İZMİR KÂTİP ÇELEBİ UNIVERSITY

İZMİR Uluslararası Misafir Öğrenci Derneği
İZMİR International Guest Student Association

2. International Students SCIENCE Congress

04-05 MAY 2018
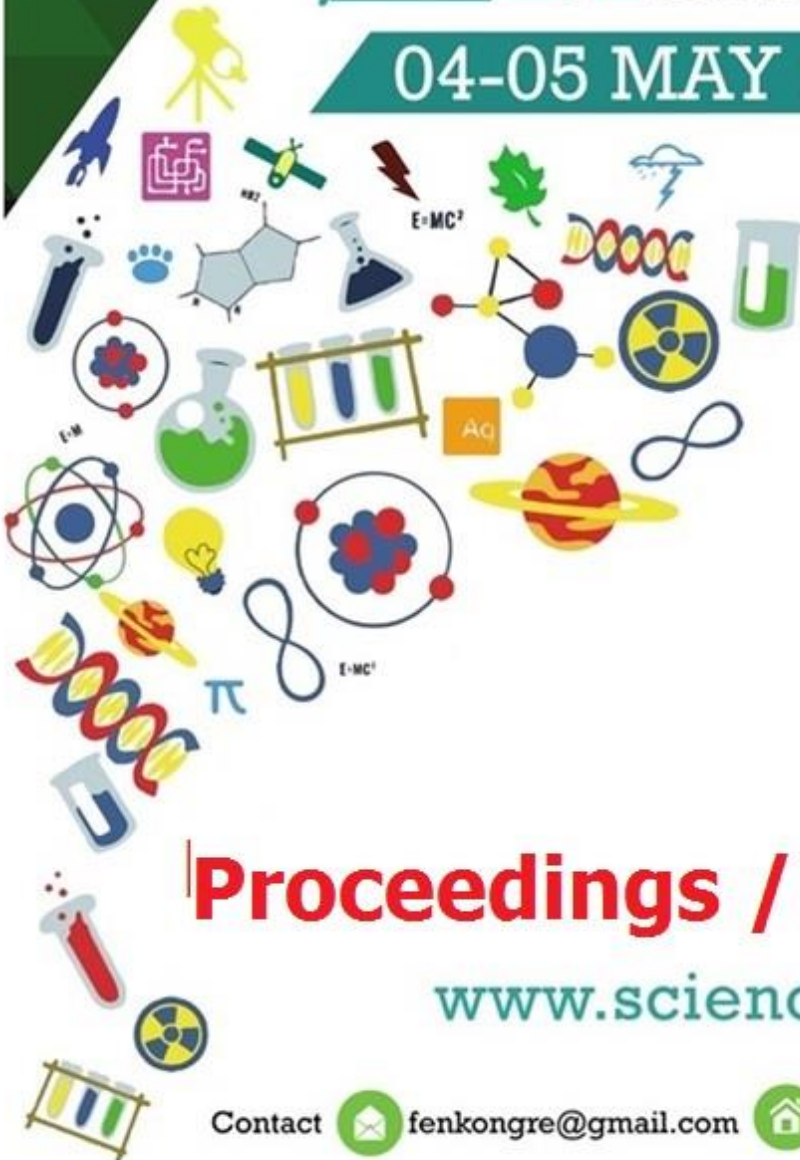
Proceedings / Bildiriler Kitabı

www.sciencecon.org

2nd International Students Science Congress Proceedings

2. Uluslararası Öğrenciler Fen Bilimleri Kongresi Bildiriler Kitabı

Editor-in-Chief / Sorumlu Editör

Mehmet Çevik

Co-editors / Yardımcı Editörler

Miftaudeen Abdul-Rahman
Ornela Lalaj
Furkan Emrem
Ahmet Aykaç

Preface

Dear Participants, Colleagues, and International Students,

It is with deep satisfaction that I write this preface to the Proceedings of the 2nd International Students Science Congress held in İzmir Kâtip Çelebi University, Turkey, May 04 - 05, 2018.

Last year's Congress that we organized for the first time in order to bring together young international researchers working in various science areas have really motivated all of us; and thus, this year we have accomplished the second congress with great enthusiasm.

The 2-day Congress had about 250 participants from more than 30 countries and 163 papers were presented in 28 sessions. In addition to the contributed papers, three intriguing invited presentations were given: by Prof. Dr. Mustafa Güden, Rector of İzmir Institute of Technology, who spoke about smart universities, by Prof. Dr. Musa Alcı of Ege University, who spoke about artificial intelligence; and by Dr. Çetin Ali Dönmez of İbni Haldun University, who spoke about cryptocurrency technologies. The audience followed these three presentations with deep interest.

The congress particularly encouraged the interaction of international research students and developing academics with the more established academic community in an informal setting to present and to discuss new and current work. Their contributions helped to make the Congress as outstanding as it has been. The Congress provided a setting for discussing recent developments in a wide variety of topics including Agricultural Engineering, Architecture, Biology and Bioengineering, Control Engineering, Chemistry and Chemical Engineering, Civil Engineering, Computer Science and Engineering, Electrical, Electronics and Communication Engineering, Geomatics Engineering, Food Engineering, Geology Engineering, Mechanical Engineering, Mathematics, Materials Science, Metallurgical and Materials Engineering, Nanotechnology, Renewable Energy, Textile Engineering, Urban and Regional Planning.

We would like to thank all participants for their contributions to the Congress program and for their contributions to these Abstract Proceedings. It is our pleasant duty to acknowledge the financial support from İzmir Kâtip Çelebi University, Federation of International Student Associations (UDEF) and İzmir International Guest Student Association.

I would like to express my sincere gratitude and appreciation to our organizing committee and all the students who worked voluntarily during the event.

The continuing success of this congress series means that planning can now proceed with confidence for the 3rd International Students Science Congress to be held in 2019.

The abstracts of all the presentations presented at the congress are published electronically as the "Abstract Book". This book can be accessed from our congress website. On the other hand, some of the authors wanted to extend their abstracts to full papers and we publish them here in electronic form again. We thank all authors, participants, and volunteers for their contributions.

Mehmet Çevik
Congress Chair

Önsöz

Değerli Katılımcılar, Meslektaşlarım ve Uluslararası Öğrenciler,

04 - 05 Mayıs 2018 tarihlerinde İzmir Kâtip Çelebi Üniversitesi'nde gerçekleştirmiş olduğumuz 2. Uluslararası Öğrenciler Bilim Kongresi Bildiriler Kitabı'na bu satırları yazmanın derin memnuniyeti içindeyim.

Geçtiğimiz yıl fen bilimleri alanlarında çalışan uluslararası genç araştırmacıları bir araya getirmek için ilk kez düzenlediğimiz kongre hepimizi gerçekten motive etti ve bu yıl ikincisini büyük bir hevesle gerçekleştirdik.

İki gün süren kongremizde 30'dan fazla ülkeden yaklaşık 250 katılımcı, 28 oturumda 163 tane bildiri sundu. Bildirilere ek olarak üç davetli konuşmacımız tarafından gerçekten ilgi çekici sunumlar yapıldı: İzmir Yüksek Teknoloji Enstitüsü Rektörü Prof. Dr. Mustafa Güden Akıllı Üniversiteler 'den bahsetti; Ege Üniversitesi'nden Prof. Dr. Musa Alcı Yapay Zeka'dan bahsetti ve İbni Haldun Üniversitesi'nden Dr. Çetin Ali Dönmez Kripto Para Teknolojileri başlıklı bir sunum gerçekleştirdi. Bu üç sunum da izleyiciler tarafından büyük ilgiyle takip edildi.

Kongre, özellikle fen bilimleri alanında eğitimlerine devam eden uluslararası öğrencilerin ve genç akademisyenlerin önlerindeki akademik camia ile etkileşimlerini gayet samimi bir ortam sunarak teşvik ederken, yeni ve güncel çalışmalarını sunmaları ve tartışmaları için de güzel bir fırsat sağlamış oldu. Onların katkıları sayesinde Kongre olabildiğince seçkin ve nitelikli bir düzeye ulaşmış oldu. Kongre, Ziraat Mühendisliği, Mimarlık, Biyoloji ve Biyomühendislik, Kontrol Mühendisliği, Kimya ve Kimya Mühendisliği, İnşaat Mühendisliği, Bilgisayar Bilimi ve Mühendisliği, Elektrik, Elektronik ve Haberleşme Mühendisliği, Harita Mühendisliği, Gıda Mühendisliği, Jeoloji Mühendisliği, Makine Mühendisliği, Matematik, Malzeme Bilimi, Metalurji ve Malzeme Mühendisliği, Nanoteknoloji, Yenilenebilir Enerji, Tekstil Mühendisliği, Kentsel ve Bölgesel Planlama, vb. çok çeşitli konulardaki son gelişmeleri tartışmak için keyifli bir ortam sağladı.

Tüm katılımcılara Kongre programına ve dolayısıyla bildiri özetleri kitabımıza yaptıkları katkılardan dolayı teşekkür ederiz. Ayrıca verdikleri maddi destek ile bu kongrenin gerçekleşmesini sağlayan İzmir Kâtip Çelebi Üniversitesi'ne, Uluslararası Öğrenci Dernekleri Federasyonu'na (UDEF) ve İzmir Uluslararası Misafir Öğrenci Derneği'ne teşekkürlerimizi arz ederiz.

Organizasyon komitemize ve etkinlikte gönüllü olarak çalışan tüm öğrencilerimize içten teşekkürlerimi ve minnettarlığımı ifade etmek isterim.

Bu kongre dizisinin başarı ile devam etmesi, 2019'da düzenlemeyi düşündüğümüz 3. Uluslararası Öğrenciler Fen Bilim Kongresi'nin organizasyonu için bize güven veriyor.

Kongremizde sunulan tüm bildirilerin özetleri "Bildiri Özetleri Kitabı"mızda elektronik kitap olarak basıldı. Bu kitaba kongre web sayfamızdan ulaşılabilir. Ayrıca, dileyen yazarlarımız bildirilerini tam metine dönüştürdüler, onları da yine elektronik ortamda burada yayınlıyoruz. Katkıları için tüm yazarlara, katılımcılara ve gönüllülere teşekkür ederiz.

Mehmet Çevik
Kongre Başkanı

vi

Organizing Committee / Düzenleme Kurulu

Mehmet Çevik

Ahmet Aykaç

Fethullah Güneş

Abdirahman Ahmed Omar

Furkan Emrem

Hichem Moulahoum

Miftaudeen Abdul Rahman

Ornela Lalaj

Shadman Sadıq

Scientific Committee / Bilim Kurulu

Prof. Dr. Abdelraouf A. Elmanama, Islamic University-Gaza
Prof. Dr. Ahmed Hussein Kamel Ahmed Elshafie, University of Malaya, Malaysia
Prof. Dr. Ahmet Türk, Manisa Celal Bayar University, Turkey
Prof. Dr. Akeel H. Ali Al-Assie, Tikrit University, Iraq
Prof. Dr. Ali Çelik, Manisa Celal Bayar University, Turkey
Prof. Dr. Amin Solaiman Badawy, University of Tikrit, Iraq
Prof. Dr. Antonio Vargas-Berenguel, Universidad de Almería, Spain
Prof. Dr. Aydın Akan, İzmir Katip Çelebi University, Turkey
Prof. Dr. Aydoğan Savran, Ege University, Turkey
Prof. Dr. Buket Okutan Baba, İzmir Katip Çelebi University, Turkey
Prof. Dr. Enver Atik, Manisa Celal Bayar University, Turkey
Prof. Dr. Erdal Çelik, Dokuz Eylül University, Turkey
Prof. Dr. Md. Ashraful Hoque, Islamic University of Technology, Bangladesh
Prof. Dr. Mehmet Ali Yurdusev, Manisa Celal Bayar University, Turkey
Prof. Dr. Mehmet Sezer, Manisa Celal Bayar University, Turkey
Prof. Dr. Musa Alcı, Ege University, Turkey
Prof. Dr. Nazar Mohammad Halim, Kabul University, Afghanistan
Prof. Dr. Nihat Sami Çetin, İzmir Katip Çelebi University, Turkey
Prof. Dr. Nilgül Çetin, İzmir Katip Çelebi University, Turkey
Prof. Dr. Nurcan Baykuş Savaşaneril, Dokuz Eylül University, Turkey
Prof. Dr. Ramazan Karakuzu, Dokuz Eylül University, Turkey
Prof. Dr. Sahib Jumaa Abdurrahman, Tikrit University, Iraq
Prof. Dr. Şerafettin Demiç, İzmir Katip Çelebi University, Turkey
Prof. Dr. Roberta Katlen Fusco Marra, Universidade Salgado de Oliveira, Brazil
Assoc. Prof. Dr. Ali Konuralp, Manisa Celal Bayar University, Turkey
Assoc. Prof. Dr. Ayşegül Alaybeyoğlu, İzmir Katip Çelebi University, Turkey
Assoc. Prof. Dr. Erkan Doğan, Manisa Celal Bayar University, Turkey
Assoc. Prof. Dr. Fatih Erdoğan Sevilgen, Gebze Technical University, Turkey
Assoc. Prof. Dr. Fethullah Güneş, İzmir Katip Çelebi University, Turkey
Assoc. Prof. Dr. Femin Yalçın, İzmir Katip Çelebi University, Turkey
Assoc. Prof. Dr. Gültekin Sınır, Manisa Celal Bayar University, Turkey
Assoc. Prof. Dr. Hubert Chapuis, Université de Lorraine, France
Assoc. Prof. Dr. Levent Çetin, İzmir Katip Çelebi University, Turkey
Assoc. Prof. Dr. Mehmet Çevik, İzmir Katip Çelebi University, Turkey
Assoc. Prof. Dr. Mehmet Ertuğrul Solmaz, İzmir Katip Çelebi University, Turkey
Assoc. Prof. Dr. Merih Palandöken, İzmir Katip Çelebi University, Turkey
Assoc. Prof. Dr. Mücahit Sütçü, İzmir Katip Çelebi University, Turkey
Assoc. Prof. Dr. Muhammad Mukhlisin, Politeknik Negeri Semarang, Indonesia
Assoc. Prof. Dr. Mustafa Can, İzmir Katip Çelebi University, Turkey
Assoc. Prof. Dr. Neritan Shkodrani, Polytechnic University of Tirana, Albania
Assoc. Prof. Dr. Ümit İşci, Gebze Technical University, Turkey

Assist. Prof. Dr. Abdulfetah Shobole, İstanbul Sabahattin Zaim University, Turkey
Assist. Prof. Dr. Adil Ali Haydir Hassan, University of Kirkuk, Iraq
Assist. Prof. Dr. Ahmet Aykaç, İzmir Katip Çelebi University, Turkey
Assist. Prof. Dr. Ali Yurddaş, Manisa Celal Bayar University, Turkey
Assist. Prof. Dr. Ali Ettehadi, İzmir Katip Çelebi University, Turkey
Assist. Prof. Dr. Aytunga Bağdatlı, Manisa Celal Bayar University, Turkey
Assist. Prof. Dr. Ceyhun Araz, Manisa Celal Bayar University, Turkey
Assist. Prof. Dr. Fabienne Dumoulin, Gebze Technical University, Turkey
Assist. Prof. Dr. İlker Polatoğlu, Manisa Celal Bayar University, Turkey
Assist. Prof. Dr. Levent Aydın, İzmir Katip Çelebi University, Turkey
Assist. Prof. Dr. M. Bahattin Akgül, Manisa Celal Bayar University, Turkey
Assist. Prof. Dr. Mohammed Wadi, İstanbul Sabahattin Zaim University, Turkey
Assist. Prof. Dr. Muhammad Imran Shakir, King Saud University, Saudi Arabia
Assist. Prof. Dr. Muhammad Shahid, The Islamia University of Bahawalpur, Pakistan
Assist. Prof. Dr. Mustafa Erol, Dokuz Eylul University, Turkey
Assist. Prof. Dr. Mustafa Erkan Turan, Manisa Celal Bayar University, Turkey
Assist. Prof. Dr. Nesrin Horzum Polat, İzmir Katip Çelebi University, Turkey
Assist. Prof. Dr. Nihad A. Jafar, Tikrit University, Iraq
Assist. Prof. Dr. Onur Ertuğrul, İzmir Katip Çelebi University, Turkey
Assist. Prof. Dr. Ozan Karaman, İzmir Katip Çelebi University, Turkey
Assist. Prof. Dr. Ömer Öztürkoğlu, Yaşar University, Turkey
Assist. Prof. Dr. Özgün Yücel, İzmir Katip Çelebi University, Turkey
Assist. Prof. Dr. Özlem Çağındı, Manisa Celal Bayar University, Turkey
Assist. Prof. Dr. Saim Kural, Manisa Celal Bayar University, Turkey
Assist. Prof. Dr. Sedat Yalçinkaya, İzmir Katip Çelebi University, Turkey
Assist. Prof. Dr. Sercan Acarer, İzmir Katip Çelebi University, Turkey
Assist. Prof. Dr. Süleyman Murat Bağdatlı, Manisa Celal Bayar University, Turkey
Assist. Prof. Dr. Utku Kürşat Ercan, İzmir Katip Çelebi University, Turkey
Assist. Prof. Dr. Violeta Rodriguez-Ruiz, The University of Cergy-Pontoise, France
Assist. Prof. Dr. Walid Sharmoukh Ahmed Moustafa, National Research Centre, Egypt
Assist. Prof. Dr. Yiğit Aksoy, Manisa Celal Bayar University, Turkey
Assist. Prof. Dr. Z. Haktan Karadeniz, İzmir Katip Çelebi University, Turkey
Dr. Ayşe Kurt Bahşı, Manisa, Turkey
Dr. Juan Manuel Casas-Solvas, University of Almeria, Spain
Dr. Manuel Cristo Martos-Maldonado, Universidad Politecnica de Madrid, Spain
Dr. Sivarama Krishna Lakkaboyana, Universiti Teknologi Malaysia, Malaysia
Dr. Zoltán Fülöp, Budapest, Hungary

Invited Speakers / Davetli Konuşmacılar

Smart Universities

Prof. Dr. Mustafa GÜDEN, Izmir Institute of Technology

Artificial Intelligence

Prof. Dr. Musa Alcı, Ege University

Cryptocurrency Technologies

Assist. Prof. Çetin Ali DÖNMEZ, Ibn Haldun University

Table of Contents

Nijer'in Balla İlçesi Tarım Havzasında Marul Üretimi Üzerine Yarasa Gübresi Uygulamalarının Etkileri

Moustapha Maman Mounirou*, Ankara Üniversitesi, Ziraat Fakültesi, Toprak Bilimi ve Bitki Besleme Bölümü, Dışkapı, Ankara, Türkiye
Karimou Ambouta Harouna, Polytechnique Üniversitesi, Ziraat Fakültesi, Toprak Bölümü, Bobo-Dioulasso 01, Burkina Faso
Adamou Didier Tidjani, Abdou Moumouni Üniversitesi, Ziraat Fakültesi, Toprak Bölümü, Niamey, Nijer
*İletişimden sorumlu yazar: mmaman@ankara.edu.tr

Özet

Araştırma, doğal arazi koşullarında 2012 yılında Balla ilçesi tarım havzası (Gouré bölgesi) deneme alanında yürütülmüştür. Deneme tesadüf blokları deneme desenine göre 3 tekerrürlü olarak kurulmuş ve bitki materyali olarak marul bitkisinin (*Lactuca sativa* L.) Maya çeşidi kullanılmıştır. Yarasa gübresinin (guano), toprakların bazı fiziksel ve kimyasal özellikleri ve marul bitkisinin verim parametreleri üzerine olan etkileri, kimyasal gübre ve ahır gübresinin etkileri ile karşılaştırılarak incelenmiştir. Toprağın ve bitkinin bazı özelliklerine (baş boyu, baş çapı, yaprak boyu ve eni, toplam verim) guano uygulamasının etkileri belirlenmiş ve uygulamaların varyans analizi Genstat 14 paket programıyla yapılmıştır.

Anahtar Kelimeler: gübreleme, yarasa gübresi, marul, Nijer Balla ilçesi
Disiplin: Ziraat Mühendisliği

GİRİŞ

Nijer Batı Afrika'da yer alan geniş bir ülkedir. Yüzölçümü 1.267.000 km^2'dir. Nijer'in nüfusu 19.865.068'e ulaşmıştır. Nüfusun %52.1'ini kadınlar, %47.9'unu ise erkekler oluşturmaktadır [1]. Nijer Cumhuriyeti, Batı Afrika'nın yüzölçümü bakımından en büyük devletidir. Güneyde Nijerya ile Benin, batıda Burkina Faso ile Mali, kuzeyde Libya ile Cezayir, doğuda Çad ile sınırları bulunmaktadır. Nijer'de 4 farklı iklim bulunmaktadır. Çöl (sahra) iklimi, karasal (sahel) iklim, sahra-sahel iklimi ve tropikal (sahel-sudan ve sudan) iklim görülmektedir.

Nijer nüfusunun %80'den fazlası tarım, hayvancılık, ormancılık ve balıkçılık ile geçimini sağlamaktadır. Geniş yüzölçümüne sahip olmasına rağmen tarıma elverişli araziler oldukça azdır. Topraklarının büyük bir kısmı çöl olmasına karşın ekonomisinde 1. sırayı yine tarım almaktadır. Tarıma elverişli alanların çoğu Nijer Irmağı kıyısındadır. Nijer hem kurak hem de tropikal iklime sahiptir. Nijer'in temel su kaynağı Nijer Nehri ve özellikle Çad Gölü olmak üzere birkaç gölden ibarettir. Tarım alanlarının çoğunda sulama yapılmamaktadır ve Nijer Nehri suları ile sulama yapılan alanlar toplam tarım alanlarının sadece %2'sini oluşturmaktadır (FAO, 2004) [2].

Topraklar da çok farklı fiziksel, kimyasal ve biyolojik özelliklere sahiptir. Toprakların organik madde içeriklerini artırmak amacıyla çok farklı organik kökenli materyaller kullanılmaktadır. Bu çalışmada hem toprak iyileştirici hem de organik gübre olarak yarasa gübresi tarım havzasında kullanılmıştır. Yarasa gübresi (guano), mağaralarda yaşayan yarasalardan elde edilen bir gübredir. Dünyada tarımsal kullanımı yaygın olan yarasa gübresinin topraklara uygulanmasıyla bitkilerde verim artışı bilinmektedir. Yarasa gübresi doğal bir gübre olarak toprakta ve bitkiler üzerindeki bazı faydaları sağlamaktadır: Toprağın su tutma kapasitesini artar. Organik madde oranı yüksektir. Verim ve ürün kalitesini yükseltmeye yardımcı olur. Toprakta pH'ı dengeler ve asidik topraklarda alüminyumu emerek bitkinin zehirlenmesini önler (Karagöz, 2014) [3]. Toprağı makro ve mikro besin elementleri yönünden zenginleştirir (Anonim 2014c) [4]. Yarasa gübresi 2002 yılında organik gübre olarak Balla havzası kullanılmaya başlamıştır. Ancak yarasa gübresiyle ilgili herhangi bir bilimsel çalışma yapılmamıştır. Bu nedenle marul bitkisinin gelişimine yarasa gübresi uygulamalarının etkisini saptamak amacıyla bu araştırma gerçekleştirilmiştir. Daha iyi üretim için bitki gelişimi ve verime guano uygulamasının uygun miktarının belirlenmesi amaçlanmıştır.

MATERYAL VE YÖNTEM

Deneme tesadüf blokları deneme desenine göre 3 tekerrürlü olarak kurulmuş ve bitki materyali olarak marul bitkisinin (Lactuca sativa L.) Maya çeşidi kullanılmıştır. Denemede, farklı kimyasal ve organik gübreler kullanılmış olup deneme konuları aşağıdaki gibidir:

1) Kontrol (T)
2) Kimyasal gübre K.G 15-15-15 gübresi NPK (200 kg ha^{-1}) üre (50 kg ha^{-1})
3) Ahır gübresi A.G (25 t ha^{-1})
4) Düşük doz yarasa gübresi G1 (3.5 t ha^{-1})
5) Orta doz yarasa gübresi G2 (6.5 t ha^{-1})
6) Yüksek doz yarasa gübresi G3 (10 t ha^{-1})
7) G1+K.G
8) G2+K.G
9) G3+K.G
10) A.G+K.G
11) G1+A.G
12) G2+A.G
13) G3+A.G
14) G1+A.G+K.G
15) G2+A.G+K.G
16) G3+A.G+K.G olacak şekilde uygulama yapılmıştır.

Kullanılmış olan yarasa gübresi Şekil 1'de görülmektedir.

Şekil 1. Yarasa gübresi

Bitkinin bazı özelliklerine (baş çapı, yaprak boyu ve eni, toplam verim) guano uygulamasının etkileri belirlenmiştir.

Baş çapı: Parselden hasat edilen bitkide başların ölçülüp ortalaması alınmak suretiyle belirlenmiştir.

Yaprak boyu ve eni: Yaprak boyu ve eni milimetrik cetvel yardımıyla ölçülerek cm cinsinden tespit edilmiştir.

Toplam verim: Her uygulamada kenar tesirleri de dikkate alınarak her parselin orta kısmından hasat edilen bitkinin ağırlığı hassas terazide tartılarak elde edilmiştir.

BULGULAR VE TARTIŞMA

Deneme kullanılan toprak aynı yerden alınmış olup 0-20 cm derinliğe kadar ve yarasa gübresi bazı fiziksel ve kimyasal özelliklerinin analizleri yapılmıştır. Abdou Moumouni Üniversitesi Ziraat Fakültesi Toprak Bilimi Bölümü laboratuvarda analizleri edilmiştir.

Tablo 1'de görüldüğü gibi, Nijer'de tarım yapılan sulu toprakların tekstürünü %36.32 kum, %40.02 silt, %23.66 kil oluşturmaktadır. Balla ilçesi sulu tarım topraklarında katyon değişim kapasitesinin (KDK) 25.05 meq 100 g^{-1} olduğu görülmektedir. Toprakların toplam azot (%0.2) ve magnezyum (1186 mg kg^{-1}) içerikleri bakımından fazla düzeyde olduğu belirlenmiştir. Toplam fosfor ise (546 mg kg^{-1}) düzeyde olduğu tespit edilmiştir. Toprakların değişebilir K (10.4 mg kg^{-1}) yüksek düzeydedir. Balla

ilçesi tarım havzası topraklarının potasyum bakımından çok zengin olduğu tespit edilmiştir. Jeolojik yapısı, iklim durumu, özellikle de sıcak ve kurak iklim koşulları nedeniyle topraklarının yarayışlı potasyum kapsamları zengindir.

Tablo 1. Denemede kullanılan tarım topraklarının bazı fiziksel ve kimyasal özellikleri

İçerik	Miktar	İçerik	Miktar
Kum (S) , %	36.32	Karbon, %	3.9
Silt (Si), %	40.02	Toplam N, %	0.2
Kil (C), %	23.66	Toplam P, mg kg^{-1}	546
Tekstür sınıfı	Tın	K, mg kg^{-1}	10,4
Katyon değişim kapasitesi (KDK), meq 100g^{-1}	25.5	Mg, mg kg^{-1}	1186

Denemede Kullanılan Gübrelerinin Bazı Fiziksel ve Kimyasal Özellikleri

Tarla denemesinde kullanılan organik gübrelere ait bazı fiziksel ve kimyasal özellikler Tablo 2' de verilmiştir.

Tablo 2. Yarasa gübresi ve ahır gübresinin bazı fizikokimyasal özellikleri

Özellik	pH	EC mS cm^{-1}	N %	P mg kg^{-1}	K mg kg^{-1}	C %	OM %	C/N
Yarasa gübresi	9.12	2.38	9.8	5090	6571	47	80	5
Ahır gübresi	8.02	0.44	1.1	2531	3491	29	50	26

Bu çalışmada değişik organik kökenli materyallerin (yarasa gübresi ve ahır gübre) kimyasal (N, P, K, pH, EC, C, C/N, organik Madde) analizleri yapılarak, elde edilen veriler değerlendirilmiştir. Analiz sonuçlarına göre örneklerin pH değerleri 8.2-9.12 arasında değişmektedir. En düşük pH ahır gübresi, en yüksek pH ise yarasada belirlenmiştir. Çalışmada materyal olarak seçilen organik gübrelerin tuz içerikleri 0.44-2.38 mS cm^{-1} arasında değişmektedir. Ahır gübresi orta tuzlu, yarasada ise çok tuzlu olarak belirlenmiştir. Organik madde içerikleri %50-80 arasında değişmektedir. En yüksek organik madde içeriği yarasa gübresinde, en düşük organik madde içeriği ahır gübresinde belirlenmiştir. Gübrelerin azot içerikleri %1.1-8.9 arasında değişmektedir. En düşük değer ahır gübresinde, en yüksek yarasa (%9.8) gübresinde tespit edilmiştir. Genel olarak incelendiğinde yarasa gübresinin N, P, K, pH, EC, C ve organik madde içeriklerinin ahır gübresine göre daha yüksek olduğu tespit edilmiştir (Tablo 2). Bunların sebebi, hayvanların beslenme şekilleri ve fizyolojileri olarak yorumlanabilir.

Toplam Verim

Kimyasal ve organik gübre uygulamalarının marul bitkisi toplam verim özelliklerine üzerine etkileri Şekil 2'de verilmiştir.

Tüm organik gübre uygulamalarıyla bitkinin toplam verim özellikleri kontrole göre önemli düzeyde artış göstermiştir. En yüksek toplam verim düşük doz guano (G1) ve ahır gübresinin birlikte uygulandığı bitkilerde görülmüştür (Şekil 2).
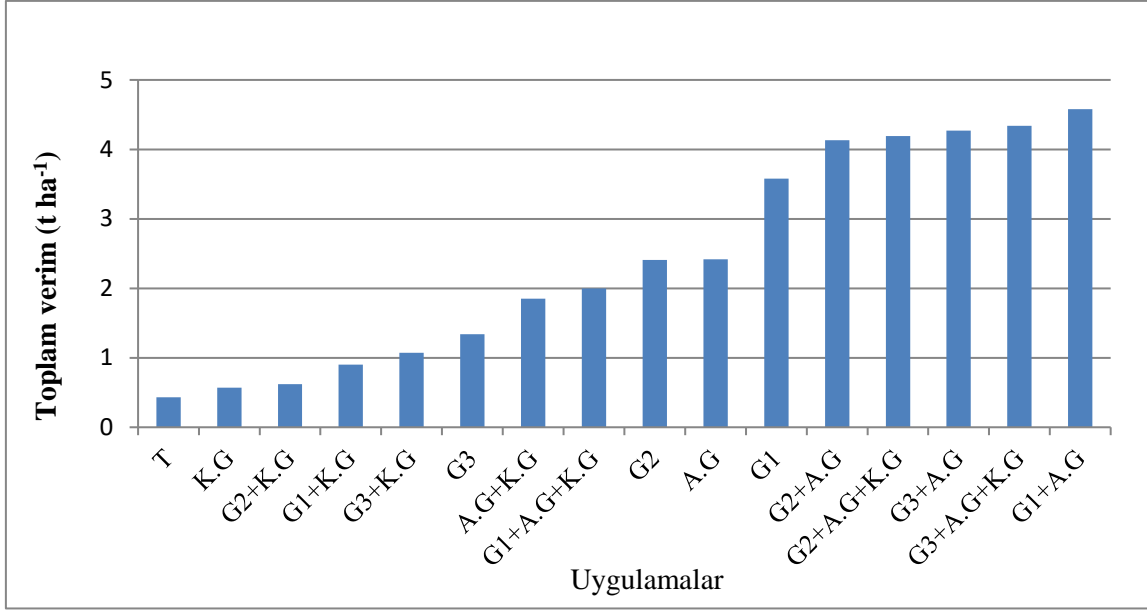
Şekil 2. Balla İlçesi deneme alanında kimyasal ve organik gübre uygulamalarının marul bitkisi toplam verimine etkileri

SONUÇ

Yarasa gübresinin düşük doz uygulamasının toplam verime (3.58 t ha-1) etkisi, ahır gübresine göre (2.42 t ha-1) daha fazla olmuştur. Benzer şekilde guanonun toplam verime etkisi kimyasal gübre (0.57 t ha-1) etkisine göre 6 kat daha fazla bulunmuştur.

Hayvanların beslenme şekilleri ve fizyolojilerinin farklı olması nedeniyle gübrelerin fizikokimyasal özelliklerinin farklılık gösterdiği ve bunun da bitki gelişimine farklı şekilde etki ettiği görülmüştür.

REFERANSLAR

[1] INS, Institut National de la Statistique du Niger, Tableau de Bord Social. http://www.stat-niger.org/statistique/file/DSEDS/TBS_2016.pdf, 2016 (03 Nisan 2017'de ulaşılmıştır).

[2] Mission FAO/PAM d'évaluation des récoltes et des disponibilités alimentaires au Nijer. Organisation des Nations Unies pour l'alimentation et l'agriculture et Programme Alimentaire Mondial. Rome. ftp://ftp.fao.org/docrep/fao/007/j3969f/j3969f00.pdf), 2004 (04 Mart 2013'de ulaşılmıştır).

[3] K. Karagöz, Yarasa gübresinin tarımda kullanılma olanakları, Alınteri Zirai Bilimler Dergisi 27 (2015) 35-42.

[4] Anonim, Yarasa Gübresinin Faydaları, https://www.gubreler.com/bilgiler_yarasa-gubresi-ve-faydalari_70.htm (12 Şubat 2017'de ulaşılmıştır).

Water Resources, Use and Irrigation Systems in Niger

Abdoul Nasser Aboubacar Dan Badaou*, Üstün Şahin, Fatih Mehmet Kızıloğlu
Ataturk University, Faculty of Agriculture, Department of Agricultural Structures and Irrigation, Erzurum-Turkey
*Corresponding author: danbadaouabdoulnasser@yahoo.fr

Abstract

Niger is a landlocked country in West Africa covering 126.7 Mha. Yearly total evaporation varies between 1700-2100 mm. The area of cultivated land approximately covers 15 Mha and irrigable land potential is estimated at 0.27 Mha. Agricultural and livestock sectors are the main source of economic activity in the country and employ 83% of the active population.

This study aims to present Niger's available water resources, the sectors of use as well as the various irrigation systems practiced. Given our limited resources, we have used extensively the databases of the services of the Ministry of Hydraulics, ECOWAS and especially FAO which are very active bodies of the field in Niger. Our research also led us to visit some sites, to carry out surveys and evaluations of existing irrigation systems. Our data was essentially collected and processed using SPHINX 5.0 PLUS software.

Keywords: Niger, irrigation, drainage, water resources, water use
Discipline: Agricultural Engineering

I.   INTRODUCTION

There are two major river basins in Niger: the Eastern Niger Basin and The Niger Basin. Niger's hydrological network includes over 1000 ponds of which about 175 are permanent. Niger has a total area of 4317589 ha of wetlands of international importance in 2013. Total renewable water resources are estimated to be 33,650 km3/year but the vast majority coming from inward flows (more than 30 km3/year). Much of the surface water, however, leaves the country (32.4 km3/year) to Nigeria. So the dependency index is very high (89.6%). Niger currently has about 10 dams with a total capacity about 76 million m3. The main international rivers are the Niger River, Lake Chad, Komadougou Yobe, Goulbi Maradi and the Iullemeden aquifer system. The hydraulic potential of Niger remains weakly mobilized. In fact, less than 3% of total renewable resources are exploited in 2005.

The volume of surface water collected for livestock was estimated at 0.045 km3 in 2005 [1], total water withdrawals for agriculture was estimated at 0.66 km3 in 2005 [2] and the main industries annual water is estimated at 0.033 km3 in 2005 [3].

The source of irrigation water was groundwater for a large majority of the farms practicing irrigation from wells and catch basins for 64% and boreholes for 5% of them, surface water for 18%, drinking water supply for 1% and the remaining (17%) escaping from the hydrographic system. Irrigation techniques used on irrigated farms are mainly dominated by manual surface irrigation (74%) and surface irrigation (21.4%) with moto-pomp. Pressurized techniques are almost non-existent (2.3%) use sprinkling and 0.5% drops only in small irrigation and the rest (1.8%) using uncontrolled submersion. The drainage system of irrigation water in excess, is carried out gravitarily for the most part through drains or open-air colaces. Although drainage requirement is high in the country, the drainage systems are not sufficient.

Niger is a landlocked country (see Figure 1) in West Africa covering an area of 126.7 Mha. ¾ of the country is located in the desert zone (the north) while the rest is in the Sahelo-Sudan zone. The area of cultivated land covers 15 Mha in 2011 [2].

Figure 1. Map of Niger and the neighboring countries

Niger's climate is continental Sahelian type, characterized by two seasons: a short rainy season (June to September), and a long dry season (October to May) and annual rainfall is characterized by significant spatio-temporal and interannual variability. These phenomena increase the risks of drought and desertification that have consequences on agro-sylvo pastoral productions. Thus, according to this rainfall, four climatic zones, shown in Figure 2, can be distinguished from North to South:

- The Saharian: about 65% of the territory, with a desert climate and less than 100 mm of rainfall;
- The Sahelo-Saharian (12.2% of the territory): receiving between 100-300 mm of rainfall and with a sub-desert climate;
- The Sahelo-Sudanian (21.9% of the territory): receiving between 300-600 mm;
- The Sudanian (0.9% of the territory): receiving more then 600 mm/year and is covered with savannah vegetation.
- Yearly total evaporation is too high, varies between 1700-2100 mm therefore the water deficit is important.
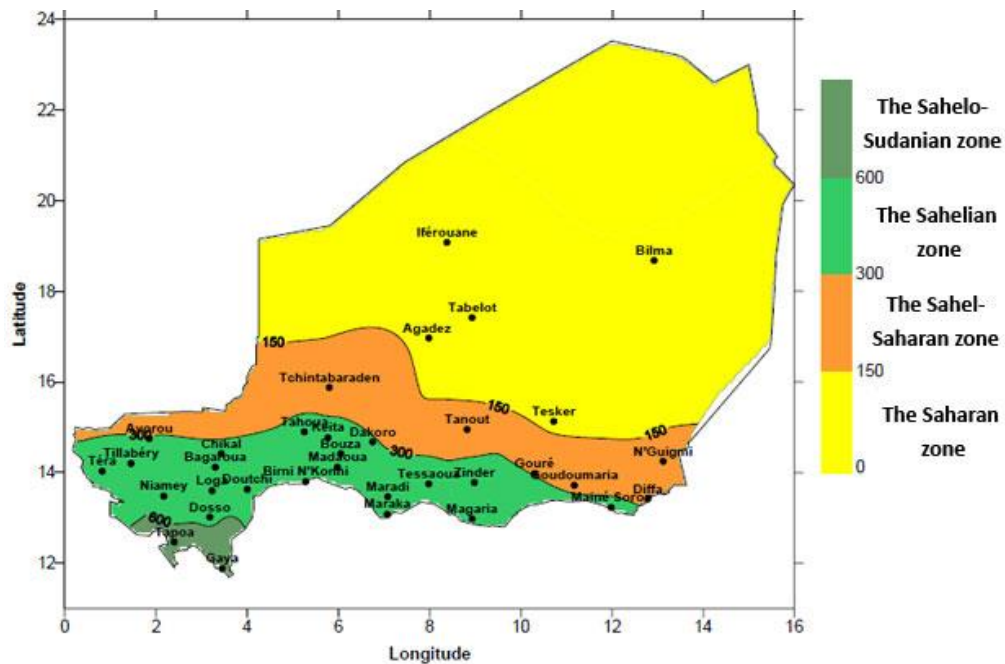
Figure 2. Niger and its climatic zones

6

Rainfed agriculture is the main source of food needs for the population, as well as the main activity in rural areas (83% of the active population). Rice production produced on irrigation schemes contributes about 1% of the population's food. Nevertheless agriculture remains extensive with low agronomic performance due to frequent droughts and a gradual decline in soil fertility. The main food crops are millet and sorghum and main cash crops are cowpeas, groundnuts and cotton [4].

II. WATER RESOURCES

There are two major river basins in Niger:
- The Eastern Niger Basin which includes: Komadougou Yobe, the Korama and Lake Chad.
- The Niger Niger Basin including the Niger River and its tributaries, the valleys of the western side of the Aïr (Telwa), the valleys and koris of Ader-Doutchi (Keita Valley, Badaguichiri, Maggia), Dallols (Bosso, Maouri and Foga) and Goulbi (N'Maradi, Kaba, Kebi and Mai Farou).

Niger has a total area of 4,317,589 ha of wetlands of international importance in 2013. In addition, the hydrological network includes over 1,000 ponds of which about 175 are permanent and generally connected to underground aquifers, such as the Tabalack and Madarounfa ponds [5]. Surface renewable water resources are estimated at more than 31 km3/year, of which only a very small portion is produced within the country (1 km3/year): the vast majority coming from inward flows from Mali (28 km3/year) and a lesser extent from Burkina Faso (1 km3/year) and Nigeria (0.2 km3/year), as well as from the border flow (1.15 km3/year). The dependency index is thus very high (89.6%). Internal groundwater resources are estimated at 2.5 km3/year. The country's internal renewable resources are estimated at 3.5 km3/year while the total renewable water resources amount to 33.65 km3/year. Much of the surface water, however, leaves the country (32.4 km3/year) to Nigeria. Non-renewable groundwater (fossils) is estimated at 2000 km3/year, a small proportion of which is exploited by mining companies. Most of the surface runoff comes from the Niger River (90%) and its tributaries from the right bank. In the Lake Chad basin, the water resources consist of Lake Chad and Komadougou Yobe. Niger currently has about 10 dams with a total capacity about 76 million m3. The Kandadji Dam, under construction on the Niger River in the Tillaberi region, will be the largest dam in the country (1.6 billion m3).

III. USE OF WATER

The hydraulic potential of Niger remains weakly mobilized. In fact, less than 3% of total renewable resources are exploited in 2005. The country has 55 drinking water production centers producing 0.062 km3 and 57 distribution centers for a distributed water volume of 0.052 km3. No volume is measured for rural water supply, but an estimate of total harvest for communities in 2005 is 0.294 km3 [3]. The volume of surface water collected for breeding from the Niger River and its tributaries was estimated at 0.045 km3 in 2005 [1]; however, this represents only a small portion of the Nigerian herd. Most of it is drinking from groundwater and other sources of surface water. In the same way, the volume of surface water collected for irrigated agriculture from the Niger River and its tributaries was estimated at 0.454 km3 in 2005 [1]. But, irrigated agriculture also uses groundwater and other surface water sources (Maggia and Komadougou). Total water withdrawals for agriculture were estimated at 0.66 km3 in 2005 [2]. The annual water requirements of the main industries provided by the water and sanitation sector benchmark in Niger [6] (MHE, 1997) are estimated at 0.022 km3 in 1999 and 0.033 km3 in 2005 [3].

IV. IRRIGATION AND DRAINAGE; EVOLUTION OF IRRIGATION DEVELOPMENT

Three factors contributed to the rapid development of irrigation: successive droughts from 1972 to 1973 and from 1983 to 1984; high yields obtained rapidly in irrigated rice and vegetable crops and the commitment of the State, farmers' organizations and several donors. The construction of the first hydro-agricultural developments in Niger dates from the colonial period with the site of Koutoukalé in 1934 and Say in 1945 [7]. Since independence, the State is interested in irrigation perimeters by managing and developing them. Since then, more than 51 perimeters were built between 1964 and 1994 [8] and most of which were intended for rice growing (Niamey area) and the others for polyculture (Tahoua region). While these hydro-agricultural developments covered less than 6000 ha in the late 1970s, the 66 perimeters with total water control covered 13744 ha at the end of 2011. They are managed by cooperatives with the support of the National Office of Hydro Agricultural Facilities (ONAHA). Initially it mainly used traditional irrigation techniques (manual watering), but pumping from the 1970s multiplies its potential. The totality of this small irrigation covers 86150 ha in 2010, of which a large

portion 68150 ha was initially off-season perimeters. Of these areas, 77291 ha were actually irrigated in 2010 [9]. Crops cultivated and irrigated on this small irrigation, also frequently referred as 'horticultural' crops in the country, are estimated at 80630 ha for the 2010-2011 season, to which should be added nearly a million fruit trees. Irrigation development has accelerated over the last 5 years with an average annual increase of 6.3% compared to only 3.1% over the last 10 years. The source of irrigation water was groundwater for a large majority of the farms practicing irrigation from wells and catch basins for 64% and boreholes for 5% of them, surface water for 18%, drinking water supply for 1% and the remaining (17%) escaping from the hydrographic system. Irrigation techniques used on irrigated farms are mainly dominated by manual surface irrigation (74%) and surface irrigation (21.4%) with moto-pomp. Pressurized techniques are almost non-existent (2.3%) use sprinkling and 0.5% drops only in small irrigation and the rest (1.8%) using uncontrolled submersion. The drainage system of irrigation water in excess is carried out gravitarily for the most part through drains or open-air colaces. Although drainage requirement is high in the country, the drainage systems are not sufficient [10].

REFERENCES

[1] Etat des lieux des ressources en eau et leurs usages agricoles et domestiques en Afrique de l'Ouest, Economic Community of West African States, 2010.

[2] AQUASTAT Irrigation water requirement and water withdrawal by country, United Nations Food and Agriculture Organization, 2012.

[3] AQUASTAT main database, United Nations Food and Agriculture Organization, 2013.

[4] Rapport sur l'Etat de l'environnement au Niger, Direction de l'environnement. Ministry of Hydraulics, Environment and the Fight against Desertification, Niger, 2005.

[5] Les Zones Humides Du Niger. Ministry of Hydraulics, Environment and the Fight against Desertification, 2006.

[6] Schéma Directeur de mise en valeur et de gestion des ressources en eau: le référentiel du secteur de l'eau et de l'assainissement au Niger. Ministry of Hydraulics and Environment, 1997.

[7] Stratégie Nationale de Développement de l'irrigation et de la Collecte des Eaux de Ruissellement, Ministry of Agricultural Development, 2005.

[8] Projets et programmes de développement de l'irrigation au Niger (1960-2010) : Eléments pour un bilan. Center of Studies and Information on Small Irrigation, CEIPI, 2011.

[9] Revue des Dépenses Publiques 2010 du Secteur Rural. Interministerial Steering Committee of the Rural Development Strategy, CIP-SDR, 2011.

[10] Recensement Général de l'Agriculture et du Cheptel (RAGC 2005-2007). Volume IX Résultats définitifs Horticulture, FAO Project GCP/NER//EC. Ministry of Agricultural Development, Ministry of Animal Resources, MDA-MRA, 2008.

The Effect of ACTIVIA Yogurt on the Lipid Profile and Blood Sugar

Fahad Khalaf Yaseen, Department of Pathological Analysis (Mycology), Al Door Technical Institute, Northern Technical University, Salahdeen, Iraq
Abeer Saleh Hasan, Department of Pathological Analysis (Medical Biochemistry), Al Door Technical Institute, Northern Technical University, Salahdeen, Iraq
Hanan Shihab Ahmad, Department of Pathological Analysis (Animal physiology), Al Door Technical Institute, Northern Technical University, Salahdeen, Iraq
Elsayed Zaabout, Faculty of Agriculture, Biotechnology Program, Ain Shams University, Egypt
Ali Awad Aldulaimi, School of Environmental and Natural Resource Sciences, Faculty of Science and Technology, University Kebangsaan Malaysia, 43600 Bangi, Selangor, Malaysia.
Shadmaan Tariq Sadiq*, School of Natural Sciences, Faculty of Science, Ege University, Izmir, Turkey
*Corresponding author:shadmantsm@gmail.com

Abstract

Activia Yogurt® is a yogurt prepared by bacterial fermentation of milk. What makes Activia significantly different from the rest of the dairy species is its probiotics (yeast and bacteria); this type of probiotics is able to survive in the digestive system, especially the large intestine. The objective is to know the effect of *Activia Yogurt* on the body weight and blood sugar. This study was done in the Department of Pathological Analysis/Al Door Technical Institute/Iraq for the period from November 2016 to April 2017, dosage of a group (Treatment Group) of 25 person of Activia Yogurt (200 ml) and the effect of the oral dosage of Activia on the body weight and blood sugar of the body of the treatment group and the observation of changes and results after the dosage and compared with the control group that deals with water instead of Activia. After 30-day dose (Activia Yogurt) of the treatment group, the results showed that the glucose level and body weight decreased at a significant level (P<0.05) compared to control group. Blood glucose and body weight was significantly less among treatment group than control group. A significant statistical negative correlation between (body weight, blood glucose) and Activia Yogurt dosage follow up.

Keywords: blood sugar, Calcium, gastrointestinal disease, Activia yoghurt
Discipline: Biology

INTRODUCTION

Yogurt is one of the most famous fermented dairy products in the world and consumed semi-solid and has increased its popularity and consumption in the world after the Russian scientist Metchnikoff research on the importance of milk consumption in prolonging life. It has also been widely accepted by consumers as a healthy food because it contains a range of energy-rich nutrients and fat in large quantities, making it nutrient dense food. In particular, yogurt can provide the body with large amounts of calcium in a biological form. Moreover, yogurt has many basic health benefits of nutrition, such as improved lactose tolerance, a potential role in body weight and fat loss and a variety of health attributes associated with probiotic bacteria

Activia yogurt is scientifically proven to help reduce gastrointestinal symptoms. Activia is prepared by bacterial fermentation of milk. What makes Activia significantly different from the rest of the dairy species is its probiotics (yeast and bacteria), this type of bio-enhancer is able to survive in the digestive system, especially the large intestine. Activia also contains bacteria that help digest lactose, which helps some people who are unable to digest lactose and milk products and help reduce gastrointestinal diseases. In addition to that, it has been shown that Activia contribute to weight control and exercise. This is due to the calcium metal present in the milk and its derivatives and its efficiency in maintaining a healthy weight and controlling weight gain and obesity. Yogurts that contain probiotics, such as Danone's Activia line are good for those who have digestive disorder. Probiotics can help regulate your digestive system by helping reduce bloating as well as difficult and painful defecation [1-4].

Standard yogurt is a mixture of milk whole, low-fat or skimmed and creamy textures that has been fermented by lactic acid, producing bacteria such as lactobacillus bulgaricus and Streptococcus thermophilus. Other strains of bacteria, such as acidophilus, may also be added.

Activia yogurt contains many of the same component found in Standard yogurt but Activia also contains Bifidobacterium lactis DN-173 010 (CNCM 1-2494) strain used in the Industry of Activia, which helps regulate digestion, it is also known as Bifidus Regularis, which is found only in Activia products [5,6].

The characteristic of healthy milk is due to the growth or presence of lactic acid bacteria in it. This includes protection of the body from intestinal disorders and the ease of digestion of lactose. The bacteria that initiates the conversion of a large part of lactose into lactic acid, lowering blood cholesterol, improve the immunological properties; help digest protein, absorption of calcium and iron. Calcium are more readily available in the yogurt than milk. Metchnikoff reported that the bacteria bulgaricus L. eliminates toxins from rotting bacteria in the intestines by producing acidity and Bacteriocin (Lactic acid bacteria). The most significant studies confirm that the health effects of Lactic acid bacteria and Yogurt are due to alteration of the Microbial content of the intestines, where an increase in the number of Lactic acid bacteria works to eliminate the growth of pathogenic bacteria and thus reduce the chances of infection and disease [3,7].

PATIENT AND METHOD

Experience Design: This study was done in the Department of Pathological Analysis / Al Door Technical Institute for the period from November 2016 to April 2017. In this experiment, 50 students of the technical institute / Al door, ranging in age from 23-25 years of age and weighing between 60 and 98 kg, were fed with food and natural water continuously and in sufficient quantities throughout the research period. Samples of the experiment (students) were divided into two groups each group 25 students as follows:

Control Group: 25 persons was given 200 ml of sterile water in the morning for 30 days.

Treatment Group: 25 persons was given 200 ml of Activia yogurt in the morning for 30 days.

At the end of the experiment, weight measurement was performed and blood samples were withdrawn from each student. The centrifugation process was carried out on all samples at a speed of 2500 cycles/min for 15 minutes to obtain serum, which was stored at -20°C, until it was used to estimate the criteria under study.

Statistical Analysis: The results were analyzed using the General Linear Model (SAS) method. The Duncun Test (1955) was used to determine the significance of the differences between the mean factors affecting the studied traits at the probability level ($P<0.05$).

RESULT AND DISCUSSION

Effect of oral dosage of Activia yogurt in body weight

Table 1 shows the effect of oral administration of Activia in body weight after 30 day dose of the treatment group. The results showed that the body weight decreased at a significant level ($P <0.05$) compared to the control group. The decrease in these cases may be due to the nature and concentrations of active ingredients in Activia yogurt. It contains high concentrations of lactic acid bacteria and the substances produced by vitamins and organic acids, which leads to easy digestion of food and absorption in the body [14]. While the most studies confirmed that the health effects of lactic acid bacteria and yogurt are due to the change of the microbial content of the intestines, where there is an increase in the number of bacteria lactic acid works to eliminate the growth of Pathogenic bacteria and harmful substances and fat burning and thus lead to weight reduction, lactic acid bacteria has the ability to absorb and bind fat, especially cholesterol with yellow salts, causing re-absorption into the body, and may be a mechanism to lower cholesterol and fatty substances by inhibiting the key enzymes responsible for its formation [8].

Table 1. Effect of oral dosage of Activia yogurt on body weight.

Group	Body weight before treatment	Body weight after treatment
Control Group	70±1.50 a	71±1.00 A
Treatment Group	70.1.75 a	67±1.24 B

In addition, some studies have indicated that some types of lactic acid bacteria, especially those used in the study, can use cholesterol from carbonic sources in their metabolic processes and reduce body weight [9]. Researchers at the University of Knoxville have found that calcium directly influence weight loss efforts. Foods rich in calcium, especially dairy, have been shown to increase body fat breakdown and preserve metabolism during dieting [2].

Yogurt specifically has been studied as a calcium rich food that helps burn fat, promotes weight loss and Protect the meager muscle mass, because the muscle mass is essential for maintaining high metabolism. Eating yogurt every day can also know to lower LDL "bad cholesterol". Many adults have problems digesting milk products because they do not produce enough of the enzyme lactase. Yogurt naturally contains lactase, making it a healthy alternative for those who cannot tolerate other milk products [4].

Bifidus Regularis is a probiotic specifically added to Activia yogurt (Danone) to aid in digestive health. A study showed that daily consumption of yogurt with Bifidobacterium lactis DN-173 010 improved digestive symptoms in women with minor digestive problems. "A 2011 study published in "Pediatrics" found that children suffering from constipation who were given yogurt containing the exclusive bacterial strain had an increase in their stool production [5]. Also the company of Danone's has funded four studies that found that the consumption of the fermented milk containing living Bifidobacterium animalis DN-173 010 was able to improve colonic transit time (CTT) in humans. Activia Speeding up transit time of their GI tracts (called transit time). Speeding up transit time "can lead to a reduction in the quantity of gas present in the digestive tract and a reduction of the bloating sensation in healthy individuals," says Miguel Freitas, Danone's scientific affairs manager [10, 11]. Eating low-fat, calcium-rich yogurt could help prevent acid reflux [12].

Effect of Oral dosage of Activia yogurt on blood sugar
Table 2 shows the effect of the oral dosage of Activia yogurt on blood sugar (glucose), after the 30 day dose of the treatment group. The results showed that the glucose decreased at a significant level (P<0.05) compared with the control group. This may be due to the fact that yogurt contains vitamins B12, vitamin C, minerals and folic acid with few other compounds that lead to increased liver activity and blood sugar regulation [2, 13, 14].

Table 2. Effect of oral dosage of Activia yogurt on blood sugar

Group	Glucose (mg/dl)
Control Group	80±0.98 A
Treatment Group	74+1.00 A

The results of the study also showed a significant decrease in the blood chemistry, especially blood sugar, which we are studying in the analysis of the sample fasting blood sugar, with treatment group content ranges (72-85mgldl). Where the results for people who do not eat Activia with the diet control group (95.43-110 mg/dl). The study found the effectiveness of the Activia yogurt and its unique components, such as Probiotic Yeast and (Lactobacillus, Streptococcus, Bifidobacterium) bacteria in reducing blood sugar and weight loss by adopting a balanced diet and many of the best benefits of Activia as a treatment for gastrointestinal diseases such as colon and stomach ulcers [3]. Because of the extra sugar added to many types of Activia, diabetics may experience problems with blood sugar levels [15, 16]. Recent research touts the dairy food connection to weight loss and diabetes prevention and the advantages of probiotics or good bacteria found in cultured products [2, 15]. Activia yogurt is rich in protein, vitamins B and basic minerals like calcium and low in carbohydrates and fat, promotes weight

loss and protect their lean muscle mass that activates the liver and improving the metabolism of carbohydrates and fats in the body [2]. Almost, all the results showed that there was a direct correlation between weight loss and blood sugar [2, 3, 7, 9].

CONCLUSION

It was found through the study that yogurt Activia has an impact on body weight, where the reduction of body weight after the treatment. The study also showed that yogurt Activia has no effect on serum sugar, where it was found through the results of the absence of significant differences before and after treatment.

REFERENCES

[1] M.C. Mckinley, The nutrition and health benefits of yoghurt, International Journal of Dairy Technology 58 (2005) 1-12.

[2] J. Shafer, J. Burnett, What to eat with Diabetes: Best Yogurts, Diabetic living, 2013.

[3] S.E. Gilliland, Health and nutritional benefits from lactic acid bacteria, FEMS Microbiol Rev. 7 (1990) 175-188.

[4] E. Braverman, For consistent weight loss, eat yogurt every day, Huffpost, 2009.

[5] J. Corleone, What is the difference between Activia and regular yogurt, livestrong.com, 2011.

[6] L. Kubicová, Z. Kádeková, Marketing strategy of the new product introduction on the market. Polityki Europejskie, Finanse i Marketing 5 (2011) 78-90.

[7] A. Ljungh, T. Wadstrom Lactobacillus Molecular Biology: From Genomics to Probiotics. Caister Academic Press. 2009.

[8] M. Ito, H. Sawada, K. Ohishi, Y. Yoshida, W. Yokoi, T. Watanabe, T. Yokokura, Suppressive effects of bifidobacteria on lipid peroxidation in the colonic mucosa of iron-overloaded mice. J. Diary Sci. 84 (2001) 1583-1589.

[9] D.I. Pereira, G.R. Gibson, Cholesterol assimilation by lactic acid bacteria and bifidobacteria isolated from the human gut. Applied Environmental Microbiology 68 (2002) 4689-4693.

[10] D. Schard, M. Freitas, Helpful bacteria: should you take probiotics?, Bioscience and Microflora. 2001, 20: 43.

[11] M. Bouvier, S. Meance and *et al.* Effects of consumption of a milk fermented by the probiotic strain bifidobacterium animalis DN-173 010 on colonic transit times in healthy humans, Bioscience and Microflora, 20 (2001) 43- 48.

[12] M. Shenker, Is Danone Activia good for digestion and acid reflux? livestrong.com, 2017.

[13] N. Butler, Diabetes and B12: What you need to know, Health Line, 2015.

[14] D.R. Wilson, 5 Vitamins to boost your metabolism and promote weight loss, Health Line, 2016

[15] S. Kaye, Side effects of Activia. livestrong.com, 2015.

[16] Slidge, Activia Yogurt Discussion, The global diabetes community, 2013.

Türkiye'de Yetiştirilen Bazı Keçi Irklarında Hipofiz Spesifik Transkripsiyon Faktörü-1 (Pit-1) Geni PstI Polimorfizminin RFLP Yöntemi ile Belirlenmesi

Mahamat Ali Amine Ouchar*, Birol Dağ, İbrahim Aytekin
Selçuk Üniversitesi, Ziraat Fakültesi, Zootekni Bölümü, Konya, Türkiye
*İletişimden sorumlu yazar: amine.ouchar@gmail.com

Özet

Bu araştırmada amaç büyüme ve gelişmenin düzenlenmesinde memelilerde aday gen olarak kabul edilen Hipofiz Spesifik Transkripsiyon Faktörü-1 (Pituitary-specific Transcription Factor; Pit-1) geninin ekzon 6 bölgesindeki PstI polimorfizmini Türkiye'de yetiştirilen 6 farklı keçi ırkında belirlemektir. Araştırmada 36 baş Kıl, 18 baş Tiftik, 43 baş Kilis, 37 baş Honamlı, 46 baş Halep ve 37 baş Saanen ırkı olmak üzere toplam 217 baş keçide Pit-1 geni *PstI* polimorfizmi (450 bç) Restriksiyon Fragman Uzunluk Polimorfizmi (RFLP) yöntemi ile araştırılmıştır.

Kıl, Tiftik, Kilis, Honamlı, Halep ve Saanen ırklarında T ve C allel frekansları sırasıyla 0.986 ve 0.014, 0.861 ve 0.139, 0.942 ve 0.058, 0.932 ve 0.068, 0.957 ve 0.043 ile 0.824 ve 0.176 olarak tespit edilmiştir. Bütün ırklarda CC genotipi tespit edilmemiş olup, TT ve TC genotip frekansları bakımından ise sırasıyla 0.972 ve 0.028, 0.722 ve 0.278, 0.884 ve 0.116, 0.865 ve 0.135, 0.913 ve 0.087 ile 0.649 ve 0.351 olarak bulunmuştur. Bütün ırklar dikkate alındığında T ve C allel frekanslarını 0.924 ve 0.076, TT, TC ve CC genotip frekanslarını ise 0.848, 0.152 ve 0.000 olarak tespit edilmiştir.

Pit-1 geni ekzon 6 bölgesi *PstI* polimorfizmi bakımından hem ırklar bazında hem de genel değerlendirme yapıldığında populasyonların Hardy-Weinberg dengesinde olduğu belirlenmiştir (P>0.05).

Anahtar Kelimeler: Pit-1, PstI polimorfizm, keçi, PCR, RFLP
Disiplin: Biyoteknoloji

Abstract

The aim of this study is to determine *PstI* polymorphism in the exon 6 region of the Pituitary-specific Transcription Factor (Pit-1) gene which is regarded as a candidate gene in mammals in regulating growth and development in 6 different goat breeds reared in Turkey. *PstI* polymorphism in Pit-1 gene (450 bp) was investigated by Restriction Fragment Length Polymorphism (RFLP) method in a total of 217 goats including 36 Hair, 18 Angora, 43 Kilis, 37 Honamlı, 46 Halep and 37 heads of Saanen breeds.

T and C allele frequencies in Hair, Angora, Kilis, Honamlı, Halep and Saanen breeds were found to be 0.986 and 0.014, 0.861 and 0.139, 0.942 and 0.058, 0.932 and 0.068, 0.957 and 0.043 and 0.824 and 0.176, respectively. CC genotype was not detected in all breeds and TT and TC genotype frequencies were found to be 0.972 and 0.028, 0.722 and 0.278, 0.884 and 0.116, 0.865 and 0.135, 0.913 and 0.087 and 0.649 and 0.351 respectively. When all breeds were taken into consideration, T and C allel frequencies were found to be 0.924 and 0.076, and TT, TC and CC genotype frequencies were found to be 0.848, 0.152 and 0.000.

It was determined that populations were in Hardy-Weinberg equilibrium when both the breed and the general evaluation were made in terms of *PstI* polymorphism in the exon 6 region of the Pit-1 gene (P> 0.05).

Keywords: Pit-1, *PstI* polymorhism, goat, PCR, RFLP
Discipline: Biotechnology

GİRİŞ

Türkiye'de keçi yetiştiriciliği denildiğinde genel olarak akla kıl keçileri gelmektedir. Keçi varlığı ise 10 634 672 milyon baş olup, toplam keçi varlığının yaklaşık % 98'ini Kıl keçi ve melezleri, %2'sini ise Tiftik keçileri oluşturmaktadır. Çiftlik hayvanları içerisinde payı ise %17,6'dır [1]. Küçükbaş hayvan yetiştiriciliği, genel olarak zayıf meralar, nadas, anız ve bitkisel üretime uygun olmayan alanları değerlendirerek et, süt, yapağı, kıl ve deri gibi ürünlere dönüştüren bir üretim faaliyetidir. Türkiye'nin doğal kaynaklarının, genellikle çayır-meraların koyun ve keçi türlerinin yetiştirilmesine daha uygun oluşu, kırsal kesimdeki halkın tüketim alışkanlıkları gibi sebepler, küçükbaş hayvan yetiştiriciliği için

uygun bir ortam oluşturmaktadır. Küçükbaş hayvan yetiştiriciliğinin bu önemine karşılık son yıllarda koyun ve keçi sayısında önemli ölçülerde gözlemlenen düşüşler, üretimde azalmaya neden olsa da [2] son yıllarda bu alana yönelik teşvik ve ıslah projeleri ile bir miktarda olsa iyileşme sağlanmaktadır. Keçi yetiştiriciliği genellikle az gelişmiş ve gelişmekte olan ülkelerde yapılan geleneksel bir hayvansal üretim koludur. Kırsal ve ormanlık bölgelerdeki dar gelirli aileler için önemli bir geçim ve besin kaynağı oluşturmaktadır. Bir özelliği de başka bir şekilde değerlendirilemeyen dağlık, fundalık ve taşlık arazilerin keçi yetiştiriciliği ile süt ve et gibi ürünlerin elde edilmesinde kullanılmasıdır [3].

Çiftlik hayvanlarında verim artışı genotipin ve/veya çevrenin iyileştirilmesi ile mümkün olacağından, populasyonların genetik yapıları hakkında bilgi sahibi olunması damızlık seçiminde başarıyı artırır. Özellikle polimorfik özellikler ile üzerinde durulan özellikler arasında yüksek bir korelasyon olması, erken dönemde tespitinin yapılabilirliği ve cinsiyete bağlı olmama gibi kriterlerin varlığı seleksiyonda yetiştiricilere kayda değer bir katkı sağlamaktadır. Günümüze kadar çiftlik hayvanlarında birçok aday gen çalışılmış ve bu genler ile ekonomik önemi olan verim özellikleri arasındaki ilişkiler araştırılmıştır. Bu genlerden birisi olan Pitüiter Spesifik Transkripsiyon Faktörü-1 (POU1F1/Pit-1) geni büyüme ve gelişmenin düzenlenmesinde memelilerde aday gen olarak kabul edilmektedir. Pit-1 geni POU familyası [4] sınıf 1 hipofiz transkripsiyon faktörü (POU1F1, POU domain class 1 transcription factor 1) olarak isimlendirilmekte ve memelilerde büyüme hormonu (BH), prolaktin (PRL) ve tirotropin (TSH) ekspresyonundan sorumlu olan [5, 6, 7, 8] bir gendir. Keçi kromozomlarında 1q21- 22'de lokalize olup, POU ve homeo-alan bölgeleri içeren 6 ekzondan meydana gelmektedir [9]. Bu genin bağlanma yeri, ekzon 1'deki transkripsiyonun varsayılan başlangıcından 350 kb aşağıdadır [10]. Bu gende meydana gelen bazı mutasyonlar memelilerde GH, PRL ve TSH hormonlarının düzenini bozmakta ve ayrıca hipofizer gelişmede anormalliklere (hipoplazi) de neden olduğu bildirilmektedir [10].

Bu araştırmada amaç Pit-1 geninin ekzon 6 bölgesindeki *PstI* polimorfizmini Türkiye'de yetiştirilen 6 farklı keçi ırkında belirlemektir.

MATERYAL VE METOT

Çalışmada, 36 Kıl, 18 Tiftik, 43 Kilis, 37 Honamlı, 46 Halep ve 37 Saanen ırkı olmak üzere toplam 217 baş hayvandan kan örnekleri alınmıştır. Steril ve tek kullanımlık enjektörler kullanılarak *Vena jugularis*'ten alınan kanlar 10 ml'lik EDTA'lı tüpler içine konulmuş ve soğuk zincirde Selçuk Üniversitesi Ziraat Fakültesi Zootekni Bölümü Biyoteknoloji Laboratuvarına getirilmiştir. Kanlar genomik DNA izolasyonları yapılıncaya kadar -20ºC'de derin dondurucuda muhafaza edilmiştir.

DNA izolasyonunda QuickGene DNA (DB-S) kiti kullanılmıştır (Fujifilm Corp., Tokyo, Japan). DNA izolasyonundan sonra tüm örnekler Nanodrop spektrofotometre'de ölçülmüş (ND1000; NanoDrop Technologies, USA) ve DNA konsantrasyonları belirlenmiştir. Pit-1 geninin ekzon 6 bölgesindeki 450 bç'lik bölgenin PCR ile çoğaltılmasında 5'–CCATCATCTCCCTTCTT–3' ve 5'–AATGTACAATGTGCCTTCTGAG –3' nükleotit sekanslarına sahip primerler kullanılmıştır [11]. PCR'da kullanılan kimyasallar ve konsantrasyonları toplamda 10 µL olmak üzere 2 µL DNA, 1X Master mix, 0.25 µM primerler ve 5.5 µL ddH$_2$O olup, PCR işlemi 95°C'de 4 dk başlangıç ayrılmasından sonra toplam 33 döngü olmak üzere ayrılma için 94°C'de 45 sn, bağlanma için 54.5 °C'de 45 sn, uzama için 72 °C'de 1 dk ve son uzama için 72 °C'de 10 dk koşullarında gerçekleştirilmiştir. İlgili gen bölgesinde polimorfizmi belirlemek amacıyla 10 µL PCR ürününe, 1 U *PstI* kesim enzimi, 1X Buffer ve 7 µL ddH$_2$O ilave edilmiş ve 37°C'de 30 dk muamele edilmiştir. RFLP yöntemi ile çoğaltılan ve *PstI* restriksiyon enzimi ile kesilen DNA örnekleri % 2.5'lik agaroz jelde yürütülmüş ve UV altında görüntüleri alınarak genotipler belirlenmiştir.

Allel ve genotip frekansları ile popülasyonların dengede olup olmadıklarının analizlerinde POPGENE 32 istatistik programından yararlanılmıştır [12].

SONUÇLAR VE TARTIŞMA

PCR-RFLP metodu ile çoğaltılan Pit-1 gen bölgesi ve *PstI* kesim enzimi ile elde edilen genotipleri Şekil 1'de verilmiştir.
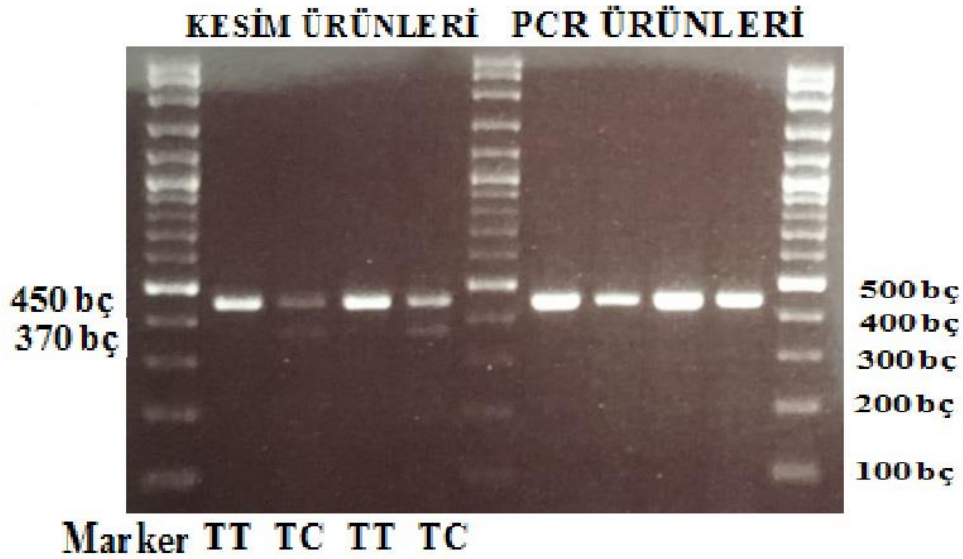
Şekil 1. PCR-RFLP metodu ile çoğaltılan Pit-1 gen bölgesi ve *PstI* kesim enzimi ile elde edilen genotipler (M: Markör, PCR ürünleri: 450 bç; TT: 450 bç ve TC: 450 bç ve 370 bç)

Tablo 1'de Pit-1 geni ekzon 6 bölgesi *PstI* polimorfizminin Türkiye'de yetiştirilen 6 farklı keçi ırkındaki genotip ve allel frekansları verilmiştir.

Tablo 1. Türkiye'de yetiştirilen 6 farklı keçi ırkındaki Pit-1/*PstI* polimorfizmi bakımından genotip ve allel frekansları

		Genotip frekansları			Allel frekanları		
Irklar	N	TT (n)	TC (n)	CC (n)	T	C	χ^2
Kıl	36	0.972 (35)	0.028 (1)	0	0,986	0.014	0.007 (p>0.05)
Tiftik	18	0.722 (13)	0.278 (5)	0	0.861	0.139	0.468 (p>0.05)
Honamlı	37	0.865 (32)	0.135 (5)	0	0.932	0.068	0.194 (p>0.05)
Halep	46	0.913 (42)	0.087 (4)	0	0.957	0.044	0.095 (p>0.05)
Saanen	37	0.649 (24)	0.351 (13)	0	0.824	0.176	1.680(p>0.05)
Kilis	43	0.884 (38)	0.116 (5)	0	0.942	0.058	0.164 (p>0.05)
Toplam	217	0.848 (184)	0.152 (33)	0	0.924	0.076	1.470 (p>0.05)

χ^2: Hardy-Weinberg denge testi

Bu çalışmada Türkiye'de yetiştirilen 6 farklı keçi ırkında Pit-1/*PstI* polimorfizmi bakımından T ve C allel frekansları dikkate alındığında genel olarak T alleli 0.861 ile 0.986 aralıklarında, C alleli ise 0.014 ile 0.176 aralıklarında tespit edilmiş olup, T allel frekansının yüksek olduğu bulunmuştur. Genotip frekansları bakımından ise aynı eğilim TT genotipleri lehinde olduğu Tablo 1'den de görülmektedir. Bununla birlikte 6 keçi ırkında da CC genotipi hiç tespit edilmemiştir. Genel olarak 217 baş keçi değerlendirildiğinde Pit-1/*PstI* polimorfizmi bakımından T ve C allel frekansları sırasıyla 0.924 ve 0.076 olarak, TT, TC ve CC genotip frekansları ise sırasıyla 0.848, 0.152 ve 0.000 olarak tespit edilmiştir. Ayrıca, çalışmadaki ırklarda allel frekans dağılımlarının Hardy-Weinberg dengesinde olduğu tespit edilmiştir (p>0.05).

Pit-1/*PstI* polimorfizmi bakımından keçilerde yapılan çalışmalara literatürde oldukça sınırlı olup, Lan ve ark.'nın [11] Moğolistan'da 847 baş Beyaz Kaşmir keçilerinde yaptıkları çalışmada, T ve C allel frekanslarını sırası ile 0.959 ve 0.041 olarak bulmuşlar ve populasyonu Hardy-Weinberg dengesinde (p<0.05) olduğunu bildirmişlerdir. Ayrıca araştırıcılar, Pit-1/*PstI* polimorfizmi ile kaşmir verimleri arasındaki ilişkiler önemli olduğunu bildirmişlerdir. Saleha ve ark.'nın [13] Mısır ve Suudi Arabistan'da yetiştirilen Barki, Zaribi, Ardi ve Masri ırklarında *PstI* polimorfizmi belirlemek amacıyla yaptıkları çalışmalarında T allel frekanslarının 0.250 ile 0.840 ve C allel frekanslarının ise 0.160 ile 0.650 arasında değiştiğini bildirmişlerdir. Dagong ve ark. (2016) [14], 72 baş Marica, Kacang ve Peranakan Ettawa ırkı keçilerde PCR-RFLP yöntemi ile Pit-1/*PstI* gen polimorfizmi çalışmışlardır. Çalışmada T ve C allel frekanslarını sırası ile 0.76 ve 0.24 olarak bildirmişlerdir. Araştırıcılar sonuç olarak, Endonezya yerli

keçilerinde Pit-1 polimorfizmlerinin doğal büyüme ve karkas kalitesine olan ilişkisini bulmak için gelecekteki araştırmalarda kullanılabileceğini ifade etmişlerdir.

Sonuç olarak bu çalışmanın Türkiye'de yetiştirilen keçi ırklarında Pit-1/*PstI* polimorfizmi bakımından literatüre katkı sağlayacağı beklenmekte olup, ayrıca söz konusu gene ait bölgenin daha fazla sayıda keçide veya gen bölgesinin tamamının farklı moleküler metotlar ile incelenmesi ırklara ilişkin daha detaylı bilgileri ortaya çıkaracaktır. Yani bu gendeki polimorfizmlerin verim özellikleri ile ilişkisini konu alan ileride yapılacak seleksiyon çalışmalarında tercih edilecek allelin belirlenmesine yardımcı olacaktır.

REFERANSLAR

[1] http://www.tuik.gov.tr/Start.do (Erişim tarihi:03.05.2018)

]2] M. Kaymakçı, N. Koşum, T. Taşkın, Y. Akbaş. Menemen koyunlarında kimi verim özelliklerinin belirlenmesi üzerine bir araştırma. Ege Üniversitesi Ziraat Fakültesi Dergisi 43 (2006) 63-74.

]3[M. Kaymakçı, Y. Aşkın. Keçi Yetiştiriciliği. Ege Üniversitesi Ziraat Fakültesi, Bornova, İzmir, 1997, 294.

]4[W. Herr, R.A. Sturm, R.G. Clerc, L.M. Corcoran, D. Baltimore, P.A. Sharp, H.A. Ingraham, M.G. Rosenfeld, M. Finney, G. Ruvkun, The POU domain: a large conserved region in the mammalian pit-1, oct-1, oct-2, and Caenorhabditis elegans unc-86 gene products. Genes and Development 2 (1988) 1513-1516.

[5] B.R. Haugen, W.M. Wood, D.F. Gordon, E.C. Ridgeway, A Thyrotropespecific Variant of Pit-1 Transactivates the Thyrotropin _ Promoter, The Journal of Biological Chemistry 268 (1993) 20818-20824.

[6] R. Renaville, N. Gengler, E. Vrech, A. Prandi, S. Massart, C. Corradini, C. Bertozzi, F. Mortiaux, A. Burny, D. Portetelle, Pit-1 Gene Polymorphism, Milk Yield, and Conformation Traits for Italian Holstein-Friesian Bulls, J. Dairy Sci. 80 (1997) 3431–3438.

[7] P. Kopp, J.L. Jameson, Thyroid Disorders, In: Jameson JL and Collins FS. eds. Principles of Molecular Medicine. *Humana Press*, Totowa. NJ, 1998, 459-473.

[8] S. Miyai, S. Yoshimura, Y. Iwasaki, S. Takekoshi, R.V. Lloyd, R.Y. Osamura, Induction of GH, PRL, and TSH beta mRNA by transfection of Pit-1 in a human pituitary adenoma-derived cell line, Cell Tissue Res 322 (2005) 269-277.

[9] J.R. Woollard, C.K. Tuggle, A.P. de Leon, Rapid communication: Localization of POU1F1 to bovine, ovine, and caprine 1q21-22, Journal of Animal Science 78 (2000) 242-243.

[10] P.W. Howard, S.F. Jue, R.A. Maurer, Expression of the Synaptotagmin I Gene is Enhanced by Binding of the Pituitary- Specific Transcription Factor, POU1F1. Mol. Endocrinol. 23 (2009) 1563-1571.

[11] X.Y. Lan, M.J. Li, H. Chen, L.Z. Zhang, Y.J. Jing, T.B. Wei, G. Ren, X. Wang, X.T. Fang, C.L. Zhang, C.Z. Lei, Analysis of caprine pituitary specific transcription factor-1 gene polymorphism in indigenous Chinese goats. Molecular Biology Reports. (2009) doi: 10.1007/s11033-008-9232-5

[12] F.C. Yeh, R.-C. Yang, T.B.J. Boyle, Z.-H. Ye, J.X. Mao, F.C. Yeh, R.C. Yang, Z.H. Ye, R. Yang, T. Boyle, Z. Ye, PopGene, the user-friendly shareware for population genetic analysis, molecular biology and biotechnology center, Canada, 10 (1997) 295-301.

[13] S.Y.M. Alakilli, K.F. Mahrous, L.M. Salem, E.S. Ahmed, Genetic polymorphism of five genes associated with growth traits in goat, African Journal of Biotechnology 11 (2012) 14738-14748.

[14] M.I.A. Dagong, L. Rahim, S.R.A. Bugiwati, K.I. Prahesti, Genetic Polymorphisms of Pituitary Specific Transcription Factor-1 (Pit-1) Gene from Indonesian Local Goat Population Reared in South Sulawesi Province, Advances in Environmental Biology 10 (2016) 121-125.

Production of Biofuel by Catalyzed Process from Green Macroalgae

Ammar Alsaho*, Feza Geyikçi
Ondokuz Mayıs University, Faculty of Engineering, Dept. of Chemical Engineering, 55139 Atakum, Samsun, Turkey
*Corresponding author: ammar.alsaho88@gmail.com

Abstract

Biofuel production from algae is widely developed at different scales as a potential source of both economic and environmental benefits and renewable energy. First and second generation biofuels are produced from various food plants and plant seed oil products. Algae have been identified as a potential source for producing biofuels that can replace transportation fuels derived from fossil energy sources because of the different advantages of the previous two generations of feed stocks. There are four basic ways to produce biofuel. Microemulsions, thermal cracking (pyrolysis), dilution and transesterification can be used. The most commonly used method is transesterification. The transesterification reaction is affected by the molar ratio of alcohol / glycerin, catalysts, reaction temperature, reaction time and free fatty acids and water content of oils or fats. The main stage in this study is the production of renewable biofuels, which are algae biomass with transesterification process. 99.7% pure methanol as the alcohol and 99.9% pure sodium hydroxide (NaOH) as catalyst were used for the transesterification reaction. Through our results the best conditions for the transesterification process are: concentration of catalyst (NaOH) is 0.75% of the lipid content (0.097gr), reaction time, 80 min, and the methanol amount, 8gr. FTIR spectra for characterization algal biofuel was applied.

Keywords: biofuel, oil extraction, algae, transesterification
Discipline: Chemical Engineering

INTRODUCTION

This century witnessed a rise in conventional energy prices and the rising fears of instability of supply and the possibility of near depletion, which necessitated the importing countries to search for the energy and especially advanced countries in search for unconventional sources of energy to get rid of oil prices soaring and environmental impacts devastating, and found the sources of renewable energy, including biofuels made from plants and agricultural crops and waste [1]. Biofuels are fuel produced directly or indirectly from biomass, which means the substance of a biological origin (except for substances buried in geological formations that have been converted into fossil fossils) [2]. Global warming due to the greenhouse effect, nowadays known as the most important world's environmental problem, is the result of harmful emissions such as SOx and NOx, mainly CO2 emissions, which are the result of combustion [3]. For all these reasons, the world is looking for new sources of energy that are safe, renewable, economical and environmentally friendly and sustainable. Renewable energies such as wind, sun, water and bio-fuels produced from renewable biomaterials, such as vegetable or animal oils made of poly-chain of saturated hydrocarbons [3, 4]. However, the use of vegetable oil in the production of biofuels increases the risk of global food safety. For this reason algae, researchers and specialists emphasize the importance of being a safe and reliable source of renewable energy in the petroleum industry [5]. Algae represent the third generation of raw materials that used as a source of biofuels production upper than second-generation crops [6, 7]. Algae is an important species that grows fast, spread over a wide area and easily adapts to environmental conditions [8]. Biofuel production from algae provides the highest yield and energy [9]. Thermal and chemical methods are applied to reduce the viscosities of vegetable and algae oils. The most commonly used method for production purposes is the transesterification method, in which the chemical reactions and the parameters connected to them are closely monitored [10, 11].

MATERIALS AND METHODS

Algal sampling: In this study, algae is used for the production of biodiesel was (Ulva lactuca) obtained from the Black Sea coast in the Turkish city of Samsun.

Oil extraction: Dried algal biomass (50g) was taken in solvent mixture (300 ml) of n-hexane. The content were refluxed for 4 hrs.

Evaporation: The solvent was removed by using rota-evaporator under vacuum to get the algal oil and release hexane solutions.

Mixing of catalyst and methanol: The catalyst is typically sodium hydroxide (NaOH) or potassium hydroxide (KOH). The solid catalyst is dissolved in methanol to prepare the methoxide solution [12].

Transesterification of algal oil: The mixture of catalyst and methanol was poured into the algal oil in a conical Flask, and stirred vigorously using a magnetic stirrer. And adding an excess quantity of methanol to confirm the equilibrium displacement of the products so that methyl ester is generated [13].

Separation of biodiesel: The biofuel was decanted into a separate beaker, and the quantity sediment (glycerin, pigments, etc.) was measured.

Washing: the biofuel is slowly washed with warm water to remove residual catalyst and soaps then the water is removed. In some systems, biofuel is distilled to remove impurities [14].

The steps of the experiment are shown in Figure 1.

Oil extraction   **Evaporation**   **Transesterification**   **Seperation**   **Washing**
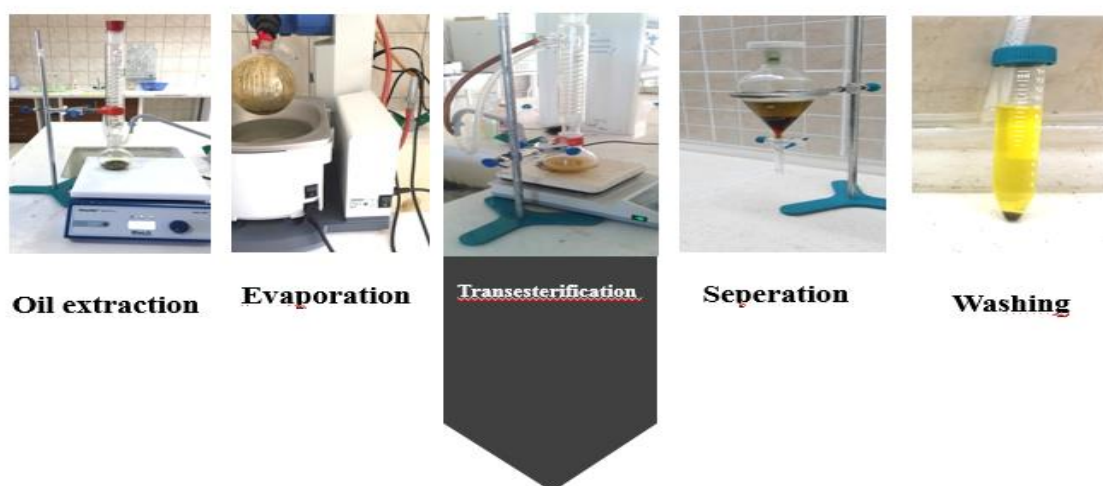
Figure 1. Steps of the Experiments

RESULTS AND DISCUSSION

The study was based on three samples of studied algae, equal in weight. Different conditions were applied for each sample in terms of temperature, reaction time, percentage of the catalyst used, and quantity of methanol used, to determine optimal conditions for the production of biofuel from macroalgae. Table 1 and Table 2 shows the conditions applied for each sample and the results of the interaction.

Table 1. The samples, conditions applied and the results

Test No	Reaction temperature (°C)	Amount of metanol (gr)	Amount of catalyst (gr)	Reaction time (min)	Amount of biofuel produced (gr)
1	50	15	0.13	60	7.92
2	62	8	0.097	80	10
3	75	5	0.26	120	3.67

Table 2. The concentration of catalyst and molar ratio of alcohol / oil

Test No	MeOH/oil molar	%,gNaOH/glipid
1	9/1	1
2	6/1	0.75
3	3/1	2

Effect of methanol amount on the amount of biofuel produced:

Referring to Figure 2, when methanol amount increased to the 8gr, the best lipid conversion rate was got. And then decreased with further increase in methanol amount. But if the methanol amount is less than 5gr, the algae cannot be completely immersed into methanol.
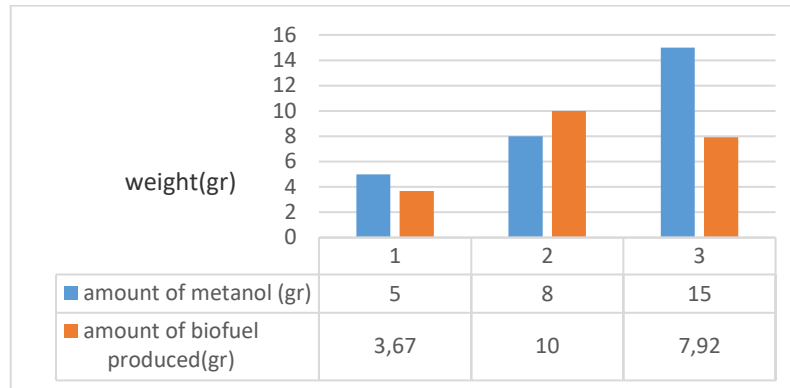
Figure 2. Influence of amount of methanol on the amount of biofuel produced

Effect of catalyst amount on the amount of biofuel produced:

The highest amount of biofuel is achieved when the amount of Sodium hydroxide (NaOH) is 0,097gr that means 0,75% of weight oil. The lipid conversion rate is decreased sharply when the concentration of NaOH increased to 2.0% and then continued to decline with the increase of catalyst concentration (Figure 3).
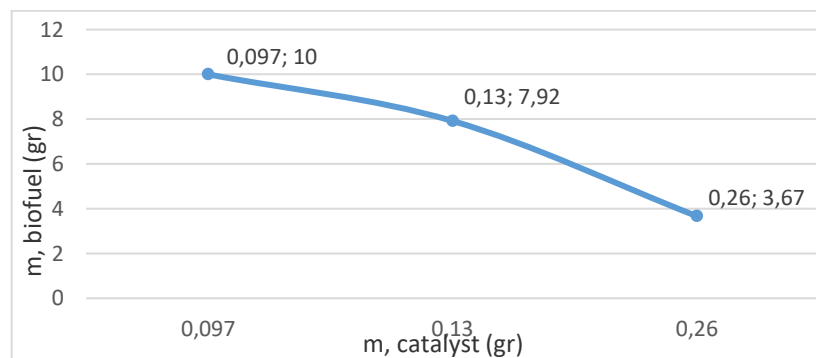
Figure 3. Influence of different amount of catalyst on the amount of biofuel produced

Effect of reaction time on amount of biofuel produced:

Figure 4 shows that the amount of biofuel produced increases with an increase in reaction time up to 80 minutes and then begins to decrease by increasing time. The maximum amount of biofuel produced (lipid conversion rate) was reached when the reaction time was 80min.
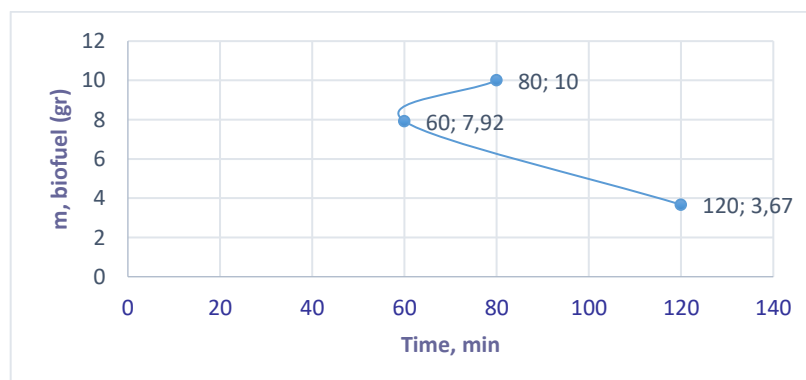
Figure 4. Influence of reaction time on the amount of biofuel produced

Effect of reaction temperature on amount of biofuel produced:

Figure 5 shows the best temperature of the reaction was 62Co, which is less than the boiling point of the methanol (64.7Co). This means that the reaction of the ester occurs without evaporation of methanol. At the highest temperature calculated 75Co, which is higher than the boiling point of methanol, which leads to a decrease in the rate of conversion of the lipid and increases the speed of side reactions, such as the reaction of sapon and form glycerin.
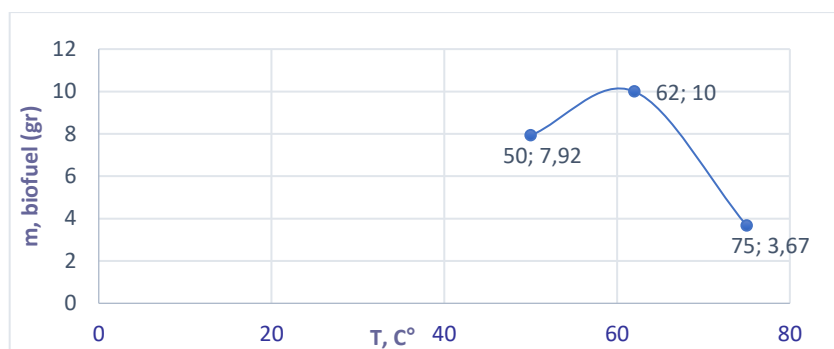
Figure 5. Influence of reaction temperature on the amount of biofuel produced

FTIR spectra for algal biofuel:

Through Figure 6 we note that C=O carbonyl compound are the strong C=O stretching absorption bands in the region of 1850-1550 cm-1. C-O-C (Ethers), these stretching vibrations produce a strong band in the 1250-950 cm-1 region. C-H, adsorption bands 2750-3050 cm-1 correspond to the asymmetric and symmetric vibration modes. Absorption of the O-H group ranges from the value of 3650 cm-1, and we note that the absorption rate is weak.
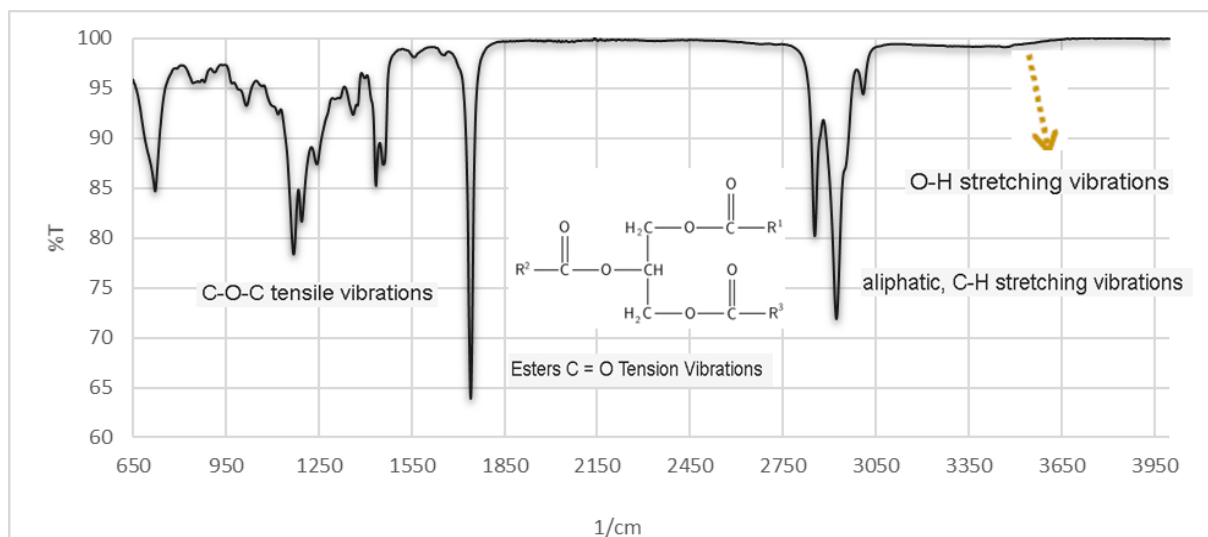
Figure 6. FTIR Spectra for Algal Biofuel

CONCLUSION

Algae are an excellent economic option for the production of biofuels for their availability and the possibility of farming on simple terms and at low cost. Transesterification is the most effective and economical method of reducing oil viscosity to produce biofuels. Through our results we found the optimal conditions for the production of biofuel in the process of Transesterification as follows: concentration of catalyst (NaOH) is 0,75% of the lipid amount(0,097gr), reaction time is 80min, and the methanol amount is 8gr. At temperatures above 60°C, It was found that 62 °C was better than 50 and 75°C. Our results in this study confirm the possibility of producing biofuels from macroalgae and thus can be considered a renewable source of energy. Although previous studies have confirmed the

superiority of microalgae on macroalgae in the production of biofuels in larger quantities, but most of these studies are still in the laboratory testing. Future studies should rely on microalgae and macroalgae as a source of mainly biofuel production.

Acknowledgements

REFERENCES

[1] A. Demirbas, Biodiesel: A realistic fuel alternative for diesel engines, ISBN 978-1-84628-994-1, Springer, London, 2008.

[2] لجنة الزراعة ، الوقود الحيوي فاو،منظمة الاغذية والزراعة للامم المتحدة: (بلا) http://www.fao.org/docrep/meeting/009/j4313a.htm#thr/ 2009.

[3] A. Bajhayiya, S.K. Mandotra, M.R. Suaeela, K. Toppo, S. Ranade. Algal Biodiesel: the next generation biofuel for India, Asian J. Exp. Biol. Sci. 1 (2010) 728-739.

[4] A. Demirbas, Biofuels: Securing the planet's future energy needs, ISBN 978-1-84882-010-4, Springer, London, 2009.

[5] D. Olivier, An Algae-Based Fuel, Biofutur, No. 255, May 2005.

[6] B. K. Bansal, M. P. Sharma, Prospects of biodiesel production from vegetables oils in India, Renew. Sustain. Energy. Rev 9 (2005) 363–78.

[7] Y. Chisti, Biodiesel from microalgae. Biotechnology Advances 25 (2007) 294-306.

[8] P. Spolaore, C. Joannis, C. Duran, E. Isambert, Commercial applications of microalgae. J. Biosci. Bioeng. 101 (2006) 87-96.

[9] E. Çılgın, 3. Nesil Biyoyakıt Teknolojisi Alglerin bir Dizel Motorunda Performans ve Egzoz Emisyonlarına Etkisinin Araştırılması, Iğdır Üni. Fen Bilimleri Enst. Der. 5 (2015) 33-41.

[10] M. Turhan, Su yosunlarının kimyasal yöntemlerle sıvı ve gaz yakıtlara dönüştürme ve biyodizel eldesi. Yüzüncü Yıl Üniversitesi. Fen Bilimleri Enstitüsü. Van – 2011.

[11] Z. Öner, Biyodizel üretiminde adsorban maddelerin rolünün incelenmesi. Çukurova Üniversitesi. Fen Bilimleri Enstitüsü, 2011.

[12] F. Yaşar, Yosun yağından biyodizel üretimi ve bir dizel motorunda alternatif yakıt olarak kullanılması. Batman, 2016.

[13] N. Adnan Ali, D.S.M., (Botryococcus braunii) في انتاج الوقود الحيوي استعمال سلالة محلية من طحلب مجلة (Using Native Strain of Botryococcus braunii algae to Product biofuel). جامعة البعث 2015. -6 العدد 73- المجلد

[14] F. Ahmad, A.U. Khan, A. Yasar, Transesterification of oil extracted from different species of algae for biodiesel production, African Journal of Environmental Science and Technology 7 (2013) 358-364.

Free Coupled Vibrations of Angle-Ply Laminated Composite Cantilever Beams

Mohammed Kashama Guzunza*
Institut National du Bâtiment et des Travaux Publics, Kinshasa, Democratic Republic of the Congo
Dokuz Eylül Univ., Dept. of Civil Engineering, İzmir, Türkiye
Mehmet Çevik, İzmir Katip Çelebi Univ., Dept. of Mechanical Engineering, Çiğli Main Campus, İzmir, Türkiye
*Corresponding author: kashmedguzunza@gmail.com

Abstract

Coupled free vibration analysis of angle-ply laminated composite beams with cantilever end conditions is performed by finite elements (FE) method. The effect of material coupling between out-of-plane bending, in-plane bending, torsional, and axial modes of vibration is taken into account. The rotary inertia and shear deformation effects are included in the analysis. Numerical applications are carried out for symmetric and anti-symmetric angle-ply and cross-ply beams. Natural frequencies and mode shapes are analyzed. Coupling occurs between out-of-plane bending and torsional modes in symmetric angle-ply beams, between out-of-plane bending and in-plane bending modes in anti-symmetric angle-ply beams, and between in-plane bending and torsional modes in anti-symmetric cross-ply beams. Parametric studies are performed to study the effects of material orthotropicity and length-to-thickness ratios on natural frequencies. The validity of the FE model is shown by comparing the results with those available in the literature.

Keywords: Angle-ply laminated composite beam, free coupled vibration, finite element analysis
Discipline: Civil Engineering

1. INTRODUCTION

In the last few decades, research and development in composite materials have shown a tremendous increase. In many cases, metals are replaced by laminated composites because of their high strength-to-weight and stiffness-to-weight ratios. Elseways, new problems emerge with these materials and further research is required for a better understanding of their vibrational behavior.

Out-of-plane bending vibration analysis of laminated composite beams is carried out by many researchers [1-7]. Shear deformation and rotary inertia are considered in these studies; however, bending vibrations are assumed uncoupled from torsion. In symmetric cross-ply laminated beams bending and torsion vibrations are always uncoupled [8]; but coupling occurs in anti-symmetric laminations. In some studies, the effect of material coupling between the bending and torsion modes are taken into account. Yıldırım and Kıral [9] studied the out-of-plane bending and torsion problem of symmetric cross-ply laminated beams and presented the rotary inertia and shear deformation effects using various beam theories. Kadivar and Mohebpour [10] studied the dynamic response of symmetric cross-ply and unsymmetric angle-ply laminated beams taking into account the characteristic (bend-stretch, shear-stretch, and bend-twist) couplings. Banerjee [11] derived exact expressions for the frequency equation and mode shapes of composite Euler-Bernoulli beams by taking into account the coupling between the bending and torsional modes of deformation. Ramtekkar [12] developed a six-node, plane stress mixed FE model for the natural vibrations of laminated composite beams and obtained natural frequencies of axial, bending and shear modes, and presented various mode shapes. Murthy [8] derived a refined 2-node beam element based on higher order shear deformation theory for axial-flexural-shear coupled deformation in asymmetrically stacked composite beams. Most of the studies on vibrations of laminated composites are related with cross-ply beams; whereas there are very few studies on the coupled vibrations of angle-ply laminated beams. In this study, coupled vibrational behavior of angle-ply laminated beams with cantilever end conditions is modeled and analyzed.

2. FE MODELING OF THE COMPOSITE BEAM

The geometry and coordinates of the laminated composite beam are illustrated in Figure 1. The length, height and width of the beam are represented by *L*, *h,* and *b*, respectively. To simulate the out-of-plane bending, in-plane (xy-plane) bending, torsional and axial vibrations of the beam, the ANSYS 10 FE analysis software is used. 8-noded, linear layered 3-dim shell element (Shell 99) having 6-dof at each

node is used for modeling. This element takes into account the rotary inertia and shear deformation effects. The clamped-free (C-F) end conditions are considered.
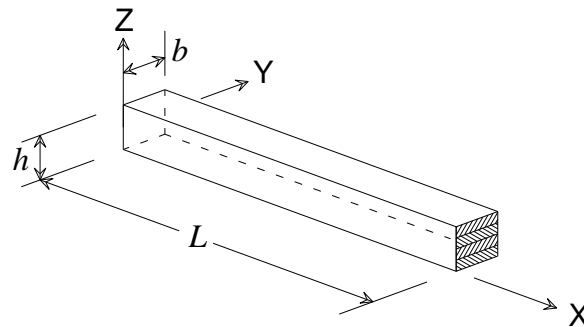
Figure 1. Geometry and coordinates of the laminated composite beam.

3. VALIDATION OF THE MODEL

In order to validate the accuracy of the present model, numerical results are compared with reported values in literature considering three examples. The material properties are given in Table 1. In this table, E, G, v and ρ are the modulus of elasticity, shear modulus, Poisson's ratio and density. Subscripts L and T denote the longitudinal and transverse directions, respectively, with respect to the fibers.

Table 1. Material properties used in comparison examples.

	E_L (GPa)	E_T (GPa)	G_{LT} (GPa)	G_{TT} (GPa)	v_{LT}	ρ (kg/m³)
Material 1 AS/3501-6 Graphite/epoxy	144.8	9.65	4.14	3.45	0.3	1389.23
Material 2 (dimensionless)	$40E_T$	E_T	$0.6\,E_T$	$0.5\,E_T$	0.25	

Example 1. Symmetric 4-layered angle-ply (θ/−θ/−θ/θ) laminated beams having Clamped-Clamped (C-C) boundary conditions made up of Material 1 with L/h=15 is considered. In Table 2, results from analytical solution [1] and first-order shear deformation theories [10] are considered for the comparison of present results. The present model yielded results in good agreement with the results of FSDT-3 since it takes into account both bend-twist coupling and Poisson effect.

Table 2. Comparison of dimensionless natural frequencies of symmetric angle-ply beams

	Ply angle						
	0	15	30	45	60	75	90
Analytical [1]	4.8487	4.6635	4.0981	3.1843	2.1984	1.6815	1.6200
FSDT-1 [10]	4.8712	4.6835	4.1118	3.1908	2.2006	1.6814	1.6207
FSDT-2 [10]	4.8712	4.1071	3.3806	2.6199	1.9611	1.6604	1.6207
FSDT-3 [10]	4.8629	4.0082	2.8762	1.9330	1.6290	1.6063	1.6161
Present	4.8457	4.0455	2.9444	1.9974	1.6542	1.6110	1.6183

Example 3. An anti-symmetric cross-ply (0º/90º) laminated beam made up of Material 2 with L/h=10 is considered for various boundary conditions. The obtained dimensionless natural frequencies ($\bar{\omega} = \omega L^2 \sqrt{\rho / E_T h^2}$) are compared in Table 3, with the FSDT, higher order shear deformation theory (HSDT) [2] and HSDT with FE Method [8]. The results are in good agreement with references.

Table 3. Comparison of dimensionless natural frequencies of anti-symmetric cross-ply beams

	Boundary conditions			
	C-F	C-C	C-S	S-S
FSDT [2]	−	13.077	9.871	6.883
HSDT [2]	2.544	13.660	10.130	6.945
HSDT-FEM [8]	2.541	13.657	10.124	6.908
Present	2.5337	13.1011	9.8983	6.8725

4. NUMERICAL RESULTS AND DISCUSSION

In this section, natural frequencies and mode shapes are discussed and the effects of various parameters are investigated. All layers have the same thickness

4.1. Natural frequencies and mode shapes of laminated beams

The first 8 dimensionless natural frequencies of 4-layer symmetrically and anti-symmetrically laminated cross-ply and angle-ply composite beams are presented in Tables 4a and 4b, respectively. (Material 2, *L/h*=10, square section). The mode shapes of the first 8 modes are shown in Figures 2-13.

Table 4(a). Dimensionless natural frequencies of symmetrically laminated composite beams

Mode number	Angle-ply ($\theta/-\theta/-\theta/\theta$)							Cross-ply 0/90/90/0
	$\theta = 0$	$\theta = 15$	$\theta = 30$	$\theta = 45$	$\theta = 60$	$\theta = 75$	$\theta = 90$	
1	5.5977	4.1192	2.5874	1.5291	1.1370	1.0283	1.0092	2.7857
2	5.6047	5.4060	2.9271	1.5661	1.1429	1.0311	1.0103	3.5063
3	15.8155	18.9675	14.0617	9.0560	6.8944	6.2694	6.1199	14.9495
4	22.8598	21.3679	17.9574	9.6901	7.0698	6.3606	6.1638	15.4381
5	23.0594	30.0386	21.5193	20.7949	17.6890	15.9981	15.0178	17.3569
6	47.2304	42.0286	33.5231	23.4775	18.3790	16.8443	15.7081	35.3797
7	47.4661	62.1645	45.2326	24.1882	19.4097	17.3862	16.3420	38.9382
8	48.2146	65.9002	48.8151	26.6350	19.8709	18.0538	16.5762	44.4996

Table 4(b). Dimensionless natural frequencies of anti-sym. laminated composite beams

Mode number	Angle-ply ($\theta/-\theta/\theta/-\theta$)			Cross-ply (0/90/0/90)
	$\theta = 30$	$\theta = 45$	$\theta = 60$	
1	2.8039	1.5516	1.1392	2.5859
2	2.8853	1.5783	1.1483	2.7802
3	15.0284	9.2857	6.9438	14.0385
4	17.5187	9.6333	7.0608	14.8257
5	21.9065	21.2165	17.6494	15.4288
6	35.1784	23.9628	18.5150	33.4078
7	44.2363	24.0849	19.3667	34.9788
8	47.4902	26.4406	20.3819	44.4032
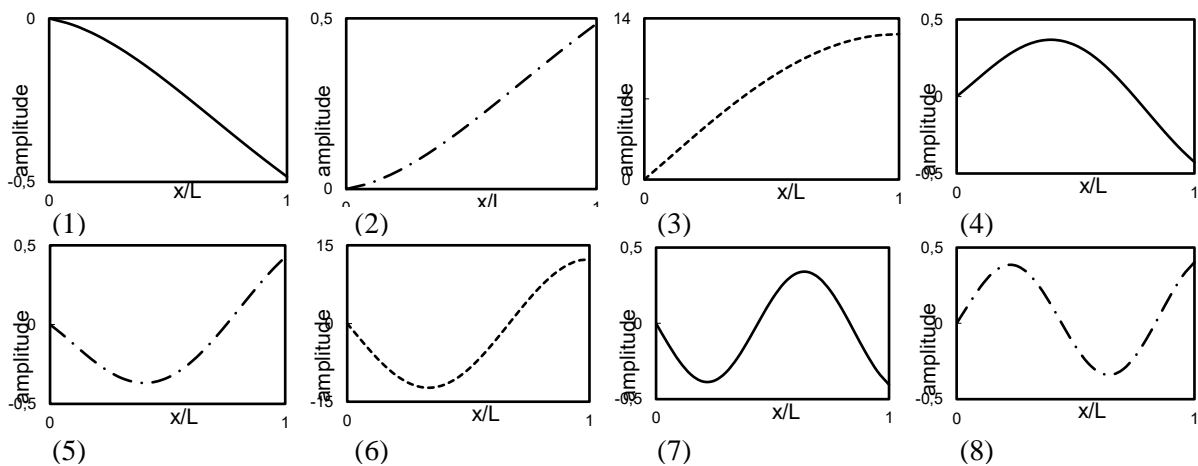
(1) (2) (3) (4)
(5) (6) (7) (8)
Figure 2. First eight modeshapes of (0°/0°/0°/0°) laminated beam.
—— out-of-plane bending; –·–·– in-plane bending; ······· torsion; – – – axial vibrations

The modeshapes for (0°) and (90°) uni-directional laminations are shown in Figures 2 and 8 where all the modes are uncoupled. In Figure 2, the 1st, 4th, and 7th modes are pure out-of-plane bending; the 2nd, 5th and 8th modes are pure in-plane bending; and 3rd and 6th modes are pure torsional modes. In Figure 8, the 1st, 3rd, and 7th modes are pure in-plane bending; the 2nd, 4th and 8th modes are pure out-of-plane bending; the 5th mode is pure torsional, and the 6th mode is pure axial mode.
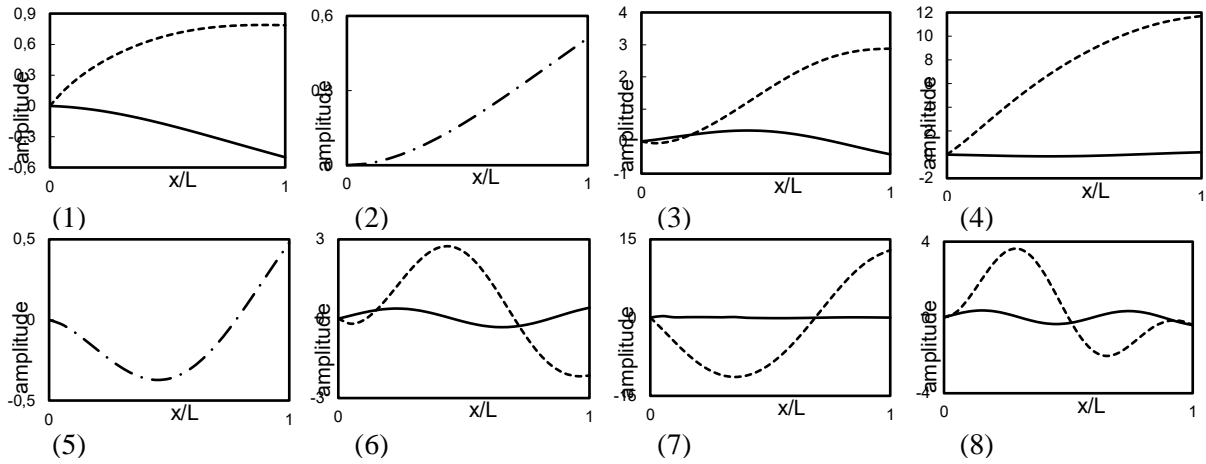
Figure 3. First eight modeshapes of symmetric (15°/-15°/-15°/15°) laminated beam.
──── out-of-plane bending; ─·─·─ in-plane bending; ······· torsion; ─ ─ ─ axial vibrations
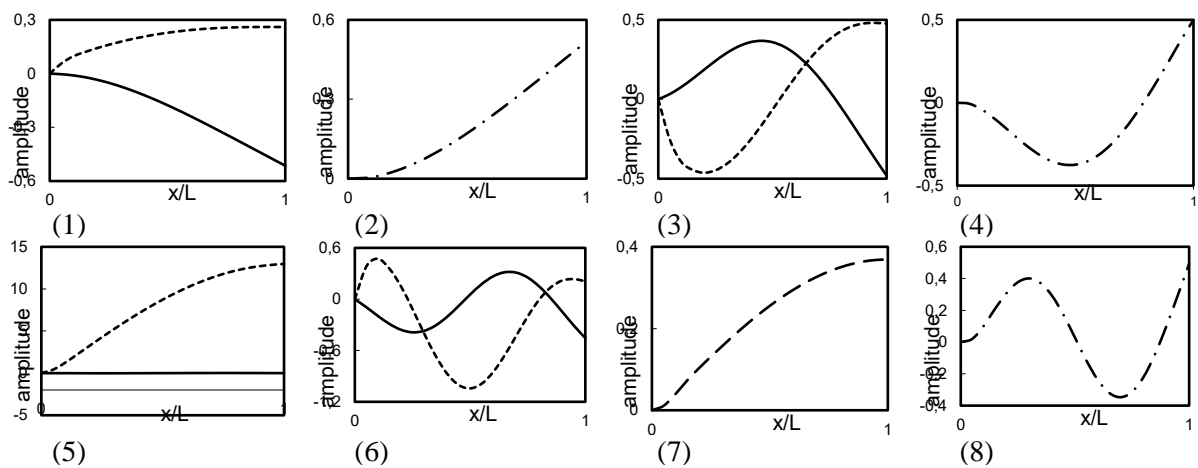
Figure 4. First eight modeshapes of symmetric (30°/-30°/-30°/30°) laminated beam.
──── out-of-plane bending; ─·─·─ in-plane bending; ······· torsion; ─ ─ ─ axial vibrations
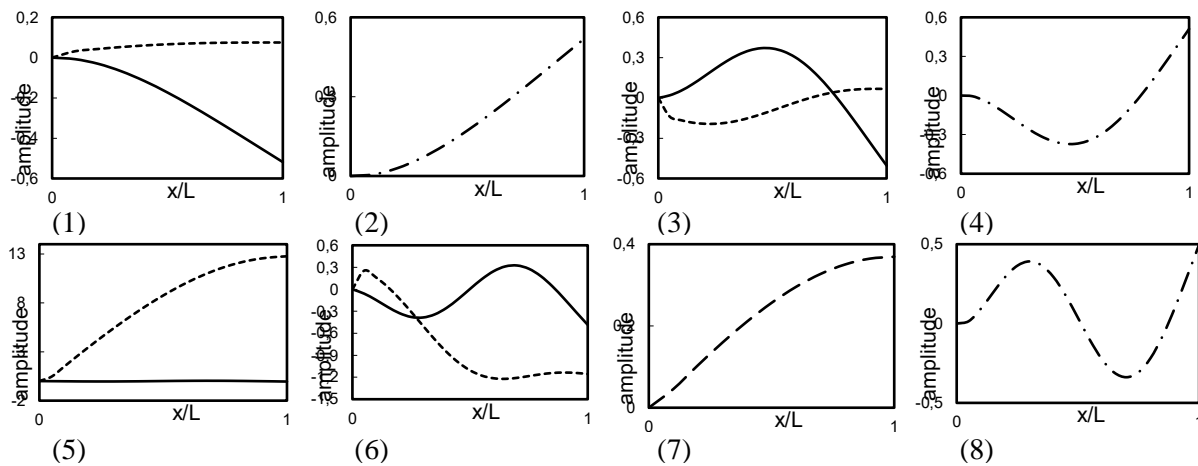
Figure 5. First eight modeshapes of symmetric (45°/-45°/-45°/45°) laminated beam.
──── out-of-plane bending; ─·─·─ in-plane bending; ······· torsion; ─ ─ ─ axial vibrations

In Figures 3-7, the modeshapes for angle-ply symmetric stacking sequences are shown. It is seen that the in-plane bending modes and axial modes are always uncoupled. In Figure 3, the 1st, 3rd, 6th and 8th modes are out-of-plane bending-torsion coupled while the 4th and 7th modes are pure torsional. In Figure 4, the 1st, 3rd and 6th modes are out-of-plane bending-torsion coupled; the 5th mode is pure torsional, and the 7th mode is purely axial.
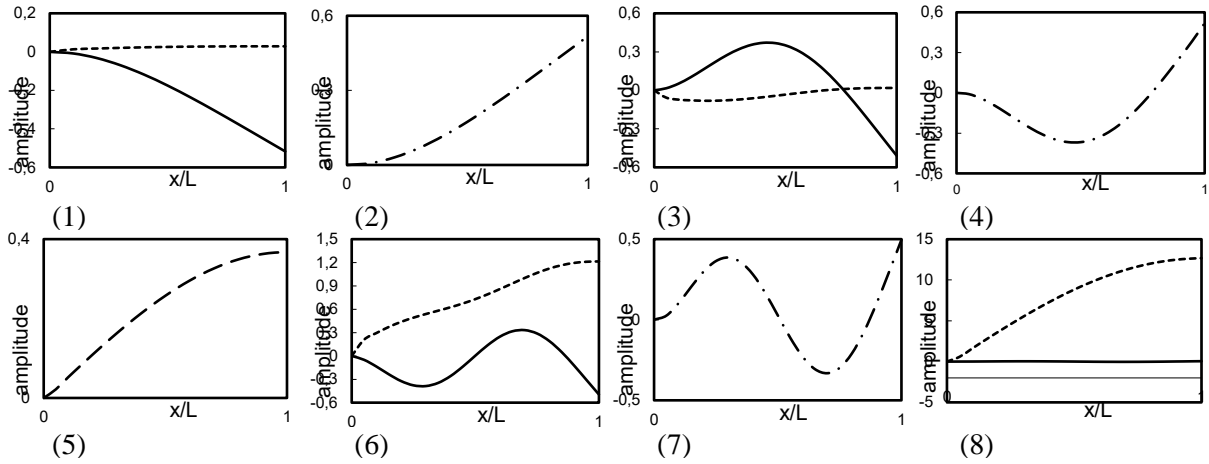
Figure 6. First eight modeshapes of symmetric (60°/-60°/-60°/60°) laminated beam.

——— out-of-plane bending; — · — · — in-plane bending; ······· torsion; — — — axial vibrations
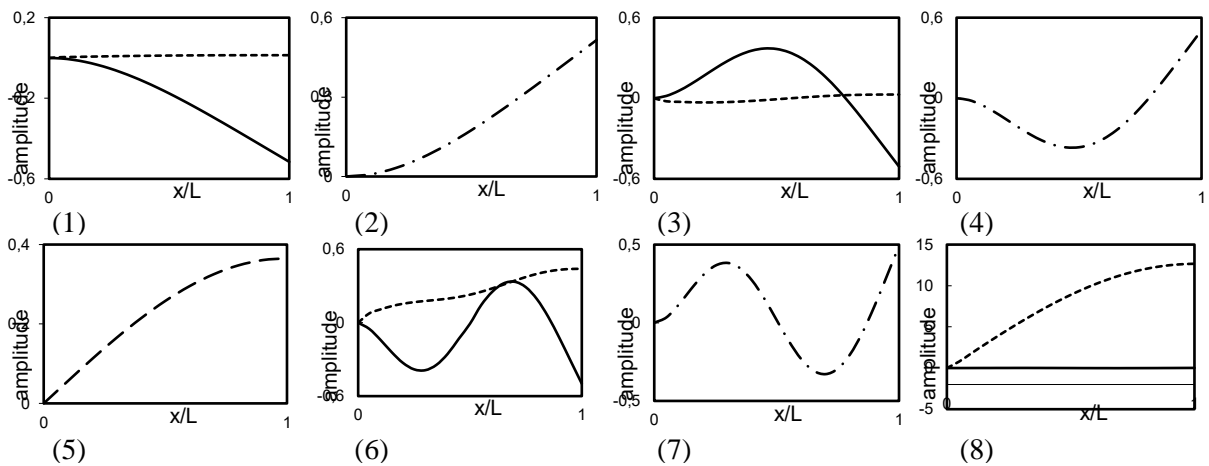
Figure 7. First eight modeshapes of symmetric (75°/-75°/-75°/75°) laminated beam.

——— out-of-plane bending; — · — · — in-plane bending; ······· torsion; — — — axial vibrations
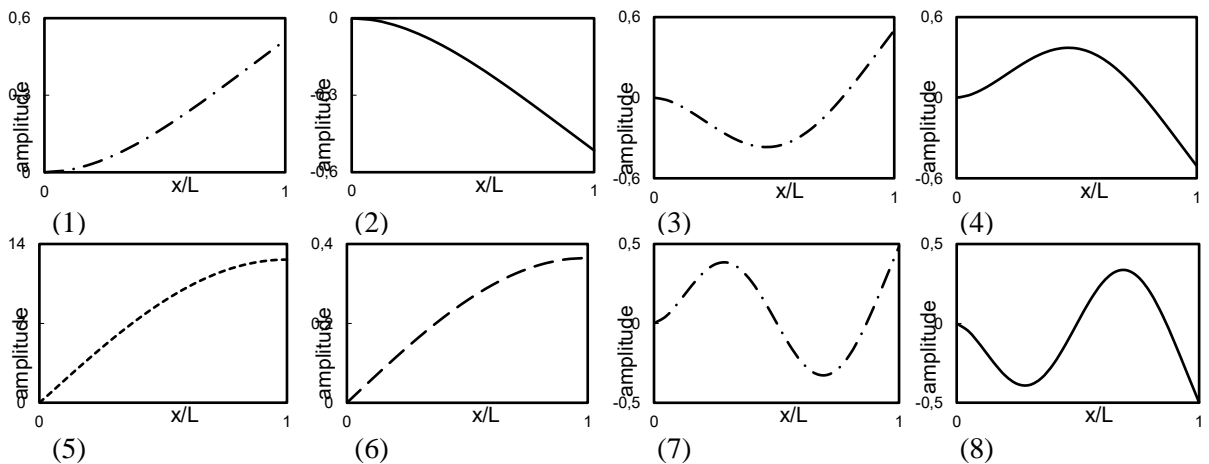
Figure 8. First eight modeshapes of (90°/90°/90°/90°) laminated beam.

——— out-of-plane bending; — · — · — in-plane bending; ······· torsion; — — — axial vibrations

It may be observed from Figure 5 that, in the 1st mode, bending vibrations are almost unaffected by torsion; the 5th mode is pure torsional; the 7th mode is pure axial; the 3rd and 6th modes are coupled modes. Figures 6-7 reveal that, in the 1st and 3rd modes, bending vibrations are almost unaffected by torsion; the 5th modes are pure axial; the 8th modes are pure torsional, and the 6th modes are coupled modes.
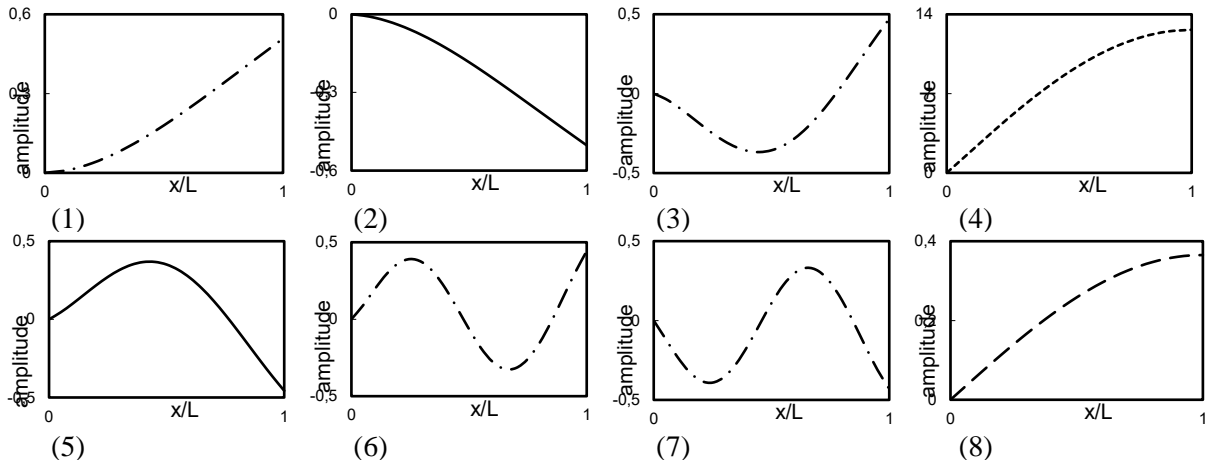
Figure 9. First eight modeshapes of symmetric (0°/90°/90°/0°) laminated beam.
—— out-of-plane bending; –·–·– in-plane bending; ······· torsion; – – – axial vibrations
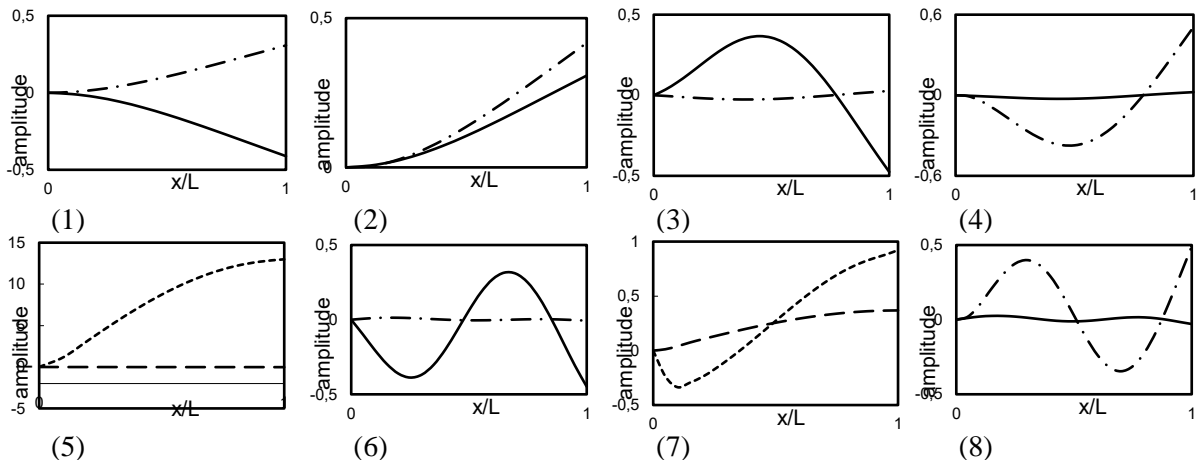
Figure 10. First eight modeshapes of anti-symmetric (30°/-30°/30°/-30°) laminated beam.
—— out-of-plane bending; –·–·– in-plane bending; ······· torsion; – – – axial vibrations
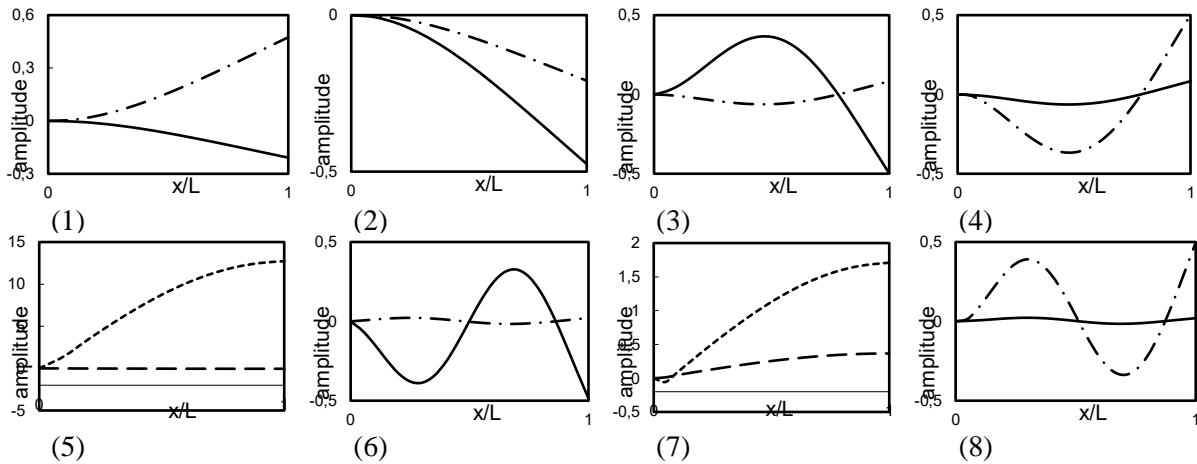
Figure 11. First eight modeshapes of anti-symmetric (45°/-45°/45°/-45°) laminated beam.
—— out-of-plane bending; –·–·– in-plane bending; ······· torsion; – – – axial vibrations

2nd International Students Science Congress
4-5 May 2018, Izmir - Turkey

İZMİR
KÂTİP ÇELEBİ
UNIVERSITY
2010

İZMİR
Uluslararası
Misafir
Öğrenci
Derneği
◆ İZMİR International Guest Student Association

It is obvious that torsional vibration is less sensitive to coupling than bending vibration. Increasing ply angle will decrease the frequencies of axial vibration modes because of decreasing axial rigidity. Frequencies of pure torsional modes increase with the increase in ply angle. Figure 9 presents the modeshapes for symmetric cross-ply lamination where all the modes are uncoupled.
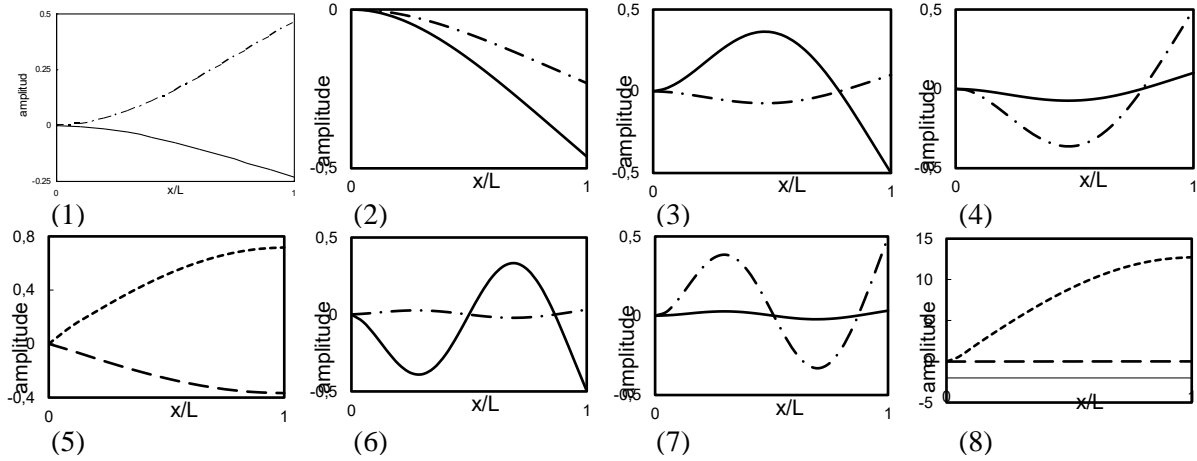
Figure 12. First eight modeshapes of anti-symmetric (60°/-60°/60°/-60°) laminated beam.
—— out-of-plane bending; —·—·— in-plane bending; ······· torsion; − − − axial vibrations
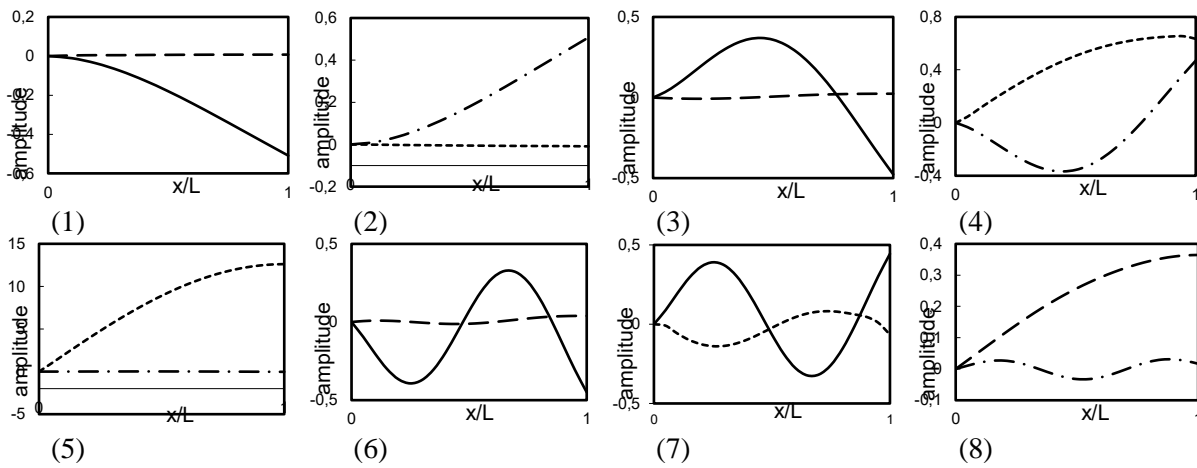
Figure 13. First eight modeshapes of anti-symmetric (0°/90°/0°/90°) laminated beam.
—— out-of-plane bending; —·—·— in-plane bending; ······· torsion; − − − axial vibrations

4.2. Effect of Stacking Sequence

In Figures 10-12, the modeshapes for angle-ply anti-symmetric stacking sequences are shown. Unlike symmetric stacking-sequences, coupling takes place between out-of-plane bending and in-plane bending modes in this case; that is, bending modes are uncoupled from torsional modes. It can be further noted that torsional modes are either uncoupled or coupled with axial modes. The fifth modes in Figures 10 and 11, and the eighth mode in Figure 12 are pure torsional modes. The seventh modes in Figures 10 and 11, and the fifth mode in Figure 12 are axial-torsional coupled modes. In Figure 13, the modeshapes for anti-symmetric cross-ply lamination scheme is displayed. In this case, coupling is evident between in-plane bending and torsional modes. Out-of-plane bending and axial vibration modes are observed to slightly affect each other.

4.3. Effect of Material Orthotropicity

To investigate the effect of degree of orthotropicity of the layers, E_L/E_T ratio of 4-layered angle-ply beams are varied by 1, 2, 5, 10, 20, 40 and 80. Variation of fundamental dimensionless out-of-plane bending and torsional frequencies of angle-ply beams are presented in Figures 14(a) and 14(b), respectively. It is understood from Figure 14(a) that the influence of modulus ratio is to increase the out-of-plane bending frequency of (0°) beam. The effect of modulus ratio on the out-of-plane frequency

decreases as the ply angle increases. It is evident from Figure 14(b) that the modulus ratio has almost no effect on the torsional frequency of (0°) and (90°) beams. In angle-ply beams, increasing orthotropicity ratio will result in an increase in fundamental torsional frequency.
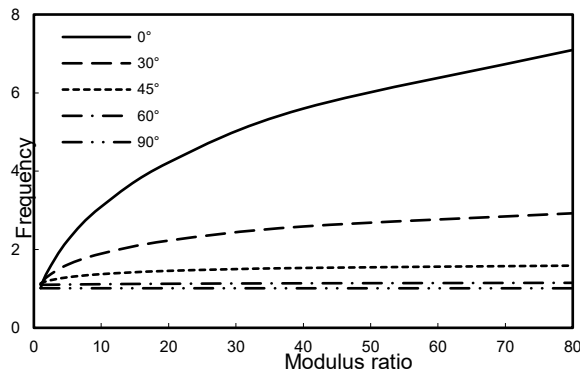
Figure 14(a). Variation of out-of-plane bending frequencies of symmetric angle-ply beams with respect to modulus ratio.
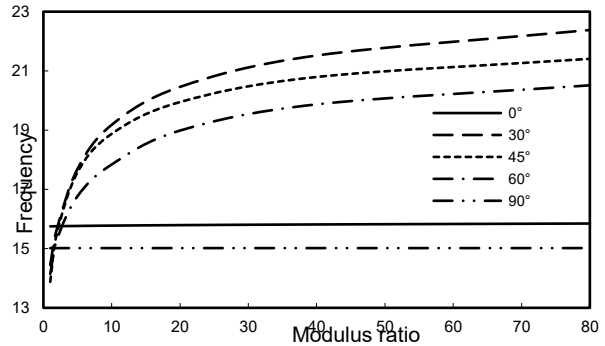
Figure 14(b). Variation of torsional frequencies of symmetric angle-ply beams with respect to modulus ratio.

4.4. Effect of length-to-thickness (*L/h*) ratio

To analyze the effect of *L/h* ratio, the variation of dimensionless out-of-plane and torsional frequencies of angle-ply ($\theta/-\theta/-\theta/\theta$) beams with respect to *L/h* ratio are illustrated in Figures 15(a) and 15(b), respectively. From Figure 15(a) one can conclude that the *L/h* ratio has almost no effect on the dimensionless out-of-plane bending frequency of angle-ply beams. It has an increasing effect merely on (0°) uni-directional beam. As displayed in Figure 15(b), however, increasing *L/h* ratio will result in an increase in the dimensionless torsional frequency for all lamination schemes.
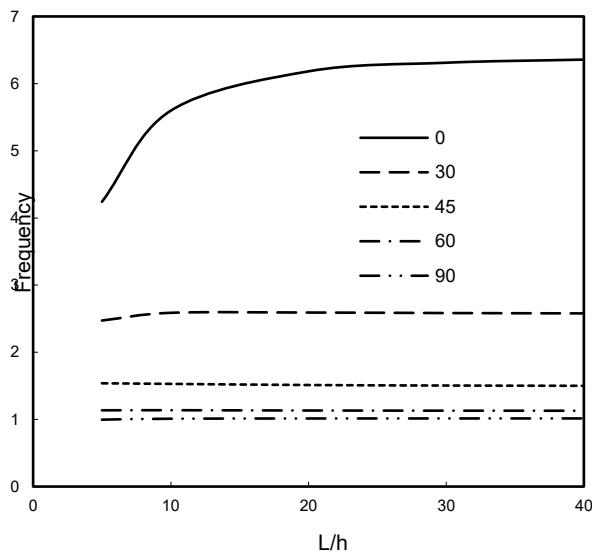
Figure 15(a). Variation of out-of-plane bending frequencies of angle-ply beams wrt *L/h* ratio.
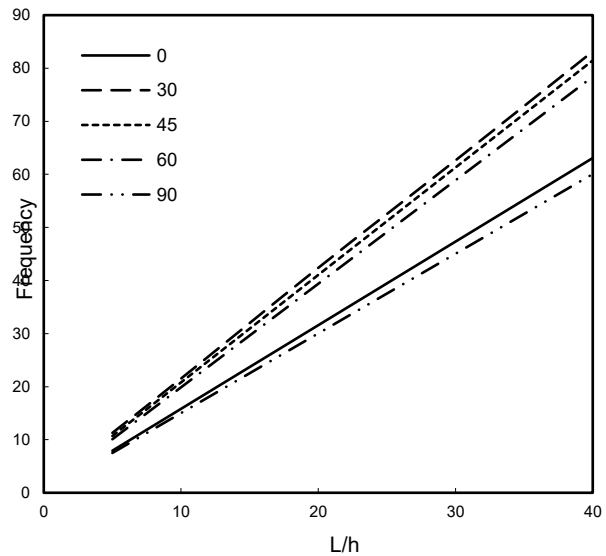
Figure 15(b). Variation of torsional frequencies of angle-ply beams wrt *L/h* ratio.

5. CONCLUSION

Free coupled vibrations of angle-ply and cross-ply laminated composite beams with cantilever end conditions are analyzed by using ANSYS. The following conclusions are drawn from this study:

1. In symmetric cross-ply beams and when the ply angle is 0 or 90°, out-of-plane, in-plane, torsional and axial modes are all uncoupled.
2. In symmetric angle-ply beams, coupling occurs between out-of-plane bending and torsion modes; torsional vibration is less sensitive to coupling than bending vibration. In-plane bending and axial modes are absolutely uncoupled in this case.

3. In symmetric angle-ply beams, increase in ply angle will result in an increase in pure torsional frequencies and in a decrease in axial frequencies. Out-of-plane and in-plane bending frequencies also decrease with increasing ply angle.

4. In anti-symmetric angle-ply beams, coupling takes place between out-of-plane bending and in-plane bending modes; i.e. bending modes are uncoupled from torsional modes. Torsional modes are either uncoupled or coupled with axial modes.

5. In anti-symmetric cross-ply beams, coupling is evident between in-plane bending and torsional modes. Out-of-plane bending and axial vibration modes are observed to slightly affect each other.

6. The effect of modulus ratio is to increase the out-of-plane frequency of the angle-ply beam but this effect decreases significantly as the ply angle increases. Increasing modulus ratio will result in an increase in torsional frequency but it has almost no effect on (0°) and (90°) beams.

7. Dimensionless torsional frequency increases with the increase in *L/h* ratio, irrespective of the lamination scheme.

REFERENCES

[1] K. Chandrashekhara, K. Krishnamurthy, S. Roy, Free vibration of composite beams including rotary inertia and shear deformation, Composite Structures 14 (1990) 269-279.

[2] A.A. Khdeir, J.N. Reddy, Free vibration of cross-ply laminated beams with arbitrary boundary conditions, International Journal of Engineering Science 32 (1994) 1971-1980.

[3] P. Si, B. Basa, Free vibration analysis of laminated composite beams, Indian Journal of Scientific Research 14(2) (2017) 270-275.

[4] H. Matsunaga, Vibration and buckling of multilayered composite beams according to higher order deformation theories, Journal of Sound and Vibration 246(1) (2001) 47-62.

[5] M. Aydoğdu, Vibration analysis of cross-ply laminated beams with general boundary conditions by Ritz method, International Journal of Mechanical Sciences 47(11) (2005) 1740-1755.

[6] M. Tahani, Analysis of laminated composite beams using layerwise displacement theories, Composite Structures 79(4) (2007) 535-547.

[7] R.-A. Jafari-Talookolaei, M. Abedi, M. Attar, In-plane and out-of-plane vibration modes of laminated composite beams with arbitrary lay-ups, Aerospace Science and Technology, 66 (2017) 366-379.

[8] M.V.V.S. Murthy, D.R. Mahapatra, K. Badarinarayana, S. Gopalakrishnan, A refined higher order finite element for asymmetric composite beams, Composite Structures 67(1) (2005) 27-35.

[9] V. Yıldırım, E. Kıral, Investigation of the rotary inertia and shear deformation effects on the out-of-plane bending and torsional natural frequencies of laminated beams, Composite Structures 49(3) (2000) 313-320.

[10] M.H. Kadivar, S.R. Mohebpour, Finite element dynamic analysis of unsymmetric composite laminated beams with shear effect and rotary inertia under the action of moving loads, Finite Elements in Analysis and Design 29(3-4) (1998) 259-273.

[11] J.R. Banerjee, Explicit analytical expressions for frequency equation and mode shapes of composite beams, International Journal of Solids and Structures 38(14) (2001) 2415-2426.

[12] G.S. Ramtekkar, Y.M. Desai, A.H. Shah, Natural vibrations of laminated composite beams by using mixed finite element modelling, Journal of Sound and Vibration 257(4) (2002) 635-651.

Assessment and Comparison of the Performance of a Deep Learning Based Face Recognition System Built on Two Different Platforms

Sufiyan N-Yo *, Ergun Erçelebi
University of Gaziantep, Dept. of Electrical and Electronics Engineering, Gaziantep, Turkey
*Corresponding author: nyoaksufiyan@gmail.com

INTRODUCTION

The goal of this paper is to present the results and compare the performance assessment of a deep learning based face recognition system built on both the Raspberry Pi 3B and a typical Intel Core i7 processor.

Face recognition has been an active research field since the 1970's [1]. Over the years many methods were developed, most of them achieved good performance. Recent advancement of machine learning and deep learning techniques has accelerated the performance (accuracy and speed) of face recognition systems significantly. Face recognition systems are mainly used for security and entertainment purposes. However, these recent deep learning based face recognition systems require a large amount of data and huge computational resources to run in real time.

In this project, we implemented and tested a pre-trained deep learning based face recognition system on both an inexpensive embedded system (Raspberry Pi 3B) and a typical Intel Core i7 processor Dell laptop. Our main aim is to assess and compare the performance (accuracy and speed) of these two systems in order to find out if both the Raspberry Pi 3B and the typical Intel Core i7 processor laptop can support real-time face recognition while using recent deep-learning techniques.

METHOD

In the literature, there are many methods to chose from but we selected the best and most recent deep learning based method called 'Face_recognition'[2]. The system is classified into 2 main parts, face detection, and face recognition part. We used a combination of different deep learning and machine learning algorithms such as Convolutional Neural Networks (CNNs) [3], Histogram of Oriented Gradients (HOG) [4], Support Vector Machines (SVM) [5] and open source libraries. We followed four major steps for realizing this project: face detection, face posing and projecting, face encoding and classification this is shown in Figure 1. For the face detection, we used the HOG method because it is faster. After detecting the face we used a modified version of face landmark estimation algorithm [6] to generate 5 face landmarks that reposition and center the face before passing it on to a pre-trained face_recognition model built with CNN which generates 128 embeddings for the face. We then used an SVM classifier to identify the face.
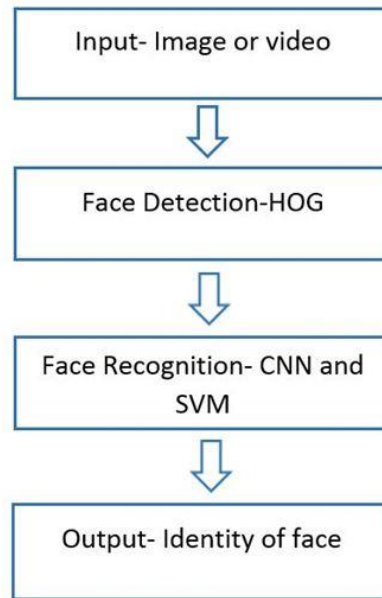
Figure 1. General structure of the face recognition system

EXPERIMENTS AND RESULTS

We tested our system on both platforms with a small dataset of 40 images including 8 different people. We carried out all experiments using Python as the programing language. Our system was able to detect and classify faces with approximately 96.88% accuracy on both platforms. Table 1 and 2 show the results of the time analysis of the recognition system on the Raspberry Pi 3 B and Intel core i7 laptop respectively using test images of four different sizes. Even with the smallest size test image (180 pixels), the Raspberry Pi 3B took 2.88s (0.35fps) as compare to 0.33s (3.06 fps) for the typical Intel Core i7. The face location step, in particular, took longer to complete in both platforms. This is because both our platforms use only a single CPU core. This can be improved by using a GPU for the recognition.

The results show that the Raspberry Pi 3B is slow to run the CNN based recognition system in real time while the typical Intel Core i7 processor has achieved real-time face recognition. The runtime performance of the Raspberry Pi 3B can be improved by running all of its 4 CPU cores at the same time. Our results show that recent deep-learning methods are equally applicable to platforms with limited computational resources.

Table 1. Time analysis of the system on Raspberry Pi 3B

Image Size [p]	Face Locations Time		Face Landmarks Time		Encode Face Time		End-to-End Time	
	s	fps	s	fps	s	fps	s	fps
180	2.25	0.44	0.02	46.45	0.63	1.58	2.88	0.35
240	4.11	0.24	0.02	46.14	0.62	1.60	4.73	0.21
450	14.89	0.07	0.02	45.30	0.62	1.60	15.61	0.06
730	39.87	0.03	0.02	44.91	0.62	1.60	40.23	0.02

Table 2. Time analysis of the system on a typical Intel Core i7 processor

Image Size [p]	Face Locations Time		Face Landmarks Time		Encode Face Time		End-to-End Time	
	s	fps	S	fps	s	fps	s	fps
180	0.18	5.55	0.01	110.45	0.12	8.24	0.33	3.06
240	0.31	3.23	0.01	111.37	0.13	7.46	0.50	2.00
450	1.06	0.94	0.01	111.26	0.14	7.30	1.24	0.81
730	2.72	0.37	0.01	108.68	0.14	7.31	2.89	0.35

The system was also tested for accuracy on both platforms. A total of 8 images of 8 different individuals was used to train the CNN. We tested the system on 32 test images and a live video test was also carried out. Figure 2 shows the training dataset while Figure 3 shows the results of the accuracy experiments. Then we tested our system on live video, which is shown in Figure 4. Our system reached a performance of 96.88% accuracy for both platforms which is near the reported 99.38% [2] of the original method used.

Figure 2. Training dataset
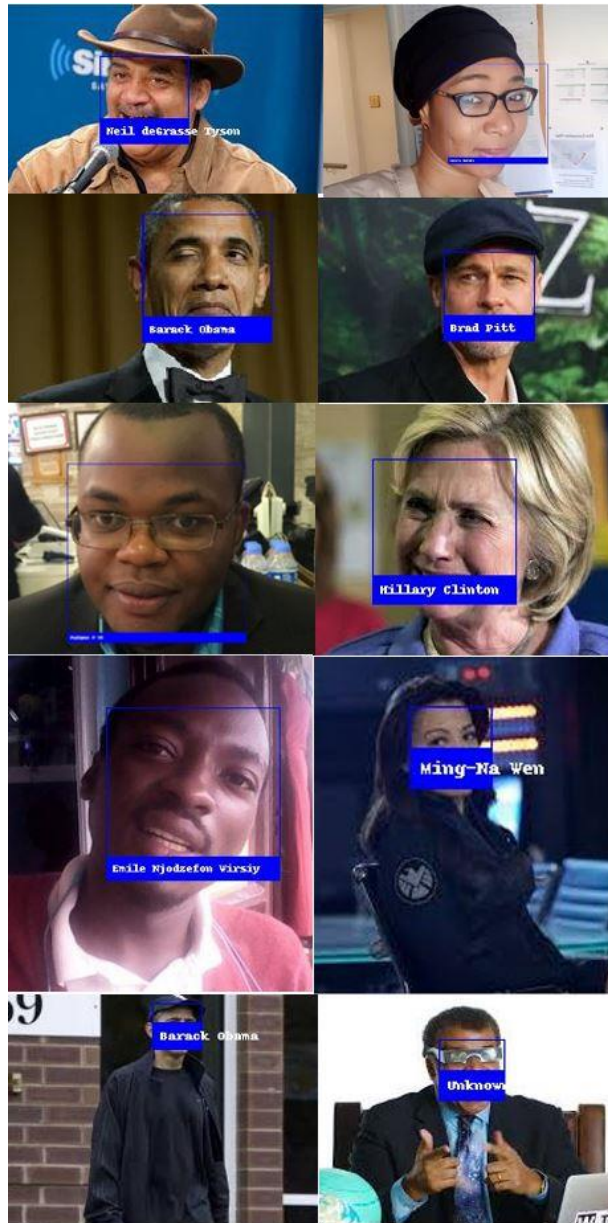
Figure 3. Results after experiments

Figure 4. Detected and recognized face from a live video

CONCLUSION

Our experiments and results show inexpensive hardware such as the Raspberry Pi 3 and a typical Intel Core i7 can support the recent deep learning based face recognition systems in terms of accuracy. However, the Raspberry Pi 3B does not support real-time face recognition using the pre-trained 'Face_recognition' method.

REFERENCES

[1] Takeo Kanade, Picture processing system by computer complex and recognition of human faces. Doctoral dissertation, Kyoto University. (1973) 3952:83–97.

[2] Adam G., Ageitgey/face_recognition. [Online] Available at: https://github.com/ageitgey/face_recognition#face-recognition, 2017 [Accessed 24 Feb. 2018].

[3] Yoshua B., Goodfellow Ian J., Aaron C., *Deep learning*, Book in preparation for MIT Press, 2015.

[4] N. Dalal and B. Triggs, Histograms of oriented gradients for human detection, inProc. IEEE Int. Conference on Computer Vision Pattern Recognition. (2005), pp. 886–893.

[5] B. Amos, B. Ludwiczuk, M. Satyanarayanan. OpenFace: A general-purpose face recognition library with mobile applications. CMU-CS-16-118, CMU School of Computer Science, Tech. Rep., 2016.

[6] Kazemi V., Josephine S. One millisecond face alignment with an ensemble of regression trees, In CVPR, Columbus, OH, USA ,ISSN:1063-6919., 10.1109/CVPR. (2014) 1867-1874.

Eğitsel Mobil Uygulama Tasarımı

Ali Özdemir, Manisa Celal Bayar Üniv., Matematik Bölümü, Manisa, Türkiye
Ayşegül Alaybeyoğlu, İzmir Katip Çelebi Üniv., Bilgisayar Mühendisliği Bölümü, Çiğli Ana Kampüs, İzmir, Türkiye
Kadriye Filiz Balbal*, Manisa Celal Bayar Üniv., Matematik Bölümü, Manisa, Türkiye
*İletişimden sorumlu yazar: kfbalbal@gmail.com

Özet

Günümüzde mobil teknolojiler hayatımızın her alanında gittikçe artan bir öneme sahiptir. Bireyler günlük işlerini halletmek, eğlenmek, öğrenmek gibi ihtiyaçlarını karşılamak için mobil teknolojileri kullanmaktadırlar. Zamandan ve mekândan bağımsız olması ve kolaylıkla kullanılabiliyor olması, mobil teknolojilerin en önemli özelliklerindendir. Ayrıca, her yaştan bireye de hitap etmektedir. Daha çok oyun ve eğlence amacıyla kullanılan mobil teknolojilerin eğitim alanında da kullanılması kaçınılmazdır. Ancak, eğitsel amaçlı geliştirilen mobil uygulama sayısı yeterli değildir. Eğitim alanında daha çok ve çeşitli mobil uygulama geliştirilmesine ihtiyaç vardır. Çalışmamızda, bu ihtiyaca yönelik eğitsel bir mobil uygulama tasarımı gerçekleştirilmiştir.

Anahtar Kelimeler: mobil uygulama, mobil öğrenme, eğitsel, tasarım
Disiplin: Bilgisayar Bilimi ve Mühendisliği

1. GİRİŞ

Ülkemizde eğitsel mobil uygulama konusu henüz yeni sayılabilecek bir konudur. Daha çok oyun ve eğlence amacıyla kullanılan mobil uygulamalar yaygındır. Mobil uygulamaların eğitim alanında da kullanılması kaçınılmazdır. Ancak, eğitsel amaçlı geliştirilen mobil uygulama sayısı yeterli değildir. Eğitim alanında daha çok ve çeşitli mobil uygulama geliştirilmesine ihtiyaç vardır. Çalışmamızda, bu ihtiyaca yönelik eğitsel bir mobil uygulama tasarımı gerçekleştirilmiştir. [1]'de mobil öğrenme ortamlarının, yaşam boyu öğrenme, fakında olmadan öğrenme, ihtiyaç anında öğrenme, zaman ve mekandan bağımsız öğrenme, yer ve şartlara göre ayarlanan öğrenme gibi avantajlara sahip olduğu belirtilmektedir. [2]'de eğitim teknolojilerinin temelinde bilginin sahip olduğu dolaşım ve paylaşım hızına erişme amacının olduğu belirtilmektedir. Eğitimde mobil uygulamalara yönelik yapılan çok sayıda araştırma mevcuttur [3-6]. Önerilen eğitsel mobil uygulama, öğrencilerin sosyal bilgiler dersinde veya tarih dersinde birçok tarihi ve turistik öneme sahip yerleri öğrenmesinden yola çıkılarak geliştirilmiştir. Derslerde öğrenilen yerlere gidip görmek, öğrenmenin kalıcılığı açısından önemlidir. Ancak her öğrenci bu imkâna sahip değildir. Geliştirdiğimiz eğitsel mobil uygulama ile öğrencilerin fiziksel olarak bu yerlere gidemeseler bile, bir nebze de olsa bilgilenme şansları olması ve öğrendiklerini pekiştirerek kalıcı bir şekilde öğrenmeleri beklenmektedir. Çalışma kapsamında geliştirilen eğitsel mobil uygulama, İzmir'in tarihi ve turistik yerlerini sanal ortamda görme ve gezme imkânı sunmaktadır.

2. GELİŞTİRİLEN EĞİTSEL MOBİL UYGULAMA

Şekil 1'de tasarlamış olduğumuz sistemin ara yüz görüntüleri verilmiştir. Çalışma kapsamında geliştirilen eğitsel mobil uygulama, İzmir'in tarihi ve turistik yerlerini sanal ortamda görme ve gezme imkânı sunmaktadır. Öğrenciler, sosyal bilgiler dersinde veya tarih dersinde öğrendikleri tarihi yerleri, geliştirilen eğitsel mobil uygulama ile mobil cihazlarından sanal olarak kolayca görebilmekte ve sanal tur atabilmektedir. Böylece, öğrencilerin fiziksel olarak bu yerlere gitme ve görme imkânları olmasa bile geliştirdiğimiz uygulama sayesinde bir nebze de olsa bilgilenme şansları olmakta, öğrendiklerini pekiştirerek kalıcı bir şekilde öğrenmektedirler. Çalışma kapsamında geliştirilen mobil uygulamada öğrenciler, bu tarihi ve turistik yerlerin tarihi önemi ile ilgili kısaca bilgi edinebilmektedirler. Çalışmamızda sadece İzmir'in tarihi ve turistik yerlerine yönelik bir eğitsel mobil uygulama tasarımı yapılmıştır. Ülkemizin her karış toprağındaki tarihi zenginlik göz önüne alındığında, gelecek çalışmalarda daha kapsamlı mobil uygulama tasarımlarının yapılabileceği düşünülmektedir. Tasarlamış olduğumuz sistem ile öğrenci görmek istediği mekânı seçince, telefonunu çevresinde döndürdüğünde seçtiği yerin çevresini görebilmektedir. Kullanıcı isterse seçtiği tarihi ve turistik yerin önemi ile ilgili

bilgi de edinebilmektedir. Kullanıcı, görmek ve bilgi edinmek istediği tarihi ve turistik yeri açılan listeden seçebilmektedir. Böylece Öğrenciler, sosyal bilgiler dersinde veya tarih dersinde öğrendikleri tarihi yerleri, geliştirilen eğitsel mobil uygulama ile mobil cihazlarından sanal olarak kolayca görebilmekte ve sanal tur atabilmektedir. Çalışmanın gerçekleştiriminde MIT App Inventor 2 teknolojisinden yararlanılmıştır.

(a)

(b)
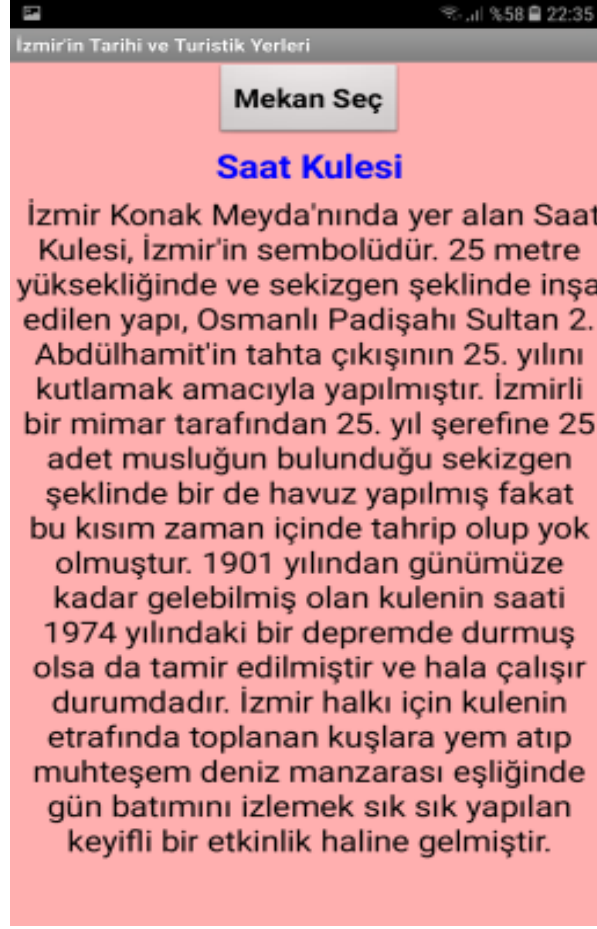
(c)

(d)

Şekil 1. Sistem Arayüzleri

3. SONUÇ

Bu çalışmada öğrencilerin sosyal bilgiler dersinde veya tarih dersinde öğrendikleri tarihi yerleri, mobil cihazlarından sanal olarak kolayca görebilecekleri ve sanal tur atabilecekleri bir mobil uygulaması geliştirilmiştir. Öğrencilerin bizzat ziyaret edipte göremeyecekleri tarihi ve turistik yerleri sanal ortamdan göstererek öğrendikleri bilgilerin daha kalıcı olması sağlanması hedeflenmiştir. Çalışma kapsamında İzmir'in tarihi ve turistik yerlerine yönelik bir eğitsel mobil uygulama tasarımı yapılmıştır. Gelecek çalışmalarda daha kapsamlı mobil uygulama tasarımlarının gerçekleştirilmesi planlanmaktadır. Ayrıca geliştirilen sistem sosyal bilgiler ve tarih dersini alan öğrenciler üzerinde uygulanıp, anket çalışmaları ile görüşler alınarak analizler yapılması ve geliştirilen sistemin öğrencinin öğrenmesi üzerindeki etkisinin incelenmesi düşünülmektedir.

REFERANSLAR

[1] M. Bulun, B. Gülnar, M. S. Güran, Eğitimde mobil teknolojiler, The Turkish Online Journal of Educational Technology, 3(2) (2004) 165-169.

[2] M. Barkan, Eğitim İletişiminin Kavramsal Temelleri ve İşlevleri, Anadolu Üniversitesi İletişim Bilimleri Fakültesi Yayınları, Eskişehir, 1994.

[3] N. Menzi, N. Önal, E. Çalışkan, Mobil teknolojilerin eğitim amaçlı kullanımına yönelik akademisyen görüşlerinin teknoloji kabul modeli çerçevesinde incelenmesi. Ege Eğitim Dergisi, 13(1) (2012).

[4] A. H. Işık, O. Özkaraca, İ. Güler, Mobil Öğrenme ve Podcast. XII. Akademik Bilişim (2011).

[5] M. K. Oran, Ş. Karadeniz, İnternet tabanlı uzaktan eğitimde mobil öğrenmenin rolü, Akademik Bilişim'07-IX. Akademik Bilişim (2007).

[6] Mobil Eğitim ve Örnek Uygulamalar. https://prezi.com/bed3e5yqukah/mobil-egitim-ve-ornek-uygulamalar/, 2015 (9 Ağustos 2018'de ulaşılmıştır)

Three-Phase Modular Multilevel Converter (MMC) Inverter Simulation

Emile N. Wirsiy*, Ahmet M. Vural
Gaziantep University, Dept. of Electrical & Electronics Engineering, Gaziantep, Turkey
*Corresponding author: wirsiyemile@gmail.com

Abstract
Detailed models of the modular multilevel converter (MMC) are not as common as equivalent circuit and simplified models. This paper proposes a detailed model of an inverter built using half bridge sub module topology. MMCs have been getting a lot of attention recently because of their superior characteristics like redundancy, scalability etc. when compared to other voltage source converter (VSC) types. Sub module capacitor voltages and circulating currents are some issues which are normally associated with MMCs. Most researchers have used additional control circuits to curb them but these circuits increase size and cost of the overall system. In this work, a modulation technique known as carrier phase shifted sinusoidal pulse width modulation (CPS-SPWM) has been realized which tries to reduce the capacitor voltage fluctuations in submodules without an additional circuit. The proposed inverter has been verified in a simulation environment and results as well as total harmonic distortion analysis obtained are satisfactory.

Keywords: modular multilevel converter, carrier phase shift, Half Bridge Sub-Module, simulation
Discipline: Electrical Engineering

INTRODUCTION
Most industrial applications require medium or high power for proper functioning. Power converters hold the solution to this as well as ever increasing power demands and play a vital role in the power industry. Nowadays, the MMC is a major topic for research because of their numerous advantages and simplicity. MMCs are mostly utilized in HVDC and FACTS applications.

Diode clamped, flying capacitor, cascaded H-bridge converters are all multilevel converters like MMC that use DC voltage to produce a stair-like AC sinusoidal output in which the number of output stairs increases with the increase in the number of levels [1]. MMC introduced in 2002 by Rainer Marquardt differs from the former and all voltage source converters in their redundancy, modular design, low harmonic and switching frequency, reduced converter losses and their highly scalable nature [2].

Many models have been proposed in the past including detailed models [4], average value models [3], equivalent circuit models and simplified models [5]. Reference [5] proposed a detailed and efficient simplified MMC model for electromagnetic transient (EMT) simulation programs with a reduction in the simulation time. A Thevenin equivalent MMC model and control circuit was introduced in reference [6]. Detailed MMC models always take much time when being simulated and the sub module structure to be used in the building of a converter has to be decided on by the researcher. Reference [3] reduced the computational time of the MMC model by using resistors in place of IGBTs as well as voltage sources and diodes. Reference [4] proposed an MMC model with circulating control strategy and capacitor voltage balancing control in addition with the CPS-SPWM. Though this model was accurate, the extra control circuits greatly increase the size and cost of the overall system.

This paper presents a detailed simulation model of an inverter (DC to AC) which uses a modulation technique that tries to mitigate capacitor voltage fluctuations between sub modules. The detailed model that has been proposed uses the CPS-SPWM technique which provides satisfactory results when verified in a simulation environment without any additional control circuit or filters. The total harmonic distortion (THD) of the output AC voltages and currents has also been analyzed.

METHOD AND RESULTS
The fundamental building blocks of an MMC are the modulation technique and the circuit components. Figure 1 shows the implementation of the inverter model and the half bridge topology is shown in Figure 2. The MMC is made up of 6 arms; 3 upper arms and 3 lower arms. These arms are sub modules connected in series to one another. One phase consists of an upper arm and a lower arm. Half bridge (HB) or full bridge (FB) sub modules of MMC can be used. HB submodules are made up of two IGBTs, two anti-parallel diodes and a DC storage capacitor. A sub module can either be inserted or

bypassed. HB modules have been chosen because of their low semiconductor losses and their low cost. In this work the carrier phase shifting sinusoidal pulse width modulation (CPS-SPWM) method provides the gate signals of the IGBTs of the series connected HB sub modules. Four triangular waves with a phase difference of $90°$ are compared with a reference sine wave and the resulting pulses serve as gate signals to the IGBTs. Four (n) sub modules give rise to five $(n + 1)$ output voltage levels which can be seen in Figure 1 below. The necessary MMC equations used for calculation of circuit parameters are

$$V_c = \frac{V_{dc}}{n} \tag{1}$$

$$n_{carriers} = n_{levels} - 1 = 5 - 1 = 4 \tag{2}$$

$$\varphi_{carriers} = \frac{360°}{n_{carriers}} = \frac{360°}{4} = 90° \tag{3}$$

$$V_{AC} = \frac{V_{DC}}{2} * m \tag{4}$$

The following parameters are used; $V_{dc} = 10KV$, modulation index $m = 0.9$, n=4, sub module capacitor voltage $V_c = 2.5KV$ which can be substituted into Equation (4) above to calculate the expected peak AC voltage

The DC voltage is divided into half between the upper arm and the lower arm and at a particular time, only four sub modules are inserted per phase while the others are bypassed. A load of 10Ω is connected across the AC output and the results have been plotted in Figures 3, 4 and 5.
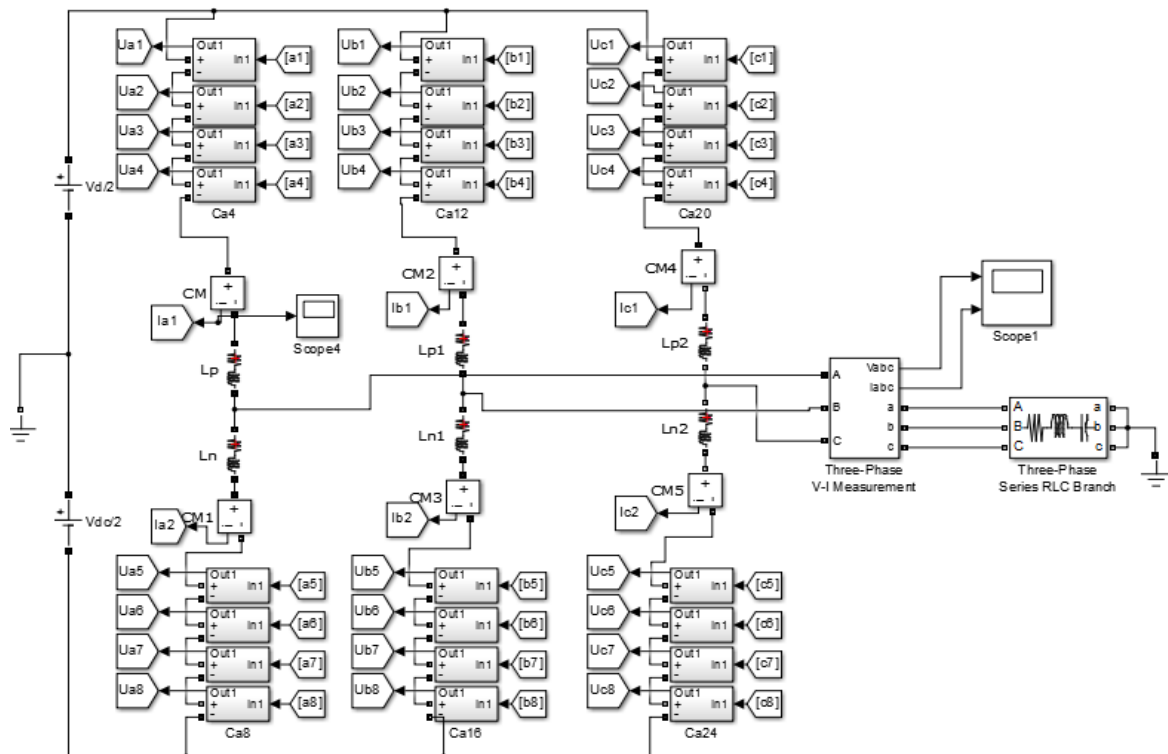
Figure 1. Inverter implementation.

2ⁿᵈ International Students Science Congress
4-5 May 2018, Izmir - Turkey

İZMİR
KÂTİP ÇELEBİ
UNIVERSITY
2010

İZMİR
Uluslararası
Misafir
Öğrenci
Derneği
◆ İZMIR International Guest Student Association
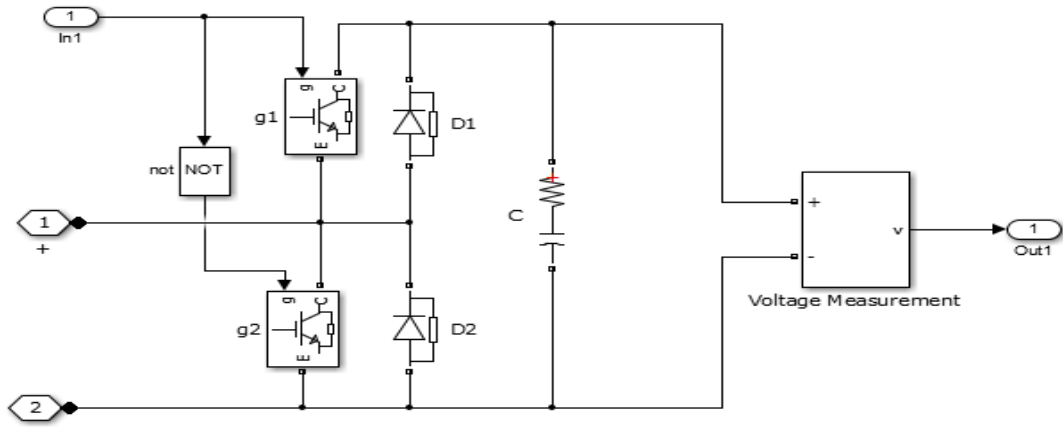
Figure 2. HB sub module topology.

The line to neutral AC voltage and current obtained at the output is plotted against time below;
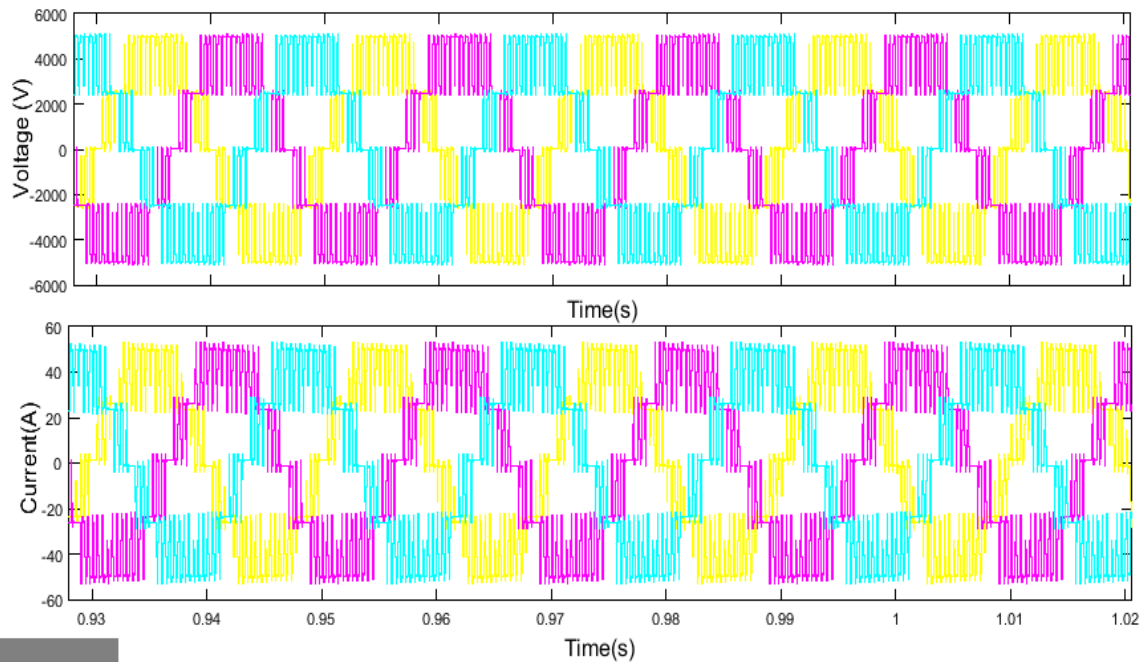
Figure 3. Three-Phase AC output.

A staircase waveform can be seen from Figure 3 which is a result of the four HB sub modules in a given phase arm. The amplitude of the AC voltage is approximately equals to $5KV$ which is the same value gotten when the calculations are done using Equation (4).

42

(a)

(b)
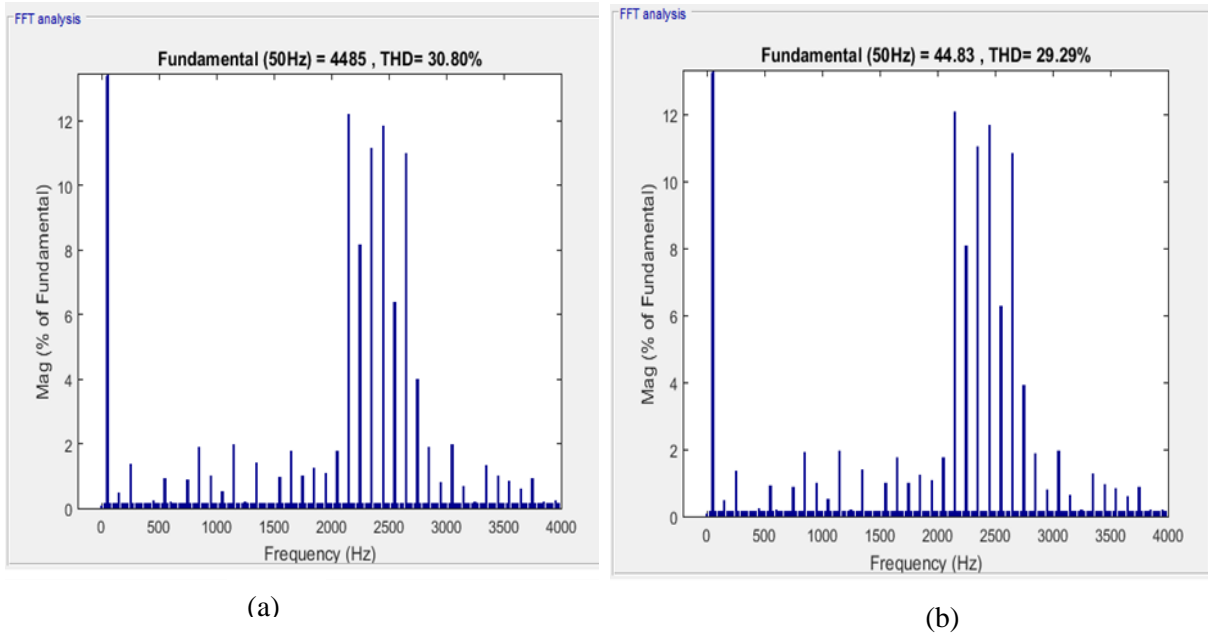
Figure 4. FFT and THD analysis.

Total harmonic Distortion (THD) of the line to neutral voltage as well as current is done and the results are presented in Figure 4(a) and 4(b), respectively. THD values are 30.80% and 29.29% for voltage and current in a 5-level MMC inverter. These results are logical given that only four submodules have been used per arm.
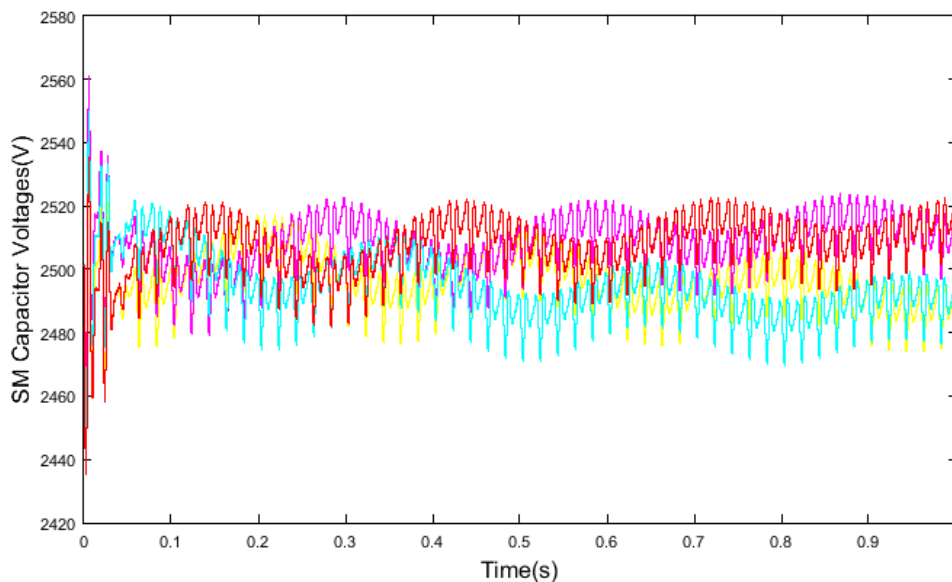
Figure 5. Sub module capacitor voltages of one arm.

The CPS-SPWM technique makes sure that the upper and lower arms are inversely commutated reason why $n + 1$ output levels exist [7]. The number of inserted sub modules are always constant that is why the capacitor voltage fluctuations are greatly reduced as shown in Figure 5.

CONCLUSION

The output voltage in Figure 3 is a five-level staircase waveform as expected since four half bridge MMC sub modules per arm are used. Total harmonic distortion (THD) of the corresponding output

43

voltage is 30.7% which can be reduced by adding more half bridge submodules per arm. Capacitor voltages of submodules are approximately equal to the expected value V_c showing that the modulation technique tries to balance them. MMC superior characteristics can be verified from this detailed model especially the little or no filter requirement characteristics of this type of VSCs.

REFERENCES

[1] J-S. Lai and F. Z. Peng, Multilevel converters-a new breed of power converters, IEEE Transactions on Industry Applications, 32 (1996) 509-517.

[2] R. Marquardt, A. Lesniscar, An innovative modular multilevel converter topology suitable for a ide power range, 2003 IEEE Bologna PowerTech Conference, 2003, Italy.

[3] H. Saad, K. Jacobs, W. Lin and D. Jovcic, Modelling of MMC including half-bridge and Full-bridge sub modules for EMT study, 2016 Power Systems Computation Conference, Genoa, 2016, pp. 1-7

[4] S. C. Zheng, W. F. Wang and M. L. Cao, Research and simulation on modular multilevel topology, IEEE 11th Conference on Industrial Electronics and Applications (ICIEA), Hefei, 2016, pp. 866-871.

[5] R.Vidal-Albalate, E. Belenguer, H. Beltran, R. Blasco-Gimenez, Efficient model for modular multi-level converter simulation, Mathematics and Computers in Simulation 130 (2016) 167-180.

[6] E. N. Abildgaard, M. Molinas, Modelling and Control of the MMC, Energy Procedia 20 (2012) 227-236.

[7] B. Li, R. Yang, D. Xu, G. Wang, W. Wang, D. Xu, Analysis of the phase-shifted carrier modulation for modular multilevel converters, IEEE Trans. Power Electron 30 (2015) 297–310.

An Analysis of Bluetooth 5 in Comparison to Bluetooth 4.2

Cornel Andrew Lyatuu*, Oğuzhan Urhan
Kocaeli Univ., Dept. of Electronics and Communication Engineering, Umuttepe, İzmit, Kocaeli, Türkiye
*Corresponding author: lyatuuacornel@gmail.com

Abstract

Bluetooth is a wire free standard of technology aimed at short distance communication. Its early versions are known as the Bluetooth classic whose range was between 10 to 100 meters depending on the version. The classic versions range from Bluetooth 1.0 to Bluetooth 3.0 after which need for longer ranges and lower energy consumption led to the rise of Bluetooth Low Energy 4.0 through to the current version 5 specification. User demands and an advancement in technology has led to release of more Bluetooth versions with features that aim at improving the communication protocol.

The main disadvantage for Bluetooth had always been its range limitations hence despite being one of the most commonly used communication protocol in many consumer electronics devices and being available in nearly 5 billion devices, it never really hit its full adoption capacity. With Bluetooth 5's extended range and higher speeds plus the possibility of a mesh protocol Bluetooth now boasts the ability to compete with other communication technologies like ZigBee and Wi-Fi.

This paper at analyzes the new Bluetooth 5 protocol specification in comparison to Bluetooth 4.2 in regards to the power consumption, range capabilities, data throughput and Bit Error Rate (BER).

The project consists of a client Bluetooth 5 capable SoC (System on Chip) in direct communication with a peripheral. The peripheral must be connected to the computer and will serve as the tester while the client responds to the requests that are sent by the tester. In the process of this interaction, different readings that pertain to throughput, range capabilities and power consumption are recorded for analysis. The SoC employed for this system is Nordic Semiconductor's nRF52840 which is a Bluetooth 5 ready SoC.

Keywords: Bluetooth low energy, Bluetooth 4.2 specification, Bluetooth 5 specification
Discipline: Electronics and Communication Engineering

INTRODUCTION

Bluetooth and its logo are a trademark of a private trade association called the Bluetooth Special Interest Group (SIG). Bluetooth was envisioned with the role of uniting ubiquitous technological devices from different industries minus employing wires, but instead using low energy short range radio frequencies found all over the world, Bluetooth. In 1994 the original concept of Bluetooth was born by Ericsson who started a research on the possibility of replacing cables that were used to connect technological accessories to each other for data transfer. The research found the possibility of a large market base for such a technology but that would require the different manufacturers of the said devices to come together to ensure all their devices supported the touted technology. To this end therefore, the Bluetooth SIG was founded in 1997 by a combination of companies namely Ericsson, IBM, Nokia, Intel and Toshiba. The first technical specification of the new technology was version 1.0A, released in the year 1999 the same year that 3Com, Lucent, Microsoft & Motorola joined Bluetooth SIG.

The second technical specification, released in the year 2000 was version 1.0B and then version 1.1. Later in 2005 version 2.0 was introduced, followed by version 2.1 with an improved data rate in the year 2007. In April 2009 Bluetooth SIG introduced version 3.0 with AMP (Alternate MAC/PHY) as the main new feature of the of the version and the addition of high rate data transport with 802.11 [1-3]. Nevertheless, Bluetooth was losing market to other technologies like WIFI, Zigbee among others and a drastic change of the protocol was needed to ensure Bluetooth remained relevant. To these ends a drastic shift in the Bluetooth came about with the introduction of Bluetooth Low Energy, also known as Bluetooth Smart ready, in 2011. Bluetooth Low Energy (BLE)'s first version was 4.0 released in 2011, subsequently versions 4.1, 4.2nd currently 5.0 joined the Bluetooth family with each version aspiring to position Bluetooth as the technology of choice for all short distance wireless communication solutions [4-6].

2nd International Students Science Congress
4-5 May 2018, Izmir - Turkey

İZMİR
KÂTİP ÇELEBİ
UNIVERSITY
2010

İZMİR
Uluslararası
Misafir
Öğrenci
Derneği
◆İZMİR International Guest Student Association

EXPERIMENT SETUP

The Block diagram of the utilized system is given in Figure 1. As seen from this figure two Bluetooth modules utilized for the tests. These modules are capable of running both Bluetooth 4.2 and 5 protocols. The details of hardware and software employed is described below.
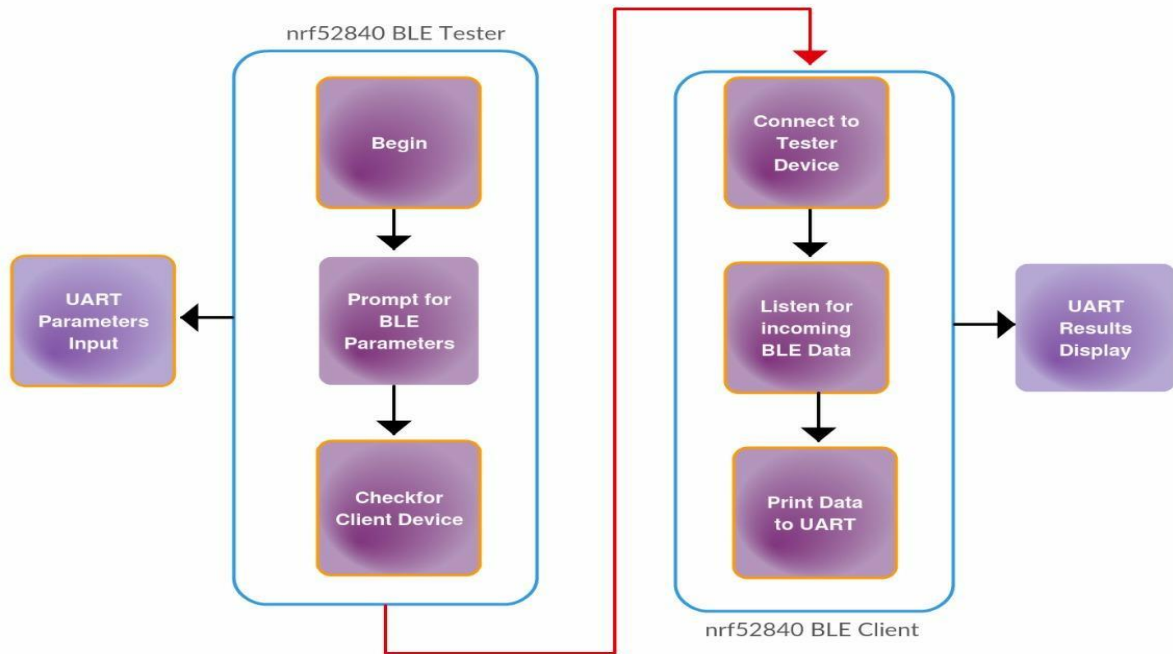
Figure 6. The test bed utilized.

The system tested consists of two nRF52840 chips directly in communication with each other. One kit has to remain attached to the PC and will act as the master whereas the other kit will be the slave. Both kits are loaded with the ATT_MTU throughput firmware from Nordic Semiconductor before being configured for throughput tests. In order to configure the master and slave, button 1 has to be pressed on the master kit and button 2 on the preferred kit. The master kit sets configurations, connects to the slave and send data.

BLE 5 has 3 variants: 1M PHY which is the standard Bluetooth radio stack used in Bluetooth 4.2 and mandatorily had to be included in Bluetooth 5. The 2M PHY, this is a new radio stack introduced with Bluetooth 5 protocol for improved throughput. The Coded PHY, introduced with Bluetooth 5 for increased range for Bluetooth.

Other configurations that can be tweaked for improved performance include; Connection interval, MTU size, DLE and Connection event Length extension.

RESULTS

The 2 meters test was carried out indoors, whereas the 50 and 100 meters test were carried out outside with few barriers. At 450 meters, the 1M PHY and 2M PHY could not carry out the test despite slave kit detection, hence the lack of results for that distance in the case of 1M and 2 M.

The coded test accepted device discovery and the running. The Table 1 shows a summary of the different measurements of throughput obtained from different test scenarios.

Table 1. A Summary of the throughput results at different test scenarios.

Distance (M)	Throughput (Kbps)		
	BLE 5 (2M)	BLE 4.2& 5 (1M)	BLE 5 (Coded)
2	1113	671	50
50	950	528	25
100	923	505	24.75
150	908	271	23.86
200	638,5	213	23.5
250	568	168	22
300	324.2	136.6	21
350	201.6	98	19
450			11

The results are then graphically depicted in Figure 2. As can be seen, the longer the distance the lower the throughput for all the different BLE versions. Nevertheless, BLE 5 2M mode goes further in range compared to the standard 1M of 4.2
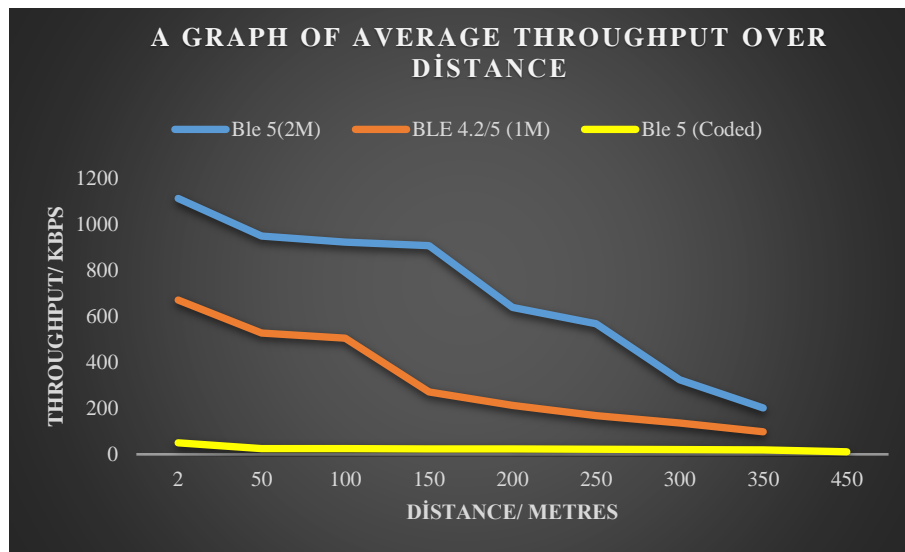
Figure 7. Throughput vs distance for the different Bluetooth versions

With the help of an amperemeter and a voltmeter, the different voltage and current readings were measured during the tests. Using the formula P (power) = I (current) * V (voltage) the average current was converted to power as in Table 2. The power is then multiplied by time to get the total energy consumed in watt-second (W.s).

Table 2. The range of current consumption at different distances

	Voltage V	Current A	Power W	Time s	Energy W. s
LE Coded PHY					
2	2,971	0,006	0.00178	163,861	2,92099
50	2,969	0,00585	0.01737	327,723	5,69211
100	2,965	0,00581	0.01723	331,033	5,70259
200	2,964	0,00577	0.01710	348,641	5,62556
300	2,962	0,00575	0.00170	390,146	6,64477
LE 2M PHY					
2	2,968	0,0095	0.02820	6.361	0,17936
50	2,97	0,00865	0.02570	8,624	0,22156
100	2,97	0,00861	0.02557	8,877	0,227
200	2,97	0,00855	0.02540	12,832	0,32585
300	2,97	0,00851	0.02527	25,272	0,63874
LE 1M PHY					
2	2,968	0,00955	0.02834	12,21	0,34609
50	2,964	0,0089	0.02638	15,517	0,40933
100	2,964	0,00887	0.02630	16,224	0,42654
200	2,964	0,00884	0.02620	38,465	1,00785
300	2,963	0,0088	0.02607	59,978	1,56389

From Table 2 above and the graphical representation in Figure 3 below, it is observed that despite consuming a higher input power, 2M is the most energy efficient as it takes a shorter time hence consumes lower energy levels. Thus, making 2M of BLE 5 the most efficient variant of BLE versions present at the moment. Despite consuming a lot of power, Coded version of BLE 5 may still be considered suitable for distance critical applications.
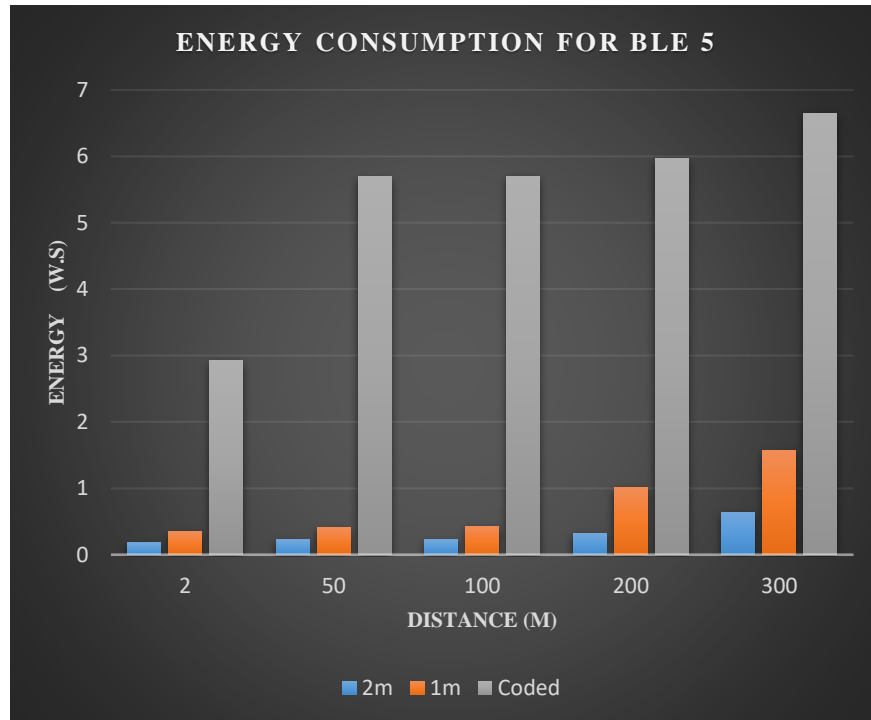
Figure 8. A graph showing power consumption over distance

CONCLUSION

From the experiments carried out, Bluetooth 5 shows a substantial increase in range capabilities and data rate. However, it is imperative to note that for an improvement in any of the said settings, there must always be a drawback. An increase in the data rate through the 2M PHY leads to an increased input power consumption, nevertheless this can be mitigated by the increase speed that ensures data transfer takes a shorter time thus reducing on the energy consumed over time.

The 1M PHY used by BLE 4.1 and standard 4.2 radio has a lower data rate at 1Mbps and a reduced input power consumption but due to lower speeds compared to 2M PHY this ensures that the energy consumption of 1M PHY is higher than that of 2M PHY.

The Coded PHY LE has a much-lowered data rate to ensure the distance is more than doubled. Due to the decreased throughput, this PHY consumes the lowest amount of input power but then takes very long time for data transfer which then leads to a high energy consumption over time.

In conclusion, Bluetooth 5 has proved an ideal technology for low powered long-life applications since its energy consumption is quite low yet it has an improved data rate and range capabilities.

The results obtained and conclusions derived above can be based upon for the deployment of BLE in home automation and other IoT projects as the results show a very big improvement in the capabilities of Bluetooth and its ability to compete with other technologies for connectivity.

REFERENCES

[1] Bluetooth, Our History. https://www.Bluetooth.com/about-us/our-history (Accessed 17 Dec 2017)
[2] T. C. Michael, Development of the Bluetooth version 1.0, Emerging Technologies Symposium: Broadband, Wireless Internet Access, Richardson, TX, USA, 10-11 April (2000)
[3] B. Chatschik, An overview of the Bluetooth wireless technology, IEEE Communication Magazine 39(12) (2001) 86-94.
[4] R. Franklin, Whither Bluetooth, IEEE Pervasive Computing, DOI: 10.1109/MPRV.2008.63
[5] ITECHTICS, Bluetooth 4 Vs. Bluetooth 5: A feature comparison.
 https://www.itechtics.com/Bluetooth-4-vs-Bluetooth-5-feature-comparison/. (Accessed 8 May. 2018).
[6] DIGNITED, Bluetooth 5 vs. Bluetooth 4: The 7 differences between the two versions. http://www.dignited.com/23114/Bluetooth-5-vs-Bluetooth-4/ (Accessed 8 May 2018).

Colorless Wavelength Division Multiplexing Passive Optical Networks (WDM PONs)

Mahmoud Alhalabi[*], *Necmi Taşpınar*
Erciyes University, Faculty of Engineering, Dept. of Electrical and Electronics Engineering, Kayseri, Turkey
Fady I. El-Nahal
Islamic University of Gaza, Electrical Engineering Department, Gaza, Palestine
[*]Corresponding author: eng.halabi@hotmail.com

Abstract

We have demonstrated a bidirectional Wavelength Division Multiplexing-Passive Optical Network (WDM-PON) system based on the wavelength locked Fabry-Perot laser diode (FP-LD) with two cascaded array waveguide gratings (AWGs). The system was demonstrated without dispersion compensation for both 10 Gbps downstream and 2.5 Gbps upstream signals respectively. This network is classified to 10GPON Standard. FP-LD will be used at optical network unit (ONU) as transmitter, so it can re-modulate the downstream signal with upstream data and then re-sent upstream towards the central office (CO). The BER performance of our system shows that our proposed scheme is effective low cost system and the injection locked FP-LD is a low cost colorless transmitter for high-speed optical access exploiting WDM technology.

Keywords: Wavelength Division Multiplexing-Passive Optical Network, Fabry-Perot laser diode, Reflective Semiconductor Optical Amplifiers
Discipline: Electronics and Communication Engineering

I.   INTRODUCTION

Wavelength Division Multiplexing-Passive Optical Network (WDM-PON) systems have been proposed to increase the channel capacity in existing optical fibers networks. WDM-PON has been proposed as a key solution for next-generation networks [1-3]. Design of low cost optical network unit (ONU) for WDM-PON is desirable. The wavelength re-use model with the Reflective Semiconductor Optical Amplifiers (RSOA) has lately been evaluated for deployment in WDM-PON [4-7]. The wavelength re-use system has a shared advantage that the optical signal modulated with downstream data is re-used to transfer the upstream data through the RSOA in the ONU. The wavelength re-use scheme would allow realizing the simplest WDM-PON system, therefore reducing the equipment and maintenance costs [8-15]. Fabry Perot Laser Diode (FP-LD) has been proposed as an uplink transmitter and modulator for WDM access networks [16-20]. The FP-LD is injection-locked with the downstream wavelength at the ONU, where the original downstream data can be mostly blocked while the upstream data can be sent on the same injection-locked wavelength by concurrently directly-modulating the FP-LD [17]. In this article, we will use FP-LD in ONU as an upstream source in our proposed WDM-PON system. Furthermore, a comparison between RSOA and FP-LD based systems is also included.

II.   PROPOSED ARCHITECTURE

The proposed PON architecture is shown in Figure 1. In downlink, CW laser with 193.1 THz frequency is modulated by MZM using 10 Gbps NRZ downstream data to form the required downstream signal. The generated signal is sent to the first AWG multiplexer at CO and then it is sent over Single Mode Fiber (SMF). It passes through the second AWG at Remote node (RN) where it is routed to the desired ONU. At the ONU, using optical splitter, part of the multiplexed signal is received by a balanced receiver. For uplink, the remaining part of the downstream multiplexed signal from the splitter is re-modulated using a 2.5 Gbps NRZ upstream data by FP-LD in the ONU. The re-modulated OOK signal re-pass through the AWG which demultiplexed the upstream signal then it is sent over the SMF. The upstream demultiplexed signal passes through the first AWG then it is received in CO. By using a circulator to isolate the upstream signal from the downstream signal, the upstream signal is received by a Photo Detector (PD) at the CO.
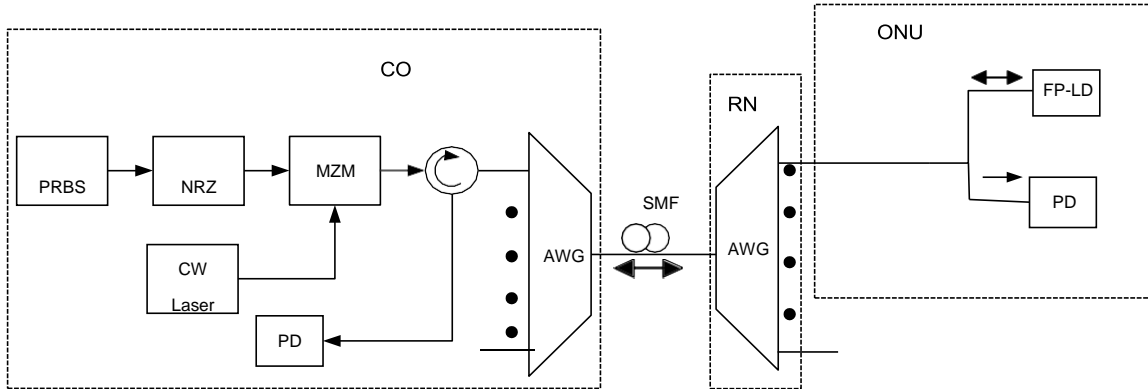
Figure 1. Block diagram of the proposed bidirectional PON system model.

The parameters used in the proposed system are listed in Table 1.

Table 1. Simulation parameters.

Parameter	Value
Layout Parameter	
Bit rate (downstream)	10 Gbps
Bit rate (upstream)	2.5 Gbps
Optical Transmitter (CW laser)	
Laser Power input, P_{in}	1mW (0 dBm)
Frequency/Wavelength	193.1 THz / 1550 nm
Laser line Width	10 MHz
Optical link	
Length	10 km
Attenuation	0.2 dB/km
Dispersion	16.75ps/(nm×km)
Optical Receiver (PIN PD)	
Responsivity	1 A/W
Dark Current	10 nA
Fabry Perot Laser Diode	
Bias current	40 mA
Modulation peak current	10 mA
Front facet reflectivity	0.99
Rear facet reflectivity	0.9

III. RESULTS AND DISCUSSION

A commercial package is used to design the proposed WDM-PON system [21]. BER analyzer is used to measure the BER, where a BER of 1×10^{-13} for the downstream signal and a BER of 3.6×10^{-12} for the upstream signal were achieved respectively. The eye diagrams of the downlink and uplink are shown in Figures 2 and 3, respectively.
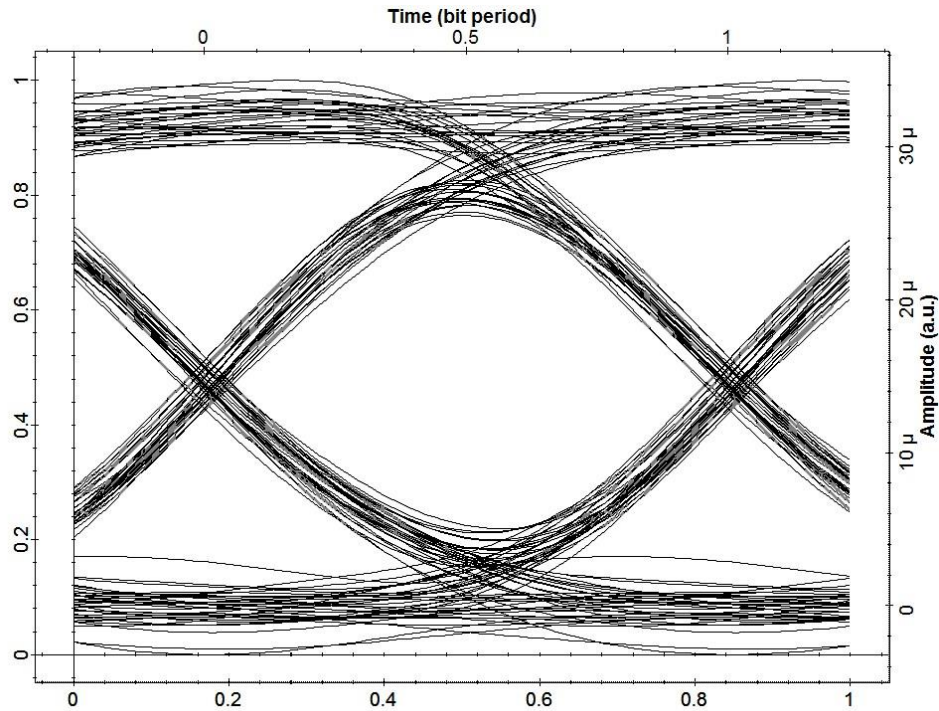
Figure 2. Eye diagram of downstream signal at ONU.
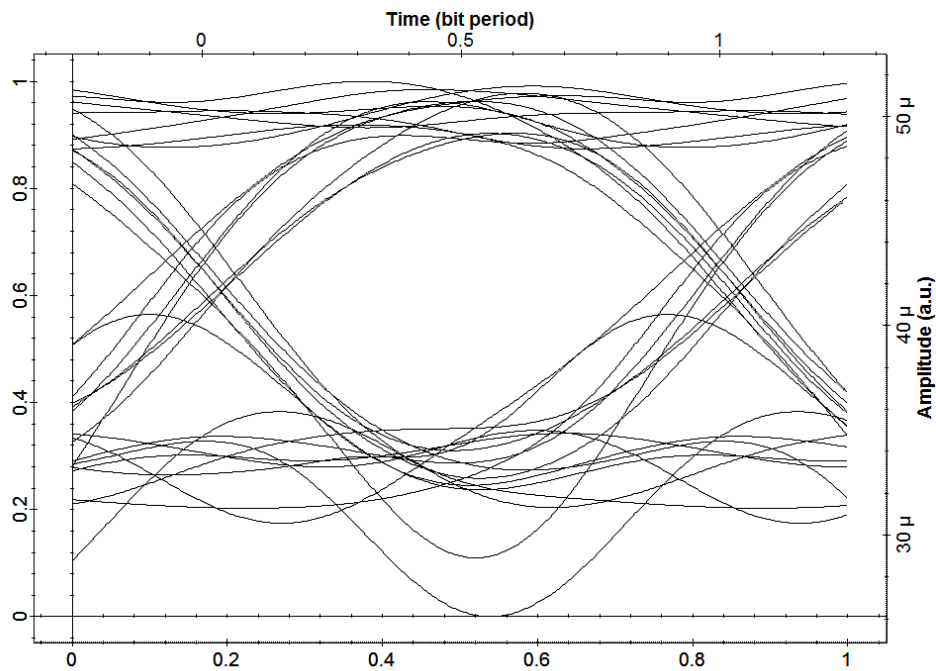
Figure 3. Eye diagram for upstream signal at CO.

BER versus Received power

The BER versus downstream-received power Pd curves for the downstream and upstream signals are shown in Figure 4. It is clear from the results that the BER performance for both downlink and uplink is satisfactory. It is noted that the BER goes down with increasing Pd from -18 dBm to -8 dBm for both downlink and uplink signals. When Pd = -18 dBm, the BER = 1×10^{-13} for downlink and 6×10^{-11} for uplink respectively. When Pd = -8 dBm, the BER = 1×10^{-16} for the downlink signal and 2.7×10^{-18} for the uplink respectively. For the uplink it is noted that for Pin ≥ -13 dBm, the BER is nearly constant. This can be explained by the fact that the FP-LD is operating in the gain saturation region.

52
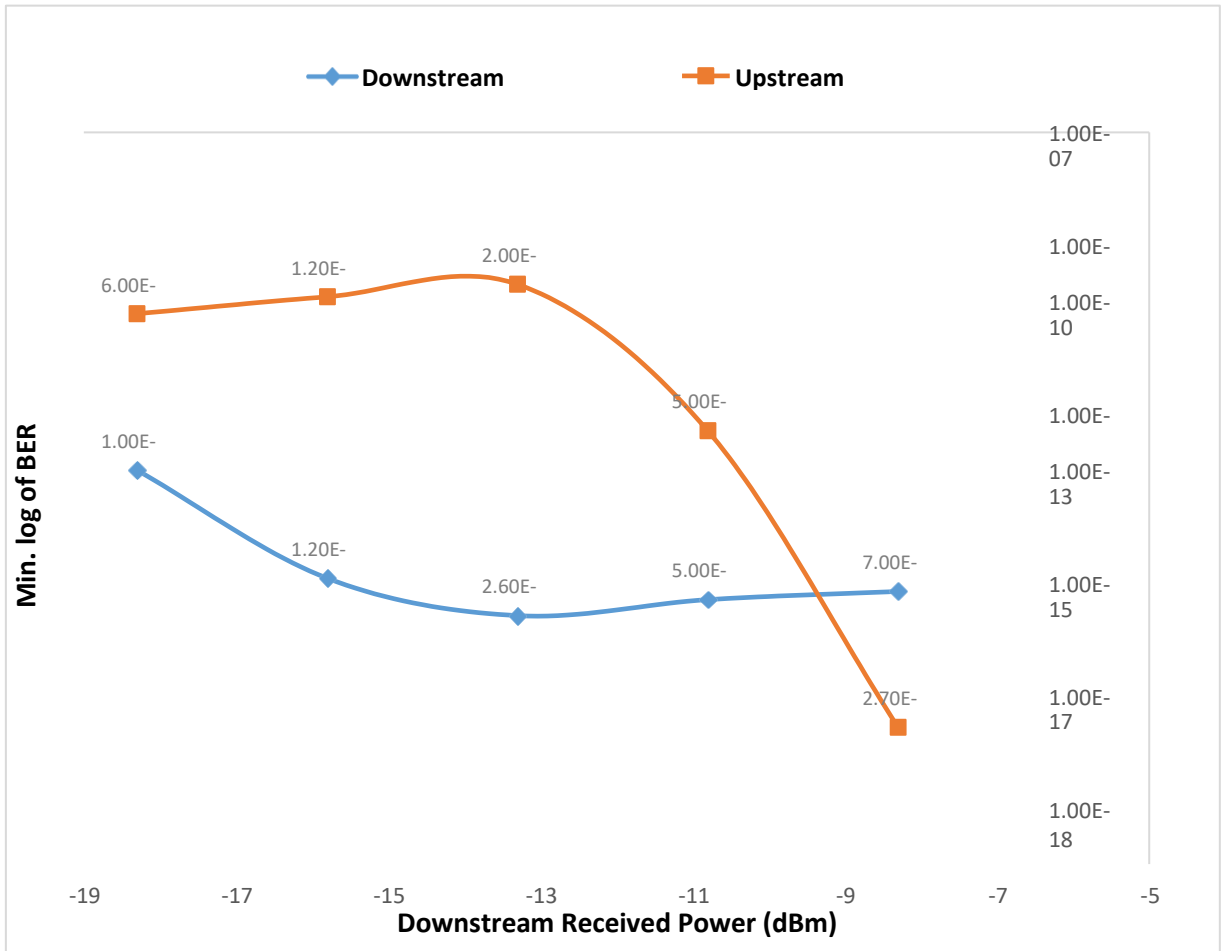
Figure 4. BER versus Downstream received power at ONU for downstream and upstream.

Upstream BER versus FP-LD bias current

The effect of FP-LD bias current on upstream BER at the CO has been investigated. Figure 5 shows upstream BER versus the bias current of FP-LD. It is clear from the results that the BER decreases with increasing bias current I_b , where it is 5.7×10^{-10} at I_b=30 mA and 1.5×10^{-17} at I_b=60 mA.
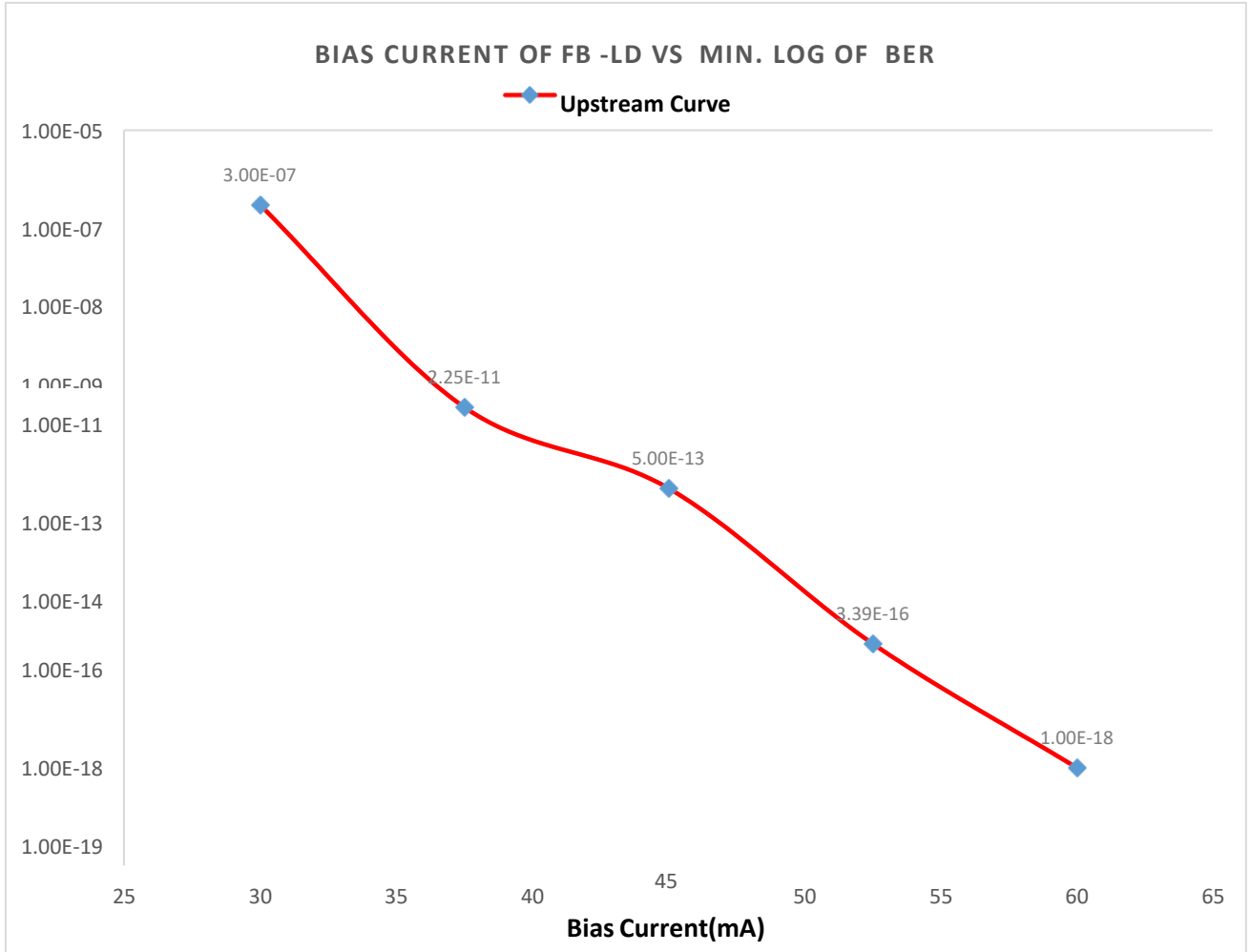
Figure 5. BER versus bias current of FP-LD for upstream signal.

WDM-PON based on FP-LD versus WDM-PON based on RSOA:

A comparison between WDM-PON based on FP-LD and WDM-PON based on RSOA has been carried out, where the FP-LD was replaced by an RSOA at the ONU. The variation of BER of the upstream signal with input power for both FP-LD and RSOA systems has been investigated. The results are shown in Figure 6. It is clear from the results that the BER decreases with increasing the input power for both systems but the performance of the FP-LD system surpass that of the RSOA system. For example, when P_{in}= 0 dBm, the BER = 6×10^{-11} for the FP-LD systems while it is 1×10^{-6} for the RSOA system. When P_{in}= 10 dBm, the BER = 2×10^{-18} for the FP-LD systems while it is 5.6×10^{-8} for the RSOA system. This can be explained by the fact that increasing FP-LD injection power could improve the modulation frequency while increasing RSOA injection power cannot help to improve its modulation injection power as it is already operating in the saturation region. Moreover, the FP-LD system is cost effective compared with the RSOA system.
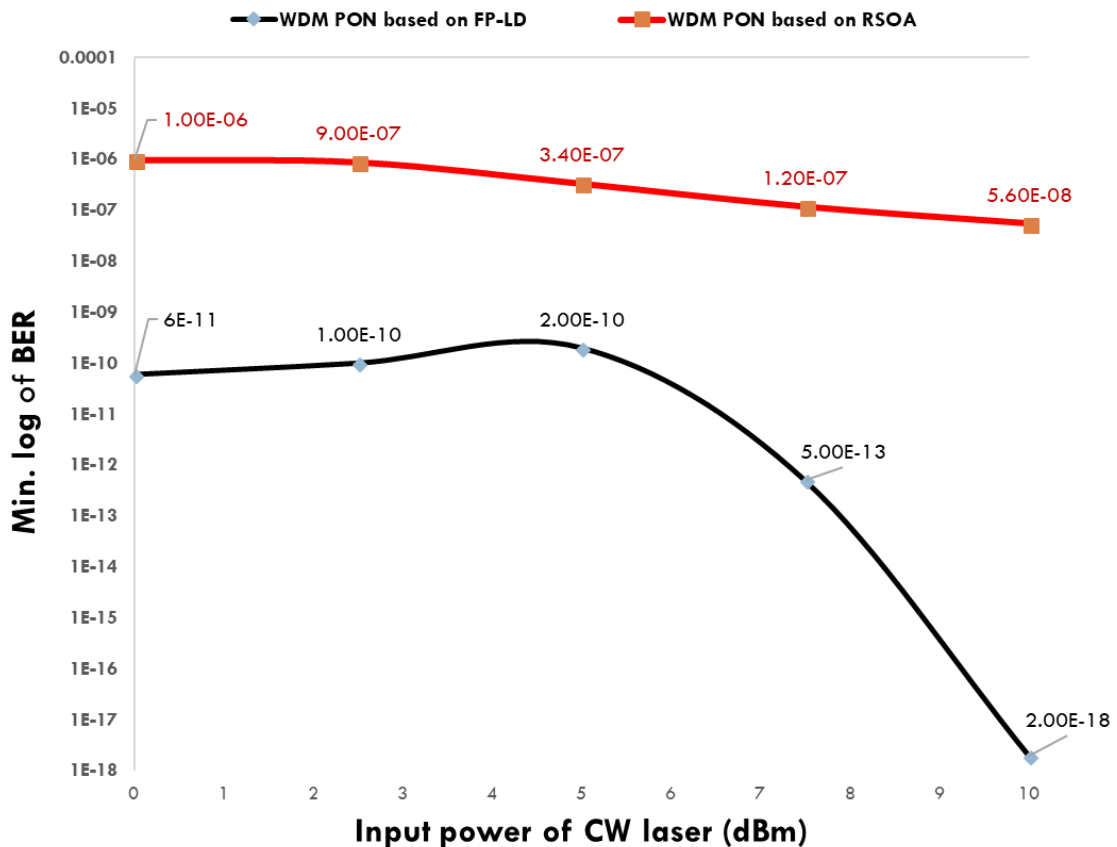
Figure 6. BER versus input power for both WDM PON based on RSOA and WDM PON based on FP-LD.

IV. CONCLUSION

A novel bidirectional WDM-PON system employing a 10 Gb/s signal for down-link and a 2.5 Gb/s signal for up-link has been demonstrated. FP-LD has been used for re-modulation of a down-link signal. The FP-LD is injection-locked with the downstream wavelength at the ONU, where the original downstream data can be mostly blocked while the upstream data can be sent on the same injection-locked wavelength by concurrently directly-modulating the FP-LD. As a result, both the upstream and downstream signals share the same wavelength for better wavelength utilization efficiency. Furthermore, a comparison between WDM-PON based on FP-LD and WDM-PON based on RSOA has been carried out. The results showed that the performance of the FP-LD system surpass that of the RSOA system. Moreover, the FP-LD system provides a cost effective solution to meet the higher data rates in future's WDM-PON access networks.

REFERENCES

[1] E. Wong, Next-Generation Broadband Access Networks and Technologies, J. Lightwave Technol., 30, (2012) 597-608.

[2] F.T. An, D. Gutierrez, K.S. Kim, J.W. Lee, L.G. Kazovsky, SUCCESS-HPON: a next generation optical access architecture for smooth migration from TDM–PON to WDM– PON, IEEE Commun. Mag. 43 (2005) 540-547.

[3] S.-J. Park, C.-H. Lee, K.-T. Jeong, H.-J. Park, J.-G. Ahn, K.-H. Song, Fiber-to the- home services based on wavelength-division-multiplexing passive optical network, J. Lightwave Technol. 22 (2004) 2582–2591.

[4] F.I. El-Nahal, A. Hakeim, M. Husein, Radio over fiber access network architecture employing RSOA with downstream OQPSK and upstream re-modulated OOK data, Int. J. Light Electron Opt. 123 (2012) 1301-1303.

[5] M. Brunero, P. Parolari, R. Brenot and M. Martinelli, 20-Gb/s polarization division multiplexed WDM PON transmitter based on self seeded RSOAs, 18th Italian National Conference on Photonic Technologies, pp. 1-4, 2016.

[6] J. Yu, B. Kim, N. Kim, Wavelength Re-use Scheme with Reflective SOA for WDM-PON Link, 3 (2008) 1704-1710.

[7] S. Y. Kim, S. B. Jun, Y. Takushima, E. S. Son and Y. C. Chung, Enhanced performance of RSOA-based WDM-PON by using Manchester coding, J. Optical Networking 6 (2007) 624-630.

[8] Y. C. Chung, Recent Advancement in WDM PON Technology, Tech. Dig. ECOC 2011, Geneva, Paper Th.11.C.4.

[9] J. Prat, C. Arellano, V. Polo, C. Bock, Optical network unit based on a bidirectional reflective semiconductor optical amplifier for fiber-to-the home networks, IEEE Photon. Technol. Lett. 17 (2005) 250-252.

[10] M.D. Feuer, J.M. Wiesenfeld, J.S. Perino, C.A. Burrus, G. Raybon, S.C. Shunk, N.K. Dutta, Single-port laser-amplifier modulators for local access, IEEE Photon. Technol. Lett. 8 (1996) 1175-1177.

[11] N. Buldawoo, S. Mottet, F. Le Gall, D. Sigonge, D. Meichenin, S. Chelles, A semiconductor laser amplifier-reflector for the future FTTH applications, in: Proc. Eur. Conf. Opt. Commun. (ECOC 1997), Edinburgh, UK, 1997, pp. 196–199.

[12] J. M. Kang, S.K. Han, A novel hybrid WDM/SCM-PON sharing wavelength for upand down-link using reflective semiconductor optical amplifier, IEEE Photon. Technol. Lett.

[13] G.C. Kassar, N. Calabretta, I.T. Monroy, Simultaneous optical carrier and radio frequency re-modulation in radio-over-fiber systems employing reflective SOA modulators, in: Lasers and Electro-Optics Society (LEOS 2007), 2007, pp. 798–799.

[14] A. Kaszubowska, L. Hu, L.P. Barry, Remote down-conversion with wavelength reuse for the radio/fiber uplink connection, IEEE Photon. Technol. Lett. 18 (2006) 562–564.

[15] T. Kuri, K. Kitayama, Y. Takahashi, A single light-source configuration for full-duplex 60- GHz-band radio-on-fiber system, IEEE Trans. Microw. Theory Tech. 51 (2003) 431–439.

[16] L.Y. Chan, C.K. Chan, D.T.K Tong, E Tong and L.K. Chen, Upstream traffic transmitter using injection-locked Fabry-Perot laser diode as modulator for WDM access networks, Electronics Letters, Vol. 38, No. I, 2002.

[17] Z. Xu, Y. Wen, C. Chae, Y. Wang, and C. Lu, 10 Gb/s WDM-PON Upstream Transmission Using Injection-locked Fabry-Perot Laser Diodes, in Lightwave Department, Institute for Infocomm Research, Singapore 119613, 2006.

[18] C.H. Yeh, C.W. Chow, H.Y. Chen, J.Y. Sung and Y.L. Liu, Demonstration of using injection-locked Fabry-Perot laser diode for 10 Gbit/s 16-QAM OFDM WDM-PON, Electronics Letters 48 (2012) 940–942.

[19] J. H. Lee et al., Single, Depolarized, CW Super continuum-Based Wavelength-Division-Multiplexed Passive Optical Network Architecture With C Band OLT, L-Band ONU, and U- Band Monitoring, IEEE J. Light. Tech. 25 (2007) 2891-2897.

[20] Q.T. Nguyen et al., Bidirectional Transmission in Colourless WDM-PON based on Injection Locked Fabry-Perot Laser at 2.5 Gbit/s using Low-Cost Seeding Source, in: Proc. Eur. Conf. Opt. Commun. (ECOC 2009), Vienna, Austria, Paper 6.5.1.

[21] OptiSystem Package from Optiwave.

Cocoa Butter Production and its Compounds

Vassiriki Cisse*, Fahri Yemişçioğlu, Onur Özdikicierler
Ege University, Department of Food Engineering, Bornova 35100, İzmir, Türkiye
*Corresponding author: aboubakcisse@hotmail.com

Abstract

Cocoa beans -seeds of the Theobroma cocoa L. tree- are the primary raw material used for the preparation of cocoa, chocolate and other chocolate products, which are highly valued by consumers around the world. The dominant constituent of cocoa bean is cocoa fat (50-57%), called cocoa butter. Cocoa butter is a natural fat, very valued for its specific textural properties and for consisting a carrier of many bioactive compounds. The most abundant fatty acids present in cocoa butter are: stearic acid (C18:0, 29-38%), oleic acid (C18:1, 29-38%) and palmitic acid (C16:0, 20-26%). Linoleic (C18:2, 2-4%), arachidic (C20:0, 1%), alfa-linolenic (C18:3, 0.1%), palmitoleic (C16:1, 0.25%) and behenic acids (C22:0, 0.2%) can be also found in cocoa butter. Small quantities of myristic (C14:0, 0.2-0.3%) and recently discovered in cocoa butter lauric acid (C12:0, 0.01%) can also be found. The presence of endogenic essential unsaturated fatty acid, which although not being synthesized in human body, determine its proper functioning, increases the nutritional value of cocoa butter. Compounds responsible for desirable properties of cocoa butter are triacylglycerols. Present in cocoa butter acylglycerols, are symmetrical triacylglycerols, and they consist around 90% of all triacylglycerols present in cocoa butter. The most important triacylglycerols of cocoa butter contain saturated palmitic, stearic acids and mono-unsaturated oleic acid in an sn-2 position are: 1,3- dipalmitoyl-2-oleoyl-glycerol (POP, 15-16%), 1-palmitoyl-3-stearoyl-2-oleoyl-glycerol (POS, 35- 38%), and 1,3-distearoyl-2-oleoyl-glycerol (SOS, 23-26%). Unsymmetrical triacylglycerols can be found only in trace amounts. The unsaponifiable fat fraction of cocoa butter includes plant sterol esters, which belong to phytosterol compound group. In the biggest quantities following sterols can be found: sitosterol (12.33mg/kg), stigmasterol (6.01mg/kg), campesterol (1.87mg/kg) and Δ5-avenasterol (0.61mg/kg). Furthermore in cocoa butter a presence of vitamin E isomers has been proven, mainly γ-tocopherol (93.90mg/kg) with trace amounts of α-tocopherol (4.20mg/kg), β- tocopherol (3.70mg/kg) and tocotrienols (<10mg/kg).

Due to all functionality that this oil has, we extracted cocoa butter from the cocoa bean so we found areas of production, especially chocolate (dark chocolate) and other. The purpose of this study is to give an idea about the transformation of cocoa bean into cocoa butter and its potential compounds.

Keywords: Theobroma cocoa L, cocoa butter, chocolate, cocoa mass, cocoa powder
Discipline: Food Engineering

INTRODUCTION

Cocoa is a fruit produced in general in tropical localities, especially in South America, West Africa, Asia [1]. The cocoa fruit comes from the genus tree Theobroma of the family Malaceae [2]. Generally it has yellow, red, purple color and has 3 types of varieties which are: forestero (90%) is more produced in West Africa such as Côte d'Ivoire, Ghana; very resistant to diseases and insects; Criollo (5%) is generally produced in South America like Brazil, less resistant but of very good flavor; Trinitario (15%) is the hybrid or result of Forestero/criollo coupling [3,4]. Cocoa fruits are characterized by 25 mm long, 15 mm wide, 8 mm thick, contain 16-60 grains of which puples (water 80%, glucose 15%, pectin 5%). Cocoa beans are extracted from cocoa fruits obtained by cutting, fermenting and drying. cocoa beans are the raw materials for the production of cocoa butter, cocoa powder and cocoa liquor (Figure 1). After drying, the moisture content is 5-8%, fat 50-55%, starch 7%, mineral 6%, cell 4%, theobromine 2%, protein 20% and water 5% [4]. The cacao beans obtained are subjected to processing procedures such as cleaning, scraping, roasting, spraying. Thus it is obtained the nib after scraping and the cocoa liquor after the spraying. The cocoa liquor is pressed to obtain cocoa butter (Figure 2). Cocoa butter is a natural fat of great value because of its sensory and textural properties in food, cosmetics and pharmaceutical production. It has a high proportion of bioactive compound with phytosterols (sitosterols, 12.33 mg / kg, stigmasterols, 6.01 mg / kg, campesterols, 1.87 mg / kg, delta 5 avenaterols, 0.61 mg / kg); tocopherols (gamma 93.90 mg / kg, alpha 4.20 mg / kg, beta 3.70 mg / kg) and tocotrienols (<10 mg / kg) [5, 6, 7, 8]. Cocoa butter is light yellow in color and solid at room temperature because of its

physicochemical composition. These chemical characteristics are based on saturated fatty acids (stearic acid, 29-38%, palmitic acid, 20-26%, arachidic acid 0.1%, behenic acid 0.2%, lauric acid 0.01 5, myristic acid 0 , 2-0.3%); unsaturated fatty acids (oleic acid 29-38%, linoleic acid 2-4%, linolenic alfa acid 0.1%, palmitoleic acid 0.25%). In cocoa butter around 1% of free fatty acids, 0.3-0.5% of diacylglycerols and 0.1% of monoglycerides also can be found and triglycerides of which palmitic and stearic acid are predominantly in position 1 and 3; oleic acid is in position 2: 1,3-dipalmitoyl-2-oleylglycerol (POP, 15-16%), 1-palmitoyl-3-stearoyl-2-oleoylglycerol (POS, 35-38%) and 1,3-distearoyl -2-oleoyl-glycerol (SOS 23-26%) [9, 10, 11, 12]. The triglycerides of cocoa butter are generally symmetrical because of the oleic acid in position 2. These physical characteristics (TAG) determine these very important textural properties and these abilities to crystallize the stable forms during the technological processes. Because of these properties, he is responsible for the important characteristics of chocolate (luster, hardness, brittleness and melting in the mouth) [10]. The TAGs of cocoa butter in solid state crystallize and show some forms called polymorphism. Polymorphism is a phenomenon of transformation into several forms of TAG in the form of: Gamma (I), Alpha (II), beta prime 2 (III), beta prime 1 (IV), beta 2 (V), beta 1 (VI). In the formulation of chocolate, the desired and most desirable form is beta 2 (V) [13, 14, 15, 16]. Many industrial producers use cocoa butter in food products like chocolate, coating, CBE; cosmetics (pomade, cream) and medications, because of these physicochemical properties.

Figure 1. Cocoa beans and cocoa butter

MATERIALS AND METHODS

Materials

The cocoa beans were purchased from Ivorian company situated in Port-Bouet, Abidjan, Cote d'Ivoire. Cocoa shells were removed manually from cocoa beans and the nibs were smashed approximately below 1 mm with a mortar and pestle before being analyzed to determine the yield, Free Fat Acid, triglycerides , phytosterols and antioxidant content. The nibs were stored in a dark closed container to prevent from humidity and light at room temperature (24°C). The cocoa butter were purchased from magazine of food and cosmetic in Abidjan, Cote d'Ivoire.

Cocoa butter extraction procedure

The cocoa butter was obtained using the technic of Soxhlet extraction with approximately 10 g of cocoa nibs into the thimble and solvent was added in 150 ml round bottom flask for 90°C during 6h. The cocoa butter obtained from the extraction procedure mentioned below was analyzed with those parameters of free fat content, triglyceride, phytosterols and antioxidant content and the solvent was evaporated by rotary evaporator at 45°C -15 mn. The yield of cocoa butter was calculated using the formula below:

$$\text{Yield (\%)} = \frac{\text{Weight of flask (after)} - \text{Weight of flask (before)}}{\text{Weight of sample}} \times 100$$

TAG Composition

The TAG compositions of cocoa butter was obtained by HPLC in a Hewlett Packard Series 1100 HPLC System equipped with a refractive index (RI) detector. A Zorbax Eclipse XDB C-18 (250 x 4.6 mm, Agilent Technologies Inc., USA) column in series with Microsorb MV (250 x 4.6 mm, Rainin

```
                    ┌─────────────────────────────┐
                    │  Harvesting of cococa pod    │
                    └─────────────────────────────┘
                              │
                    ┌─────────────────────────────┐
                    │         Transport            │
                    └─────────────────────────────┘
                              │
                    ┌─────────────────────────────┐
                    │      Opening of pod          │
                    └─────────────────────────────┘
                              │
 ┌──────────────┐   ┌─────────────────────────────┐   ┌──────────────────────────────┐
 │ Cocoa beans  │◄──│       Fermentation          │──►│ Fermented pulp (water, pulp) │
 └──────────────┘   └─────────────────────────────┘   │ and ethanol distil alcoholic │
                              │                         │ spirits)                     │
                    ┌─────────────────────────────┐   └──────────────────────────────┘
                    │      Drying of beans         │
                    └─────────────────────────────┘
                              │
                    ┌─────────────────────────────┐
                    │     Roasting of beans        │
                    └─────────────────────────────┘
                              │
                    ┌─────────────────────────────┐
                    │     Cracking of beans        │
                    └─────────────────────────────┘
                              │
 ┌──────────────┐   ┌─────────────────────────────┐   ┌──────────────────────────────┐
 │    Nibs      │◄──│        winnowing            │──►│          Shells              │
 └──────────────┘   └─────────────────────────────┘   └──────────────────────────────┘
                              │
                    ┌─────────────────────────────┐
                    │         Grinding             │
                    └─────────────────────────────┘
                              │
                    ┌─────────────────────────────┐
                    │         Pressing             │
                    └─────────────────────────────┘
                              │
                    ┌─────────────────────────────┐
                    │    **Chocolate liquor**      │
                    └─────────────────────────────┘
                         │             │
 ┌─────────────────┐                   ┌──────────────────┐
 │ **Cocoa powder**│                   │ **Cocoa butter** │
 └─────────────────┘                   └──────────────────┘
```
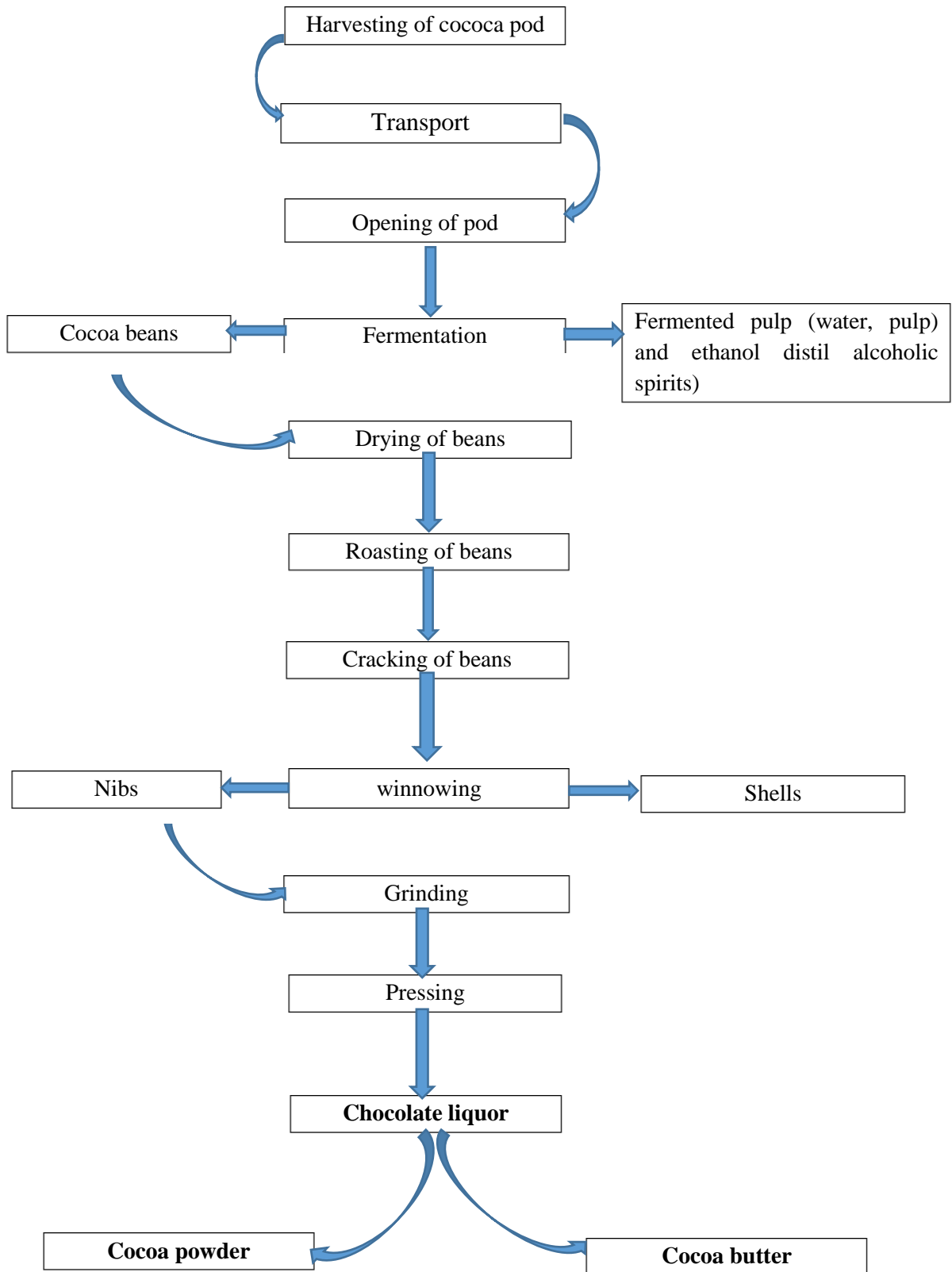
Figure 2. Processing of production of Cocoa Butter, Cocoa Powder and Chocolate liquor

Instrument Co. Inc., USA) column was used for the analysis with a mobile phase of 85:15 (v/v) acetone and acetonitrile at a flow rate of 0.8 mL/min. Each sample was dissolved in acetone or acetone/chloroform (2:1, v/v) to make a 5% solution. The injection volume was 20 μL. All TAG contents were given in percentage area.

Fatty Acid Composition

Fatty acid composition of cocoa butter was determined using gas chromatographic system (7820 A, Agilent, USA). Sample was prepared followed the method done by [16]. Separation was carried out on Trace TR-FAME capillary column (0.25 μm, 60 m Å ~ 0.25 mm, Thermo Fisher, USA) under the following conditions: 1 μL aliquot was injected into the column with a split ratio of 50:1. The injector and detector temperature were set at 250°C. Nitrogen was used as carrier gas and set at 1 mL/min. the initial temperature was 120°C and hold for 3 min and then to 176°C at 8°C/min for 28 min, and then to 215°C at 3 C/min for 20 min. The fatty acid contents were given in terms of percentage area.

Oxidative Analysis

Iodine value (IV) : The IV measures the number of reactive doublebonds present in cocoa butter. A higher IV number indicates more double bonds in the cocoa butter. IV was determined according to AOCS method Cd 1d- 92 [17].

Peroxide value (PV) : The PV measures the oxidation processes in oil. PV of cocoa butter was determined according to AOCS method Cd 8-53 [17].

Acid value (AV) : The acid value (which is twice the free fatty acid (FFA) value) measures the amount of fatty acids separated from glycerol molecules. The amount of free fatty acid present in cocoa butter was estimated by determining the quantity of alkali that must be added to the fat to become neutral. Acid value of cocoa butter was determined according to AOCS method Ca 5a-40 [18].

Slip Melting Point (SMP)

SMP was analyzed using method adopted with minor modifications. Briefly, three capillary tubes were filled with sample up to10 mm high, then left to solidify and refrigerated at $10 \pm 1°C$ for 16 h. The capillary tubes were attached to a thermometer and suspended in a beaker containing distilled water. The water was stirred and the heat was applied, the temperature of the water was recorded when the fat column in each tube rises.

Statistical Analysis

The data were obtained in duplicate or triplicate and reported as mean and standard deviations. Analysis was carried out by SPSS program (version 19.0) at $p < 0.05$.

RESULTS AND DISCUSSION

Yield determination

Extraction of cocoa butter (CB) using soxhlet extraction (ethanol) SE-ethanol gave an average yield of 30.1% as shown in Table 1, grouping the percentage of the three extraction tests. In view of these values, the amount of cocoa butter obtained by SE-ethanol is low compared with other methods. This was reported by Jahural [19], in one of his studies on CB extraction. This BC value was obtained under the effect of the high temperature of SE (78°C) against 60°C for the methods of supercritical carbon dioxide SCO2 and supercritical carbon dioxide-ethanol SCO2-ethanol. The temperature has an effect on the yield of oils, in particular CB. According to the approach of Asep et al. [20], SE-ethanol is beneficial but has a low yield than SE-Hexane because of its potential to get clear products of sample residues, fast and does not require a lot of solvent. the high yield of CB by SE-hexane may be the effect of its attractiveness to oils or fats. Salajegheh et al., 2013 [21] , reported that ethanol used with supercritical extraction has a strong yield due to the solubility of it, carbon dioxide.

Table 1. Yield determination using soxhlet extraction with ethanol

Method of extraction	1	2	3
SE-Ethanol	28,99 ±0,32	30,70 ±0,52	32,01 ±0,71

.

Phytosterol content

According to Table 2, the values of phytosterol are presented according to sub-sterols (beta sitosterol, campesterol and stigmasterol). The cocoa butter obtained by the soxhlet extraction contains more amount of beta sitosterol (12,33 mg / kg) than stigmasterol (6,01 mg / kg), campesterol (1,87 mg / kg) and Δ5-avenasterol (0,61 mg/ kg). The phytosterol yield of the cocoa butter is 20,82 mg / kg.

A study by Wang and Weller, 2006 [22]; the Cocoa Butter extraction (SCO2, USE, SE, SCO2-ethanol) revealed that the Soxhlet method had a low phytosterol yield compared to other methods and that the SCO2-ethanol method had a high yield due to its moderate pressure (35 MPa) and temperature (60°C). [23] revealed that the hexane used for the extraction of CB had a low yield in terms of phytosterol compound against the polar solvent (ethanol).

Table 2. Phytosterol composition (μg/g) after CB extraction using soxhlet extraction-ethanol

Method of extraction	Beta sitosterol	Campesterol	Stigmasterol	Δ5-avenasterol	Total phytosterol
SE-ethanol	12.33 ±0,06	1.87 ± 0,02	6.01 ±0,04	0.61 ± 0,01	20,82 ± 0,03

Antioxidant Assay (AA) and Total Phenolic Content (TPC)

Figures 3 and 4 show the results of the DPPH and TPC test of the cocoa butter obtained after repeated analysis. For Figure 3, using SE, the Cocoa Butter DPPH test shows values: 43.79% (1), 45.01% (2), 46.32% (3). This gives an average of 45.04% DPPH for cocoa butter. Figure 4, the total phenolic content showed values of 20.78 mg GAE / 100 g (1), 22.01 mg GAE / 100 g (2), 21.69 mg GAE / 100 g (3).

According to some articles [11] the DPPH and TPC values are significantly lower than other extraction methods such as SCO2 and SCO2 - ethanol. This was due to the high temperature and the direct contact between the solvent and the liquor during the extraction process.

A study was conducted by [24] revealed that the variability of phenolic compounds was due to cocoa bean variation, solvent usage and extraction techniques. Extraction techniques can be influenced by pressure, temperature, and level of homogenization.
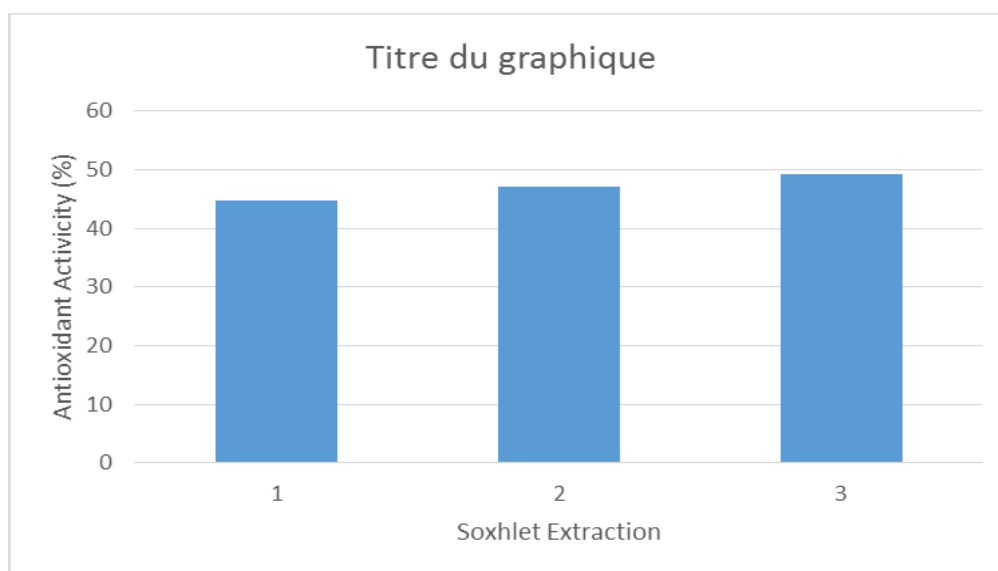
Figure 3. DPPH assay for soxhlet extraction methods
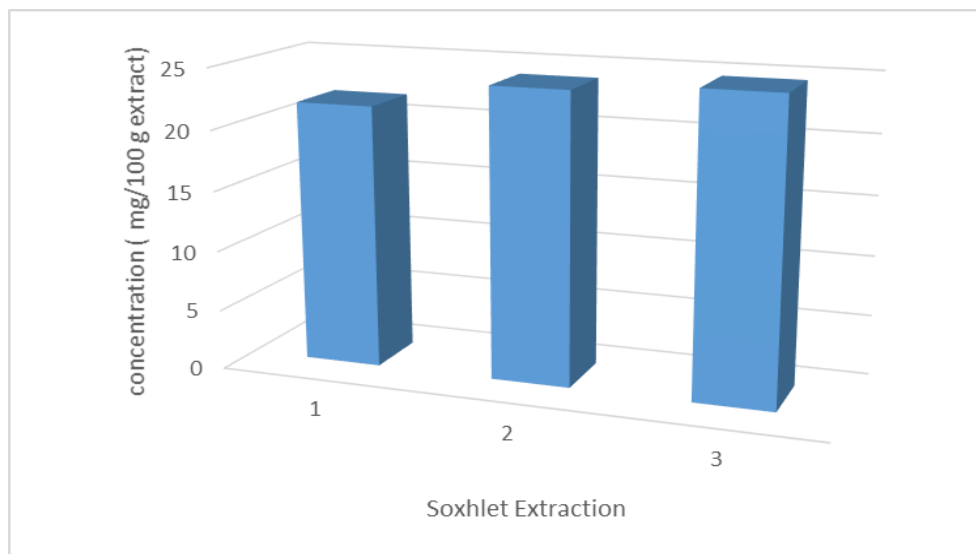
Figure 4. TPC values for different types of extraction methods

Cocoa Butter fatty acids and Triglycerides composition

As shown in Tables 3 and 4, the analysis results of fatty acids and triglycerides of cocoa butter after Soxhlet extraction with ethanol were regrouped. Those in Table 1 showed the values of saturated fatty acids and unsaturated fatty acids. The saturated fatty acids were composed in major of the palmitic acid (20-26%) and stearic acid (29-38%). They had an average amount of 65.51% which confers its predominant on the total amount of fatty acid. Oleic acid (29-38%) was the major unsaturated fatty acid in cocoa butter. The average amount of unsaturated fatty acid is 44.49% of the cocoa butter.

Table 3. Cocoa Butter fatty acids composition after soxhlet extraction

Fatty Acids	C12:0	C14:0	C16:0	C16:1	C18:0	C18:1	C18:2	C18:3	C20:0	C22:0
SE-ethanol/ Amount (%)	0.01	0.2-0.3	20-26	0.25	29-38	29-38	2-4	0.1	1	0.2

stearic acid (C18:0), oleic acid (C18:1,), palmitic acid (C16:0,). Linoleic acid (C18:2), arachidic acid (C20:0), alfa-linolenic acid (C18:3), palmitoleic acid (C16:1), behenic acid (C22:0) myristic acid (C14:0) and lauric acid (C12:0)

Table 4. Triglycerides composition of cocoa butter obtained after soxhlet extraction.

Triglycerides	POP	POS	SOS	DAG	MAG	FFA
SE-ethanol / Amounts (%)	15-16	35- 38	23-26	0.3-0.5	0.1	1

1-dipalmitoyl-2-oleoyl-glycerol (POP) , 1-palmitoyl-3-stearoyl-2-oleoyl-glycerol (POS) , 1,3-distearoyl-2-oleoyl- glycerol (SOS) , 1% free fatty acids, 0.3-0.5% diacylglycerols and 0.1% monoglycerides.

According to the study conducted by [19] the major fatty acid components of cocoa butter were oleic acid 34.5% and stearic acid 34.5%. Stearic acid has an apolar chain which confers solubility in organic solvent.

Asep et al., [20] showed at the end of their study on cocoa butter extraction that the 3 major fatty acids of cocoa butter were C 16: 0 (28.03-29.90%), C 18: 0 (34, 95%), C 18: 1 (31.01-31.82%), obtained after extraction with ethanol and these values were identical to those obtained using isopropanol.

The results obtained from the analysis of triglycerides using HPLC are shown in Table 2. The results showed that the cocoa butter contained 3 major TAGs including POP 15-23% (1,3 dipalmitoyl-2-oleoyl glycerol). ; POS 35-43% (1-palmitoyl 3-stearoyl-2-oleoyl glycerol); SOS 23-26% (1,3 distearoyl-2-oleoyl glycerol). These 3 TAGs had more than 80% of Cocoa butter's TAGs. POP, POS, SOS are symmetrical triglycerides due to the position of oleic acid in position 2.

According to the results obtained by [25] after analysis of CB by HPLC, cocoa butter had POS (43,48-45.85%), SOS (27.26-30.6%) and POP (20.19-23.15%) the results of Rossi et al. [25] corroborate those obtained after analysis.

Oxidative Analysis and Slip Melting Point (SMP)

The results obtained from the analysis of iodine, peroxide, acid and melting point indices were presented in Table 5. The value of the iodine number were 34.09 g I2/100 g of Cocoa Butter. This value was insignificant due to the similarity in fatty acid composition of the butter extracted. As reported by Bhatnager and Krishna [23], the iodine value of Niger seeds was insignificant when applied with different types of solvents.

Table 5. Slip melting point, Iodure value, Peroxyde value and Acid value of cocoa butter after soxhlet extraction

Characteristics	SMP (°C)	IV (g I_2/ 100g)	PV (meq O_2/kg)	AV (%)
SE-Ethanol / Amounts	$37 \pm 0,12$	$34,09 \pm 0,6$	$2,02 \pm 1,2$	$1,75 \pm 0,01$

SMP (Slip melting point) , IV (İodure value) , PV (Peroxide Value) , AV (Acid Value)

Those of peroxide value of cocoa butter (Table 1) showed 2.02 meq O2. According to pattern, the PV value obtained during SE-Ethanol was almost identical to those of the other methods (SCO2, USE, SCO2-Ethanol) when comparing the values. The peroxide index being the first oxidation product, gives an idea of the level of oxidative of the butter or oil extracted.

The acidity level of CB (Table 5) is high. Comparing this value to the other values of the other extraction methods is considerable. The high temperature during the extraction process and the period of exposure of ethanol to cocoa nibs can accelerate the hydrolysis of fatty acids and glycerol and thus accelerate the rancidity.

The melting point of the cocoa butter was shown in Table 5 with a value of 34°C. This value indicates that cocoa butter is solid or semi-solid at room temperature and that it melts when its temperature reaches 34°C. According to Bindu Naik and Vijay Kumar, cocoa butter has a sharp melting point ranges from 27 to 35°C.

CONCLUSION

The yield of cocoa butter, oxidative values (IV, PV, AV), phytosterols, antioxidant content (AA, TPC), fatty acids composition, triglycerides and Sharp Melting Point of cocoa butter was obtained by analysis after using of soxhlet extraction-ethanol. The results obtained was the yield of phytosterols (20,82 mg /kg), Antioxidant contents (AA, 45.04 %; TPC, 21,49mg GAE/100g) , Oxidation values (PV, 2,02 meq O2/kg ; AV, 1.75 mg KOH/g ; IV,34,09 g I2/ 100 g oil), SMP (34°C), Fatty acids (SFA, 65.51% ; UFA, 44.49%) and Triglycerides (more than 80 %). With Ethanol, the yield of cocoa butter is low compared to apolar solvent. These characteristics are constitued the physicochemical characteristics which determinate the textural value of cocoa butter and it is important in chocolate production process, cosmetic and pharmaceutic products.

REFERENCES

[1] B. Bujjsse, E.J. Feskens, F.J. Kok, D. Kromphout, Cocoa intake, blood pressure, and cardiovascular mortality: the Zutphen Elderly Study, Arch. Int. Med., 166 (2006) 411-417.

[2] B. Acquaah, Cocoa Development in West Africa. Ghana University Press, Accra (1999).

[3] M. Barel, Qualité du cacao : L'impact du traitement post- récolte. Edition Quae RD 10 (2013): 17-20.

[4] Ö. Tokuşoğlu, Kakao Çikolata ve Çikolatalı Ürünler Bilimi ve Teknolojisi, İzmir 2015.

[5] M. Lipp, E. Anklam, Review of cocoa butter and alternative fats for use in chocolate – Part A. Compositional data. Food Chem 62 (1998) 73-97.

[6] V.K.S. Shukla, Confectionery Lipids. In: Shahidi F, editor. Bailey's Industrial Oil and Fat Products. Hoboken: John Wiley & Sons Inc. (2005) 159-173.

[7] R.R. Carpenter, J.F. Hammerstone, L.J.Jr. Romanczyk, W.M. Aitken, Lipid composition of Herrania and Theobroma seeds, J Am Oil Chem Soc. 71 (1994) 845-851.

[8] K. Staphylakis, D. Gegiou, Free, esterified and glucosidic sterols in Cocoa. Lipids 11 (1985) 723-728.

[9] J.E. Spangenberg, F. Dionisi, Characterization of cocoa butter and cocoa butter equivalents by bulk and molecular carbon isotope analyses: implications for vegetable fat quantification in chocolate. J Agric Food Chem 49 (2001) 4271-4277.

[10] M. Lipp, Simoneau C, Ulberth F, Anklam E, Crews C, Brereton P, De Greyt W, Schwack W, Wiedmaier C, Composition of genuine cocoa butter and cocoa butter equivalents. J Food Compos Anal 14 (2001) 399-408.

[11] E.O. Afoakwa, Paterson A, Fowler M, Vieira J, Effects of tempering and fat crystallisation behaviour on microstructure, mechanical properties and appearance in dark chocolate systems. J Food Engin 89 (2008) 128-136.

[12] M.A. Bootello, Hartel RW, Garcés HR, Martínez-Force E, Salas JJ, Evaluation of high oleic-high stearic sunflower hard stearins for cocoa butter equivalent formulation. Food Chem 134 (2012) 1409-1417.

[13] P. Lonchampt, Hartel RW, Fat bloom in chocolate and compound coatings. Eur J Lipid Sci Technol 106 (2004) 241-274.

[14] R. Wille, E. Lutton, Polymorphism of cocoa butter. J Am Oil Chem Soc. 43 (1966) 491-496.

[15] P. Dimick, Principles of cocoa butter crystallization. Manuf. Confect. 71 (1991) 109-114.

[16] S.V. Vaeck, Polymorphie einiger. Naturfette Rev Int Choc 6 (1951) 350-354.

[17] American Oil Chemists' Society (AOCS). Method Cd 1d-92. Official Methods and Recommended Practices of the American Oil Chemists' Society Champaign (1993).

[18] American Oil Chemists' Society (AOCS). Method Ca 5a-40. Official Methods and Recommended Practices of the American Oil Chemists' Society Champaign (1993).

[19] M.H.A. Jahurul, I.S.M. Zaidul, N.A.N. Norulaini, F. Sahena, M.Z. Abedin, K. Ghafoor, A.K. Mohd Omar, Characterization of crystallization and melting profiles of blends of mango seed fat and palm oil mid-fraction as cocoa butter replacers using differential scanning calorimetry and pulse nuclear magnetic resonance, Food Research International Journal 55 (2014) 103-109.

[20] E.K. Asep, S. Jinap, T.J. Tan, A.R. Russly, S. Harcharan, S.A.H. Nazimah, The effects of particle size, fermentation and roasting of cocoa nibs on supercritical fluid extraction of cocoa butter, Journal of Food Engineering 85 (2008) 450–458.

[21] D. Salajegheh, A. Vaziri, D. Bastani, Supercritical extraction of cocoa butter from cocoa seed, using pure carbon dioxide, carbon dioxide with ethanol as co-solvent and ethane. Middle East Journal of Scientific Research 13 (2013) 1010-1015.

[22] L. Wang, C.L. Weller, Recent advances in extraction of nutraceuticals from plants. Trends in Food Science and Technology Journal 17 (2006): 300–312.

[23] A.S. Bhatnagar, A.G.G. Krishna, Effect of extraction solvent on oil and bioactives composition of commercial Indian Niger (Guizotia abyssinica (L.f.) Cass.) Seed. Journal of American Oil Chemists Society 90 (2013) 1203–1212.

[24] A. Azizah, Nik Ruslawati, N. and Swee Tee, T. Extraction and characterization of antioxidant from cocoa by-products. Food Chemistry Journal 64 (1999) 199–202.

[25] M. Rossi, C. Arnoldi, G. Salvioni, A. Schiraldi, Characterization of cocoa extracts obtained with supercritical carbon dioxide. Italian Journal of Food Science 3 (1989) 41–50.

Some Soft Fixed Point Results for Soft near Metric Spaces

Simge Öztunç*, Manisa Celal Bayar University, Faculty of Art and Science, Department of Mathematics, Manisa, Turkey
Ali Mutlu, Manisa Celal Bayar University, Faculty of Art and Science, Department of Mathematics, Manisa, Turkey
Kaan Özdemir, Manisa Celal Bayar University, The Institute of Natural and Applied Sciences, Manisa, Turkey,
*Corresponding author: simge.oztunc@cbu.edu.tr

Abstract

In the current study we defined a new metric called the soft near metric due to the near metric (or weak metric) which is defined by Fagin, Kumar and Sivakumar [1] in 2003. We use the contractive mappings for soft fixed theorems by using soft near metric.

Keywords: soft metric, soft near metric, soft fixed point theorems
Discipline: Mathematics, Topology

INTRODUCTION

The theory of soft set is a progressing rapidly as a new subject of mathematics which propounded by Molodtsov [2] in 1999 and investigated by Maji et al [3]. Soft sets has many applications especially in computer science modeling problems in engineering, economics, medical and social science. Also it has significant theorical properties which are studied in [4, 5, 6].

On the other hand Fixed Point Theory is a fascinating subject, with an enormous number of applications in various fields of mathematics for example engineering, physics, medicine and economics. In addition to this soft metric was defined by Das, Samanta [7] in 2013 and Hosseinzadeh [8] in 2017.

In current study we defined a new metric called the soft near- metric due to the near-metric (or weak metric) which is defined by Fagin, Kumar and Sivakumar [1] in 2003. We use the contractive mappings for soft fixed theorems by using soft near metric.

1. PRELIMINARIES

Definition 1.1. [2] A pair (F, A) is said to be a soft set over the universe U, where F is a mapping given by $F : A \to P(U)$.

In other words, a soft set over U is a parameterized family of subsets of the universe U. For any parameter $x \in A, F(x)$ may be considered as the set of $x-$ approximate elements of the soft set (F, A).

Definition 1.2. [3] Let (F, A) and (G, B) be two soft sets over U. We say that (F, A) is a soft subset of (G, B) and denote it by $(F, A) \widetilde{\subset} (G, B)$ if

(1) $A \subseteq B$, and

(2) $F(a) \subseteq G(a)$, for all $a \in A$.

(F, A) is said to be a soft super set of (G, B), if (G, B) is a soft subset of (F, A). We denote it by $(F, A) \widetilde{\supset} (G, B)$.

Definition 1.3. [3] Let (F, A) and (G, B) be two soft sets over U. The union of (F, A) and (G, B) is soft set (H, C), where $c = A \cup B$ and for all $e \in C$,

$$f(x) = \begin{cases} F(e), & e \in A - B \\ G(e), & e \in B - A \\ F(e) \cup G(e), & e \in A \cap B \end{cases}.$$

We write $(F, A) \widetilde{\cup} (G, B) = (H, C)$.

Definition 1.4. [3] Let (F, A) and (G, B) be two soft sets over U. The intersection of (F, A) and (G, B) is a soft set (H, C), where $C = A \cap B$ and for all $e \in C$, $H(e) = F(e) \cap G(e)$. We write $(F, A) \tilde{\cap} (G, B) = (H, C)$.

Definition 1.5. [3] Let (F, A) be soft set over U. The relative complement of (F, A) is denoted by $(F, A)^c$ and is defined $(F, A)^c = (F^c, A)$, where $F^c : A \rightarrow P(U)$ is a mapping given by $F^c(a) = U - F(a)$ for all $a \in A$.

Definition 1.6. [3] Let (F, A) and (G, B) be two soft sets over U. Then $(F, A) - (G, B)$ is a soft set $(x, F(x)) : F(x) \notin G(B), x \notin B$.

Definition 1.7. [3] Let (F, A) be soft set over U. Then

$(1) (F, A)$ is said to be null soft set denoted by $\tilde{\varnothing}$ if for every $a \in A, F(a) = \varnothing$.

$(2) (F, A)$ is said to be absolute soft set denoted by $\tilde{A}$ if for every $a \in A, F(a) = U$.

Definition 1.8. [8] Let $A \subseteq E$ be a set of parameters. We say the ordered pair (a, r) is a soft parametric scalar if $r \in R$ and $a \in A$. The parametric scalar (r, a) called nonnegative if $r \geq 0$. Let (a, r) and (b, r') be two soft parametric scalars. We say (a, r) is no less than (b, r') and we write $(a, r) \pm (b, r')$, if $r \geq r'$.

Definition 1.9. [8] Let $A \subseteq E$ be a set of parameters. Let (a, r) and (b, r') be two soft parametric scalars. Then we define addition between soft parametric scalars and scalar multiplication on soft parametric scalars as follows
$(a, r) \hat{e} (b, r') = (a, b, r + r')$, and
$\lambda(a, r) = (a, \lambda r)$, for every $\lambda \in R$.

Definition 1.10. [8] Let (F, A) be a soft set over X. We call a function f on (F, A) is parametric scalar valued, if there are functions $f_1 : A \rightarrow A$ and $f_2 : F(A) \rightarrow R$ such that $f(F, A) = (f_1, f_2)(A, F(A))$.

Similarly, we can extent above defined parametric scalar valued function as $f : (F, A) \times (F, A) \rightarrow (A, R)$ by $f(A \times A, F(A) \times F(A)) = (f_1, f_2)(A \times A, F(A) \times F(A))$, where $f_1 : A \times A \rightarrow A$ and $f_2 : F(A) \times F(A) \rightarrow R$.

Definition 1.11. [8] Let (F, A) be a soft set over X and let $\tilde{\pi} : A \times A \rightarrow A$ be parametric function. We say the parametric scalar valued function $\mathcal{D} : (F, A) \times (F, A) \rightarrow (A, R^+\{0\})$ a soft meter on (F, A) if $\mathcal{D}$ satisfies in the following conditions:

$(1) \mathcal{D}((a, F(a)), (b, F(b))) \pm (\tilde{\pi}(a, b), 0)$, and equality holds, whenever $a = b$.

$(2) \mathcal{D}((a, F(a)), (b, F(b))) = \mathcal{D}((b, F(b)), (a, F(a)))$, for all $a, b \in A$.

$(3) \mathcal{D}((a, F(a)), (c, F(c))) \circ \mathcal{D}((a, F(a)), (b, F(b))) \hat{e} \mathcal{D}((b, F(b)), (c, F(c)))$, for all $a, b, c \in A$.

We say the pair $((F, A), \mathcal{D})$ is a soft metric space over X.

Definition 1.12. [1] Assume X is a not null set and $d : X \times X \rightarrow [0, \infty]$ satisfy the following conditions for all $x, y \in X$ and all distinct $u, v \tilde{\in} X$ each of which is dissimilar from x and y.
(NM1) $d(x, y) = 0 \Leftrightarrow x = y$
(NM2) $d(x, y) = d(y, x)$
(NM3) $d(x, y) \leq Cd(x, z) + d(z, y)$
At that time d is named a rectangular metric and the pair (X, d) is named a near metric spaces. (NMS)

Definition 1.13. [9] $X \neq \varnothing$ and an element $x \in X$ is a fixed point of $f : X \rightarrow X$ if $f(x) = x$.

Definition 1.14. [9] Let T be a mapping of a metric space M into M. We say that T is a contraction mapping if there exists a number k such that $0 < k < 1$ and

66

$$p(Tx, Ty) \le kp(x, y) \qquad (\forall x, y \in M).$$

Theorem 1.15. [9] Any contraction mapping of a complete non-empty metric space M into M has a unique fixed point in M.

2. SOME FIXED POINT THEOREMS FOR STEINHAUS SOFT METRIC SPACES

Let $\tilde{\pi} : A \times A \to A$ be a scalar valued parametric function. The parametric scalar valued function $D_N : (F, A) \times (F, A) \to (A, R^+ \cup \{0\})$ is called to be a near soft metric on (F, A) if D_N satisfies the following conditions:

NSM1) $D_N((a, F(a)), (b, F(b))) \ge (\tilde{\pi}(a, b), 0),$ and equality holds whenever $a = b.$

NSM2) $D_N((a, F(a)), (b, F(b))) = (\tilde{\pi}(a, b), 0) \Leftrightarrow$ for all $((a, F(a)), (b, F(b))) \in (F, A),$ $(a, F(a)) = (b, F(b))[$ for all $a, b \in A, a = b]$

NSM3) $D_N((a, F(a)), (b, F(b))) = D_R((b, F(b)), (a, F(a))),$ for all $a, b \in A$

NSM4) $D_N((a, F(a)), (c, F(c))) \le (c, r) D_N((a, F(a)), (b, F(b))) + D_N(b, F(b)), (c, F(c)))$ for all $a, b, c \in A$ and $(c, r) \ge (1, r)$

Then we say the pair $((F, A), D_N)$ is a near soft metric space over X.

Definition 2.1. [8] Let (F, A) be a soft set over X. A soft sequence in (F, A) is a function $f : N \to (F, A)$ by setting $f(n) = (F_n, A)$ such that (F_n, A) is a soft subset of (F, A) for $n \in N,$ and we denote it by $\{(F_n, A)\}_{n=1}^{\infty}$.

Definition 2.2. Let (F, A) be a soft set over X. Let D_R be a near soft metric on $(F, A),$ $\{(F_n, A)\}_{n=1}^{\infty}$ be a soft sequence in (F, A) and $(x, F(x)) \in (F, A)$. Then we say $\{(F_n, A)\}_{n=1}^{\infty}$ converges to $(x, F(x)),$ if for every positive number ò, there exists a naturel number N such that for every natural number n which $n \ge N,$ we have

$$D_N(a, F_n(a),) \le (\tilde{\pi}(a, x), ò).$$

Definition 2.3. Let (F, A) be a soft set over X. Let D_N be a near soft metric on (F, A) and $\{(F_n, A)\}_{n=1}^{\infty}$ be a soft sequence in (F, A). Then we say $\{(F_n, A)\}_{n=1}^{\infty}$ is a Cauchy soft sequence, if for every positive number ò, there exists a natural number N such that for every natural number n, m which $n, m \ge N,$ we have

$$D_N((a, F_n(a)), (a, F_m(a))) \le (\tilde{\pi}(a, a), ò).$$

Proposition 2.4. Let $((F, A), D_N)$ be a near soft metric space over X, and let $\{(F_n, A)\}_{n=1}^{\infty}$ be a convergent soft sequence in (F, A). Then $\{(F_n, A)\}_{n=1}^{\infty}$ is a Cauchy soft sequence.

Definition 2.5. Let (F, A) be a soft set over X, let D_N be a near soft metric on (F, A). We say that (F, A) is a complete rectangular soft metric space if every Cauchy soft sequence converges in (F, A).

Theorem 2.6. Let $((F, A), D_N)$ and $((F', A'), D'_N)$ be two near soft metric spaces over X and Y respectively. Let $f = (f_1, f_2) : ((F, A), D_N) \to ((F', A'), D'_N)$ be a soft mapping. Then f is soft continuous if and only if for every $(x, F(x)) \in (F, A)$ and every positive number ò, there exists a positive number δ such that for every $(y, F(y)) \in (F, A)$

67

$$\mathcal{D}'_N((f(x,F(x))),f((y,F(y)))) \leq (\tilde{\pi}'(\tilde{\pi}(x,y)),\grave{o})$$

whenever $\mathcal{D}'_N(f(x,F(x))),f((y,F(y))) \leq (\tilde{\pi}(x,y)),\delta)$.

Definition 2.7. Let $((F,A),\mathcal{D}_N)$ be a near soft metric space over X and $f:((F,A),\mathcal{D}_N) \rightarrow ((F,A),\mathcal{D}_N)$ be a soft mapping. We say that f is soft contractive if there is a positive number c with $0<c<1$ such that

$$\mathcal{D}_N((f(x,F(x))),f((y,F(y)))) \leq c\,\mathcal{D}_N((x,F(x)),(y,F(y))), \text{ for all } x,y \in A.$$

Theorem 2.8. Soft contractive mapping is soft continuous in near soft metric space $((F,A),\mathcal{D}_N)$.

Definition 2.9. Let $((F,A),\mathcal{D}_N)$ be a complete near soft metric space over X and let $f:((F,A),\mathcal{D}_N) \rightarrow ((F,A),\mathcal{D}_N)$ be a soft mapping. A fixed soft set for f is a soft subset of (F,A) such as $(x,F(x))$ such that $f((x,F(x)))=(x,F(x))$.

Theorem 2.10. (Banach Contraction Theorem for Near Soft Metric Space)

Let $((F,A),\mathcal{D}_N)$ be a complete near soft metric space over X, and $f:((F,A),\mathcal{D}_N) \rightarrow ((F,A),\mathcal{D}_N)$ be near soft contractive mapping. Then f has unique fixed soft set.

Proof: Let (F_0,A) be an arbitrary soft point in (F,A). We construct the soft sequence $\{(F_n,A)_{n=1}^{\infty}\}$ as follows:

$$(F_{n+1},A)=f((F_n,A))=f^{n+1}((F_0,A)) \qquad (n=0,1,2,...) \tag{2.1}$$

Since f is soft contraction, then there exists a $0<c<1$ such that for all $n \geq 1$

$$\mathcal{D}_R((F_{n+1},A),(F_n,A))=\mathcal{D}_R(f,((F_n,A)),f((F_{n-1},A)))$$

$$\leq \mathcal{D}_R((F_n,A),(F_{n-1},A)) \tag{2.2}$$

By induction for $n=0,1,2,...$ we conclude that

$$\mathcal{D}_R((F_{n+1},A),(F_n,A)) \leq c^n \mathcal{D}_R((F_1,A),(F_0,A)) \tag{2.3}$$

Now by using rectangular property of soft metric for all $(F_0,A) \in (F,A)$, we have

$$\mathcal{D}_R((F_0,A),f^4((F_0,A))) \leq \mathcal{D}_R((F_0,A),f((F_0,A)))+\mathcal{D}_R((F_0,A),f^2((F_0,A)))$$

$$+\mathcal{D}_R(f^2((F_0,A)),f^4((F_0,A)))$$

$$\leq \mathcal{D}_R((F_0,A),f((F_0,A)))+c\,\mathcal{D}_R((F_0,A),f((F_0,A)))$$

$$+c^2\mathcal{D}_R(f((F_0,A)),f^2((F_0,A)))$$

Similarly;

$$\mathcal{D}_R((F_0,A),f^6((F_0,A))) \leq \mathcal{D}_R((F_0,A),f((F_0,A)))+\mathcal{D}_R((F_0,A),f^2((F_0,A)))$$

$$+\mathcal{D}_R(f^2((F_0,A)),f^3((F_0,A)))+\mathcal{D}_R(f^3((F_0,A)),f^4((F_0,A)))$$

$$+\mathcal{D}_R(f^4((F_0,A)),f^6((F_0,A)))$$

$$\leq \mathcal{D}_R((F_0,A),f((F_0,A)))+c\,\mathcal{D}_R((F_0,A),f((F_0,A)))$$

$$+c^2\mathcal{D}_R((F_0,A),f((F_0,A)))+c^3\mathcal{D}_R((F_0,A),f^2((F_0,A)))$$

$$+c^4\mathcal{D}_R((F_0,A),f^2((F_0,A)))$$

$$\leq \sum_{i=1}^{3}c^i\mathcal{D}_R((F_0,A))+c^4\mathcal{D}_R((F_0,A),f^2((F_0,A))) \quad \forall (F_0,A) \in (F,A)$$

By induction for $k=2,3,4,...$

$$D_R((F_0, A), f^{2k}((F_0, A))) \leq \sum_{i=0}^{2k-3} c^i D_R((F_0, A), f((F_0, A))) + c^{k-2} D_R((F_0, A), f^2((F_0, A)))$$

Moreover for all $(F_0, A) \in (F, A)$;

$$\begin{aligned}
D_R((F_0, A), f^5((F_0, A))) &\leq D_R((F_0, A), f((F_0, A))) + D_R((F_0, A), f^2((F_0, A))) \\
&\quad + D_R(f^2((F_0, A)), f^3((F_0, A))) + D_R(f^3((F_0, A)), f^4((F_0, A))) \\
&\quad + D_R(f^4((F_0, A)), f^5((F_0, A))) \\
&\leq \sum_{i=0}^{4} c^i D_R((F_0, A), f((F_0, A)))
\end{aligned}$$

By induction for $k = 0, 1, 2, \ldots$

$$D_R((F_0, A), f^{2k+1}((F_0, A))) \leq \sum_{i=0}^{2k} c^i D_R((F_0, A), f((F_0, A)))$$

By using (2) inequality for $k = 0, 1, 2, \ldots$

$$\begin{aligned}
D_R(f^n((F_0, A)), f^{n+2k}((F_0, A))) &\leq c^n D_R((F_0, A), f^{2k}((F_0, A))) \\
&\leq c^n \Big[\sum_{i=0}^{2k-3} c^i (D_R((F_0, A), f((F_0, A))) + D_R((F_0, A), f^2((F_0, A)))) \\
&\quad + c^{k-2}(D_R((F_0, A), f((F_0, A))) + D_R((F_0, A), f^2((F_0, A))))\Big] \\
&\leq c^n \Big[\sum_{i=0}^{2k-2} c^i (D_R((F_0, A), f((F_0, A))) + D_R((F_0, A), f^2((F_0, A))))\Big] \\
&\leq \frac{c^n(1-c^{2k-1})}{1-c}\Big[D_R((F_0, A), f((F_0, A))) + D_R((F_0, A), f^2((F_0, A)))\Big] \\
&\leq \frac{c^n}{1-c}\Big[D_R((F_0, A), f((F_0, A))) + D_R((F_0, A), f^2((F_0, A)))\Big]
\end{aligned}$$

Similarly for $k = 0, 1, 2 \ldots$ (2.3) inequality

$$\begin{aligned}
D_R(f^n((F_0, A)), f^{n+2k+1}((F_0, A))) &\leq c^n D_R((F_0, A), f^{2k+1}((F_0, A))) \\
&\leq c^n \Big[\sum_{i=0}^{2k} c^i (D_R((F_0, A), f((F_0, A))))\Big] \\
&\leq \frac{c^n}{1-c}\Big[D_R((F_0, A), f((F_0, A))) + D_R((F_0, A), f^2((F_0, A)))\Big]
\end{aligned}$$

Thus;

$$D_R((F_0, A), f^{n+m}((F_0, A))) \leq \frac{c^n}{1-c}\Big[D_R((F_0, A), f((F_0, A))) + D_R((F_0, A), f^2((F_0, A)))\Big]$$

Since every convergent soft sequence is soft Cauchy Sequence $\{(F_n, A)\}_{n=1}^{\infty}$ is a soft Cauchy sequence in (F, A). Since (F, A) is a complete soft metric space, then there exists $(x, F(x)) \in (F, A)$ such that $\{(F_n, A)\}_{n=1}^{\infty}$ converges to $(x, F(x))$. Since f is a soft continuous, therefore $f((F_n, A))$ converges to $f((x, F(x)))$. As well as, according to definition of $\{(F_n, A)\}_{n=1}^{\infty}$, $f((F_n, A))$ converges to $(x, F(x))$. It follows that (Theorem 2.6) that $f((x, F(x))) = (x, F(x))$.

Now prove the uniqueness property of $(x, F(x))$. Suppose that there exists another element $(y, F(y)) \in (F, A)$ such that $f((y, F(y))) = (y, F(y))$ and $(x, F(x)) \neq (y, F(y))$. Then

$$D_R((x, F(x)), (y, F(y))) = D_R(f((x, F(x))), f((y, F(y))))$$
$$\leq c D_R((x, F(x)), (y, F(y)))$$

Then above inequality implies that $c > 1$, which is a contradiction. This completes the proof. ∎

Lemma 2.11. Let $A \subseteq E$ be a set of parameters, (a, r) and (b, r') be two soft parametric scalars such that for every $\grave{o} > 0$, if $(a, r) \prec (b, r' + \grave{o})$, then $(a, r) \circ (b, r')$.

Theorem 2.12. Let $((F, A), D_R)$ be a complete rectangular soft metric space over X, and let $T = (T_1, T_2) : ((F, A), D_R) \rightarrow ((F, A), D_R)$ be a soft continuous mapping such that $T(a, F(a)) = (T_1(a), T_2(F(a))) = (T_1(a), F(T_1(a)))$ for every $(a, F(a)) \in (F, A)$ and it satisfies for some parametric scalar valued $\varphi : (F, A) \rightarrow (A, R^+)$

$$D_R(T((a, F(a))), (a, F(a))) < \varphi((a, F(a))) - \varphi(T(a, F(a))) \tag{2.4}$$

Then $\{T^n((a, F(a)))\}$ converges to a fixed soft set, for every $(a, F(a)) \in (F, A)$.

Proof: Let $T = (T_1, T_2)$ and $\varphi = (\varphi_1, \varphi_2)$. Now, if $T((a, F(a))) = (T_1(a), T_2(F(a)))$, we set $T((a, F(a))) = (a_1, F(a_1))$, then

$$\varphi(T((a, F(a)))) = (\varphi_1(a_1), \varphi_2(F(a_1))) = (b_1, r_1).$$

Similarly we write $T^n((a, F(a))) = (a_n, F(a_n))$ for $n = 1, 2, \ldots$

Thus;

$$\varphi(T^n((a, F(a)))) = (\varphi_1(a_n), \varphi_2(F(a_n))) = (b_n, r_n)$$

The condition 2.4 implies that

$$D_R(T((a, F(a))), (a, F(a))) + \varphi(T(a, F(a))) < \varphi((a, F(a))) \tag{2.5}$$

Therefore by Lemma 2.11 $\varphi(T((A, F(a)))) < \varphi((a, F(a)))$.

This implies that $\varphi(T^2((a, F(a)))) \leq \varphi(T((a, F(a))))$. If we continuous this method we obtained $\varphi(T^{n+1}((a, F(a)))) \leq \varphi(T^n((a, F(a))))$

This means that $\{\varphi(T^n((a, F(a))))\}$ is a decreasing and so the sequence $\{r_n\}$ of real numbers is decreasing. Hence there is an $r \in R$ such that

$$\lim_{n \to \infty} \varphi(T^n((a, F(a)))) = (b, r) \text{ (for all } b \in A) \tag{2.6}$$

Clearly (b, r) is nonnegative. Then for all $n, m \in N$ with $m \geq n$, we have by using soft rectangular property;

$$D_R(T^n((a, F(a))), T^m((a, F(a)))) \leq D_R(T^n((a, F(a))), T^{n+1}((a, F(a))))$$
$$+ D_R(T^{n+1}((a, F(a))), T^{n+2}((a, F(a)))) + D_R(T^{n+2}((a, F(a))), T^m((a, F(a))))$$
$$\leq D_R(T^n((a, F(a))), T^{n+1}((a, F(a)))) + D_R(T^{n+1}((a, F(a))), T^{n+2}((a, F(a))))$$
$$+ D_R(T^{n+2}((a, F(a))), T^{n+3}((a, F(a)))) + D_R(T^{n+3}((a, F(a))), T^{n+4}((a, F(a))))$$
$$+ D_R(T^{n+4}((a, F(a))), T^m((a, F(a))))$$
$$\leq D_R(T^n((a, F(a))), T^{n+1}((a, F(a)))) + D_R(T^{n+2}((a, F(a))), T^{n+3}((a, F(a))))$$
$$+ D_R(T^{n+3}((a, F(a))), T^{n+4}((a, F(a)))) + D_R(T^{n+4}((a, F(a))), T^{n+5}((a, F(a))))$$
$$+ D_R(T^{n+5}((a, F(a))), T^{n+6}((a, F(a)))) + D_R(T^{n+6}((a, F(a))), T^m((a, F(a))))$$
$$\leq D_R(T^n((a, F(a))), T^{n+1}((a, F(a)))) + D_R(T^{n+1}((a, F(a))), T^{n+2}((a, F(a))))$$
$$+ \cdots + D_R(T^{n+2k}((a, F(a))), T^m((a, F(a))))$$
$$\leq \varphi(T^n((a, F(a)))) - \varphi(T^{n+1}((a, F(a)))) + \varphi(T^{n+1}((a, F(a)))) - \varphi(T^{n+2}((a, F(a))))$$

$$+ \cdots + \varphi(T^{n+2k}((a, F(a))) - \varphi(T^m((a, F(a)))$$

$$\leq \varphi(T^n((a, F(a))) - \varphi(T^m((a, F(a)))$$

Thus $\lim\limits_{m,n \to \infty} D_R(T^n((a, F(a))), T^m((b, F(b)))) = (b, 0).$

Therefore $\{T^n((a, F(a)))\}$ is a soft Cauchy sequence. Thus there exist $(x, F(x)) \in (F, A)$ such that

$$\lim\limits_{n \to \infty} T^n((a, F(a)) = (x, F(x)). \qquad \blacksquare$$

REFERENCES

[1] R. Fagin, R. Kumar, D. Sivakuma, Comparing Top k Lists, SIAM Journal on Discrete Mathematics 17 (2003) 134-160.

[2] D. Molodtsov, Soft set theory-First result, Comput. Math. Appl. 37 (1999) 19- 31.

[3] P. K. Maji, R. Biswas, A. R. Roy, Soft Set Theory, Comput. Math. Appl. 45 (2003) 555-562.

[4] Ç.G.Aras, A. Sönmez, H. Çakallı, On Soft Mappings, ArXiv, Computers & Mathematics with Applications 60(9) (2013) 1-12.

[5] Ç.G. Aras, H. Poşul, On some new operations in Probabilistic Soft Set Theory, European Journal of Pure and Applied Mathematics 9(3) (2016) 333-339.

[6] I. Zorlutuna, H. Çakır, On continuity of Soft Mappings, Appl. Math. Inf. Sci. 9(1), (2015), 403-409.

[7] S. Das, S.K.Samanta, Soft Metric, Annals of Fuzzy Mathematics and Informatics 6 (2013) 77-94.

[8] H. Hosseinzadeh, Fixed Point Theorems on Soft Metric Spaces, Journal of Fixed Point Theory and Applications 19 (2017) 1625–1647.

[9] S. Banach, Sur les opérations dans les ensembles abstraits et leur application aux équations intégrales. Fund Math. 3 (1922) 133-181.

A Numerical Method for Solving Functional Differential Equations with Delays

Ömür Kıvanç Kürkçü*, Izmir University of Economics, Department of Mathematics, Izmir, Turkey
Ersin Aslan, Manisa Celal Bayar Üniv., Department of Software Engineering, Manisa, Turkey
Mehmet Sezer, Manisa Celal Bayar Üniv., Department of Mathematics, Manisa, Turkey
*Corresponding author e-mail: omur.kivanc@ieu.edu.tr

Abstract

In this study, we implement a matrix-collocation method based on Dickson polynomials with a parameter-α to numerically solve the functional differential equations with delays. We scrutinize the behavior of the obtained solutions of illustrative numerical examples with the help of α. Thus, we determine stableness of the solutions corresponding to a proper α-interval. All results indicate the efficiency of the present method.

Keywords: Collocation points, Dickson polynomials, matrix method
Discipline: Mathematics

INTRODUCTION

In recent years, functional differential equations have received much attention by many authors, who study on mathematics, physics, biology and engineering and etc. We often encounter a problem, since these equations cannot be solved easily. Instead of this, the highly effective numerical methods have been employed for obtaining the approximate solutions of the equations. Some well-known of them are Taylor [1,2], Dickson matrix-collocation [3-6], Adomian decomposition [7], He's homotopy perturbation [8] and variational iteration methods [9]. In this study, we apply the matrix-collocation method based on the Dickson polynomials including a parameter-α to the functional linear differential equations with delays. The Dickson polynomial solutions are investigated in figures and tables. In addition, the behaviors of the solutions are discussed in terms of different parameter-α. Hence, the parameter-α enables us to observe the consistency of the solutions for its different values. Besides, we make comparison between the present results and the existed results found in literature. The functional differential equation with delays we consider in this study

$$\sum_{k=0}^{m} P_k(t) y^{(k)}(\alpha_k t + \tau_k) = g(t), \ a \le t \le b, \tag{1}$$

subject to the initial conditions

$$\sum_{k=0}^{m-1} a_{ik} y^{(k)}(a) = \eta_i, \ i = 0,1,\ldots,m-1. \tag{2}$$

METHOD

In this study, the method forms a basis of the operational matrices, collocation points and the Dickson polynomials with the parameter-α. The functions are transformed into the operational matrices and the values of them at collocation points are written in these matrices. In order to obtain sensitive results, we construct a computer program, which is easily applied to the mentioned equations.

We find the Dickson polynomial solution of Eq. (1) in the form [3-6]:

$$y(t) \cong y_N(t) = \sum_{n=0}^{N} y_n D_n(t, \alpha), \tag{3}$$

where y_n unknown Dickson coefficients.

The collocation points we use in the matrices are defined to be

$$t_i = a + \left(\frac{b-a}{N}\right)i \ , \ i = 0,1,\ldots,N \ , \ a = t_0 < t_1 < \ldots < t_N = b \ .$$

The matrix relation of the Dickson polynomial solution (3) is

$$y(t) \cong y_N(t) = \boldsymbol{D}(t,\alpha)\boldsymbol{Y} \ , \ \boldsymbol{D}(t,\alpha) = \boldsymbol{X}(t)\boldsymbol{S}(\alpha) \Rightarrow y(t) = \boldsymbol{X}(t)\boldsymbol{S}(\alpha)\boldsymbol{Y}$$

where

$$\boldsymbol{X}(t) = \begin{bmatrix} 1 & t & t^2 & \cdots & t^N \end{bmatrix} \text{ and } \boldsymbol{Y} = \begin{bmatrix} y_0 & y_1 & \cdots & y_N \end{bmatrix}^T .$$

By using the collocation points, we give the following matrix relations for Eq. (1):

$$[W]_{(N+1)\times 1} = \sum_{k=0}^{m} \boldsymbol{P}_k \boldsymbol{X}^{(k)} \boldsymbol{S}(\alpha) \boldsymbol{Y} , \tag{4}$$

where

$$\boldsymbol{W} = \begin{bmatrix} W(t_0) \\ W(t_1) \\ \vdots \\ W(t_N) \end{bmatrix} , \ \mathbb{P}_k = \begin{bmatrix} P_k(t_0) & 0 & \cdots & 0 \\ 0 & P_k(t_1) & \cdots & 0 \\ \vdots & \vdots & \ddots & \vdots \\ 0 & 0 & \cdots & P_k(t_N) \end{bmatrix} ,$$

$$\boldsymbol{X}^{(k)} = \begin{bmatrix} \boldsymbol{X}^{(k)}(\alpha_k t_i + \tau_k) \end{bmatrix} = \begin{bmatrix} 1 & (\alpha_k t_i + \tau_k)^{(k)} & \cdots & \left((\alpha_k t_i + \tau_k)^N\right)^{(k)} \end{bmatrix} .$$

The fundamental matrix equation is obtained as

$$\boldsymbol{WY} = \boldsymbol{G} \ .$$

After removing the last m row of W in (4), we add the initial conditions (2) into the relation (4). Thus,

$$\tilde{\boldsymbol{W}}\boldsymbol{Y} = \tilde{\boldsymbol{G}} \Rightarrow \boldsymbol{Y} = \left(\tilde{\boldsymbol{W}}\right)^{-1}\tilde{\boldsymbol{G}} \ .$$

By obtaining the unknown Dickson coefficients, we finally reach the Dickson polynomial solution (3).

NUMERICAL EXAMPLES

We consider three examples to illustrate the efficiency of the method. The behavior of the solutions is demonstrated in figures and numerical results are tabulated.

Example 1. [10] Consider Hayes equation used for stability theory

$$y'(t) = \varepsilon y(t) + \beta y(t-\tau) + g(t), \ 0 \le t \le 1$$

subject to initial conditions $y(0) = y'(0) = 1$. The exact solution is $y(t) = e^t$. For delay parameter $\tau = 1$, different parameters ε and β. Solving the problem, we then illustrate different curves with respect to α in Figure 1.

Example 2. [11] Consider the oscillator equation with delayed damping

$$y''(t) + y'(t-1) + y(t) = 1 - \sin(2-t) + 0.5\sin(2-t), \ 1 \le t \le 2$$

subject to initial conditions $y(1) = 0.459698$ and $y'(1) = 0.841471$. The exact solution is

$$y(t) = 1 - \cos(t) + 0.5(t-1)\cos(t-1) - 0.5\sin(t-1).$$
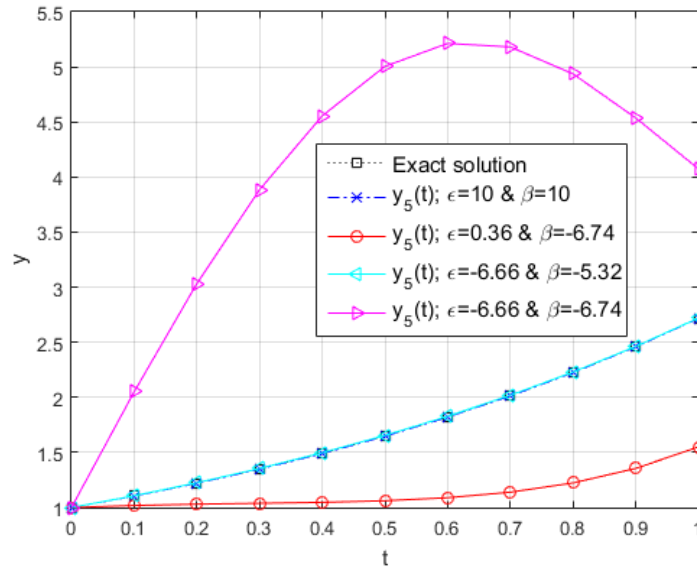
Figure 1. The behavior of the Dickson polynomial solution with respect to ε and β for Example 1.

Let us solve the problem by taking N=9. In Table 1, we compare the present results with those obtained by spline approximation method [11]. As seen from there, the better results are obtained. Figure 2 shows the consistency between the exact and Dickson polynomial solution and also Figure 3 demonstrates the contour lines of them.

Table 1. Comparison of the absolute errors $\left|e_N(t_i)\right| = \left|y(t) - y_N(t)\right|$ and $\left|e_N^*(t_i)\right| = \left|y'(t) - y_N'(t)\right|$ for Example 2

t_i	$\left|e_9(t_i)\right|$ $\alpha = 0.1$	Spline method $\left|e_9(t_i)\right|$ [11]	$\left|e_9^*(t_i)\right|$ $\alpha = 0.1$	Spline method $\left|e_9^*(t_i)\right|$ [11]
1.25	$1.98e-04$	$1.27e-02$	$1.25e-03$	$4.40e-02$
1.50	$7.20e-04$	$2.39e-02$	$2.56e-03$	$4.32e-02$
1.75	$1.42e-03$	$3.32e-02$	$2.98e-03$	$2.86e-02$
2.00	$2.15e-03$	$3.72e-02$	$2.75e-03$	$1.83e-03$

Example 3. Consider third-order multiple delay differential equation with variable coefficients

$$y'''(t) - t^2 y''(t+1) + e^t y'(0.5t-1) - (t^3+1)y(t-\pi) = g(t), \ 0 \le t \le 1$$

subject to the initial conditions $y(0) = 0$, $y'(0) = 1$ and $y''(0) = 0$. Here, the exact solution is $y(t) = \sin(t)$ and

$$g(t) = e^t \cos(1-0.5t) - \cos(t) - (1+t^3)\sin(t) + t^2 \sin(t+1).$$

We solve this problem by taking N=10 and $\alpha \in \left[-5 \times 10^{3}, 5 \times 10^{3} \right]$. We illustrate the Dickson polynomial solution as both diagram and contour lines in Figures 4 and 5, respectively.
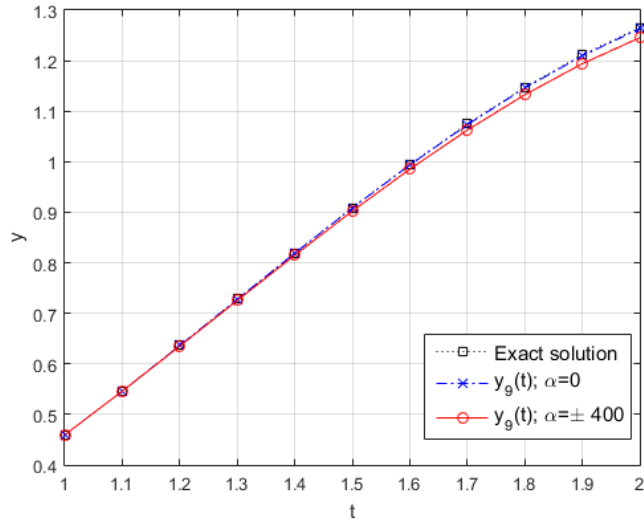
Figure 2. The behavior of the exact and Dickson polynomial solution with respect to α for Example 2

(a)   (b)
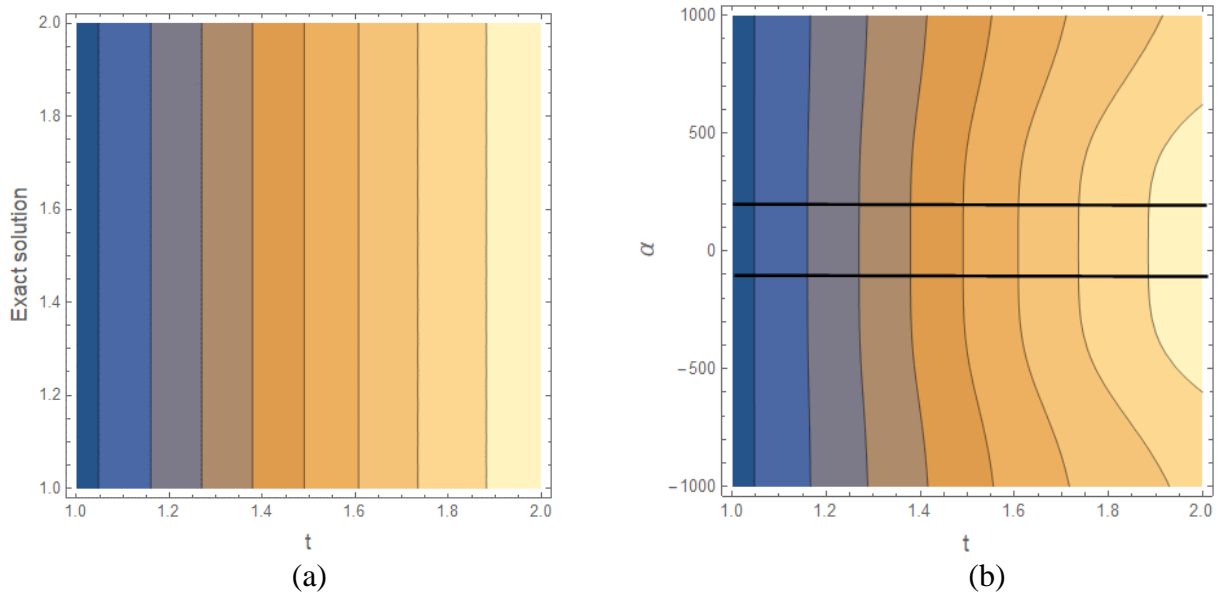
Figure 3. (a) The contour plot of the exact solution, (b) the stable contour area of the Dickson polynomial solution with $\alpha \in \left[-100, 100 \right]$ for Example 2.

2nd International Students Science Congress
4-5 May 2018, Izmir - Turkey

İZMİR
KÂTİP ÇELEBİ
UNIVERSITY
— 2010 —

İZMİR
Uluslararası
Misafir
Öğrenci
Derneği
◆ İZMİR International Guest Student Association
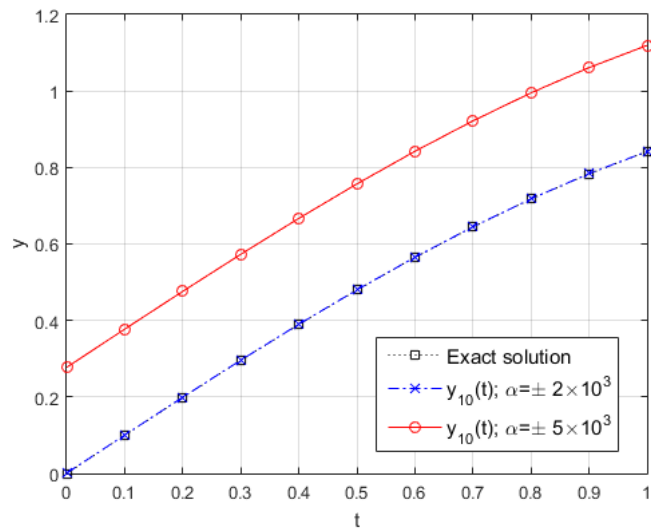
Figure 4. The behavior of the exact and Dickson polynomial solution with respect to α for Example 3
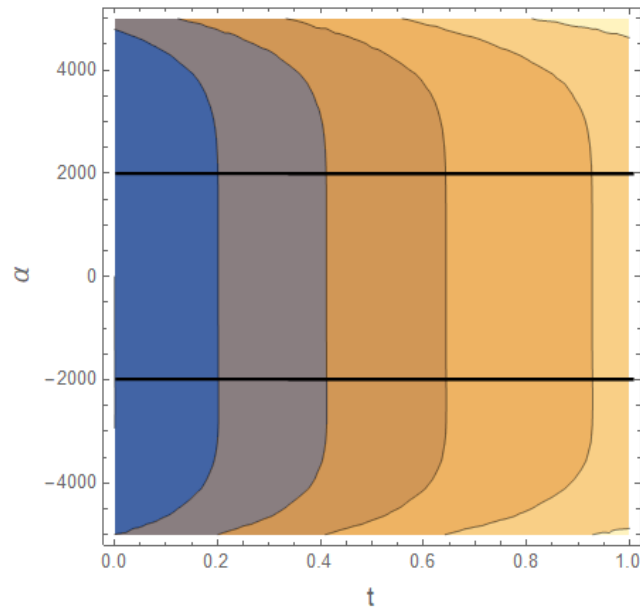
Figure 5. The stable contour area of the Dickson polynomial solution with $\alpha \in \left[-2 \times 10^{3}, 2 \times 10^{3} \right]$ for Example 3.

CONCLUSIONS

We discuss the behaviors of the solutions in Figures 1-5 and Table 1. We observe that our solutions coincide with the exact solutions. In addition, the consistent numerical results are obtained and the parameter-α plays an important role in these results as seen in Figures 2 and 4. Thus, we conclude that present method is effective and practical to solve the functional linear differential equations with delays.

REFERENCES

[1] M. Gülsu, M. Sezer, A Taylor collocation method for solving high-order linear pantograph equations with linear functional argument, Numer. Methods Partial Differ. Eqns. 27 (2011) 1628–1638.
[2] M. Sezer, Taylor polynomial solution of Volterra integral equations, Int. J. Math. Educ. Sci. Technol. 25 (1994) 625–633.

[3] Ö.K. Kürkçü, E. Aslan, M. Sezer, A numerical approach with error estimation to solve general integro-differential–difference equations using Dickson polynomials, Appl. Math. Comput. 276 (2016) 324–339.

[4] Ö.K. Kürkçü, E. Aslan, M. Sezer, A novel collocation method based on residual error analysis for solving integro-differential equations using hybrid Dickson and Taylor polynomials, Sains Malays. 46 (2017) 335–347.

[5] Ö.K. Kürkçü, E. Aslan, M. Sezer, Ö. İlhan, A numerical approach technique for solving generalized delay integro-differential equations with functional bounds by means of Dickson polynomials, Int. J. Comput. Methods 15 (2018) doi.org/10.1142/S0219876218500391.

[6] Ö.K. Kürkçü, E. Aslan, M. Sezer, A numerical method for solving some model problems arising in science and convergence analysis based on residual function, Appl. Numer. Math. 121 (2017) 134–148.

[7] G. Adomian, A review of the decomposition method in applied mathematics, J. Math. Anal. Appl. 135 (1988) 501–544.

[8] J.H. He, Homotopy perturbation technique, Comput. Methods Appl. Mech. Eng. 178 (1999) 257–262.

[9] J.H. He, Variational iteration method-a kind of non-linear analytical technique: Some examples, Int. J. Nonlinear Mech. 34 (1999) 699–708.

[10] T. Insperger, G. Stépán, Semi-discretization for time-delay systems: stability and engineering applications, Applied Mathematical Sciences 178, Springer, New York, 2011.

[11] H.T. Banks, F. Kappel, Spline approximations for functional differential equations, J. Diff. Eqns. 34 (1979) 496–522.

A Combined Numerical Approach Based upon Genocchi Series for Solution of Functional Integro-Differential Equations

Ülker Başar*, Mehmet Sezer
Manisa Celal Bayar Univ., Department of Mathematics, Muradiye, Manisa, Turkey
*Corresponding author: ulkerbasar@hotmail.com

Abstract

In this article, we introduce a new operational matrix method based on Genocchi series and collocation points. This method is developed for the approximate solution of high-order generalized linear Volterra-Fredholm integro-differential equations with mixed functional arguments under the mixed conditions. Besides, some numerical examples having the exact solution are performed to demonstrate the validity and applicability of the method.

Keywords: collocation points, Genocchi polynomials, matrix method
Discipline: Mathematics

INTRODUCTION

In recent years, it is well known that there exists an increasing interest in the implementation of the models to high-order linear problems of the mentioned type in biological science, mathematical physics and engineering mathematics. Also, the numerical solution methods of them have been developed very quickly and intensely by many authors. Since the beginning of 1994, the most common functions related with Taylor [1], Chebyshev [2], Laguerre [3], Hermite [4], Dickson [5], Bernstein [6], Bessel [7], Bernoulli [8], Taylor-Lucas [9], and Jacobi [10] methods depend on collocation method have been used by Sezer et al. to solve high-order linear various type of equations such as differential, difference, integral or Volterra-Fredholm integro-differential difference equations. In this study, we examine the high-order generalized linear functional integro-differential equations with constant and functional delays

$$\sum_{k=0}^{m_1}\sum_{j=0}^{m_2} D_{kj}(x) = f(x) + \sum_{r=0}^{m_3}\sum_{s=0}^{m_4} I_{rs}(x), \ (\max\{m_1, m_3\} = m, \ \{x, t, u_{rs}(x), v_{rs}(x)\} \in [a, b]) \tag{1}$$

so that $\quad D_{kj}(x) = P_{kj}(x) y^{(k)}(h_{kj}(x)) \quad$ and $\quad I_{rs}(x) = \int_{u_{rs}(x)}^{v_{rs}(x)} K_{rs}(x, t) y^{(r)}(g_{rs}(t)) dt,$

via mixed conditions

$$\sum_{k=1}^{m}\sum_{l=1}^{L} a_{j,k,l} y^{(k)}(\gamma_l) = \lambda_j, \ (j=1,2,...,m, \quad a \le \gamma_l \le b). \tag{2}$$

Here, $D_{kj}(x)$ and $I_{rs}(x)$ are the functional differential part and functional integro-differential part of Eq.(1); $f(x), P_{kj}(x), K_{rs}(x,t),) \ g_{rs}(t), h_{kj}(x), u_{rs}(x)$ and $v_{rs}(x)$ are functions defined on the interval $a \le x, t \le b$; $a_{j,k,l}, \gamma_l$ and λ_j are appropriate constants. Our aim in this work is to find the approximate solution of the problem (1)-(2) in the finite Genocchi series form

$$y(x) \cong y_N(x) = \sum_{n=1}^{N} a_n G_n(x), \ (a \le x \le b), \tag{3}$$

where $G_n(x)$, n=1,2,...,N denote the Genocchi polynomials[10] ; a_n, n=1,2,...,N are unknown Genocchi coefficients to be determined and N is any positive integer chosen such that $N \ge m$; Genocchi polynomials $G_n(x)$, n=1,2,...,N, are given by

$$G_n(x) = \sum_{k=1}^{n} \binom{n}{k-1} G_{n-k+1} x^{k-1}, \ \ n=1,2,...,N; \ \ (G_{n-k+1}:\text{Genocchi numbers}).$$

METHOD

The technique we used in this study is a modification of Genocchi matrix and collocation methods. This modification is based on first, taking truncated Genocchi series of the functions in equation and then substituting their matrix forms into the given equation. Thereby, the equation reduces to a matrix equation which corresponds to a system of linear algebraic equations with unknown Genocchi coefficients. Hence, the solution is obtained in terms of Genocchi polynomials. For this purpose, by means of the operational matrix procedures mentioned in previous section [5-10], we firstly write the matrix forms of the truncated Genocchi series defined by (3) and its derivatives and then, the matrix forms of expressions in Eq.(1):

$$y(x) \cong y_N(x) = \mathbf{G}(x)\mathbf{A} = \mathbf{X}(x)\mathbf{MA} \Rightarrow y_N^{(k)}(x) \cong y_N^{(k)}(x) = \mathbf{G}^{(k)}(x)\mathbf{A} = \mathbf{X(x)}\mathbf{B}^k\mathbf{MA},$$

$$y_N^{(k)}(h_{kj}(x)) \cong y_N^{(k)}(h_{kj}(x)) = \mathbf{X}(h_{kj}(x))\mathbf{B}^k\mathbf{MA}, \ \ y_N^{(k)}(h_{kj}(x)) \cong y_N^{(k)}(h_{kj}(x)) = \mathbf{X}(h_{kj}(x))\mathbf{B}^k\mathbf{MA} \quad (4)$$

$$\mathbf{K}_{rs}(x,t) = X(x)K_{rs}X^T(t); \ \ \mathbf{K}_{rs} = [k_{ij}^{rs}], \ \ k_{ij}^{rs} = \frac{1}{i!\,j!}\frac{\partial K^{i+j}(0,0)}{\partial x^i \partial t^j}, \ \ (i,j=0,1,...,N-1)$$

where

$$\mathbf{G}(x) = \begin{bmatrix} G_1(x) & G_2(x) & ... & G_N(x) \end{bmatrix}, \ \mathbf{A} = \begin{bmatrix} a_1 & a_2 & ... & a_N \end{bmatrix}^T, \ \mathbf{X}(x) = \begin{bmatrix} 1 & x & x^2 & ... & x^{N-1} \end{bmatrix},$$

$$\mathbf{X}(h_{kj}(x)) = \begin{bmatrix} 1 & h_{kj}(x) & (h_{kj}(x))^2 & ... & (h_{kj}(x))^{N-1} \end{bmatrix}, \ \ \mathbf{B}^0 : \text{unit matrix},$$

$$\mathbf{M}^T = \begin{bmatrix}
\binom{1}{0}G_1 & 0 & 0 & ... & 0 \\
\binom{2}{0}G_2 & \binom{2}{1}G_1 & 0 & ... & 0 \\
\binom{3}{0}G_3 & \binom{3}{1}G_2 & \binom{3}{2}G_1 & ... & 0 \\
... & ... & ... & ... & ... \\
\binom{N}{0}G_N & \binom{N}{1}G_{N-1} & \binom{N}{2}G_{N-2} & ... & \binom{N}{N-1}G_1
\end{bmatrix}_{NxN}, \mathbf{B} = \begin{bmatrix}
0 & 1 & 0 & 0 & ... & 0 \\
0 & 0 & 2 & 0 & ... & 0 \\
0 & 0 & 0 & 3 & ... & 0 \\
... & ... & ... & ... & ... & ... \\
0 & 0 & 0 & 0 & 0 & N-1 \\
0 & 0 & 0 & 0 & 0 & 0
\end{bmatrix}_{NxN}$$

Now we substitute the matrix relations (4) and the collocation points defined by $x_i = a + \frac{b-a}{N-1}(i-1), \ i=1,2,...,N$ into Eq(1) ; afterwards, by performing necessary regulations, we obtain the following fundamental matrix equation for Eq.(1):

$$\left\{ \sum_{k=0}^{m_1} \sum_{j=0}^{m_2} \mathbf{P}_{kj} \mathbf{X}_{kj} \mathbf{B}^k - \sum_{r=0}^{m_3} \sum_{s=0}^{m_4} \bar{\mathbf{X}} \bar{\mathbf{K}}_{rs} \bar{\mathbf{Q}}_{rs} \mathbf{B}^r \right\} \mathbf{MA} = \mathbf{F} \Leftrightarrow \mathbf{WA} = \mathbf{F} \Leftrightarrow [\mathbf{W} : \mathbf{F}]; \tag{5}$$

$$\mathbf{X}_{kj} = \begin{bmatrix} \mathbf{X}(h_{kj}(x_1)) \\ \mathbf{X}(h_{kj}(x_2)) \\ \vdots \\ \mathbf{X}(h_{kj}(x_N)) \end{bmatrix} = \begin{bmatrix} 1 & h_{kj}(x_1) & h_{kj}^2(x_1) & ... & h_{kj}^{N-1}(x_1) \\ 1 & h_{kj}(x_2) & h_{kj}^2(x_2) & ... & h_{kj}^{N-1}(x_2) \\ 1 & h_{kj}(x_3) & h_{kj}^2(x_3) & ... & h_{kj}^{N-1}(x_3) \\ ... & ... & ... & ... & ... \\ 1 & h_{kj}(x_N) & h_{kj}^2(x_N) & ... & h_{kj}^{N-1}(x_N) \end{bmatrix}_{NxN}, \mathbf{F} = \begin{bmatrix} f(x_1) \\ f(x_2) \\ \vdots \\ f(x_N) \end{bmatrix}_{Nx1}$$

$$\mathbf{P}_{kj} = diag\begin{bmatrix} P_{kj}(x_1) & P_{kj}(x_2) & ... & P_{kj}(x_N) \end{bmatrix}, \quad \bar{\mathbf{X}} = diag\begin{bmatrix} \mathbf{X}(x_1) & \mathbf{X}(x_2) & ... & \mathbf{X}(x_N) \end{bmatrix}_{NxN^2}$$

$$\bar{\mathbf{K}}_{rs} = diag\begin{bmatrix} \mathbf{K}_{rs} & \mathbf{K}_{rs} & ... & \mathbf{K}_{rs} \end{bmatrix}_{N^2xN^2}, \quad q_{mn}^{rs}(x_i) = \begin{bmatrix} \int_{u_{rs}(x_i)}^{v_{rs}(x_i)} t^m (g_{rs}(t))^n dt \end{bmatrix}; \quad i=1,2,...,N$$

$$\mathbf{Q}_{rs}(x_i) = \begin{bmatrix} q_{00}^{rs}(x_i) & q_{01}^{rs}(x_i) & ... & q_{0(N-1)}^{rs}(x_i) \\ q_{10}^{rs}(x_i) & q_{11}^{rs}(x_i) & ... & q_{1(N-1)}^{rs}(x_i) \\ ... & ... & ... & ... \\ q_{(N-1)0}^{rs}(x_i) & q_{(N-1)1}^{rs}(x_i) & ... & q_{(N-1)(N-1)}^{rs}(x_i) \end{bmatrix}_{NxN}, \quad \bar{\mathbf{Q}}_{rs} = \begin{bmatrix} \mathbf{Q}_{rs}(x_1) \\ \mathbf{Q}_{rs}(x_2) \\ \vdots \\ \mathbf{Q}_{rs}(x_N) \end{bmatrix}_{N^2xN}$$

Besides, by means of the matrix relations (4), we get the following fundamental matrix equation for the conditions (2):

$$\sum_{k=1}^{m} \sum_{l=1}^{L} a_{j,k,l} \mathbf{X}(\gamma_l) \mathbf{B}^k \mathbf{A} = \lambda_j \Leftrightarrow \mathbf{U}_j \mathbf{A} = \lambda_j \Leftrightarrow [\mathbf{U}_j : \lambda_j] \text{ (j=1,2,...,m).} \tag{6}$$

After removing the any m rows of the matrix $[\mathbf{W} : \mathbf{F}]$ defined by (5), we add the row matrices $[\mathbf{U}_j : \lambda_j]$ (j=1,2,...,m) given in (6) for the conditions (2) according to the matrix-collocation techniques [1-3,8-10]. Thereby, the new desired matrix as follows;

$$\tilde{\mathbf{W}}\mathbf{A} = \tilde{\mathbf{F}} \Leftrightarrow [\tilde{\mathbf{W}} : \tilde{\mathbf{F}}].$$

By solving this matrix equation (or the corresponding algebraic system), the matrix A is uniquely determined and hence, Eq.(1) has a unique solution under the conditions (2).

NUMERICAL EXAMPLE

The technique of this research is practical in getting the solution of high-order linear functional integro-differential equations by means of Genocchi polynomials. We show the numerical solutions by using the below example [5]

We can take into consideration the second order integro-differential-difference equation with variable delays to find out the solution by means of Genocchi polynomials as follows;

$$(x^2+1)y''(0.2x)+xy'(x-1)-(x-1)y(x+2)+y(x)=f(x)+2\int_0^1 xy'(t)dt+\int_0^{(\frac{x}{2}+1)}(xt^2+tx^2)y''(t)dt,$$

$(0 \le x,t \le 1)$ with boundary conditions $y(0)=-1$ and $y'(1)=3$. Here

$$f(x)=-\frac{1}{3}x^4-\frac{5}{2}x^3-x^2-\frac{14}{3}x+6.$$

The approximate solution $y_3(x)$ is assumed as the truncated Genocchi series

$$y(x)=y_3(x)=\sum_{n=1}^{3}a_nG_n(x), \ (0 \le x \le 1).$$

Here the known expressions are

$$m=2, \ N=3, \ \lambda_1=2, \ \lambda_2=1, \ u_{10}(x)=u_{20}(x)=0, \ v_{10}(x)=1, \ v_{20}(x)=\frac{x}{2}+1,$$

$$K_{10}(x,t)=1, \ K_{20}(x,t)=xt^2+tx^2, \ h_{10}(x)=x-1, \ h_{20}=0.2x, \ P_{00}(x)=1,$$

$$P_{01}(x)=-(x-1), \ _{10}(x)=x, \ P_{20}(x)=x^2+1, \ h_{00}(x)=x, \ h_{01}(x)=x+2, \ .$$

The collocation points for $N=2$ are determined as $\left\{x_0=0, \ x_1=\frac{1}{2}, \ x_2=1\right\}$ and the fundamental

matrix equation from (5) is written as

$$\left\{\sum_{k=0}^{2}\sum_{j=0}^{1}\mathbf{P}_{kj}\mathbf{X}_{kj}\mathbf{B}^k-\sum_{r=0}^{2}\sum_{s=0}^{0}\bar{\mathbf{X}}\bar{\mathbf{K}}_{rs}\bar{\mathbf{Q}}_{rs}\mathbf{B}^r\right\}\mathbf{MA}=\mathbf{F} \ ;$$

$$\mathbf{P}_{00}(x)=\begin{bmatrix}1&0&0\\0&1&0\\0&0&1\end{bmatrix}, \ \mathbf{P}_{01}(x)=\begin{bmatrix}1&0&0\\0&\frac{1}{2}&0\\0&0&0\end{bmatrix}, \ \mathbf{P}_{10}(x)=\begin{bmatrix}0&0&0\\0&\frac{1}{2}&0\\0&0&1\end{bmatrix}, \ \mathbf{P}_{20}(x)=\begin{bmatrix}1&0&0\\0&\frac{5}{4}&0\\0&0&2\end{bmatrix},$$

$$\mathbf{X}_{00}(x)=\begin{bmatrix}1&0&0\\1&\frac{1}{2}&\frac{1}{4}\\1&1&1\end{bmatrix}, \ \mathbf{X}_{01}(x)=\begin{bmatrix}1&2&4\\1&\frac{5}{2}&\frac{25}{4}\\1&3&9\end{bmatrix}, \ \mathbf{X}_{10}(x)=\begin{bmatrix}1&-1&1\\1&\frac{-1}{2}&\frac{1}{4}\\1&0&0\end{bmatrix}, \ \mathbf{X}_{20}(x)=\begin{bmatrix}1&0&0\\1&\frac{1}{10}&\frac{1}{100}\\1&\frac{1}{5}&\frac{1}{25}\end{bmatrix},$$

$$\mathbf{B}^0=\begin{bmatrix}1&0&0\\0&1&0\\0&0&1\end{bmatrix}, \ \mathbf{B}^1=\begin{bmatrix}0&1&0\\0&0&2\\0&0&0\end{bmatrix}, \ \mathbf{B}^2=\begin{bmatrix}0&0&2\\0&0&0\\0&0&0\end{bmatrix}, \ \mathbf{M}=\begin{bmatrix}1&-1&0\\0&2&-3\\0&0&3\end{bmatrix} \ \mathbf{F}=\begin{bmatrix}6&\frac{37}{12}&\frac{-5}{2}\end{bmatrix}^T$$

$$\bar{\mathbf{X}}=Diag\begin{bmatrix}\mathbf{X}(x_0)&\mathbf{X}(x_1)&\mathbf{X}(x_2)&\mathbf{X}(x_3)\end{bmatrix}, \ \bar{\mathbf{K}}=Diag\begin{bmatrix}\mathbf{K}&\mathbf{K}&\mathbf{K}&\mathbf{K}\end{bmatrix},$$

$$\bar{\mathbf{Q}}=Diag\begin{bmatrix}\mathbf{Q}&\mathbf{Q}&\mathbf{Q}&\mathbf{Q}\end{bmatrix}.$$

The augmented matrix for this basis matrix relation is computed as

$$\begin{bmatrix}\mathbf{W}; & \mathbf{F}\end{bmatrix}=\begin{bmatrix}2&2&12;&6\\\frac{3}{2}&2&\frac{25}{4};&\frac{37}{12}\\1&1&\frac{-9}{2};&\frac{-5}{2}\end{bmatrix}$$

By using the matrix form (6), the matrix relations for the boundary conditions $y(0) = -1$ and $y'(1) = 3$ are computed as

$$\begin{bmatrix} \mathbf{U}_0; & \boldsymbol{\lambda}_0 \end{bmatrix} = \begin{bmatrix} 1 & -1 & 0; & -1 \end{bmatrix} \text{ and } \begin{bmatrix} \mathbf{U}_1; & \boldsymbol{\lambda}_1 \end{bmatrix} = \begin{bmatrix} 0 & 2 & 3; & 3 \end{bmatrix}.$$

Thereby, we achieve the desired augmented matrix form and according to the matrix-collocation method as follows:

$$\begin{bmatrix} \tilde{\mathbf{W}}; & \tilde{\mathbf{F}} \end{bmatrix} = \begin{bmatrix} 2 & 2 & 12; & 6 \\ 1 & -1 & 0; & -1 \\ 0 & 2 & 3; & 3 \end{bmatrix}.$$

By solving this system, the Genocchi series solution is obtained as

$$A = (\tilde{\mathbf{W}})^{-1}\tilde{\mathbf{F}} \Rightarrow A = [0\ 1\ 1/3]^T; y_3(x) = G(x)A = X(x)MA,$$

$$y_3(x) = a_1 G_1(x) + a_2 G_2(x) + a_3 G_3(x) = x^2 + x - 1$$

which is the exact solution. In similar way, the same solution is obtained for $N > 2$.

CONCLUSIONS

In this article, a new operational matrix method based on the Genocchi polynomials is derived and applied together with the collocation technique to numerically solve the linear integro- differential difference equations with delays. Besides, the experiment is performed to show the effectualness and trueness of our method. Also, the presented method can be developed for nonlinear functional integro-differential equations.

REFERENCES

[1] M. Gülsu, M. Sezer, A Taylor collocation method for solving high-order linear pantograph equations with linear functional argument, Numer. Methods Partial Differ. Eqns. 27 (2011) 1628-1638.
[2] A. Akyüz, M. Sezer, Chebyshev polynomial solutions of systems of high-order linear differential equations with variable coefficients, Applied Mathematics and Computation 144 (2003) 237-247.
[3] M. Gülsu, B. Gürbüz, Y. Öztürk, M. Sezer, Laguerre polynomial approach for solving linear delay difference equations, Applied Mathematics and Computation 217 (2011) 6765-6776.
[4] S. Yalçınbaş, M. Aynigül, M. Sezer, A Collocation method using Hermite polynomials for approximate solution of pantograph equations, J. Franklin Institute 348 (2011) 1128-1139.
[5] Ö. K. Kürkçü, E. Aslan, M. Sezer, A Numerical approach with error estimation to solve general integro-differential-difference equations using Dickson Polynomials, Applied Mathematics and Computation 276 (2016) 324-339.
[6] O. R. Işık, M. Sezer, Z. Güney, Bernstein series solution of a class of linear integro-differential equations with weakly singular kernel, Applied Mathematics and Computation 217 (2011) 7009-7020.
[7] Ş. Yüzbaşı, M. Sezer, N. Şahin, Bessel polynomial solutions of high-order linear Volterra integro-differential equations, Computers and Mathematics with Applications 62 (2011) 1940-1956.
[8] M. Sezer, K. E. Biçer, Bernoulli matrix collocation method for solving general functional integro-differential equations with hybrid delays, J. Inequalities and Special Functions (2017) 85-99.
[9] N.Baykuş Savaşaneril, M. Sezer, Hybrid Taylor-Lucas collocation method for numerical solution of high-order Pantograph type delay differential equations with variables delays, Appl. Math. Inf. Sci. 11 (2017) 1795-1801.
[10] M.M. Bahşi, M. Çevik, M. Sezer, Jacobi polynomial solutions of Volterra integro-differential equations with weakly singular kernel, New Trends in Mathematical Sciences 6 (2018) 24-38.
[11] A. Isah, C. Phang, Operational matrix based on Genocchi polynomials for solution of delay differential equations, Ain Shams Engineering Journal (2017).

Some Soft Fixed Point Theorems by Using Steinhaus Transform Soft Metric

Simge Öztunç*, Manisa Celal Bayar University, Faculty of Art and Science, Department of Mathematics, Manisa, Turkey
Ali Mutlu, Manisa Celal Bayar University, Faculty of Art and Science, Department of Mathematics, Manisa, Turkey
Nurettin Yılmaz, Manisa Celal Bayar University, The Institute of Natural and Applied Sciences, Manisa, Turkey,
*Corresponding author: simge.oztunc@cbu.edu.tr

Abstract

In this paper we focus on the biotope transform metric or Steinhaus transform metric which is introduced by Marczewski and Steinhaus [1] in 1957. We define the Steinhaus transform soft metric by using soft sets and acquire new properties concerning with contractive mappings. Also we present some different useful examples. Then we apply the Steinhaus transform metric to some soft fixed point theorems by using contractive mappings.

Keywords: soft metric, Steinhaus transform soft metric, soft fixed point theorems.
Discipline: Mathematics, Topology

INTRODUCTION

The concept of soft sets was introduced by D. Molodtsov [2] in 1999 and soft set theory became an alternative and useful tool for computer science, modeling problems in engineering, economics, medical and social science. Theoretical properties of soft set theory has also been studied by some mathematicians. Maji et al. [3] defined some operations on soft sets. Zorlutuna et al. [4] worked on continuity of soft mappings and soft topological spaces. On the other hand soft fixed point theory became on interesting area of fixed point theory. The concept of soft metric is defined by Das and Samanta [5] in 2012. However, Hosseinzadeh [6] in 2017 improved the theory which is revealed by Das and Samanta. In other respects Steinhaus transform metric (in other words biotope transform metric) was propounded by Marczawski and Steinhaus [1] in 1954. In present paper we defined a new soft metric named Steinhaus transform soft metric, by using soft metric and acquire new properties concerning with contractive mappings.

1. PRELIMINARIES

Definition 1.1. [2] A pair (F, A) is said to be a soft set over the universe U, where F is a mapping given by $F : A \rightarrow P(U)$.

In other words, a soft set over U is a parameterized family of subsets of the universe U. For any parameter $x \in A, F(x)$ may be considered as the set of $x-$ approximate elements of the soft set (F, A).

Definition 1.2. [3] Let (F, A) and (G, B) be two soft sets over U. We say that (F, A) is a soft subset of (G, B) and denote it by $(F, A) \tilde{\subset} (G, B)$ if

(1) $A \subseteq B,$ and

(2) $F(a) \subseteq G(a),$ for all $a \in A.$

(F, A) is said to be a soft super set of $(G, B),$ if (G, B) is a soft subset of $(F, A).$ We denote it by $(F, A) \tilde{\supset} (G, B).$

Definition 1.3. [3] Let (F, A) and (G, B) be two soft sets over U. The union of (F, A) and (G, B) is soft set $(H, C),$ where $c = A \cup B$ and for all $e \in C,$

$$f(x) = \begin{cases} F(e), & e \in A - B \\ G(e), & e \in B - A \\ F(e) \cup G(e), & e \in A \cap B \end{cases}.$$

We write $(F, A) \tilde{\cup} (G, B) = (H, C).$

Definition 1.4. [3] Let (F, A) and (G, B) be two soft sets over U. The intersection of (F, A) and (G, B) is a soft set (H, C), where $C = A \cap B$ and for all $e \in C$, $H(e) = F(e) \cap G(e)$. We write $(F, A) \tilde{\cap} (G, B) = (H, C)$.

Definition 1.5. [3] Let (F, A) be soft set over U. The relative complement of (F, A) is denoted by $(F, A)^c$ and is defined $(F, A)^c = (F^c, A)$, where $F^c : A \to P(U)$ is a mapping given by $F^c(a) = U - F(a)$ for all $a \in A$.

Definition 1.6. [3] Let (F, A) and (G, B) be two soft sets over U. Then $(F, A) - (G, B)$ is a soft set $(x, F(x)) : F(x) \notin G(B), x \notin B$.

Definition 1.7. [3] Let (F, A) be soft set over U. Then

(1) (F, A) is said to be null soft set denoted by $\tilde{\varnothing}$ if for every $a \in A, F(a) = \varnothing$.

(2) (F, A) is said to be absolute soft set denoted by $\tilde{A}$ if for every $a \in A, F(a) = U$.

Definition 1.8. [6] Let $A \subseteq E$ be a set of parameters. We say the ordered pair (a, r) is a soft parametric scalar if $r \in R$ and $a \in A$. The parametric scalar (r, a) called nonnegative if $r \geq 0$. Let (a, r) and (b, r') be two soft parametric scalars. We say (a, r) is no less than (b, r') and we write $(a, r) \pm (b, r')$, if $r \geq r'$.

Definition 1.9. [6] Let $A \subseteq E$ be a set of parameters. Let (a, r) and (b, r') be two soft parametric scalars. Then we define addition between soft parametric scalars and scalar multiplication on soft parametric scalars as follows
$(a, r) \hat{e} (b, r') = (a, b, r + r')$, and
$\lambda(a, r) = (a, \lambda r)$, for every $\lambda \in R$.

Definition 1.10. [6] Let (F, A) be a soft set over X. We call a function f on (F, A) is parametric scalar valued, if there are functions $f_1 : A \to A$ and $f_2 : F(A) \to R$ such that $f(F, A) = (f_1, f_2)(A, F(A))$.

Similarly, we can extent above defined parametric scalar valued function as $f : (F, A) \times (F, A) \to (A, R)$ by $f(A \times A, F(A) \times F(A)) = (f_1, f_2)(A \times A, F(A) \times F(A))$, where $f_1 : A \times A \to A$ and $f_2 : F(A) \times F(A) \to R$.

Definition 1.11. [6] Let (F, A) be a soft set over X and let $\tilde{\pi} : A \times A \to A$ be parametric function. We say the parametric scalar valued function $\mathcal{D} : (F, A) \times (F, A) \to (A, R^+\{0\})$ a soft meter on (F, A) if $\mathcal{D}$ satisfies in the following conditions:

(1) $\mathcal{D}((a, F(a)), (b, F(b))) \pm (\tilde{\pi}(a, b), 0)$, and equality holds, whenever $a = b$.

(2) $\mathcal{D}((a, F(a)), (b, F(b))) = \mathcal{D}((b, F(b)), (a, F(a)))$, for all $a, b \in A$.

(3) $\mathcal{D}((a, F(a)), (c, F(c))) \circ \mathcal{D}((a, F(a)), (b, F(b))) \hat{e} \mathcal{D}((b, F(b)), (c, F(c)))$, for all $a, b, c \in A$.

We say the pair $((F, A), \mathcal{D})$ is a soft metric space over X.

Definition 1.12. Let (F, A) be a soft set over X and let $\tilde{\pi} : A \times A \to A$ be parametric function. We say the parametric scalar valued function $\mathcal{D} : (F, A) \times (F, A) \to (A, R^+\{0\})$ a soft meter on (F, A) if $\mathcal{D}$ satisfies in the following conditions:

(1) $\mathcal{D}_p((a, F(a)), (b, F(b))) \pm (\tilde{\pi}(a, b), 0)$, and equality holds, whenever $a = b$.

(2) $\mathcal{D}_p((a, F(a)), (b, F(b))) = \mathcal{D}((b, F(b)), (a, F(a)))$, for all $a, b \in A$.

(3) $\mathcal{D}_p((a, F(a)), (c, F(c))) \circ \mathcal{D}((a, F(a)), (b, F(b))) \hat{e} \mathcal{D}((b, F(b)), (c, F(c)))$, for all $a, b, c \in A$.

(4) $\mathcal{D}_p((a, F(a)), (b, F(b))) = \dfrac{2\mathcal{D}((a, F(a)), (b, F(b)))}{\mathcal{D}((a, F(a)), (c, F(c))) \,\hat{e}\, \mathcal{D}_p((b, F(b)), (c, F(c))) \,\hat{e}\, \mathcal{D}((a, F(a)), (b, F(b)))}$

We say the pair $((F, A), \mathcal{D}_p)$ is a soft Steinhaus transform metric space over X.

Definition 1.13. [7] $X \neq \varnothing$ and an element $x \in X$ is a fixed point of $f : X \to X$ if $f(x) = x$.

Definition 1.14. [7] Let T be a mapping of a metric space M into M. We say that T is a contraction mapping if there exists a number k such that $0 < k < 1$ and

$$p(Tx, Ty) \leq kp(x, y) \qquad (\forall x, y \in M).$$

Theorem 1.15. [7] Any contraction mapping of a complete non-empty metric space M into M has a unique fixed point in M.

2. SOME FIXED POINT THEOREMS FOR STEINHAUS SOFT METRIC SPACES

Definition 2.1. [6] Let (F, A) be a soft set over X. A soft sequence in (F, A) is a function $f : N \to (F, A)$ by setting $f(n) = (F_n, A)$ such that (F_n, A) is a soft subset of (F, A) for $n \in N$, and we denote it by $\{(F_n, A)\}_{n=1}^{\infty}$.

Definition 2.2. Let (F, A) be a soft set over X. Let $\mathcal{D}_P$ be a Steinhaus transform soft metric on (F, A), $\{(F_n, A)\}_{n=1}^{\infty}$ be a soft sequence in (F, A) and $(x, F(x)) \in (F, A)$. Then we say $\{(F_n, A)\}_{n=1}^{\infty}$ converges to $(x, F(x))$, if for every positive number $\grave{o}$, there exists a naturel number N such that for every natural number n which $n \geq N$, we have

$$\mathcal{D}_P(a, F_n(a),) \leq (\tilde{\pi}(a, x), \grave{o}).$$

Theorem 2.3. Let (F, A) be a soft set over X, let $\mathcal{D}$ be a meter on (F, A), $(F_n, A)_{n=1}^{\infty}$ be a soft sequence in (F, A). If (F, A), $(F_n, A)_{n=1}^{\infty}$ is convergent in (F, A), then it converges to unique element of (F, A).

Proof: Assume towards a contradiction that there are elements $(x, F(x))$,

$(y, F(y)) \in (F, A)$ such that $(F_n, A) \to (x, F(x))$ and $(F_n, A) \to (y, F(y))$,

for every $n \in N$. Then by condition (3) of Definition 3.8, for every $a \in A$, we have

$\mathcal{D}_P((x, F(x)), (y, F(y))) = \dfrac{2\mathcal{D}((x, F(x)), (y, F(y)))}{\mathcal{D}((x, F(x)), (z, F(z))) \,\hat{e}\, \mathcal{D}((y, F(y)), (z, F(z))) \,\hat{e}\, \mathcal{D}((a, F(a)), (b, F(b)))}$

$^{\circ}\ 2\mathcal{D}((x, F(x)), (y, F(y))) \}$

$^{\circ}\ 2[\mathcal{D}((x, F(x)), (a, F_n(a))) \,\hat{e}\, \mathcal{D}((a, F_n(a)), (y, F(y)))] \}$ \hfill (2.1)

Now, let $\grave{o}$ be an arbitrary positive number. Since $(F_n, A)_{n=1}^{\infty}$ converges to $(x, F(x))$ and $(y, F(y))$, so there are natural numbers N_1 and N_2 such that for every $n > N_1$ and $n > N_2$,

$\mathcal{D}((x, F(x)), (a, F_n(a)))\ ^{\circ}\ (\tilde{\pi}(x, a), \grave{o}/4)\ ^{\circ}\ 2(\tilde{\pi}(x, a), \grave{o}/4)$ \hfill (3.2)

and

$\mathcal{D}_p((a, F_n(a)), (y, F(y)))\ ^{\circ}\ (\tilde{\pi}(a, y), \grave{o}/4)\ ^{\circ}\ 2(\tilde{\pi}(a, y), \grave{o}/4)$ \hfill (2.2)

Now, suppose that $n \geq max\{N_1, N_2\}$. Then by (3.1), (3.2) and (3.3), we have

$$\mathcal{D}_p((x, F(x)), (y, F(y)))\ ^{\circ}\ 2((\tilde{\pi}(x, a), \grave{o}/4) \,\hat{e}\, (\tilde{\pi}(a, y), \grave{o}/4))$$

$$^{\circ}\ 2(\{\tilde{\pi}(x, a), \tilde{\pi}(a, y)\}, \grave{o}/2) \}$$

$$^{\circ}\ (\{\tilde{\pi}(x, a), \tilde{\pi}(a, y)\}, \grave{o}) \} \qquad (2.3)$$

This means that $D_p((x,F(x)),(y,F(y)))\,^\circ\,(\{\tilde{\pi}(x,a),\tilde{\pi}(a,y)\},\grave{o})\}$, for every $\grave{o}>0$ and $a\in A$.
Therefore, $D_p((x,F(x)),(y,F(y)))=(\tilde{\pi}(x,y),0)$. Then condition (1) of Definition 3.8, implies that $x=y$, and consequently, $(x,F(x))=(y,F(y))$. ∎

Definition 2.4. Let (F,A) be a soft set over X. Let D_p be a Steinhaus transform soft metric on (F,A) and $\{(F_n,A)\}_{n=1}^{\infty}$ be a soft sequence in (F,A). Then we say $\{(F_n,A)\}_{n=1}^{\infty}$ is a Cauchy soft sequence, if for every positive number $\grave{o}$, there exists a natural number N such that for every natural number n,m which $n,m\geq N$, we have

$$D_p((a,F_n(a)),(a,F_m(a)))\leq(\tilde{\pi}(a,a),\grave{o}).$$

Proposition 2.5. Let $((F,A),D_p)$ be a Steinhaus transform soft metric space over X, and let $\{(F_n,A)\}_{n=1}^{\infty}$ be a convergent soft sequence in (F,A). Then $\{(F_n,A)\}_{n=1}^{\infty}$ is a Cauchy soft sequence.

Definition 2.6. Let (F,A) be a soft set over X, let D_p be a Steinhaus transform soft metric on (F,A). We say that (F,A) is a complete Steinhaus transform soft metric space if every Cauchy soft sequence converges in (F,A).

Theorem 2.7. Let $((F,A),D_p)$ and $((F',A'),D'_p)$ be two Steinhaus transform soft metric spaces over X and Y respectively. Let $f=(f_1,f_2):((F,A),D_p)\to((F',A'),D'_p)$ be a soft mapping. Then f is soft continuous if and only if for every $(x,F(x))\in(F,A)$ and every positive number $\grave{o}$, there exists a positive number δ such that for every $(y,F(y))\in(F,A)$

$$D'_p((f(x,F(x))),f((y,F(y))))\leq(\tilde{\pi}'(\tilde{\pi}(x,y)),\grave{o})$$

whenever $D'_p(f(x,F(x))),f((y,F(y)))\leq(\tilde{\pi}(x,y)),\delta)$.

Definition 2.8. Let $((F,A),D_p)$ be a Steinhaus transform soft metric space over X and $f:((F,A),D_p)\to((F,A),D_p)$ be a soft mapping. We say that f is soft contractive if there is a positive number c with $0<c<1$ such that

$$D_p((f(x,F(x))),f((y,F(y))))\leq cD_p((x,F(x)),(y,F(y))),\text{ for all }x,y\in A.$$

Theorem 2.9. Soft contractive mapping is soft continuous in Steinhaus transform soft metric space $((F,A),D_p)$.

Definition 2.10. Let $((F,A),D_p)$ be a complete Steinhaus transform soft metric space over X and let $f:((F,A),D_p)\to((F,A),D_p)$ be a soft mapping. A fixed soft set for f is a soft subset of (F,A) such as $(x,F(x))$ such that $f((x,F(x)))=(x,F(x))$.

Theorem 2.11. Let $((F,A),D_P)$ be a complete Steinhaus transform soft metric space over X, and $f:((F,A),D_P)\to((F,A),D_P)$ be Steinhaus transform soft contractive mapping. Then f has unique fixed soft set.

Proof: Let (F_0,A) be an arbitrary soft point in (F,A). We construct the soft sequence $\{(F_n,A)_{n=1}^{\infty}\}$ as follows:

$$(F_{n+1},A)=f((F_n,A))=f^{n+1}((F_0,A))\qquad(n=0,1,2,...)\tag{2.4}$$

Since f is soft contraction, then there exists a $0<c<1$ such that for all $n\geq 1$

$$D_P((F_{n+1},A),(F_n,A))=\frac{2D((F_{n+1},A),(F_n,A))}{D((F_{n+1},A),(F_i,A))\,\hat{e}\,D((F_n,A),(F_i,A))\,\hat{e}\,D((F_{n+1},A),(F_n,A))}$$

86

$$= \frac{2\mathcal{D}(f(F_n,A),f(F_{n-1},A))}{\mathcal{D}(f(F_n,A),f(F_{i-1},A))\,\hat{e}\;\mathcal{D}(f(F_{n-1},A),f(F_{i-1},A))\,\hat{e}\;\mathcal{D}(f(F_n,A),f(F_{n-1},A))}$$

$$^{\circ}\;\; 2\mathcal{D}(f(F_n,A),f(F_{n-1},A))$$

$$^{\circ}\;\; 2c\,\mathcal{D}((F_n,A),(F_{n-1},A))\;\}. \tag{2.5}$$

By induction for $n = 0,1,2,...,$ we conclude that

$$\mathcal{D}_p(F_{n+1},A),(F_n,A))^{\circ}\;\; 2^n \cdot c^n\,\mathcal{D}(F_1,A),(F_0,A))\;\} \tag{2.6}$$

For any $i > m > n$, we have

$$\mathcal{D}_P(F_n,A),(F_m,A)) = \frac{2\mathcal{D}((F_n,A),(F_m,A))}{\mathcal{D}((F_n,A),(F_i,A))\,\hat{e}\;\mathcal{D}((F_m,A),(F_i,A))\,\hat{e}\;\mathcal{D}((F_n,A),(F_m,A))}$$

$$^{\circ}\;\; 2\mathcal{D}_p((F_n,A),(F_m,A))$$

$$^{\circ}\;\; 2[\mathcal{D}((F_n,A),(F_{n+1},A))\,\hat{e}\;\cdots\hat{e}\;\mathcal{D}((F_{m-1},A),(F_m,A))]$$

$$^{\circ}\;\; 2[c^n\,\mathcal{D}((F_1,A),(F_0,A))\,\hat{e}\;\cdots\hat{e}\;c^{m-1}\mathcal{D}((F_1,A),(F_0,A))]$$

$$= (2\cdot c^n\,\hat{e}\;2\cdot c^{n+1}\,\hat{e}\;\cdots\hat{e}\;2\cdot c^{m-1})\mathcal{D}((F_1,A),(F_0,A))$$

$$^{\circ}\;\; (\sum_{n=0}^{\infty}(2c)^n)\mathcal{D}((F_1,A),(F_0,A))$$

$$= \frac{1}{1-2c}\,\mathcal{D}((F_1,A),(F_0,A)).\;\} \tag{2.7}$$

Thus, (2.7) shows that $(F_n,A)_{n=1}^{\infty}$ is a Cauchy soft sequence in (F,A). Since (F,A) is a complete Steinhaus transform soft metric space, then there exist $(x,F(x)) \in (F,A)$ such that $(F_n,A)_{n=1}^{\infty}$ converges to $(x,F(x))$. Since f is soft continuous, therefore, by Theorem 2.3, $f((F_n,A))$ converges to $f((x,F(x)))$. As well as, according to the definition of $(F_n,A)_{n=1}^{\infty}, f((F_n,A))$ converges to $(x,F(x))$. It follows from Theorem 2.3 that $f((x,F(x))) = (x,F(x))$.

To prove the uniqueness property of $(x,F(x))$, suppose that there exist another element $(y,F(y)) \in (F,A)$ such that $f((y,F(y))) = (y,F(y))$ and $(x,F(x)) \neq (y,F(y))$. Then

$$\mathcal{D}_P((x,F(x)),(y,F(y))) = \mathcal{D}_P(f((x,F(x))),f((y,F(y))))$$

$$\leq c\,\mathcal{D}_p((x,F(x)),(y,F(y))).$$

Then above inequality implies that $c > 1$, which is a contradiction. This completes the proof. ∎

Lemma 2.12. Let $A \subseteq E$ be a set of parameters, (a,r) and (b,r') be two soft parametric scalars such that for every $\grave{o} > 0$, if $(a,r) \prec (b,r'+\grave{o})$, then $(a,r)^{\circ}\;(b,r')$.

Theorem 2.13. Let $((F,A),\mathcal{D}_P)$ be a complete Steinhaus transform soft metric space over X, and let $T = (T_1,T_2):((F,A),\mathcal{D}_P) \to ((F,A),\mathcal{D}_P)$ be a soft continuous mapping such that $T((a,F(a))) = (T_1(a),T_2(F(a))) = (T_1(a),F(T_1(a)))$ for every $(a,F(a)) \in (F,A)$ and it satisfies for some parametric scalar valued $\varphi:(F,A) \to (A,\square^{+})$

$$\mathcal{D}_P(T((a,F(a)),(a,F(a)))) \prec \varphi((a,F(a))) - \varphi(T(a,F(a))). \tag{2.8}$$

Then $T^n((a,F(a)))$ converges to a fixed soft set, for every $(a,F(a)) \in (F,A)$.

Proof: Let $T = (T_1, T_2)$ and $\varphi = (\varphi_1, \varphi_2)$. Now, if $T((a, F(a))) = (T_1(a), T_2(F(a)))$, we set $T((a, F(a))) = (a_1, F(a_1))$, then

$$\varphi(T((a, F(a)))) = (\varphi_1(a_1), \varphi_2(F(a_1))) = (b_1, r_1).$$

Similarly, we write $T^n((a, F(a))) = (a_n, F(a_n))$ for $n = 1, 2, \ldots$. Thus,

$$\varphi(T^n((a, F(a)))) = (\varphi_1(a_n), \varphi_2(F(a_n))) = (b_n, r_n).$$

This implies that

$$\mathcal{D}_P(T((a, F(a)), (a, F(a)))) \, \hat{e} \, \varphi(T((a, F(a)))) \prec \varphi((a, F(a))) \} \tag{2.9}$$

$$\frac{2\mathcal{D}(T((a, F(a)), (a, F(a))))}{\mathcal{D}(T((a, F(a)), (c, F(c)))) \, \hat{e} \, \mathcal{D}(T((a, F(a)), (c, F(c)))) \, \hat{e} \, \mathcal{D}(T((a, F(a)), (a, F(a))))} \, \hat{e} \, \varphi(T((a, F(a)))) \tag{2.10}$$

$$\prec \varphi((a, F(a)))$$

Therefore, by Lemma 2.12., $\{ \varphi(T((a, F(a)))) \, ° \, \varphi((a, F(a))) \}$. This implies that $\varphi(T^2((a, F(a)))) \, ° \, \varphi(T((a, F(a))))$.

If we continue this method, we obtain $\varphi(T^{n+1}((a, F(a)))) \, ° \, \varphi(T^n((a, F(a))))$. This means that $\varphi(T^n((a, F(a))))$ is a decreasing and so the sequence r_n of real numbers is decreasing. Hence there is an $r \in \square$ such that

$$\lim_{n \to \infty} \varphi((a, F(a))) = (b, r) \quad \text{for all } b \in A. \tag{2.11}$$

Clearly (b, r) is nonnegative. Then for all $n, m, p \in N$ with $p \geq m \geq n$, we have

$$\mathcal{D}_P(T^n((a, F(a)), T^m((a, F(a)))))$$

$$= \frac{2\mathcal{D}(T^n((a, F(a)), T^m((a, F(a)))))}{\mathcal{D}(T^n((a, F(a)), T^p((a, F(a)))) \, \hat{e} \, \mathcal{D}(T^m((a, F(a)), T^p((a, F(a)))) \, \hat{e} \, \mathcal{D}(T^n((a, F(a)), T^m((a, F(a)))))}$$

$$° \, 2\mathcal{D}(T^n((a, F(a)), T^m((a, F(a)))))$$

$$° \, 2[\mathcal{D}(T^n((a, F(a)), T^{n+1}((a, F(a)))) \, \hat{e} \, \mathcal{D}(T^{n+1}((a, F(a)), T^{n+2}((a, F(a)))) \, \hat{e}$$

$$\mathcal{D}(T^{n+2}((a, F(a)), T^{n+3}((a, F(a)))) \, \hat{e} \, \cdots \hat{e} \, \mathcal{D}(T^{m-1}((a, F(a)), T^m((a, F(a)))))]$$

$$° \, 2\sum_{i=n}^{m-1} \mathcal{D}(T^i((a, F(a)), T^{i+1}((a, F(a)))))$$

$$° \, 2\varphi(T^n((a, F(a)))) - 2\varphi(T^{n+1}((a, F(a)))) \}$$

$$+ 2\varphi(T^{n+1}((a, F(a)))) - 2\varphi(T^{n+2}((a, F(a)))) \, \hat{e} \, \cdots \hat{e} \, 2\varphi(T^{m-1}((a, F(a)))) - 2\varphi(T^m((a, F(a))))$$

$$= 2\varphi(T^n((a, F(a)))) - 2\varphi(T^m((a, F(a)))).$$

Thus, $\lim_{m \cdot n \to \infty} \mathcal{D}_P(T^n((a, F(a)), T^m((a, F(a))))) = (b, 0)$. (See Definition 2.2) Therefore, $T^n((a, F(a)))$ is a soft Cauchy sequence. Thus, there exists $(x, F(x)) \in (F, A)$ such that $\lim_{n \to \infty} T^n((a, F(a))) = (x, F(x))$. ∎

REFERENCES

[1] E. Marczewski, H. Steinhaus, On a certain distance of sets and the corresponding distance of functions, Colloquium Mathematicae 6 (1958) 319–327.

[2] D. Molodtsov, Soft set theory-First result, Comput. Math. Appl. 37 (1999) 19-31.

[3] P. K. Maji, R. Biswas and A. R. Roy, Soft Set Theory, Comput. Math. Appl. 45 (2003) 555-562.

[4] I.Zorlutuna, and H. Çakır, On Continuity of Soft Mappings, Appl. Math. Inf. Sci. 9 (2015) 403-409.

[5] S. Das, S.K.Samanta, Soft Metric, Annals of Fuzzy Mathematics and Informatics 6 (2013) 77-94.

[6] H. Hosseinzadeh, Fixed Point Theorems on Soft Metric Spaces, Journal of Fixed Point Theory and Applications 19 (2017) 1625-1647.

[7] S. Banach, Sur les opérations dans les ensembles abstraits et leur application aux équations intégrales. Fundamenta Mathematicae 3(1) (1922) 133-181.

A Note on Certain Limitation Matrices

Faruk Özger*, İzmir Katip Çelebi Univ., Dept. of Engineering Sciences, Çiğli Main Campus, İzmir, Türkiye
*Corresponding author: farukozger@gmail.com

Abstract
Limitation matrices are widely used in functional analysis and operator theory since they are very useful tools. One of the main goal is to assign a limit for divergent sequences or series. This aim is achieved by considering a transform rather than the original sequence or series. This can be done in various different ways. A short survey related to certain limitation matrices is given in this study.

Keywords: limitation matrix, matrix domain
Discipline: Mathematics

1. INTRODUCTION

Let $A = (a_{nk})$ an be an infinite matrix of complex numbers. A sequence $x = (x_k) \in \omega$ is said to be limitable/summable A to a complex number ξ if the A–limit of x is ξ, i.e.,

$$\lim_{n\to\infty}(Ax)_n = \lim_{n\to\infty}\sum_{k=0}^{\infty} a_{nk}x_k = \xi,$$

and is denoted by $x \to \xi(A)$.

Let infinite matrix $T = (t_{nk})_{n,k=0}^{\infty}$ is said to be a triangle if $t_{nk} = 0$ $(k > n)$ and $t_{nn} \neq 0$ for all n.

A subspace X of ω is said to be a BK space if it is a Banach space with continuous coordinates $P_n: X \to \mathbb{C}$ $(n = 0,1,\dots)$ where $P_n(x) = x_n$ for all $x \in X$. An FK-space whose topology is normable is called a BK space. A BK space $X \supset \phi$ is said to have AK if every sequence $x = (x_k)_{k=0}^{\infty} \in X$ has a unique representation

$$x = \sum_{k=1}^{\infty} x_k e^{(k)}, \quad that \; is, \quad x = \lim_{n\to\infty}\sum_{k=1}^{n} x_k e^{(k)}.$$

The letters **A** and **K** stand for **A**bschnitts**k**onvergenz, the German word for sectional convergence.

A sequence $(b_n)_{n=0}^{\infty}$ in a linear metric space X is called a Schauder basis if, for each $x \in X$, there exists a unique sequence $(\lambda_n)_{n=0}^{\infty}$ of scalars such that $x = \sum_{n=0}^{\infty} \lambda_n b_n$.

The spaces c and c_0 of convergent and null sequences given by

$$c := \left\{x = (x_k) \in \omega: \lim_{k\to\infty}|x_k - L| = 0 \; for \; some \; L \in \mathbb{C}\right\},$$
$$c_0 := \left\{x = (x_k) \in \omega: \lim_{k\to\infty} x_k = 0\right\}.$$

The space ℓ_p of absolutely p summable sequences is defined as

$$\ell_p := \{x = (x_k) \in \omega: \sum_{k=0}^{\infty} |x_k|^p < \infty\}, \quad (0 < p < \infty).$$

The space ℓ_∞ of bounded sequences is defined by

$$\ell_\infty := \left\{x = (x_k) \in \omega: \sup_{k\in\mathbb{N}}|x_k| < \infty\right\}.$$

The β dual of a set X is

$$X^\beta = \{y = (y_k) \in \omega: \sum_{k=0}^{\infty} x_k y_k \; converges \; for \; every \; x \in X\}.$$

Let $\dagger \in \{\alpha, \beta, \gamma\}$, then we have $c^\dagger = c_0^\dagger = \ell_\infty^\dagger = \ell_1$ and $\ell_p^\dagger = \ell_q$ $(1 \leq p < \infty)$.

2. LIMITATION METHODS

The classical summability theory deals with a generalization of the concept of the convergence of sequences and series of real or complex. Note that, this survey is benefited from [12-16].

Italian analyst Ernesto Cesàro first introduced the Cesàro method of order α for a positive integer α in "Sur la multiplication des séries, Bulletin des Sciences Mathématiques (2) vol. 14, 114–120, 1980". The more general C_α methods (where $\alpha > -1$) were introduced by K. Knopp in "Sitzungsberichte d. Berliner Math. Ges. vol. 7, 1–12, 1907".

Definition 2.1 *(Cesàro method)* *Let* $\alpha \in \mathbb{R}$ *be given. Then* $C_\alpha = (c_{nk}^{(\alpha)})$ *defined by*

$$c_{nk}^{(\alpha)} = \begin{cases} \dfrac{\binom{n-k+\alpha-1}{n-k}}{\binom{n+\alpha}{n}} & \text{if } k \leq n \\ 0 & \text{if } k > n \end{cases} \quad (k, n \in \mathbb{N}_0)$$

is called the Cesàro method of order α.

The most important method of summability is the arithmetic means of a sequence which is known as Cesàro method of order 1. This method is defined by the matrix $C_1 = (c_{nk})_{n,k=0}^\infty$ where

$$c_{nk} = \begin{cases} \dfrac{1}{n+1} & (0 \leq k \leq n) \\ 0 & (k > n) \end{cases} (n = 0, 1, \dots).$$

If $y = (y_k)_{k=0}^\infty$ is any sequence then we write

$$\sigma_n(y) = \frac{1}{n+1} \sum_{k=0}^n y_k \quad (n = 0, 1, \dots) \quad (1.1)$$

for the C_1 means of the sequence y. The equality in (1.1) transform a sequence y into the sequence $(\sigma_n)_{n=0}^\infty$; therefore this is referred to as the sequence-to-sequence transformation for the C_1 method. Some studies of Cesàro method can be seen in [4,7,10].

Theorem 2.2 *If* $\{a_n\}_{n=0}^\infty$ *converges to L then* $\{a_n\}_{n=0}^\infty$ *is* C_1 *convergent to L (but not conversely).*

Definition 2.3 *(Hölder Method)* *Let* C_1 *be the Cesàro method of order one and let* $\alpha \in \mathbb{N}_0$. *Then*
$$H^\alpha = (C_1)^\alpha \quad \{\text{that is}, H^0 = I \text{ and } H^\alpha = (C_1)H^{\alpha-1} \quad (\alpha \geq 1)\}$$
is called Hölder matrix of order α or briefly the H^α matrix and **-method, respectively.

The advantage of the matrices H^α is that many of their proeprties can be derived from corresponding properties of C_1. A decisive disadvantage is the direct handling of those matrices since there does not exist a simple formula for their matrix coefficients. This circumstance is one reason, among others, that we consider also the Cesàro methods C_α which turn out to be equivalent and consistent with H^α. However, unlike the Hölder matrices, it is more difficult to handle products of Cesàro matrices because, for example, the product of two Cesàro matrices is not in general a Cesàro matrix.

In 1921 Hausdorff established a number of properties of these matrices, which now bear his name, including necessary and sufficient conditions for regularity in "F. Hausdorff, Summationsmethoden und Momentfolgen I, II, Math. Z., 9, 1921".

Definition 2.3 *(Hausdorff Method) Let* Let $\lambda = (\lambda_n)_{n=0}^\infty$ be a complex sequence, $M = (m_{nk})_{n,k=0}^\infty$ be the diagonal matrix with $m_{nn} = \lambda_n$ $(n = 0, 1, \dots)$, and D be the matrix with $d_{nk} = (-1)^k \binom{n}{k}$ for all n and k. The matrix $H(\lambda) = DMD$ is called the Hausdorff matrix associated with the sequence λ, and the entries of $H(\lambda)$ is given by

$$h_{nk} = \begin{cases} \sum_{j=k}^{n} (-1)^{j+k} \binom{n}{j}\binom{j}{k} \lambda_j & (0 \leq k \leq n) \\ 0 & (k > n) \end{cases} (n = 0,1, \dots).$$

Remark 2.4 *The Hölder matrices are all Hausdorff matrices; indeed we have $H^\alpha = H(\lambda)$ with $\lambda_n = (n+1)^{-\alpha}$ for $n = 0,1, \dots$. If $\lambda_n = (n+1)^{-1}$ for $n = 0,1, \dots$ we obtain $H^\alpha = C_1$. If $\lambda_n = \binom{(n+\alpha)^{-1}}{\alpha}$ for $n = 0,1, \dots$ we obtain Cesàro method of order α. If $\lambda_n = (r+1)^{-n}$ for $n = 0,1, \dots$ we obtain Euler mean E^r of order r.*

Definition 2.5 *(Euler Method)* Let $r > 0$. The Euler method E^r of order r is defined by the matrix $E = (e_{nk})_{n,k=0}^{\infty}$ with

$$e_{nk}^r = \begin{cases} \binom{n}{k} (1-r)^{n-k} r^k & (0 \leq k \leq n) \\ 0 & (k > n) \end{cases} (n = 0,1, \dots).$$

The E^r transform of the sequence $x = (x_k)_{k=0}^{\infty}$ is defined by

$$\tau_n^r = \frac{1}{(1-r)^n} \sum_{k=0}^{n} \binom{n}{k} r^{n-k} x_k \quad \text{for all } n = 0,1, \dots$$

The matrix E^r is invertable and its inverse is $(E^r)^{-1} = E^{1/r}$ with $r \neq 0$.

Much of the work on the Euler transform of order r was done by K. Knopp in articles "Über das Eulersche Summierungsverfahren, I and II, Math. Z. vol. 15, 226–253, 1922. The original Euler transformation (when $r = 1/2$) was given by L. Euler in Institutiones calculi differentialis in 1755.

Definition 2.6 *(Taylor Method)* Let $r \in \mathbb{C}\backslash\{0\}$. Then, the Taylor method T^r is defined by the matrix $T = (t_{nk}^r)$, where

$$t_{nk}^r = \begin{cases} \binom{k}{n} (1-r)^{n+1} r^{k-n} & (k > n) \\ 0 & (0 \leq k \leq n) \end{cases} (n = 0,1, \dots).$$

In case $r = 0$, it is immediate that $T^0 = I$. The matrix T^r is invertable and its inverse is $(T^r)^{-1} = T^{-r/(1-r)}$ provided $r \neq 1$.

Definition 2.7 Riesz Method *(Weighted Means)* Let $\boldsymbol{t} = (\boldsymbol{t_k})$ be a sequence of non-negative real numbers with $\boldsymbol{t_0 > 0}$ and write
$$T_n = \sum_{k=0}^{n} t_k \quad \text{for all } n \in \mathbb{N}.$$
Then the Riesz Means with respect to the sequence $t = (t_k)$ is defined by the matrix $R^t = (r_{nk}^t)$ which is given by

$$r_{nk}^t = \begin{cases} \frac{t_k}{T_n} & (0 \leq k \leq n) \\ 0 & (k > n) \end{cases} (n = 0,1, \dots).$$

It is obvious that the Riesz matrix R^t is reduced in the case $t = e$ to the Cesàro method of order 1.

Definition 2.8 *(Nörland Method)* The convolution $a * b$ of the sequences a and b is defined by
$$(a * b)_n = \sum_{k=0}^{n} a_k b_{n-k} \quad \text{for all } n = 0,1, \dots$$
The convolution of sequences is commutative, $a * b = b * a$. Let $p = (p_k)_{k=0}^{\infty}$ be a complex sequence with $p_0 = 1$ such that the sequence $P = p * e$ satisfies $P_n = (p * e)_n \neq 0$ for all n. Then the Nörlund method (N, p) is defined by the matrix $A = (a_{nk})_{n,k=0}^{\infty}$ with

$$a_{nk} = \begin{cases} \frac{p_{n-k}}{P_n} & (0 \leq k \leq n) \\ 0 & (k > n) \end{cases} (n = 0,1, \dots).$$

Hence, we have $A_n x = \frac{(p*x)_n}{(p*e)_n}$ for arbitrary sequences $x = (x_k)_{k=0}^{\infty}$ and $\sum_{k=0}^{n} a_{nk} = A_n e = 1$ for all $n = 0,1, \dots$ The $n-th$ Nörlund mean of a sequence $x = (x_k)_{k=0}^{\infty}$ is defined by

$$(N,p)_n x = \frac{(p*x)_n}{(p*e)_n} = \frac{1}{P_n} \sum_{k=0}^{n} p_{n-k} x_n.$$

It is obvious that the Nörlund matrix (N,p) is reduced in the case $p = e$ to the Cesàro method of order 1.

Definition 2.9 (*Abel Method*) Let $(a_n)_{n=0}^{\infty}$ be a real sequence s_n be the partial sums of the sequence $(a_n)_{n=0}^{\infty}$. Then $\sum_{n=0}^{\infty} a_n x^n$ be convergent for $|x| < 1$. If

$$\sum_{n=0}^{\infty} a_n x^n = (1-x) \sum_{n=0}^{\infty} s_n x^n \to s \quad (x \to 1^-)$$

then the series $\sum_n$ and the sequence $(a_n)_{n=0}^{\infty}$ are said to be Abel summable to s. The corresponding method of summability is called the Abel method.

Theorem 2.10 *If $\{a_n\}_{n=0}^{\infty}$ converges to L then $\{a_n\}_{n=0}^{\infty}$ is A (Abel) convergent to L (but not conversely).*
E. Borel first defined the Borel exponential method in the article "Mémoire sur les séries divergentes, Annls. scient. Éc. norm. sup. Paris (3), vol. 16, 9–136, 1899". G.H. Hardy improved and corrected some Borel's results in an article in "On differentiation and integration of divergent series, Trans. Camb. Phil. Soc., vol. 19, 297–321, 1904".

Definition 2.11 (*Borel Method*) *Let $(s_n)_{n=0}^{\infty}$ be a real sequence and $\sum_{n=0}^{\infty} s_n x^n /n!$ be convergent for all $x \in \mathbb{R}$. If*

$$\sigma(x) = e^{-x} \sum_{n=0}^{\infty} \frac{x^n}{n!} s_n \to s \quad (x \to \infty)$$

then the sequence $(s_n)_{n=0}^{\infty}$ is said to be Borel summable to s; this is denoted by $s_n \to s(B)$ $(n \to \infty)$. The corresponding method of summability is called the Borel method.

3. MATRIX TRANSFORMATIONS IN SEQUENCE SPACES

The study of matrix maps between sequence spaces originates from a natural problem in classical summability theory, namely to characterize all infinite matrices that transform every convergent sequence into a convergent sequence. This problem was solved by O. Toeplitz, who established the following three necessary and sufficient conditions for an infinite matrix $A = (a_{nk})_{n,k=0}^{\infty}$ to map the space c of all convergent sequence into itself

$$(i) \ \sup_{n} \sum_{k=0}^{\infty} |a_{nk}| < \infty,$$

$$(ii) \ \lim_{n \to \infty} a_{nk} = \alpha_k \ for \ each \ k \ and \ (iii) \ \lim_{n \to \infty} \sum_{k=0}^{\infty} a_{nk} = \alpha.$$

The difficult part of the proof was to show the necessity of the so–called row norm condition (i); the original proof used the classical analytical method of the gliding hump.

By characterizing a class of all continuous linear operators between X and Y, we mean establishing necessary and sufficient conditions for a continuous linear operator to map X into Y. So, $A \in (X,Y)$ if and only if

$(Ax)_n$ converges for all n and all $x \in X$ and
$Ax \in Y$ for all $x \in X$.

In particular, if L is represented by a matrix A, this means to establish necessary and sufficient conditions on the entries A to be in the class (X,Y).

Assume that $A = (a_{ij})$ is an infinite matrix of real or complex numbers a_{nk}, where $k, n \in \mathbb{N}$ and $x = (x_k) \in \omega$. Then we obtain the sequence Ax, the A-transform of x, by the usual matrix product

$$Ax = \begin{bmatrix} a_{0,0} & a_{0,1} & a_{0,2} & \cdots & a_{0,k} & \cdots \\ a_{1,0} & a_{1,1} & a_{1,2} & \cdots & a_{1,k} & \cdots \\ . & . & . & . & . \\ . & . & . & . & . \\ . & . & . & . & . \\ a_{n,0} & a_{n,1} & a_{n,2} & \cdots & a_{n,k} & \cdots \\ . & . & . & . & . \\ . & . & . & . & . \\ . & . & . & . & . \end{bmatrix} \begin{bmatrix} x_0 \\ x_1 \\ . \\ . \\ . \\ x_n \\ . \\ . \\ . \end{bmatrix} = \begin{bmatrix} a_{00}x_0 + a_{01}x_1 + a_{02}x_2 + \cdots \\ a_{10}x_0 + a_{11}x_1 + a_{12}x_2 + \cdots \\ . \\ . \\ . \\ a_{n0}x_0 + a_{n1}x_1 + a_{n2}x_2 + \cdots \\ . \\ . \\ . \end{bmatrix}.$$

Hence, in this way, we transform the sequence x into the sequence $Ax = \{(AX)_n\}$ with

$$(Ax)_n = \sum_k a_{nk} x_k \text{ for all } n \in \mathbb{N}, (3.1)$$

provided the series on the right hand side of (3.1) converges for each $n \in \mathbb{N}$. Recent results about matrix transformations can be found in [1-3, 8-11].

Matrix transformations are applied on measures of non–compactness of operators to establish some estimates or identities for the Hausdorff measure of non–compactness of linear operators between certain sequence spaces. Some examples can be seen in [5, 6].

4. SOME EXAMPLES OF REGULAR MATRICES

It is known that arithmetics mean, Cesaro means, Euler means, Taylor means, Riesz means, Nörland means, Hausdorff matrices, Borel matrix, Abel matrix and A^r matrix are regular.

Example 4.1 *Consider the infinite matrix* $A^r = (a_{nk}^r)$ *for* $0 < r < 1$:

$$a_{nk}^r = \begin{cases} \dfrac{r^k+1}{n+1} & \text{if } 0 \leq k \leq n, \\ 0 & \text{if } k > n. \end{cases}$$

The A^r matrix is a regular matrix since

- $\lim\limits_{n\to\infty} a_{nk}^r = \lim\limits_{n\to\infty} \dfrac{r^k+1}{n+1} = 0$ for each k,

- $\lim\limits_{n\to\infty} \sum_{k=0}^{\infty} a_{nk}^r = \lim\limits_{n\to\infty} \sum_{k=0}^{n} \dfrac{r^k+1}{n+1} = \lim\limits_{n\to\infty} \left(1 + \dfrac{1-r^{n+1}}{(1-r)(1+n)}\right) = 1$ and

- $\sup\limits_{n\in\mathbb{N}} \sum_{k=0}^{\infty} |a_{nk}^r| = \sup\limits_{n\in\mathbb{N}} \sum_{k=0}^{n} \left|\dfrac{r^k+1}{n+1}\right| \dfrac{1}{n+1} \sum_{k=0}^{n} |(r^k + 1)| = \sup\limits_{n\in\mathbb{N}} \dfrac{1}{n+1} \sum_{k=0}^{n} |(r^k + 1)| = \sup\limits_{n\in\mathbb{N}} \left[1 + \dfrac{1-r^{n+1}}{(1-r)(1+n)}\right] \leq M.$

REFERENCES

[1] A.M. Jarrah, E. Malkowsky, Ordinary, absolute and strong summability and matrix transformations, Filomat 17 (2003) 59–78.

[2] A. Karaisa, F. Özger, Almost difference sequence space derived by using a generalized weighted mean. J. Comput. Anal. Appl. 19(1) (2015) 27–38.

[3] A. Karaisa, F. Özger, On almost convergence and difference sequence spaces of order m with core theorems, Gen. Math. Notes 26(1) (2015) 102–125.

[4] E. Malkowsky, F. Özger, A note on some sequence spaces of weighted means, Filomat 26(3) (2012) 511-518.

[5] E. Malkowsky, F. Özger, A. Alotatibi, Some notes on matrix mappings and their Hausdorff measure of noncompactness, Filomat 285 (2014) 1059-1072.

[6] E. Malkowsky and F. Özger, Compact operators on spaces of sequences of weighted means, AIP Conf. Proc. 1470 (2012) 179–182.

[7] E. Malkowsky, F. Özger, V. Veličković, Some spaces related to Cesaro sequence spaces and an application to crystallography, MATCH Commun. Math. Comput. Chem. 70(3) (2013) 867–884.

[8] E. Malkowsky, F. Özger, V. Veličković, Some mixed paranorm spaces, Filomat, 31(4) (2017) 1079–1098.

[9] E. Malkowsky, F. Özger, V. Veličković, Matrix transformations on mixed paranorm spaces, Filomat 31(10) (2017) 2957–2966.

[10] V. Veličković, E. Malkowsky, F. Özger, Visualization of the spaces $W(u, v; \ell_p)$ and their duals, AIP Conf. Proc. 1759, (2016), doi: 10.1063/1.4959634.

[11] F. Özger, F. Başar, Domain of the double sequential band matrix $B(\tilde{r}, \tilde{s})$ on some Maddox's spaces, Acta Mathematica Scientia 34(2) (2014) 394–408.

[12] F. Başar, Summability Theory and Its Applications, Bentham Science Publishers, Monographs, 2012.

[13] J. Boos, Classical and Modern Methods in Summability, Oxford University Press, 2000.

[14] K. Zeller, W. Beekmann, Theorie der Limitierungsverfahren, Springer Verlag, Heidelberg, Berlin, New York, 1968.

[15] M. Stieglitz, H. Tietz, Matrixtransformationen in Folgenräumen. Eine Ergebnisubersicht, Math. Z. 154 (1977), 1–16.

[16] R.G. Cooke, Infinite Matrices and Sequence Spaces, Macmillan and Co. Limited, London, 1950.

[17] A. Wilansky, What Infinite Matrices Can Do, Mathematics Magazine, 58 (5) (1985)., 281–283.

[18] A. Wilansky, Summability through Functional Analysis, North–Holland Mathematics Studies 85, Amsterdam, New York, Oxford, 1984.

2nd International Students Science Congress
4-5 May 2018, Izmir - Turkey

İZMİR
Uluslararası
Misafir
Öğrenci
Derneği
◆İZMİR International Guest Student Association

İZMİR
KÂTİP ÇELEBİ
UNIVERSITY
2010

On Infinite Matrices

Faruk Özger*, İzmir Katip Çelebi Univ., Dept. of Engineering Sciences, Çiğli Main Campus, İzmir, Türkiye
*Corresponding author: farukozger@gmail.com

Abstract
Infinite matrices have many applications in pure and applied mathematics as well as in other fields of sciences. A short survey related to infinite matrices and their properties and applications is given in this study.

Keywords: infinite matrix, linear matrix equation
Discipline: Mathematics

1. INTRODUCTION

An infinite matrix $A = (a_{ij})$ of complex numbers is a double sequence of complex numbers defined by a function A from the set $\mathbb{N} \times \mathbb{N}$ into the complex field $\mathbb{C}$. In other words,

$$A = \begin{bmatrix} a_{0,0} & a_{0,1} & a_{0,2} & \cdots & a_{0,k} & \cdots \\ a_{1,0} & a_{1,1} & a_{1,2} & \cdots & a_{1,k} & \cdots \\ \cdot & \cdot & \cdot & \cdot & \cdot \\ \cdot & \cdot & \cdot & \cdot & \cdot \\ \cdot & \cdot & \cdot & \cdot & \cdot \\ a_{n,0} & a_{n,1} & a_{n,2} & \cdots & a_{n,k} & \cdots \\ \cdot & \cdot & \cdot & \cdot & \cdot \\ \cdot & \cdot & \cdot & \cdot & \cdot \\ \cdot & \cdot & \cdot & \cdot & \cdot \end{bmatrix}.$$

The addition and scalar multiplication of the infinite matrices $A = (a_{ij})$ and $B = (b_{ij})$ are defined by

$$A + B = \left(a_{ij} + b_{ij}\right) \text{ and } \lambda A = (\lambda a_{ij}),$$

where λ is a scalar. The product AB of matrices A and B is defined by

$$(AB)_{ij} = \sum_k a_{ik} \, b_{kj} \text{ for all } i, j \in \mathbb{N} \tag{1}$$

provided the series in (1) converge for all $i, j \in \mathbb{N}$, where $(AB)_{ij}$ denotes the entry of the matrix AB in the ith row and j^{th} column. Since the series on the right hand side of (1) may diverge for some,or all values of i, j; the product AB of the infinite matrices A and B may not exist.

Definition 1.1. If every row of a matrix A contains only a finite number of non–zero elements, then A is said to be *row–finite*. If the same is true with respect to every column, then A is said to be *column–finite*.

Definition 1.2. If A and B are both different from 0, and if $AB = 0$, then B is called the *right zero–divisor* of A and A is called a *left zero–divisor* of B which are denoted by A^0 and ^0B, respectively.

Definition 1.3. When the sum converges, $\sum_i a_{ii}$ is called the *trace* of the matrix A, and is denoted by $tr(A)$. This concept is used in some applications of the quantum theory of radiation.

Definition 1.4. (triangular matrix, triangle) A matrix $A = a_{nk}$ is called a (lower) triangular matrix if $a_{nk} = 0$ $(k, n \in \mathbb{N}_0$ with $k > n)$. A lower triangular matrix $A = a_{nk}$ with $a_{nn} \neq 0$ $(n \in \mathbb{N}_0)$ is called a triangle or normal matrix.

2. COMPARISON OF FINITE AND INFINITE MATRIX THEORIES

In the finite theory determinants play a fundamental part; but their value is lost, to a very large extent, in the theory of infinite matrices. Whereas the theory of finite matrices is a branch of Algebra, the theory of infinite matrices is a branch of Analysis. As compared to the case with finite $n \times n$ matrices, an infinite matrix A may be left (right) invertible, but not right (left) invertible. Also an infinite matrix may have more than oe left (right) inverse. Note that, the results in [1-7] are widely used in this survey.

***Example* 2.1.** The infinite matrix $A = a_{nk}$ (which is not triangular) has no right–hand inverse, but it does have an infinite number of left–hand inverses:

$$a_{nk} = \begin{cases} 1 & \text{if } n = k = 0 \\ 1 & \text{if } k = n + 1 \text{ or } k = n - 1 \text{ and } n \geq 1 \\ 0 & \text{otherwise .} \end{cases}$$

The explicit form of the matrix $A = a_{nk}$ is

$$A = \begin{bmatrix} 1 & 1 & 0 & 0 & 0 & \cdots \\ 1 & 0 & 1 & 0 & 0 & \cdots \\ 0 & 1 & 0 & 1 & 0 & \cdots \\ 0 & 0 & 1 & 0 & \ddots & \\ \cdot & \cdot & \cdot & & \ddots & \\ \cdot & \cdot & \cdot & \cdot & & \\ \cdot & \cdot & \cdot & \cdot & & \end{bmatrix}.$$

Consider the following system of an infinite number of linear equations in infinitely many known unknowns $x_0, x_1, x_2, \ldots$

$$\sum_k a_{ik} x_k = y_i \text{ for all } i \in \mathbb{N}. \tag{2}$$

If we construct a n infinite matrix $A = a_{ik}$ with the coefficients a_{ik} of the unknowns x_k and denote the vectors of the unknowns and constants by X and Y can be expressed in a matrix form as follows:

$$AX = Y. \tag{3}$$

This is a system of linear equations as follows:

$$a_{00}x_0 + a_{01}x_1 + a_{02}x_2 + \cdots + a_{0k}x_n + \cdots = y_0$$
$$a_{10}x_0 + a_{11}x_1 + a_{12}x_2 + \cdots + a_{1k}x_n + \cdots = y_1$$
$$\cdots$$
$$a_{n0}x_0 + a_{n1}x_1 + a_{n2}x_2 + \cdots + a_{nk}x_n + \cdots = y_n$$
$$\cdots$$

It is possible to express this system with the following matrix multiplication of infinite matrices:

$$Ax = \begin{bmatrix} a_{0,0} & a_{0,1} & a_{0,2} & \cdots & a_{0,k} & \cdots \\ a_{1,0} & a_{1,1} & a_{1,2} & \cdots & a_{1,k} & \cdots \\ \cdot & \cdot & \cdot & \cdot & \cdot & \\ \cdot & \cdot & \cdot & \cdot & \cdot & \\ \cdot & \cdot & \cdot & \cdot & \cdot & \\ a_{n,0} & a_{n,1} & a_{n,2} & \cdots & a_{n,k} & \cdots \\ \cdot & \cdot & \cdot & \cdot & \cdot & \\ \cdot & \cdot & \cdot & \cdot & \cdot & \\ \cdot & \cdot & \cdot & \cdot & \cdot & \end{bmatrix} \begin{bmatrix} x_0 \\ x_1 \\ \cdot \\ \cdot \\ \cdot \\ x_n \\ \cdot \\ \cdot \\ \cdot \end{bmatrix} = \begin{bmatrix} a_{00}x_0 + a_{01}x_1 + a_{02}x_2 + \cdots \\ a_{10}x_0 + a_{11}x_1 + a_{12}x_2 + \cdots \\ \cdot \\ \cdot \\ \cdot \\ a_{n0}x_0 + a_{n1}x_1 + a_{n2}x_2 + \cdots \\ \cdot \\ \cdot \\ \cdot \end{bmatrix} = \begin{bmatrix} y_0 \\ y_1 \\ \cdot \\ \cdot \\ \cdot \\ y_n \\ \cdot \\ \cdot \\ \cdot \end{bmatrix}.$$

A left inverse of the infinite matrix A is used to find a solution of the linear matrix equation.
Let us suppose that the left inverse of a matrix A exists, such that $^{(-1)}AA = I$. Then, under certain conditions, if we multiply both sides of (3) on the left by $^{(-1)}A$, we obtain the solution of (3) as $X = {}^{(-1)}AY$.
A very important application of infinite matrices is used in the theory of summability of divergent sequences and series.

***Example* 2.2.** A simple example of this is the *Cesàro mean of order one* which is the well-known method of summability and is defined by the infinite matrix $C_1 = (c_{nk})$, as follows;

$$c_{nk} = \begin{cases} \dfrac{1}{n+1} & \text{if } 0 \leq k \leq n, \\ 0 & \text{if } k > n. \end{cases}$$

The C_1-transform of a sequence $x = (x_k)$ is the sequence $y = (y_n)$ defined by

$$y_n = (C_1 x)_n = \frac{1}{n+1} \sum_{k=0}^{n} x_k \text{ for all } n \in \mathbb{N}.$$

One can easly see that the C_1-transform of the sequence $x = \{(-1)^k\}$ which is obviously bounded but divergent, is the null sequence

$$y = y_n = \left\{ \frac{1 + (-1)^n}{2(n+1)} \right\}.$$

A further important application of infinite matrices is the Heisenberg–Dirac theory of quantum mechanics. Here two basic problems consist in solving two linear equations in infinite matrices:
- For a given matrix A, the *quantization equation* which is in the form $AX - XA = I$.
- For a given matrix A and a diagonal matrix D, the equation is in the form $AX - XD = 0$.

Infinite matrices are applied in function theory in connection with the analytic continuation of holomorphic functions and the boundary behavior of a power series.
- Infinite matrices are applied in applied analysis for the generation of iteration methods for the solution of a linear system of equations, and for the acceleration of convergence in approximation theory.
- Infinite matrices are applied in the theory of Fourier series for both the creation and acceleration of convergence of a Fourier series.
- They are also applied in other fields of mathematics like probability theory (law of large numbers) and the number theory (prime number theory which can be deduced from Wiener's Tauberian theorem).

For an overview of the extensive literature use, for example, MathSciNet with Classification: 40xx, 46XX, 47xx. Recent results about the application of infinite matrices can be found in [8-16].

3. SOME CHARACTERISTIC PROPERTIES OF INFINITE MATRICES

Since the product of two diagonal matrices D and E is the diagonal matrix

$$DE = diag(d_0e_0, d_1e_1, d_2e_2, \dots) = diag(e_0d_0, e_1d_1, e_2d_2, \dots) = ED,$$

multiplication is *commutative* for diagonal matrices. But in general, products of matrices are not commutative, since $\sum_k a_{ik} b_{kj}$ is not equal to $\sum_k b_{ik} a_{kj}$ for every i, j, even assuming that both series converge for every i, j, in general.

Multiplication of infinite matrices is not *associative*, in general. For example, if $a_{ij} = c_{ij} = 1$ for all $i, j \in \mathbb{N}$, and if

$$\sum_j \left(\sum_i b_{ij} \right) \neq \sum_i \left(\sum_j b_{ij} \right) \tag{4}$$

then $(AB)C \neq A(BC)$, where $\{(AB)C\}_{ij}$ and $\{A(BC)\}_{ij}$ are given by the left and right hand sides of (4). As an example of a matrix satisfying (4) we can define the matrix $B = (b_{ij})_{i,j \in \mathbb{N}}$ by

$$b_{ij} = \begin{cases} 2^{-i} & \text{if } j = 0, i \in \mathbb{N}_1, \\ 2^{-j} & \text{if } i = 0, j \in \mathbb{N}_1, \\ 0 & \text{otherwise.} \end{cases}$$

Then, it is easily seen that

$$\sum_j \left(\sum_i b_{ij} \right) = b_{00} + \sum_{i=1}^{\infty} b_{i0} = 1 \text{ and } \sum_i \left(\sum_j b_{ij} \right) = b_{00} + \sum_{i=1}^{\infty} b_{0j} = -1$$

Example 3.1. Consider the following matrices

$$A = \begin{bmatrix} 1 & -1 & 1 & -1 & \cdots \\ 0 & 0 & 0 & 0 & \cdots \\ \cdot & \cdot & \cdot & \cdot & \ddots \\ \cdot & \cdot & \cdot & \cdot \\ \cdot & \cdot & \cdot & \cdot \end{bmatrix}, \quad B = \begin{bmatrix} 1 & 1 & 1 & 1 & \cdots \\ 0 & 1 & 1 & 1 & \cdots \\ 0 & 0 & 1 & 1 & \cdots \\ & \ddots & \ddots & \ddots & \ddots \end{bmatrix}$$

$$\text{and } C = \begin{bmatrix} 0 & 0 & \cdots \\ 1 & 0 & \cdots \\ 0 & 0 & \cdots \\ 1 & 0 & \cdots \\ \cdot & \cdot & \cdots \end{bmatrix} \text{ then } AB = \begin{bmatrix} 1 & 0 & 1 & 0 & \cdots \\ 0 & 0 & 0 & 0 & \cdots \\ \cdot & \cdot & \cdot & \cdot & \ddots \\ \cdot & \cdot & \cdot & \cdot \\ \cdot & \cdot & \cdot & \cdot \end{bmatrix}$$

and $(AB)C = 0$. However, BC, and thus $A(BC)$, does not exist.

Theorem 3.2. *A lower triangular matrix $A = a_{nk}$ is invertible if and only if $a_{nn} \neq 0$ for all $n \in \mathbb{N}$. Moreover, if A is invertible then it has a unique right hand inverse which is also a left hand inverse.*

Example 3.3. *A lower triangular matrix $A = a_{nk}$ with non–zero diagonal elements may not has a unique left–hand inverse.:*

$$a_{nk} = \begin{cases} 1 & \text{if } n = k = 0 \\ 1 & \text{if } k = n - 1 \text{ or } k = n \text{ and } n \geq 1 \\ 0 & \text{otherwise.} \end{cases}$$

The unique right–hand inverse is $B = b_{nk}$, where

$$b_{nk} = \begin{cases} 0 & \text{if } k > n \\ (-1)^{n+k} & \text{if } k \leq n. \end{cases}$$

Note that B is also a left–hand inverse. However, the matrix $C = c_{nk}$, where is also a left–hand inverse.

Theorem 3.4. *(triangle) If A is a triangle, then the following statements hold:*
  a) For each $y \in \omega$ there exists a unique solution of the system of equations $AX = Y$.
  b) There exists a unique right inverse B of A. Moreover, B is also a triangle and a left inverse. So A^{-1} exists.
  c) The matrix A may have more than one left inverse, but there is exactly one that is also a triangle, namely A^{-1}.

Theorem 3.5. *(Silverman–Toeplitz)* A matrix $A = (a_{nk})$ is regular if and only if
  a) $\lim\limits_{n\to\infty} a_{nk} = 0$ for each $k = 0,1,2,...$,
  b) $\lim\limits_{n\to\infty} \sum_{k=0}^{\infty} a_{nk} = 1$ for each $k = 0,1,2,...$ and
  c) $\sup\limits_{n\in\mathbb{N}}\{\sum_{k=0}^{\infty} |a_{nk}|\} \leq M$ for some $M > 0$.

It is known that arithmetics mean, Cesaro means, Euler means, Taylor means, Riesz means, Nörland means, Hausdorff matrices, Borel matrix, Abel matrix and A^r matrix are regular.

Example 3.6. *Consider the infinite matrix* $A^r = (a_{nk}^r)$ *for* $0 < r < 1$:

$$a_{nk}^r = \begin{cases} \dfrac{r^k+1}{n+1} & \text{if } 0 \leq k \leq n, \\ 0 & \text{if } k > n. \end{cases}$$

The A^r matrix is a regular matrix since

- $\lim\limits_{n\to\infty} a_{nk}^r = \lim\limits_{n\to\infty} \dfrac{r^k+1}{n+1} = 0$ for each k,

- $\lim\limits_{n\to\infty} \sum_{k=0}^{\infty} a_{nk}^r = \lim\limits_{n\to\infty} \sum_{k=0}^{n} \dfrac{r^k+1}{n+1} = \lim\limits_{n\to\infty} \left(1 + \dfrac{1-r^{n+1}}{(1-r)(1+n)}\right) = 1$ and

- $\sup\limits_{n\in\mathbb{N}} \sum_{k=0}^{\infty} |a_{nk}^r| = \sup\limits_{n\in\mathbb{N}} \sum_{k=0}^{n} \left|\dfrac{r^k+1}{n+1}\right| \dfrac{1}{n+1} \sum_{k=0}^{n} |(r^k+1)| = \sup\limits_{n\in\mathbb{N}} \dfrac{1}{n+1} \sum_{k=0}^{n} |(r^k+1)| = \sup\limits_{n\in\mathbb{N}}\left[1 + \dfrac{1-r^{n+1}}{(1-r)(1+n)}\right] \leq M.$

Example 3.7. It is possible to find a sequence which is not A^r–limitiable.

Theorem 3.8. Every convergent sequence $x = (x_n)$ is C_1–summable and $\lim_{n\to\infty} x_n = \lim_{n\to\infty}(C_1 x)_n$.

Theorem 3.9. A regular matrix cannot sum all bounded sequences.

REFERENCES
[1] A. Peyerimhof, Lectures on Summability, Lecture Notes in Mathematics 107, Springer Verlag, Heidelberg, Berlin, New York, 1969.

[2] F. Başar, Summability Theory and Its Applications, Bentham Science Publishers, Monographs, 2012.

[3] J. Boos, Classical and Modern Methods in Summability, Oxford University Press, 2000.

[4] R.G. Cooke, Infinite Matrices and Sequence Spaces, Macmillan and Co. Limited, London, 1950.

[5] B.E. Rhoades, Fixed Point Iterations Using Infinite Matrices, Transactions of the American Mathematical Society, 196 (1974) 161–176.

[6] O. Toeplitz, Uberallgemeine Mittelbildungen, Prace. Mat. Fiz., 1911(22) (1911) 113–119.

[7] A. Wilansky, What Infinite Matrices Can Do, Mathematics Magazine, 58(5) (1985) 281–283.

[8] E. Malkowsky, F. Özger, A note on some sequence spaces of weighted means, Filomat 26(3) (2012) 511-518.

[9] E. Malkowsky, F. Özger, A. Alotatibi, Some notes on matrix mappings and their Hausdorff measure of noncompactness, Filomat 285 (2014) 1059-1072.

[10] E. Malkowsky and F. Özger, Compact operators on spaces of sequences of weighted means, AIP Conf. Proc. 1470 (2012) 179–182.

[11] E. Malkowsky, F. Özger, V. Veličković, Some spaces related to Cesaro sequence spaces and an application to crystallography, MATCH Commun. Math. Comput. Chem. 70(3) (2013) 867–884.

[12] E. Malkowsky, F. Özger, V. Veličković, Some mixed paranorm spaces, Filomat, 31(4) (2017) 1079–1098.

[13] E. Malkowsky, F. Özger, V. Veličković, Matrix transformations on mixed paranorm spaces, Filomat 31(10) (2017) 2957–2966.

[14] V. Veličković, E. Malkowsky, F. Özger, Visualization of the spaces $W(u, v; \ell_p)$ and their duals, AIP Conf. Proc. 1759, (2016), doi: 10.1063/1.4959634.

[15] F. Özger, F. Başar, Domain of the double sequential band matrix $B(\tilde{r}, \tilde{s})$ on some Maddox's spaces, Acta Mathematica Scientia 34(2) (2014) 394–408.

[16] F. Özger, Some geometric characterizations of a fractional Banach set, Commun. Fac. Sci. Univ. Ank. Ser. A1 Math. Stat. 68(1) (2019) 546-558.

A Numerical Solution of Cauchy Problem for Partial Differential Equations by Means of Pell Polynomials

Seda Çayan*, Manisa Celal Bayar University, Department of Mathematics, Manisa, Turkey
Mehmet Sezer, Manisa Celal Bayar University, Department of Mathematics, Manisa, Turkey
Mehmet Çevik, İzmir Kâtip Çelebi University, Department of Mechanical Engineering, İzmir, Turkey
*Corresponding author: seda_cayan@hotmail.com

Abstract

In this study, we present a novel efficient numerical method for the approximate solution of Cauchy problem for partial differential equations, which are encountered in science and engineering branch. This technique is a matrix method based on collocation points along with the truncated Pell series, and reduces the solution of problem to the solution of a matrix equation which corresponds to a system of algebraic equations with unknown Pell coefficients. The approximate solutions subject to initial conditions are obtained in terms of Pell polynomials. Some examples with error analysis techniques are given to demonstrate the validity and applicability of the present method, and the comparisons are made with existing results.

Keywords: Pell polynomials, matrix and collocation methods, Cauchy problem, partial differential equations
Discipline: Mathematics

1. INTRODUCTION

This study is about partial differential equations, and especially with Cauchy's Problem (or initial value problem) concerning them. The Cauchy problem is one of the major problems in the theory of partial differential equations and occurs in several physical applications such as Maxwell's equations, the equations of compressible flow, motion of elastic bodies, magneto-hydrodynamics and others [1]. Cauchy problem is properly posed if two assumptions are satisfied: (1) existence of solutions for sufficiently many initial data, (2) continuous dependence of solutions on their initial data [2]. In this study, we consider the second order linear partial differential equation

$$A(x,t)\frac{\partial^2 u}{\partial x^2} + B(x,t)\frac{\partial^2 u}{\partial x \partial t} + C(x,t)\frac{\partial^2 u}{\partial t^2} + D(x,t)\frac{\partial u}{\partial x} + E(x,t)\frac{\partial u}{\partial t} + F(x,t)u = G(x,t) \quad (1)$$

under the initial conditions

$$u(x,c) = f(x) \quad , \quad u_t(x,c) = m(x) \, , \ a \le x \le b \, , \ c \le t \le d \quad (2)$$

Here $A(x,t), B(x,t), C(x,t), D(x,t), E(x,t), F(x,t)$ and $G(x,t)$ are functions and $f(x)$, $m(x)$ are continuous functions [3-5]. We assume the approximate solution of the problem (1-2) in the truncated Pell series form

$$u(x,t) \cong u_N(x,t) = \sum_{m=0}^{N}\sum_{n=0}^{N} a_{m,n} P_{m+1,n+1}(x,t) \, ; \ P_{m+1,n+1}(x,t) = P_{m+1}(x)P_{n+1}(t) \quad (3)$$

where $u_N(x,t)$ is approximate solution of Eq. (1); $a_{m,n}$, $(m,n=0,1,\ldots,N)$ are unknown Pell polynomials coefficients; N is chosen as any positive integer such that $N \ge 2$.

Pell Polynomials are defined by the generating function [6]:

$$(1-2xt-t^2)^{-1} = \sum_{n=0}^{\infty} P_{n+1}(x)t^n .$$

From standard methods, we obtain the explicit representations of Pell polynomials [7]:

$$P_n(x) = \sum_{k=0}^{[(n-1)/2]} \binom{n-k-1}{k} 2^{n-2k-1} x^{n-2k-1} \quad (4)$$

2. FUNDAMENTAL MATRIX RELATIONS

Let us consider Eq. (1) and find the matrix forms of the equation. First, we can write Pell polynomials (4) in the matrix form:

$$[u(x,t)] \cong [u_N(x,t)] = \mathbf{P}(x)\overline{\mathbf{P}}(t)\mathbf{A} \tag{5}$$

where

$$\mathbf{P}(x) = [P_1(x) \quad P_2(x) \quad P_3(x) \quad \cdots \quad P_{N+1}(x)] \;, \; \overline{\mathbf{P}}(t) = diag(\mathbf{P}(t), \mathbf{P}(t), \mathbf{P}(t), ..., \mathbf{P}(t))$$

$$\mathbf{A}_i = [a_{i,0} \quad a_{i,1} \quad a_{i,2} \quad \cdots \quad a_{i,N}]^T \;, \; (i = 0,1,2,...,N) \; , \; \mathbf{A} = [\mathbf{A}_0 \quad \mathbf{A}_1 \quad \mathbf{A}_2 \quad \cdots \quad \mathbf{A}_N]^T$$

$$\mathbf{A} = [a_{0,0} \quad a_{0,1} \quad a_{0,2} \quad \cdots \quad a_{0,N} \quad a_{1,0} \quad a_{1,1} \quad a_{1,2} \quad \cdots \quad a_{1,N} \quad \cdots \quad a_{N,0} \quad a_{N,1} \quad a_{N,2} \quad \cdots \quad a_{N,N}]^T$$

Also, we can use the relation

$$\mathbf{P}(x) = \mathbf{X}(x)\mathbf{S} \text{ and } \overline{\mathbf{P}}(t) = \overline{\mathbf{X}}(t)\overline{\mathbf{S}} \tag{6}$$

where

$$\mathbf{X}(x) = [1 \quad x \quad x^2 \quad \cdots \quad x^N] \;, \quad \overline{\mathbf{X}}(t) = diag(\mathbf{X}(t), \mathbf{X}(t), \mathbf{X}(t), ..., \mathbf{X}(t))$$

$$\mathbf{S} = \begin{bmatrix} 1 & 0 & 0 & \cdots & 0 \\ 0 & 2^1 \binom{1}{0} & 0 & \cdots & 0 \\ 2^0 \binom{1}{1} & 0 & 2^2 \binom{2}{0} & \cdots & 0 \\ \vdots & \vdots & \vdots & \ddots & \vdots \\ 2^0 \binom{N-\left(\frac{N-1}{2}\right)-1}{\frac{N-1}{2}} & 0 & 2^2 \binom{N-\left(\frac{N-3}{2}\right)-1}{\frac{N-3}{2}} & \cdots & 2^{N-1} \binom{N-\left(\frac{N-N}{2}\right)-1}{\left(\frac{N-N}{2}\right)} \\ 0 & 2^1 \binom{N-\left(\frac{N-2}{2}\right)-1}{\frac{N-2}{2}} & 0 & \cdots & 2^{N-1} \binom{N-\left(\frac{N-N}{2}\right)-1}{\left(\frac{N-N}{2}\right)} \end{bmatrix}^T \begin{array}{l} \text{if } N \text{ is} \\ \text{odd} \\ \\ \text{if } N \text{ is} \\ \text{even} \end{array}$$

$$\mathbf{S}^0 = \mathbf{I} = \begin{bmatrix} 1 & 0 & \cdots & 0 \\ 0 & 1 & \cdots & 0 \\ \vdots & \vdots & \ddots & \vdots \\ 0 & 0 & \cdots & 1 \end{bmatrix}, \; \mathbf{B}^0 = \mathbf{I} = \begin{bmatrix} 1 & 0 & \cdots & 0 \\ 0 & 1 & \cdots & 0 \\ \vdots & \vdots & \ddots & \vdots \\ 0 & 0 & \cdots & 1 \end{bmatrix}, \; \mathbf{B} = \begin{bmatrix} 0 & 1 & 0 & \cdots & 0 \\ 0 & 0 & 2 & \cdots & 0 \\ \vdots & \vdots & \vdots & \ddots & \vdots \\ 0 & 0 & 0 & \cdots & N \\ 0 & 0 & 0 & \cdots & 0 \end{bmatrix}$$

$$\overline{\mathbf{S}} = diag(\mathbf{S}, \mathbf{S}, \mathbf{S}, ..., \mathbf{S}), \; \overline{\mathbf{B}} = diag(\mathbf{B}, \mathbf{B}, \mathbf{B}, ..., \mathbf{B})$$

On the other hand, the relation between the matrix $\mathbf{X}(x)$, $\overline{\mathbf{X}}(t)$ and its derivatives [8-10] $\mathbf{X}'(x)$, $\mathbf{X}''(x)$,..., $\mathbf{X}^{(k)}(x)$ and $\overline{\mathbf{X}}'(t)$, $\overline{\mathbf{X}}''(t)$,..., $\overline{\mathbf{X}^{(k)}}(t)$ are

$$\mathbf{X}'(x) = \mathbf{X}(x)\mathbf{B} \;, \; \mathbf{X}''(x) = \mathbf{X}(x)\mathbf{B}^2 \;,..., \; \mathbf{X}^{(k)}(x) = \mathbf{X}(x)\mathbf{B}^k \tag{7}$$

$$\overline{\mathbf{X}}'(t) = \overline{\mathbf{X}}(t)\overline{\mathbf{B}} \;, \; \overline{\mathbf{X}}''(t) = \overline{\mathbf{X}}(t)\overline{\mathbf{B}}^2 \;,..., \; \overline{\mathbf{X}^{(k)}}(t) = \overline{\mathbf{X}}(t)\overline{\mathbf{B}^{(k)}} \tag{8}$$

Then, we organize the following matrix relations of derivative forms of $u(x,t)$ with (5-8):

$$\left[u(x,t)\right]=\mathbf{P}(x)\overline{\mathbf{P}}(t)\mathbf{A}=\mathbf{X}(x)\mathbf{S}\overline{\mathbf{X}}(t)\overline{\mathbf{S}}\mathbf{A}\,,\;\left[u_x(x,t)\right]=\mathbf{P}'(x)\overline{\mathbf{P}}(t)\mathbf{A}=\mathbf{X}(x)\mathbf{B}\mathbf{S}\overline{\mathbf{X}}(t)\overline{\mathbf{S}}\mathbf{A}\quad(9)$$

$$\left[u_t(x,t)\right]=\mathbf{P}(x)\overline{\mathbf{P}}'(t)\mathbf{A}=\mathbf{X}(x)\mathbf{S}\overline{\mathbf{X}}(t)\overline{\mathbf{B}}\overline{\mathbf{S}}\mathbf{A}\,,\;\left[u_{xt}(x,t)\right]=\mathbf{P}'(x)\overline{\mathbf{P}}'(t)\mathbf{A}=\mathbf{X}(x)\mathbf{B}\mathbf{S}\overline{\mathbf{X}}(t)\overline{\mathbf{B}}\overline{\mathbf{S}}\mathbf{A}$$

$$\left[u_{xx}(x,t)\right]=\mathbf{P}''(x)\overline{\mathbf{P}}(t)\mathbf{A}=\mathbf{X}(x)\mathbf{B}^2\mathbf{S}\overline{\mathbf{X}}(t)\overline{\mathbf{S}}\mathbf{A}\,,\;\left[u_{tt}(x,t)\right]=\mathbf{P}(x)\overline{\mathbf{P}}''(t)\mathbf{A}=\mathbf{X}(x)\mathbf{S}\overline{\mathbf{X}}(t)\overline{\mathbf{B}}^2\overline{\mathbf{S}}\mathbf{A}$$

By substituting the relations (9) into Eq.(1) we have the fundamental matrix form for Eq.(1):

$$\left\{\begin{matrix}[A(x,t)]\mathbf{X}(x)\mathbf{B}^2\mathbf{S}\overline{\mathbf{X}}(t)\overline{\mathbf{S}}+[B(x,t)]\mathbf{X}(x)\mathbf{B}\mathbf{S}\overline{\mathbf{X}}(t)\overline{\mathbf{B}}\overline{\mathbf{S}}+[C(x,t)]\mathbf{X}(x)\mathbf{S}\overline{\mathbf{X}}(t)\overline{\mathbf{B}}^2\overline{\mathbf{S}}+\\ [D(x,t)]\mathbf{X}(x)\mathbf{B}\mathbf{S}\overline{\mathbf{X}}(t)\overline{\mathbf{S}}+[E(x,t)]\mathbf{X}(x)\mathbf{B}\overline{\mathbf{X}}(t)\overline{\mathbf{B}}\overline{\mathbf{S}}+[F(x,t)]\mathbf{X}(x)\mathbf{S}\overline{\mathbf{X}}(t)\overline{\mathbf{S}}\end{matrix}\right\}\mathbf{A}=[G(x,t)];$$

$$\underbrace{\qquad\qquad\qquad\qquad\qquad\qquad\qquad\qquad\qquad\qquad\qquad\qquad\qquad}_{\mathbf{W}(x,t)}$$

or shortly

$$\mathbf{W}(x,t)\mathbf{A}=G(x,t)$$

and then, using collocation points defined by

$$x_i=a+\frac{b-a}{N}i\quad,\quad t_j=c+\frac{d-c}{N}j\quad,\quad i,j=0,1,2,\dots,N\,.$$

$$\mathbf{W}=\begin{bmatrix}\mathbf{W}_1 & \mathbf{W}_2 & \cdots & \mathbf{W}_N\end{bmatrix}^T\;;\;\mathbf{W_i}=\begin{bmatrix}\mathbf{W}(x_i,t_0) & \mathbf{W}(x_i,t_1) & \cdots & \mathbf{W}(x_i,t_N)\end{bmatrix}^T$$

$$\mathbf{G}=\begin{bmatrix}\mathbf{G}_0 & \mathbf{G}_1 & \cdots & \mathbf{G}_N\end{bmatrix}^T\;;\;\mathbf{G}_i=\begin{bmatrix}G(x_i,t_0) & G(x_i,t_1) & \cdots & G(x_i,t_N)\end{bmatrix}^T\quad,\quad i=0,1,2,\dots,N$$

or shortly

$$\mathbf{W}\mathbf{A}=\mathbf{G}\text{ or }[\mathbf{W};\mathbf{G}]\qquad\qquad(10)$$

Thus, the fundamental matrix equation of (1) is defined. Similarly, we are able to obtain the corresponding matrix form for the conditions (2) by using the relations (5-8). Thus, we have the matrix form of (2):

$$\left[u(x,c)\right]=\mathbf{P}(x)\overline{\mathbf{P}}(c)\mathbf{A}=\mathbf{X}(x)\mathbf{S}\overline{\mathbf{X}}(c)\overline{\mathbf{S}}\mathbf{A}\,,\;\left[u_t(x,c)\right]=\mathbf{P}(x)\overline{\mathbf{P}}'(c)\mathbf{A}=\mathbf{X}(x)\mathbf{S}\overline{\mathbf{X}}(c)\overline{\mathbf{B}}\overline{\mathbf{S}}\mathbf{A}\quad(11)$$

By substituting the relation (11) into equations (2) we have matrix form of (2):

$$\underbrace{\mathbf{X}(x)\mathbf{S}\overline{\mathbf{X}}(c)\overline{\mathbf{S}}}_{\mathbf{U}_1(x,t)}\mathbf{A}=f(x)\Rightarrow\mathbf{U}_1(x,t)\mathbf{A}=f(x),\;\underbrace{\mathbf{X}(x)\mathbf{S}\overline{\mathbf{X}}(c)\overline{\mathbf{B}}\overline{\mathbf{S}}}_{\mathbf{U}_2(x,t)}\mathbf{A}=m(x)\Rightarrow\mathbf{U}_2(x,t)\mathbf{A}=m(x)$$

and by putting collocation points,

$$\mathbf{U}_1=\begin{bmatrix}\mathbf{U}_1(x_1,c) & \mathbf{U}_1(x_2,c) & \cdots & \mathbf{U}_1(x_N,c)\end{bmatrix}^T,\;\mathbf{U}_2=\begin{bmatrix}\mathbf{U}_2(x_1,c) & \mathbf{U}_2(x_2,c) & \cdots & \mathbf{U}_2(x_N,c)\end{bmatrix}^T$$

$$\mathbf{F}=\begin{bmatrix}f(x_0) & f(x_1) & f(x_2) & \cdots & f(x_N)\end{bmatrix}^T,\;\mathbf{M}=\begin{bmatrix}m(x_0) & m(x_1) & m(x_2) & \cdots & m(x_N)\end{bmatrix}^T$$

$$\mathbf{U}_1\mathbf{A}=\mathbf{F}\text{ or }[\mathbf{U}_1;\mathbf{F}]\text{ and }\mathbf{U}_2\mathbf{A}=\mathbf{M}\text{ or }[\mathbf{U}_2;\mathbf{M}]\qquad(12)$$

To obtain the solution of (1) under the conditions (2), the following augmented matrix is constructed by replacing the row matrices (10) by the $(N+1)+(N+1)$ rows of the matrix (12), so we get the new augmented matrix

$$[\tilde{\mathbf{W}};\tilde{\mathbf{G}}] = \begin{bmatrix} \mathbf{W};\mathbf{G} \\ \mathbf{U}_1;\mathbf{F} \\ \mathbf{U}_2;\mathbf{M} \end{bmatrix}$$

Then we solve the system $\mathbf{A} = (\tilde{\mathbf{W}})^{-1}\tilde{\mathbf{G}}$ if $rank(\tilde{\mathbf{W}}) = rank(\tilde{\mathbf{W}};\tilde{\mathbf{G}}) = (N+1)^2$ and $\mathbf{A}$ is uniquely determined. In this way, the unknown Pell polynomials coefficients are obtained. Thus, the approximate solution $u(x,t)$ is found in the form of (3).

3. ERROR ANALYSIS

In this section, the error estimation [8-10] for equation (3) is given; it improves the accuracy of the Pell polynomials solution. The resulting equation must be satisfied approximately, that is, for $x = x_r$, $0 \le x_r \le 1$ and $t = t_s$, $0 \le t_s \le 1$:

$$E_N(x_r,t_s) = \left| \begin{matrix} A(x_r,t_s)u_{xx}(x_r,t_s) + B(x_r,t_s)u_{xt}(x_r,t_s) + C(x_r,t_s)u_{tt}(x_r,t_s) + \\ D(x_r,t_s)u_x(x_r,t_s) + E(x_r,t_s)u_t(x_r,t_s) + F(x_r,t_s)u(x_r,t_s) - G(x_r,t_s) \end{matrix} \right| \cong 0$$

where $E_N(x_r,t_s) \le 10^{-k_{rs}} = 10^{-k}$ (k is positive integer). If $\max 10^{-k_{rs}} = 10^{-k}$ is prescribed, then the truncation limit N is increased until the difference $E_N(x_r,t_s)$ at each of the points becomes smaller than the prescribed 10^{-k}. On the other hand, we use absolute error for measuring errors. If $\tilde{u}(x,t)$ is an approximation to $u(x,t)$ the absolute error is

$$e(x,t) = |u(x,t) - \tilde{u}(x,t)|$$

4. NUMERICAL EXAMPLES

The method of this study is useful in finding the solutions in terms of Pell polynomials. We illustrate the method by the following examples.

Example 1. Let us consider the problem

$$u_t(x,t) - u_{xx}(x,t) = -x - 2 \text{ , } (0 \le x \le 1 \text{ , } 0 \le t \le 1) \tag{13}$$

under the initial conditions

$$u(x,0) = x^2 \text{ , } u_t(x,0) = -x \tag{14}$$

We follow the procedure in Section 2 above and by substituting the initial conditions (14), the exact solutions of (13) is obtained as $u(x,t) = x^2 - xt$.

Example 2. Consider the following problem

$$u_{tt}(x,t) - u_{xx}(x,t) = (x+t+2)e^t \text{ , } (0 \le x \le 1 \text{ , } 0 \le t \le 1)$$

under the initial conditions

$$u(x,0) = x \text{ , } u_t(x,0) = x+1$$

where the exact solution of the problem is $u(x,t) = (x+t)e^t$.

We suppose that $u(x,t)$ is approximated by a truncated Pell series in the form

$$u(x,t) \cong \sum_{m=0}^{N} \sum_{n=0}^{N} a_{m,n} P_{m,n}(x,t) \ , \ 0 \le x \le 1, \ 0 \le t \le 1$$

By using the procedure in Section 2, the fundamental matrix relations for the equation and conditions are computed and then the Pell coefficients are found. The comparison of exact and approximate solutions for $N = 3,5,7,9$ can be seen in Figures 1 and 2 and numerical results are given in Table 1.

Table 1. Comparison of the exact and approximate solutions for $N = 3,5,7,9$ of Example 2.

x_r , t_s		Exact Solution	N = 3		N = 5		N = 7		N = 9	
x	t	u (x, t)	$\tilde{u}_3$ (x, t)	e_3 (x, t)	$\tilde{u}_5$ (x, t)	e_5 (x, t)	$\tilde{u}_7$ (x, t)	e_7 (x, t)	$\tilde{u}_9$ (x, t)	e_9 (x, t)
0.0	0.0	0.00000	0.00000	0.00000	0.00000	0.00000	0.00000	0.00000	0.00000	0.00000
0.0	0.5	0.82436	0.73996	0.84 E – 1	0.82054	0.38 E – 2	0.82428	0.80 E – 4	0.82436	0.99 E – 6
0.0	1.0	2.71828	2.16049	0.55778	2.66327	0.55 E – 1	2.7156	0.26 E – 2	2.7182	0.77 E – 4
0.5	0.0	0.50000	0.50000	0.00000	0.50000	0.00000	0.50000	0.00000	0.50000	0.00000
0.5	0.5	1.64872	1.64482	0.39 E – 2	1.64868	0.32 E – 4	1.64872	0.10 E – 6	1.64872	0.19 E – 9
0.5	1.0	4.07742	3.87731	0.20010	4.06928	0.81 E – 2	4.07726	0.16 E – 3	4.07742	0.20 E – 5
1.0	0.0	1.00000	1.00000	0.00000	1.00000	0.00000	1.00000	0.00000	1.00000	0.00000
1.0	0.5	2.47308	2.3804	0.92 E – 1	2.46909	0.39 E – 2	2.47299	0.82 E – 4	2.47308	0.10 E – 5
1.0	1.0	5.43656	4.80247	0.63409	5.37788	0.58 E – 1	5.43377	0.27 E – 2	5.43648	0.79 E – 4
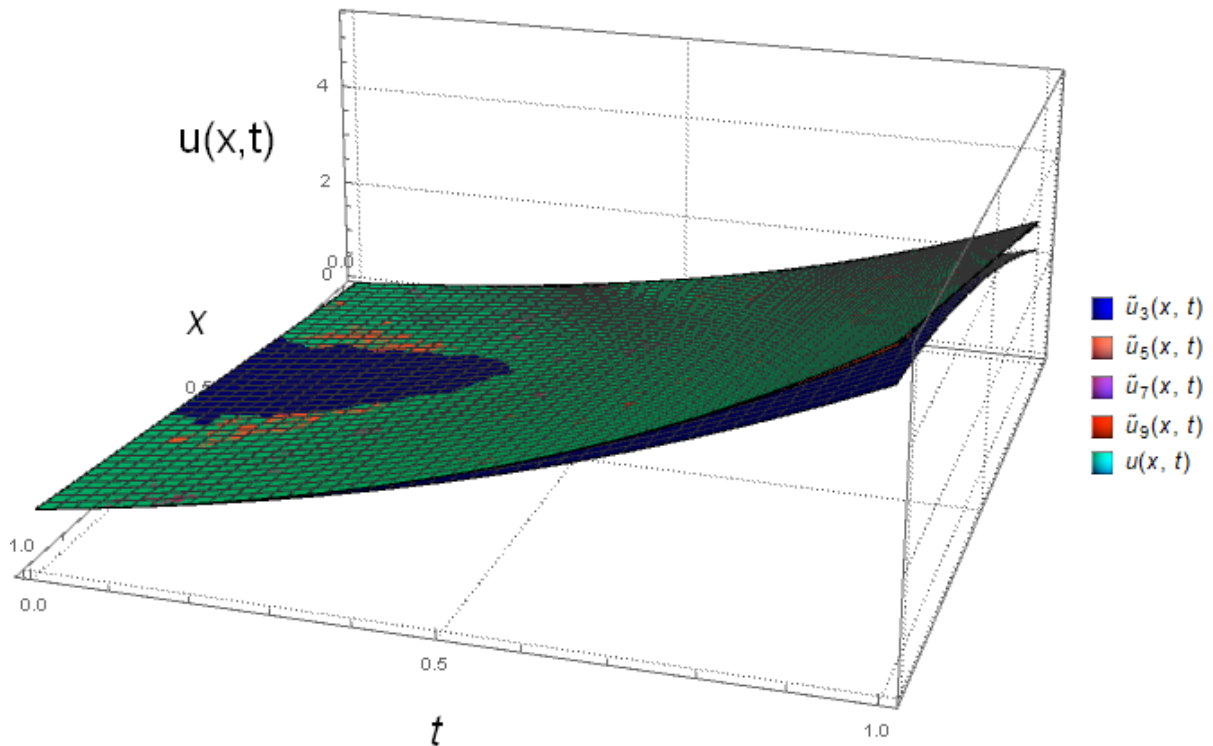
Figure 1. Exact solution and approximate solution for $N = 3,5,7,9$ in Example 2.

Error functions for $x = 0$ Error functions for $t = 0$
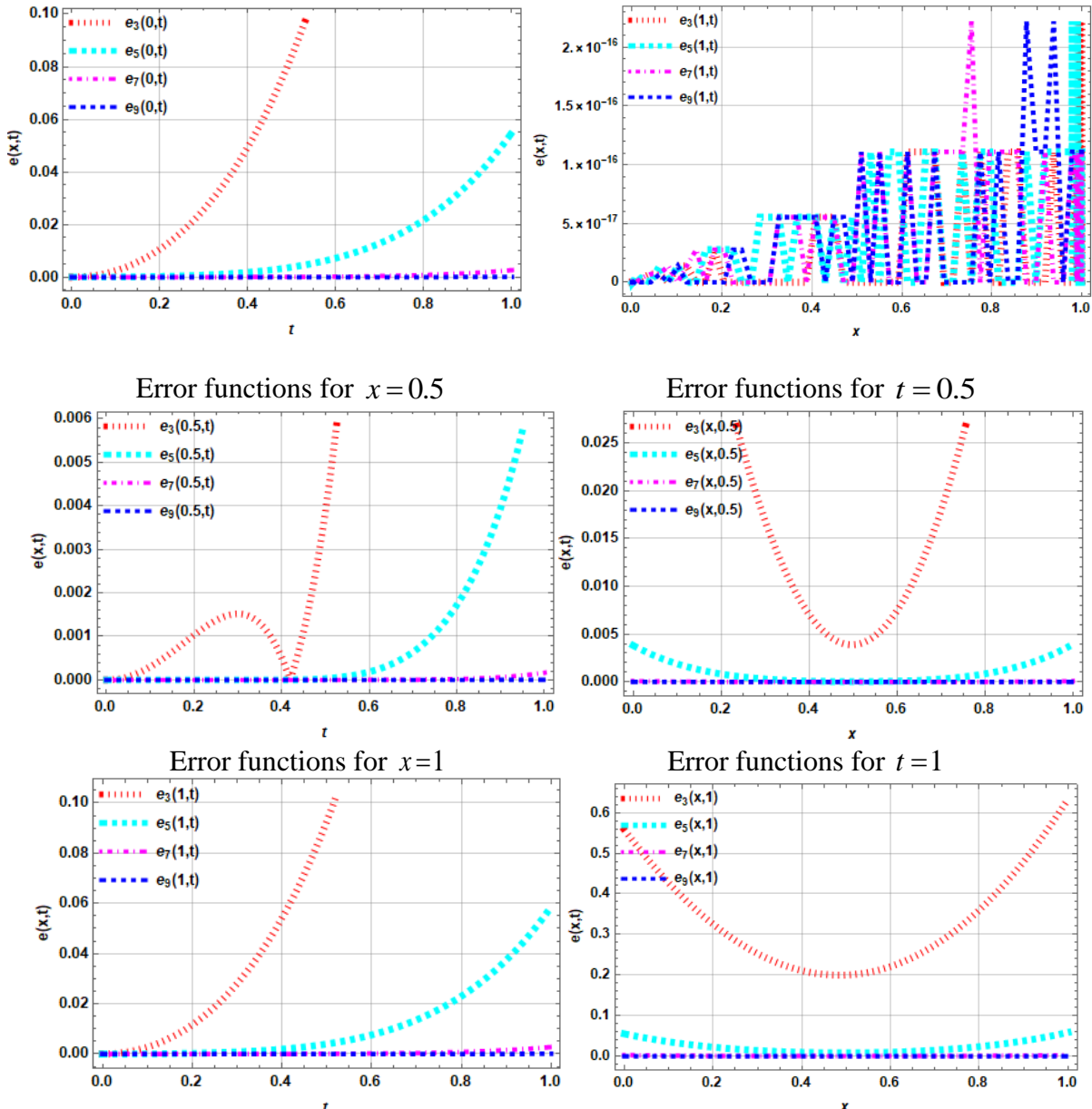
Figure 2. Error functions for $N = 3, 5, 7, 9$ in Example 2

5. CONCLUSION

The purpose of our paper is to provide an approximate solution of Cauchy Problem for partial differential equations. To this aim, we transformed the Pell polynomials from algebraic form to matrix form. After that, we found an approximate solution using fundamental matrix relations. We applied the method to two numerical examples in order to show its usefulness of this method. The numerical results show that the method proves well and the accuracy improves when N is increased.

REFERENCES

[1] P.D. Lax, On Cauchy's problem for hyperbolic equations and the differentiability of solutions of elliptic equations. Communications on Pure and Applied Mathematics, 8 (1955) 615-633.

[2] H.O. Fattorini, Encyclopedia of Mathematics and its Applications: The Cauchy Problem. Cambridge University Press, UK, 1983.

[3] J.D. Logan, Applied Partial Differential Equations. Springer International Publishing. 2015.

[4] S. J. Farlow, Partial Differential Equations for Scientists and Engineers. Dover Publications, New York, 1993.

[5] B. Goodwine, Engineering Differential Equations: Theory and applications. Springer, 2011.

[6] G. B. Djordjevic, G.V. Milovanovic, Special Cases of Polynomials. University of Nis, Faculty of Technology, Leskovac, 2014.

[7] T. Koshy, Pell and Pell-Lucas Numbers with Applications. Springer, New York, 2014.

[8] M.M. Bahşı, M. Çevik, M. Sezer, Orthoexponential polynomial solutions of delay pantograph differential equations with residual error estimation, Applied Mathematics and Computation 271 (2015) 11-21.

[9] M.M. Bahşı, M. Çevik, M. Sezer, A numerical solution of parabolic-type Volterra partial integro-differential equations by Laguerre collocation method, New Trends in Mathematical Sciences 6 (2018) 24-38.

[10] G. Yüksel, M. Sezer, A Chebyshev series approximation for linear second-order partial differential equations with complicated conditions, Gazi University Journal of Science 26 (2013) 515-525.

Müntz-Legendre Polynomial Solutions of a Class of Delay Differential Equations having First Order Nonlinear Terms

Burcu Kalfaoğlu*, Derya Doğan Durgun, Mehmet Sezer
Manisa Celal Bayar University, Department of Mathematics, Manisa, Turkey
*Corresponding author: burcukalfaoglu35@hotmail.com

Abstract

In recent years, there exists an increasing interest on models to delay and nonlinear- type functional differential equations in many scientific areas such as biology, physics and engineering. Furthermore, the approximation methods for these problems have been developed by many authors. In this study, we consider a class of high order delay functional differential equations with variable coefficients containing first order nonlinear terms; then we develop a novel matrix-collocation method based on Müntz-Legendre polynomials to find the approximate solutions of these type equations subject to appropriate mixed conditions. The method reduces the solution of the mentioned equations to the solution of a matrix equation which corresponds to system of algebraic equations with unknown Müntz-Legendre coefficients. Besides, two numerical examples are performed to illustrate the efficiency of our method.

Keywords: Müntz-Legendre polynomials, delay functional differential equations, matrix and collocation method, nonlinear differential equation
Discipline: Mathematics

1. INTRODUCTION

Nonlinear delay differential equations and the related initial and boundary value problems play an important role in astrophysics, physics and engineering. In recent years, in order to solve these type problems arising in various branches of applied sciences, several numerical and analytical methods have been given. But it may not be possible to find the analytical solutions of such problems for all coefficient functions [1-3]. Therefore it is necessary to obtain their approximate solutions by using some numerical methods [4,6].

In this study, we consider the high-order delay nonlinear ordinary differential equation with variable coefficients

$$\sum_{k=0}^{m} P_k(x) y^{(k)}(\alpha x + \beta) + \sum_{p=0}^{1}\sum_{q=0}^{p} Q_{pq}(x) y^{(p)}(x) y^{(q)}(x) = S(x), \ 0 \le x \le 1 \tag{1}$$

with the mixed conditions

$$\sum_{k=0}^{m-1} (a_{kj} y^{(k)}(0) + b_{kj} y^{(k)}(1)) = \lambda_j, \ j = 0,1,\ldots,\text{m-1} \tag{2}$$

where $P_k(x)$, $Q_{pq}(x)$ and $S(x)$ are functions defined on the $0 \le x \le 1$; a_{kj}, b_{kj} and λ_j are appropriate real constants; $y(x)$ is an unknown function to be determined. For our purpose, we assume the approximate solution of the problem (1) (2) in the truncated Müntz-Legendre series form

$$y(x) \cong y_N(x) = \sum_{n=0}^{N} a_n L_n(x), \ 0 \le x \le 1 \tag{3}$$

where $L_n(x)$ denotes the Müntz-Legedre polynomials defined by [7-9]

$$L_n(x) = \sum_{j=n}^{N} (-1)^{N-j} \binom{N+1+j}{N-n}\binom{N-n}{N-j} x^j, \ 0 \le x \le 1 \tag{4}$$

and $a_n, (n = 0,1,...,N)$ are unknown Müntz-Legendre polynomial coefficients, and N is chosen as any positive integer such that $N \ge m$.

2. FUNDAMENTAL MATRIX RELATIONS AND METHOD

We now constitute the matrix forms of each term in Eq. (1). Firstly, we can write the solution $y_N(x)$ defined by truncated Müntz-Legendre series (3) in the matrix and its derivatives in the following matrix form [4, 5, 8, 9]:

$$\left[y(x)\right] = \mathbf{L}(x)\mathbf{A} = \mathbf{X(x)FA}, \qquad \left[y^{(k)}(x)\right] = \mathbf{L}^{(k)}(x)\mathbf{A} = \mathbf{X(x)B}^k FA,$$

$$\left[y^{(k)}(x)\right] = \mathbf{X}(\alpha x + \beta)\mathbf{B}^k FA = X(x)B(\alpha,\beta)\mathbf{B}^k FA; \tag{5}$$

where

$$\mathbf{L}(x) = \left[L_0(x)\; L_1(x)\; ...\; L_N(x)\right], \quad \mathbf{A} = \left[a_0\; a_1\; ...\; a_N\right]^T, \quad \mathbf{X}(x) = \left[1\; x\; ...\; x^N\right],$$

$$\mathbf{F}^T = \begin{bmatrix} (-1)^N\binom{N+1}{N} & (-1)^{N-1}\binom{N+2}{N}\binom{N}{N-1} & (-1)^{N-2}\binom{N+3}{N}\binom{N}{N-2} & \cdots & (-1)^1\binom{2N}{N}\binom{N}{1} & (-1)^0\binom{2N+1}{N} \\ 0 & (-1)^{N-1}\binom{N+2}{N-1} & (-1)^{N-2}\binom{N+3}{N-1}\binom{N-1}{N-2} & \cdots & (-1)^1\binom{2N}{N-1}\binom{N-1}{1} & (-1)^0\binom{2N+1}{N-1} \\ 0 & 0 & (-1)^{N-2}\binom{N+3}{N-2} & \cdots & (-1)^1\binom{2N}{N-2}\binom{N-2}{1} & (-1)^0\binom{2N+1}{N-2} \\ 0 & 0 & 0 & \ddots & \vdots & \vdots \\ \vdots & \vdots & \vdots & \cdots & (-1)^1\binom{2N}{1} & (-1)^0\binom{2N+1}{1} \\ 0 & 0 & 0 & \cdots & 0 & (-1)^0\binom{2N+1}{0} \end{bmatrix},$$

$$\mathbf{B} = \begin{bmatrix} 0 & 1 & 0 & \cdots & 0 \\ 0 & 0 & 2 & \cdots & 0 \\ \vdots & \vdots & \vdots & \ddots & \vdots \\ 0 & 0 & 0 & \cdots & N \\ 0 & 0 & 0 & \cdots & 0 \end{bmatrix}, B(\alpha,\beta) = \begin{bmatrix} \binom{0}{0}\alpha^0\beta^0 & \binom{1}{0}\alpha^0\beta^1 & \binom{2}{0}\alpha^0\beta^2 & \cdots & \binom{N}{0}\alpha^0\beta^N \\ 0 & \binom{1}{1}\alpha^1\beta^0 & \binom{2}{1}\alpha^1\beta^1 & \cdots & \binom{N}{1}\alpha^1\beta^{N-1} \\ 0 & 0 & \binom{2}{2}\alpha^2\beta^0 & \cdots & \binom{N}{2}\alpha^2\beta^{N-2} \\ \vdots & \vdots & \vdots & \ddots & \vdots \\ 0 & 0 & 0 & \cdots & \binom{N}{N}\alpha^N\beta^0 \end{bmatrix}.$$

On the other hand, the matrix form of the expression $y^{(p)}(x)y^{(q)}(x)$, by using the matrix relations (5), is obtained as follows; for p,q=0,1

$$y^{(p)}(x)y^{(q)}(x) = \mathbf{X(x)B}^p F\overline{\mathbf{X(x)B}^q F}\,\overline{A} \tag{6}$$

where

$$\overline{X(x)} = diag[\mathbf{X(x),X(x),...,X(x)}], \overline{\mathbf{B}^q} = diag[B^q, B^q,...,B^q]$$

$$\overline{F} = diag[\mathrm{F,F,...,F}], \overline{A} = [a_0 A, a_1 A,...,a_n A]^T, B^0 : \text{unit matrix.}$$

By substituting the matrix relations (5) and (6) into Eq.(1) and then, by using the collocation points defined by $x_i = \dfrac{1}{N}i$, $i = 0,1,...,N$, we obtain the system of matrix equations

$$\sum_{k=0}^{m} P_k(x_i) X(x_i) B(\alpha,\beta) B^k F A + \sum_{p=0}^{1} \sum_{q=0}^{p} Q_{pq}(x_i) X(x_i) B^p F \overline{X(x_i) B^q F} \overline{A} = S(x_i),$$

or briefly, the corresponding fundamental matrix equation

$$\sum_{k=0}^{m} \mathbf{P_k} \mathbf{X} \mathbf{B}(\alpha,\beta) \mathbf{B^k} \mathbf{F} \mathbf{A} + \sum_{p=0}^{1} \sum_{q=0}^{p} \mathbf{Q_{pq}} \mathbf{L_{pq}} \overline{\mathbf{A}} = \mathbf{S} \Leftrightarrow \mathbf{W} \mathbf{A} + \mathbf{V} \overline{\mathbf{A}} = \mathbf{S} \Leftrightarrow [\mathbf{W}; \mathbf{V} : \mathbf{S}] \qquad (7)$$

or more clearly
$$\left[\mathbf{W};\mathbf{V}:\mathbf{G}\right] = \begin{bmatrix} w_{00} & w_{01} & \dots & w_{0N} & ; & v_{00} & v_{01} & \dots & v_{0,(N+)^2} & : & S(x_0) \\ w_{10} & w_{11} & \dots & w_{1N} & ; & v_{10} & v_{11} & \dots & v_{1,(N+1)^2} & : & S(x_1) \\ w & & & & & & & & & & \\ \dots & \dots & \dots & \dots & ; & \dots & \dots & \dots & \dots & : & \dots \\ w_{N0} & w_{N1} & \dots & w_{NN} & ; & v_{N0} & v_{N1} & \dots & v_{N,(N+1)^2} & : & S(x_N) \end{bmatrix}$$

where

$$\mathbf{W} = \sum_{k=0}^{2} \mathbf{P_k} \mathbf{X} \mathbf{B}(\alpha,\beta) \mathbf{B^k} \mathbf{F} = [w_{ij}], \mathbf{V} = \sum_{p=0}^{2} \sum_{q=0}^{p} \mathbf{Q_{pq}} \mathbf{L}_{pq} = [v_{ij}]_{(N+1)\times(N+1)^2}; \ i=0,1,\dots,N; \ j=0,1,\dots,(N+1)^2$$

$$\mathbf{X} = \begin{bmatrix} \mathbf{X}(x_0) \\ \mathbf{X}(x_1) \\ \vdots \\ \mathbf{X}(x_N) \end{bmatrix} = \begin{bmatrix} 1 & x_0 & x_0^2 & \cdots & x_0^N \\ 1 & x_1 & x_1^2 & \cdots & x_1^N \\ \vdots & \vdots & \vdots & \cdots & \vdots \\ 1 & x_N & x_N^2 & \cdots & x_N^N \end{bmatrix}, \mathbf{P}_k = \begin{bmatrix} P_k(x_0) & 0 & 0 & 0 \\ 0 & P_k(x_1) & 0 & 0 \\ \vdots & \vdots & \ddots & \vdots \\ 0 & 0 & 0 & P_k(x_N) \end{bmatrix}, \mathbf{S} = \begin{bmatrix} S(x_0) \\ S(x_1) \\ \vdots \\ S(x_N) \end{bmatrix}$$

$$\boldsymbol{Q}_{pq} = \begin{bmatrix} Q_{pq}(x_0) & 0 & 0 & 0 \\ 0 & Q_{pq}(x_1) & 0 & 0 \\ \vdots & \vdots & \ddots & \vdots \\ 0 & 0 & 0 & Q_{pq}(x_N) \end{bmatrix}, \quad \boldsymbol{L}_{pq} = \begin{bmatrix} y^{(p)}(x_0) y^{(q)}(x_0) \\ y^{(p)}(x_1) y^{(q)}(x_1) \\ \vdots \\ y^{(p)}(x_N) y^{(q)}(x_N) \end{bmatrix} = \begin{bmatrix} \mathbf{X}(x_0) \mathbf{B}^p F \overline{\mathbf{X}(x_0) \mathbf{B}^q F} \\ \mathbf{X}(x_1) \mathbf{B}^p F \overline{\mathbf{X}(x_1) \mathbf{B}^q F} \\ \vdots \\ \mathbf{X}(x_N) \mathbf{B}^p F \overline{\mathbf{X}(x_N) \mathbf{B}^q F} \end{bmatrix}.$$

Using the matrix relation (5), the fundamental matrix equation corresponding to the mixed conditions (2) is obtained as

$$\sum_{k=0}^{m-1} (a_{kj} \mathbf{X}(0) \mathbf{B}^k F + b_{kj} \mathbf{X}(1) \mathbf{B}^k F) A = \lambda_j, \ j = 0,1,\dots,m-1 \Leftrightarrow \mathbf{U} A + \mathbf{O}^* \overline{A} = \lambda \Leftrightarrow \left[\mathbf{U}; \mathbf{O}^* : \lambda\right] \qquad (8)$$

or clearly

$$\left[\mathbf{U}; \mathbf{O}^* : \lambda\right] = \begin{bmatrix} u_{00} & u_{01} & \dots & u_{0N} & ; & 0 & 0 & \dots & 0 & : & \lambda_0 \\ u_{10} & u_{11} & \dots & u_{1N} & ; & 0 & 0 & \dots & 0 & : & \lambda_1 \\ \dots & \dots & \dots & \dots & ; & \dots & \dots & \dots & \dots & : & \dots \\ u_{N0} & u_{N1} & \dots & u_{NN} & ; & 0 & 0 & \dots & 0 & : & \lambda_{m-1} \end{bmatrix}.$$

To calculate the coefficients $a_n \ (n=0,1,\dots,N)$ related to the approximate solution (3) of the problem (1)-(2), by replacing the m row matrices (8) by the last m rows (or any m rows) of the augmented matrix (7), we obtain the new augmented matrix as follows;

$$[\tilde{\mathbf{W}};\tilde{\mathbf{v}}:\tilde{\mathbf{G}}]=\begin{bmatrix} w_{00} & W_{01} & \cdots & W_{0N} & ; & v_{00} & V_{01} & \cdots & V_{0,(N+1)^2} & : & S(x_0) \\ w_{10} & W_{11} & \cdots & W_{1N} & ; & V_{10} & V_{11} & \cdots & V_{1,(N+1)^2} & : & S(x_1) \\ \cdots & \cdots & \cdots & \cdots & ; & \cdots & \cdots & \cdots & \cdots & : & \cdots \\ W_{N-m,0} & W_{N-m,1} & \cdots & W_{N-m,N} & ; & V_{N-m,0} & V_{N-m,1} & \cdots & V_{N-m,(N+1)^2} & : & S(x_{N-m}) \\ u_{00} & U_{01} & \cdots & U_{0N} & ; & 0 & 0 & \cdots & 0 & : & \lambda_0 \\ U_{10} & U_{11} & \cdots & U_{1N} & ; & 0 & 0 & \cdots & 0 & : & \lambda_1 \\ \cdots & \cdots & \cdots & \cdots & ; & \cdots & \cdots & \cdots & \cdots & : & \cdots \\ U_{m-1,0} & U_{m-1,1} & \cdots & U_{m-1,N} & ; & 0 & 0 & \cdots & 0 & : & \lambda_{m-1} \end{bmatrix} \qquad (9)$$

From the nonlinear algebraic system (9), that is, from the matrix equation $\tilde{\mathbf{W}}\mathbf{A} + \tilde{\mathbf{v}}\overline{A} = \tilde{\mathbf{G}}$, the unknown Müntz-Legendre coefficients a_n $(n = 0,1,...,N)$ are determined. Thus, the truncated Müntz-Legendre series solution (3) is obtained.

3. NUMERICAL EXAMPLES AND CONCLUSIONS

Example 1. Consider the second order nonlinear differential equation

$$y''(x) - 2xy'(x) + 4y(x) + y'(x)y(x) = 2x^3 - 2x - 2, \ 0 \le x \le 1,$$

subject to the boundary conditions $y(0) = -1$ and y(1)=0. The exact solution of this problem is $y(x) = x^2 - 1$.

Here the known expressions are

$$P_0(x) = 4, \ P_1(x) = -2x, \ P_2(x) = 1, \ Q_{10}(x) = 1, \ S(x) = 2x^3 - 2x - 2, \ \alpha = 1, \ \beta = 0.$$

The set of collocation points is obtained as $\{x_o = 0, \ x_1 = \frac{1}{2}, \ x_2 = 1\}$ for N=2. Then, by using the procedure in Section 2, the fundamental augmented matrix equations of this problem can be written as

$$\mathbf{WA} + \mathbf{V}\overline{\mathbf{A}} = \mathbf{S} \Leftrightarrow$$

$$[\mathbf{W};\mathbf{V}:\mathbf{S}] = \begin{bmatrix} 32 & 10 & 2 & ; & -36 & 0 & 0 & -12 & 0 & 0 & 0 & 0 & 0 & ; & -2 \\ 16 & 8 & 4 & ; & 1 & 3/2 & -1/2 & -1/2 & -3/4 & 1/4 & -1/2 & -3/4 & -1/2 & ; & -11/4 \\ 40 & 26 & 10 & ; & 8 & 8 & 8 & 6 & 6 & 6 & 2 & 2 & 2 & ; & -2 \end{bmatrix}$$

and

$$\mathbf{UA} + \mathbf{O}^*\overline{\mathbf{A}} = \lambda \Leftrightarrow [\mathbf{U};\mathbf{O}^*:\lambda] = \begin{bmatrix} 3 & 0 & 0 & ; & 0 & 0 & 0 & 0 & 0 & 0 & 0 & 0 & 0 & ; & -1 \\ 1 & 1 & 1 & ; & 0 & 0 & 0 & 0 & 0 & 0 & 0 & 0 & 0 & ; & 0 \end{bmatrix}.$$

Consequently, the desired augmented matrix from Eq.(9) becomes

$$\tilde{\mathbf{W}}\mathbf{A} + \tilde{\mathbf{v}}\overline{A} = \tilde{\mathbf{G}} \Leftrightarrow [\tilde{\mathbf{W}};\tilde{\mathbf{v}}:\tilde{\mathbf{G}}] = \begin{bmatrix} 32 & 10 & 2 & ; & -36 & 0 & 0 & -12 & 0 & 0 & 0 & 0 & ; & -2 \\ 3 & 0 & 0 & ; & 0 & 0 & 0 & 0 & 0 & 0 & 0 & 0 & ; & -1 \\ 1 & 1 & 1 & ; & 0 & 0 & 0 & 0 & 0 & 0 & 0 & 0 & ; & 0 \end{bmatrix};$$

from the solution of this nonlinear algebraic system, the Müntz-Legendre coefficients are obtained as $\{a_0 = -1/3, \ a_1 = -1, \ a_2 = -2/3\}$ and thereby, the approximate solution of the problem is determined as

$$y(x) = -1/3 L_o(x) + L_1(x) - 2/3 L_2(x)$$
$$= x^2 - 1$$

which is the exact solution.

Example 2. We now consider the first order delay nonlinear differential equation

$$y'(x) - 2y\left(\frac{1}{2}x - 1\right) + y^2(x) = x^2 + x + 2, \ 0 \le x \le 1$$

with the initial condition y(0)=1.

The exact solution of this problem is $y(x) = x + 1$. The known expressions are $P_0(x) = -2, \ P_1(x) = 1, \ Q_{00}(x) = 1, \ S(x) = x^2 + x + 2, \ \alpha = 1/2, \ \beta = -1$. We seek the approximate solution with truncated Müntz-Legendre series for N=2:

$$y(x) = \sum_{n=0}^{2} a_n L_n(x), \ 0 \le x \le 1.$$

The set of collocation points is obtained as $\{x_o = 0, \ x_1 = \frac{1}{2}, \ x_2 = 1\}$ for N=2. Then, by using the procedure in Section 2, the fundamental augmented matrix equations of this problem can be written as

$$\mathbf{WA} + \mathbf{V}\overline{\mathbf{A}} = \mathbf{S} \Leftrightarrow$$

$$[\mathbf{W}; \mathbf{V} : \mathbf{S}] = \begin{bmatrix} -62 & -22 & -2; & 9 & 0 & 0 & 0 & 0 & 0 & 0 & 0 & 0; & 2 \\ -\dfrac{149}{4} & -\dfrac{85}{4} & -\dfrac{1}{8}; & 1/4 & 3/8 & -1/8 & 3/8 & 9/16 & -3/16 & -1/8 & -1/16 & 1/16; & 11/4 \\ -15 & -1/2 & 3/2; & -2 & 1 & 1 & -2 & 1 & 1 & -2 & 1 & 1; & 4 \end{bmatrix}$$

and

$$\mathbf{UA} + \mathbf{O}^*\overline{\mathbf{A}} = \lambda \Leftrightarrow [[\mathbf{U}; \mathbf{O}^* : \lambda]] = [3 \ \ 0 \ \ 0; \ \ 0 \ \ 0 \ \ 0 \ \ 0 \ \ 0 \ \ 0 \ \ 0 \ \ 0 \ \ 0; \ \ 1];$$

thereby, the desired augmented matrix from Eq.(9) becomes

$$\tilde{\mathbf{W}}\mathbf{A} + \tilde{\mathbf{V}}\overline{\mathbf{A}} = \tilde{\mathbf{G}} \Leftrightarrow [\tilde{\mathbf{W}}; \tilde{\mathbf{V}} : \tilde{\mathbf{G}}] = \begin{bmatrix} -62 & -22 & -2; & 9 & 0 & 0 & 0 & 0 & 0 & 0 & 0 & 0; & 2 \\ 3 & 0 & 0; & 0 & 0 & 0 & 0 & 0 & 0 & 0 & 0 & 0; & 1 \\ -15 & -1/2 & 3/2; & -2 & 1 & 1 & -2 & 1 & 1 & -2 & 1 & 1; & 4 \end{bmatrix}.$$

Thus, from the solution of this nonlinear system, the Müntz-Legendre coefficients are obtained as $\{a_0 = 1/3, \ a_1 = -5/4, \ a_2 = 35/12\}$ and thereby, the approximate solution of the problem is determined as

$$y(x) = 1/3 L_o(x) - 5/4 L_1(x) + 35/12 L_2(x)$$
$$= x + 1$$

which is the exact solution.

Consequently, we have presented the Müntz-Legendre Matrix-Collocation method for solving a class of nonlinear delay ordinary differential equations. The method has been applied to two examples having exact solution. Thereby, it is seen from the obtained results that the method can be used to solve such equations.

REFERENCES
[1] I. Fried, Numerical Solution of Differential Equations, Academic Press, New York, 1979.
[2] D. W. Jordan, P. Smith, Nonlinear Ordinary Differential Equations: An introduction for Scientists and Engineers, 4th Edition. Oxford University Press, New York, 2007.

[3] M. Gülsu, M. Sezer, On the solutions of the Riccati equation by the Taylor matrix method, J. Appl. Math. 27 (1996) 821-834.

[4] N. Baykuş Savaşaneril, M. Sezer, Hybrid Taylor-Lucas collocation method for numerical solution of high-order pantograph type delay differential equations with variables delays, Appl. Math. Inf. Sci. 11 (2017) 1795-1801.

[5] B. Gürbüz, M. Sezer, Laguerre polynomial approach for solving Lane–Emden type functional differential equations, Appl. Math. Comput. 242 (2014) 255-264.

[6] G. Yüksel, M. Gülsu, M. Sezer, Chebyshev polynomial solutions of a class of second-order nonlinear ordinary differential equations, Journal of Advanced Research in Scientific Computing 3 (2011) 11-24.

[7] Q. Wu, A new exceptional polynomial for the integer transfinite diameter of [0,1], Journal de Théorie des Nombres de Bordeaux 15 (2003) 847-861.

[8] Ş. Yüzbaşı, E. Gök, M. Sezer, A numerical method for solving systems of higher-order linear functional differential equations, Open Physics 14 (2016) 15–25.

[9] Ş. Yüzbaşı, E. Gök, M. Sezer, Müntz-Legendre matrix method to solve the delay Fredholm integro-differential equations with constant coefficients, New Trends in Mathematical Sciences 3 (2015) 159-167.

A Numerical Approach Based on Abel Polynomials for Solving Nonlinear Duffing Differential Equations

İbrahim Güleç*, Manisa Celal Bayar University, Department of Mathematics, Manisa, Turkey
Mehmet Sezer, Manisa Celal Bayar University, Department of Mathematics, Manisa, Turkey
Nurcan Baykuş Savaşaneril, Dokuz Eylül University, İzmir Vocational School, İzmir, Turkey
*Corresponding author: ibogulec310@gmail.com

Abstract

In this study, we present a novel efficient numerical procedure for the approximate solution of second order nonlinear Duffing differential equations in terms of Abel polynomials. This technique is a matrix method based on collocation points along with the truncated Abel series, and reduces the solution of nonlinear differential equation to the solution of a matrix equation which corresponds to system of nonlinear algebraic equations with unknown coefficients. The approximate solutions subject to initial conditions are obtained in terms of Abel polynomials. Besides, two examples are given to demonstrate validity and the applicability of the method and the obtained results are discussed.

Keywords: Abel polynomials, matrix and collocation methods, Duffing equation, nonlinear differential equations
Discipline: Mathematics

1. INTRODUCTION

Nonlinear Duffing differential equations arise in the study of the nonlinear problems and the related initial and boundary value problems play an important role in various scientific fields such as physics, astrophysics, engineering, biology and communication theory [1-7]. In recent years, to solve these problems both analytically and numerically, several numerical and analytical methods have been given [3-9]. But it may not be possible to find the analytical solutions of such problems having variable coefficients. So, in this study, we consider the Duffing differential equation, one of the most fundamental equations in the study of the nonlinear problems, defined by

$$\sum_{k=0}^{2} P_k(x) y^{(k)}(x) + Q(x) y^3(x) = f(x), \ a \le x \le b \tag{1}$$

with the initial conditions

$$\sum_{k=0}^{1} a_{kj} y^{(k)}(a) = \lambda_j, \ j = 0,1 \tag{2}$$

where $P_k(x)$, $Q(x)$ and $f(x)$ are functions defined on the interval $a \le x \le b$; a_{kj} and λ_j are appropriate real constants; $y(x)$ is an unknown function to be determined. For our purpose, we assume the approximate solution of the problem (1) (2) in the truncated Abel series form

$$y(x) \cong y_N(x) = \sum_{n=0}^{N} b_n A_n(x, \alpha), \ a \le x \le b \tag{3}$$

where $A_n(x, \alpha)$ denotes the Abel polynomials defined by

$$A_n(x, \alpha) = \sum_{k=0}^{n-1} \binom{n-1}{k} (-n\alpha)^{n-k-1} x^{k+1}, \ A_0(x, \alpha) = 1, \ n = 1, ..., N \tag{4}$$

and $a_n, (n = 0,1, ..., N)$ are unknown Abel polynomial coefficients, α is a real parameter, N is chosen as any positive integer such that $N \ge m$. The Abel polynomial sequence form a polynomial sequence, the nth term of which is of the form (4), is named after Niels Henrik Abel (1802-1829), the Norwegian mathematician; it is of binomial type: conversely, every polynomial sequence of binomial type may be obtained from the Abel sequence in the umbral calculus [10, 11].

2. FUNDAMENTAL MATRIX RELATIONS AND METHOD

In this section we convert the expressions defined in (1) and (2) to the matrix forms by the following procedure: Firstly, the function y(x) defined by (3) and its derivatives can be written in the matrix form

$$y(x) \cong y_N(x) = A(x,\alpha)B = X(x)G(\alpha)B$$
$$y^{(k)}(x) \cong y_N^{(k)}(x) = A^{(\mathbf{k})}(x,\alpha)B = \mathbf{X}(\mathrm{x})\mathbf{C}^k G(\alpha)B, \, k = 0,1,2$$

(5)

where

$$A(x,\alpha) = \begin{bmatrix} A_0(x,\alpha) & A_1(x,\alpha) & A_2(x,\alpha) & \cdots & A_N(x,\alpha) \end{bmatrix}$$

$$B = \begin{bmatrix} b_0 & b_1 & b_2 & \cdots & b_N \end{bmatrix}^T \qquad X(x) = \begin{bmatrix} 1 & x & x^2 & \cdots & x^N \end{bmatrix}$$

$$G(\alpha) = \begin{bmatrix} 1 & 0 & 0 & 0 & \cdots & & 0 \\ 0 & 1 & -2\alpha & 9\alpha^2 & \cdots & (-N\alpha)^{N-1}\binom{N-1}{0} \\ 0 & 0 & 1 & 1 & \cdots & (-N\alpha)^{N-2}\binom{N-1}{1} \\ 0 & 0 & 0 & 0 & \cdots & & 0 \\ \vdots & \vdots & \vdots & \vdots & \ddots & & \vdots \\ 0 & 0 & 0 & 0 & 0 & (-N\alpha)^0\binom{N-1}{N-1} \end{bmatrix}, C = \begin{bmatrix} 0 & 1 & 0 & \cdots & 0 \\ 0 & 0 & 2 & \cdots & 0 \\ \vdots & \vdots & \vdots & \ddots & \vdots \\ 0 & 0 & 0 & \cdots & N \\ 0 & 0 & 0 & \cdots & 0 \end{bmatrix}.$$

In a similar way to the matrix equations (5), it follows that the matrix representation of $y^3(x)$ becomes [5, 6]

$$y^3(x) = A(x,\alpha)\bar{A}(x,\alpha)\bar{\bar{A}}(x,\alpha)\bar{\bar{B}}$$
$$= X(x)G(\alpha)\bar{X}(x)\bar{G}(\alpha)\bar{\bar{X}}(x)\bar{\bar{G}}(\alpha)\bar{\bar{B}}$$

(6)

where

$$\bar{X}(x) = \begin{bmatrix} X(x) & 0 & \cdots & 0 \\ 0 & X(x) & \cdots & 0 \\ \vdots & \vdots & \ddots & \vdots \\ 0 & 0 & \cdots & X(x) \end{bmatrix}_{(N+1)\times(n+1)^2} \qquad \bar{G}(\alpha) = \begin{bmatrix} G(\alpha) & 0 & \cdots & 0 \\ 0 & G(\alpha) & \cdots & 0 \\ \vdots & \vdots & \ddots & \vdots \\ 0 & 0 & \cdots & G(\alpha) \end{bmatrix}_{(N+1)^2\times(N+1)^2}$$

$$\bar{\bar{X}} = \begin{bmatrix} \bar{X}(x) & 0 & \cdots & 0 \\ 0 & \bar{X}(x) & \cdots & 0 \\ \vdots & \vdots & \ddots & \vdots \\ 0 & 0 & \cdots & \bar{X}(x) \end{bmatrix}_{(N+1)^2\times(N+1)^3} \qquad \bar{\bar{G}}(\alpha) = \begin{bmatrix} \bar{G}(\alpha) & 0 & \cdots & 0 \\ 0 & \bar{G}(\alpha) & \cdots & 0 \\ \vdots & \vdots & \ddots & \vdots \\ 0 & 0 & \cdots & \bar{G}(\alpha) \end{bmatrix}_{(N+1)^3\times(N+1)^3}$$

116

2nd International Students Science Congress
4-5 May 2018, Izmir - Turkey

İZMİR
KÂTİP ÇELEBİ
UNIVERSITY
2010

İZMİR
Uluslararası
Misafir
Öğrenci
Derneği
◆ IZMIR International Guest Student Association

$$
B = \begin{bmatrix} b_0 \\ b_1 \\ \vdots \\ b_N \end{bmatrix}_{(N+1)\times 1} \qquad
\bar{B} = \begin{bmatrix} b_0 B \\ b_1 B \\ \vdots \\ b_N B \end{bmatrix}_{(N+1)^2 \times 1} \qquad
\bar{\bar{B}} = \begin{bmatrix} b_0 \bar{B} \\ b_1 \bar{B} \\ \vdots \\ b_N \bar{B} \end{bmatrix}_{(N+1)^3 \times 1}
$$

To obtain the Abel polynomial solution of Eq. (1) in the form (3), we firstly compute the Abel coefficients by means of the collocation points defined by

$$
x_i = a + \frac{b-a}{N} i, \qquad a \le x_i \le b, \qquad i = 0, 1, 2, ..., N \,.
$$

For this purpose, by substituting the collocation points into Eq. (1) and by using the matrix relations (5)-(6), we obtain the system of matrix equations

$$
\sum_{k=0}^{2} P_k(x_i) y^{(k)}(x_i) + Q(x_i) y^3(x_i) = f(x_i), \, i = 0, 1, ..., N
$$

and briefly, the matrix equation

$$
\sum_{k=0}^{2} P_k Y^{(k)} + Q Y^3 = F; \tag{7}
$$

where

$$
P_k = \begin{bmatrix} P_k(x_0) & 0 & 0 & \cdots & 0 \\ 0 & P_k(x_1) & 0 & \cdots & 0 \\ 0 & 0 & P_k(x_2) & \cdots & 0 \\ \vdots & \vdots & \vdots & \ddots & \vdots \\ 0 & 0 & 0 & 0 & P_k(x_N) \end{bmatrix} \qquad
Q = \begin{bmatrix} Q(x_0) & 0 & 0 & \cdots & 0 \\ 0 & Q(x_1) & 0 & \cdots & 0 \\ 0 & 0 & Q(x_2) & \cdots & 0 \\ \vdots & \vdots & \vdots & \ddots & \vdots \\ 0 & 0 & 0 & 0 & Q(x_N) \end{bmatrix}
$$

$$
Y^{(k)} = \begin{bmatrix} y^{(k)}(x_0) \\ y^{(k)}(x_1) \\ \vdots \\ y^{(k)}(x_N) \end{bmatrix} = XC^k G(\alpha) B, \qquad
X = \begin{bmatrix} X(x_0) \\ X(x_1) \\ \vdots \\ X(x_N) \end{bmatrix} = \begin{bmatrix} 1 & x_0 & \cdots & x_0^N \\ 1 & x_1 & \cdots & x_1^N \\ \vdots & \vdots & \ddots & \vdots \\ 1 & x_N & \cdots & x_N^N \end{bmatrix}, \qquad
F = \begin{bmatrix} f(x_0) \\ f(x_1) \\ \vdots \\ f(x_N) \end{bmatrix}
$$

$$
Y^3 = \begin{bmatrix} y^3(x_0) \\ y^3(x_1) \\ \vdots \\ y^3(x_N) \end{bmatrix} = \begin{bmatrix} X(x_0)G(\alpha)\bar{X}(x_0)\bar{G}(\alpha)\bar{\bar{X}}(x_0)\bar{\bar{G}}(\alpha) \\ X(x_1)G(\alpha)\bar{X}(x_1)\bar{G}(\alpha)\bar{\bar{X}}(x_1)\bar{\bar{G}}(\alpha) \\ \vdots \\ X(x_N)G(\alpha)\bar{X}(x_N)\bar{G}(\alpha)\bar{\bar{X}}(x_N)\bar{\bar{G}}(\alpha) \end{bmatrix} \bar{\bar{B}} = A^* \bar{\bar{B}} \,.
$$

Therefore, by means of the matrix relation (7) and its matrices in the fundamental matrix equation corresponding to Eq. (1) becomes as follows;

$$
\sum_{k=0}^{2} P_k X C^k G(\alpha) B + Q A^* \bar{\bar{B}} = F \Leftrightarrow WB + V\bar{\bar{B}} = F \Leftrightarrow [\mathbf{W}; \mathbf{V} : \mathbf{F}] \tag{8}
$$

and clearly

$$[\mathbf{W};\mathbf{V}:\mathbf{F}] = \begin{bmatrix} w_{0,0} & w_{0,1} & \cdots & w_{0,N} & ; & v_{0,0} & v_{0,1} & \cdots & v_{0,(n+1)^3} & : & f(x_0) \\ w_{1,0} & w_{1,1} & \cdots & w_{1,N} & ; & v_{1,0} & v_{1,1} & \cdots & v_{1,(N+1)^3} & : & f(x_1) \\ \vdots & \vdots & \ddots & \vdots & ; & \vdots & \vdots & \ddots & \vdots & : & \vdots \\ w_{N,0} & w_{N,1} & \cdots & w_{N,N} & ; & v_{N,0} & v_{N,1} & \cdots & v_{N,(N+1)^3} & : & F(x_N) \end{bmatrix}$$

Next, by means of relations (5), we can obtain the corresponding matrix forms for the initial conditions (2) as

$$\sum_{k=0}^{1} a_{kj} \mathbf{X(a)B}^k G(\alpha) = \lambda_j, \ j = 0,1 \Leftrightarrow \mathbf{UB} + \mathbf{O}^* \overline{\overline{B}} = \lambda \Leftrightarrow \left[\mathbf{U};\mathbf{O}^* : \lambda \right], \mathbf{B}^0 = diag[1,1,...,1] \tag{9}$$

or clearly

$$\left[\mathbf{U};\mathbf{0}^* : \lambda \right] = \begin{bmatrix} u_{00} & u_{01} & \cdots & u_{0N} & ; & 0 & 0 & \cdots & 0 & ; & \lambda_0 \\ u_{10} & u_{11} & \cdots & u_{1N} & ; & 0 & 0 & \cdots & 0 & ; & \lambda_1 \end{bmatrix}$$

Consequently, to obtain the solution of Eq.(1) under the conditions (2), by replacing the row matrices of (9) by the last two rows of the augmented matrix (8), we have the required augmented matrix as follows;

$$[\tilde{\mathbf{W}};\tilde{\mathbf{V}}:\tilde{\mathbf{G}}] = \begin{bmatrix} w_{00} & w_{01} & \cdots & w_{0N} & ; & v_{00} & v_{01} & \cdots & v_{0,(N+1)^3} & : & f(x_0) \\ w_{10} & w_{11} & \cdots & w_{1N} & ; & v_{10} & v_{11} & \cdots & v_{1,(N+1)^3} & : & f(x_1) \\ \vdots & \vdots & \vdots & \vdots & ; & \vdots & \vdots & \vdots & \vdots & : & \vdots \\ w_{N-2,0} & w_{N-2,1} & \cdots & w_{N-2,N} & ; & v_{N-2,0} & v_{N-2,1} & \cdots & v_{N-2,(N+1)^3} & : & f(x_{N-2}) \\ u_{00} & u_{01} & \cdots & u_{0N} & ; & 0 & 0 & \cdots & 0 & : & \lambda_0 \\ u_{10} & u_{11} & \cdots & u_{1N} & ; & 0 & 0 & \cdots & 0 & : & \lambda_1 \end{bmatrix},$$

$$\tag{10}$$

From the nonlinear algebraic system (10), that is, from the matrix equation $\tilde{W}B + \tilde{V}\overline{\overline{B}} = \tilde{F}$ the unknown Abel polynomial coefficients a_n $(n = 0,1,...,N)$ are determined. Thus, the truncated Abel series solution (3) is obtained. By solving the matrix Eq. (10), the unknown Abel coefficients b_n are determined. Thus, we get Abel polynomial solution

$$y_N(x) = \sum_{n=0}^{N} b_n A_n(x,\alpha) \ .$$

3. NUMERICAL EXAMPLES AND CONCLUSIONS

The method used in this study is useful in finding the solutions of Duffing equations in terms of Abel polynomials. We illustrate it by the following examples. Numerical computations have been done using Mathematica 9.

Example 1. Consider the Duffing equation in the following type

$$2y''(x) - y'(x) - y(x) + y^3(x) = e^{3x}, \ 0 \le x \le 1$$

with initial conditions $y(0) = 0$ and $y'(0) = 1$ having the exact solution $y(x) = x$.

Here, the known functions are defined as

$$P_0(x) = 1, \qquad P_1(x) = -x, \qquad P_2(x) = 1, \qquad Q(x) = 1, \qquad f(x) = x^3$$

Firstly, for $N=2$, we search the approximate solution in the form of the truncated Abel series

$$y(x) = \sum_{n=0}^{2} a_n A_n(x, \alpha).$$

Thereafter, we determine the collocation points as

$$\left\{ x_0 = 0, \qquad x_1 = \frac{1}{2}, \qquad x_2 = 1 \right\}$$

and by taking $\alpha = \frac{1}{2}$, , we obtain the matrix $G(1/2)$ as

$$G(\frac{1}{2}) = \begin{pmatrix} 1 & 0 & 0 \\ 0 & 1 & -1 \\ 0 & 0 & 1 \end{pmatrix}$$

Thus, by means of the collocation points and the developed method, the fundamental matrix equation of Eq. (1) is obtained as follows

$$\{ \mathbf{P_0 X C^0 G}(\frac{1}{2}) + \mathbf{P_1 X C G}(\frac{1}{2}) + \mathbf{P_2 X C^2 G}(\frac{1}{2}) \} \mathbf{B} + \mathbf{Q A^* \bar{\bar{B}}} = \mathbf{F}$$

where

$$\mathbf{P_0} = \mathbf{P_2} = \mathbf{C^0} = \mathbf{Q} = \begin{bmatrix} 1 & 0 & 0 \\ 0 & 1 & 0 \\ 0 & 0 & 1 \end{bmatrix}, \qquad \mathbf{P_2} = \begin{bmatrix} 0 & 0 & 0 \\ 0 & -\frac{1}{2} & 0 \\ 0 & 0 & -1 \end{bmatrix}, \qquad \mathbf{F} = \begin{bmatrix} 0 \\ \frac{1}{8} \\ 1 \end{bmatrix},$$

$$\mathbf{C^1} = \begin{bmatrix} 0 & 1 & 0 \\ 0 & 0 & 2 \\ 0 & 0 & 0 \end{bmatrix}, \qquad \mathbf{C^2} = \begin{bmatrix} 0 & 0 & 2 \\ 0 & 0 & 0 \\ 0 & 0 & 0 \end{bmatrix}, \qquad \mathbf{X} = \begin{bmatrix} X(0) \\ X(\frac{1}{2}) \\ X(1) \end{bmatrix} = \begin{bmatrix} 1 & 0 & 0 \\ 1 & \frac{1}{2} & \frac{1}{4} \\ 1 & 1 & 1 \end{bmatrix},$$

$$\bar{X} = \begin{bmatrix} 1 & 0 & 0 & 0 & 0 & 0 & 0 & 0 & 0 \\ 0 & 0 & 0 & 1 & \frac{1}{2} & \frac{1}{4} & 0 & 0 & 0 \\ 0 & 0 & 0 & 0 & 0 & 0 & 1 & 1 & 1 \end{bmatrix}.$$

Hence, the augmented matrix corresponding to this fundamental matrix equation becomes

$$[W;V:F] = \begin{bmatrix} 1 & 0 & 2 & ; & 1 & 0 & 0 & 0 & 0 & 0 & 0 & 0 & 0 & 0 & 0 & 0 & 0 & 0 & 0 & 0 & 0 & 0 & 0 & 0 & 0 & 0 & 0 & 0 & : & 0 \\ \frac{1}{2} & 0 & \frac{7}{4} & ; & 1 & -1 & 1 & -1 & 1 & -1 & |1 & -1 & 1 & -1 & 1 & -1 & 1 & -1 & 1 & -1 & 1 & -1 & 1 & -1 & 1 & -1 & 1 & : & \frac{1}{8} \\ 2 & 2 & 3 & ; & 1 & -6 & 4 & -6 & 36 & -24 & 4 & -24 & 16 & -6 & 36 & -216 & 144 & -24 & 144 & -96 & 4 & -24 & 16 & -24 & 144 & -96 & 16 & -96 & 64 & : & 1 \end{bmatrix}$$

Besides, we find the augmented matrix for the initial conditions in the forms

$$[U_0 ; 0 : l_0] = [1 \ 0 \ 0; 0 \ 0 \ 0 \ 0 \ 0 \ 0 \ 0 \ 0 \ 0 \ 0 \ 0 \ 0 \ 0 \ 0 \ 0 \ 0 \ 0 \ 0 \ 0 \ 0 \ 0 \ 0 \ 0 \ 0 \ 0 \ 0 \ 0 \ 0 : 0]$$

and

$$[U_1 ; 0 : l_1] = [0 \ 1 \ -1; 0 \ 0 \ 0 \ 0 \ 0 \ 0 \ 0 \ 0 \ 0 \ 0 \ 0 \ 0 \ 0 \ 0 \ 0 \ 0 \ 0 \ 0 \ 0 \ 0 \ 0 \ 0 \ 0 \ 0 \ 0 \ 0 \ 0 \ 0 : 1] .$$

These matrices are combined according to the rules of the method and the resultant matrix is the algebraic system as follows

$$\left[\tilde{W};\tilde{V}:\tilde{F}\right]=\begin{bmatrix} 1 & 0 & 2 & ; & 1 & 0 & 0 & 0 & 0 & 0 & 0 & 0 & 0 & 0 & 0 & 0 & 0 & 0 & 0 & 0 & 0 & 0 & 0 & 0 & 0 & 0 & 0 & 0 & 0 & 0 & 0 & : & 0 \\ 1 & 0 & 0 & ; & 0 & 0 & 0 & 0 & 0 & 0 & 0 & 0 & 0 & 0 & 0 & 0 & 0 & 0 & 0 & 0 & 0 & 0 & 0 & 0 & 0 & 0 & 0 & 0 & 0 & 0 & 0 & : & 0 \\ 0 & 1 & -1 & ; & 0 & 0 & 0 & 0 & 0 & 0 & 0 & 0 & 0 & 0 & 0 & 0 & 0 & 0 & 0 & 0 & 0 & 0 & 0 & 0 & 0 & 0 & 0 & 0 & 0 & 0 & 0 & : & 1 \end{bmatrix}$$

By solving this system, the matrix of unknown coefficients becomes $B = [0\ 1\ 0]^T$; thereby, the approximate solution is obtained as

$$y_2(x) = b_0 A_0\left(x, \frac{1}{2}\right) + b_1 A_1\left(x, \frac{1}{2}\right) + b_2 A_2\left(x, \frac{1}{2}\right) = A_1\left(x, \frac{1}{2}\right) \Rightarrow y_2(x) = x,$$

which is the exact solution.

Example 2. We consider the Duffing equation

$$2y''(x) - y'(x) - y(x) + y^3(x) = e^{3x}, \qquad 0 \le x \le 1$$

under the initial conditions $y(0) = 1$ and $y'(0) = 1$ with the exact solution $y(0) = e^x$.

Here, the functions $P_0(x) = -1$, $P_1(x) = -1$, $P_2(x) = 2$, $Q(x) = 1$, $f(x) = e^{3x}$ are the known functions. Firstly, for $N=2$, we search the approximate solution in the form of the truncated Abel series

$$y = \sum_{n=0}^{2} b_n A_n(x, \alpha).$$

Then, we determine the collocation points as

$$\left\{x_0 = 0 \quad x_1 = \frac{1}{2} \quad x_2 = 1\right\}$$

and by taking $\alpha = -\frac{1}{8}$, we get the matrix $G(-1/8)$ as

$$G\left(-\frac{1}{8}\right) = \begin{vmatrix} 1 & 0 & 0 \\ 0 & 1 & \frac{1}{4} \\ 0 & 0 & 1 \end{vmatrix}.$$

Thus, by means of the collocation points and the developed method, the fundamental matrix equation for Eq.(1) becomes

$$\{\mathbf{P_0 X C^0 G}(-\frac{1}{8}) + \mathbf{P_1 X C^1 G}(-\frac{1}{8}) + \mathbf{P_2 X C^2 G}(-\frac{1}{8})\}B + \mathbf{QA}^*\overline{\overline{\mathbf{B}}} = \mathbf{F}$$

where

$$P_0 = \begin{bmatrix} 1 & 0 & 0 \\ 0 & 1 & 0 \\ 0 & 0 & 1 \end{bmatrix} \quad P_1 = \begin{bmatrix} 1 & 0 & 0 \\ 0 & 1 & 0 \\ 0 & 0 & 1 \end{bmatrix}, \quad P_2 = \begin{bmatrix} 2 & 0 & 0 \\ 0 & 2 & 0 \\ 0 & 0 & 2 \end{bmatrix} \quad C^0 = \begin{bmatrix} 1 & 0 & 0 \\ 0 & 1 & 0 \\ 0 & 0 & 1 \end{bmatrix}, \quad C^1 = \begin{bmatrix} 0 & 1 & 0 \\ 0 & 0 & 2 \\ 0 & 0 & 0 \end{bmatrix},$$

$$C^2 = \begin{bmatrix} 0 & 0 & 2 \\ 0 & 0 & 0 \\ 0 & 0 & 0 \end{bmatrix}, \quad Q = \begin{bmatrix} 1 & 0 & 0 \\ 0 & 1 & 0 \\ 0 & 0 & 1 \end{bmatrix}, \quad X = \begin{bmatrix} X(0) \\ X(\frac{1}{2}) \\ X(1) \end{bmatrix} = \begin{bmatrix} 1 & 0 & 0 \\ 1 & \frac{1}{2} & \frac{1}{4} \\ 1 & 1 & 1 \end{bmatrix}, \quad F = \begin{bmatrix} 1 \\ e^{3/2} \\ e \end{bmatrix},$$

$$\bar{X} = \begin{bmatrix} 1 & 0 & 0 & 0 & 0 & 0 & 0 & 0 & 0 \\ 0 & 0 & 0 & 1 & \frac{1}{2} & \frac{1}{4} & 0 & 0 & 0 \\ 0 & 0 & 0 & 0 & 0 & 0 & 1 & 1 & 1 \end{bmatrix}.$$

Hence, the augmented matrix corresponding to this fundamental matrix equation becomes

$$[\mathbf{W;V:F}] = \left[\begin{array}{ccc|cccccccccccccccccccccccccccc|c} -1 & -1 & \frac{15}{4} & ; & 1 & 0 & 0 & 0 & 0 & 0 & 0 & 0 & 0 & 0 & 0 & 0 & 0 & 0 & 0 & 0 & 0 & 0 & 0 & 0 & 0 & 0 & 0 & 0 & 0 & : & 1 \\ -1 & -\frac{3}{2} & \frac{19}{8} & ; & 1 & \frac{1}{2} & \frac{3}{8} & \frac{1}{2} & \frac{1}{4} & \frac{3}{16} & \frac{3}{8} & \frac{3}{16} & \frac{9}{64} & \frac{1}{2} & \frac{1}{4} & \frac{3}{16} & \frac{1}{4} & \frac{1}{8} & \frac{3}{32} & \frac{3}{16} & \frac{3}{32} & \frac{9}{128} & \frac{3}{8} & \frac{3}{16} & \frac{9}{64} & \frac{3}{16} & \frac{3}{32} & \frac{9}{128} & : & 4.481 \\ -1 & -2 & \frac{1}{2} & ; & 1 & \frac{1}{2} & \frac{3}{16} & \frac{9}{64} & \frac{3}{8} & \frac{3}{16} & \frac{1}{2} & \frac{3}{16} & \frac{1}{4} & \frac{1}{8} & \frac{3}{32} & \frac{9}{128} & \frac{9}{64} & \frac{3}{32} & \frac{9}{64} & \frac{9}{128} & \frac{3}{16} & \frac{1}{4} & \frac{1}{8} & \frac{3}{8} & \frac{3}{32} & \frac{9}{64} & \frac{3}{4} & \frac{3}{16} & \frac{9}{512} & : & 20.085 \end{array} \right]$$

and the augmented matrices for the initial conditions $y(0) = 1$ and $y'(0) = 1$;

$$[\mathbf{U}_0;\mathbf{0}:l_0] = [1 \ 0 \ 0; 0 \ 0 \ 0 \ 0 \ 0 \ 0 \ 0 \ 0 \ 0 \ 0 \ 0 \ 0 \ 0 \ 0 \ 0 \ 0 \ 0 \ 0 \ 0 \ 0 \ 0 \ 0 \ 0 \ 0 \ 0 \ 0 \ 0 \ 0:1]$$

$$[\mathbf{U}_1;\mathbf{0}:l_1] = [0 \ 1 \ \frac{1}{4}; 0 \ 0 \ 0 \ 0 \ 0 \ 0 \ 0 \ 0 \ 0 \ 0 \ 0 \ 0 \ 0 \ 0 \ 0 \ 0 \ 0 \ 0 \ 0 \ 0 \ 0 \ 0 \ 0 \ 0 \ 0 \ 0 \ 0 \ 0 \ 0:1]$$

.

These matrices are combined according to the rules of the method and the resultant augmented matrix becomes

$$[\tilde{\mathbf{W}};\tilde{\mathbf{V}}:\tilde{\mathbf{F}}] = \left[\begin{array}{ccc|ccccccccccccccccccccccccccccc|c} -1 & -1 & \frac{15}{4} & ; & 1 & 0 & 0 & 0 & 0 & 0 & 0 & 0 & 0 & 0 & 0 & 0 & 0 & 0 & 0 & 0 & 0 & 0 & 0 & 0 & 0 & 0 & 0 & 0 & 0 & : & 1 \\ 1 & 0 & 0 & ; & 0 & 0 & 0 & 0 & 0 & 0 & 0 & 0 & 0 & 0 & 0 & 0 & 0 & 0 & 0 & 0 & 0 & 0 & 0 & 0 & 0 & 0 & 0 & 0 & 0 & : & 1 \\ 0 & 1 & \frac{1}{4} & ; & 0 & 0 & 0 & 0 & 0 & 0 & 0 & 0 & 0 & 0 & 0 & 0 & 0 & 0 & 0 & 0 & 0 & 0 & 0 & 0 & 0 & 0 & 0 & 0 & 0 & : & 1 \end{array} \right]$$

which is the nonlinear algebraic system. Matrix of unknown coefficients by solving this system in the form $\mathbf{B} = [1 \ 7/8 \ 1/2]^T$; therefore, the approximate solution of the given problem is obtained as follows;

$$y(x) = A_0(x, -\frac{1}{8}) + \frac{7}{8}A_1(x, -\frac{1}{8}) + \frac{1}{2}A_2(x, -\frac{1}{8}) = 1 + x + \frac{1}{2}x^2$$

which is the first three terms in the Maclaurin expansion of the exact solution $y(x) = e^x$.

Consequently, a very simple but effective Abel matrix method was proposed for the numerical solution of the nonlinear Duffing equation. One of the advantages of this method that is the solution is expressed as a truncated Abel series, then (x) can be easily evaluated for arbitrary values of x by using the computer program without any computational effort. From the given illustrative examples, it can be seen that the Abel series approach can obtain very accurate and satisfactory results. However, the main point is that the polynomial expansion is highly ill-posed when α is larger than 1. This method can be improved with new strategies to solve the other nonlinear equations.

REFERENCES

[1] I. Fried, Numerical Solution of Differential Equations, Academic Press, NY, 1979.

[2] D. W. Jordan, P. Smith, Nonlinear Ordinary Differential Equations: An Introduction for Scientists and Engineers, Oxford University Press, NY, 2007.

[3] A. C. King, J. Billingham, S. R. Otto, Differential Equations: Linear, Nonlinear, Ordinary, Partial, Cambridge University Press, NY, 2003.

[4] E. Yusufoğlu, Numerical solution of Duffing equation by the Laplace decomposition algorithm, Applied Mathematics and Computation 177 (2006) 572–580

[5] G. Yüksel, M. Gülsu, M. Sezer, Chebyshev polynomial solutions of a class of second-order nonlinear ordinary differential equations. Journ. Adv. Res. Sci. Comput. 3 (2011) 11-24.

[6] A. Anapalı, Y. Öztürk, M. Gülsu, Numerical solutions of Duffing equations involving linear integral with shifted Chebyshev polynomials, AKU J. Sci. Eng. 15 (2015) 1-11.

[7] B. Bülbül, M. Sezer, Numerical solution of Duffing equation by using an improved Taylor matrix method, Journal of Applied Mathematics 2013 (2013), 1-6

[8] N. Baykuş Savaşaneril, M. Sezer, Hybrid Taylor-Lucas collocation method for numerical solution of high-order pantograph type delay differential equations with variables delays, Appl. Math. Inf. Sci. 11 (2017) 1795-1801.

[9] A. Akyüz-Daşcıoğlu, H. Çerdik-Yaslan, The solution of high-order nonlinear ordinary differential equations by Chebyshev series, Appl. Math. Comput. 217 (2011) 5658-5666.

[10] D.S. Kim, T.Kim, S-H. Lee, S-H. Kim, Some identities of Bernoulli, Euler and Abel polynomials arising from umbral calculus, Advances in Difference Equations 2013:15 (2013) 8 pages.

[11] D.V. Kruchinin, V.V. Kruchinin, Application of a composition of generating functions for obtaining explicit formulas of polynomials, J. Math. Anal. Appl. 404 (2013) 161-171.

A New Perturbation-Iteration Method for Solving Delay Differential Equations

M. Mustafa Bahşı*, Manisa Celal Bayar Univ., Kırkağaç Vocational School, Kırkağaç, Manisa, Turkey
Mehmet Çevik, İzmir Katip Çelebi Univ., Dept. of Mechanical Engineering, Çiğli Main Campus, İzmir, Turkey
*Corresponding author: mustafa.bahsi@cbu.edu.tr

Abstract
In this study, the Perturbation-Iteration method is used to solve the delay differential equations. Two examples are presented to verify the efficiency of the method. It is demonstrated that the proposed method gives better results than those of some other methods in the literature. The present method can be useful in developing new algorithms since they can be generated in various forms according to the number of correction terms in perturbation expansion and the order of derivation in Taylor expansion.

Keywords: delay differential equations, Perturbation-Iteration algorithm, numerical solution
Discipline: Mathematics

INTRODUCTION
The delay differential equation is a special type of functional differential equations. Delay differential equations have been used mathematical model of the various areas, such as car-following models, population dynamics, economics, fluid dynamics, etc. Many researchers have studied on numerical solution and stability analysis of these equations.

In this study, we consider the delay differential equations with closed form

$$F\left(u^{(k)}, \ldots, u', u, u_\tau, \varepsilon, x\right) = 0$$

where $u = u(x)$ and $u_\tau = u(x - \tau)$ such that τ is constant. This problem is solved by the Perturbation-Iteration method.

PERTURBATION-ITERATION METHOD
Perturbation-Iteration method is defined by PIA(n, m). Here, n denotes the number of correction terms in the perturbation expansions and m denotes the order of the derivatives in the Taylor expansion [1]. For the calculating of correction terms, n is smaller than or equal to m. In this study, we generate PIA(1,1) algorithms. Taking only one correction term in the perturbation expansion, the straightforward expansion for the solution of each iteration can be written as follows:

$$u_{n+1} = u_n + \varepsilon(u_c)_n$$

where $(u_c)_n$ is the nth correction term. When we substitute the straightforward expansion into the equation and expand it in a Taylor series with first derivatives to obtain

$$
\begin{aligned}
F\left(u_n^{(k)}, \ldots, u_n', u_n, (u_\tau)_n, 0\right) &+ F_{u^{(k)}}\left(u_n^{(k)}, \ldots, u_n', u_n, (u_\tau)_n, 0\right)\varepsilon\left(u_c^{(k)}\right)_n + \cdots \\
&+ F_{u'}\left(u_n^{(k)}, \ldots, u_n', u_n, (u_\tau)_n, 0\right)\varepsilon(u_c')_n \\
&+ F_u\left(u_n^{(k)}, \ldots, u_n', u_n, (u_\tau)_n, 0\right)\varepsilon(u_c)_n \\
&+ F_{u_\tau}\left(u_n^{(k)}, \ldots, u_n', u_n, (u_\tau)_n, 0\right)\varepsilon((u_\alpha)_c)_n \\
&+ F_\varepsilon\left(u_n^{(k)}, \ldots, u_n', u_n, (u_\tau)_n, 0\right)\varepsilon = 0
\end{aligned}
$$

where $(\ )'$ denotes differentiation with respect to the independent variable and

$$F_{u^{(k)}} = \frac{\partial F}{\partial u^{(k)}}, \ldots, F_{u'} = \frac{\partial F}{\partial u'}, F_u = \frac{\partial F}{\partial u}, F_{u_\tau} = \frac{\partial F}{\partial u_\tau}, F_\varepsilon = \frac{\partial F}{\partial \varepsilon}$$

Bearing in mind that all derivatives are evaluated at $\varepsilon = 0$, and rewriting the equation in the following more suitable form

$$F_{u^{(k)}}\left(u_c^{(k)}\right)_n + \cdots + F_{u'}(u_c')_n + F_u(u_c)_n + F_{u_\tau}((u_\tau)_c)_n = -F_\varepsilon - \frac{F}{\varepsilon}$$

One may easily notice that this is a variable coefficient pantograph equation. Starting with an initial guess u_0, first we determine $(u_c)_0$ from the PIA(1,1) algorithm and then substitute it into the straightforward expansion for calculating u_1. This iteration procedure is repeated using the straightforward expansion and the PIA(1,1) algorithm until the iteration converges to a satisfactory solution.

NUMERICAL EXAMPLES

Example 1. Consider the fourth order linear delay differential equation [2, 3]

$$\left(e^x u'''(x)\right)' + \frac{e^{x-\frac{1}{2}}}{16}u(x-1) = 0, \qquad 0 \leq x \leq 1$$

with the initial condition

$$u(0) = 0, \qquad u'(0) = -1/2, \qquad u'(0) = 1/4, \qquad u'(0) = -1/8$$

which the exact solution is $u(x) = e^{-\frac{x}{2}}$. The equation can be written in the following form:

$$F\left(u^{(iv)}, \dots, u, u_\tau, \varepsilon, x\right) = u^{(iv)}(x) + u'''(x) + \frac{\varepsilon}{16e^{\frac{1}{2}}}u(x-1) = 0$$

where ε is the artificially introduced perturbation parameter. The nonzero terms of PIA(1,1) algorithm are

$$F_{u^{(iv)}} = 1, F_{u'''} = 1, F_\varepsilon = \frac{1}{16e^{\frac{1}{2}}}u_n(x-1) \text{ and } F = u_n^{(iv)}(x) + u_n'''(x)$$

For this example, the equation of the PIA(1,1) algorithm reduces to

$$\left(u_c^{(iv)}\right)_n(x) + (u_c''')_n(x) = -\frac{1}{16e^{\frac{1}{2}}}u_n(x-1) - u_n^{(iv)}(x) - u_n'''(x)$$

When applying the iteration formula, we take the following trivial solution as the initial function, which satisfies the given initial conditions

$$\left(u_c^{(iv)}\right)_n(x) + (u_c''')_n(x) = -\frac{1}{16e^{\frac{1}{2}}}u_n(x-1) - u_n^{(iv)}(x) - u_n'''(x)$$

and using the PIA(1,1) algorithm of the problem, the first iteration solution is

$$u_1(x) = \frac{1}{384} \frac{e^{-x}\left(-71 + 48e^{\frac{1}{2}}\right)}{e^{\frac{1}{2}}} + \frac{7}{2048} e^{-\frac{1}{2}x^4} - \frac{1}{3840} e^{-\frac{1}{2}x^5} + \frac{1}{92160} e^{-\frac{1}{2}x^6}$$

$$- \frac{71}{2304} e^{-\frac{1}{2}x^3} + \frac{x^3}{48} - \frac{1}{768} \frac{x^2\left(-71 + 48e^{\frac{1}{2}}\right)}{e^{\frac{1}{2}}}$$

$$+ \frac{1}{384} \frac{x\left(-71 + 48e^{\frac{1}{2}}\right)}{e^{\frac{1}{2}}} - \frac{1}{384} \frac{-71 + 48e^{\frac{1}{2}}}{e^{\frac{1}{2}}}$$
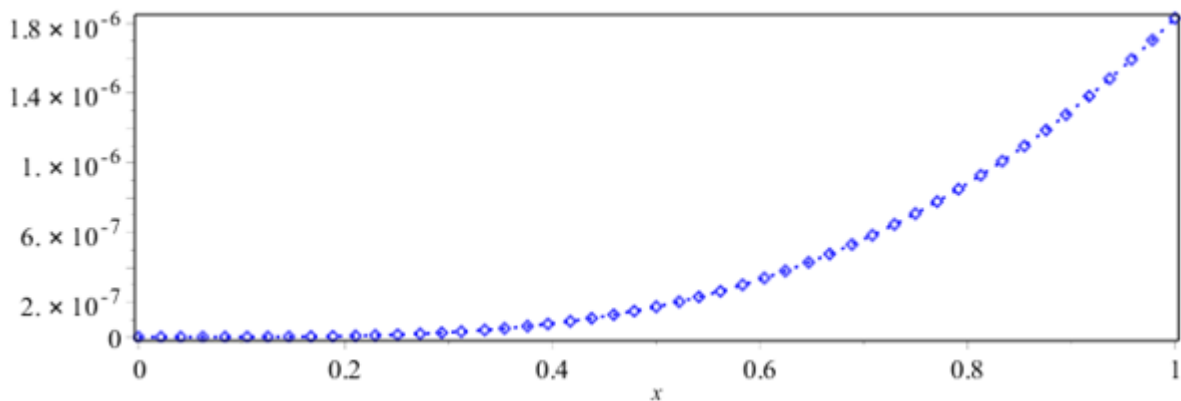
Figure 1. The absolute error function of the first iteration solution by PIA(1,1).

Then, we determine the absolute maximum error for u_n as,

$$E_n = \| u_n(x) - u(x)\|_\infty = max\{| u_n(x) - u(x)|, 0 \le x \le 1\}$$

The absolute maximum errors E_n for different values of n are given in the Table, and it is seen that the error decreases continually as n increases.

Table 1. The absolute maximum errors E_n.

n	1	2	3	4	5	6
E_n	$1.82e-6$	$7.51e-9$	$4.50e-11$	$3.22e-13$	$2.43e-15$	$4.98e-17$

Example 2. Consider the initial value problem of third-order differential equation with delay [2]

$$u'''(x) = -u(x) - u(x - 0.3) + e^{-x+0.3}, \qquad 0 \le x \le 1$$

with initial conditions

$$u(0) = 1, \qquad u'(0) = -1, \qquad u''(0) = 1.$$

which has the exact solution $u(x) = e^{-x}$. The problem can be written in the following form:

$$F\left(u^{(iv)}, \dots, u, u_\tau, \varepsilon, x\right) = u'''(x) + u(x) - e^{-x+0.3} + \varepsilon u(x - 0.3) = 0$$

where $\varepsilon = 1$ is the artificially introduced perturbation parameter. The nonzero terms of the equation in PIA(1,1) algorithm are

$$F_{u'''} = 1, F_u = 1, F_\varepsilon = u_n(x - 0.3) \text{ and } F = u_n'''(x) + u_n(x) - e^{-x+0.3}$$

125

The PIA(1,1) algorithm of the problem is obtained by

$$(u_c''')_n(x) + (u_c)_n(x) = -u_n(x - 0.3) - u_n'''(x) - u_n(x) + e^{-x+0.3}$$

The initial trial function is selected as

$$u_0(x) = 1 - x + \frac{1}{2}x^2$$

The approximate first iteration solution is obtained as

$$
\begin{aligned}
u_1(x) = &-\frac{269}{200} + \frac{13}{10}x - \frac{x^2}{2} + \frac{1}{3}e^{-x+\frac{3}{10}} + \frac{1}{3}xe^{-x+\frac{3}{10}} + \frac{443}{200}e^{-x} \\
&+ \left(\frac{3}{100} - \frac{1}{3}e^{\frac{3}{10}}\right)e^{\frac{x}{2}}cos\left(\frac{\sqrt{3}x}{2}\right) \\
&+ \frac{1}{90}\left(-9 + 10e^{\frac{3}{10}}\right)\sqrt{3}e^{\frac{x}{2}}sin\left(\frac{\sqrt{3}}{2}x\right)
\end{aligned}
$$
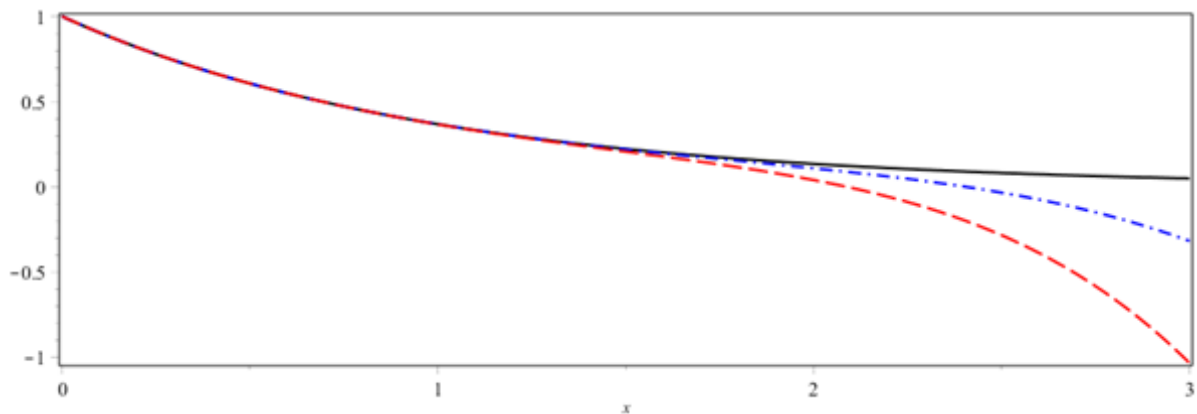
Figure 2. Comparison of the first iteration solutions of the VIM (red line) and PIA(1,1) (blue line) with exact solution (black line).
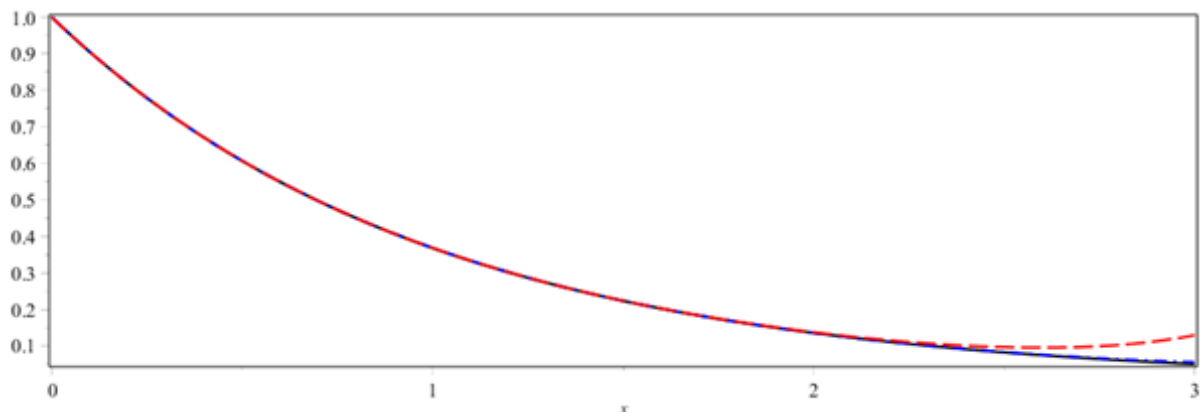
Figure 3. Comparison of the second iteration solutions of the VIM (red line) and PIA(1,1) (blue line) with exact solution (black line).
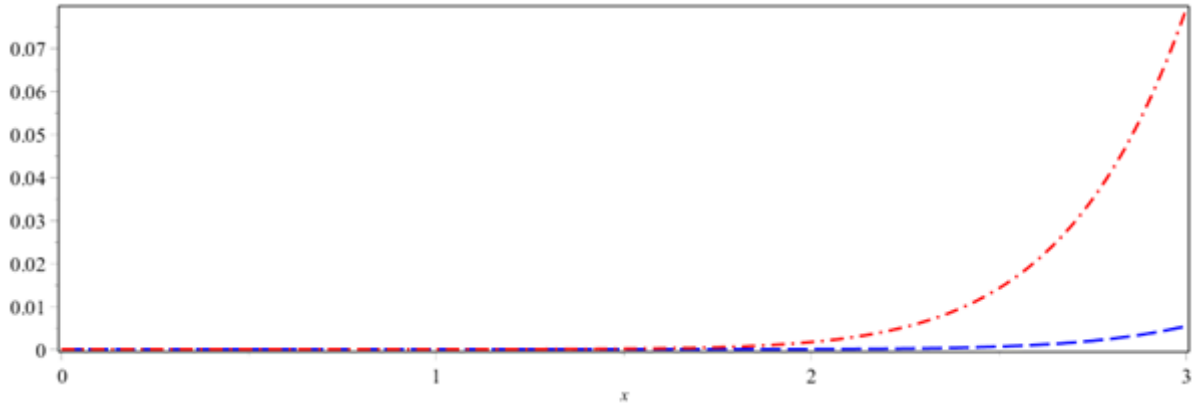
Figure 4. Comparison of the absolute error functions the third iteration solutions of the VIM (red line) and PIA(1,1) (blue line).

CONCLUSION

In this study, the new perturbation-iteration method is employed for the first time to numerically solve the delay differential equations. The comparative results showed that the method highly efficient and reliable two examples. PIA(1,1) algorithm gave better results for the results as Variational Iteration Method. It is anticipated that the present method can be useful in developing new algorithms since they can be generated in various forms according to the number of correction terms in perturbation expansion and the order of derivation in Taylor expansion.

REFERENCES

[1] M. M. Bahşı, M. Çevik, Numerical solution of pantograph-type delay differential equations using Perturbation-Iteration Algorithms, Journal of Applied Mathematics, Article ID 139821 (2015) 1-10 https://doi.org/10.1155/2015/139821.

[2] M. M. Bahşı, M. Çevik, M. Sezer, Orthoexponential polynomial solutions of delay pantograph differential equations with residual error estimation, Applied Mathematics and Computation 271 (2015) 11-21.

[3] M. Çevik, M. M. Bahşı, M. Sezer, Solution of the delayed single degree of freedom system equation by exponential matrix method, Applied Mathematics and Computation 242 (2014) 444-453.

New Transition Curves via a New Spiral Curve

Aslı Ayar*, Bayram Şahin**
Ege University, Dept. of Mathematics, Bornova, 35100, Izmir, Turkey
*Corresponding author: asliayar1@gmail.com
** Corresponding author: bayram.sahin@ymail.com

Abstract

It is known that spirals have been used in many applications such as railway, highway or robotic design. Therefore it is important to find new spirals for CAD (computer-aided design). In this paper, we consider a $\lambda\mu-$Bézier like curve and find spiral conditions for it. Then we propose a research problem for constructing spiral transitions by using the spiral curve obtained in this paper.

Keywords: $\lambda\mu-$Bézier like polynomials, Bezier spiral
Discipline: Mathematics, Computer Science and Engineering

INTRODUCTION

Although Bezier curves have been used for design, these curves are not useful for certain cases. For instance they are not appropriate for representing closed curves. Considering curves with shape parameters, researchers have started to modify representation of curves [2, 4, 6, 8, 9]. Thus, rational curves, trigonometric curves and Bézier like curves with exponential functions are obtained.

In this paper, we consider Bézier like curves with exponential functions, introduced by Zhu and Han in [10]. Basis functions of these curves were obtained by adding two exponential functions to Bernstein basis functions. These two exponential functions have two shape parameters, λ and μ. Then by incorporating control points with these basis functions, the curve is defined and is called $\lambda\mu-$Bézier like curve with two shape parameters.

Also spirals, which are commonly used in CAD and CAM, are very important for technological design. Because their curvature varies monotonically with their arc length. They do not have cusps, loops or inflection points by definition. Consequently the spirals are used in many applications such as satellite orbit, railway, highway or robotic design. In [1], the authors found a spiral Bézier curve and then they constructed many transition curves by using this spiral. Later they extended their result for general case [2, 3], see also [5] and [8].

In this paper, we obtain certain conditions for a $\lambda\mu-$Bézier like curve with two shape parameters to be a spiral and propose an open problem to the interested readers.

BACKGROUND, NOTATIONS AND CONVENTIONS

Parametric form of an any vector **U** is $\mathbf{U} = u_x + u_y$ and norm of its is formulated as $\|\mathbf{U}\| = \sqrt{u_x^2 + u_y^2}$.

Positive angles are measured anti-clockwise. The dot product of two vectors, **U** and **V** is $\mathbf{U}.\mathbf{V} = u_x v_x + u_y v_y$ and the cross product of these two vectors is defined as $\mathbf{U} \times \mathbf{V} = \|\mathbf{U}\|\|\mathbf{V}\|\sin\theta$ where the angle θ is positive angle. The derivative of function **f** is denoted by $\mathbf{f}'$.

The signed curvature of a Bezier like curve $f(t)$ is defined by [7]

$$\kappa(t) = \frac{f'(t) \times f''(t)}{\|f'(t)\|^3} \tag{1}$$

The radius of curvature r is given by $r = \frac{1}{\kappa}$. If $\kappa(t) = 0, t \in [0,1]$ then the curve f (t) reduces to straight line. If $\kappa(t) = 0$, then the curve has a point of inflection. If t is the unit tangent vector to f (t) at t, then the orientation of the unit normal vector n to f (t) at t, is such that the angle is anti-clockwise from t to n is $\pi/2$.

We now define $\lambda\mu-$Bézier like basis functions with two shape parameters and discuss some of their properties.

Definition 1. [10] For $t \in [0, 1]$, $\lambda\mu-$Bezier like basis functions with two shape parameters $\lambda, \mu \in [0, \infty)$ are defined as:

$$A_0(t; \lambda) = (1 - t)^3 e^{-\lambda t},$$
$$A_1(t; \lambda) = (1 - t)^2 [1 + 2t - (1 - t)e^{-\lambda t}],$$
$$A_2(t; \mu) = t^2 [1 + 2t - (1 - t)e^{-\mu(1-t)}],$$
$$A_3(t; \mu) = t^3 e^{-\mu(1-t)},$$

(2)

$$A_0(t; \lambda) + A_1(t; \lambda) + A_2(t; \mu) + A_3(t; \mu) = 1$$

(3)

For $\lambda, \mu = 0$, the $\lambda\mu-$Bézier like basis functions are linear cubic Bernstein basis functions.
We now construct the $\lambda\mu-$Bézier like curve with two shape parameters as follows:

Definition 2. [10] Given the control points $\mathbf{P}_i$ ($i = 0, 1, 2, 3$) in E^2, we define the $\lambda\mu-$Bezier like curve with two shape parameters as:

$$f(t; \lambda, \mu) = \sum_{i=0}^{3} A_i(t; \lambda, \mu) P_i = A_0(t; \lambda)P_0 + A_1(t; \lambda)P_1 + A_2(t; \mu)P_2 + A_3(t; \mu)P_3$$

(4)

$$t \in [0, 1], \lambda, \mu \in [0, \infty)$$

The curve defined by (4) satisfies some geometric properties which can be obtained easily from the properties of the basis functions.

$$f(0; \lambda, \mu) = P_0$$
$$f(1; \lambda, \mu) = P_1$$

(5)

Using derivative of basis functions, we have

$$f'(0; \lambda, \mu) = (\lambda + 3)(P_1 - P_0)$$
$$f'(1; \lambda, \mu) = (\mu + 3)(P_3 - P_2)$$
$$f''(0; \lambda, \mu) = (\lambda^2 + 6\lambda + 6)(P_0 - P_1) + 6(P_2 - P_1)$$
$$f''(1; \lambda, \mu) = (\mu^2 + 6\mu + 6)(P_3 - P_2) + 6(P_1 - P_2)$$

(6)

$\lambda\mu-$BEZIER LIKE SPIRAL WITH TWO SHAPE PARAMETERS

In this section, we are going to find a new spiral under certain conditions for $\lambda\mu-$Bézier like curve given in definition 1.

Theorem 1. Let beginning and ending unit tangent vectors be $\mathbf{t}_0$ and $\mathbf{t}_1$ respectively. The beginning point of curve is $\mathbf{P}_0$ and it is given. An ending curvature value is $c > 0$. We define the $\lambda\mu-$Bézier like curve with two shape parameters

$$\mathbf{f}(t; \lambda, \mu) = \sum_{i=0}^{3} A_i(t; \lambda, \mu) \mathbf{P}_i = A_0(t; \lambda)\mathbf{P}_0 + A_1(t; \lambda)\mathbf{P}_1 + A_2(t; \mu)\mathbf{P}_2 + A_3(t; \mu)\mathbf{P}_3$$

$$t \in [0, 1], \lambda, \mu \in [0, \infty)$$

with

$$\mathbf{P}_1 = \mathbf{P}_0 + a\, \mathbf{t}_0$$
$$\mathbf{P}_2 = \mathbf{P}_1 + b\, \mathbf{t}_0 = \mathbf{P}_0 + (a + b)\, \mathbf{t}_0$$
$$\mathbf{P}_3 = \mathbf{P}_2 + d\, \mathbf{t}_1 = \mathbf{P}_0 + (a + b)\mathbf{t}_0 + d\, \mathbf{t}_1$$

(7)

for $a, b, d > 0$. Suppose θ is the positive angle from $\mathbf{t}_0$ to $\mathbf{t}_1$ and $0 < \theta < \pi/2$. The $\lambda\mu-$Bézier like curve is a spiral segment when

$$a = \frac{\left(12 + 16\mu + 3\mu^2 + \sqrt{(12 + 16\mu + 3\mu^2)^2 + 72e^{-\lambda}(3 + \mu)\cos^2\theta}\right)\sin\theta}{6c(3 + \mu)^2}$$

(8)

$$b = \frac{\left(12 + 16\mu + 3\mu^2 + \sqrt{(12 + 16\mu + 3\mu^2)^2 + 72e^{-\lambda}(3 + \mu)\cos^2\theta}\right)^2 \sec\theta\tan\theta}{216c(3 + \mu)^2}$$

(9)

and

$$d = a\sec\theta$$

(10)

This $\lambda\mu-$Bézier like spiral has

$$\kappa(0) = 0$$

(11)

$$\kappa(1) = c, \quad \kappa'(1) = 0$$

(12)

and $\kappa'(t) \neq 0$ for $0 \leq t < 1$.

Proof. Let $\mathbf{n}_0$ be the normal vector at $\mathbf{P}_0$. Since $\mathbf{t}_1 = \cos\theta\mathbf{t}_0 + \sin\theta\mathbf{n}_0$ and substitute $\mathbf{P}_1$, $\mathbf{P}_2$, $\mathbf{P}_3$ from (7) into (4) to obtain

$$\mathbf{f}(t) = \big(a\,A_1(t;\lambda) + (a+b)A_2(t;\mu) + (2a+b)A_3(t;\mu)\big)\mathbf{t}_0 + A_3(t;\mu)a\tan\theta\,\mathbf{n}_0. \tag{13}$$

Then take the derivative to obtain

$$\mathbf{f}'(t) = \big(aA_1'(t;\lambda) + (a+b)A_2'(t;\mu) + (2a+b)A_3'(t;\mu)\big)\mathbf{t}_0 + A_3'(t;\mu)a\tan\theta\,\mathbf{n}_0, \tag{14}$$

$$\mathbf{f}''(t) = \big(aA_1''(t;\lambda) + (a+b)A_2''(t;\mu) + (2a+b)A_3''(t;\mu)\big)\mathbf{t}_0 + A_3''(t;\mu)a\tan\theta\,\mathbf{n}_0. \tag{15}$$

Substituting expressions $A_1'(t;\lambda), A_2'(t;\mu), A_3'(t;\mu), A_1''(t;\lambda), A_2''(t;\mu), A_3''(t;\mu)$ into (14) and (15), we obtain

$$\mathbf{f}(t) = x(t)\mathbf{t}_0 + y(t)\mathbf{n}_0,$$
$$\mathbf{f}'(t) = x'(t)\mathbf{t}_0 + y'(t)\mathbf{n}_0, \tag{16}$$
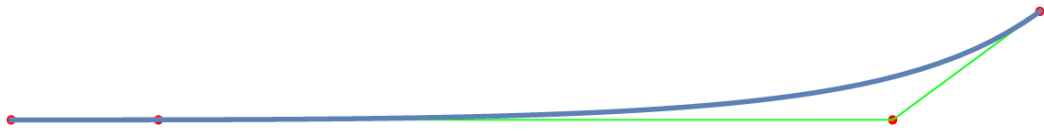
Figure 1. A spiral curve example ($\theta = 36$, $\lambda = 3.11$, $\mu = 2.09$, $c = 1.43$)

and

$$\mathbf{f}''(t) = x''(t)\mathbf{t}_0 + y''(t)\mathbf{n}_0. \tag{17}$$

where

$$\begin{aligned}
x'(t) &= a\big(A_1'(t;\lambda)\big) + (a+b)A_2'(t;\mu) + (2a+b)A_3''(t;\mu)\\
y'(t) &= A_3'(t;\mu)a\tan\theta\\
x''(t) &= a\big(A_1''(t;\lambda)\big) + (a+b)A_2''(t;\mu) + (2a+b)A_3''(t;\mu)\\
y''(t) &= A_3''(t;\mu)a\tan\theta
\end{aligned} \tag{18}$$

The curvature and its derivative are given by

$$\kappa(t) = \frac{x'(t)\,y''(t) - x''(t)\,y'(t)}{\{x'^2(t) + y'^2(t)\}^{3/2}} \tag{19}$$

and

$$\kappa'(t) = \frac{\big(\mathbf{f}'(t)\times\mathbf{f}'''(t)\big)\big(\mathbf{f}'(t)\mathbf{f}'(t)\big) - 3\big(\mathbf{f}'(t)\times\mathbf{f}''(t)\big)\big(\mathbf{f}'(t)\mathbf{f}''(t)\big)}{\|\mathbf{f}'(t)\|^5} \tag{20}$$

$$\kappa'(t) = \frac{A(t)}{\|\mathbf{f}'(t)\|^5} \tag{21}$$

respectively, where

$$\begin{aligned}
A(t) &= \big(\mathbf{f}'(t)\times\mathbf{f}'''(t)\big)\big(\mathbf{f}'(t)\mathbf{f}'(t)\big) - 3\big(\mathbf{f}'(t)\times\mathbf{f}''(t)\big)\big(\mathbf{f}'(t)\mathbf{f}''(t)\big)\\
&= (x'\,y''' - x'''\,y')(x'^2 + y'^2) - 3(x'y'' - x''\,y')(x'\,x'' - y'\,y'')
\end{aligned} \tag{22}$$

Set

$$A(t) = a(t)b(t) - 3c(t)d(t),$$

where

$$\begin{aligned}
a(t) &= \mathbf{f}'(t)\times\mathbf{f}'''(t) = x'(t)\,y'''(t) - x'''(t)\,y'(t)\\
b(t) &= \mathbf{f}'(t)\mathbf{f}'(t) = x'^2(t) + y'^2(t)\\
c(t) &= \mathbf{f}'(t)\times\mathbf{f}''(t) = x'(t)\,y''(t) - x''(t)\,y'(t)\\
d(t) &= \mathbf{f}'(t)\mathbf{f}''(t) = x'(t)\,x''(t) - y'(t)\,y''(t)
\end{aligned}$$
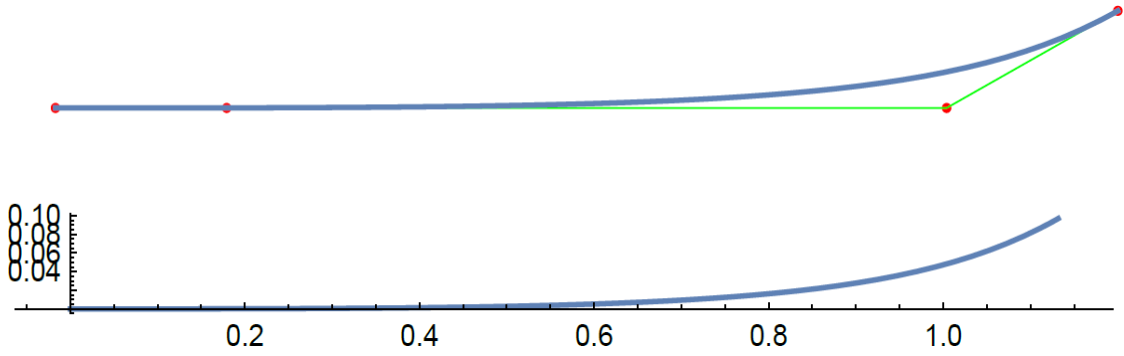
Figure 2. Spiral curve ($\theta = 28$, $\lambda = 2.2846$, $\mu = 2.1020$, $c = 1.94$)

$$a\,(t) = a\,e^{-t(\lambda-\mu)-2\mu}\,\tan\theta\Big((6+18t\mu+9t^2\mu^2$$
$$+ t^3\mu^3)\,\Big(a\Big(e^\mu(t-1)^2(3-(t-1)\lambda)e^{t(\lambda+\mu)}t^2(3+t\mu)\Big)-6be^{t\lambda+\mu}(t-1)t\Big)$$
$$+ t^2(3$$
$$+ t\mu)\Big(12be^{t\lambda+\mu}\,a\Big(e^\mu(6-18(t-1)\lambda+9(t-1)^2\lambda^2-(t-1)^3\lambda^3)$$
$$+ e^{t(\lambda+\mu)}(6+18t\mu+9t^2\mu^2+t^3\mu^3)\Big)\Big)\Big),$$

$$b\,(t) = e^{-2(t\lambda+\mu)}\Big(6be^{t\lambda+\mu}(t-1)t + a\Big(e^{\mu(t-1)^2(-3+(t-1)\lambda)} - e^{t(\lambda+\mu)}t^2(3+t\mu)\Big)\Big)^2$$
$$+ a^2 e^{2(t-1)\mu}\,t^4(3+t\mu)^2\tan^2\theta,$$

(23)

$$c\,(t) = -a\,e^{-t\lambda-\mu+t\mu}\,\tan\theta\Big(6be^{t\lambda}t(-3-5t\mu-t^2(\mu-4)\mu+t^3\mu^2)$$
$$+ a(t-1)\Big((t-1)^2t\lambda^2(3+u\mu)+3(6+6t\mu+t^2(\mu-4)\mu-t^3\mu^2)$$
$$+ (t-1)\lambda\left(-6-t^2\mu^2+t^3\mu^2-6t(2+\mu)\right)\Big)\Big),$$

$$d\,(t) = -e^{-2(t\lambda+\mu)}\Big(6be^{t\lambda+\mu}(t-1)t$$
$$+ a\Big(e^\mu(t-1)^2(-3+(t-1)\lambda)-e^{t(\lambda+\mu)}t^2(3+t\mu)\Big)\Big)\Big(-6be^{t\lambda+\mu}(2t-1)$$
$$+ a\Big(e^\mu(t-1)(6-6(t-1)\lambda+(t-1)^2\lambda^2)+e^{t(\lambda+\mu)}t(6+6t\mu+t^2\mu^2)\Big)\Big)$$
$$+ a^2 e^{2(t-1)\mu}t^3(3+t\mu)(6+6t\mu+t^2\mu^2)\tan^2\theta.$$

If $t = 0$, from (18), it follows
$$\begin{aligned}
x'(0) &= a\,(3+\lambda),\\
y'(0) &= 0,\\
x''(0) &= 6b - a(6+6\lambda+\lambda^2),\\
y''(0) &= 0,\\
x'''(0) &= 6(a\,e^{-\mu}-2b)+a(6+18\lambda+9\lambda^2+\lambda^3),\\
y'''(0) &= 6a\,e^{-\mu}\tan\theta
\end{aligned}$$
Using these equations in (22), we get

$$A(t) = a(0)b(0) - 3c(0)d(0) = 6a^4 e^{-\mu}(3+\lambda)^3\tan\theta.$$

131
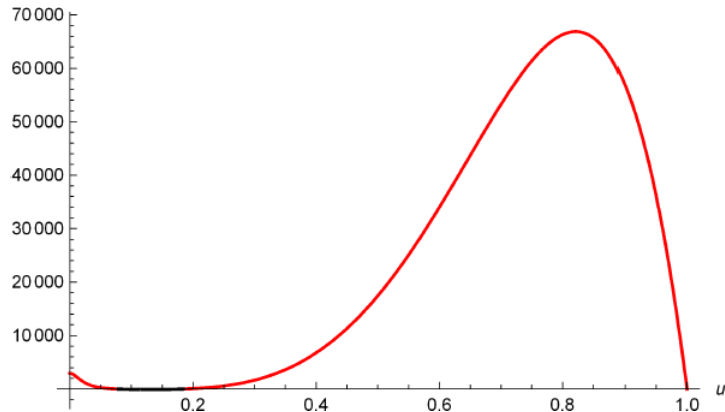
Figure 3. Graphic of A(t) ($\theta = 74, \lambda = 32.11, \mu = 1, c = 2.02$)
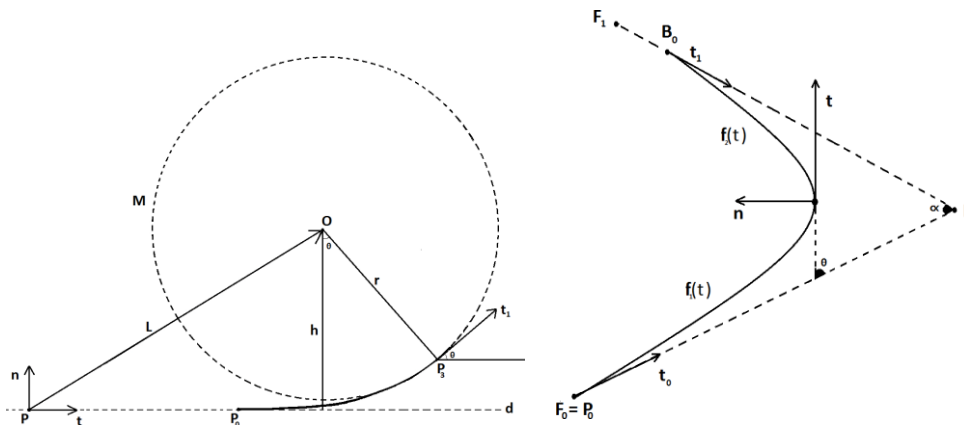
Figure 4. (a) Line to circle transition   (b) Line to Line transition

From (21), the beginning curvature value

$$\kappa'(0) = \frac{A(0)}{\|f'(0)\|^5}$$

(11) and (12) follows substitution of t = 0 and t = 1 into (19) and (20):

$$\kappa(0) = 0, \quad \kappa(1) = c, \quad \kappa'(1) = 0.$$

It also follows from (20), $A(0) > 0$, and $\lim_{t \to \infty} A(t) > 0$ if $\lambda > 0$ and $\mu > 1$. For the case of $\mu = 1$, see also Figure 2. Hence value of $\kappa'(t)$ decreases on $0 \leq t < 1$, and when $t = 1$, $\kappa'(1) = 0$. So that $\kappa'(t)$ does not change sign on $0 \leq t < 1$.

Therefore, we obtain certain conditions for a $\lambda\mu$−Bézier like curve with two shape parameters to be a spiral. When a $\lambda\mu$−Bézier like curve is a spiral, we can construct transition curves (Line to circle,
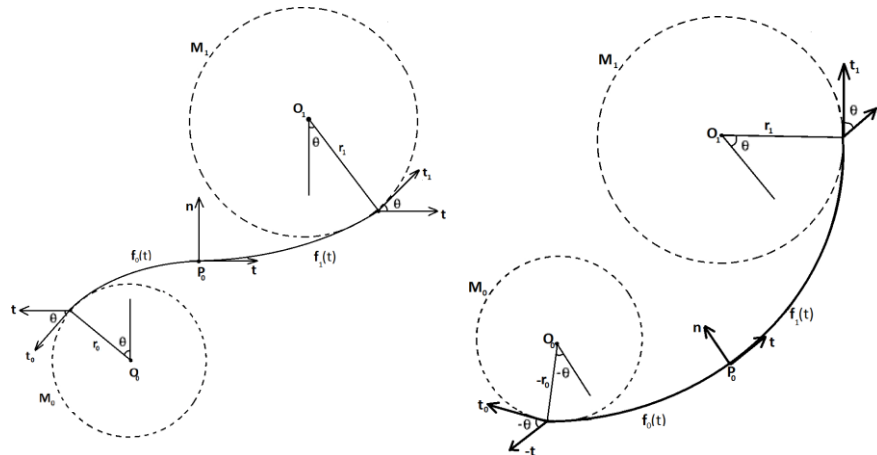
Figure 5. 1-Circle to circle with S shaped. 2-Circle to circle with a C-shaped.

Circle to circle with C shaped, Circle to circle with S shaped, Line to line transition curves) by using the spiral we find in previous theorem, see Figures 2 and 3. Therefore we propose the following problem.

Open Problem: By using the spiral obtained in this paper, construct transition curves in the forms; Line to circle, Circle to circle with C shaped, Circle to circle with S shaped, Line to line transition curves.

REFERENCES

[1] D.J. Walton and D.S. Meek, A planar cubic Bezier spiral, Journal of Computational and Applied Mathematics 72 (1996), 85-100.

[2] D.J. Walton, D.S. Meek and Md, A. Jamaludin, Planar G^2 transition curves composed of cubic Bézier spiral segments, Journal of Computational and Applied Mathematics 157 (2003) 453-476.

[3] D.J. Walton and D.S. Meek, A further generalization of the planar cubic Bézier spiral, Journal of Computational and Applied Mathematics 236 (2012) 2869-2882.

[4] G. Farin, Curves and Surfaces for CAGD: A Practical Guide, Academic Press, 2002.

[5] Z. Habib, M. Sakai, Spiral transition curves and their applications, Scientiae Mathematicae Japonicae Online (e-2004) 251-262.

[6] H.G. Timmer, Alternative representation for parametric cubic curves and surfaces, Computer-Aided Design, 12 (1980) 25-28.

[7] R.S. Millman, G.D. Parker, Elements of Differential Geometry, Englewood Cliffs, N.J. Prentice-Hall, 1977.

[8] U. Bashira, M. Abbasa, M.N. Awangb, Md. A. Jamaludin, The quadratic trigonometric Bézier curve with single shape parameter, Journal of Basic and Applied Scientific Research 2 (2012) 2541-2546.

[9] U. Bashir, M. Abbas, J. Md, Ali, The G^2 and C^2 rational quadratic trigonometric Bézier curve with two shape parameters with applications, Applied Mathematics and Computation 219 (2013) 10183-10197.

[10] Y. Zhu and X. Han, Curves and surfaces construction based on new basis with exponential functions, Acta Appl. Math. 129 (2014) 183-203.

On Ruled Surfaces Defined by Smarandache Curve

Amine Yılmaz*, Bayram Şahin
Ege University, Dept. of Mathematics, Bornova, 35100, İzmir, Turkey
*Corresponding author: amineyilmaz2020@hotmail.com

Abstract

In the surfaces theory, it is well-known that a surface is called to be a ruled surface if it is generated by a continuously moving of a straight line in the space. Since a ruled surface is obtained by a line movement, its geometry has many nice properties and such surfaces have been studied by many authors, see: [4, 5, 6] and references therein. Ruled surfaces are also important subject in many applications. In particular, such surfaces have been used in computer aided engineering design (CAD) [7].

In differential geometry, one can obtain a new curve by using a regular curve [4, 5, 8]. In this direction, Smarandache curves have been defined and studied in [11]. More precisely, if the position vector of a curve β is composed by the Frenet frame's vectors of another curve α, then the curve β is called a Smarandache curve [11]. Special Smarandache curves in the Euclidean and Minkowski spaces are studied by many authors [1, 2, 9, 10, 11, 12].

In this talk, we first obtain binormal surface generated by TN-Smarandache curve and investigate singular point of this surface. Then we derive main properties of binormal surfaces such as striction curve, distribution parameter, Gauss curvature, mean curvature and geodesic curvature. By using these main properties, we obtain certain results on Gauss curvature and geodesic curvature of binormal surface. We also check the minimality of such surfaces by using its mean curvature. Finally, we give an example to illustrate our results.

Keywords: Frenet frame, Smarandache curve, Binormal surface, Euclidean space
Discipline: Mathematics

INTRODUCTION

Ruled surfaces are surfaces which are generated by moving a straight line continuously in the 3-dimensional Euclidean space. Ruled surfaces are one of the most important topics of differential geometry. Also, geometrical properties of these surface are richer than the other surface due to generated with line. In [3, 4, 5], many geometers have investigated the many properties of these surfaces.

There have been many studies on the differential geometry of curves in the 3-dimensional Euclidean space. In the differential geometry, a new curve produced from a known curve is one of the most studied areas of research. Thus, it is possible to compare generated curve by initial curve. In [11], the authors defined a regular curve in Minkowski space-time, whose position vector is composed by Frenet frame vectors on another regular curve, This new curve is called a Smarandache curve. After that, special Smarandache curves have been investigated in differential geometers [1, 9, 12]. Also, surfaces family with common Smarandache geodesic curve have been investigated in [2].

In this talk, we investigated singular points of the binormal surface defined TN-Smarandache curve according to Frenet frame in Euclidean space. And we obtained striction curves, distribution parameters, Gauss curvatures and mean curvatures of the this surfaces. We give some important results and illustrate an example.

PRELIMINARIES

In this section, we recall some basic topics from [5, 8].Euclidean 3-space provided with the standard flat metric given by

$$<,>=dx_1^2+dx_2^2+dx_3^2,$$

where x_1, x_2, x_3 is a rectangular coordinate system of E^3. Then, the norm of an arbitrary vector $\varphi \in E^3$ is defined by

$$\|\varphi\|=\sqrt{\langle\varphi,\varphi\rangle}.$$

2nd International Students Science Congress
4-5 May 2018, Izmir - Turkey

İZMİR
Uluslararası
Misafir
Öğrenci
Derneği
◆ IZMIR International Guest Student Association

İZMİR
KÂTİP ÇELEBİ
UNIVERSITY
2010

Let $\varphi = \varphi(s)$ be a regular curve in E^3. If $\left\| \varphi'(s) \right\| = 1$, the curve is called the unit speed curve. Also, if the tangent vector of this curve forms a constant angle with a constant axes, the this curve is called a general helix.

Denote by $\left\{ \vec{T}, \vec{N}, \vec{B} \right\}$ the moving Frenet-Serret frame along the curve $\overrightarrow{\varphi}$ in the space E^3. For an arbitrary unit speed curve with the first and the second curvature, $\mathcal{K}$ and τ, the Frenet-Serret formulae are given by

$$\begin{bmatrix} \vec{T'} \\ \vec{N'} \\ \vec{B'} \end{bmatrix} = \begin{bmatrix} 0 & \kappa & 0 \\ -\kappa & 0 & \tau \\ 0 & -\tau & 0 \end{bmatrix} \cdot \begin{bmatrix} \vec{T} \\ \vec{N} \\ \vec{B} \end{bmatrix}$$

where

$$\left\langle \vec{T}, \vec{T} \right\rangle = \left\langle \vec{N}, \vec{N} \right\rangle = \left\langle \vec{B}, \vec{B} \right\rangle = 1$$
$$\left\langle \vec{T}, \vec{N} \right\rangle = \left\langle \vec{T}, \vec{B} \right\rangle = \left\langle \vec{N}, \vec{B} \right\rangle = 0$$

Definition 1. A regular curve in E^4, whose position vector is obtained by Frenet frame vectors on another regular curve, is called Smarandache curve [11].

From [1], we have the following information for such curves:

Let $\sigma = \sigma(s)$ be a unit speed regular curve and $\left\{ T_\sigma, N_\sigma, B_\sigma, \kappa_\sigma, \tau_\sigma \right\}$ be Frenet apparatus of this curve. TN-Smarandache curve of $\sigma(s)$ curve is defined by

$$\vec{\alpha}(s_\alpha) = \frac{1}{\sqrt{2}} (T_\sigma + N_\sigma).$$

Denote by $\left\{ T_\alpha, N_\alpha, B_\alpha, \kappa_\alpha, \tau_\alpha \right\}$ the Frenet apparatus of a curve α. The tangent vector and principal normal of the curve α can be written as follows:

$$T_\alpha = \alpha' = \frac{-\kappa_\sigma \vec{T}_\sigma + \kappa_\sigma \vec{N}_\sigma + \tau_\sigma \vec{B}_\sigma}{\sqrt{2\kappa_\sigma^2 + \tau_\sigma^2}}, \tag{1}$$

$$N_\alpha = \frac{\lambda_1 \vec{T}_\sigma + \lambda_2 \vec{N}_\sigma + \lambda_3 \vec{B}_\sigma}{\sqrt{\lambda_1^2 + \lambda_2^2 + \lambda_3^2}}, \tag{2}$$

where

$$\lambda_1 = -[\kappa_\sigma^2 (2\kappa_\sigma^2 + \tau_\sigma^2) + \tau_\sigma (\tau_\sigma \kappa_\sigma' - \kappa_\sigma \tau_\sigma')],$$
$$\lambda_2 = -[\kappa_\sigma^2 (2\kappa_\sigma^2 + 3\tau_\sigma^2) + \tau_\sigma (\tau_\sigma^3 - \tau_\sigma \kappa_\sigma' + \kappa_\sigma \tau_\sigma')],$$
$$\lambda_3 = \kappa_\sigma [\tau_\sigma (2\kappa_\sigma^2 + \tau_\sigma^2) - 2(\tau_\sigma \kappa_\sigma' - \kappa_\sigma \tau_\sigma')].$$

The binormal vector of the curve α is given by the following:

$$B_\alpha = \frac{[\kappa_\sigma \lambda_3 - \tau_\sigma \lambda_2]\vec{T}_\sigma + [\kappa_\sigma \lambda_3 + \tau_\sigma \lambda_1]\vec{N}_\sigma - \kappa_\sigma [\lambda_1 + \lambda_2]\vec{B}_\sigma}{\sqrt{\lambda_1^2 + \lambda_2^2 + \lambda_3^2} \sqrt{2\kappa_\sigma^2 + \tau_\sigma^2}} \tag{3}$$

[1].

Also, tangent of the binormal vector of the curve α which will be used in later calculations as

$$B_\alpha' = \frac{\sqrt{2}(\omega \vec{T}_\sigma + \phi \vec{N}_\sigma + \psi \vec{B}_\sigma)}{(\lambda_1^2 + \lambda_2^2 + \lambda_3^2)^{\frac{3}{2}} (2\kappa_\sigma^2 + \tau_\sigma^2)^2}, \tag{4}$$

where

135

$$\omega = (\kappa_\sigma' \lambda_3 + \kappa_\sigma \lambda_3' - \tau_\sigma' \lambda_2 - \tau_\sigma \lambda_2' - \kappa_\sigma^2 \lambda_3 - \kappa_\sigma \tau_\sigma \lambda_1)(\lambda_1^2 + \lambda_2^2 + \lambda_3^2)(2\kappa_\sigma^2 + \tau_\sigma^2)$$

$$-(\kappa_\sigma \lambda_3 - \tau_\sigma \lambda_2)[(\lambda_1 \lambda_1' + \lambda_2 \lambda_2' + \lambda_3 \lambda_3')(2\kappa_\sigma^2 + \tau_\sigma^2) + (2\kappa_\sigma \kappa_\sigma' + \tau_\sigma \tau_\sigma')(\lambda_1^2 + \lambda_2^2 + \lambda_3^2)],$$

$$\phi = (\kappa_\sigma' \lambda_3 + \kappa_\sigma \lambda_3' + \tau_\sigma' \lambda_1 + \tau_\sigma \lambda_1' + \kappa_\sigma^2 \lambda_3 + \kappa_\sigma \tau_\sigma \lambda_1)(\lambda_1^2 + \lambda_2^2 + \lambda_3^2)(2\kappa_\sigma^2 + \tau_\sigma^2)$$

$$-(\kappa_\sigma \lambda_3 + \tau_\sigma \lambda_1)[(\lambda_1 \lambda_1' + \lambda_2 \lambda_2' + \lambda_3 \lambda_3')(2\kappa_\sigma^2 + \tau_\sigma^2) + (2\kappa_\sigma \kappa_\sigma' + \tau_\sigma \tau_\sigma')(\lambda_1^2 + \lambda_2^2 + \lambda_3^2)],$$

$$\psi = (-\kappa_\sigma' \lambda_1 - \kappa_\sigma \lambda_1' - \kappa_\sigma' \lambda_2 - \kappa_\sigma \lambda_2' + \tau_\sigma^2 \lambda_1 + \kappa_\sigma \tau_\sigma \lambda_3)(\lambda_1^2 + \lambda_2^2 + \lambda_3^2)(2\kappa_\sigma^2 + \tau_\sigma^2)$$

$$+\kappa_\sigma(\lambda_1 + \lambda_2)[(\lambda_1 \lambda_1' + \lambda_2 \lambda_2' + \lambda_3 \lambda_3')(2\kappa_\sigma^2 + \tau_\sigma^2) + (2\kappa_\sigma \kappa_\sigma' + \tau_\sigma \tau_\sigma')(\lambda_1^2 + \lambda_2^2 + \lambda_3^2)]$$

[12].

Definition 2. A set of one-parameter of lines are called ruled surfaces. Such surfaces are represented by the vector equation

$$X(s,v) = \sigma(s) + v\beta(s), \tag{5}$$

where $\sigma(s)$ is its base curve and $\beta(s)$ is its direction of the ruled surface [4].

Definition 3. Let $M \subset E^3$ be a surface and $\sigma : I \subset R \to E^3$ be a regular curve. Also, let $\{T_\sigma, N_\sigma, B_\sigma, \kappa_\sigma, \tau_\sigma\}$ be Frenet apparatus of this curve. M is said to be the binormal surface of a curve σ if M can be parametrized as

$$X(s,v) = \sigma(s) + vB_\sigma(s),$$

[4].

The parametrization of the striction curve and distribution parameter on the ruled surface (5) are given by, respectively

$$\overline{\sigma}(s) = \sigma(s) - \frac{\langle T_\sigma, \beta' \rangle}{\langle \beta', \beta' \rangle} \beta(s), \tag{6}$$

$$P = \frac{\det(\beta, \beta', \sigma')}{\|\beta'\|^2}. \tag{7}$$

The standard unit normal vector field U on a surface $X(s,v)$ can be defined by

$$U = \frac{X_s \wedge X_v}{\|X_s \wedge X_v\|} = \frac{X_s \wedge X_v}{\sqrt{EG - F^2}},$$

where $X_s = \dfrac{\partial X(s,v)}{\partial s}$ and $X_v = \dfrac{\partial X(s,v)}{\partial v}$. Respectively, the first and second fundamental forms of the surface $X(s,v)$ are given by

$$I = Eds^2 + 2Fdsdv + Gdv^2,$$
$$II = eds^2 + 2fdsdv + gdv^2,$$

where

$$E = \langle X_s, X_s \rangle, F = \langle X_s, X_v \rangle, G = \langle X_v, X_v \rangle,$$
$$e = \langle U, X_{ss} \rangle, f = \langle U, X_{sv} \rangle, g = \langle U, X_{vv} \rangle.$$

The Gaussian curvature K and mean curvature H are defined by, respectively

$$K = \frac{eg - f^2}{EG - F^2}, \tag{8}$$

$$H = \frac{Eg + Ge - 2Ff}{2(EG - F^2)}$$

(9)

[5].

BINORMAL SURFACES DEFINED BY TN-SMARANDACHE CURVE ACCORDING TO FRENET FRAME

Let $\sigma : I \rightarrow E^3$ be a curve. TN-Smarandache curve of $\sigma(s)$ curve is written as follows

$$\vec{\alpha}(s_\alpha) = \frac{1}{\sqrt{2}}(T_\sigma + N_\sigma).$$

We denote the Frenet apparatus of a curve α by $\{T_\alpha, N_\alpha, B_\alpha, \kappa_\alpha, \tau_\alpha\}$. We consider the following binormal surface

$$X(s,v) = \alpha + vB_\alpha$$

(10)

with TN-Smarandache curve of $\sigma(s)$.

We first have following result

Theorem 1. If $\sigma(s)$ is helix, the binormal surface $X(s,v)$ defined by (10) have singular points. And, if $\sigma(s)$ isn't helix, the binormal surface $X(s,v)$ defined by (10) have non-singular surface.

Proof: We can calculate that

$$X_s \wedge X_v = \alpha' \wedge B_\alpha + vB_\alpha' \wedge B_\alpha = -N_\alpha + vB_\alpha' \wedge B_\alpha.$$

(11)

Then $P_0 = X(s_0, v_0)$ is a singular point of binormal surface $X(s,v)$ defined by (10) if and only if

$$\left\| \frac{\partial X(s,v)}{\partial s} \wedge \frac{\partial X(s,v)}{\partial v} \right\| = 0.$$

Thus, we write

$$vB_\alpha' \wedge B_\alpha = N_\alpha \Rightarrow v = \frac{1}{\det(B_\alpha', B_\alpha, N_\alpha)},$$

$$v = \frac{(\lambda_1^2 + \lambda_2^2 + \lambda_3^2)^{\frac{5}{2}}(2\kappa_\sigma^2 + \tau_\sigma^2)^{\frac{3}{2}}}{\left\{ \begin{array}{l} \sqrt{2}(\kappa_\sigma \tau_\sigma' - \tau_\sigma \kappa_\sigma')[\lambda_3(\omega - \phi) - \psi(\lambda_1 - \lambda_2)] \\ + \sqrt{2}(2\kappa_\sigma^2 + \tau_\sigma^2)(\tau_\sigma \lambda_2 \psi - \tau_\sigma \lambda_3 \phi + \kappa_\sigma \lambda_1 \phi - \kappa_\sigma \lambda_2 \omega) \end{array} \right.},$$

(12)

$$B_\alpha' \wedge B_\alpha = \frac{\sqrt{2}\left\{ \begin{array}{l} [\phi(-\kappa_\sigma \lambda_1 - \kappa_\sigma \lambda_2) - \psi(\kappa_\sigma \lambda_3 + \tau_\sigma \lambda_1) \\ -\omega(-\kappa_\sigma \lambda_1 - \kappa_\sigma \lambda_2) + \psi(\kappa_\sigma \lambda_3 - \tau_\sigma \lambda_2) \\ +\omega(\kappa_\sigma \lambda_3 + \tau_\sigma \lambda_1) - \phi(\kappa_\sigma \lambda_3 - \tau_\sigma \lambda_2)] \end{array} \right.}{(\lambda_1^2 + \lambda_2^2 + \lambda_3^2)^2(2\kappa_\sigma^2 + \tau_\sigma^2)^{\frac{5}{2}}}.$$

(13)

Substituting (12) and (13) values in (11) equation, we obtain as

$$\frac{\lambda_1}{\sqrt{\lambda_1^2 + \lambda_2^2 + \lambda_3^2}} = \left\{ \begin{array}{l} \dfrac{(\lambda_1^2 + \lambda_2^2 + \lambda_3^2)^{\frac{5}{2}}(2\kappa_\sigma^2 + \tau_\sigma^2)^{\frac{3}{2}}}{\left\{ \begin{array}{l} \sqrt{2}(\kappa_\sigma \tau_\sigma' - \tau_\sigma \kappa_\sigma')[\lambda_3(\omega - \phi) - \psi(\lambda_1 - \lambda_2)] \\ +(2\kappa_\sigma^2 + \tau_\sigma^2)[\lambda_2(\tau_\sigma \psi - \kappa_\sigma \omega) + \phi(-\tau_\sigma \lambda_3 + \kappa_\sigma \lambda_1)]] \end{array} \right.}, \\ \cdot \dfrac{\sqrt{2}[\phi\kappa_\sigma(2\kappa_\sigma^2 + \tau_\sigma^2) - \psi(\kappa_\sigma \tau_\sigma' - \tau_\sigma \kappa_\sigma')]}{(\lambda_1^2 + \lambda_2^2 + \lambda_3^2)^2(2\kappa_\sigma^2 + \tau_\sigma^2)^{\frac{3}{2}}} \end{array} \right.$$

$$\frac{\lambda_2}{\sqrt{\lambda_1^2+\lambda_2^2+\lambda_3^2}} = \begin{cases} \dfrac{(\lambda_1^2+\lambda_2^2+\lambda_3^2)^{\frac{5}{2}}(2\kappa_\sigma^2+\tau_\sigma^2)^{\frac{3}{2}}}{\begin{cases}\sqrt{2}(\kappa_\sigma\tau_\sigma^{'}-\tau_\sigma\kappa_\sigma^{'})[\lambda_3(\omega-\phi)-\psi(\lambda_1-\lambda_2)] \\ +(2\kappa_\sigma^2+\tau_\sigma^2)[\lambda_2(\tau_\sigma\psi-\kappa_\sigma\omega)+\phi(\kappa_\sigma\lambda_1-\tau_\sigma\lambda_3)]]\end{cases}}, \\[2em] \cdot\dfrac{\sqrt{2}[(2\kappa_\sigma^2+\tau_\sigma^2)(\psi\tau_\sigma-\omega\kappa_\sigma)+\psi(\kappa_\sigma\tau_\sigma^{'}-\tau_\sigma\kappa_\sigma^{'})]}{(\lambda_1^2+\lambda_2^2+\lambda_3^2)^2(2\kappa_\sigma^2+\tau_\sigma^2)^{\frac{3}{2}}} \end{cases}$$

$$\frac{\lambda_3}{\sqrt{\lambda_1^2+\lambda_2^2+\lambda_3^2}} = \begin{cases} \dfrac{(\lambda_1^2+\lambda_2^2+\lambda_3^2)^{\frac{5}{2}}(2\kappa_\sigma^2+\tau_\sigma^2)^{\frac{3}{2}}}{\begin{cases}\sqrt{2}(\kappa_\sigma\tau_\sigma^{'}-\tau_\sigma\kappa_\sigma^{'})[\lambda_3(\omega-\phi)-\psi(\lambda_1-\lambda_2)] \\ +(2\kappa_\sigma^2+\tau_\sigma^2)[\lambda_2(\tau_\sigma\psi-\kappa_\sigma\omega)+\phi(\kappa_\sigma\lambda_1-\tau_\sigma\lambda_3)]]\end{cases}}. \\[2em] \cdot\dfrac{\sqrt{2}[(\kappa_\sigma\tau_\sigma^{'}-\tau_\sigma\kappa_\sigma^{'})(\omega-\phi)-\psi\tau_\sigma(2\kappa_\sigma^2+\tau_\sigma^2)]}{(\lambda_1^2+\lambda_2^2+\lambda_3^2)^2(2\kappa_\sigma^2+\tau_\sigma^2)^{\frac{3}{2}}} \end{cases}$$

From this we have

$$\begin{cases} \omega-\phi=\psi \\ \lambda_1=-\lambda_2=-\lambda_3 \,. \\ \kappa_\sigma=\tau_\sigma \end{cases} \tag{14}$$

respectively. Substituting ω,ϕ,ψ and $\lambda_1,\lambda_2,\lambda_3$ in the first and the second equations of (14), we obtain

$$\kappa_\sigma=\tau_\sigma \Rightarrow \frac{\tau_\sigma}{\kappa_\sigma}=1.$$

In that case, if $\sigma(s)$ is helix, the binormal surface $X(s,v)$ defined by (10) have singular points. And, if $\sigma(s)$ isn't helix, the binormal surface $X(s,v)$ defined by (10) have non-singular surface.

Theorem 2. The striction curve is the base curve of a surface $X(s,v)$ defined by (10).

Proof: Substituting (1) and (4) equations in (6), one can obtain the assertion.

Theorem 3. The distribution parameter of a surface $X(s,v)$ defined by (10) as follows

$$P=\frac{-\sqrt{2}(\lambda_1\omega+\lambda_2\phi+\lambda_3\psi)(\lambda_1^2+\lambda_2^2+\lambda_3^2)(2\kappa_\sigma^2+\tau_\sigma^2)}{2(\omega^2+\phi^2+\psi^2)}$$

Proof: It is obvious.

Theorem 4. The Gauss curvature and the mean curvature of a surface $X(s,v)$ defined by (10) are given by

$$K=\frac{-2(\lambda_1\omega+\lambda_2\phi+\lambda_3\psi)^2}{(\lambda_1^2+\lambda_2^2+\lambda_3^2)^4(2\kappa_\sigma^2+\tau_\sigma^2)^4 E^2},$$

$$
H = \frac{
\begin{cases}
\sqrt{2}v^2[(2\kappa_\sigma^2 + \tau_\sigma^2)(\kappa_\sigma b_1\phi - \kappa_\sigma b_2\omega + \tau_\sigma b_2\psi - \tau_\sigma b_3\phi) \\
+ (\kappa_\sigma\tau_\sigma' - \tau_\sigma\kappa_\sigma')(-b_1\psi + b_2\psi + b_3\omega - b_3\phi)] \\
- (\lambda_1^2 + \lambda_2^2 + \lambda_3^2)^{\frac{9}{2}}(2\kappa_\sigma^2 + \tau_\sigma^2)^4\sqrt{E} \\
+ \sqrt{2}v[(2\kappa_\sigma^2 + \tau_\sigma^2)(\kappa_\sigma\lambda_1\phi - \kappa_\sigma\lambda_2\omega + \tau_\sigma\lambda_2\psi - \tau_\sigma\lambda_3\phi) \\
.(\lambda_1^2 + \lambda_2^2 + \lambda_3^2)^3(2\kappa_\sigma^2 + \tau_\sigma^2)^{\frac{5}{2}} \\
+ \sqrt{2}v[(\kappa_\sigma\tau_\sigma' - \tau_\sigma\kappa_\sigma')(-\lambda_1\psi + \lambda_2\psi + \lambda_3\omega - \lambda_3\phi)] \\
.(\lambda_1^2 + \lambda_2^2 + \lambda_3^2)^3(2\kappa_\sigma^2 + \tau_\sigma^2)^{\frac{5}{2}} \\
- v(\lambda_1 b_1 + \lambda_2 b_2 + \lambda_3 b_3)(\lambda_1^2 + \lambda_2^2 + \lambda_3^2)^{\frac{3}{2}}(2\kappa_\sigma^2 + \tau_\sigma^2)^{\frac{3}{2}}\sqrt{E}
\end{cases}
}{2(\lambda_1^2 + \lambda_2^2 + \lambda_3^2)^5(2\kappa_\sigma^2 + \tau_\sigma^2)^6 E^{\frac{3}{2}}},
$$

respectively.

Proof: From (10), we have

$$
X_s = \begin{cases}
\left(\dfrac{-\kappa_\sigma}{\sqrt{2\kappa_\sigma^2 + \tau_\sigma^2}} + \dfrac{\sqrt{2}v\omega}{(\lambda_1^2 + \lambda_2^2 + \lambda_3^2)^{\frac{3}{2}}(2\kappa_\sigma^2 + \tau_\sigma^2)^2}\right)\vec{T}_\sigma \\
+\left(\dfrac{\kappa_\sigma}{\sqrt{2\kappa_\sigma^2 + \tau_\sigma^2}} + \dfrac{\sqrt{2}v\phi}{(\lambda_1^2 + \lambda_2^2 + \lambda_3^2)^{\frac{3}{2}}(2\kappa_\sigma^2 + \tau_\sigma^2)^2}\right)\vec{N}_\sigma \\
+\left(\dfrac{\tau_\sigma}{\sqrt{2\kappa_\sigma^2 + \tau_\sigma^2}} + \dfrac{\sqrt{2}v\psi}{(\lambda_1^2 + \lambda_2^2 + \lambda_3^2)^{\frac{3}{2}}(2\kappa_\sigma^2 + \tau_\sigma^2)^2}\right)\vec{B}_\sigma
\end{cases},
$$

$$
X_v = B_\alpha = \frac{[\kappa_\sigma\lambda_3 - \tau_\sigma\lambda_2]\vec{T}_\sigma + [\kappa_\sigma\lambda_3 + \tau_\sigma\lambda_1]\vec{N}_\sigma - \kappa_\sigma[\lambda_1 + \lambda_2]\vec{B}_\sigma}{\sqrt{\lambda_1^2 + \lambda_2^2 + \lambda_3^2}\sqrt{2\kappa_\sigma^2 + \tau_\sigma^2}}.
$$

The components of the first and the second fundamental forms are obtain

$$
\begin{cases}
E = 1 + \dfrac{2v^2(\omega^2 + \phi^2 + \psi^2)}{(\lambda_1^2 + \lambda_2^2 + \lambda_3^2)^3(2\kappa_\sigma^2 + \tau_\sigma^2)^4}, \\
F = 0 \\
G = 1,
\end{cases}
$$

and

$$
\begin{cases}
e = \dfrac{\begin{aligned}
&[\lambda_1(\lambda_1^2 + \lambda_2^2 + \lambda_3^2)^3(2\kappa_\sigma^2 + \tau_\sigma^2)^{\frac{5}{2}} + vb_1]u_1 \\
&+[\lambda_2(\lambda_1^2 + \lambda_2^2 + \lambda_3^2)^3(2\kappa_\sigma^2 + \tau_\sigma^2)^{\frac{5}{2}} + vb_2]u_2 \\
&[\lambda_3(\lambda_1^2 + \lambda_2^2 + \lambda_3^2)^3(2\kappa_\sigma^2 + \tau_\sigma^2)^{\frac{5}{2}} + vb_3]u_3
\end{aligned}}{(\lambda_1^2 + \lambda_2^2 + \lambda_3^2)^3(2\kappa_\sigma^2 + \tau_\sigma^2)^{\frac{9}{2}}}, \\[2em]
f = \dfrac{-\sqrt{2}(\lambda_1\omega + \lambda_2\phi + \lambda_3\psi)}{(\lambda_1^2 + \lambda_2^2 + \lambda_3^2)^2(2\kappa_\sigma^2 + \tau_\sigma^2)^2\sqrt{E}}, \\[1em]
g = 0
\end{cases}
$$

respectively, where u_1, u_2, u_3 are components of the $U(s,v)$ unit normal vector of $X(s,v)$ defined by (10). Making use of the data described above in (8) and (9) the Gauss curvature K and mean curvature H are obtain.

EXAMPLE

Let $\vec{\sigma}(s)$ be unit speed curve in E^3 defined by

$$\sigma = \vec{\sigma}(s) = (\cos s, \sin s, s). \tag{15}$$

See in Figure 1.
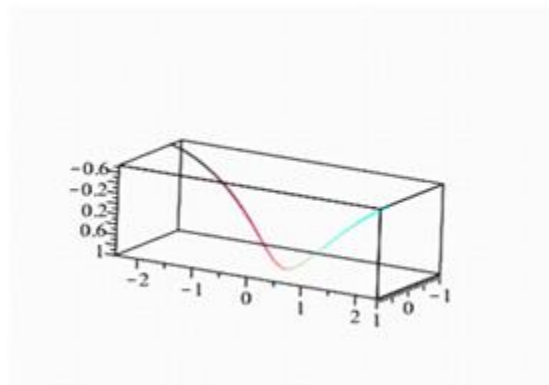
Figure 1. The curve $\sigma = \vec{\sigma}(s)$

One can calculate its Frenet-Serret apparatus as the following

$$\vec{T}(s) = (-\sin s, \cos s, 1),$$
$$\vec{N}(s) = (-\cos s, -\sin s, 0),$$
$$\vec{B}(s) = (\sin s, -\cos s, 0).$$

140

TN-Smarandache curve of $\vec{\sigma}(s)$ curve in (15) is defined by

$$\alpha(s_\alpha) = \frac{1}{\sqrt{2}}(T(s)+N(s)) = (\frac{-\sin s - \cos s}{\sqrt{2}}, \frac{\cos s - \sin s}{\sqrt{2}}, \frac{1}{\sqrt{2}}).$$

The tangent vector of the curve α can be written as follows

$$\alpha^{'} = \frac{d\alpha}{ds_\alpha}\frac{ds_\alpha}{ds} = (\frac{-\cos s + \sin s}{\sqrt{2}}, \frac{-\sin s - \cos s}{\sqrt{2}}, 0) \tag{16}$$

and hence

$$T_\alpha = \frac{d\alpha}{ds_\alpha}\frac{ds_\alpha}{ds} = (\frac{-\cos s + \sin s}{\sqrt{2}}, \frac{-\sin s - \cos s}{\sqrt{2}}, 0),$$

where

$$\left\langle T_\alpha \frac{ds_\alpha}{ds}, T_\alpha \frac{ds_\alpha}{ds} \right\rangle = 1 \Rightarrow \frac{ds_\alpha}{ds} = 1.$$

Thus, we have

$$N_\alpha = (\frac{\sin s + \cos s}{\sqrt{2}}, \frac{-\cos s + \sin s}{\sqrt{2}}, 0), \tag{17}$$

$$B_\alpha = T_\alpha \wedge N_\alpha = (0,0,1).$$

Thus, we obtain the following binormal surface

$$X(s,v) = \alpha + vB_\alpha = (\frac{-\sin s - \cos s}{\sqrt{2}}, \frac{\cos s - \sin s}{\sqrt{2}}, \frac{1}{\sqrt{2}} + v). \tag{18}$$

with TN-Smarandache curve of $\vec{\sigma}(s)$.
See in Figure 2.
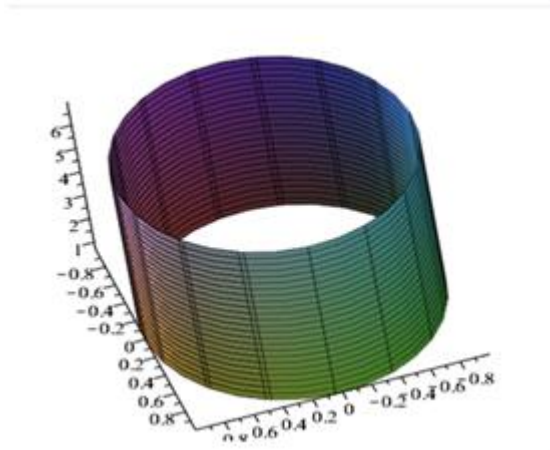
Figure 2. Binormal surface

From (18), we have

$$X_s = (\frac{-\cos s + \sin s}{\sqrt{2}}, \frac{-\sin s - \cos s}{\sqrt{2}}, 0),$$

$$X_v = (0,0,1),$$

$$X_{ss} = (\frac{\sin s + \cos s}{\sqrt{2}}, \frac{-\cos s + \sin s}{\sqrt{2}}, 0),$$

$$X_{vv} = 0,$$

$$X_{sv} = 0.$$

141

The components of the first and second fundamental forms are obtain

$$\begin{cases} E = 1, \\ F = 0, \\ G = 1 \end{cases}$$

and

$$\begin{cases} e = -1, \\ f = 0, \\ g = 0 \end{cases}$$

respectively.

Thus, the striction curve $\gamma(s)$, distribution parameter P and mean curvature H of $X(s,v)$ defined by (18) as follows

$$\gamma(s) = \alpha - \frac{\left\langle \alpha^{'}, B_{\alpha}^{'} \right\rangle}{\left\langle B_{\alpha}^{'}, B_{\alpha}^{'} \right\rangle} B_{\alpha}$$

Substituting (16) and (17) values in above equation, we have

$$\left\langle \alpha^{'}, B_{\alpha}^{'} \right\rangle = 0 \Rightarrow \gamma(s) = \alpha.$$

Therefore, the striction curve is the base curve of $X(s,v)$ defined by (18).

$$P = \frac{\det(B_{\alpha}, B_{\alpha}^{'}, \alpha^{'})}{\left\| B_{\alpha}^{'} \right\|^{2}}$$

Substituting (16) and (17) values in above equation, we have

$$P = 0.$$

Thus, $X(s,v)$ defined by (18) is developable.

$$H = \frac{Ge}{2(EG - F^{2})} = \frac{-1}{2}.$$

$X(s,v)$ defined by (18) is not the minimal surface.

REFERENCES

[1] A.T. Ali, Special Smarandache curves in Euclidean space, Int. J. Math. Combin. 2 (2010) 30-36.

[2] G.Ş. Atalay, E. Kasap, Surfaces family with common Smarandache geodesic curve according to Bishop frame in Euclidean space, Math. Sciences and Applications E-Notes 4 (2016) 164-174.

[3] M. Çetin, Y. Tuncer, M.K. Karacan, Smarandache curves according to Bishop frame in Euclidean 3-space, Gen. Math. Notes 20 (2014) 50-66.

[4] A. Gray, E. Abbena, S. Salamon, Modern Differential Geometry of Curves and Surfaces with Mathematica®. *Chapman & Hall/CRC, Boca Raton, FL.* 2006.

[5] H.H. Hacısalihoğlu, Diferensiyel Geometri Cilt II, Ankara Üniversitesi Yayınları. 2000.

[6] S. Izumiya, N. Takeuchi, Singularities of ruled surfaces in R-3, Math. Proceedings of Cambridge Philosophical Soc. 130 (2001) 1-11.

[7] A. Saxena, B. Sahay, Computer Aided Engineering Design, Springer, 2005.

[8] T. Shifrin, Differential Geometry: A first course in curves and surfaces. Preminary Version, 125 pp. University of Georgia, 2011

[9] S. Şenyurt, S. Sivas, Smarandache eğrilerine ait bir uygulama, Ordu Üniversitesi Bilimsel Teknik Dergisi 3 (2013) 46-60.

[10] S. Şenyurt, A. Çalışkan, Smarandache curves of Mannheim curve couple according to Frenet frame, Mathematical Sciences and Applications E-Notes 5 (2017) 122–136.

[11] M. Turgut, S. Yılmaz, Smarandache curves in Minkowski space-time, Int. J. Math. Combin. 3 (2008) 51-55.

[12] A. Yılmaz, Doğru Kongrüansları ve Geometrik Modellemesi, Ege Üniversitesi Fen Bilimleri Enstitüsü, Doktora Tezi, 2018.

Medicinal Plants Hold the Future of Drug Discovery

Jonathan Kulah, University of Liberia, College of Science and Technology, Biological Science,
Capitol Hill Monrovia, 9020 Montserrado Liberia
jnkulah11@gmail.com

Abstract

This study aims at calling the attention of pharmaceutical researchers to the significance of medicinal plants, and how they might be utilized in the discovery of new drugs. One of such plants is the *Moringa oleifera*. Previous research finding has established it as one of the indispensable medicinal plants capable of responding to many health cases. Additionally, this study establishes Targeted Drug Delivery Systems (TDDS) as a means of increasing the efficiency and effectiveness of possible drug molecules. Moreover, some challenges associated with medicinal plants are identified, with proposed plausible solutions, in the hope that the global network of herbal scientists would pursue further projects in order to produce drugs from these plants and apply them in a more efficient way to maximizing TDDS.

Keywords: medicinal plants, herbalism, herbs, *Moringa oleifera*, Targeted Drug Delivery System (TDDS)
Discipline: Molecular Biology, Pharmaceutical Plants/Drug Discovery

INTRODUCTION

Medicinal plants hold great potential for future drug discovery in the global health sector. Medicinal plants are species used in herbalism for health purposes. Such plants contain compounds and molecules that pharmaceutical drugs use or mimic, and they ease the symptoms of or cure diseases or sicknesses [1]. The use of medicinal plants dates far back to the primitive age when there were no form of formal medical establishments or hospitals. The use of medicinal plants has advanced through the ages; particularly in Africa, Asia and South America. During times of health disasters such as plagues or wars, wounded warriors or sick civilians were treated using herbs. Currently about 80% of the world's total population utilizes herbal treatment. For example 65% of India's rural population, about 40% of China's healthcare, 71% of Chile's population, and 40% of Columbia's population rely on such treatments [1].

More than 65% of children in Ghana, Mali, Nigeria, Zambia, Liberia and many other African countries regularly use tea, ginger or mint to treat common flu. They also use herbs and other plants for the primary treatment of high fever, diarrhea, dysentery, ulcer, jaundice, elephantiasis, and snake bites. A recent study conducted in Ghana West Africa showed that 52 species of plants belonging to 28 plant families were used for the successful treatment and management of 42 diseases and ailments. [2]. Medicinal plants were commonly harvested from the soil and prepared in the form of decoctions (67%) and infusions (33%). Oral administration of the herbals was the most common (77%) route of administration whereas the least used routes were nasal (1%) and rectal (2%) [2].

Among the many medicinal plants used today, *Moringa oleifera* (Figure 1) is notable because it contains 92 nutrients, 46 natural antioxidants, several anti-inflammatory compounds and has the ability to treat more than 300 known diseases. *Moringa oleifera* very rich in vitamins and serves beyond medical boundaries in that it is maximized economically for cosmetic uses and is drought resistant, growing in tropical and subtropical regions of the world [3]. *Moringa oleifera* like many other plants, holds high probability for reducing the spread of cancer as well as sustaining the lives of people living with HIV/AIDS [4]. It is one of the plants used in the targeted drug delivery system.

Targeted drug delivery system is a special system for delivering a drug selectively to a specific targeted site of action. It involves the use of a carrier system/engineered vector (nanoparticles, polymers, liposomes, microcapsules etc.), a targeting molecule (proteins, antibodies, hormones, etc) and a drug molecule. In the simplest terms, this drug delivery system aims at improving efficiency, reducing side effects, increasing drug concentration at required sites without interaction with other organs/tissues achieving better pharmacological response [5].

Figure 1. *Moringa oleifera* leaves

MATERIALS AND METHODS

According to Aja et al. [6], extracts from *Moringa oleifera* were obtained by the following procedures and materials:

Firstly, the *Moringa oleifera* plant (leaves and seeds) were gathered from Abakaliki Area and identified by taxonomist from the Department of Applied Biology at Ebonyi State University. Some of the leaves and seeds were stored for future research and reference purposes. Next the leaves were destalked, washed with distilled water and allowed to dry as well as the dehusked seeds. With a time interval enough to avoid fungal growth on one side, the leaves and seeds were turned. After drying, the leaves and seeds were separately milled in an electric blender and stored in a labeled airtight container at 4°C in a refrigerator. In order to prepare the extracts, 40 g of dried MO leaves and seed powder was mixed with 300ml methanol in an orbital shaker for 24h at room temperature. Using Whatman No. 1 filter paper, the aqueous solution was filtered to remove undesired solid substances at 3h interval. Using a rotary evaporator, liquid from the combined extracts was evaporated, dried and stored at 4°C in two different sterile containers [6].

Although specific chemical composition of the *Moringa oleifera* extracts were not further analyzed, theorectically, the crude extracts can be dissolved in Dichloromethane (DCM). Thin Layer Chromatography (TLC) (as shown in Figure 2) along with UV light can be utilized to analyze active chemical agent present. Then the active chemicals can be separated with Column Chromatography using silica gel in DCM solvent as shown in Figure 3 [7].

Figure 2. Ideal labeled Thin Layer Chromatography (TLC).

Figure 3. Column Chromatography using Selica gel and DCM solvent.

RESULTS AND DISCUSSION

Based on Vergara-Jimenez et al. [8] the bioactive components from *Moringa oleifera* extracts can be predicted to contain:

- Vitamins: Vitamin A, Vitamin C and Vitamin E
- Polyphenol: Flavonoids [myrectin (5.8mg/g), quercetin (0.207mg/g) and kaempferol (7.57mg/g)], Phenolic acids, Chlorogenic acid (CGA)
- Alkaloids, Glucosinolates and Isothiocyonates
- Tannins (13,2-20.6g/kg *Moringa oleifera* leaves)
- Saponins (64-81g/kg *Moringa oleifera* leaves)

Moringa oleifera has been reported to have many effects on the prevention of chronic diseases, including [8];

- Antioxidant effect; having beta-carotene and due to high antioxidant present and redox property, can be used to treat cancer, hypertension, cardiovascular diseases and other inflammatory conditions.
- Anti-inflammatory and immunomodulatory effect
- Anti-Hyperglycemic (Antidiabetic) Effect
- Anticancer effect; Moringa oleifera extracts were reported to protect organism and cell from oxidative DNA damage, increasing the efficacy of chemotherapy
- Hypolipidemic effects; lipids regulation, reducing cholesterol utilizing flavonoids, Saponins etc.
- Hypotensive effects; niazinin A, niazinin B, niazimicin and niazinin A + B isolated from Moringa oleifera leaves extracts reportedly showed blood pressure lowering effect in rats.

Table 1 shows compounds that can be extracted from *Moringa oleifera*, their postulated function, model organism that were used for different disease(s) [8].

Table 1. Bioactive Components in *Moringa Oleifera* and their Positive Effects on Chronic Disease.

Compounds	Postulated Function	Model Used	Disease Protection
Flavonoids: Quercitin	Hypolipidemic and anti-diabetic properties	Zucker rat	Diabetes
	Lower hyperlipidemia	Rabbits	Atherosclerosis
	Decrease expression of DGAT	Guinea Pigs	NAFLD
	Inhibition of cholesterol esterase and α-glucosidase	In vitro study	Cardiovascular disease and Diabetes
	Inhibits activation of NF-kB	High fat fed Mice	Cardiovascular disease
Chlorogenic Acid	Glucose lowering effect	Diabetic rats	Diabetes
	Cholesterol lowering in plasma and liver	Zucker rat	Cardiovascular disease
	Decrease expression of CD68, SERBP1c	Guinea pigs	NAFLD
	Anti-obesity properties	High-fat induced obesity rats	Obesity
	Inhibit enzymes linked to T2D		Diabetes
Alkaloids	Cardioprotection	Cardiotoxic-induced rats	Cardiovascular disease
Tannins	Anti-inflammatory	Rats	Cardiovascular/Cancer
Isothiocyanates	Decreased expression of inflammatory markers	RAW Macrophages	Cardiovascular disease
	Reduction in insulin resistance	Mice	Diabetes
	Inhibition of NF-kB signaling	Cancer breast cells	Cancer
B-Sitosterol	Decrease cholesterol absorption	High-fat fed rats	Cardiovascular disease

CONCLUSION

Conclusively, out of the many examples of medicinal plants, *Moringa oleifera* is used as potential antioxidant, anticancer, anti-inflammatory, antidiabetic and antimicrobial agent. *Moringa oleifera* is reported to have 7 times more vitamin C than oranges, 10 times more vitamin A than carrots, 17 times more calcium than milk, 9 times more protein than yoghurt, 15 times more potassium than bananas and 25 times more iron than spinach. Additionally, beyond medical studies *Moringa oleifera* is used economically for cosmetic and oleic oil produced from the seeds [3].

Due to technological advancements, and very minimum collaboration efforts between herbal scientists and traditional herbal doctors, the knowledge of most traditional herbalists who treat patients with these medicinal plants is gradually fading away. Also, the challenge associated with the unregulated usage of these herbs has been of major concern globally, as it poses danger to the increase in health risk and side effects associated with overdose, toxicity and poisoning. Researchers need to get more involved in understanding medicinal plants for drug discovery so as to provide dosage regulations and assist traditional herbalists in more significant ways; and thereby improve their drug testing methods as well.

One major advantage of the use of medicinal plants by scientists in recent decades is that it has significantly reduced the ethical challenge of the use of humans for drug testing. Most importantly, with the utilization of Targeted Drug Delivery System, the therapeutic index, specification, efficiency and effectiveness of existing drugs as well as potential newly synthesize drugs from medicinal plants can be increased [5]. Therefore it is safe to state that in order to improve both diet and drug discovery with less side effect, researchers and scientists should consider medicinal plants in line with targeted drug delivery system.

REFERENCES

[1] A. Sofowora, Medicinal plants and traditional medicine in Africa. John Wiley and Sons Ltd, 1982.
[2] A.A. Boadu, A. Asase, Documentation of herbal medicines used for the treatment and management of human diseases by some communities in Southern Ghana, Evidence-Based Complementary and Alternative Medicine, Article ID 3043061 (2017) 1-12.
[3] F. Anwar, S. Latif, M. Ashraf, A.H. Gilani, Moringa oleifera: a food plant with multiple medicinal uses. Phytotherapy Research 21 (2007) 17-25.
[4] T. G. Monera, C.C. Maponga, Prevalence and patterns of Moringa oleifera use among HIV positive patients in Zimbabwe: a cross-sectional survey. Journal of Public Health in Africa 3 (2012) e6.
[5] E. Gullotti, Y. Yeo, Extracellularly activated nanocarriers: a new paradigm of tumor targeted drug delivery, Molecular Pharmaceutics 6 (2009) 1041-1051.

[6] P.M. Aja, N. Nwachukwu, U.A. Ibiam, I.O. Igwenyi, C.E. Offor, U.O. Orji, Chemical constituents of Moringa oleifera leaves and seeds from Abakaliki, Nigeria. American Journal of Phytomedicine and Clinical Therapeutics 2 (2014) 310-321.

[7] V.A. Ogundele, O.E. Fadeyi, Isolation, characterization and derivatization of some bioactive components in Moringa oleifera leaves, Natural Products Chemistry & Research 3 (2015) 1-4.

[8] M. Vergara-Jimenez, M. M. Almatrafi, M.L. Fernandez, Bioactive components in Moringa oleifera leaves protect against chronic disease, Antioxidants 6 (2017) 91.

Gemi Sevk Sistemlerinde Dinamik Etki Arttırma Kütlesi (DEAK) Etkisinin İncelenmesi

Şevki Akkoca*, Süleyman Murat Bağdatlı
Manisa Celal Bayar Üniversitesi, Makine Mühendisliği Bölümü,
Şehit Prof. Dr. İlhan Varank Kampüsü, Manisa, Türkiye
*İletişimden sorumlu yazar: sevkiakkoca@gmail.com, murat.bagdatli.cbu.edu.tr

Özet

Bu çalışmada, bir gemi sevk sistemine ait pervanenin su içindeki polar kütle atalet momenti (J_P) değerinin dikkate alınmadan, bahse konu sistemin tasarımının gerçekleştirilmesi durumunda, makinenin teorik olarak hesaplanan işletme devirlerinde oluşabilecek rezonans etkileri araştırılmıştır. Yukarıda belirtilen nedenle, gemi sevk sisteminde meydana gelebilecek rezonans etkisinin ortadan kaldırılması maksadıyla, Dinamik Etki Arttırma Kütlesi (DEAK) olarak kullanılan J_d kütle atalet momentine sahip bir disk, pervane ile redüktör arasına yerleştirilmiştir. DEAK'ın eklenmesi ile, sistemin doğal frekansları değiştirilmiştir. Bu değişiklik sayesinde, sistemin rezonans frekansın da titreşim hareketi yapmasının önüne geçilmiştir.

Anahtar Kelimeler: burulma, güç aktarma organları, gemi, redüktör, şaft, titreşim
Disiplin: Makina Mühendisliği

GİRİŞ

Günümüzde deniz ulaşımda kullanılan deniz araçlarının hareket etmesini makine ile pervane arasındaki şaft ve redüktör sisteminin çalışması sağlamaktadır. Bahse konu gemi sevk sistemlerinin tasarımlarında pervanenin su içindeki polar kütle atalet momenti (J_P) değerinin dikkate alınmadan yapılması durumunda makinenin teorik olarak hesaplanan işletme devirlerinde rezonans etkilerinden kaynaklı titreşimden dolayı aktarma ve taşıma sistemlerinde yağ kaçırma, aşınma, şaft yataklanma sorunları vb. arızaların meydana gelmesine neden olabilmektedir. Bu nedenle, gemi çalışmaya başladıktan sonra alınacak önlemlerin uygulanması hem daha zor hem de maliyetli olması sebebiyle gemi inşa esnasında teorik ve deneysel çalışmalar yapılmaktadır. Bu çalışmalar ana makine, yardımcı makinelerde, pervane titreşim analizi üzerine olduğu gibi yapısal titreşim analizlerini de içermektedir. Gemide titreşim analizinin gerekli olduğu sistemlerden biri de şaft sistemidir. Şaft titreşimleri ile ilgili çok çeşitli çalışmalar mevcuttur. Alarçin ve Korkmaz [1], çalışmalarında, gemi ana makine şaft sisteminde titreşimlerin yoğun olarak görüldüğü ekipmanları dikkate alarak meydana gelen titreşimlerin analizini yapmıştır. Referans aldıkları bir gemi modeline ait ana makine şaft pervane bilgilerini dikkate alarak şaft ve pervane üzerindeki burulma ve eksenel titreşimleri incelemişlerdir. Özgen [2], bir elektrik motoru, iki kanatlı bir pervane ve motordan aldığı döndürme momentini pervaneye ileten iki yerden yataklı, içi dolu, tek kademeli bir şaftan oluşan sevk sistemi modelinin doğal frekanslarını, diferansiyel denklem çözümüne dayanan analitik yöntemle ve nümerik yöntemlere dayanan yaklaşık çözümle çözümlemiştir, çalışmasında daha sonra ivmeölçer ile ölçüm yaparak analitik ve nümerik yöntemlerle bulunan frekansları karşılaştırmıştır. Ünsan ve İnsel [3], yaptıkları çalışmalarında, gemi seyir tecrübelerinde şaft yataklarından ivmeölçer yardımı ile titreşim ölçümleri alınmasını ve titreşim analizi yapılmasının önemi vurgulamıştır. Hara, Furukawa ve Andshoda [4], Building Block yaklaşımı kullanarak ana makine ve şaft sisteminin titreşim analizini yapmıştır ve referans aldıkları gemiye ilişkin titreşim ölçümü verileri ile karşılaştırılmıştır. Maurice [5], eserinde, makine gücünün aktarılmasını sağlayan mil ve benzeri dönen parçalarda oluşan burulma titreşiminin hesaplamalarının nasıl yapılacağını göstermiştir. Tahralı [6], eserinde, şaft,mil ve redüktörden oluşan farklı serbestlik derecelerindeki sistemlere ait burulma titreşimlerinin matematik modellemelerini yaparak doğal frekanslarını hesaplamıştır. Yapılan çalışmalardan da görüleceği üzere, mühendislik mekaniğinin günümüzü uğraştıran dinamik problemlerden en önemlilerinden birisi titreşimdir. Makine mühendislerince yapılan çalışmaların amacı, bu istenmeyen titreşimin ortadan kaldırılması veya zararsız hale getirilmesidir.

2nd International Students Science Congress
4-5 May 2018, Izmir - Turkey

İZMİR
Uluslararası
Misafir
Öğrenci
Derneği
◆ İZMİR International Guest Student Association

İZMİR
KÂTİP ÇELEBİ
UNIVERSITY
2010

Bu çalışmada, Şekil 1'deki gemi sevk sisteminde meydana gelebilecek rezonans etkisinin ortadan kaldırılması maksadıyla, Dinamik Etki Arttırma Kütlesi (DEAK) olarak kullanılan J_0 kütle atalet momentine sahip bir disk, pervane ile redüktör arasına yerleştirilmesi suretiyle sistemin doğal frekanslarının parametrik hesaplamaları yapılmıştır.
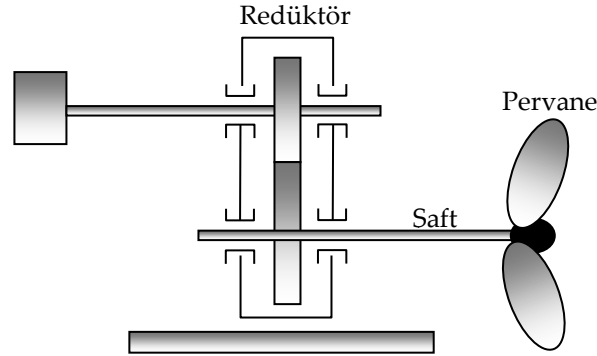
Şekil 1. Motor, redüktör sistemi, şaft ve pervane parçalarından oluşan gemi sevk sistemi modeli

GEMİ TAHRİK SİSTEMİNİN MODELLENEREK İRDELENMESİ

Şekil 1'deki modelde, tek bir ana makineye bağlı pervane şaftındaki serbest burulma titreşimleri incelenmiştir. Burada j_P değeri, pervane kütle atalet momentine eşit olarak ele alınmıştır. $k_{beş}$ değeri redüktöre kadar olan pervane milindeki her bir yay katsayılarının pervane miline indirgenmesi ile elde edilmiştir. Genel olarak büyük kütle atalet momentli elemanlar, küçük salınımlar ile titreşim yaparlar. Küçük kütle atalet momentli elemanlar ise büyük salınımlar ile titreşim yaparlar. Burada pervanenin kütle atalet momenti büyük olmasına rağmen, sistemde meydana getirdiği titreşimlerin belirlenebilmesi maksadıyla şekil 1'deki modelin Şekil 2'deki matematik modeli verilmiştir.
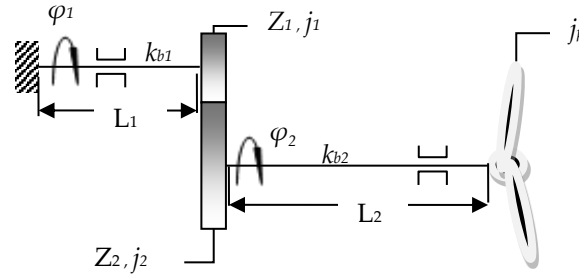
Şekil 2. Gemi sevk sistemine ilişkin matematik model
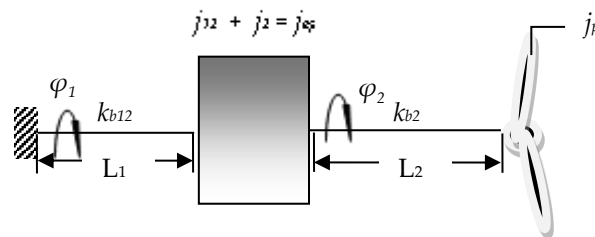
Şekil 3. 2.mile (pervane şaftı) indirgemesi yapılmış matematik model
(kütle atalet momentleri toplanmış $=j_{eş}$)

k_{b12}, k_{b2}: Buralma Yay Sabiti $\left[Nmm/radyan\right]$

φ_1, φ_2: Burulma Açısı $\left[radyan\right]$

$j_{eş}$, j_p: Kütle Atalet Momenti $\left[kgmm^2\right]$

$$j_{eş}\ddot{\varphi}_1 = -k_{b12}\varphi_1 - k_{b2}\left(\varphi_1 - \varphi_2\right) \tag{1}$$

$$j_p\ddot{\varphi}_2 = -k_{b2}\left(\varphi_2 - \varphi_1\right) \tag{2}$$

$$\varphi_1 = Ae^{i(\omega t+\phi)} \qquad ve \qquad \varphi_2 = Be^{i(\omega t+\phi)} \tag{3}$$

Yukarıdaki (1) ve (2) denklemlerinin ortak çözümü yapılırsa aşağıdaki titreşim hareketine ilişkin doğal frekans (4) denklemi elde edilir.

$$\omega^4 - \left[\frac{k_{b12}+k_{b2}}{j_{eş}} + \frac{k_{b2}}{j_p}\right]\omega^2 + \frac{k_{b12}k_{b2}}{j_{eş}j_p} = 0 \tag{4}$$

Yukarıdaki parametrik denklemin çözümünden dört adet doğal frekans değeri elde edilir. Bu doğal frekans değerlerden birinin, makinenin teorik işletme devirleri ile çakışması durumunda rezonans etkisinden kaynaklanan arızalar meydana gelebilecektir. Bahse konu istenmeyen rezonans durumu gibi bir problem ile karşılaşılması durumunda, gemi sevk sistemi tasarımını baştan yapmak yerine bir J_d kütle atalet momentine sahip bir disk, pervane ile redüktör arasına yerleştirilebilmektedir. Eklenen bu kütleye Dinamik Etki Arttırma Kütlesi **(DEAK)** denir. DEAK eklenmiş Şekil 4'deki matematiksel modele ilişkin sistemin rezonans bölgesi aralıkları değişmektedir.
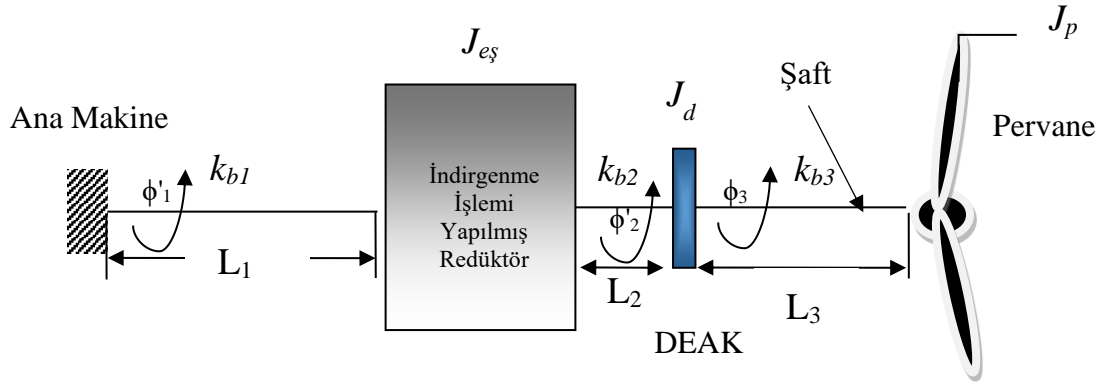
Şekil 4. DEAK eklenmiş gemi sevk sisteminin matematiksel modeli

$$j_{eş}\ddot{\varphi}'_1 = -k_{b12}\varphi'_1 - k_{b2}\left(\varphi'_1 - \varphi'_2\right) \tag{5}$$

$$j_d\ddot{\varphi}'_2 = -k_{b2}\left(\varphi'_2 - \varphi'_1\right) - k_{b3}\left(\varphi'_2 - \varphi'_3\right) \tag{6}$$

$$j_p\ddot{\varphi}'_3 = -k_{b3}\left(\varphi'_3 - \varphi'_2\right) \tag{7}$$

Yukarıdaki (5), (6) ve (7) denklemlerinin ortak çözümü yapılırsa aşağıdaki titreşim hareketine ilişkin doğal frekans (8) denklemi elde edilir.

$$\omega^6 - \left(\frac{k_{b12} + k_{b2}}{j_{e\c{s}}} + \frac{k_{b2} + k_{b3}}{j_d} + \frac{k_{b3}}{j_p} \right) \omega^4 + \left(\frac{\begin{array}{c} k_{b12}k_{b2} + k_{b2}k_{b3} + k_{b3}k_{b12} + \\ \hline j_{e\c{s}} \, j_d \end{array}}{} + \frac{k_{b2}k_{b3} + k_{b12}k_{b2}}{j_d \, j_p} + \frac{(k_{b12} + k_{b2})k_{b3}}{j_{e\c{s}} \, j_p} \right) \omega^2 - \frac{k_{b12}k_{b2}k_{b3}}{j_{e\c{s}} \, j_d \, j_p} = 0 \qquad (8)$$

Yukarıdaki parametrik denklemin çözümünden altı adet doğal frekans değeri elde edilir.

3. SONUÇ

Yukarıda yapılan parametrik hesaplamalardan anlaşılacağı üzere, gemi sevk sistemine ilişkin doğal frekans hesaplamaları yapılmadan tasarlanan ve montajı tamamlanan gemi sevk sistemlerinde büyük genliklerde burulma titreşimleri meydana gelmesi durumunda; uygun bir materyalden yapılmış dinamik damperin sevk sisteminin uygun bir yerine montajı yapılmak suretiyle, istenmeyen zararlı burulma titreşim problemlerinin çözülebileceği değerlendirilmektedir.

REFERANSLAR

[1] F. Alarçin, F.C. Korkmaz, Vibration analysis of ship main engine and shaft system, Journal of Engineering and Natural Sciences, Sigma 3 (2012) 310-319.

[2] O. Özgen, Pervane şaftı titreşim analizi, Yıldız Teknik Üniversitesi, FBE Gemi İnşaatı ve Gemi Makineleri Mühendisliği Ana Bilim Dalı, Yüksek Lisans Tezi, 2010.

[3] Y. Ünsan, M. İnsel, Gemi inşaatı sektöründe karşılaşılan problemin çözümü için yapılan tam ölçekli endüstriyel ölçümler ve örnekler, Harita ve Kadastro Mühendisleri Odası, Mühendislik Ölçmeleri STB Komisyonu, 2. Mühendislik Ölçmeleri Sempozyumu, İstanbul, 2005.

[4] T. Hara, T. Furukawa, K. Shoda, Vibration analysis of main engine shaft system by building block approach, Bulletin of the MESJ (1995) 77-81.

[5] M.L. Adams, Rotating Machinery Vibrations: From Analysis to Troubleshooting, CRC Press, New York, 2001.

[6] N. Tahralı, Makine Dinamiği Mekanik Titreşimler Çözümlü Problemler- 2. Fasikül: Burulma Titreşimleri, Eğitim Yayınları A.Ş., İstanbul, 1988.

Effects of Design Parameters in a Flux Modulated Magnetic Gearing System

Ahmed Mozamel*, Department of Mechanical Engineering, University of Nyala, Sudan
Kemal Yıldızlı, Department of Mechanical Engineering, Ondokuz Mayıs University, Turkey
Hakan Öktem, Department of Civil Aviation Electric and Electronics, Ondokuz Mayıs University, Turkey
Corresponding author: ahmadeiah@gmail.com

Abstract

In this paper, the effects of the design parameters of a flux modulated magnetic gearing system with emphasis on volume optimization are investigated. The flux modulated magnetic gearing system have been modeled and analyzed by using 2D finite element method (ANSYS Maxwell). The study is concerned with selection of an optimum volume of the rectangular shape elements as the variable parameters of magnetic gear system (Permanent magnets, flux modulators and air-gaps), by considering the width and length are fixed on the elements under study, and then optimizing the height length of the variable parameters. The effects of the design parameters on the magnetic flux densities, magnetic forces, magnetic torques and the magnetic energy distributions are discussed. The results show that, the maximum torques are affected by iron-segments volume, pole-pairs volume and air-gap thickness, the volume ratio ranges are obtained as follow: for the modulator the volume ratio $V_{iron-segment}/V_{pole-pair}$ can be ranged between $1\ to\ 1.5$, the permanent magnet pole-pair volume ratio $V_{pole-pair}/V_{iron-segment}$ can be laid between $1.4\ to\ 1.5$ and the minimum air-gap is between $0.25mm\ to\ 1.5mm$ height.

The ANSYS Maxwell model of a flux modulated magnetic gearing system considered on this study is consisting of an iron segments rotor which is held stationary, high speed rotor (inner rotor) connected to the input shaft and low speed rotor (outer rotor) connected to the output shaft. The stationary iron segments rotor would rigidly attach to the fixed cover. The high speed rotor attaches to the electric motor, while the low speed rotor rotates under magnetic dipole moment effects of a rate proportional to the gearing ratio $G_r = 3.5:1$.

Keywords: Magnetic gears, permanent magnet, flux density, magnetic torque density
Discipline: Mechanical Engineering

INTRODUCTION

Magnetic gearing can be designed almost for each mechanical gear type. However, there are only a few magnetic gear types (Flux modulated, harmonic and planetary magnetic gear) can demonstrate competitive torque capability against mechanical counterparts [1]. After a Neodymium Iron Boron magnet (NdFeB) have been developed in the 1980s, the magnetic gears technology has drastically improved in effectiveness and is therefore receiving increasingly more attention from industry and research institutions [2]. There are many researches has been published on magnetic gears is clearly indicates that, the flux modulated magnetic gear appear to be the most promising and the most likely magnetic gear topology to select to achieve success on the large scale magnetic gears. The flux modulated magnetic gear was proposed by Atallah in 2001 [3]. In recent years, there has been growing interest in the research of magnetic gears. This gear can realize equal magnetic pole coupling with different numbers of permanent magnet pole-pairs. Flux modulated magnetic gear adopts a coaxial topology and exceeds the limit of the traditional magnetic gears that adopt the parallel shaft; therefore, flux modulated magnetic gear significantly improves PM utilization rate [4]. Moreover, flux modulated magnetic gear can generate a high torque and a high torque density. It can be extensively used in the medical, vehicular, navigational, aerospace, and other fields because of its advantages, such as no contact between input and output shafts, high efficiency, free from lubrication, little noise, and inherent overload protection [5]. The wear, tear, chipping, micro pitting, noise, vibrations and tooth fracture are some kinds of failure occurs due to contact. By the use of magnetic gearing system the conventional failures can be reduced to great extent [3, 4, 6]. This paper aims to presents a geometrical optimization (volume) of some design parameters like the modulator volume (iron-segments), the permanent magnet

2nd International Students Science Congress
4-5 May 2018, Izmir - Turkey

İZMİR
KÂTİP ÇELEBİ
UNIVERSITY
2010

İZMİR
Uluslararası
Misafir
Öğrenci
Derneği
◆IZMIR International Guest Student Association

pole-pair volume and the air-gap volume, on a flux modulated magnetic gearing system. A geometrical optimization (volume) of the flux modulated design parameters is modeled and simulated using the finite-element method in order to investigate the best volume effects of the design parameters. The performance and magnetic topologies are evaluated to cover different heights of the modulator pieces, the permanent magnet pole-pairs and the air-gaps, since the width and length are considered to be fixed.

THE FLUX MODULATED MAGNETIC GEARING SYSTEM

The flux modulated magnetic gearing is mechanically least complex and can potentially realize both high torque density and high efficiency. Thus, it might be the magnetic gear technology that is closest to the commercial applications [7]. The flux modulated magnetic gearing appears to be one of the most promising magnetic gear designs. The magnetic gearing system shown in Figure 1, is composed of the inner rotor and outer rotor and fixed iron segments rotor, all the components are concentric, and the system has two air-gaps. The permanent magnet pole-pairs are positioned uniformly on the inner surface of the outer rotor and outer surface of the inner rotor. When the inner rotor runs, the magnetic flux of the permanent magnets field in the outer air-gap is modulated by an iron segments (fixed rotor) to rotate the outer rotor in opposite direction.
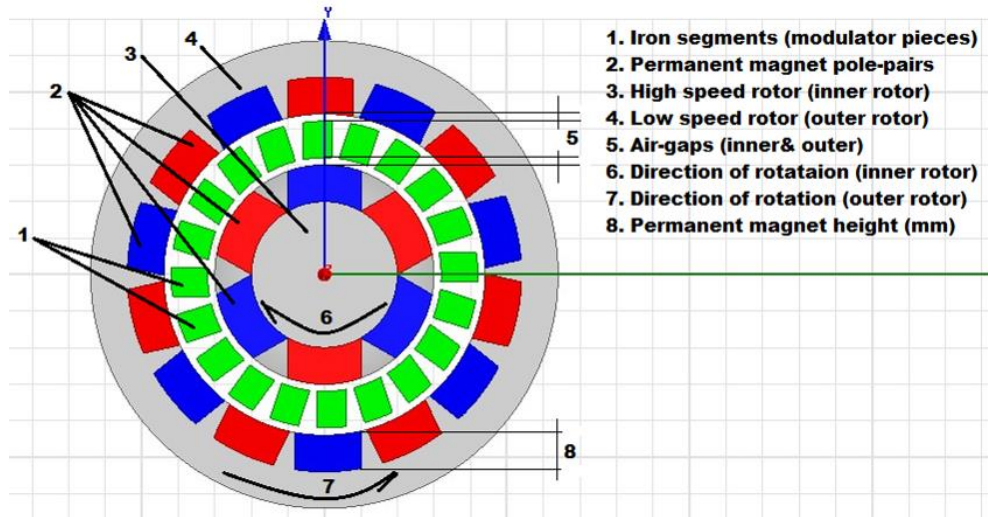
Figure 1. Flux modulated magnetic gearing components.

In a flux modulated magnetic gearing systems, the flux modulator is the key to the magnetic gearing effects. Mechanically the pole pieces on the modulator need to withstand strong magnetic forces exerted by both high speed and low speed PM rotors. Therefore, when choosing the number of pole pairs and modulator segments in the magnetic gear, it is desirable to choose suitable volume of iron segments related to the PM volume that capable to maintain strong magnetic fields. Considering the iron segments rotor is fixed, the specifications of two-dimensional finite element model of the system shown in Table 1 are generated. It can be shown that the numbers of pole-pairs on the inner rotor or outer rotor can be given by Equation 2 below [1]:

$$p_{ml} = |mp_h + kN_s| \tag{1}$$

where $m = 1,3,5,...$ and $k = 0, \pm1, \pm2, \pm3$, N_s is the number of iron segments of the modulator and p_{ml} is the number of magnetic pole-pairs on the outer rotor. To enable the flux modulated magnetic gear to work, the number of pole-pairs of the outer rotor p_l should be equal to p_{ml}. The largest asynchronous space harmonic is usually realized when $m = 1$ and $k = -1$.

$$N_s = p_h + p_l \tag{2}$$

153

The gear ratio (G_r) of a magnetic gear is governed by Equation 3. The selection of numbers of pole pairs and numbers of iron segments for realizing required gear ratios could have significant influence on the magnetic gears performance [8]. Magnetic gears therefore are somewhat limited in the range of gear ratios that are practically achievable. In addition, the number of pole pairs should be small to keep the fundamental frequency, and therefore the electromagnetic losses low [9].

$$G_r = \frac{N_s - p_h}{p_h} = \frac{\omega_h}{\omega_l} = -\frac{p_l}{p_h} \tag{3}$$

The relationship between the number of PM pole-pairs of the inner rotor and outer rotor, p_h and p_l, and the number of iron segments in the modulator Ns, and their respective angular velocity ω_h, ω_l and ω_m, is governed by the following equation [2,5,8]:

$$N_s \times \omega_m = \omega_h p_h + \omega_l p_l \tag{4}$$

DESIGN OF A FLUX MODULATOR

The objective of this study is to evaluate the effects of design parameters of a flux modulated magnetic gear system using a geometrical optimization (volume) in order to maximize the output torque and torque density of the magnetic gearing system. Ten promising iron-segments volume are $0.5\,mm, 1\,mm, 1.5\,mm, ..., 5\,mm$ heights with fixed air gap height of $1mm$. The length and width of the system of $40\,mm$ and $20\,mm$ respectively are considered to be fixed. The design specifications of the magnetic gear are determined as given in table 1.

Table 1. Design specifications

Specification	value	Unit
Gear ratio	3.5:1	-
Input speed (rpm)	3000	rpm
Remanence of (NdFeB) permanent magnets, Br (tesla)	1.25	tesla
Number of permanent magnets pole-pairs on inner rotor	3	-
Number of permanent magnets pole-pairs on outer rotor	7	-
Number of iron-segments pieces (modulator pieces)	10	-
Permeability for air regions	$4 \times \pi \times 10^{-7}$	Tm/A
Permanent magnet dimensions (length×width)	40×20	mm

Employing an optimum design parameters volume not only offering additional mechanical strength to the system, but also some performance benefits. It is possible to divide the design parameters (iron-segments, PM pole-pairs, air-gaps) into different volumes, by making the magnitude of length and width fixed, $40\,mm$ and $20\,mm$ respectively, while the value of height increases by $1\,mm$ height/ iteration for both iron-segments, PM pole-pairs and $0.25\,mm$ height/ iteration for the air-gaps. For this magnetic gearing design, analyzing 10 design models with various volumes of design parameters has been deemed to be sufficient. To investigate the effects, which expected to affect the performance of the magnetic gear topologies of a flux modulated magnetic gears, a $2D\,FE$ design is modeled and the simulation is run over $500\,ms$ with time steps of $20\,ms$.

As illustrated in Figure 1, the $2D\,FE$ design of a flux modulated magnetic gearing system, consists of an iron segments rotor which is held stationary, high speed rotor (inner rotor) connected to the input shaft and low speed rotor (outer rotor) connected to the output shaft. The stationary iron segments rotor would rigidly attach to the fixed cover. The high speed rotor attaches to the electric motor, while the low speed rotor rotates under magnetic dipole moment effects with a rate proportional to the gear ratio governed by Equation 3. During the working, the magnetic fields established by the two permanent magnet rotors are modulated by the iron segments fixed rotor, which is located in between these two

rotors to produce working field harmonics corresponding to the pole-pairs of each permanent magnet rotor. The magnetic flux travels radially from the permanent magnet, the S-pole on the inner rotor across the first air-gap to the iron segment modulator and then to the next permanent magnet on the outer rotor, with N-pole through the second air gap and then go back to the magnet with the S-pole to form a closed flux loop as shown in Figure 2 and Figure 3.
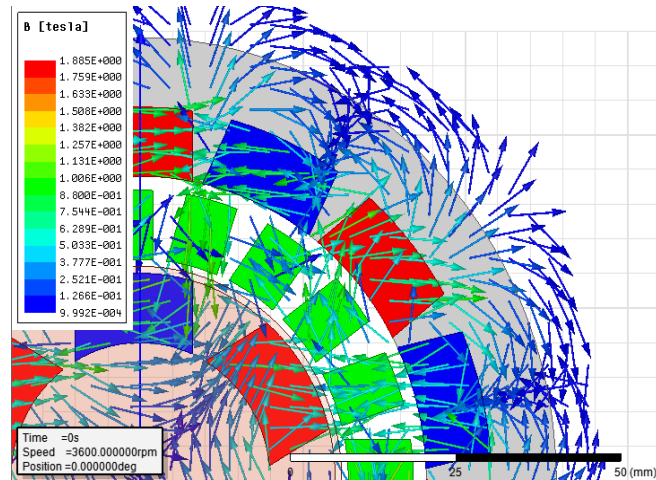

Figure 2. Magnetic flux vector topology

Figure 2 shows plots of the magnetic flux vector topology for the flux modulated magnetic gear system. The analysis also shows how the modulator pieces reverse the direction of rotation and guiding the flux density on the system. In addition to that, it represents the magnitude of magnetic flux densities.
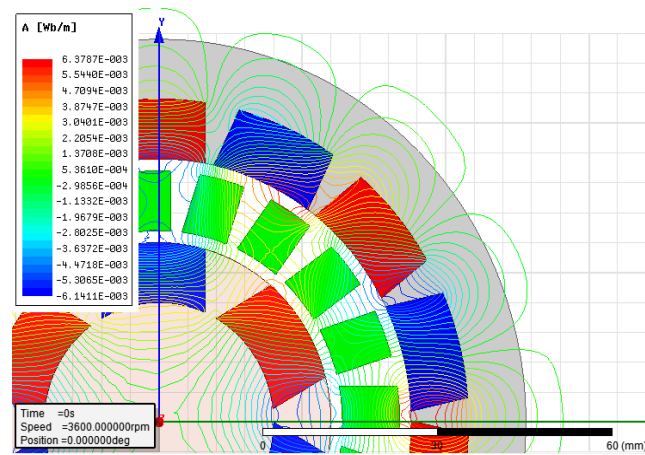
Figure 3. Magnetic flux lines topology

Figure 3 shows plots of the magnetic flux lines topology, it is the line where the magnetic force vectors acting tangent to the lines. High concentrations of lines in any region means strong magnetic field at that region.
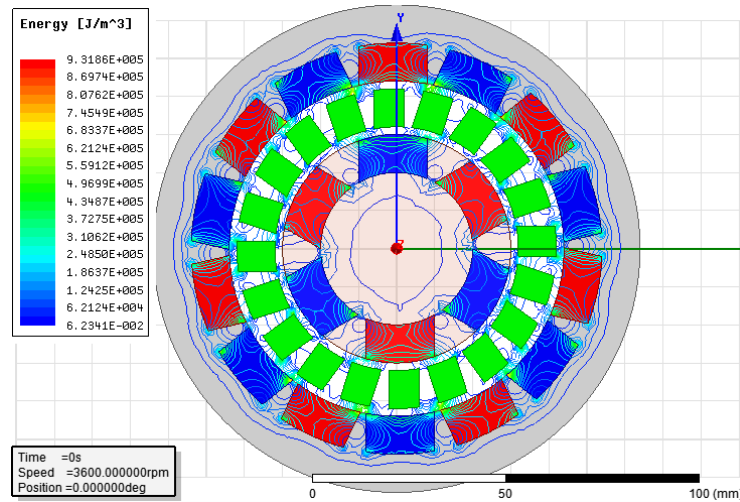
Figure 4. Magnetic energy lines topology

Figure 4 depicts the magnetic energy lines topology, where the potential energy of *PM* of magnetic moment, is defined as the mechanical work of magnetic force on realignment of the vector of the magnetic dipole moment. It shows that, the maximum magnetic energy concentrated at the permanent magnets corners.
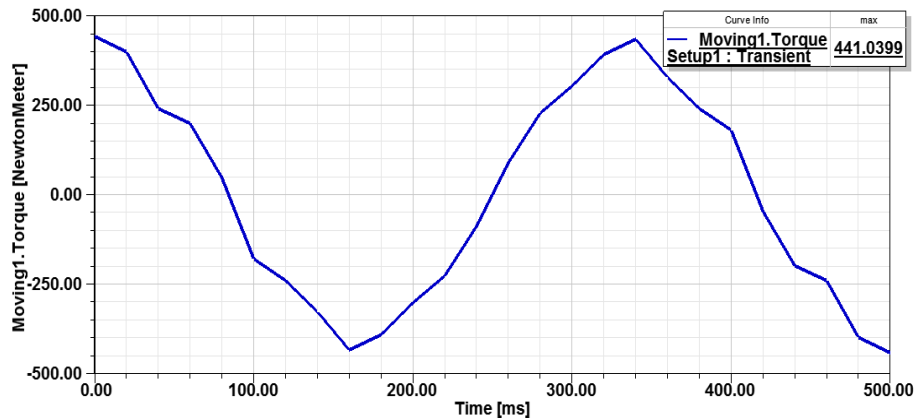
Figure 5. Magnetic transient torque

Figure 5 shows that, the output shaft transient torque change sinusoidally with time in (ms). The period of the transmitted torque waveform is 500 ms and maximum transmitted torque is 440 Nm.

ANALYSIS AND RESULTS

a. The Flux Modulator Volume Analysis

Figure 6 shows the flux modulator (iron-segment) volume analysis, which includes: (a) Magnetic flux, (b) Magnetic force, (c) Magnetic torque and (d) Magnetic energy. Since the magnetic pole-pair volume is assumed to be fixed, the maximum flux density and corresponding magnetic force, magnetic torque and magnetic energy increases with decreases the iron segment volume. The effect of the iron-segments (modulators) in Figure 6 (a, b and c) shows that, the significant results of magnetic flux, magnetic force and magnetic torque achieved related to the volume ratio $V_{iron-segment}/V_{pole-pair}$ rates are between $1\ to\ 1.5$ of the ratio, where the magnetic energy rapidly increases. Therefore, the torque decrease quickly with increases the modulator volume and then remains constant. Thus the field modulation presents satisfying magnetic torque acting on outer rotor.

(a)

(b)

(c)

(d)
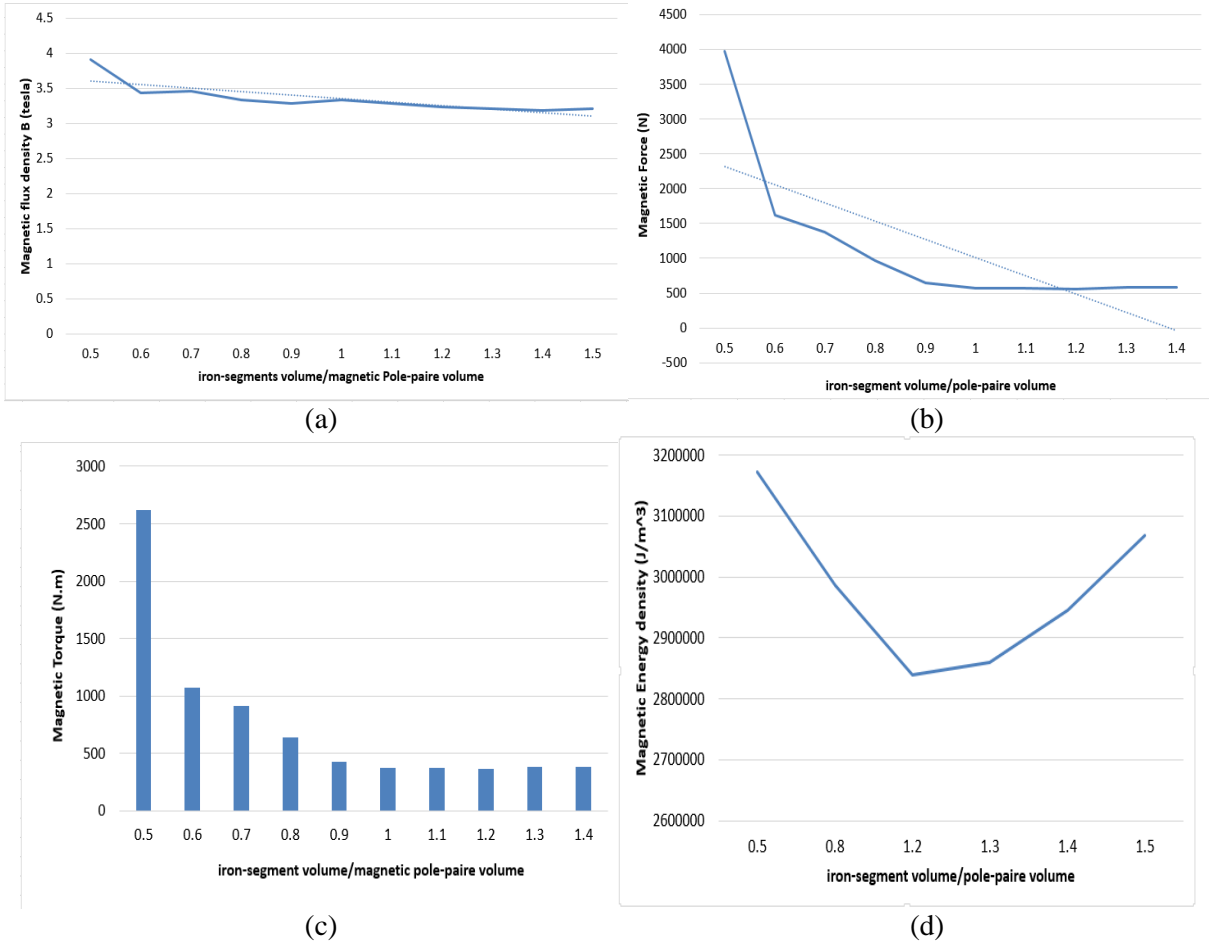
Figure 6. The flux modulator volume analysis:
(a) flux density, (b) magnetic force, (c) magnetic torque and (d) magnetic energy.

b. The Permanent Magnet Volume Analysis

Figure 7. Represent PM pole-pair volume analysis: (a) flux density, (b) magnetic force, (c) magnetic torque and (d) magnetic energy. The curves indicate that, with increases the PM pole-pair volume magnitude, the magnetic flux density, the magnetic force, the magnetic torque and magnetic energy gradually increases respectively. Meanwhile, the modulator volume remains unchangeable; therefore the corresponding magnetic flux, magnetic force, magnetic torque and magnetic energy increases proportionally with increases permanent magnet pole-pair volume to certain values and then the magnetic energy decreases as shown in Figure 7. (d), because of increases of magnetic flux leakages, to control that, the volume ratio $V_{pole-pair}/V_{iron-segment}$ must be laid between $1.4\ to\ 1.5$ in x coordinate. High performance level of PMs indicates that, better transmission capacity and better utilization rate of the PMs related to the optimum volume.
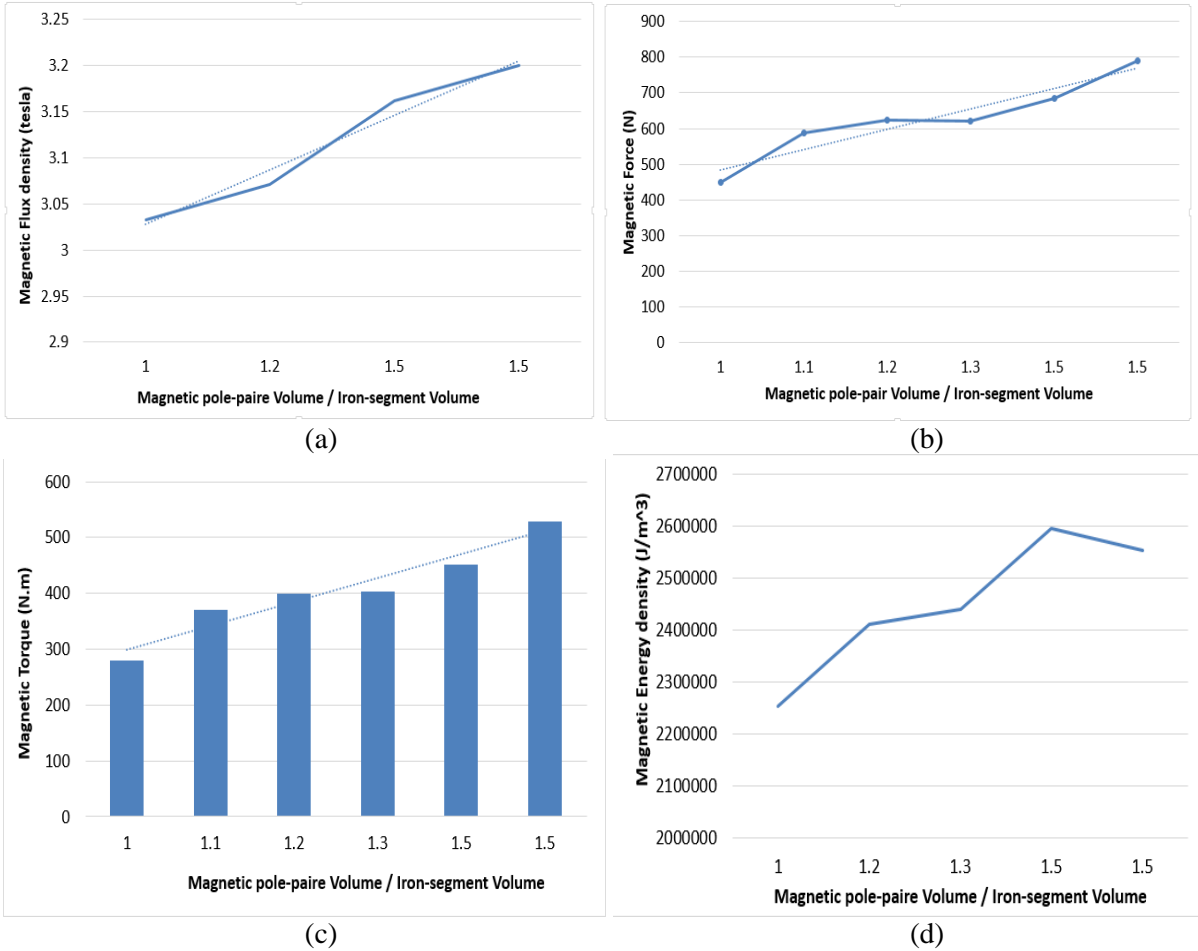
Figure 7. Permanent magnet volume analysis:
(a) flux density, (b) magnetic force, (c) magnetic torque and (d) magnetic energy.

c. Air-gap Volume Analysis

An air-gap is a nonmagnetic part of a magnetic circuit. It is usually connected magnetically in series with the rest of the circuit, so that a substantial part of the magnetic flux flows through the gap. An air-gap is a very essential design parameters part of any magnetic circuit in which there is a relative movement between different parts. The air-gap can take different form, shape and size depending on the type of magnetic circuit and its shape. In some design it might be large, or as small as possible. The smallest practical gap for industrial machines is around 0.2 mm [10]. Figure 8. (a, b, c and d), illustrated that, the maximum magnetic flux and corresponding magnetic force, magnetic torque and magnetic energy on the outer rotor air-gap increases gradually with decreases the air-gap (height). The coupling areas between the modulators and permanent magnets on the outer rotor, remains constant while examining the air-gap height from 0.25 mm to 2 mm in step of 0.25 mm/iteration, therefore, the torque reach equilibrium when the PMs thicken to a certain extent.
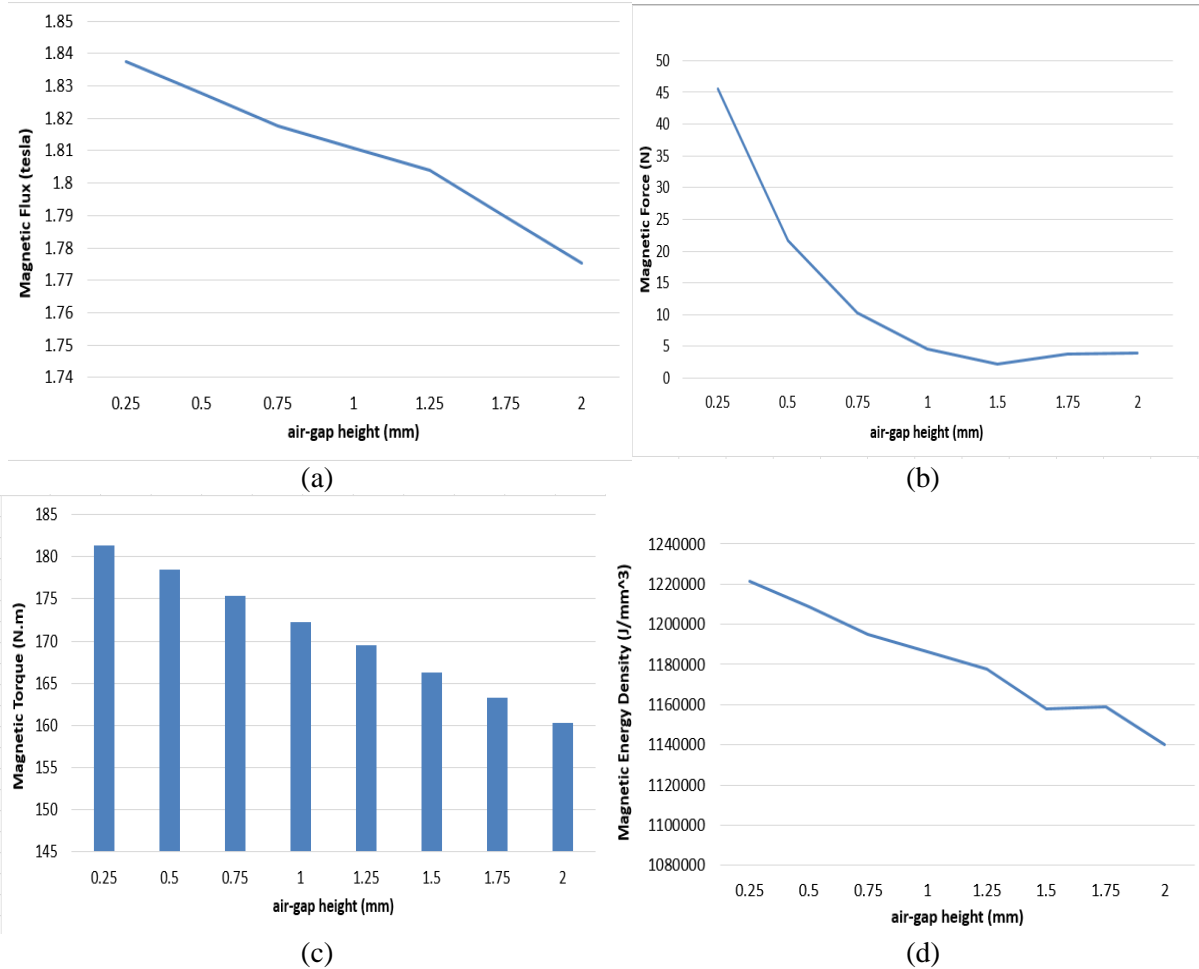
Figure 8. Air-gap volume analysis:
(a) flux density, (b) magnetic force, (c) magnetic torque and (d) magnetic energy.

CONCLUSIONS

This paper optimized the effects of some design parameters of a flux modulated magnetic gearing system by using FE analysis. Since the maximum torque and torque density of a flux modulated magnetic gearing system are evidently affected by design parameters, particularly the modulator volume, permanent magnet pole-pair volume and air-gap volume. By considering the length and width are fixed for the all components, the results show that, the optimum results obtained when the modulator volume ratio rates $V_{iron-segment}/V_{pole-pair}$ kept between $1\ to\ 1.5$ of the ratio, the PM pole-pair volume ratio rates $V_{pole-pair}/V_{iron-segment}$ laid between $1.4\ to\ 1.5$ of the ratio and the minimum air-gaps selected to be between $0.25\ mm\ to\ 1.5\ mm$ height. The magnetic torque decreases with increases the air-gap volume and modulator volume because of increasing the magnetic field losses. However, it is rapidly increase with increasing the permanent magnet volume.

REFERENCES

[1] A. Matthee, Development of a magnetic gear for dry-cooling power plant applications, Stellenbosch University, Master Thesis, 2017.
[2] F.T. Jørgensen, Design and construction of permanent magnetic gears, Department of Energy Technology, Aalborg University, 2010.
[3] X. Yin, Y. Fang, P.-D. Pfister, A novel single-PM-array magnetic gear with HTS bulks, IEEE Transactions On Applied Superconductivity 27 (2017)
[4] R.-J. Wang, A. Matthee, S. Gerber, P. Tlali, Effects of employing an iron segments in flux modulated magnetic gearing system, IEEE Magnetics Letters, 2016

[5] S. Gerber, R-J. Wang, Evaluation of a prototype magnetic gear, Industrial Technology (ICIT), 2013 IEEE International Conference, 2013

[6] A. Matthee, S. Gerber, R-J Wang, A high performance concentric magnetic gear, The 23rd Southern African Universities Power Engineering Conference (2015) 203-207.

[7] X-h. Hao, H-f. Zhang, J-d. Men, Electromechanical integrated magnetic gear, Advances in Mechanical Engineering 8 (2016) 1–14.

[8] Y-C. Wu, W-T. Tseng,Y-T. Chen, Torque ripple suppression in an external-meshed magnetic gear train, Advances in Mechanical Engineering, Article ID 178909 (2013) 1-7.

[9] K. Atallah, S.D. Calverley, D. Howe, High-performance magnetic gears, Journal of Magnetism and Magnetic Materials 272–276 (2004) e1727–e1729.

[10] X. Li, K-T. Chau, M. Cheng, W. Hua, Comparison of magnetic-geared permanent- magnet machines, Progress In Electromagnetics Research 133 (2013) 177-198.

İZMİR
KÂTİP ÇELEBİ
UNIVERSITY
2010

İZMİR
Uluslararası
Misafir
Öğrenci
Derneği
◆ İZMİR International Guest Student Association

Numerical Simulation of a Two-Dimensional Laminar Flow in a Tank with Heat Transfer

Mohamad Mehyo*, Ondokuz Mayis Univ., Dept. of Mechanical Engineering, Samsun, Turkey
Hesham AlRayess, Ondokuz Mayis Univ., Dept. of Civil Engineering, Samsun, Turkey
*Corresponding author: 15210438@stu.omu.edu.tr

Abstract

Applying the fundamental laws of mechanics to fluid gives the governing equation for a fluid. Partial differential equations are discretized into a system of algebraic equations. All algebraic equations are solved numerically to render the solution field. This equation is nonlinear partial differential equations because of that it is not possible to solve this equation analytically for most engineering problems. However, it is possible to obtain approximate computer-based solutions to the governing equations for a variety of engineering problems. One of CFD applications is a numerical analysis of two-dimensional flow with heat transfer in enclosures of importance in thermal science. Among numerical approaches for the analysis of mass flow and heat transfer. In this paper, the finite-volume method was used to study two-dimensional laminar flow in a tank with heat transfer. As a result of the deflectors, the flow describes a complex trajectory (due to obstacles). The simulations have been performed using the CFD Fortran 90 Coding. The system of formally linear algebraic equations consisting of the discretization equations of all domain nodes for any generic variable to which the general conservation equation, was solved by an iterative technique line-by-line, which is based on The SIMPLE (Semi-Implicit Method for Pressure-Linked Equations) algorithm. By taking the coarsest mesh (32, 22), adapting the program in order to perform a numerical simulation of the flow for the configuration and the conditions outlined previously. It was obtained which are presented, generated by the post-processing program (Tecplot 360).

Keywords: CFD, 2D flow, heat transfer, simulation
Discipline: Mechanical Engineering

1. INTRODUCTION

Computational Fluid Dynamics (CFD) is a theoretical method of scientific and engineering investigation concerned with the development and application of a virtual video -camera like tool – a software which is used to analyze a fluid dynamics as well as heat and mass transfer problem; for a unified cause-and-effect study. Here, the software results in a fluid-dynamic a movie where each picture consists of a flow property (velocity, pressure, temperature, vorticity, and stream-function). Each flow property can result in one movie. Thus, a large number of the fluid dynamic movie can be generated for a scientific understanding and engineering related study of a particular fluid dynamics problem. Representation, as well as mathematical-modeling of flow, are needed to create a fluid-dynamic movie in CFD [1]. Applying the fundamental laws of mechanics to a fluid gives the governing equation for a fluid. Partial differential equations are discretized into a system of algebraic equations. And all algebraic equations are then solved numerically to render the solution field.

CFD is useful in a wide variety of applications. Thus it can be used to simulate the flow over a vehicle. For instance, it can be used to study the interaction of propellers or rotors with the aircraft fuselage. And rotors and propellers can be represented with models of varying complexity [2].

Among numerical approaches for the analysis of mass flow and heat transfer. For example, discretization by using the finite-volume method which is, in this paper, used to study two-dimensional laminar flow in a tank with heat transfer. The flow describes a complex trajectory as a result of the deflectors (due to obstacles). The simulations shown below have been performed using the CFD Fortran 90 Coding.

2. PROPOSED SYSTEM DESCRIPTION AND BORDER CONDITIONS

Figure 1 shows schematically the cross-section, in vertical section, of a tank where water flows in the indicated direction. The flow, supposedly in laminar regime, describes a complex trajectory as a result of the obstacles A, B and C, all of aluminum, with the following dimensions:

A and B: (6 cm × 0.8 cm) centered at positions x = 3.2 and 8.8 cm, respectively. The obstacle C of 3 cm × 0.8 cm dimensions is welded to B, and the corresponding contact thermal resistance can be neglected. In the obstacle B there is an internal heat generation, at the rate of $\dot{q}_{g,B} = 10^7 \ W/m^3$.
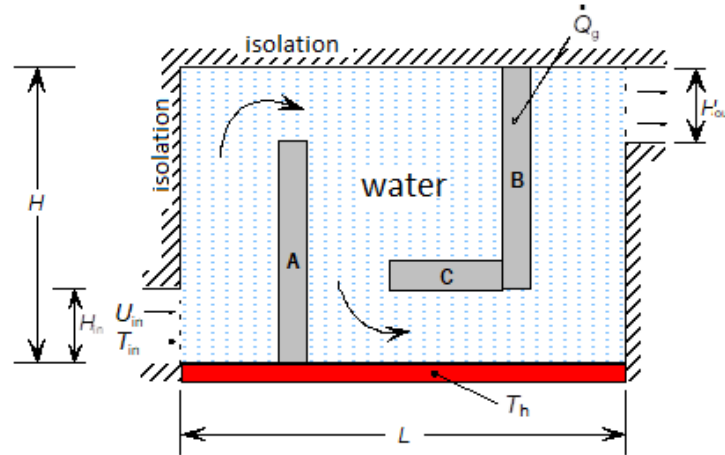

Figure 1. Diagram of the straight section of a tank where water flows, indicating the most relevant dimensions and some border conditions (*H*=0.08 m, *L*=0.12 m, H_{in}= H_{out}= 0.02 m; T_{in}=10 ºC, T_h=100 ºC; U_{in}=0.01 m/s)

3. CFD ANALYSIS PROCESS

3.1. Mathematical Models

In a preliminary analysis of the problem, the relevant variables in equation (1), dependent and independent variables have already been selected, resulting in a set of conservation equations to solve: in a reduced number to the essential and in a form as simple as possible. The next step in the method of numerical integration of differential equations is called discretization, whose main function is "transforming the differential (conservation) differential equations into 'algebraic equations' (approximate, but resolvable) [3].

The general equation of conservation in Cartesian coordinates and tensor notation is:

$$\frac{\partial(\rho\phi)}{\partial t} + \frac{\partial}{\partial x_j}\left(\rho u_j \phi - \Gamma_\phi \frac{\partial \phi}{\partial x_j}\right) = S_\phi \tag{1}$$

where ϕ can acquire different meanings: continuity 1, X momentum u, Y momentum v, Z momentum w, and energy h. Assuming the problem can be considered two dimensional, The conservation equation is integrated by applying a power balance to a small region of the domain (finite control volume as shown in Figure 2) involving the mesh node [4].
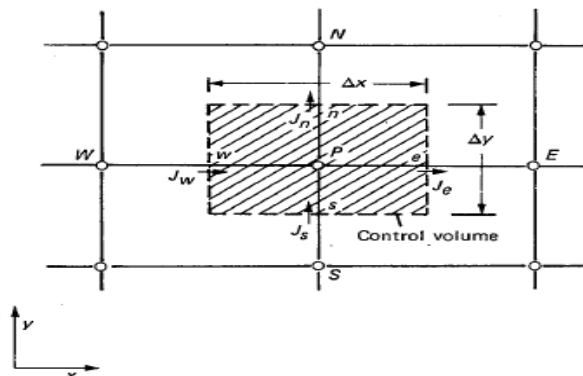
Figure 2. The control volume of the two-dimensional situation [3]

The two-dimensional discretization equation can be written as:

$$a_p \phi_p = a_E \phi_E + a_W \phi_W + a_N \phi_N + a_S \phi_S + b \qquad (2)$$

where values ($\phi_p, \phi_E, \phi_W, \phi_N, \phi_S$ and so on) are the unknown values at time $t + \Delta t$. The neighbor coefficients a_E, a_W, a_N, and a_S represent the convection and diffusion influence at the four faces of the control volume. The term b results from the addition to the previous term.

3.2. Solution Method

The problem of pressure-velocity coupling, as well as that of non-linearities of advective terms, is solved by the SIMPLE algorithm of Patankar and Spalding [5], which will be further developed. In this algorithm, the mass flows through the faces of the control volumes are calculated based on approximate values or estimates of velocity components. Starting from an estimate for the pressure distribution, we solve the equations of the momentum, as well as an equation for the local pressure corrections, which is deduced from the continuity equation. The latter provides a pressure correction field which is in turn used to update the velocity fields. The iterative process begins by using arbitrary velocity and pressure distributions, continuing with the progressive improvement of these fields, iterating the iteration, until convergence is achieved [3]. As it is shown in Figure 3.
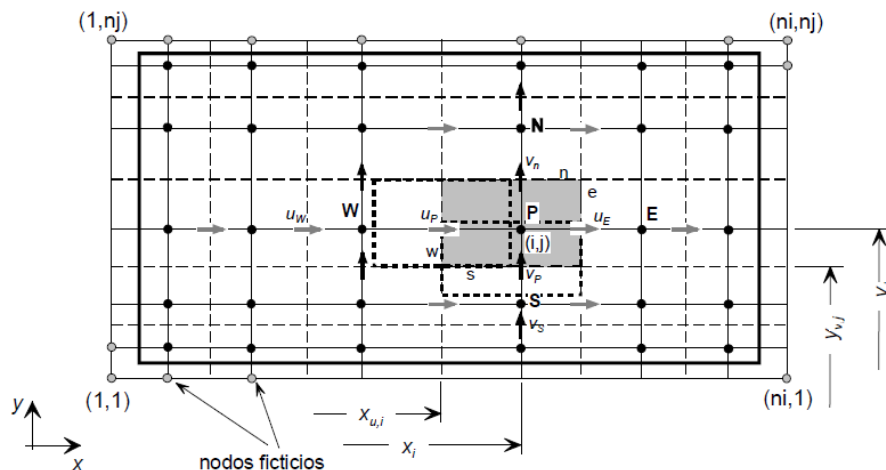
Figure 3. Scheme of a main Cartesian mesh, indicating the offset location of the horizontal u and vertical v components of the velocity.

For the pressure-correction equation, from the continuity equation and after integrating it, in order to two- dimensional form, and substituting for all the velocity components the expressions given by the velocity-correction formulas, after rearrangement, the discretization equation for the pressure correction p' is obtained:

$$a_P p'_P = a_E p'_E + a_W p'_W + a_N p'_N + a_S p'_S + b \qquad (3)$$

Since the values of the density is available only at the main grid points, the interface densities such as may calculated by any convenient interpolation. The term b represents a "mass source" which the pressure corrections must annihilate [3].

4. RESULTS AND DISCUSSION

By taking the coarsest mesh (32, 22), adapting the program in order to perform a numerical simulation of the flow for the configuration and the conditions outlined previously. It is obtained results which are presented, generated by the post-processing program (Tecplot 360) shown in Figure 4, (a), (b), (c) and (d) respectively.

The results include the velocity, temperature, and pressure distributions. Further, the values of the total power $Q_{ger,tot}(W)$ which transmitted to the flow and the mean temperature T (^oC) and power $Q_{out}(W)$ of the outlet. Where it was defined control point near of the outlet because at this point has approximately all the shifts which are happened in the domain.
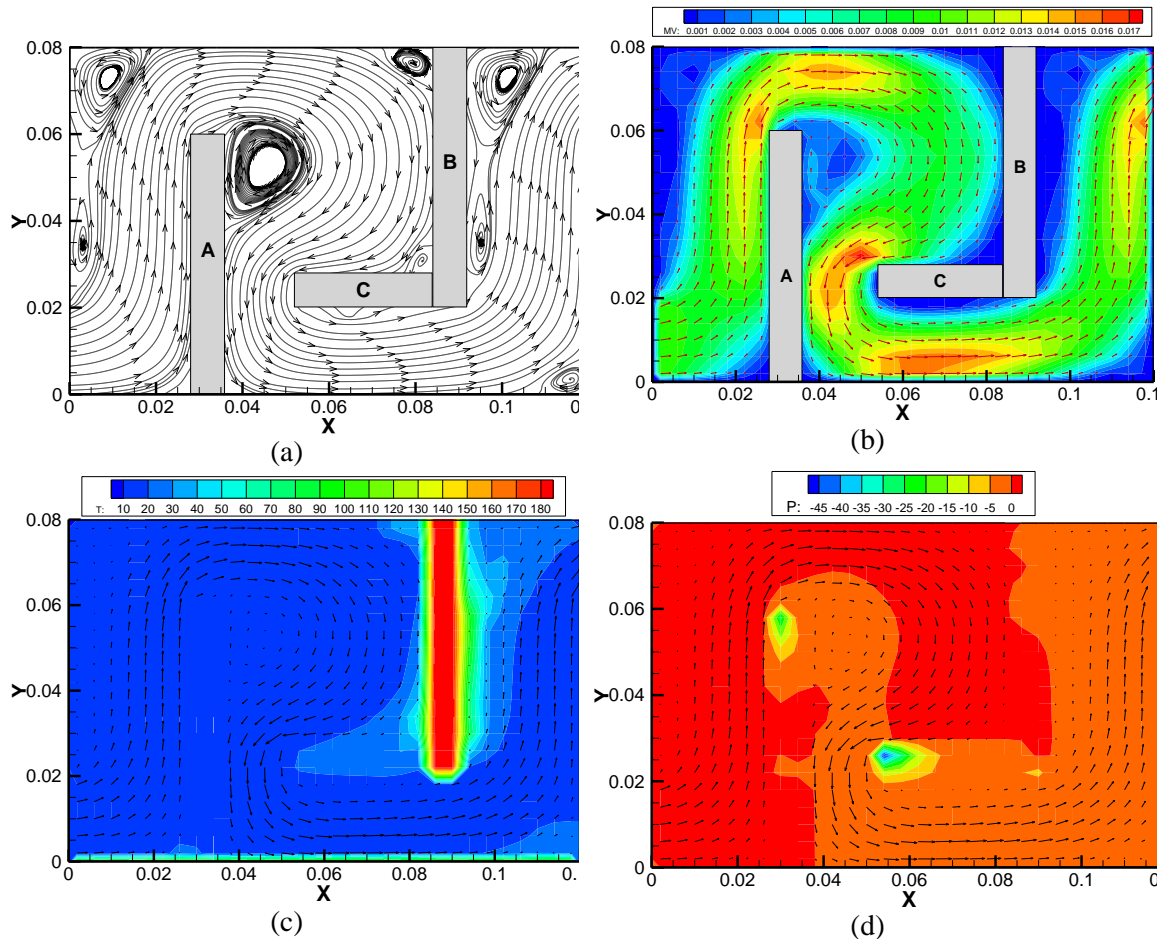

Figure 4. Representation of the flow field in the form of (a) current lines (30 × 20), (b) vectors and distribution (colored according to the value of its module) and (c) vectors and distribution of temperature; (d) vectors and distribution of pressure

By taking different values the height of the B obstacle = 4, 5, 6 and 7 cm respectively, the results of the effect of the variation of the height of the obstacle B on the flow and temperature fields are shown in Figures 5 and 6.
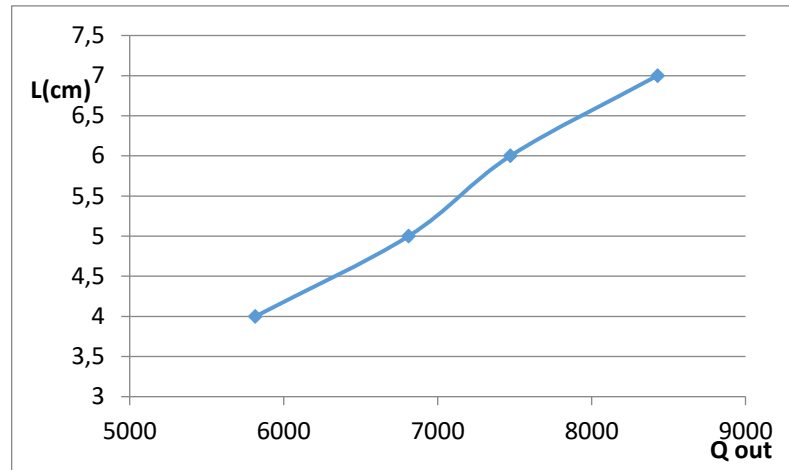
Figure 5. The curve of comparison between the values of total power through the domain depending on different values of the height of the obstacle B.

Figure 5 shows an increase in the total power at the outlet with an increase of the height of the obstacle B. and This is a logical result where the heat flux from the obstacle B is depending on the volume of this obstacle, and by increasing the height leads to increase in the volume and the increase in the power which the obstacle gives to the flow. And so it is for the mean temperature of the outlet, where Figure 6 shows an increase in the temperature with an increase of the height of the obstacle B.
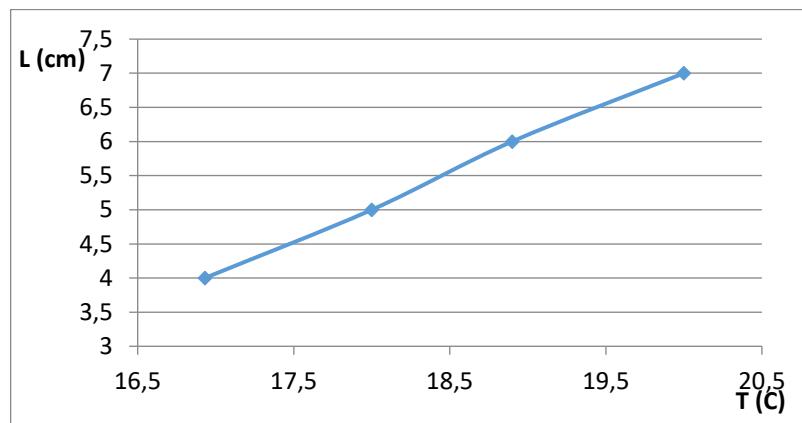
Figure 6. The curve of comparison between the values of the mean temperature of the outlet depending on different values of the height of the obstacle B.

By comparing the thermal power which transmitted to the flow from B with the total thermal power through the flow it can be noticed that the thermal power from the obstacle constitutes almost 93 % form the total thermal.

5. CONCLUSION

The system of formally linear algebraic equations consisting of the discretization equations of all domain nodes for any generic variable to which the general conservation equation, applies was solved by an iterative technique line-by-line, which is based on The SIMPLE (Semi-Implicit Method for Pressure Linked Equations) algorithm.

By taking the coarsest mesh (32, 22), adapting the program in order to perform a numerical simulation of the flow for the configuration and the conditions outlined previously. It was obtained results which are presented, generated by the post-processing program (Tecplot 360), with graphs of current lines, vectors and distribution of velocity, vectors and distribution of temperature, the vectors and distribution of pressure. The variance of the height of the obstacle B effects on the heat flux from the obstacle B. Where the amount of thermal power which transmitted to the flow is depending on the

volume of this obstacle, and by increasing the height leads to increase in the volume and the increase in the power which the obstacle gives to the flow. Therefore, it is for the mean temperature of the outlet.

REFERENCES

[1] A. Sharma, Level set method for computational multi-fluid dynamics: A review on developments, applications, and analysis, Indian Academy of Sciences (Sadhana) 40(3) (2015) 627–652.

[2] R. Bhaskaran, L. Collins, Introduction to CFD Basics, Technical report, 2002.

[3] S. V. Patankar, Numerical Heat Transfer and Fluid Flow, Hemisphere Publishing Corporation, 1980.

[4] L.A. Oliveira, Cálculo Numérico de Escoamentos com Transferência de Calor e de Massa, Dep. Engenharia Mecânica, FCTUC, 1989.

[5] S.V. Patankar, D.B. Spalding, A calculation procedure for heat, mass and momentum transfer in three-dimensional parabolic flows, International Journal of Heat and Mass Transfer 15 (1972) 1787-1806.

Finite Element Analysis of Material and Parameter Effects in Ballistic Armors

Latif Tibet Aktaş*, Izmir University of Economics, Dept. of Mechanical Engineering, Balçova, Izmir, Turkey
Mehmet Çevik, İzmir Katip Çelebi Univ., Dept. of Mechanical Engineering, Çiğli Main Campus, Izmir, Turkey
*Corresponding author: tibet.aktas@ieu.edu.tr

Abstract

The literature about the ballistic armors are mostly focused on 2 or 3 different parameter effects. The aim of this study, differently, is to find and compare the effects of specific materials on protection of composite ballistic armor plates against high-velocity projectile impact. The effects of stacking sequence for different materials, projectile type, target plate shape and impact obliquity are investigated individually. It is shown that the proposed stacking sequence decelerates the residual velocity of the projectile better than the other considered arrangements. The average percentage of kinetic energy absorption of rectangular shaped Kevlar 29/epoxy plate is considerably higher than that of circular shaped Kevlar 29/epoxy plate.

Keywords: composite, ballistic, armor, impact, finite element
Discipline: Mechanical Engineering

INTRODUCTION

Composites are very important materials in defense applications, especially in production of bulletproof systems. Bulletproof composites are used in covering the most important body parts as in helmets, vests and shields. Despite all the advantages of composite armors like mobility and lightness, they still need to be improved because their protection efficiencies against high-velocity projectile impact are not perfect. Even when the impact energy is almost absorbed and the contact of projectile with the protected asset is blocked, the residual impact energy transferred to the protected surface is still high and should be decreased.

Garcia-Avila et al. [1] manufactured high-performance light-weight composite armor system using different materials and different manufacturing methods and evaluated the ballistic tolerance of this composite armor system. They performed finite element analysis to study failure mechanisms and energy absorption of the plate. Min et al. [2] studied effect of reinforcement continuity on ballistic performance of composites made from multiply plain weave fabric. After producing continuous and discontinuous plain weave fabrics, they examined the damage morphology and confirmed the superiority of the continuously reinforced composites. Wicklein et al. [3] derivated and validated of a numerical material model that predicts the highly dynamic behavior of CFRP under high velocity impact. Additionally, they compared the numerically predicted damage within the CFRP to the delamination areas found in ultrasonic scans. Zhou et al. [4] used finite element models to predict the response of woven fabrics wiith different structural parameters. They confirmed that the plain woven fabric shows superior energy absorption over other structures in a ballistic event. Rizov [5] investigated low velocity impact behavior of two densities of ductile polyvinylchloride foam and post-impact creep response of this foam. He studied development of a damage tolerance design approach for structural foams. Toqueboeuf et al. [6] conducted dynamic compressive tests in different configurations and they found that the initial multi-axial prestress of polyurethane is one of the most important parameters for material and layered response. Deka et al. [7] investigated the response of laminated composites subjected to high velocity, multi-site impacts from a modeling and experimental viewpoint. They compared energy absorption, new surface creation and failure mechanisms from sequential and simultaneous multi-site high velocity impacts.

Ansari & Chakrabarti [8] studied numerically on a validated model. The model consisted of 19 layers of Kevlar 29 and it was impacted by blunt nosed steel projectile. The impact velocity gap was from 25 m/s to 1000 m/s and they compared residual velocities of projectile as results. In addition, the ballistic limit variation, residual velocity of projectile, failure propagation in the impacted plate and in the projectile, penetration depth, kinetic energy of the projectile, deflection and radius of damaged zone were investigated.

The literature review reveals that most of the ballistic studies are focused on 2 or 3 different parameter effects. In this study, it is intended to find and compare the effects of specific materials on protection of composite ballistic armor plates against high-velocity projectile impact. In addition, the effects of stacking sequence for different materials, projectile type, target plate shape and impact obliquity are investigated individually.

METHOD

In this study, it is intended to find and compare the effects of specific materials on protection of composite ballistic armor plates against high-velocity projectile impact. In addition, the effects of stacking sequence, shape of projectile and shape of target plate are investigated individually for different impact velocities. ANSYS/AUTODYN solver is used for modelling, numerical study and simulations.

The applicability and the accuracy of the present finite element model is validated by comparing the results with those of Ansari & Chakrabarti [8]. The present study provides results in good agreement with their results, as seen in Table 1.

Table 1. Comparison of present impact results with those of [8]

Impact velocity (m/s)	Residual velocity (m/s) [8]	Residual velocity (m/s) (present study)
200	-48,93	-48,64
300	-44,72	-38,4
500	267,24	265,49
650	442,1	431,38
850	670,5	629,17

RESULTS

The modelled plate is impacted by a flat nosed projectile made of Steel 4340 and its boundary conditions are all-clamped. Considering the unit layer weight and absorbed kinetic energy of the projectile, UHMWPE layers perform best with Kevlar 29/epoxy woven layers. The results show that the stacking sequence in which UHMWPE layers are placed in between Kevlar 29/epoxy layers one by one, decelerates the residual velocity of the projectile better than the other considered arrangements. For a unit plate area (100 mm × 100 mm), the final model ($[(K/U)_{11}/K]$) is 4,4 g lighter and slow down the projectile by 9,187% better than the 19 layers of Kevlar 29/epoxy model. Residual velocities of flat nosed cylindrical projectile for different secondary materials of target plate are presented in Table 2. On the other hand, comparison of 500 m/s impact results of full Kevlar 29/epoxy and Kevlar 29/epoxy – UHMWPE plates are shown in Table 3.

Table 2. Residual velocities of flat nosed cylindrical projectile

Material	Layer weight (g)	Total weight of the plate (g)	Residual velocity (m/s)
Pure Kevlar 29/epoxy	8,250	156,750	265,490
H100 foam	0,500	87,000	360,000
Polyurethane	6,325	139,426	330,180
UHMWPE	4,850	126,150	300,600
Graphite	11,250	183,750	299,280
S2 Glass	9,250	165,750	316,380

Table 3. Comparison of 500 m/s impact results of full Kevlar 29/epoxy and Kevlar 29/epoxy – UHMWPE plates

Composition	Total number of layers	Total thickness (mm)	Total weight (g)	Residual velocity of the projectile (m/s)
Kevlar 29/epoxy	19	9,5	156,75	265,49
Kevlar 29/epoxy - UHMWPE	23	11,5	152,35	241,10

Effect of projectile type is investigated and the tests show that the average percentage of kinetic energy absorption of Kevlar 29/epoxy - UHMWPE plate impacted by flat nosed projectile is 62,81%. For the case with conical nosed projectile, the average percentage of kinetic energy absorption of the plate is 51,96%. The impact responses are illustrated in Figures 1 and 2.
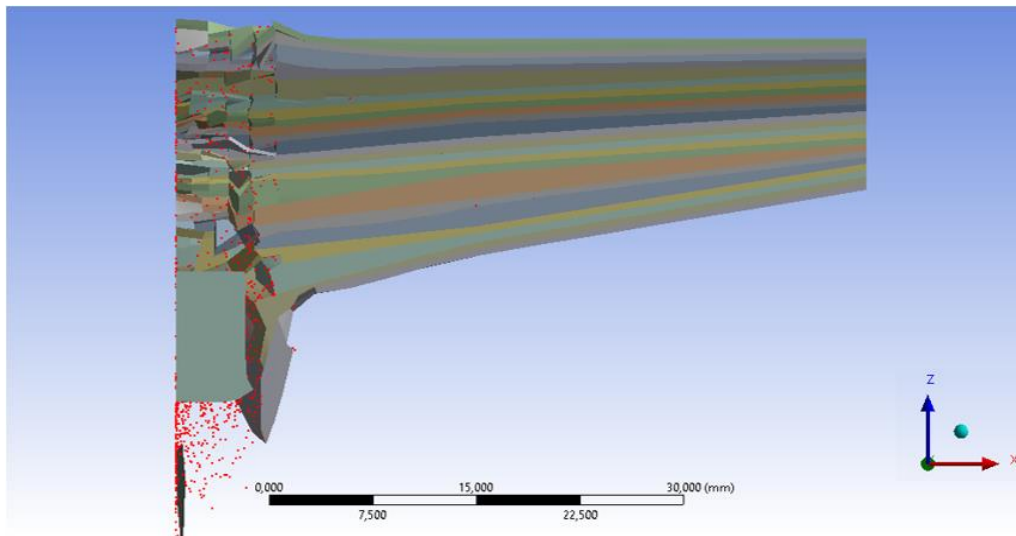
Figure 1. Impact response of 23 layers of Kevlar 29/epoxy - UHMWPE plate to rectangular nosed Steel 4340 projectile with 500 m/s impact velocity.
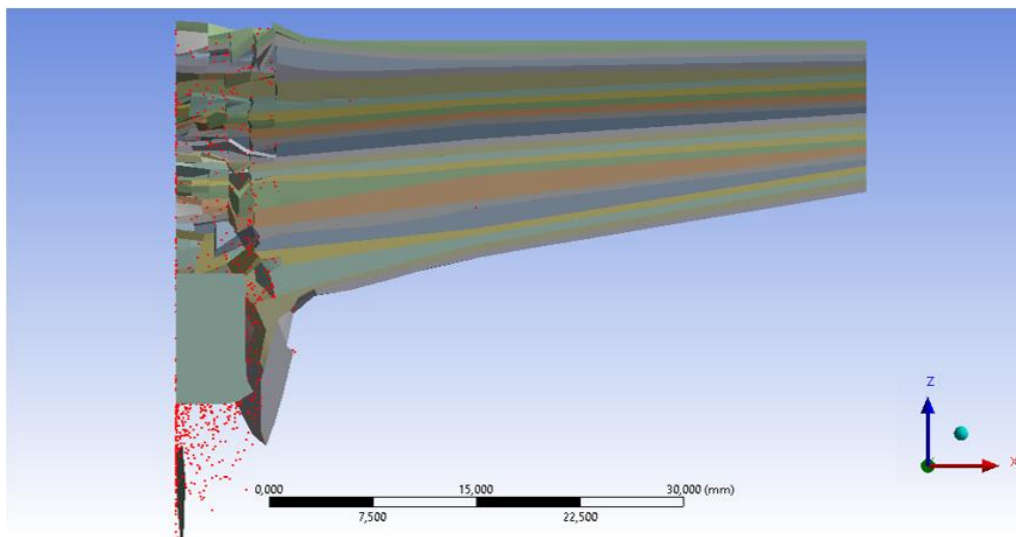
Figure 2. Impact response of 23 layers of Kevlar 29/epoxy - UHMWPE plate to conical nosed Steel 4340 projectile with 500 m/s impact velocity.

Figure 3 illustrates the comparison of the velocity variations of conical nosed and flat nosed projectiles during penetration of Kevlar 29/epoxy – UHMWPE plate for impact velocity of 500 m/s.
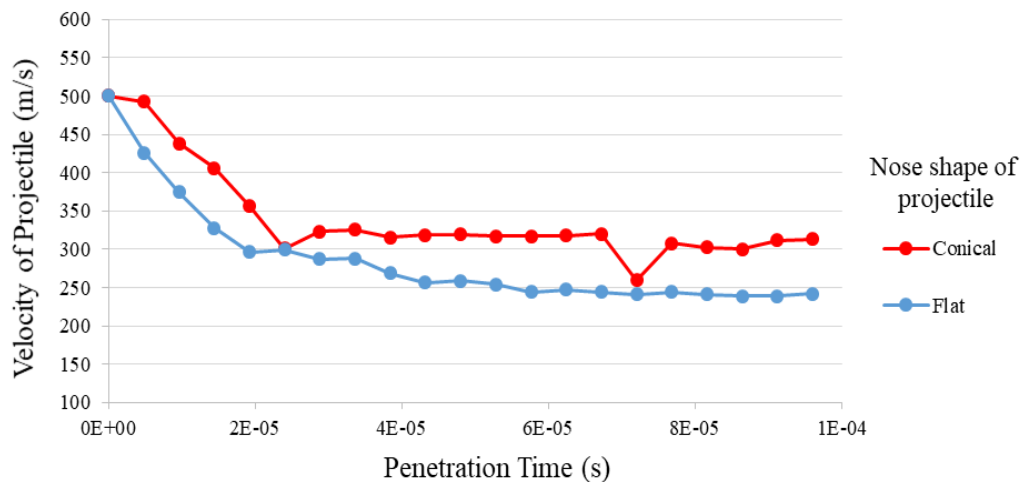
Figure 3. Comparison of the velocity variations of conical nosed and flat nosed projectiles during penetration of Kevlar 29/epoxy – UHMWPE plate for impact velocity of 500 m/s.

Effect of target plate shape is investigated and the tests show that the average percentage of kinetic energy absorption of rectangular shaped Kevlar 29/epoxy plate is 71,81% while the average percentage of kinetic energy absorption of circular shaped Kevlar 29/epoxy plate is 56,71%. 500 m/s impact results of different shape parameters for plate and projectile are compared in Table 4.

Table 4. Comparison of 500 m/s impact results of different shape parameters for plate and projectile

Shape parameter	Residual velocity of the projectile (m/s)
Rectangular shaped Kevlar 29/epoxy plate impacted by conical nosed projectile	314,00
Rectangular shaped Kevlar 29/epoxy plate impacted by flat nosed projectile	265,49
Circular shaped Kevlar 29/epoxy plate impacted by flat nosed projectile	328,97
Circular shaped Kevlar 29/epoxy plate impacted by conical nosed projectile	340,56

REFERENCES
[1] M. Garcia-Avila, M. Portanova, A. Rabiei, Ballistic performance of composite metal foams, Composite Structures 125 (2015) 202-211.
[2] S. Min, X. Chen, Y. Chai, T. Lowe, Effect of reinforcement continuity on the ballistic performance of composites reinforced with multiply plain weave fabric, Composites Part B 90 (2016) 30-36.
[3] M. Wicklein, S. Ryan, D.M. White, R.A. Clegg, Hypervelocity impact on CFRP: Testing, material modelling, and numerical simulation, International Journal of Impact Engineering 35 (2008) 1861-1869.
[4] Y. Zhou, X. Chen, A numerical investigation into the influence of fabric construction on ballistic performance, Composites Part B 76 (2015) 209-217.
[5] V.I. Rizov, Low velocity localized impact study of cellular foams, Materials and Design 28 (2007) 2632-2640.
[6] W. Toqueboeuf, B. Mortaigne, C. Cottenot, Dynamic behaviour of polycarbonate/polyurethane multi-layer for transparent armor, Journal de Physique IV Colloque, 1997, 07 (C3), C3-499-C3-504.
[7] L.J. Deka, S.D. Bartus, U.K. Vaidya, Multi-site impact response of S2-glass/epoxy composite laminates, Composites Science and Technology 69 (2009) 725-735.
[8] Md. M. Ansari, A. Chakrabarti, Impact behavior of FRP composite plate under low to hyper velocity impact, Composites Part B 95 (2016) 462-474.

Vibration Control of a 2-DOF Quarter Car with an Actuator by State Space and System Identification Methods

Levent Malgaca, Dokuz Eylül Univ., Dept. of Mechanical Engineering, Tınaztepe Campus, Izmir, Turkey
Mehmet Uyar*, Bayburt Univ., Dept. of Mechanical Engineering, Dede Korkut Campus, Bayburt, Turkey
Şefika İpek Lök, Dokuz Eylül Univ., The Graduate School of Natural and Applied Sciences, Tınaztepe Campus, Izmir, Turkey
*Corresponding author: muyar@bayburt.edu.tr

Abstract

The suspension system of cars affects the stability, the road handling and the ride comfort. In this study, the vibration control of a 2-DOF quarter car (QC) is studied with the state space (SS) and system identification (SI) methods. The finite element (FE) model of the QC is created in ANSYS. In the first approach, the SS model is extracted from the FE model. The command "SPMWRITE" is used to extract the SS model. The command is required for the modal analysis. Also, the input and output of the system should be defined. The input is considered as the step input as a road profile. The output of the system is chosen as the displacement of the body mass. In the second approach, the transfer functions of the system are obtained from the FE model by using the SI method. The ARX and ARMAX models are evaluated to find the transfer functions. The obtained transfer functions are considered in the closed-loop block diagram. Then the PID control is applied to the models. The vibrations of the body mass are successfully reduced by the active control. The closed-loop results are compared.

Keywords: vibration control, state space, system identification, finite element
Discipline: Mechanical

INTRODUCTION

The suspension system parameters affects the road handling and the ride comfort of the cars. The influence of the suspension parameters over ride and handling of the cars is popular research topics. Active vibration control affects damping properties of suspension systems. Active vibration control of a QC is studied to attenuate the excitation from a road by using the PID controller [1]. The spring and damping elements in suspension systems are used as the passive suspension parts. Also, semi-active or active suspension systems are used [2]. In active suspension systems, actuators can provide better performance characteristics. An actuator is defined between the body mass and tyre mass. The actuator generates the control force to improve the suspension performance [3, 4, 5]. To improve the performance characteristic for a QC, the various control methods were studied such as the linear quadratic regulator [6], sliding mode control [7], fuzzy logic control [8], optimal control [9].

The SI is an effective approach to obtain mathematical models of systems whose structural properties are not known or cannot be modeled [10]. The SI is a method that estimating the mathematical model of a dynamic system based on input and output data.

In the literature, there are studies to obtain experimental and theoretical dynamic models of flexible manipulators and different mechanical systems [11, 12, 13]. Sethi and Song [11, 12] used parametric and nonparametric SI methods to extract the mathematical model of a flexible beam, and then designed the controller by using the mathematical model. In another article, the SI method was applied to a flexible manipulator rotating in one axis. Experimental data was used to determine the physical parameters such as mass, moment of inertia and manipulator thickness [13].

In this study, the analysis of active vibration control of a QC model is performed with the SS and SI methods. The state space matrices of the QC are obtained from ANSYS/APDL, and then the PID control is applied to the system. The transfer functions of the QC are obtained from the FE model with the SI method by using the step road input and body response and then the PID control is applied to the system. Then, the uncontrolled and controlled responses for the two different methods are compared by MATLAB/Simulink.

2-DOF QUARTER CAR MODEL

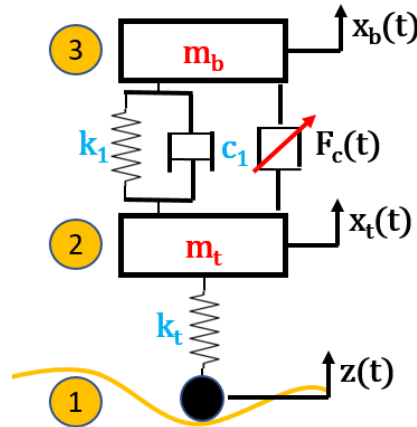The QC model considered in the study is shown in Figure 1.

Figure 1. 2-DOF QC model
(m_b = 240 kg, m_t = 36 kg, k_1 = 16000 N/m, c_1 = 980 N.s/m and k_t = 160000 N/m).

The parameters mb, mt, k1, kt, and c1 are the body mass, tyre mass, suspension stiffness, tyre stiffness and suspension damping, respectively. xb(t) and xt(t) are the displacements of body and tyre masses. z(t) is the ground motion. Fc(t) is the actuator force.

The QC is studied as the lumped parameter system in ANSYS. The FE model of the system is created by using MASS21 and COMBIN14 elements. The system consists of three nodes as shown in Figure 1. MASS21 is used for the body and tyre masses while COMBIN14 is used for the suspension.

EXTRACTION OF STATE SPACE MATRICES FROM FINITE ELEMENT MODEL

The natural frequencies and damping ratios of the system are the dynamic parameters of the QC model. After creating the FE model of the system, the modal analysis is done to find the undamped natural frequencies. The undamped natural frequencies are found as fn1 = 1.2382 Hz and fn2 = 11.135 Hz. The time step Δt and steady-state time tss depend on the natural frequencies. Therefore, the time step and steady-state time are calculated as Δt=0.407 and tss =3.67 s, respectively [14].

The state space matrices are required to obtain the mathematical model of the QC and they are obtained with SPMWRITE command in ANSYS. In the FE model, the inputs z(t) and Fc(t) are applied to the nodes 2 and 3, respectively. xb(t) and xt(t) are considered as the outputs of the system. Then, the matrices A, B, C, D are found as follow.

$$A = \begin{bmatrix} 0 & 0 & 1 & 0 \\ 0 & 0 & 0 & 1 \\ -60.53 & 0 & -3.29 & 0 \\ 0 & -4895.0 & 0 & -26.92 \end{bmatrix} \quad B = \begin{bmatrix} 0 & 0 & 0 \\ 0 & 0 & 0 \\ 950.07 & 0.0059 & 0.0645 \\ 26649.7 & 0.1665 & -0.0022 \end{bmatrix}$$

$$C = \begin{bmatrix} 0.0645 & -0.0022 & 0 & 0 \end{bmatrix} \quad D = \begin{bmatrix} 0 & 0 & 0 \end{bmatrix}$$

After obtaining the state space matrices, the open and closed-loop block diagrams are defined by using MATLAB. The closed-loop block diagram for the SS method is shown in Figure 2.
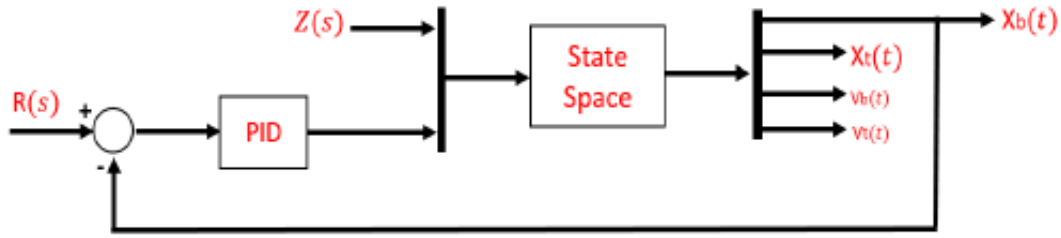
172

Figure 2. Closed-loop block diagram for the SS method.

R(s) is the reference input and Z(s) is the disturbance. xb(t), xt(t), vb(t), and vt(t) are the displacements and velocities of the body and tyre masses, respectively.

SYSTEM IDENTIFICATION METHOD

The SI method has several steps [15]. In the first stage, input and output signals are determined. Various input types can be used. The step input is used in this study. In the second stage, the model structure is determined. The SI models for the QC are chosen as parametric SI methods. The ARX and ARMAX models are used to model the system. The equations of ARX and ARMAX models are given in Eqs. 1 and 2.

$$y(t) = \frac{B(q)}{A(q)} u(t) + \frac{1}{A(q)} e(t) \tag{1}$$

$$y(t) = \frac{B(q)}{A(q)} u(t) + \frac{C(q)}{A(q)} e(t) \tag{2}$$

Then, the orders of numerator and denominator are determined. Finally, the model validation is performed whether the obtained result is suitable.

The system has two input signals Fc(t) and z(t), and two output signals xb(t) and xt(t). There are four transfer functions for the QC system. The transfer functions are given in Eq. 3.

$$\begin{Bmatrix} X_b(s) \\ X_t(s) \end{Bmatrix} = \begin{bmatrix} G_{11}(s) & G_{12}(s) \\ G_{21}(s) & G_{22}(s) \end{bmatrix} \begin{Bmatrix} Z(s) \\ F_c(s) \end{Bmatrix} \tag{3}$$

For example, G11(s) represents the relationship from Z(s) to Xb(s) and G12(s) represents the relationship from Fc(s) to Xb(s). Two different data sets are used in the SI method. These are the identification data set and validation data set. In the first data set, the transfer function of the system is estimated. In the second data set, the input signal is applied to the transfer function and the output signals are compared. The validation data set is used to check whether the system learns the noise [15].

(a)   (b)

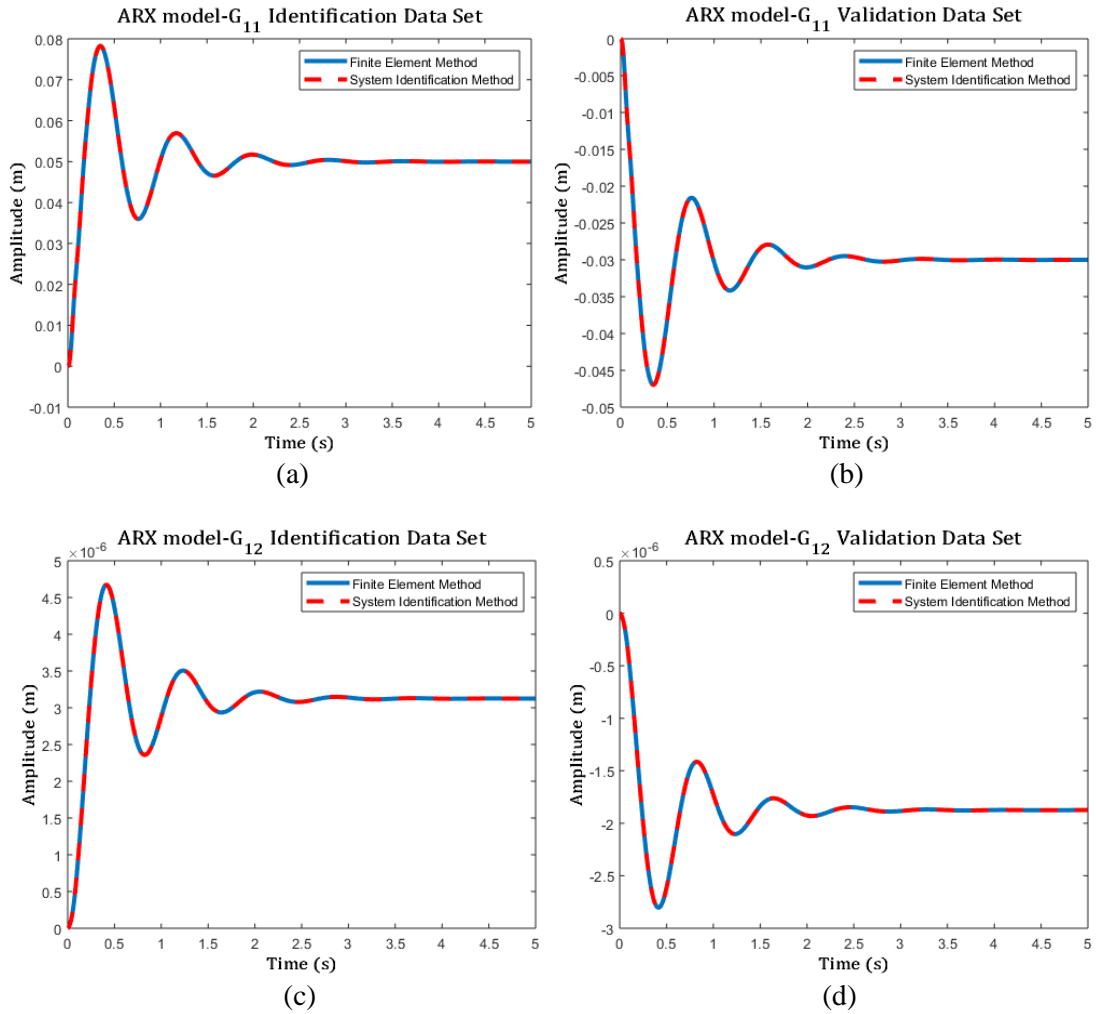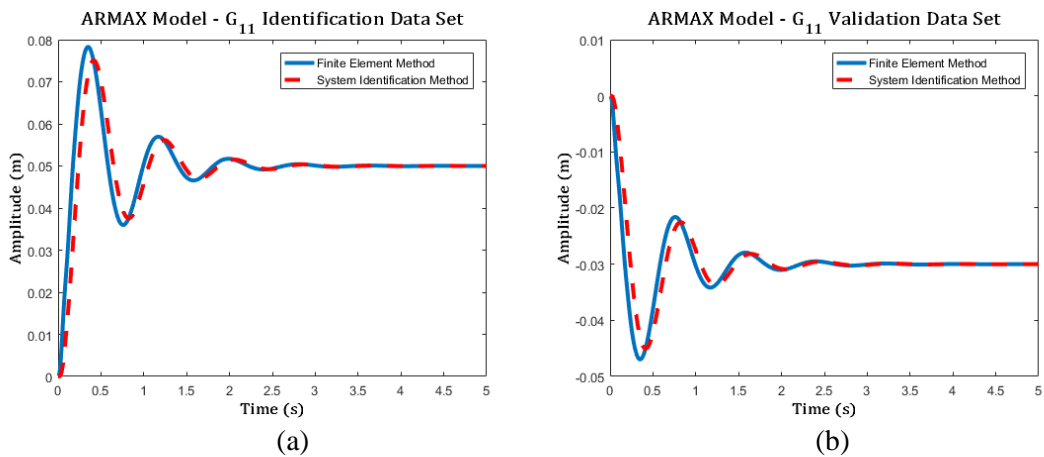(c)   (d)

Figure 3. Identification (a, c) and validation data (b, d) for the ARX model.

The two models in the SI method are compared in Figs. 3 and 4. The ARX model gives better results. The success rate for the G11(s) is found as 99.97% and the success rate for the G12(s) is found as 99.98%. The mathematical model of the system is successfully obtained by using the SI method.
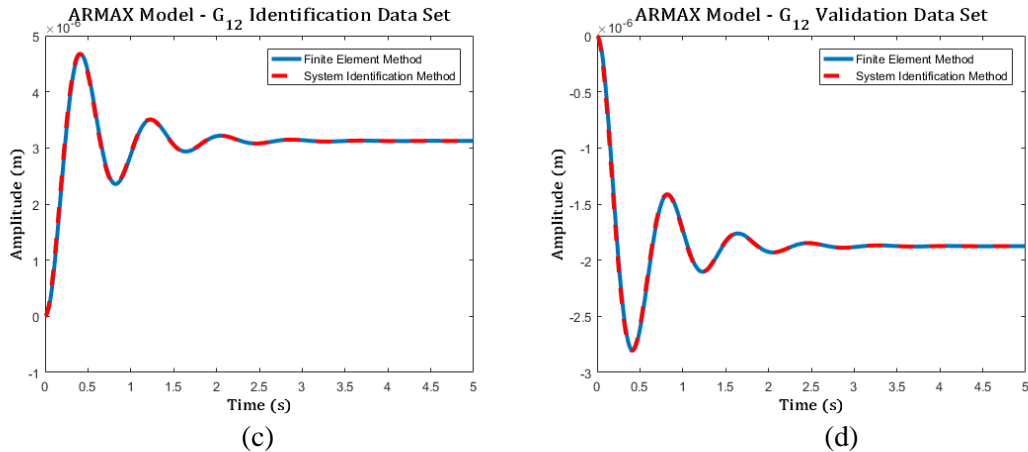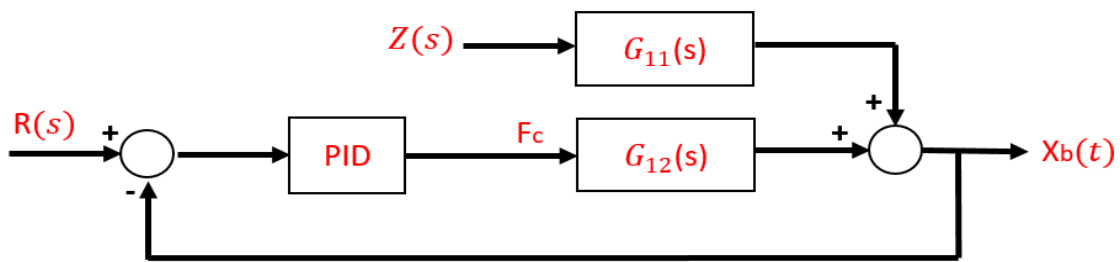

(a)   (b)

(c)   (d)

Figure 4. Identification (a, c) and validation data (b, d) for the ARMAX model.

After obtaining the transfer functions, the open and closed-loop block diagrams are defined in MATLAB. The closed-loop block diagram for the SI method is shown in Figure 5.

Figure 5. Closed-loop block diagram for the SI method.

The uncontrolled and controlled responses to the step input of 0.05 m are shown in Figure 6.
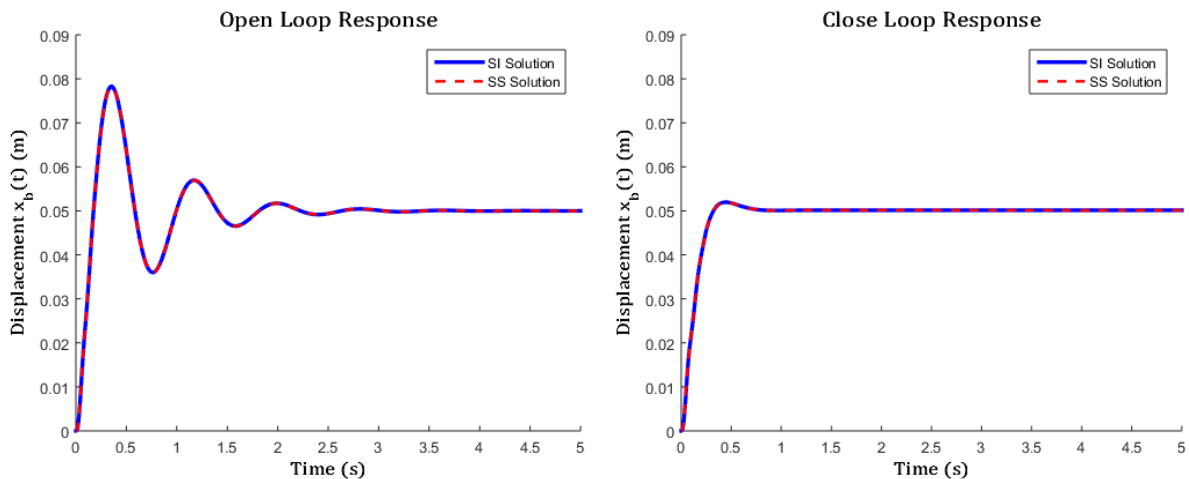
Figure 6. Uncontrolled and controlled (K_p=5000, K_i=500, K_d=2500) system responses.

As seen from Figure 6, the SS and SI solutions are in very good agreement. The body mass vibrates between 0.078 and 0.036 m in the uncontrolled response. The damping ratios of system are calculated as $\zeta 1 = 0.201$ and $\zeta 2 = 0.217$. In the controlled response, the overshoot and settling time of the system are reduced when the PID control is applied to the system.

CONCLUSIONS

In this work, active vibration control of the QC is studied. The SS and SI methods are used to obtain mathematical models of the system. The FE model of QC is created and then modal analysis is performed to find the undamped natural frequencies. The step input is defined as a road profile. The output of the system is chosen as the displacement of the body mass. The state space matrices A, B, C, and D based on the modal analysis are exported from ANSYS. Also, the transfer functions between inputs and outputs are obtained with the SI method. Then, the PID control is applied to the obtained mathematical models in MATLAB. The uncontrolled and controlled responses are compared. It is observed that the results for both methods are in good agreement.

REFERENCES

[1] N.M. Ghazaly, A.E.S. Ahmed, A.S. Ali, G.T.A. Jaber, Pid controller of active suspension system for a quarter car model, International Journal of Advances in Engineering and Technology 8 (2015) 899-909.

[2] H.Y. Chen, S.J. Huang, Adaptive control for active suspension system, In International Conference on Control and Automatic, June 2005.

[3] A. Aldair, W.J. Wang, Design an intelligent controller for full vehicle nonlinear active suspension systems, International Journal on Smart Sensing and Intelligent Systems 4 (2011) 224-243.

[4] N.M. Ghazaly, A.O. Moaaz, The future development and analysis of vehicle active suspension system, IOSR Journal of Mechanical and Civil Engineering 11 (2014) 19-25.

[5] F. Jamshidi, A. Shaabany, Robust control of an active suspension system using h2 control methods. Journal of American Science 7 (2011) 1-5.

[6] M.S. Yahaya, M.R.A. Ghani, Lqr controller for active car suspension, In Proceeding in TENCON, September 2000.

[7] I.Z.M. Darus, E. Akbari, M. Farsadi, R. Ghelichi, Observer design for active suspension system using sliding mode control. In Proceedings of IEEE Student Conference on Research and Development, December 2010.

[8] M.Hady H. Elbab, E. Allam, S. Abouel-Seoud, Performance of active suspension with fuzzy control, Technical report, SAE Technical Paper, May 2009.

[9] H. Zohoor, J. Marzbanrad, Y. Hojjat, S.K. Nikravesh, Optimal previewcontrol design of an active suspension based on a full car model, Scientia Iranica 10 (2003) 23-36.

[10] L. Ljung, System Identification: Theory for the User, 2nd Ed., Prentice-Hall, 1999.

[11] V. Sethi, G. Song, Multimodal vibration control of a flexible structure using piezoceramic sensor and actuator, Journal of Intelligent Material Systems and Structures 19 (2008) 573–582.

[12] V. Sethi, G. Song, Multimodal vibration control of a flexible structure using piezoceramics, Proceedings of the 2005 IEEE/ASME International Conference on Advanced Intelligent Mechatronics, California, USA, 24-28 July, 2005.

[13] B. Tarvirdizadeh, E. Khanmirza, M. Ebrahimi, A. Kalhor, S. Vakilipour, An efficient numerical and experimental system identification approach for a flexible manipulator, Engineering Computations 32 (2015) 2467 – 2490.

[14] N.M. Newmark, A method of computation for structural dynamics, Journal of Engineering Mechanics, ASCE 85 (1959) 67–94.

[15] K. J. Keesman, System Identification an Introduction, Springer Publications, London, 2011.

Comparison of Numerical and Analytical Methods of 4-Degree-of-Freedom System's Passive Vibration Control

Mehmet Mert İlman*, Dokuz Eylül Univ., The Graduate School of Natural and Applied Sciences, Tınaztepe Campus, İzmir, Türkiye
Şahin Yavuz, Dokuz Eylül Univ., Dept. of Mechanical Engineering, Tınaztepe Campus, İzmir, Türkiye
Hira Karagülle, Dokuz Eylül Univ., Dept. of Mechanical Engineering, Tınaztepe Campus, İzmir, Türkiye
*Corresponding author: mert.ilman@cbu.edu.tr

Keywords: vibration control, Newmark, state-space, Ansys
Discipline: Mechanical Engineering

INTRODUCTION

Structures that driven by trapezoidal velocity profiles are widely used in mechatronic applications. There are studies that inquired into the dynamic behavior of the system during motion or tried to reduce the inevitable harmful effects on the structure. Malgaca, Doğan *et al.* studied the effect of joint flexibility on modal parameters and vibration response of the servo driven composite manipulator [1]. Malgaca, Yavuz *et al.* studied the tuning of triangular velocity profile parameters in order to reduce the residual vibration of a curved beam, numerically and experimentally [2]. Karagülle *et al.* studied the same open-loop vibration control process on two-link manipulator system which is more complicated due to the change of its natural frequency during the motion [3]. Yavuz *et al.* studied the closed-loop vibration control on a four-degree-of-freedom system by integrated the LPM (lumped-parameter-model) with the Newmark numerical method [4].

The main problem of this area of research is to define a convenient model in terms of accuracy and simplicity for representing the system sufficiently and for the applying of control methods easily. In this regard, State-Space model can be used as suitable linear dynamic-model of a system. Kosarac *et al.* studied this modelling on the spindle by the help of ANSYS software and compared the impulse responses for validation [5]. In this study a one-link flexible manipulator system is considered for dynamic modelling with the State-Space model (for linearization) and the reduced-order State-Space model (for further simplification of the system). For validation of the State-Space model solution, another numerical solution called Newmark's method is established. Results of ANSYS commercial simulation software are compared with analytical solutions to verify the mathematical models. After fulfillment of the modelling, open-loop vibration control methods are applied to the system. Process scheme is shown in Figure 1.
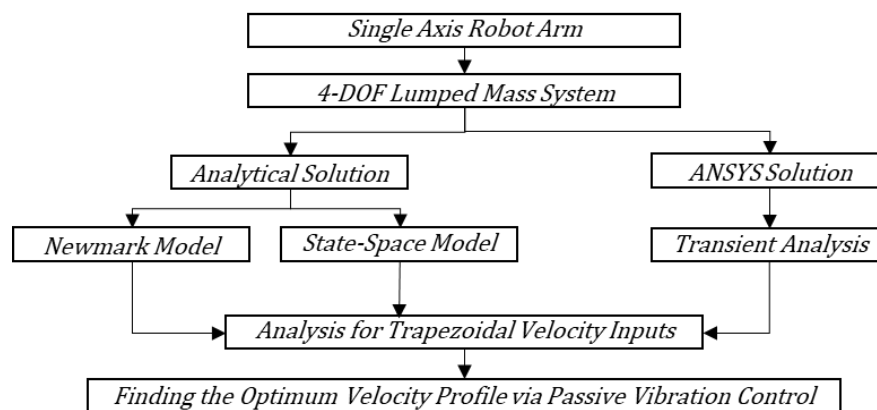

Figure 1. Process Scheme.

MODELLING OF THE SYSTEM

In this paper, one-link robot arm is used and it can be demonstrated as rotating beam and servo motor couple. The system can be modelled by rotational lumped mass model and this model can be converted to a four-degrees-of-freedom translational lumped mass model. (See Figure 2)

İZMİR KÂTİP ÇELEBİ UNIVERSITY 2010

İZMİR Uluslararası Misafir Öğrenci Derneği
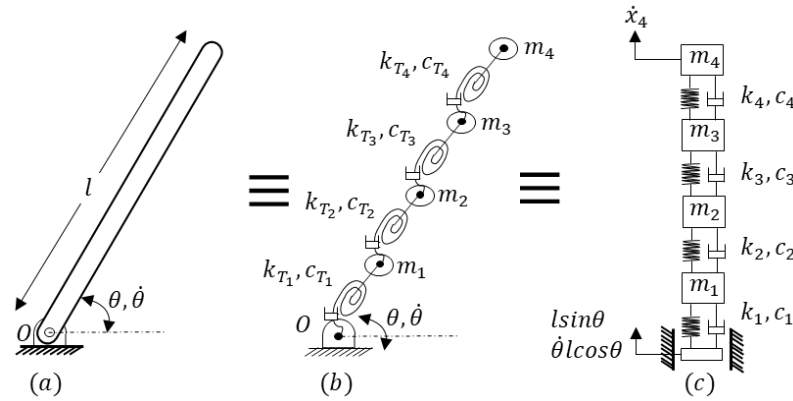◆İZMİR International Guest Student Association

Figure 2. Lumped mass model of the system. (a) One-link manipulator, (b) Rotational lumped mass model, (c) Equivalent translational lumped mass model.

In order to be sure of the modelling, it is a must to show that rotational & translational models could be equivalents. The validation is demonstrated via using two-degrees-of-freedom rotational-model's equation-of-motion-in-matrix-form (See Eq. 1) and transforming it to the equation-of-motion-of-two-degrees-of-freedom-translational-model (See Eq. 2 and 3) by assuming the distances between the masses are same (here it is symbolized with L).

$$\begin{bmatrix} I_1 & 0 \\ 0 & I_2 \end{bmatrix}\begin{bmatrix} \ddot{\theta}_1 \\ \ddot{\theta}_2 \end{bmatrix} + \begin{bmatrix} (C_{T_1}+C_{T_2}) & -C_{T_2} \\ -C_{T_2} & C_{T_2} \end{bmatrix}\begin{bmatrix} \dot{\theta}_1 \\ \dot{\theta}_2 \end{bmatrix} + \begin{bmatrix} (K_{T_1}+K_{T_2}) & -K_{T_2} \\ -K_{T_2} & K_{T_2} \end{bmatrix}\begin{bmatrix} \theta_1 \\ \theta_2 \end{bmatrix} = \begin{bmatrix} C_{T_1}\dot{\theta} \\ 0 \end{bmatrix} \tag{1}$$

$$\begin{bmatrix} I_1/L & 0 \\ 0 & I_2/L \end{bmatrix}\begin{bmatrix} \ddot{\theta}_1 L \\ \ddot{\theta}_2 L \end{bmatrix} + \begin{bmatrix} (C_{T_1}+C_{T_2})/L & -C_{T_2}/L \\ -C_{T_2}/L & C_{T_2}/L \end{bmatrix}\begin{bmatrix} \dot{\theta}_1 L \\ \dot{\theta}_2 L \end{bmatrix} + \begin{bmatrix} (K_{T_1}+K_{T_2})/L & -K_{T_2}/L \\ -K_{T_2}/L & K_{T_2}/L \end{bmatrix}\begin{bmatrix} \theta_1 L \\ \theta_2 L \end{bmatrix} = \begin{bmatrix} C_{T_1}/L\dot{\theta}L \\ 0 \end{bmatrix} \tag{2}$$

$$\begin{bmatrix} m_{eq_1} & 0 \\ 0 & m_{eq_2} \end{bmatrix}\begin{bmatrix} \ddot{X}_1 \\ \ddot{X}_2 \end{bmatrix} + \begin{bmatrix} (C_{eq_1}+C_{eq_2}) & -C_{eq_2} \\ -C_{eq_2} & C_{eq_2} \end{bmatrix}\begin{bmatrix} \dot{X}_1 \\ \dot{X}_2 \end{bmatrix} + \begin{bmatrix} (K_{eq_1}+K_{eq_2}) & -K_{eq_2} \\ -K_{eq_2} & K_{eq_2} \end{bmatrix}\begin{bmatrix} X_1 \\ X_2 \end{bmatrix} = \begin{bmatrix} C_{eq_1}\dot{Z} \\ 0 \end{bmatrix} \tag{3}$$

By using the mathematical model of the system, the mass, stiffness and damping matrices can be generated, which determines the dynamic behavior of a system. Modal analysis can be applied in order to calculate system's characteristics as undamped/damped natural frequency and damping ratio as shown in Table 1.

Table 1. Modal analysis results

Mode No	ANSYS Results	MATLAB Results		
	Natural Freq. (f_n)	Natural Freq. (f_n)	Damping Ratio (ξ)	Damped Natural Freq. (f_d)
1	1.7479 Hz	1.7479 Hz	0.0137	1.7477 Hz
2	5.0329 Hz	5.0329 Hz	0.0395	5.0290 Hz
3	7.7109 Hz	7.7109 Hz	0.0606	7.6967 Hz
4	9.4588 Hz	9.4588 Hz	0.0743	9.4326 Hz

In the results it can be seen that natural frequencies (f_n) and damped natural frequencies (f_d) are nearly same due to the low damping ratio and the natural frequencies are low as an appearance of flexible system. There is a natural frequency and a mode shape for each degree-of-freedom and the fundamental period (T_n) of the system is 0.5721 seconds.

DYNAMIC ANALYSIS OF THE SYSTEM

It is known that the system has one input and one output, so the system can be shown as SISO (single input single output) system. (See Figure 3)

Figure 3. Single input single output model of the one-link manipulator.

The input is base excitation which is in trapezoidal function form. (See Figure 4)
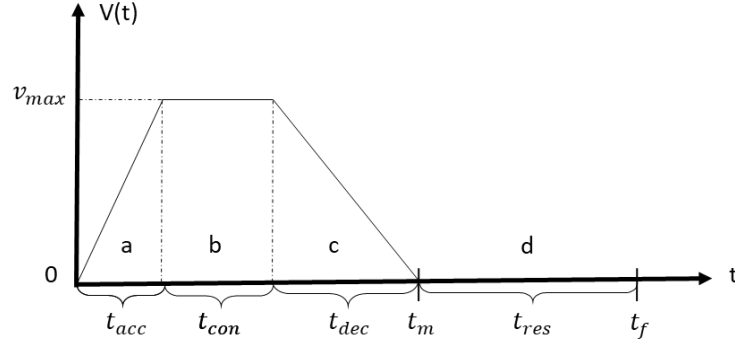

Figure 4. Trapezoidal velocity profile,
(a) acceleration state, (b) constant velocity state, (c) deceleration state, (d) stable state.

The parameters for the input, which are acceleration time (tacc), constant velocity time (tcon), deceleration time (tdec), motion time (tm), residual vibration time (tres), ending time (tf) and maximum velocity (vMAX). The parameters will be used in the vector form which is given as t= [tacc, tdec, tm, tf].

For the dynamic analysis of the system, three different solution method are used in order to validation of the methods. Firstly, the model with base excitation input is solved with ANSYS simulation program. Second method is a numerical integration method called Newmark solution and it calculates the system responses step by step by using the integration constants. (See Eq. 4,5,6,7)

$$q_{n+1} = [a_0 M + a_1 C + K]^{-1}[F_n + M(a_0 q_n + a_2 \dot{q}_n + a_3 \ddot{q}_n) + C(a_1 q_n + a_4 \dot{q}_n + a_5 \ddot{q}_n)] \qquad (4)$$

$$\ddot{q}_{n+1} = a_0(q_{n+1} - q_n) - a_2 \dot{q}_n - a_3 \ddot{q}_n \qquad (5)$$

$$\dot{q}_{n+1} = \dot{q}_n + a_6 \ddot{q}_n + a_7 \ddot{q}_{n+1} \qquad (6)$$

$$a_0 = \frac{1}{\alpha dt^2}, \quad a_1 = \frac{\delta}{\alpha dt}, \quad a_2 = \frac{1}{\alpha dt}, \quad a_3 = \frac{1}{2\alpha} - 1, \quad a_4 = \frac{\delta}{\alpha} - 1, \quad a_5 = \frac{\Delta t}{2}(a_4 - 1), \quad a_6 = \Delta t(1 - \delta),$$

$$a_7 = \delta \Delta t, \quad q_n = \begin{bmatrix} q_1(n) \\ q_2(n) \\ q_3(n) \\ q_4(n) \end{bmatrix}, \quad F_n = \begin{bmatrix} F_1(n) \\ 0 \\ 0 \\ 0 \end{bmatrix}, \quad M,C,K \in \mathbb{R}^{4x4}, \quad \alpha = \frac{1}{4}(1 + \gamma)^2, \quad \delta = \frac{1}{2} + \gamma \qquad (7)$$

In Newmark solution, the values of q are calculated at the subsequent time by knowing the initial values of q. In order to use the algorithm, adjusting the input as a force term is needed. So the base excitation is converted to the base force. (See Eq. 8)

$$F_1(n) = c_1 v(n) + k_1 x(n) \quad [N] \qquad (8)$$

After the Newmark solution, the results are compared with ANSYS solution and the matching is shown in Figure 5.
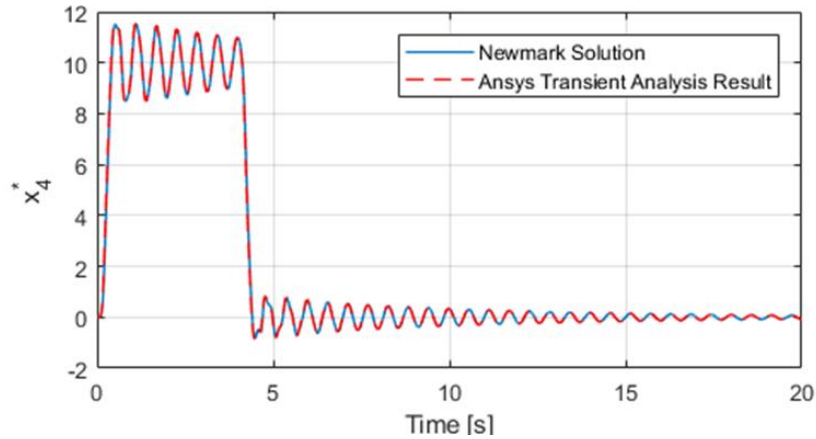
Figure 5. ASYS and Newmark solutions for base excitation, t=[0.5, 0.5, 4.5, 20], v_{max}=10 m/s

As the third dynamic analysis method, state-space modelling is used. (See Figure 6)
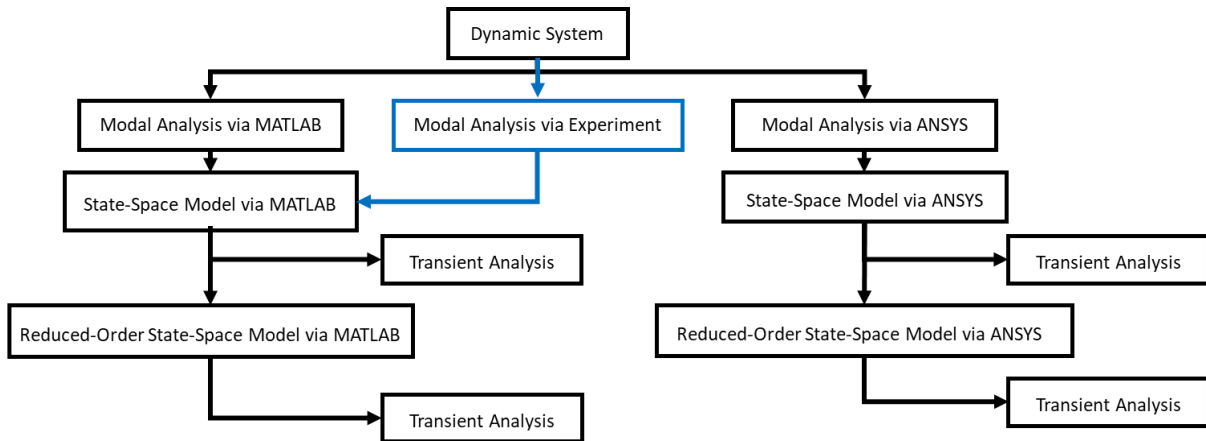

Figure 6. Process scheme for State-Space solution.

After the modal analysis, which can be both applied analytically, numerically and experimentally, by using the dynamic parameters from modal analysis state-space model of the dynamic system can be built. For complex systems, model's order can be reduced in order to simplify the system.

Because of being able to obtain dynamic parameters, building State-Space model with only an experiment is possible. During this process, the natural frequencies can be found by using FFT (Fast-Fourier-Transform), the damping ratio can be found from logarithmic decrement or half power method and the mode shapes can be found from Least Squares Finite Difference (LSFD) method or Abraham Time Domain Technique.

After the mathematical process called eigendecomposition, the equation of motion of modal coordinates is uncoupled (meaning it has only the diagonal elements). (See Eqs. 9,10)

$$\ddot{\boldsymbol{\eta}} + diag\big[2\xi_i\omega_{n_i}\big]\dot{\boldsymbol{\eta}} + diag\big[\omega_{n_i}^2\big]\boldsymbol{\eta} = \{\phi_i\}^T\{F\} \tag{9}$$

$$\{U\} = \{\phi\}\{\eta\} \tag{10}$$

$\boldsymbol{\eta}$ is the state vector, $\boldsymbol{\phi}$ is the orthonormalized eigenvector, U is the output vector of the system and Equation 10 shows the output-state verctor transform by using eigenvector. So, the system responses can be calculated with less terms and thus much more faster with the State-Space matrices given in Equations 11 and 12.

$$[\dot{\eta}] = [A][\eta] + [B][F]$$

$$[U] = [C][\eta] + [D][F] \tag{11}$$

180

where A is the system matrix, B is the input matrix, C is the output matrix and D is the feedthrough matrix, F is the input vector of the system.

$$\begin{bmatrix} \dot{\eta} \\ \ddot{\eta} \end{bmatrix} = \left[\begin{bmatrix} [0] \\ \begin{bmatrix} -\omega_1^2 & \cdots & 0 \\ \vdots & \ddots & \vdots \\ 0 & \cdots & -\omega_n^2 \end{bmatrix} \end{bmatrix} \begin{bmatrix} [I] \\ \begin{bmatrix} -2\xi_1\omega_1 & \cdots & 0 \\ \vdots & \ddots & \vdots \\ 0 & \cdots & -2\xi_n\omega_n \end{bmatrix} \end{bmatrix} \right] \begin{bmatrix} \eta \\ \dot{\eta} \end{bmatrix} + \begin{bmatrix} [0] \\ [\phi]^T[F_U] \end{bmatrix} [F]$$

$$\begin{bmatrix} U \\ \dot{U} \\ \ddot{U} \end{bmatrix} = \begin{bmatrix} [U_U][\phi] \\ [0] \\ [U_U][\phi].\begin{bmatrix} -\omega_1^2 & \cdots & 0 \\ \vdots & \ddots & \vdots \\ 0 & \cdots & -\omega_n^2 \end{bmatrix} & \begin{bmatrix} [0] \\ [U_U][\phi] \\ [U_U][\phi].\begin{bmatrix} -2\xi_1\omega_1 & \cdots & 0 \\ \vdots & \ddots & \vdots \\ 0 & \cdots & -2\xi_n\omega_n \end{bmatrix} \end{bmatrix} \begin{bmatrix} \eta \\ \dot{\eta} \end{bmatrix} + \begin{bmatrix} [0] \\ [0] \\ [U_U][\phi].[\phi]^T[F_U] \end{bmatrix} [F] \qquad (12)$$

Again organizing the input in terms of force is needed. It is known that k1 & c1 are constants for a linear system, so they can be found them with experiment, constant-velocity base input will give the k1 by adjusting the steady state value and adjusting of the decaying of the graph will give the c1. The comparison of the results of three methods shown in Figure 7.
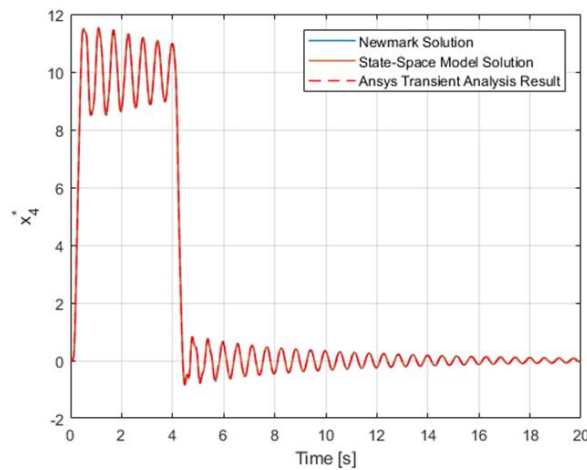

Figure 7. ASYS, Newmark and State-Space model solutions for base excitation, t=[0.5, 0.5, 4.5, 20], v$_{max}$=10 m/s.

In order to convert the full-order model to reduced-order model; mass, stiffness and damping elements must be changed entirely but model parameters will only reduce by quantity. So in order to reduce the four-degrees-of-freedom system into two-degrees-of-freedom system, it is just needed to reduce the modal parameters from four to two. In Figure 8 it can be seen that the reduced order model satisfies the full order model.
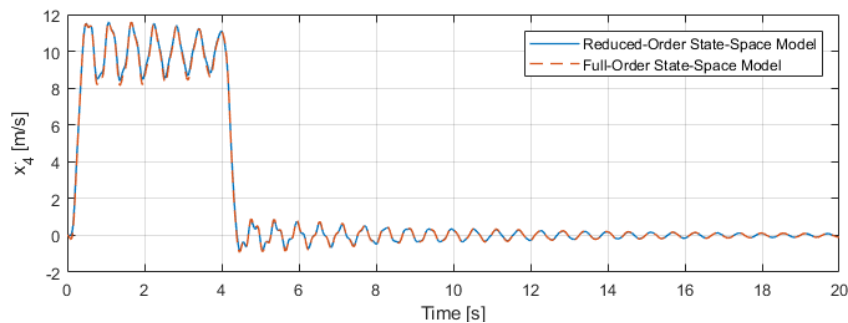

Figure 8. State-Space full-order and reduced-order model solutions for base excitation, t=[0.5, 0.5, 4.5, 20], v$_{max}$=10 m/s.

PASSIVE VIBRATION CONTROL

Same Trapezoidal velocity profiles are applied to State space model to control residual vibrations passively, except the deceleration time and the maximum velocity (vMAX), because of the changing of it depending on the deceleration time (tdec). While the inputs are being arranged, the fundamental period of the system and its multiples are chosen as deceleration time (tdec) parameter. Results of this application shown in Table 2.

Table 2. First passive vibration control application

Input No	Deceleration Time (t_{dec}) T_n=0.5721 sec	Maximum Velocity (v_{MAX})	RMS of the Residual Vibration
1	$T_n/2$	9.7395 m/s	2.0181 m/s
2	T_n	10.0910 m/s	0.2457 m/s
3	$2*T_n$	10.8758 m/s	0.2654 m/s
4	$3*T_n$	11.7930 m/s	0.2883 m/s
5	$4*T_n$	12.8792 m/s	0.3156 m/s
6	$5*T_n$	14.1858 m/s	0.3485 m/s

Figure 9 shows the difference between the outputs more clearly. In order to find the optimum value of deceleration time (tdec), the root mean square values of residual vibrations are compared as shown in Table 2, and it can be seen that the least residual vibration occurs when deceleration time equals to the fundamental period (tdec = Tn).
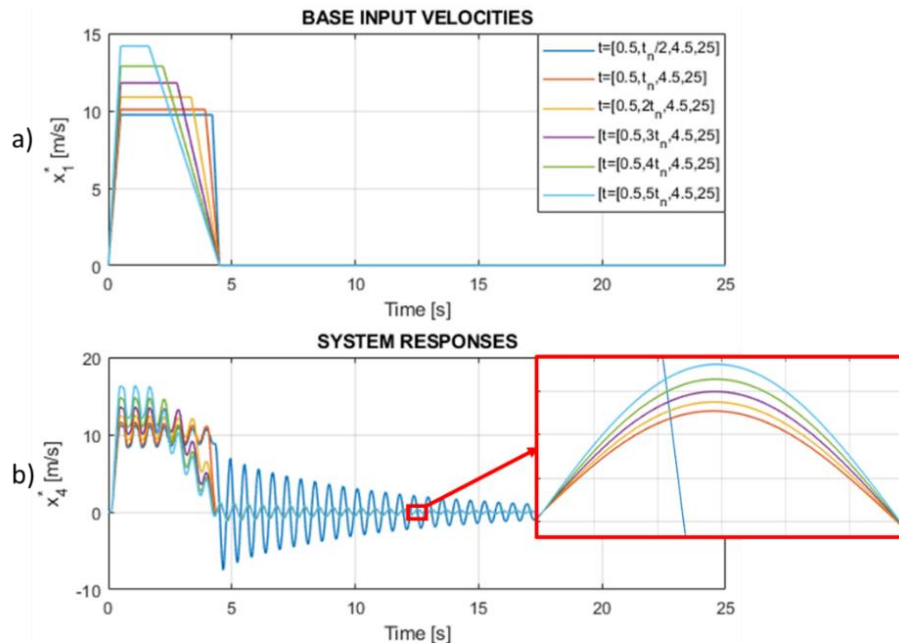

Figure 9. First passive vibration control application's graphics, (a) Input graphics, (b) Output graphics.

In second application, in order to research the best deceleration time parameter, an algorithm in code based manner is made. For gaining much more delicate results, 62.5 million data have produced. In Figure 10, the first graphic is for inputs with different deceleration times, second one is the responses of the system and third one shows the RMS values of the residual vibration responses. In the graphs, x-axis is the change of deceleration time parameter (tdec) and it is seen that, the best value with black ring is different with the fundamental period value with red ring. The elapsed time of the analysis via workstation is: 2 min 41 seconds.
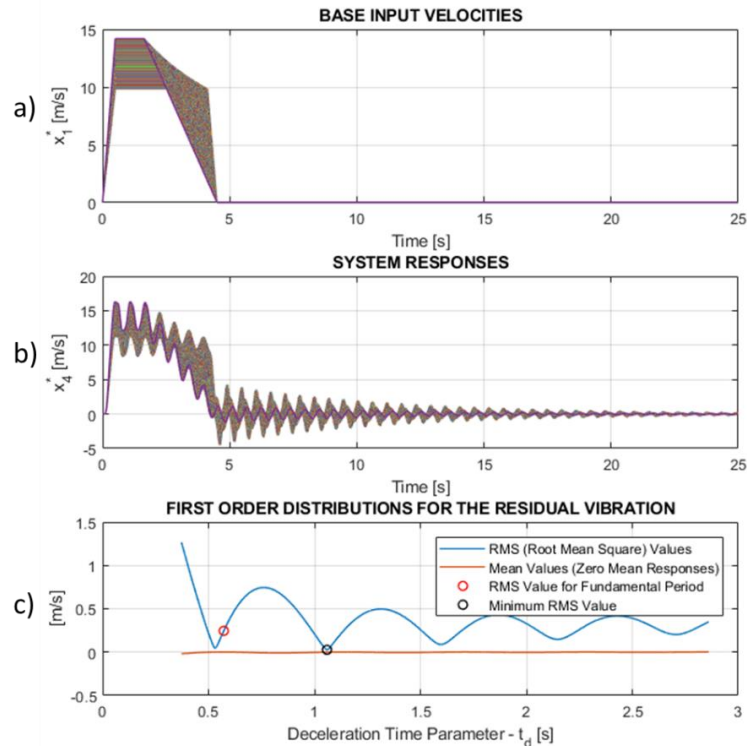
Figure 10. Second passive vibration control application's graphics,
(a) Input graphics, (b) Output graphics, (c) First-order-distribution of residual vibrations.

The state-space model responses are compared with State-Space model solutions and ANSYS transient structural solutions (See Figure 11) for comparing the two time parameters, and the validation of RMS algorithm is shown.
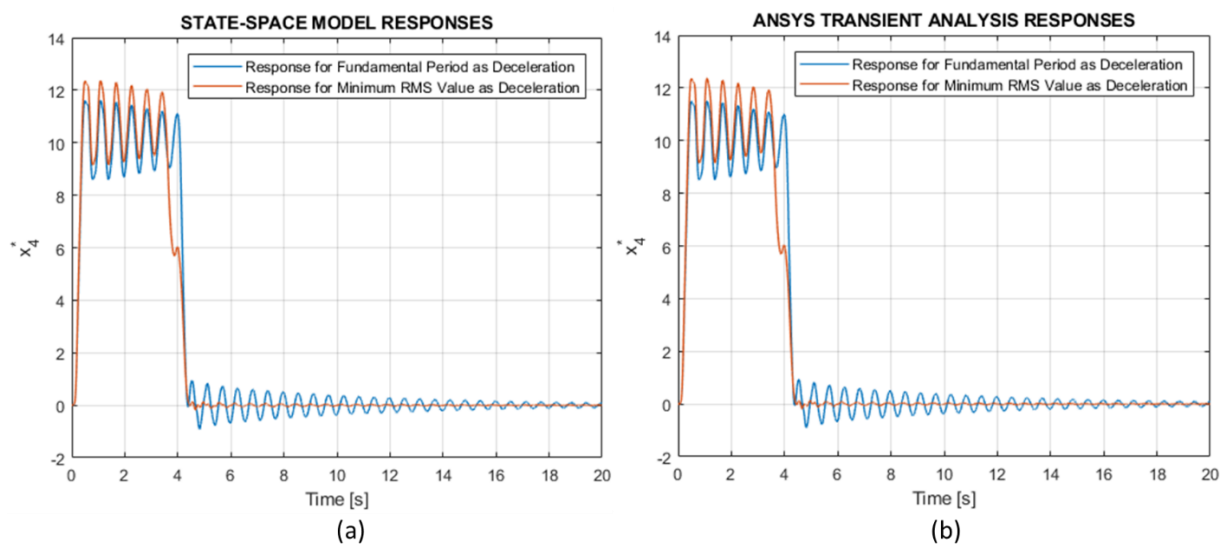

Figure 11. Comparison of best deceleration time parameter from first and second application,
(a) via state-space model solutions, (b) via ANSYS transient analysis solutions.

So it can be seen that, although the fundamental period is giving a good result - by the way it is a modal parameter, which means it can be applied to any other system - the value that found from second application is the best deceleration time value for this system. For generalizing this value for other systems, a relation between the value and modal parameters can be researched.

183

CONCLUSION

In order to minimize these harmful effects, passive vibration control is made via adjusting motion parameters of the velocity profile by considering natural periods of the system. From the results, it is observed that the numerical and analytical results are in good agreement. The passive vibration control solutions as presented in this study can be extended to simulate the control of complex mechanical systems by using experimentally modelling the system as reduced-order model.

REFERENCES

[1] L. Malgaca, H. Doğan, M. Akdağ, Ş. Yavuz, M. Uyar, B. Bidikli, Effect of joint flexibility on vibration characteristics of a composite box manipulator, Composite Structures 183 (2018) 271-277.

[2] L. Malgaca, Ş. Yavuz, M. Akdağ, H. Karagülle, Residual vibration control of a single-link flexible curved manipulator, Simulation Modelling Practice and Theory 67 (2016) 155-170.

[3] H. Karagülle, L. Malgaca, M. Dirilmiş, M. Akdağ, and Ş. Yavuz, Vibration control of a two-link flexible manipulator, Journal of Vibration and Control 23 (2015) 2023-2034.

[4] Ş. Yavuz, L. Malgaca, H. Karagülle, Analysis of active vibration control of multi-degree-of-freedom flexible systems by Newmark method, Simulation Modelling Practice and Theory 69 (2016) 136-148.

[5] A. Kosarac; et al. , State space modeling from FEM model using balanced reduction, Acta Technica Corviniensis - Bulletin of Engineering 9 (2016) 23-27.

Forced Vibration Analysis of Axially Functionally Graded Euler-Bernoulli Beam with Trigonometric Material Gradient

Sümeyye Sınır*, Bilecik Şeyh Edebali Univ., Institute of Graduate Studies, Gülümbe Campus, Bilecik, Türkiye
Mehmet Çevik, İzmir Katip Çelebi Univ., Dept. of Mechanical Engineering, Çiğli Main Campus, İzmir, Türkiye
* Corresponding author: sumeyye.sinir@bilecik.edu.tr

Abstract

Nonlinear forced vibrations of axially functionally graded Euler–Bernoulli beams are investigated. Equation of motion is derived by using Hamilton's principle with the von–Kármán's non–linear strain displacement relationships as non–linear variable–coefficient partial differential equation. The variations of material properties are assumed to be trigonometric functions, in which the axially direction of the beam. The equation of motion is non–dimensionalized in order to obtain a more general solution, then damping and forcing terms are included. The perturbation method is practiced to obtain approximate solution of the equations. In the linear order, natural frequencies and mode shapes are computed by differential quadrature method. In the nonlinear order, frequency –amplitude and frequency –response curves drawn to show the effect of nonlinear correction terms on natural frequency and the unstable regions.

Keywords: non–linear Euler–Bernoulli beam, perturbation method, differential quadrature method, forced vibration, frequency–response curves.
Discipline: Mechanical Engineering

1. INTRODUCTION

In the literature, there are many studies on various FGM structures like beams [1, 2] shells [3, 4], plates [5, 6], panels [4, 7]. Among the works on the beams, it is apparent that the greater part of publications is related with FGM beams which are graded in the thickness (transverse) direction [8-9, 13-16], still there are also numerous studies investigating FGBs with axially varying material properties [10-12, 17-18]. Free vibration analysis of the FGM beam is often considered in the literature [3-18]

In this study, the mathematical model of axially FGM Euler–Bernoulli beam including the von Kármán geometric nonlinearity is derived as at Ref. [1]. Multiple time scales method is performed in order to obtain an approximate solution for this model [1, 21]. However, the analytical solution of the variable coefficient linear differential equation at order one can be obtained only for exceptional coefficient functions by this method. Thus, the equation at order one is solved by DQM, and mode shapes and linear natural frequencies are obtained [1, 22]. The equation at order ε is tackled by multiple scales method. Consequently, multiple time scales method and DQM are used simultaneously to solve this problem for the first time in this study. The free vibration and frequency response analyses are performed. The effects of material gradient and nonlinearity are investigated.

2. EQUATION OF MOTION

The displacement field components of the Euler–Bernoulli beam theory are introduced as [1, 10-20]

$$
\begin{aligned}
u_{\hat{x}} &= -\hat{z}\frac{\partial \widehat{w}(\hat{x},\hat{t})}{\partial \hat{x}} \\
u_{\hat{y}} &= 0 \\
u_{\hat{z}} &= \widehat{w}(\hat{x},\hat{t})
\end{aligned}
\tag{1}
$$

In the above equations, $\hat{x}$–axis coincides with the centroidal axis of the undeformed beam, the $\hat{y}$–axis is the neutral axis and $\hat{z}$–axis is the symmetry axis; $(u_{\hat{x}}, u_{\hat{y}}, u_{\hat{z}})$ are displacement components of a point positioned at $(\hat{x}, \hat{y}, \hat{z})$; $\widehat{w} = \widehat{w}(\hat{x},\hat{t})$ denotes transverse deflection of a point on the $\hat{x}$–axis.

The strain field considering the von Kármán nonlinearity is [1, 2]

$$
\epsilon_{\hat{x}} = -z\widehat{w}' + \frac{1}{2}(\widehat{w}')^2
\tag{2}
$$

Equation of motion is derived by using Hamilton's principle with the von-Kármán's non-linear strain displacement relationships as non-linear variable-coefficient partial differential equation.

Substituting Eqs. (1)–(2) into Hamilton's principle [1, 19-20], the equation of motion is obtained as,

$$\left(\hat{E}(x)I\hat{w}''\right)'' + \left(\frac{\hat{E}(x)I}{2}(\hat{w}')^2\hat{w}'\right)' + \hat{\rho}(\hat{x})I\ddot{\hat{w}}'' + \hat{\rho}(\hat{x})A\ddot{\hat{w}} - \hat{q} = 0 \tag{3}$$

here $\hat{E}(x)$ is the Young's modulus, $\hat{\rho}(\hat{x})$ is density, A is the cross–sectional area and I is the moment of inertia of the beam.

The variations of material properties are assumed to be trigonometric functions, in which the axially direction of the beam. The variations of elasticity modulus and density are as [10, 23],

$$\hat{E}(\hat{x}) = E_0\left(1 + \alpha_1 cos\left(\pi\frac{\hat{x}}{L}\right)\right) \tag{4}$$

$$\hat{\rho}(\hat{x}) = \rho_0\left(1 + \alpha_2 cos\left(\pi\frac{\hat{x}}{L}\right)\right) \tag{5}$$

where $|\alpha_1| < 1$ and $|\alpha_2| < 1$ are parameters.

For the purpose of nondimensionalization, the dimensionless terms are introduced as:

$$x = \frac{\hat{x}}{L}, \qquad w = \frac{\hat{w}L}{r^2}, \qquad t = \frac{\hat{t}}{L^2}\sqrt{\frac{E_0 I}{\rho_0 A}} \tag{6}$$

where L is the length of the beam, r is the radius of gyration, and E_0 and ρ_0, are the Young's modulus and density at the starting configuration of the beam, respectively.

Substituting the dimensionless terms and after the mathematical manipulations, the equation of motion (3) reduces to,

$$Hw^{iv} + 2H'w''' + H''w'' + m\ddot{w} - \kappa H\ddot{w}'' \\ -\frac{\kappa}{2}\left(m'w'^3 + 3mw'^2w''\right) - q = 0 \tag{7}$$

Note that, κ is a small dimensionless parameter, inversely proportional to the square of slenderness ratio, $\kappa = \left(\frac{r}{L}\right)^2 \ll 1$. The new dimensionless coefficients in Eq. () are

$$H = E(x) = \frac{\hat{E}(\hat{x})}{E_0},$$

$$m = \rho(x) = \frac{\hat{\rho}(\hat{x})}{\rho_0}, \tag{8}$$

$$q = \frac{\hat{q}(\hat{x},\hat{t})L^5}{r^2 E_0 I}$$

Admitting κ equal to the perturbation parameter ε, adding external excitation having amplitude f and frequency Ω, and viscous damping having damping coefficient μ, at order ε, one finally obtains the following nonlinear equation of motion

$$Hw^{iv} + 2H'w''' + H''w'' + m\ddot{w} - \varepsilon H\ddot{w}'' \\ -\frac{\varepsilon}{2}\left(m'w'^3 + 3mw'^2w''\right) + \varepsilon\mu\dot{w} = \varepsilon f cos(\Omega t) \tag{9}$$

Since we investigate only the primary resonance case, the forcing and damping terms are ordered such that they respond the effect of nonlinearity.

3. DIRECT PERTURBATION ANALYSIS
In this section, we try to find approximate analytical solutions for Eq. (9) subject to the related boundary conditions. We apply the method of multiple time scales [21], to the partial differential

equation and boundary conditions directly. We assume the following approximate solution for the deflection in the form

$$w(x, T_0, T_1; \varepsilon) = w_0(x, T_0, T_1) + \varepsilon w_1(x, T_0, T_1) + \cdots \tag{10}$$

where, $T_0 = t$ and $T_1 = \varepsilon t$ represent the fast and slow time scales, respectively. Time derivatives are,

$$\frac{\partial}{\partial t} = D_0 + \varepsilon D_1 + \cdots$$

$$\frac{\partial^2}{\partial t^2} = D_0^2 + 2\varepsilon D_0 D_1 + \cdots \tag{11}$$

Substituting Eqs. (10) and (11) into Eq. (9) and separating terms at each order of ε, one obtains;

$$O(1): \ mD_0^2 w_0 + H_1 w_0^{iv} + 2H_1' w_0''' + H_1'' w_0'' = 0 \tag{12}$$

$$\begin{aligned}
O(\varepsilon): \ &mD_0^2 w_1 + H_1 w_1^{iv} + 2H_1' w_1''' + H_1'' w_1'' \\
&= -2mD_0 D_1 w_0 + H_2 D_0^2 w_0'' \\
&\quad + \frac{1}{2}\left(H_3' w_0'^3 + 3H_3 w_0'^2 w_0''\right) - \mu D_0 w_0 \\
&\quad + f\cos(\Omega t)
\end{aligned} \tag{13}$$

At $O(1)$ the problem is linear and we assume the following form of solution,

$$w_0(x, T_0, T_1) = \left(B_n(T_1)e^{i\omega_n T_0} + \bar{B}_n(T_1)e^{-i\omega_n T_0}\right)X_n(x) \tag{14}$$

where ω_n, B_n and $X_n = X_n(x)$ are natural frequencies, amplitude of motion and mode shapes respectively. Substituting Eq. (14) into Eq. (12), one has

$$HX_n^{iv} + 2H'X_n''' + H''X_n'' - m\omega_n^2 X_n = 0 \tag{15}$$

For pinned–pinned support, the boundary conditions are as,

$$X_n''(1) = X_n''(0) = 0 \text{ and } X_n(1) = X_n(0) = 0 \tag{16}$$

The mode shapes X_n can be obtained from the solution of Eq. (15) with differential quadrature method.

Differential quadrature method requires discretizing the domain of the problem into S points. This method is based on the assumption that the derivative of a function may be represented as the weighted linear sum of the function values at all discrete points [1, 22].

Substituting the given discretizing equations of derivative terms at Ref.[1,22] into Eq. (15), one obtains the following discretized equation of motion,

$$\begin{aligned}
&H(x_i)\sum_{j=1}^{S} c_{ij}^{(4)} X_n(x_j) + 2H'(\xi_i)\sum_{j=1}^{S} c_{ij}^{(3)} X_n(x_j) \\
&+ H''(x_i)\sum_{j=1}^{S} c_{ij}^{(2)} X_n(x_j) - \omega_n^2 m(x_i) X_n(x_i) = 0 \ , \\
&\qquad\qquad i = 1,2,3,\dots,S
\end{aligned} \tag{17}$$

Substituting the given discretizing equations of derivative into Eq. (16), the discretized form of the pinned-pinned supported boundary conditions are obtained,

$$\begin{aligned}
X_n(x_1) = 0, \quad &\sum_{j=2}^{S-1} c_{1j}^{(2)} X_n(x_j) = 0 \\
X_n(x_S) = 0, \quad &\sum_{j=2}^{S-1} c_{Sj}^{(2)} X_n(x_j) = 0
\end{aligned} \tag{18}$$

Similarly, for the points neighboring the boundary

$$X_n(x_2) = -\frac{1}{K}\sum_{j=3}^{S-2} K_1 X_n(x_j)$$

$$X_n(x_{S-1}) = -\frac{1}{K}\sum_{j=3}^{S-2} K_2 X_n(x_j)$$

(19)

where

$$K_1 = c_{Sj}^{(2)} c_{1,S-1}^{(2)} - c_{1j}^{(2)} c_{S,S-1}^{(2)}$$

$$K_2 = c_{S2}^{(2)} c_{1,j}^{(2)} - c_{12}^{(2)} c_{Sj}^{(2)}$$

(20)

Then, integrating Eq. (19) for pinned–pinned supports, yields the following algebraic system of equations

$$H(x_i)\sum_{j=3}^{S-2}\left(c_{ij}^{(4)} - \frac{c_{i2}^{(4)}K_1 + c_{iS}^{(4)}K_2}{K}\right)X_n(x_j)$$
$$+ 2H'(x_i)\sum_{j=3}^{S-2}\left(c_{ij}^{(3)} - \frac{c_{i2}^{(3)}K_1 + c_{iS}^{(3)}K_2}{K}\right)X_n(x_j)$$
$$+ H''(\xi_i)\sum_{j=3}^{S-2}\left(c_{ij}^{(2)} - \frac{c_{i2}^{(2)}K_1 + c_{iS}^{(2)}K_2}{K}\right)X_n(x_j)$$
$$- \omega_n^2 m(x_i)X_n(x_i) = 0 \; , \qquad i = 3, \ldots, S-2$$

(21)

where the linear natural frequencies ω_n and mode shapes X_n of the beam can be determent using algebraic system of equations (21).

Now, in order to tackle the nonlinear part of the problem, we substitute Eq. (14) into Eq. (13) and simplify to reveal

$$mD_0^2 w_1 + H w_1^{iv} + 2H' w_1''' + H'' w_1''$$
$$= -2D_0 D_1 (B_n e^{i\omega_n T_0} + ke)X_n$$
$$+ HD_0^2 (B_n e^{i\omega_n T_0} + ke)X_n''$$
$$+ \frac{1}{2}\{m'(B_n^3 e^{3i\omega_n T_0} + 3B_n^2 \bar{B}_n e^{i\omega_n T_0} + ke)X_n'^3$$
$$+ 3m(B_n^3 e^{3i\omega_n T_0} + 3B_n^2 \bar{B}_n e^{i\omega_n T_0} + ke)X_n'^2 X_n''\}$$
$$- i\mu\omega_n(B_n e^{i\omega_n T_0} + ke)X_n + \frac{f}{2}(e^{i\Omega T_0} + e^{-i\Omega T_0})$$

(22)

Because the homogeneous Eq. (12) has a non–trivial solution, the non–homogeneous Eq. (13) can possess a solution if and only if a solvability condition is satisfied [21]. To establish a solvability condition, one has to separate the secular and non–secular terms. There for we suggest the following solution function,

$$w_1(x, T_0, T_1) = \varphi_n(x, T_1)e^{i\omega_n T_0} + W(x, T_0, T_1) + cc$$

(23)

where φ_n represents the portion of solution related with secular terms and $W(x, T_0, T_1)$ represents the portion related with non–secular terms. In an attempt to eliminate the terms causing secularities, we substitute Eq. (23) into Eq. (13), and elaborate the related part

$$-\omega_n^2\varphi_n + H\varphi_n^{iv} + 2H'\varphi_n''' + H''\varphi_n''$$
$$= -2D_0D_1\left(B_n e^{i\omega_n T_0} + ke\right)X_n$$
$$+ HD_0^2\left(B_n e^{i\omega_n T_0} + ke\right)X_n''$$
$$+ \frac{1}{2}\left\{m'\left(B_n^3 e^{3i\omega_n T_0} + 3B_n^2\bar{B}_n e^{i\omega_n T_0} + ke\right)X_n'^3\right.$$
$$\left. + 3m\left(B_n^3 e^{3i\omega_n T_0} + 3B_n^2\bar{B}_n e^{i\omega_n T_0} + ke\right)X_n'^2 X_n''\right\}$$
$$- i\mu\omega_n\left(B_n e^{i\omega_n T_0} + ke\right)X_n + \frac{f}{2}\left(e^{i\Omega T_0} + e^{-i\Omega T_0}\right)$$

(24)

Herewith, pinned–pinned is as

$$\varphi_n''(1) = \varphi_n''(0) = 0 \text{ and } \varphi_n(1) = \varphi_n(0) = 0 \tag{25}$$

4. NON-LINEAR FREQUENCIES

In this case, there is no external load and no damping, thus

$$f = 0, \mu = 0 \tag{26}$$

From Eq.(24), the solvability condition of free vibration case is

$$D_1 B_n + ik_{1I} B_n + ik_2 B_n^2 \bar{B}_n = 0 \tag{27}$$

where

$$k_{1I} = -\frac{\omega_n}{2}\frac{\int_0^1 H X_n'' dx}{\int_0^1 m X_n^2 dx} \tag{28}$$

$$k_2 = \frac{3}{4\omega_n}\frac{\int_0^1\left(m' X_n'^3 + m X_n'^2 X_n''\right)dx}{\int_0^1 m X_n^2 dx} \tag{29}$$

The solvability condition (27) discloses the amplitude–phase modulation equations. Polar form of the complex amplitude is

$$B_n = \frac{1}{2}b_n(T_1)e^{i\beta_n(T_1)} \tag{30}$$

Substitute Eq. (30) into Eq. (27), then separate real and imaginary parts,

$$D_1 b_n = 0 \tag{31}$$

$$D_1\beta_n = -k_{1I} - \frac{k_2}{4}b_n^2 = 0 \tag{32}$$

From the real part (31), $b_n = b_0$ where b_0 is a constant amplitude. From the imaginary part (32), one obtains the nonlinear frequency as

$$\beta_n = \beta_0 + \left(-k_{1I} - \frac{k_2}{4}b_0^2\right)T_1 = \beta_0 + \left(-k_{1I} - \frac{k_2}{4}b_0^2\right)\varepsilon t \tag{33}$$

5. FORCED VIBRATION ANALYSIS

We begin the forced vibration analysis by first assuming that the frequency of external excitation comes close to one of the natural frequencies; therefore

$$\Omega = \omega_n + \varepsilon\sigma_n \tag{34}$$

where σ_n is a detuning parameter. In addition, the solvability condition of forced vibration case is obtained from Eq. (24) as

$$D_1 B_n + (k_{1R} + ik_{1I})B_n + ik_2 B_n^2\bar{B}_n + \frac{1}{2}F_n e^{i\sigma_n T_1} = 0 \tag{35}$$

where,

$$k_{1R} = \frac{1}{2} \frac{\int_0^1 \mu X_n^2 dx}{\int_0^1 m X_n^2 dx} \tag{36}$$

$$F_n = \int_0^1 f X_n \, dx \tag{37}$$

Substitute Eq. (30) into Eq. (35), then separate real and imaginary parts,

$$D_1 b_n + k_{1R} b_n - \frac{F_n}{2\omega_n} \sin(\gamma_n) = 0 \tag{38}$$

$$D_1 \gamma_n = \sigma_n + k_{1I} - \frac{k_2}{4} b_n^2 + \frac{F_n}{2\omega_n} \cos(\gamma_n) = 0 \tag{39}$$

Here, γ_n is defined by $\gamma_n = \sigma_n T_1 - \beta_n$.

For the steady–state solution, $D_1 b_n = D_1 \gamma_n = 0$; thus

$$\sigma_n = -k_{1I} - \frac{k_2}{4} b_0^2 \pm \frac{1}{2} \sqrt{\frac{F_n^2}{b_0^2} - 16 k_{1R}^2} \tag{40}$$

6. NUMERICAL RESULTS

Table 1 shows material properties for aluminum and zirconia.

Table 1. Material properties for aluminum and zirconia.

Property	Unit	aluminum	zirconia
E	GPa	70	200
ρ	Kg/m^3	2702	5700

Table 2 shows linear natural frequencies of the FGM beam according to variation of α_1 and α_2.

Table 2. Linear natural frequencies, for $\alpha_2 = 4\alpha_1$.

	Pinned–pinned				
n	$\alpha_1 = -0.2$	$\alpha_1 = -0.1$	$\alpha_1 = 0$	$\alpha_1 = 0.1$	$\alpha_1 = 0.2$
1	9.9913	9.8994	9.8696	9.8994	9.9913
2	42.4303	40.1576	39.4784	40.1576	42.4303
3	96.5374	90.3757	88.8264	90.3757	96.5374

In the nonlinear order, frequency–amplitude and frequency–response curves are drawn to show the effect of nonlinear correction terms on natural frequency and the unstable regions as in Figures 1 and 2. The effects of variation of α_1 and α_2 on natural frequencies and stability are obtained.
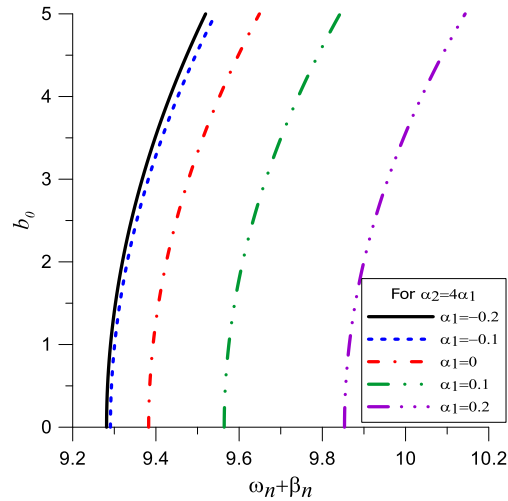
Figure 1. Nonlinear natural frequencies of pinned–pinned supported beam, first mode.
($\varepsilon = 1/100$)

The variation of natural frequencies with amplitude is shown in Figure 1 and natural frequencies increase with increasing α_1 and α_2 .
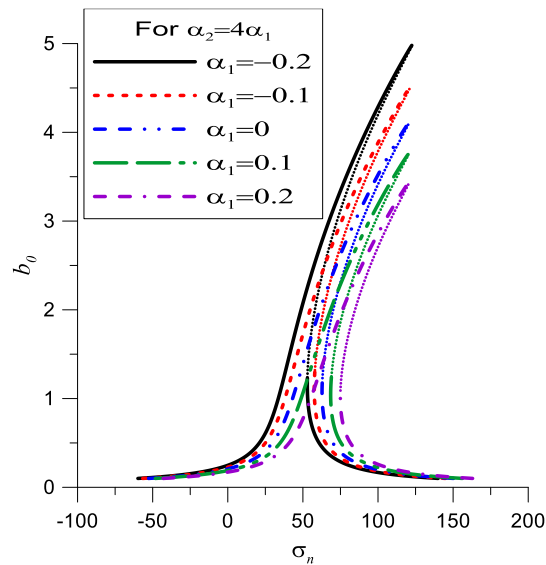

Figure 2. Nonlinear frequency–response curves of pinned–pinned supported beam, first mode.
($f = 25,\ \mu = 0.1,\ \varepsilon = 1/100$)

We observe that nonlinearity has a hardening effect and the unstable region decrease as α_1 and α_2 increase in Figure 2.

7. CONCLUSION

The mathematical model of axially FGM Euler–Bernoulli beam including the von Kármán geometric nonlinearity is derived. Multiple time scales method is used to obtain an approximate solution for this model. The equation at order one is solved by DQM, and mode shapes and linear natural frequencies are obtained. Multiple time scales method and DQM are used simultaneously to solve this problem. The free vibration and frequency response analyses are performed. The effects of material gradient and nonlinearity are investigated. It is observed that natural frequencies increase with increasing material coefficients α_1 and α_2 .

REFERENCES

[1] S. Sınır, M. Çevik, B.G. Sınır, Nonlinear free and forced vibration analyses of axially functionally graded Euler–Bernoulli beams with non–uniform cross–section, Composites: Part B 148 (2018) 123–131.

[2] B. Akgöz, Ö. Civalek, Longitudinal vibration analysis of strain gradient bars made of functionally graded materials, Composites: Part B 55 (2013) 263–268.

[3] F. Z. Jouneghani, R. Dimitri, M. Bacciocchi, F. Tornabene, Free vibration analysis of functionally graded porous doubly–curved shells based on the first–order shear deformation theory, Applied Sciences 7(12)1252 (2017) 1-20.

[4] F.Tornabene, E.Viola, Free vibration analysis of functionally graded panels and shells of revolution, Meccanica 44 (2009) 255–281.

[5] F.Tornabene, S. Brischetto, N. Fantuzzi, M. Bacciocchi, Boundary conditions in 2D numerical and 3D exact models for cylindrical bending analysis of functionally graded structures, Shock and Vibration, Article ID 2373862 (2016) 1-17.

[6] F. Tornabene, Free vibration analysis of functionally graded conical, cylindrical shell and annular plate structures with a four–parameter power–law distribution, Computer Methods in Applied Mechanics and Engineering 198 (2009) 2911–2935.

[7] F. Tornabene, E. Viola, Free vibrations of four–parameter functionally graded parabolic panels and shells of revolution, European Journal of Mechanics A/Solids 28 (2009) 991–1013.

[8] C. Jin, X. Wang, Accurate free vibration analysis of Euler functionally graded beams by the weak form quadrature element method, Composite Structures 125 (2015) 41–50.

[9] K.K. Pradhan, S. Chakraverty, Free vibration of Euler and Timoshenko functionally graded beams by Rayleigh–Ritz method, Composites: Part B 51 (2013) 175–184.

[10] Y. Huang, X.F. Li, A new approach for free vibration of axially functionally graded beams with non–uniform cross–section, Journal of Sound and Vibration 329 (2009) 2291–303.

[11] J.W. Lee, J.Y. Lee, Free vibration analysis of functionally graded Bernoulli–Euler beams using an exact transfer matrix expression, International Journal of Mechanical Sciences, 122 (2017) 1–17.

[12] S. Kumar, A. Mitra, H. Roy, Geometrically nonlinear free vibration analysis of axially functionally graded taper beams, Engineering Science and Technology, An International Journal 18 (2015) 579–593.

[13] H.T. Thai, T.P. Vo, Bending and free vibration of functionally graded beams using various higher–order shear deformation beam theories, International Journal of Mechanical Sciences 62 (2012) 57–66.

[14] M. Şimşek, Fundamental frequency analysis of functionally graded beams by using different higher–order beam theories, Nuclear Engineering and Design 240 (2010) 697–705.

[15] M. Sitar, F. Kosel, M. Brojan, Large deflections of nonlinearly elastic functionally graded composite beams, Archives of Civil and Mechanical Engineering 14 (2014) 700–709.

[16] G. Giunta, D. Crisafulli, S. Belouettar, E. Carrera, Hierarchical theories for the free vibration analysis of functionally graded beams, Composite Structures 94 (2011) 68–74.

[17] Y. Huang, L.E. Yang, Q.Z. Luo, Free vibration of axially functionally graded Timoshenko beams with non–uniform cross–section, Composites: Part B 45 (2013) 1493–1498.

[18] X.F. Li, Y.A. Kang, J.X. Wu, Exact frequency equations of free vibration of exponentially functionally graded beams, Applied Acoustics 74 (2013) 413–420.

[19] P. Khodabakhshi, J.N. Reddy, A unified beam theory with strain gradient effect and the von Kármán nonlinearity, ZAMM Journal of Applied Mathematics and Mechanics 97 (2017) 70–91.

[20] J.N. Reddy, P. Mahaffey, Generalized beam theories accounting for von Kármán nonlinear strains with application to buckling, Journal of Coupled Systems and Multiscale Dynamics 1 (2013) 120–134.

[21] A. H. Nayfeh, Introduction to Perturbation Techniques, John Wiley & Sons, New York, 1981.

[22] C. Shu, Differential Quadrature and Its Application in Engineering, Springer, 2000.

[23] H. Hein, L. Fklistova, Free vibrations of non–uniform and axially functionally graded beams using Haar wavelets, Engineering Structures 3 (2011) 3696–3701.

Influence of Thermal-oil Ageing on Mechanical and Thermal Properties of E-Glass Fibre/Epoxy Composites

Tarkan Akderya*, Mehmet Çevik
İzmir Katip Çelebi Univ., Dept. of Mechanical Engineering, Çiğli Main Campus, İzmir, Türkiye
*Corresponding author: takderya@gmail.com

Abstract

The effects of thermal-oil ageing at different temperatures on the mechanical and thermal properties of glass fiber / epoxy composite specimens are investigated. It is observed from the tensile tests that the load carrying capacities of the composite specimens subjected to thermal-oil ageing at 100 and 120 °C for 360 hours are lower than those of the non-aged one. The ageing process reduced the ductility of the specimens. Thermal-oil ageing application temperature has a detrimental effect on the thermal stability of E-glass fibre/epoxy composite specimens. The highest glass transition temperature belongs to non-aged samples and glass transition temperatures decrease as the ageing temperature increases.

Keywords: E-Glass fibre/epoxy, thermal ageing, mechanical properties, thermal stability
Discipline: Mechanical Engineering

INTRODUCTION

Polymer matrix composites (PMC's) can be used in a wide range of applications such as energy, marine, defence and aircraft industries. In addition to that, polymer matrix composite based pipes are widely used for submerged and underground transport of materials such as natural gas, oil, thermal water and wastewater. Environmental influences such as high and low temperatures, temperature changes and humidity, which are active during the service life, can affect the pot life of the pipes.

Hu et al. [1] conducted a study to investigate the effect of hygrothermal ageing on the fatigue behaviour of glass fibre / polydicyclopentadiene composite. As a result of this study; it was found that the main cause of surface degradation depends on the water absorption. Another experimental study was conducted by Rocha et al. [2] and the purpose of this study was to analyse the damage processes caused by hygrothermal ageing in an epoxy system reinforced with E-glass fibres representing the material used in the design of the wind turbine. The mechanical properties of hygrothermal aged composite specimens were reduced by up to 36% compared to those of non-aged ones.

Therefore, some experimental studies have been carried out to determine the effect of thermal-oil ageing on the mechanical and thermal properties of e-glass fibre / epoxy composite materials. The present study proposes some new aspects for e-glass fibre/epoxy composites.

MATERIAL PRODUCTION AND THERMAL-OIL AGEING APPLICATION

Vacuum-Assisted Resin Infusion Method (VARIM) were used to produce eight-layer [0/90]8s woven glass fibre/epoxy composite laminates (Figure 1). After the production process, the laminate was cut into pieces according to ASTM D3039 standard for tensile testing (Figure 2).

Two different group of specimens were heated in a 5000-ml borosilicate laboratory glass beaker filled with heat transfer fluid (Renolin Therm 320) using a heating magnetic stirrer to 100 °C and 120 °C and kept at these temperatures for 360 hours (Figure 3).
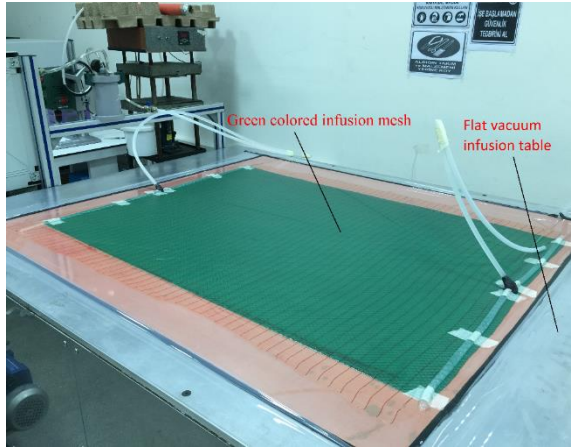
Figure 1. Glass fibre/epoxy composite material production process using VARIM.
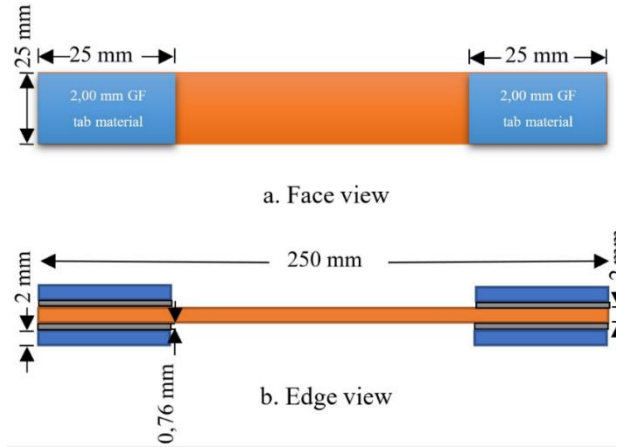

a. Face view

b. Edge view

Figure 2. Tensile test specimen geometries according to ASTM D3039.

100 °C   120 °C

Figure 3. Specimens subjected to thermal ageing at different temperatures.

RESULTS

The tensile tests used to determine the mechanical properties of the composite material were performed at room temperature using a Shimadzu 100 kN capacity device with a crosshead speed of 1mm/min and at least three pieces per parameter. Thermogravimetric analyse (TGA), Differential Thermal Analysis (DTA) and Differential Scanning Calorimetry (DSC) analyses were performed to determine how thermal-oil ageing affects thermal stability and glass transition temperatures of the composite material. TGA and DTA of the composite samples were performed using an instrument TA TGA-SDT Q600 at a flow rate of 50 ml/min under a nitrogen atmosphere at a rate of 10 °C/min. 10-20 mg samples were placed on a platinum pan and heated from 30 °C to 600 °C. DSC analysis, the determinant of the glass transition temperatures, was performed using TA DSC Q2000 instrument. The 10-15 mg samples were put into the aluminium pans and heated from 25 to 300 °C at a rate of 10 °C/min.

According to the tensile test results, the load carrying capacities of the composite specimens subjected to thermal-oil ageing at 100 and 120 °C for 360 hours are lower than those of the non-aged one. In addition to that, the ageing process reduced the ductility of the specimens (Figure 4).
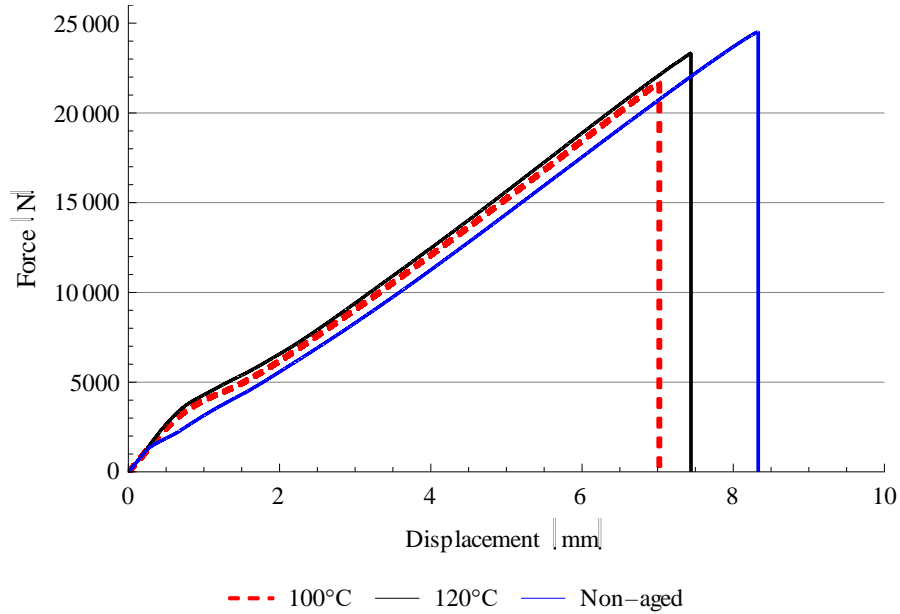
194

Figure 4. Force–Displacement graph for 360-hour thermal aged composites.

In Figure 5, the change in percentage weight of the composite sample is given by increasing the temperature as a time dependent function. According to this, the degradation rates of non-aged specimens, specimens aged at 100 and 120 °C are 22.50%, 24.95% and 26.25%, respectively (Figure 5). According to the TGA and DTA results, the onset temperature (T_{onset}°C) which is determinant of thermal stability, is 359.55 for non-aged specimens, 357.54 for the specimens aged at 100 °C and 354.74 for the specimens aged at 120 °C (Table 1). Above the onset temperature, there is a degradation in the chemical bonds in the fibres [3]. Composite materials can be safely used up to this temperature [4]. After this temperature, degradation will be accelerated and decreases in thermal stability will cause mechanical properties to drop. It is observed that, thermal-oil ageing application temperature has a detrimental effect on the thermal stability of E-glass fibre/epoxy composite specimens.
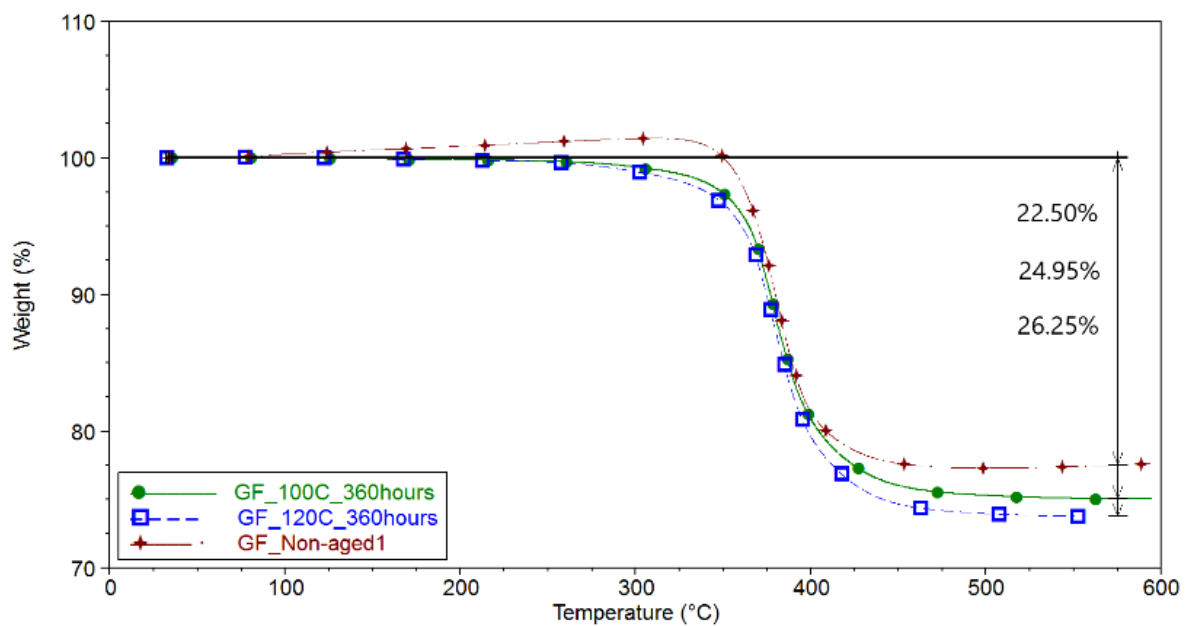

Figure 5. Weight–Temperature graph for 360-hour thermal aged composites.

Table 1. Decomposition temperatures of 360-hour aged E-Glass fibre/epoxy composites

Sample name	1st degradation step			3rd degradation step			Complex peak temp. from DTA curves			
	T_{1i} (°C)	T_{1f} (°C)	% weight loss	T_{3i} (°C)	T_{3f} (°C)	% weight loss	T_{onset} (°C)	T_{endset} (°C)	T_{peak} (°C)	Area μV·min / (mg·°C)
360h@ 100°C	261.87	357.54	3.06	357.54	405.53	16.60	363.71	388.59	374.94	0.01067
360h@ 120°C	250.95	354.74	3.55	354.74	406.01	17.57	363.44	394.31	373.98	0.01067
Non-aged	277.35	359.55	1.74	359.55	403.65	17.61	356.88	395.89	379.24	0.01037

The changes in glass transition temperature (Tg) due to the thermal ageing temperatures of the E-glass fiber / epoxy composite material are shown in Figure 6. Among the 360-hour aged ones, the lowest Tg belongs to the samples aged at 120 °C. The highest value belongs to the non-aged specimen.
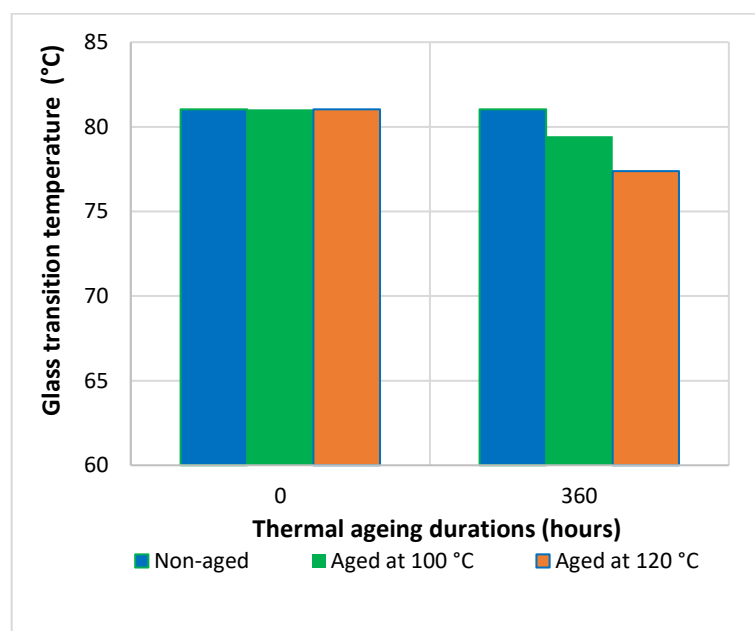

Figure 6. Glass transition temperatures - Thermal ageing durations chart.

CONCLUSION

In this study, the effects of thermal-oil ageing at different temperatures for 360 hours on the mechanical and thermal properties of glass fiber/epoxy composite specimens were investigated. The following results are obtained;

- As the thermal ageing temperature increases, the load carrying capacities of the specimens decrease.
- The increasing of the ageing temperature has a reducing effect on the thermal stability of the samples.
- The highest glass transition temperature belongs to non-aged samples and glass transition temperatures decrease as the ageing temperature increases

REFERENCES

[1] Y. Hu, A.W. Lang, X. Li, S.R. Nutt, Hygrothermal aging effects on fatigue of glass fiber/ polydicyclopentadiene composites, Polymer Degradation and Stability 110 (2014) 464-472. DOI: https://doi.org/10.1016/j.polymdegradstab.2014.10.018

[2] I.B.C.M. Rocha, S. Raijmaekers, R.P.L. Nijssen, F.P. van der Meer, L.J. Sluys, Hygrothermal ageing behaviour of a glass/epoxy composite used in wind turbine blades, Composite Structure 174 (2017) 110-122. DOI: https://doi.org/10.1016/j.compstruct.2017.04.028

[3] A.C. Milanese, M.O.H. Cioff, H.J.C. Voorwald, Thermal and mechanical behaviour of sisal/phenolic composites, Composites Part B: Engineering 43(7) (2012) 2843-2850. DOI: https://doi.org/10.1016/j.compositesb.2012.04.048

[4] K. Anbukarasi, S. Kalaiselvam, Study of effect of fibre volume and dimension on mechanical, thermal, and water absorption behaviour of luffa reinforced epoxy composites, Materials & Design 66 (2015) 321-330. DOI: https://doi.org/10.1016/j.matdes.2014.10.078

Design and Manufacture of an Industrial Low Cost Pick-and-Place Parallel Mechanism

Ünsal Dinçer, DALAN Kimya Endüstri A.Ş., Kemalpaşa Cad. No.325 35060 Pınarbaşı İzmir, Türkiye
Mehmet Çevik*, İzmir Katip Çelebi Univ., Dept. of Mechanical Engineering, Çiğli Main Campus, İzmir, Türkiye
*Corresponding author: mehmet.cevik@ikc.edu.tr

Abstract

A low-cost parallel mechanism that meets with the expectations of industry was designed and prototyped rapidly within domestic manufacturing capabilities. The manufacturing cost of this manipulator is about one third of a similar commercial manipulator in the market and will decrease significantly in subsequent productions.

Keywords: parallel mechanism, kinematic, servo, Codesys
Discipline: Mechatronics Engineering

INTRODUCTION

The aim of this study is to design and manufacture an industrial low cost parallel mechanism to be used in Dalan Kimya Soap Manufacturing Plant for quality control, and pick and place of soaps. The cost of parallel manipulators is an important aspect in their design and implementation in the industry. In the last decade, there are various studies about manufacturing low cost parallel robots in the literature. Cazalilla et al. [1] designed a low cost parallel-robot PRS that has been controlled using Oroco modules. Orocos is a real-time middleware focused on control systems. The authors mention its advantage as the capability to provide an off-the-shelf hard real-time operation, which is crucial in most of the robotics applications. Grajewski et al. [2] presented new approach to creating interactive simulations for testing tactile interaction with the user, which involves use of a low-cost device. They used a parallel kinematic structure (Delta robot) for this purpose. According to the authors, this type of application will be able in the future to support the effectiveness of virtual training, with particular emphasis on educational simulation. Another low cost and robust robot design study is carried out by Gomez et al. [3]. It is a tool for students to gain experience integrating different mechatronic fields of knowledge, as well as practicing the procedures needed to successfully accomplish their own design. Ottavino et al. [4] presented the design and kinematic performances for a low-cost parallel manipulator with 4 driven cables. A prototype has been built and tests have experienced the feasibility of the system design and its operation. The ability to work in an unexplored environment is crucial to the success of the autonomous robot's operation. The simultaneous localization and mapping is a technique used to build a map of the robot's surrounding while keeping track of its position. In recent years, significant attention has been paid to the development of this technique. One of the reasons behind this popularity is the low price [5]. A group of researchers developed a low cost parallel robot to assist impaired persons in making 3-dof movements of the forearm and wrist with a parts and machining cost of less than 1500 USD. The process of design and development of a low cost small sized in-pipe inspection robot was examined in another study [7]. Some researches focused on low cost robot parts. Gutiérrez et al. [8] manufactured a prototype of a lightweight robot arm with a low cost budget, fully functional. They used their prototype to test and fix elements for driving and controlling. They concluded some recommendations about material, reinforcements, geometry of the parts as a result of their investigation. Another research [9] is about the design of a robot gripper for a service robot that moves rapidly. The required criteria were light weight, low cost and friendly shape.

As can be concluded from these studies, there is still interest to develop low cost manipulators. The present study focuses on such a research. Custom-made parts, two servomotors, a control unit and open source code available to everyone have a much lower cost than their counterparts have in the market.

MECHANICAL DESIGN

According to preliminary inspections of manufacturing lines, the workspace required for pick and place process was determined. The total degrees of freedom of the manipulator is calculated as 2. The solid model of a new mechanism was designed via Solidworks software through inspiration of existing

two degrees-of-freedom parallel mechanisms. The kinematic equations were derived and forward and inverse kinematics solutions were obtained using Matlab software, the sign analysis was performed; then the maximum available workspace of the mechanism was drawn. The equations were verified by comparing the results obtained by Solidworks and Matlab programs. Figure 1 displays the motion analysis in Solidworks.
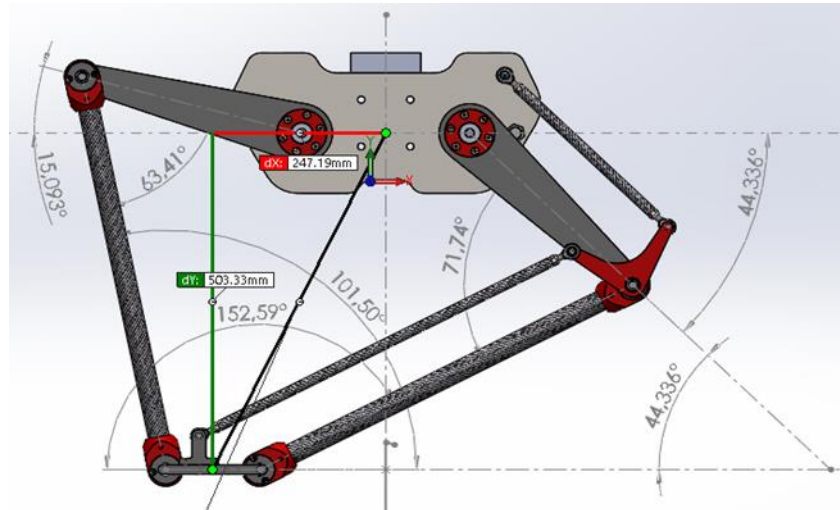

Figure 1. Motion analysis in Solidworks.

The maximal working space in the XZ-plane and the physical constraints are shown in Figure 2. An optimum working area, based on trajectory and general requirements, was determined within the maximal workspace that was determined considering the physical constraints.
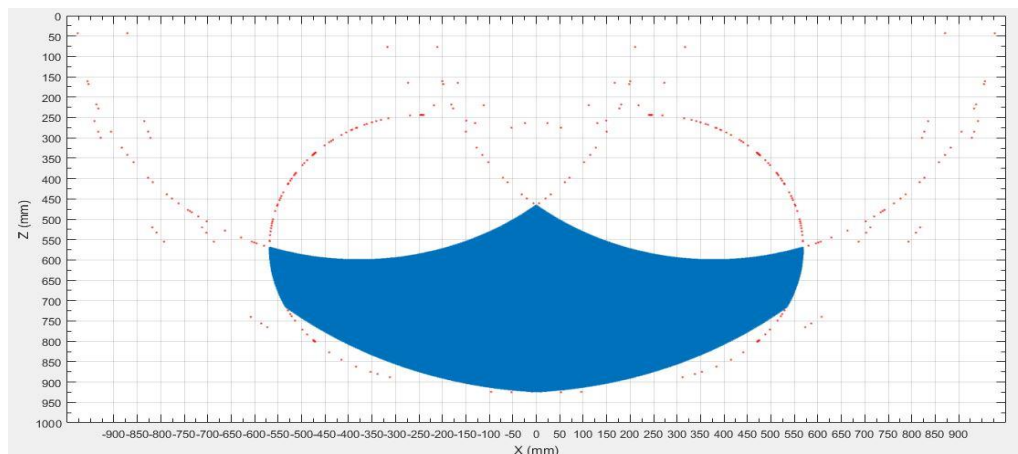

Figure 2. The maximal working space and the physical constraints.

The maximum and minimum values of joint angles, within the specified workspace, were calculated. These values were input in the servo program software.

Trajectories were generated within the specified workspace and motion analysis was carried out by Matlab and Solidworks software. The trajectory of the moving platform is determined using the widely used cubic polynomials. The advantage of spline interpolation is that it tends to greatly reduce oscillation between data points. Cubic spline interpolation gives a good approximation over the whole interval. Figure 3 illustrates the trajectory planning using cubic polynomials with via points.
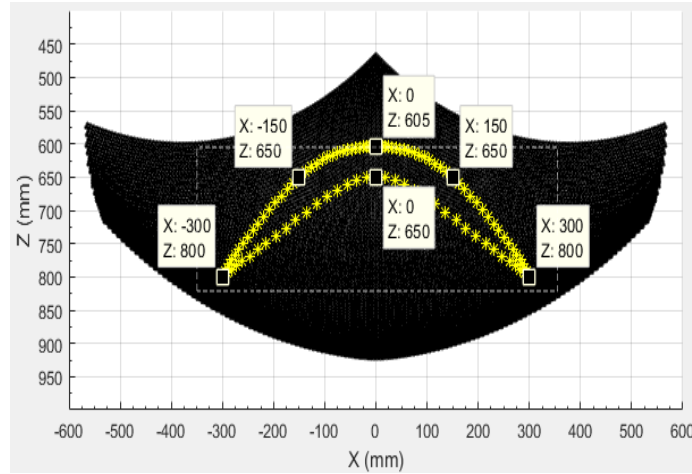
Figure 3. Trajectory planning using cubic polynomials with via points.

Upon the determination of the trajectory, position, velocity and acceleration profiles are analyzed. The required torque value in the rotary actuators were determined and an appropriate servo motor was selected accordingly. The static and transient structural analyses were performed to assess the mechanical stresses of mechanism under load condition.

MANUFACTURING

After completing the inverse and forward analyses in Matlab and verifying, the prototype is manufactured. In prototype manufacturing, some parts of mechanism were manufactured by waterjet cutting process to prevent the heating. Other parts were machined on lathe, milling and CNC within defined tolerances.
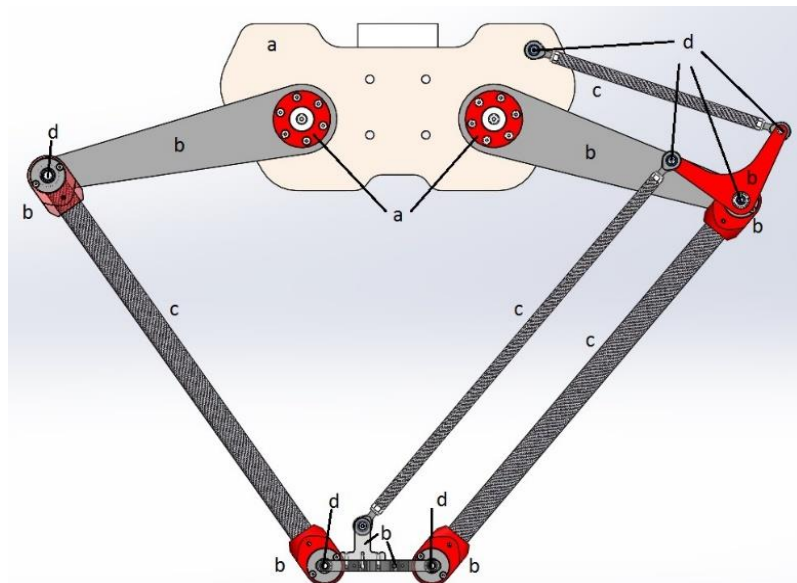

Figure 4. Material type codes of the parts of mechanism.

The materials used in manufacturing are given in Figure 4 and Table 1.

Table 1. Materials used in manufacturing the manipulator

Material	Code
AISI 1050 Carbon steel	a
7Aluminum alloy 7075	b
Carbon Fiber 3K	c
16MnCr5 - Case Hardening Steel	d

Other mechanical components used in manufacturing are lightweight, maintenance free, dry-running, polymeric spherical joint with chemical resistance and high fatigue strength, and high precision, maintenance-free, low heat planet reducer. They are shown in Figure 5.

Figure 5. Other mechanical components (left: joint, right: planet-reducer)

The Schneider brand BSH series industrial servo motors with a holding torque of 1.4 Nm are used as rotary actuator (Figure 6). This motor is selected by calculating the required moment according to the Solidworks motion analysis. Schneider brand LMC58 motion controller and Lexi32 series servo drive are utilized. The Beijer operator panel is used as the human-machine interface for remote control and adjustment of the mechanism.

Figure 6. Schneider BSH servomotor

The forward and inverse kinematic solutions and trajectory planning codes derived from Matlab, were transferred to the servo software (Codesys). Final verification of motion planning is performed by a simple five-bar mechanism constructed on a frame (Figure 7) instead of actual prototype.
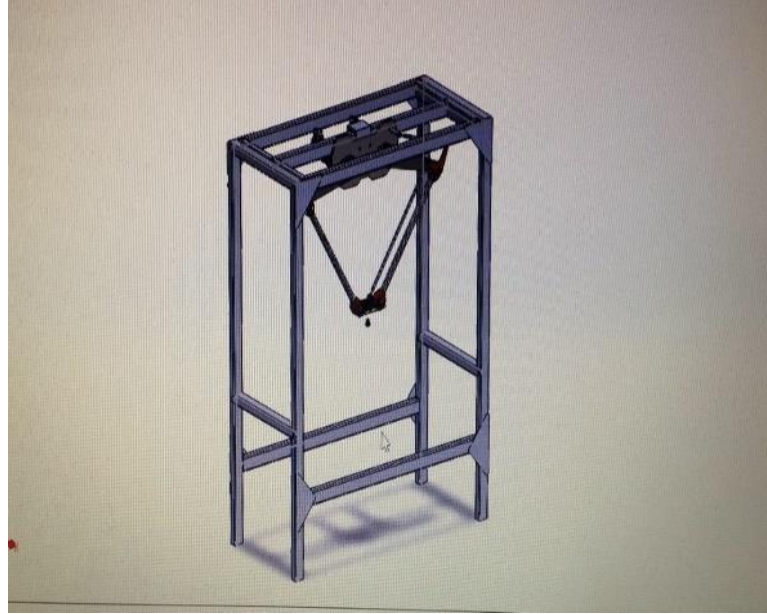

Figure 7. The five bar mechanism and the frame.

After the final verification process, original prototype (Figure 8) has been assembled on the frame.

Figure 8. Final view of the original prototype

The cost of all the materials, handwork, servomotors, control units and other components used in the prototype are about one third of a similar commercial manipulator in the market. It is obvious that the cost will decrease significantly in subsequent productions, approximately to one-fourth or less of a similar commercial one.

While the parallel mechanism is designed for soap industry, it can be modified easily to be utilized in other industries and with different dimensions. The software used is compatible with brand independent IEC 61131-3 standard and Codesys platform, and adaptable with all motion control units using Codesys.

CONCLUSION

As a result of this study, a low-cost parallel mechanism that meets with the expectations of industry was designed and prototyped rapidly within domestic manufacturing capabilities. All the necessary analysis is carried out with high precision. The cost of all the materials, handwork, servomotors, control units and other components used in the prototype are about one third of a similar commercial manipulator in the market. It is obvious that the cost will decrease significantly in subsequent productions, approximately to one-fourth or less of a similar commercial one.

REFERENCES

[1] J. Cazalilla, M. Valles, M. Diaz-Rodriguez, V. Mata, A. Soriano, A. Valera, Implementation of dynamic controllers using real-time middleware for a low-cost parallel robot, 2014 IEEE International Conference on Robotics & Automation, 2014, Hong Kong, China.

[2] D. Grajewski, F. Gorski, D. Rybarczyk, P. Owczarek, A. Milecki, P. Bun, Use of Delta Robot as an active touch device in immersive case scenarios, ICTE 2016, Riga, Latvia. Procedia Computer Science 104 (2017) 485-492.

[3] A. Gómez-Espinosa, P.D. Lafuente-Ramón, C. Rebollar-Huerta, M.A. Hernández-Maldonado, E.H. Olguín-Callejas, H. Jiménez-Hernández, E.A. Rivas-Araiza and J. Rodríguez-Reséndiz, Design and construction of a didactic 3-dof parallel links robot station with a 1-dof gripper, Journal of Applied Research and Technology 12 (2014) 435-443.

[4] E. Ottaviano, M. Ceccarelli, A. Paone, G. Carbone, A low-cost easy operation 4-cable driven parallel manipulator, Proceedings of the 2005 IEEE International Conference on Robotics and Automation, Barcelona, Spain, April 2005.

[5] Z. Xuehe, L. Ge, L. Gangfeng, Z. Jie, H. ZhenXiu, GPU based real-time SLAM of six-legged robot, Microprocessors and Microsystem, 47 (2016) 104–111.

[6] S.J. Spencer, J. Klein, K. Minakata, V. Le, J.E. Bobrow, D.J. Reinkensmeyer, A low cost parallel robot and trajectory optimization method for wrist and forearm rehabilitation using the Wii, Proceedings of the 2nd Biennial IEEE/RAS-EMBS International Conference on Biomedical Robotics and Biomechatronics, USA, 2008.

[7] Md R.A. Md Zin, Kh.S.M. Sahari, J.Md Saad, A. Anuar, A.T. Zulkarnain, Development of a low cost small sized in-pipe robot, International Symposium on Robotics and Intelligent Sensors 2012, Procedia Engineering 41 (2012) 1469-1475.

[8] S.C. Gutiérrez, R. Zotovic, M.D. Navarro, M.D. Meseguer, Design and manufacturing of a prototype of a lightweight robot arm, Manufacturing Engineering Society International Conference 2017, Spain, Procedia Manufacturing 13 (2017) 283–290.

[9] T.-J. Jung, J.-H. Oh, Design of a robot gripper for a rapid service robot, 6th IFAC Symposium on Mechatronic Systems, The International Federation of Automatic Control, China, 2013.

Synthesis of ZnO Nanostructured Photocatalysts
via Electrochemical Anodization

Ahmet Yavaş*, Saadet Güler
İzmir Katip Çelebi Univ., Dept. of Materials Science and Engineering, Çiğli Main Campus, İzmir, Türkiye
Mustafa Erol
Dokuz Eylül Univ., Dept. of Metallurgy and Materials Engineering, Tınaztepe Main Campus, İzmir, Türkiye
*Corresponding author: ahmet.yavas@ikc.edu.tr

Abstract

Zinc oxide (ZnO) nanostructures have been extensively utilized in diverse fields including photocatalysis. Several nanostructured ZnO can be fabricated via electrochemical anodization of zinc plates. In this work, ZnO nanostructures were produced on commercially pure zinc plates which have diversifying surface roughness by electrochemical anodization method under potentiometric regime. It is aimed to observe the effects of surface roughness on structural, morphological and photocatalytic properties of the anodized samples. Characterization of nanostructured ZnO samples was carried out through X-ray diffractometer (XRD) and scanning electron microscopy (SEM). The photocatalytic performance of these ZnO samples was examined by means of decomposition of methylene blue (MB) aqueous solutions under UV-Visible light irradiation.

Keywords: zinc oxide, nanostructure, photocatalyst, electrochemical anodization,
Discipline: Materials Science and Engineering

1. INTRODUCTION

Zinc oxide (ZnO) is a promising material thanks to its thermal and chemical stability, wide band gap, piezoelectricity, ferroelectricity, huge magneto-optic effect and chemical sensivity [1]. Due to these unique properties, ZnO materials have been employed in various applications such as ultraviolet lasers, solar cells, gas sensors, bio-detectors, UV light-emitting diodes, transparent conductors, piezoelectrics and photocatalysts [2, 3]. Having wide band gap (3,37 eV) and large exciton binding energy (60 meV), ZnO has been widely studied for photocatalytic applications.

In the literature, the production of ZnO nanostructures has been carried out with several techniques including chemical vapor deposition, epitaxial growth, electrodeposition, and electrochemical anodization [4]. Among these techniques, electrochemical anodization presents various superiorities as low cost, simple operation, wide compatibility and suitability for industrial procedures if compared to the others [5]. Thanks to this motivation, in the present study electrochemical anodization method was employed to grow zinc oxide nanostructures on pure zinc plates with varying surface roughness. It is aimed to show the effects of substrate roughness on the structural, morphological and photocatalytic properties of as anodized samples. The phase structure and surface morphology of the prepared nanostructures characterized by way of X-ray diffraction (XRD) and scanning electron microscope (SEM) respectively. The photocatalytic activities of the samples for the degradation of methylene blue (MB) under UV-Visible light irradiation were evaluated.

2. EXPERIMENTAL PROCEDURE

Zinc plates with square sections (25 x 25 mm2) a 2 mm thickness were mechanically polished using emery papers with varying grits (500#, 1000#, 1500# and 2000#) to create uneven surfaces. Then, the prepared samples having different surface roughness were respectively washed with ethanol, distilled water and acetone in an ultrasonic cleaner at room temperature for 20 min in air. After cleaning process, electrochemical anodization process was performed by using a setup including plate samples with varying roughness, platinum electrode and 1 wt % hydrofluoric acid aqueous solution as anode, cathode and electrolyte, respectively. The electrochemical anodization process was carried out under 10 volts for 20 minutes at room temperature while anode to cathode distance kept as 10 cm. These anodized samples were annealed at 450˚C for 1.5 h in air so as to obtain crystalline ZnO nanostructures

The crystallinity and phase structure of the ZnO nanostructures were characterized via X-Ray diffractometer (Bruker D2 phaser) Cu-Kα irradiation. Scanning electron microscope (Zeiss Sigma 300 VP) was utilized to obtain and find out the surface morphology and microstructure of the samples. The photocatalytic activities of the samples on aqueous methylene blue (MB) solutions were performed under UV light source (Osram, UltraVitalux E27, 300 W). The average irradiation intensity of the employed light source was 18 W/m2 for the visible bandwidth, 3.2 W/m2 for UV-A, 0.004 W/m2 for UV-B and 0.004 W/m2 for UV-C [11]. Methylene blue (MB) as an artificial impurity is a heterocyclic aromatic organic compound and its aqueous solution (MB+) is a cationic dye with maximum absorption of light around 664 nm [10]. The aqueous MB solutions (35 ml) were dropwise added into the beakers for each catalyst with varying roughness. Then, the catalysts were placed across to light source with a constant distance (30 cm). The change in the absorbencies of the aqueous MB solutions as a result of photocatalytic activity of the samples were recorded via UV spectrometer (1240 UV–vis/Shimadzu) for various durations. However, the photocatalytic activities of the catalysts are mostly determined through monitoring the change in the concentration of aqueous MB solutions by time. A linear Lambert Beer correlation was obtained to convert absorbencies into concentration in our previous study [11] in which the same MB solutions and equipment were used. After all, the regarding data were utilized for the calculation of the degradation reaction kinetics.

3. RESULT AND DISCUSSION

The XRD patterns of the samples were given in Figure 1. The patterns indicate that there are two different phases as zinc and zinc oxide. Presence of zinc oxide phase denotes that the anodization process was performed successfully [12]. On the other hand, Zn peaks are raised from metallic zinc plate thanks to the penetration of x-rays. The literature reveals that phase transformation and crystallinity of ZnO possess a vital effect on its photocatalytic efficiency [6-7].
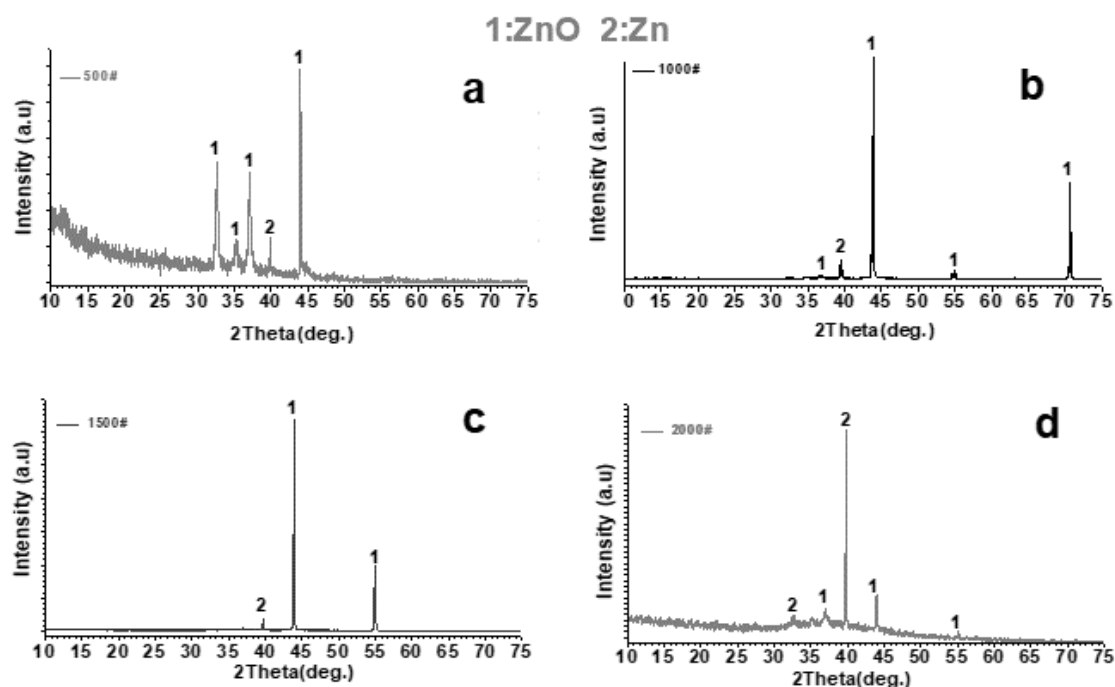

Figure 1. XRD patterns of the anodized + annealed samples for different surface roughness
(a) 500 grid, (b) 1000 grid, (c) 1500 grid, (d) 2000 grid.

The morphology and other surface parameters such as specific surface area, defect content and surface contamination have huge impact on the photocatalytic activity of ZnO [8]. Within this scope, the surface properties of all samples were evaluated with SEM images. From the SEM results in Figure 2, it can be seen that various nanostructured morphologies were obtained.
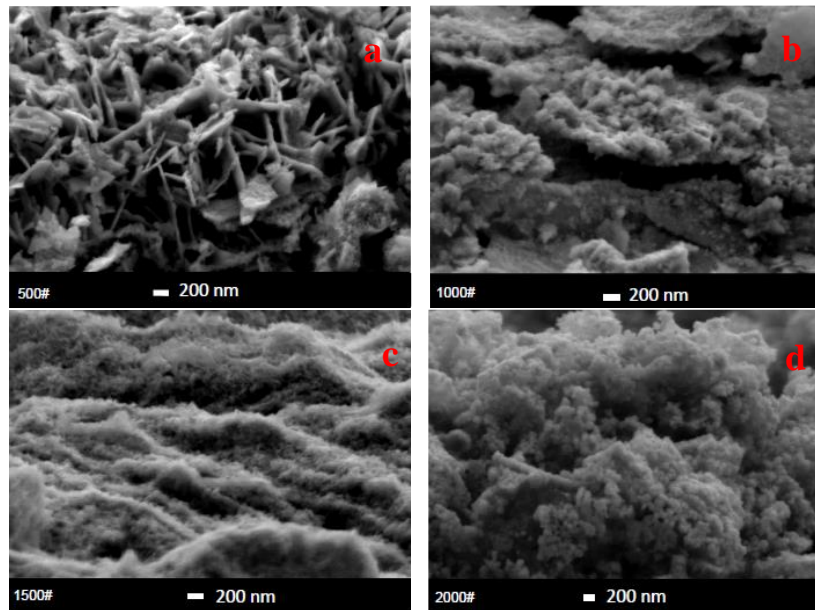
Figure 2. SEM images of the anodized + annealed ZnO samples for different surface roughness
(a) 500 grid, (b) 1000 grid, (c) 1500 grid, (d) 2000 grid.

Figure 3 reveals the photocatalytic degradation of MB by ZnO nanostructures under UV–visible light irradiation in line with the Langmiur–Hinshelwood kinetics model. According to this model, the curve of ln (C_0/C) versus irradiation time indicates a flat line and the slope of curve gives the degradation rate (k) [9]. The degradation rates are given in Table 1.
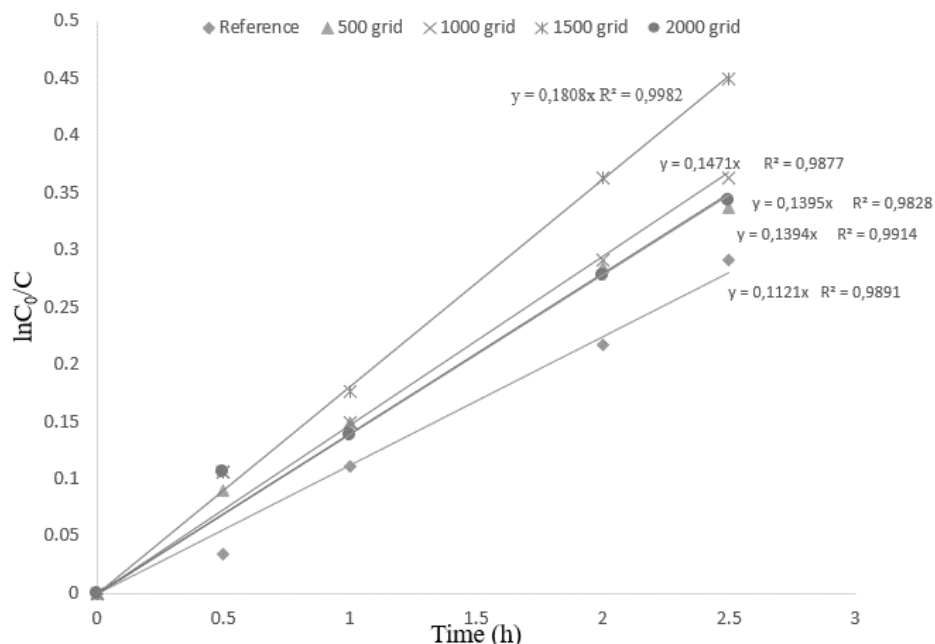

Figure 3. Photocatalytical kinetics of the ZnO nanostructures for different surface roughness.

Among the ZnO nanostructured samples, the sample 1500 grid has the best photocatalytic activity towards MB under the UV irradiation. As a final assessment, any significant relation between surface roughness (and/or grid number) and the photocatalytic activity could not be created.

206

Table 1. Photocatalytic degradation kinetic data.

Sample	(k)	R^2
REF	0.2908	0.9891
500#	0.3364	0.9914
1000#	0.3635	0.9877
1500#	0.4492	0.9982
2000#	0.3431	0.9828

4. CONCLUSIONS

ZnO nanostructures were successfully obtained for all substrates those polished with emery papers of various grids. Crystalline ZnO phases were observed for each sample. The morphologies of the samples exhibited nanostructures thanks to anodization. The photocatalytic reaction kinetics which are in a good agreement with the Langmiur–Hinshelwood kinetics model were achieved. However, the effect and the dependency of photocatalytic reaction kinetics on surface roughness could not be exposed.

A more detailed experimental approach in which the surface roughness values are precisely determined and the type of electrolyte investigated can be performed so as to create comprehensive evaluation of the process in the future.

REFERENCES

[1] P.K. Basu, N. Saha, S. Maji, H. Saha, S. Basu, Nanoporous ZnO thin films deposited by electrochemical anodization: effect of UV light, Journal of Materials Science: Materials in Electronics 19 (2008) 493-499.

[2] D. O. Miles, P. J. Cameron, D. Mattia, Hierarchical 3D ZnO nanowire structures via fast anodization of zinc, Journal of Materials Chemistry A 3 (2015) 17569-17577.

[3] S. He, M. Zheng, L. Yao, X. Yuan, M. Li, L. Ma, W. Shen, Preparation and properties of ZnO nanostructures by electrochemical anodization method, Applied Surface Science 256 (2010) 2557-2562.

[4] A. Ramirez-Canon, D. Miles, P. Cameron, D. Mattia, Zinc oxide nanostructured films produced via anodization: a rational design approach, The Royal Society of Chemistry-Advances 3 (2013) 25323-25330.

[5] M. Erol, T. Dikici, M. Toparlı, E. Çelik, The effect of anodization parameters on the formation of nanoporous TiO_2 layers and their photocatalytic activities, Journal of Alloys and Compounds 604 (2014) 66-72.

[6] T. Dikici, M. Erol, M. Toparlı, E. Çelik, Characterization and photocatalytic properties of nanoporous titanium dioxide layer fabricated on pure titanium substrates by the anodic oxidation process, Ceramic International 40 (2014) 1587-1591.

[7] T. Dikici, Temperature-dependent growth of ZnO structures by thermal oxidation of Zn coatings electrodeposited on steel substrates and their photocatalytic activities, Ceramic International 43 (2017) 8289-8293.

[8] M. Montero-Munoz, J.E. Ramos-Ibarra, J.E. Rodrigues-Paez, M.D. Teodoro, G.E. Marques, A.R. Sanabria, P.C. Cajas, C.A. Paez, B. Heinrichs, J.A.H. Coaquira, Role of defects on the enhancement of the photocatalytic response of ZnO nanostructures, Applied Surface Science 448 (2018) 646-654.

[9] J. Sun, X. Wang, J. Sun, S. Ruixia, S. Shengpeng, Q. Liping, Photocatalytic degradation and kinetics of orange G using nano-sized $Sn(IV)/TiO_2/AC$ photocatalyst, Journal of Molecular Catalysis A: Chemical 260 (2006) 241–246.

[10] M. Erol, O. Ertugrul, HIPed TiO_2 dense pellets with improved photocatalytic performance, Ceramics International 44(3) (2018) 2991-2999.

[11] M. Erol, K. Bilgin, Boron doped titaniumdioxide nanotube arrays: production, characterization and photocatalytic properties, Journal of Porous Materials 24(5) (2017) 1295-1302.

[12] S. Sreekantan, L.R. Gee, Z. Lockman, Room temperature anodic deposition and shape control of one-dimensional nanostructured zinc oxide, Journal of Alloys and Compounds 476 (2009) 513-518.

Characterization of Al7075 Alloy Processed by Equal Channel Angular Pressing (ECAP)

Mehmet Mahsun Yeşil*, İzmir Katip Çelebi Univ., Dept. of Materials Science and Engineering, İzmir, Türkiye
Ebubekir Atan, İzmir Katip Çelebi Univ., Dept. of Mechanical Engineering, İzmir, Türkiye
Mücahit Sütçü, İzmir Katip Çelebi Univ., Dept. of Materials Science and Engineering, İzmir, Türkiye
*Corresponding author: mehmet.yesil@yahoo.com

Abstract

Severe Plastic Deformation (SPD), applying extreme force to alterate and refine the structures of materials permanently, have a huge potential to improve the mechanical and structural properties of materials superiously. Equal Channel Angular Pressing (ECAP) is a kind of SPD techniques to produce submicron or nano sized particles by applying stress to the sample passing through two angular intersected channels have the same diameters. ECAP has recently been becoming one of the most favorable method in the production of nano-structured bulk materials.

One of the main objectives of this search and relating experiment is trying to understand how the properties of the material enhance under applied progressive and severe pressure. This process is directly related to the internal structure and texture of the material. A more strengthened material structure with superior properties is desired to achieve. The material strengthening has been explained by dislocation theory which based on the restricting the movement of dislocations through the crystalline lattice.

In this study, it is aimed to observe the changes in microstructural and mechanical properties of Al-7075 alloy as a result of obtaining them in micro/nano grained structures by using Equal Channel Angular Press (ECAP) technique. Consecutive ECAP experiments have been carried out in the Mechanical Laboratory of İzmir Katip Çelebi University. The rods with a diameter of 12 mm and a length of 30 mm were used as sample billets which were not subjected to any heat treatment previously. A 120 ton capacity hydraulic press with pressing speed of 2mm/s and a sensitively machined die with channels 120° intersected (Φ=120°, ψ=20°) have been used. All the ECAP experiments in this investigation have been carried out at 120 °C temperature condition. Prior to each repeating the process, the specimen was rotated using type of BC route. Then the analyses on ECAP applied samples were performed and the changes in crystal structure, microstructural and mechanical properties were investigated. Changes in the crystal grain orientations of ECAP samples were observed. At the same time, the grain size in the microstructure decreased by ECAP process. As a result, partially increase in microhardness values was determined.

Keywords: Al7075 alloy, ECAP, mechanical properties
Discipline: Materials Science and Engineering

1. INTRODUCTION

With development of technology, investigations at nano-scale levels in materials engineering has recently become a favorite field. Metallurgical structures and mechanical properties of materials have a remarkable relationship between each other. Such processes known as Severe Plastic Deformation (SPD) applying excess force to alter and refine the structures of the materials plastically have the potential to improve the mechanical and structural properties of materials superiously. SPD techniques such as rolling, drawing, extrusion that widely preferred for strengthening metals, alloys or composites have been used in industrial applications for many years.

ECAP is a kind of SPD techniques which produces submicron or nano sized grains by applying stress to the sample passing through two angular intersected channels having the same diameters. While the specimen is passing from the first channel to the second, curling at a sharp corner, it is exposed a large amount of shear strain resulting with grain refinement. The cross sectional dimensions of the specimen remains the same as the origin after each pass. Using this method keeps the waste of the material at minimum level. Then the process is repeated with the same specimen up to achieve a nearly perfect microstructure or even nanostructure. Moreover, specimen with homogeneously refined structure gain exceptional mechanical properties. On the other hand, this technique has the potential to make a leap for nano engineering inventions [1].

Al7075 alloy, preferred to use in this study, is a non-corrosive alloy as it is used in automotive applications, gears and shafts, regulating valve parts, worm gears, keys, fuse parts, aerospace and defense applications, bike frames, terrain vehicle sprockets [2].

The chemical composition and main mechanical properties of Al7075 alloy are given in Table 1 and Table 2 respectively. The rods supplied from market have been machined into intended sizes as sample billets compatible with die design.

Table 1. Chemical compositions of Al7075 alloy [3]

Fe	Si	Cu	Mn	Mg	Zn	Cr	Zi+Ti	Others	Al
0.5	0.5	1.2-2.0	0.3	2.1-2.9	5.1-6.1	0.18-0.28	0.25	0.15	Remain

Table 2. Mechanical properties of Al7075 alloy [3]

Yield Strength (MPa) min-max	Tensile Strength (MPa) min-max	Elongation min-max	Hardness (Brinell) min-max
105 (T0)	225 (T0)	17 (T0)	60 (T0)
460-505 (T3)	530-570 (T3)	10 (T3)	140 (T3)
435 (T6)	505 (T6)	12 (T6)	130 (T6)

The products provided by ECAP procedure with superior mechanical, electrical or constructional properties can be in bulk rods, sheets or even in wire forms. This method is feasible in combining with many metal forming processes, thermomechanical treatments as well SPD techniques. It has been observed a considerable increase in mechanical properties such as values of strength obtained with supporting subsequent treatments. ECAP processed Ti–6%Al–4%V alloy has been given a successful performance in dental applications and many other engineering products, for example, weight-sensitive products and special automotive components [1].

2. FUNDAMENTAL TERMS AND CONCEPTS

2.1 Material Strengthening

One of the main objectives of this research and relating experiment is trying to understand how the properties of material enhance under applied progressive and severe pressure. This process is directly related to the internal structure and texture of the material. A more strengthened material structure with superior properties is desired to achieve. The material strengthening has been explained by dislocation theory which based on the restricting the movement of dislocations through the crystalline lattice. Impurities, defects, vacancies and self-interstitials drive deviations from crystalline perfection of materials (Figure 1). That means there is no excellence in the crystal structure of the material. Thanks to deviations from crystallographic structure, it is possible to process the metals for usage. Otherwise, it would be needed huge forces and strains for deformation and refinement. Following plastic deformation, dislocations are piled up and absorbed by the sub grain boundaries. The strength can be improved by putting obstacles to slip. Generally with increasing the hardness, ductility and toughness decrease and hence the plasticity of the material sacrificed to achieve a higher yield strength [4, 5].

Dislocation propagations have been impeded with refining the grains in the internal structure of the material. The adjacent grains interact each other and due to the lattice structure they prevent each other to move in a continuous slip [4].
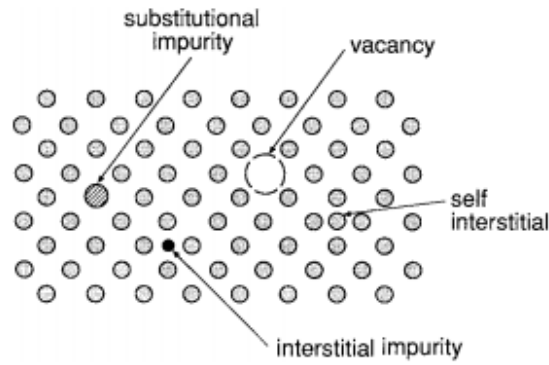
Figure 1. Point defects in a crystalline solid [4].

2.2 SPD Mechanisms

The main purpose of SPD is to refine the grained microstructure by applying excess force deforming the material irreversibly and as a result, mechanical and functional properties improved. Ability to deform plastically depends on the ability of dislocations to move (Figure 2). Motion of a large number of dislocations happens during plastic deformation as well as the amount of dislocations increases extremely [5].
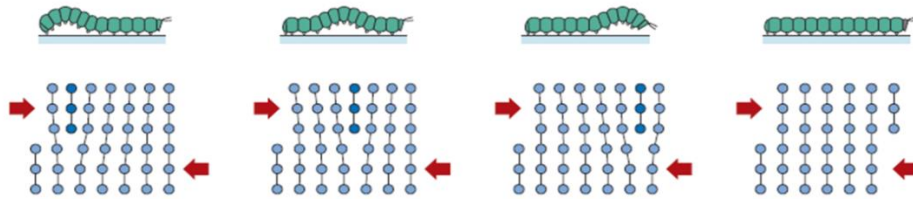

Figure 2. The analogy between caterpillar and dislocation motion [5]

While the metal subjected to a hydrostatic pressure with imposing a very huge strain the internal grains of the subjected material divide into sub grains up to micro or nano sizes which have smaller angle boundaries embedding the impurities and dislocations [6, 7].

The yield strength (σ_y) is expected to vary with grain size d according to Hall-Petch relationship (Equation 1):

$$\sigma_y = \sigma_0 + {k_y}\big/{\sqrt{d}} \tag{1}$$

where σ_0 is the lattice friction stress, and k_y is a constant of yielding.

ECAP process has a great potential to reduce the size of grains into nano levels. There have been many efforts to show the relationships between the grain size and the strengthening mechanism. However, some deviations were reported at the same time. Furthermore, for coarse-grain polycrystalline metals up to a critical point which about 10 nm, the strength increase with decreasing grain size [8-14].

3. ECAP PROCEDURE AND THE MAIN PARAMETERS

M. Furukawa et al. [15] conducted some experiments to search the principles of shear distributions and with sample rotations effects of ECAP process. They showed geometrically the shearing strain imposed to the material (Figure 3) and the directions of the shearing segments determined by the rotating of the subjected sample about its axis before each pass (Figure 4).
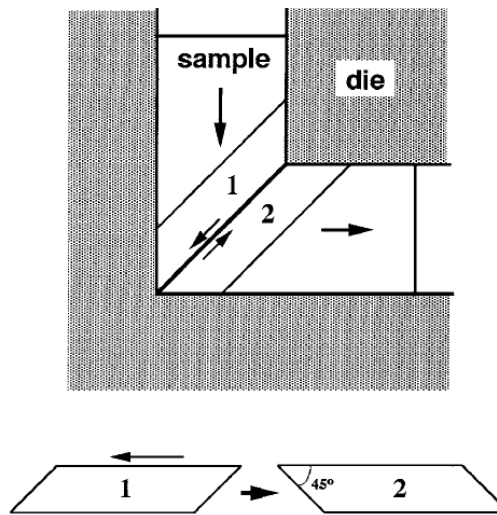
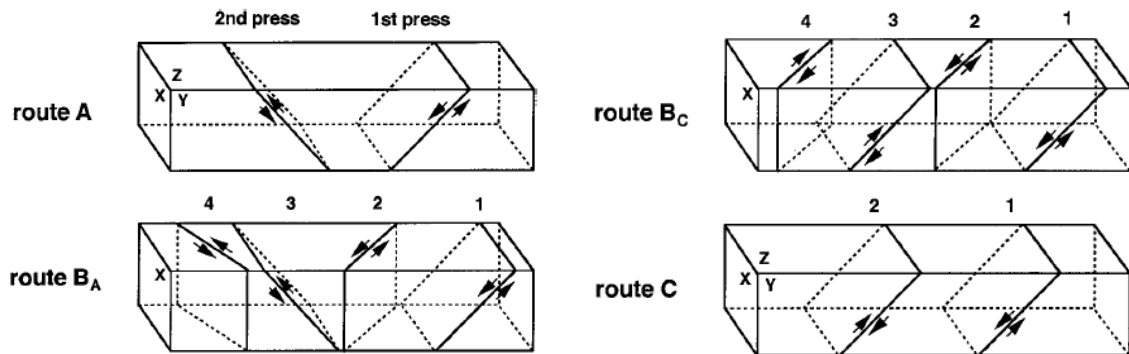Figure 3. The basic principle of shearing during ECAP [15].

Figure 4. The shearing planes concerning processing rotations [15].

S. M. Kumar et al pressed Al7075 billets through the channel with 90° die angles after annealing at 412 °C for 1 h and then cooled to room temperature. They have observed that the structure with grains of 400–440 nm achieved in route Bc after four passes [16].

M. Reddy et al studied on Al7075 alloy die angle 120° up to 3 passes and determined that ultimate tensile strength increases from 329 MPa as received, reaches about 487 MPa after first pass. The hardness value is increased from 125 HV to 197 HV at the end of third pass [17].

M. Saravanan et al. [18] studied on pure aluminum with 90° die angles at room temperature up to eight passes and determined with AFM characterization as the grain sizes reduced from 150 μm to ~620 nm.

3.1 Main Parameters of the study

Hydraulic Press, ECAP die and billet samples are the main components of the ECAP process. Throughout plenty of trials and observations we have determined the following main important parameters that must be watch out to prevent blockage of the sample and damages:

- Controllable pressing unit (Figure 5).
- The material sample with proper size for ECAP process.
- ECAP die material and design [19].
- Intersection angles of die channels [24].
- Pressing speed. Optimum: 2mm/sec [20].
- Surface quality of the channels [20].
- Plunger to push the samples throughout the channels [20].

211

- Lubrication agent applying to the specimen and to the die channels [23].
- Heating the billet sample [21].
- The number of passes repeating up to achieve a homogeneous microstructure [18].
- Rotating the sample around its axis at specified routes prior to each repeating the process [25].

Figure 5. Overall view of hydrostatic pressing machine

Using Route Bc, it was carried out under a pressure of 80 tons and a pressing speed of 2 mm/s in the present study.

Even though there is a wide range of experimental factors that influence in achievement of advanced microstructural and mechanical properties, the most important key parameters are channels geometry, contact friction and tool design [22].

3.2 ECAP Die Block

Two machined and integrated channels with the same diameter as Ø12 mm and intersecting 120 degrees have been used (Figure 6). It is made from AISI H13 DIN 1.2344 steel and have a steel block surrounded and a mount age base. There are holes through the steel block to put heating cartridges. The die of ECAP consists of two symmetrical half parts, machined from two blocks of steel and heat treated to achieve a nominal hardness of 62 HRC. These two equal cross sectioned channels were machined with outer and inner radius transition (R: 4 mm and r: 2 mm, respectively) between the two channels intersecting at 120°.

Figure 6. ECAP Die geometry and 120° intersected channels.

3.3 Methodology of Metallographic Sample Preparation

The samples with and without ECAPed were prepared for microstructural and micro hardness investigations with the metallographic sample preparation treatments (Figure 7).

Figure 7. Typical appearance of ECAPed sample billets of Al7075.

In order to carry out characterization processes transverse and longitudinal samples have taken out from center of unpassed and passed billets (Figure 8).
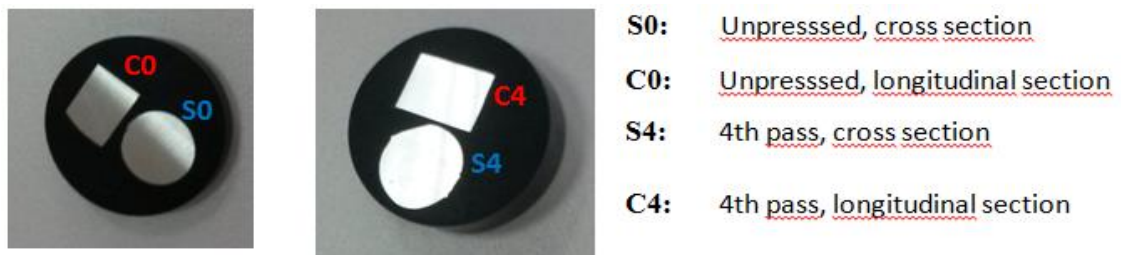

Figure 8. Samples polished and get ready for characterization tests.

4. RESULTS AND DISCUSSION
4.1 X-Ray Diffraction (XRD) Analysis of the Samples

It's revealed that ECAP process cause a considerable amount of distortion in the lattice structure of the deformed materials, since the peaks shift can be related to long range stresses as well as sub grain boundaries generated by deformation (Figure 9). Increase in dislocation density due to lattice microstrain and size effect can be correlated. Following each pass, crystal structure orientation and crystal size changes have been happened.
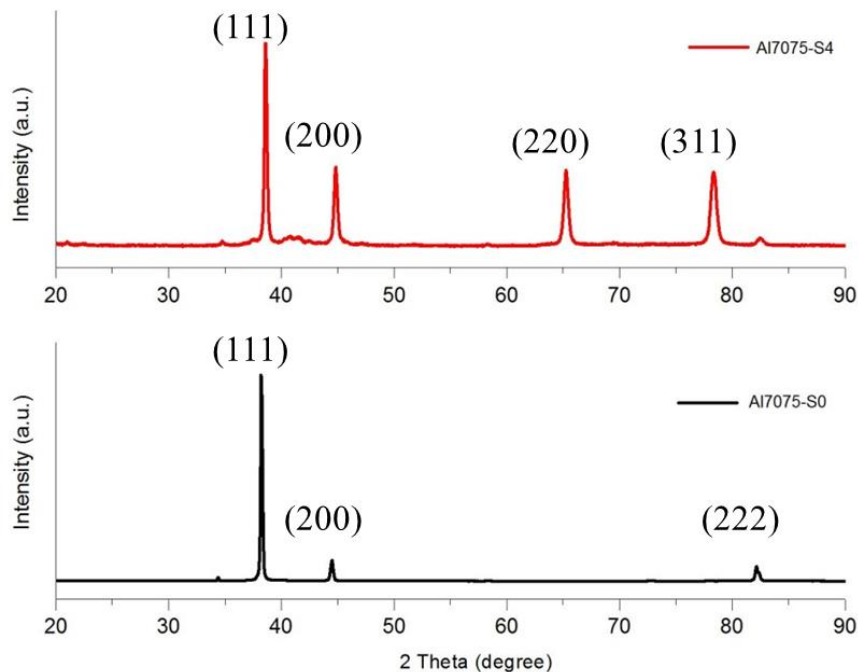

Figure 9. XRD patterns of Al7075 with fourth pass and unpassed samples.

213

2nd International Students Science Congress
4-5 May 2018, Izmir - Turkey

İZMİR
KÂTİP ÇELEBİ
UNIVERSITY
2010

İZMİR
Uluslararası
Misafir
Öğrenci
Derneği
◆ İZMİR International Guest Student Association

4.2 Optical Microscopy results

Grain orientation in rolling direction was observed on unpassed sample. In the subsequent passes shearing bands are aligned with the corner stress effect. Changes in the grain orientations of ECAPed samples happen while the grain size in the microstructure reduced (Figure 10). Passing of the samples can be repeated more than 4 times up to achieving homogenous and ultrafine grained structure.
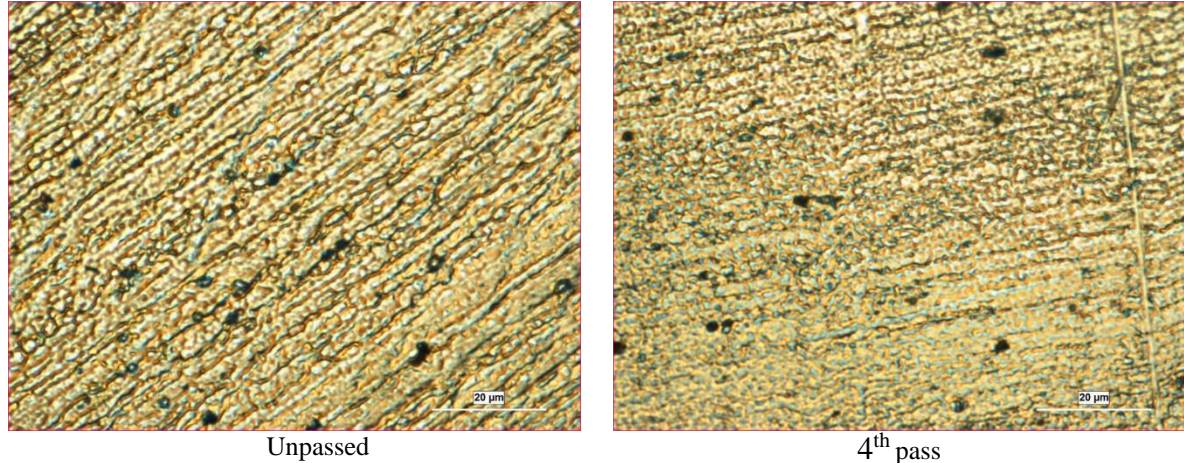

Unpassed   4th pass
Figure 10. Microstructures of longitudinal surface of the samples (1000 x)

4.3 Scanning Electron Microscope (SEM) results

The grain dividing and subgrain formation can be seen and followed even though the grain boundaries are not so much clear. The results of SEM support and are in parallel with optical microscopy data pictures. Shearing bands, grain orientations, subgrain formation have been observed while the grain refinement and more homogeneous structure promoted at the fourth pass (Figure 11).
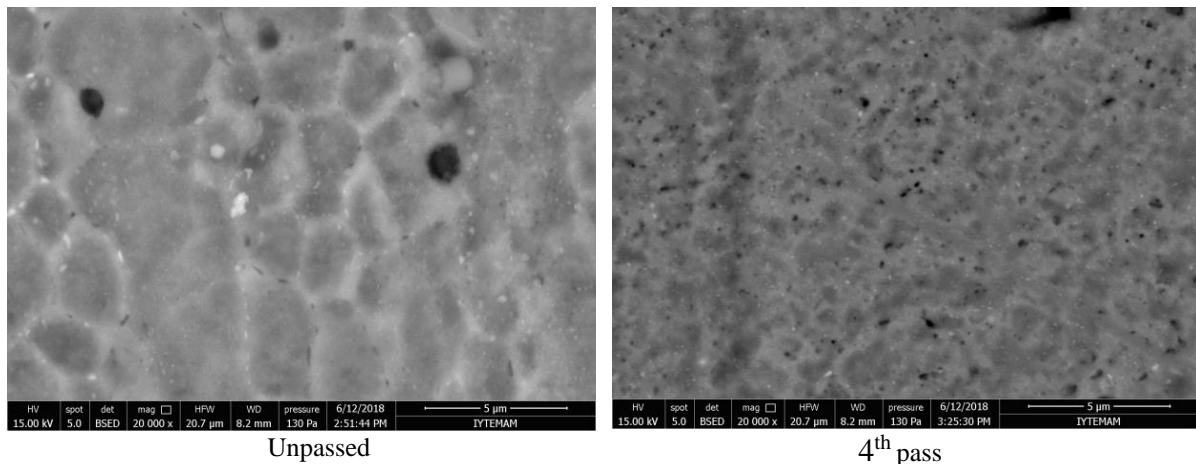

Unpassed   4th pass
Figure 11. Comparison between microstructures of unpassed and 4th pass of crossectional surface (20,000 x)

4.4 Micro Vickers hardness tests results

The mechanical properties of the samples investigated by applying the Micro Vickers hardness test. It has been determined that the hardness values up to 4th pass after ECAP increases significantly from 65HV to 92.4HV as about 30% using Bc route(Figure 12). The percentage of increase in quantitative hardness values nearly corresponds to the study done by M. Reddy et al as mentioned above [17]. Some difference may occur due to variable experimental parameters such as lubrication, heating temperature, tool design, pressing speed, etc.

Figure 12. Hardness values versus number of passes of Al 7075 samples.

5. CONCLUSION

Strength and ductility are the essential mechanical characteristics for the metallic materials. They are seem as reciprocal each other. Metallic materials have been handling and evaluating as they strong or ductile, but infrequently both at once. Plenty of ECAP experiments have shown that with reducing the grained size of the material to nano levels, an exceptional combination of high strength and ductility all at once can be achieved [1].

As a result, ECAP process can be combined with any other SPD techniques to achieve better mechanical and functional properties. The material can be cured by aging or any thermomechanical processing before or after the experiment.

Consequently, the number of passes should be repeated up to achieve an ultimate homogeneous ultrafine grained microstructure and characterization tests to the material should be applied for each pass in all points of view to determine quantitative and conceptual principles about ECAPed material.

REFERENCES

[1] R.Z. Valiev, T.G. Langdon, Principles of equal-channel angular pressing as a processing tool for grain refinement, Progress in Materials Science 51(7) (2006) 881-981.

[2] http://asm.matweb.com/search/SpecificMaterial.asp?bassnum=MA7075T6 (accessed 19 July 2018).

[3] http://www.seykoc.com.tr/icerik/alloys-1050-seykoc-aluminium?dil=en (accessed 19 July 2018).

[4] N. E. Dowling, Mechanical Behavior of Materials – Engineering Methods for Deformation, Fracture, and Fatigue, fourth edition. Pearson Education Limited, (2013).

[5] W. D. Callister Jr, Materials Science and Engineering – An Introduction, 7th Edition. John Wiley & Sons, Inc. 2004.

[6] R. Z. Valiev, R. K. Islamgaliev, I.V. Alexandrov, Bulk nanostructured materials from severe plastic deformation, Progress in Materials Science 45 (2000) 103-189.

[7] C. S. Pande, K.P. Cooper, Extreme grain refinement by severe plastic deformation: A wealth of challenging science, Acta Materialia 61 (2013) 782–817.

[8] C. S. Pande, K.P. Cooper, Nanomechanics of Hall–Petch relationship in nanocrystalline materials, Progress in Materials Science 54 (2009) 689–706.

[9] C. E. Carlton, P. J. Ferreira, What is behind the inverse Hall–Petch effect in nanocrystalline materials? Acta Materialia 55 (2007) 3749–3756.

[10] K. A. Padmanabhan, S. Sripathi, H. Hahn, H. Gleiter, Inverse Hall–Petch effect in quasi-and nanocrystalline materials, Materials Letters 133 (2014) 151–154.

[11] M.J. Starink, Dislocation versus grain boundary strengthening in SPD processed metals: Non causal relation between grain size and strength of deformed polycrystals, Materials Science and Engineering: A 705 (2017) 42–45.

[12] A. S. Mohammadabadi, K. Dehghani, A new model for inverse Hall-Petch relation of nanocrystalline materials, Journal of Materials Engineering and Performance 17 (2008) 662-666.

[13] N. Hansen, Hall–Petch relation and boundary strengthening, Scripta Materialia 51 (2004) 801–806.

[14] S.S. Quek, Z.H. Chooi, Z. Wu, Y.W. Zhang, D.J. Srolovitzc, The inverse Hall–Petch relation in nanocrystalline metals: A discrete dislocation dynamics analysis, Journal of the Mechanics and Physics of Solids 88 (2016) 252-266.

[15] M. Furukawa, Z. Horita, M. Nemoto, B. Ravisankar, T. G. Langdon, Processing of metals by equal-channel angular pressing, Journal of Materials Science 36 (2001) 2835 – 2843

[16] S. R. Kumar, K. Gudimetla, P. Venketachalam, B. Ravisankar, K. Jayasankar, Microstructural and mechanical properties of Al 7075 alloy processed by equal channel angular pressing, Materials Science and Engineering: A 533 (2012) 50-54.

[17] M. Reddy, M.S. Kumar, V. A. Kumar, Improving mechanical properties of al 7075 alloy by equal channel angular extrusion process, International Journal of Modern Engineering Research (IJMER) 3 (2013) 2713-2716.

[18] M. Saravanan, V. B. Pillai, V. M. Pai, Brahmakumar, K. R. Ravi, Equal channel angular pressing of pure aluminium-an analysis, Bull. Mater. Sci. 29 (2016) 679–684.

[19] M. Kamachia, M. Furukawa, H. Zenji, T. G. Langdon, Equal-channel angular pressing using plate samples. Materials Science and Engineering: A 361 (2003) 258–266.

[20] A. Güral, S. Tekeli, A. Aytaç, Ç. Karataş, Construction of an equal channel angular pressing unit and determination of optimum parameters for Al-Zn-Mg-Cu alloy chosen as a modal material, Journal of Polytechnic 14 (2011) 243-248.

[21] A. Yamashita, D. Yamaguchi, Z. Horita, T. G. Langdon, Influence of pressing temperature on microstructural development in equal-channel angular pressing, Materials Science and Engineering: A 287 (2000) 100–106.

[22] V. M. Segal, Slip line solutions, deformation mode and loading history during equal channel angular extrusion, Materials Science and Engineering: A 345 (2003) 36-46.

[23] P. Frint, M.F.-X. Wagner, S. Weber, S. Seipp, S. Frint, T. Lampke, An experimental study on optimum lubrication for large-scale severe plastic deformation of aluminum-based alloys, Journal of Materials Processing Technology 239 (2017) 222–229.

[24] M. A. Agwa, M. N. Ali, E. Amal, Optimum processing parameters for equal channel angular pressing, Mechanics of Materials 100 (2016) 1–11.

[25] V. M. Segal, Equal channel angular extrusion: from macromechanics to structure formation. Materials Science and Engineering: A 271 (1999) 322–333.

Two-Steps Electrochemical Process for Growth of ZnO Nanostructures on Glass/ITO Substrate

Berkant Uzunbayır, İzmir Katip Çelebi Univ., Dept. of Nanoscience & Nanotechnology, Izmir, Turkey
Ahmet Aykaç*, İzmir Katip Çelebi Univ., Dept. of Engineering Sciences, Izmir, Turkey
Mustafa Erol, Dokuz Eylül Univ., Dept. of Metallurgical and Mat. Eng., Izmir, Turkey
Tuncay Dikici, Dokuz Eylül Univ. Center for Fabrication and Application of Electronic Materials, Izmir, Turkey
Fethullah Güneş, İzmir Katip Çelebi Univ., Dept. of Mat. Science and Eng., Izmir, Turkey
*Corresponding author: ahmet.aykac@ikc.edu.tr

Abstract

In this work, such electrochemical processes consisting of two steps: electrochemical deposition and electrochemical anodization methods were employed. Electrodeposition method used for plating a thin zinc layer over Glass/ITO substrates. The process carried out under different deposition durations by constant voltage to produce ITO/Zn structures. Sequentially, electrochemical anodization method led to growth of zinc oxide nanostructures on the zinc layer. Anodization voltage and duration also kept constant. The samples were characterized by XRD and SEM to evaluate the structure and the morphology of the Glass/ITO/ZnO structures, respectively.

Keywords: electrodeposition, zinc, thin film, nanostructure, anodization
Discipline: Nanotechnology and Materials Science

INTRODUCTION

Sensors are the analytical devices, which are composed of a sensing material and transducer. When sensing material is bioselective layer, these sensors defined as biosensors. The main function of biosensors is to react with a target biomolecule such as DNA, proteins and enzymes and transforms the biologic interaction into physical signal (optical, chemical, electrical, thermal etc.) These output signals could be converted in to digital signals for data processing. Data processing and a methodology of biosensor measurements, conditions of the measurements and limitations can vary depend on the type of transducer. For detection of diseases; biosensors step ahead among various techniques because of their high sensitivity and selectivity, easy and rapid manufacturing, and simple methods.

The active sensing materials can be any kind of materials that acts as a catalyst for sensing a particular analyte or a set of analytes. In the recent years, the researcher's attention has been paid to nanomaterials since their dimensions are the same scale as the dimensions of the bio-components, which form a bioselective layer [1]. Collaborations between nanotechnology and biology have resulted in large number of new materials with desirable properties With reduction in size, novel morphological, structural, electrical, chemical, and optical properties are introduced and these novel properties of nanostructured materials marques them as a principally striking and innovative choice for biomedical applications [2].

At this stage, metal oxide nanostructures are quite attractive for biosensor applications with their intended physical properties (conductivity, luminescence and absorbance) as well as biocompatibility. Metal oxide nanostructures have extraordinary ability to promote faster electron kinetics on their surfaces. Using metal oxide nanostructures gives biosensors some unique upgrades like immobilization of enzymes, retaining their bioactivity due to the desirable microenviroment and the direct electron transfer between the enzyme's active sites and the electrode [3].

Between all metal oxide nanostructures, zinc oxide nanostructures are frequently used in biosensor applications. ZnO is a semi- conducting material that presents high surface area to volume ratio, high biocompatibility, and biosafety with non-toxicity, chemical stability, biomimetic, electrochemical activities and fast electron communication features combined with the easiness of growth has shown its novel advantages for the fabrication of electrochemical biosensors. More importantly, with an isoelectric point about 9.5, ZnO nanostructures are good source for immobilization of proteins with high bioactivity and stability by electrostatic interactions. In addition, ZnO which is n-type semiconductor with wide band-gap (3.37 eV) and high exciton binding energy (60meV) ensures intense ultraviolet (UV) photoluminescence at room temperature and it makes ZnO suitable for short wavelength optoelectronic

biosensor applications [4-8]. Also, ZnO is has a diverse shapes of growth morphologies, such as nanowires, nanocombs, nanocages, nanorings, nanohelixes, nanosprings, nanobelts [9].

The methods used to prepare ZnO nanostructures include PLD, MBE, CVD, MOCVD, and wet chemical technique, but some of these techniques have expensive equipment and the operation procedures are rather complicated [10]. On the contrary, electrochemical process presents multiple advantages over these techniques with low cost, simple operations, and wide compatibility, suitability for industrial procedures [11]. Electrochemical deposition process is a surface coating process for producing a dense, uniform, and adherent coating, usually of metal or alloys, upon a surface by the presence of electric current. The coating produced has enhancing specific properties of the surface. Electrochemical anodization process is an electrochemical passivation process which can be applied to some metallic materials having their own natural passive oxide layers. Anodizing is an electrochemical process that converts the metal surface into a decorative, durable, corrosion-resistant, anodic oxide finish.

In this research, electrochemical deposition and electrochemical anodization methods create unique two steps electrochemical process for growth of ZnO nanostructures on glass/ITO substrates.

MATERIALS AND METHODOLOGY

In this research, electrochemical deposition and electrochemical anodization methods were employed to obtain zinc oxide nanostructures on glass/ITO substrates. Electrodeposition method used for plating a thin zinc layer over Glass/ITO substrates. Sequentially, electrochemical anodization method led to growth of zinc oxide nanostructures on the zinc layer. Glass/ITO plates (10cm x 5cm) were purchased as substrates and were cut into 2.5cm x 2.5cm pieces to use as cathode. Zinc plates and platinum mesh were used as anode in deposition and anodization processes, respectively. Commercial ZnCl2 aqueous solution was used as electrolyte for electrochemical deposition. Glycerol based solution (0.5 g NH4F + 90 ml glycerol + 10 ml DDW) was prepared as electrolyte for electrochemical anodization.

ITO coated glass substrates were first annealed at 200°C for 18 hours, and then cleaned ultrasonically for 10 minutes in isopropyl alcohol and acetone, respectively, and blow dried. Electrodeposition process carried out under different deposition durations (Table 1) by keeping voltage constant (DC 0.4V) at ambient temperature to produce ITO/Zn structures. As coated substrates were washed by distilled water and dried.

Electrochemical anodization reactions were carried out in an electrochemical cell. Anodization voltage and duration kept constant as 2.0V (DC) and 15 minutes, respectively. Samples were washed by distilled water and dried. As produced samples were annealed at 200°C for 1 hour to improve ZnO film crystallinity.

Table 1. Parameter of electrochemical processes

Sample Name	Electrochemical Deposition		Electrochemical Anodization	
	Voltage	Time	Voltage	Time
S1	0.4 V	2.5 min	2.0 V	15 min
S2	0.4 V	5 min	2.0 V	15 min
S3	0.4 V	7.5 min	2.0 V	15 min
S4	0.4 V	10 min	2.0 V	15 min

The sample were characterized by XRD and SEM to evaluate the structure and the morphology of the Glass/ITO/ZnO structures, respectively.

RESULTS

We studied surface characteristics and morphology of ZnO nanostructures. The XRD results are shown in Figure 1. As seen in the graphics, preparation of ZnO layer were observed on every sample.
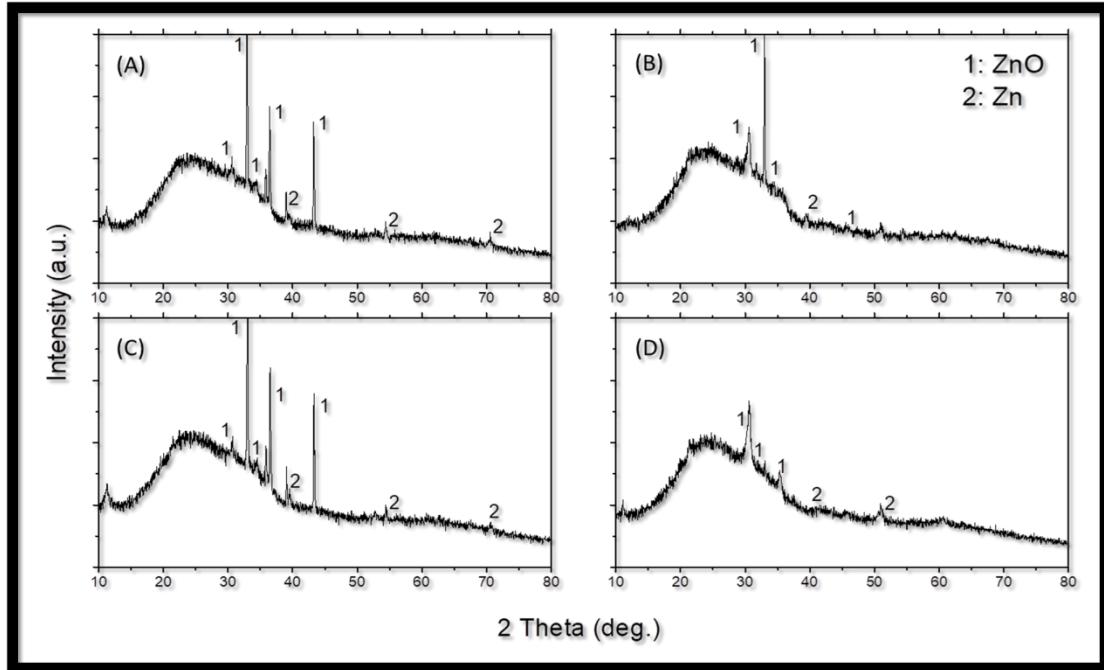
Figure 1. XRD graphics of glass/ITO/ZnO samples; (A) 2.5 min, (B) 5 min, (C) 7.5 min, (D) 10 min.

SEM images of the surfaces are shown in Figure 2. ZnO layers can be seen in all samples. But only sample D has the surface with ZnO nanostructures. This shows that if the deposition time were shorter than 10 minutes, as coated Zn layer would not be thick enough for growth of ZnO nanostructures.
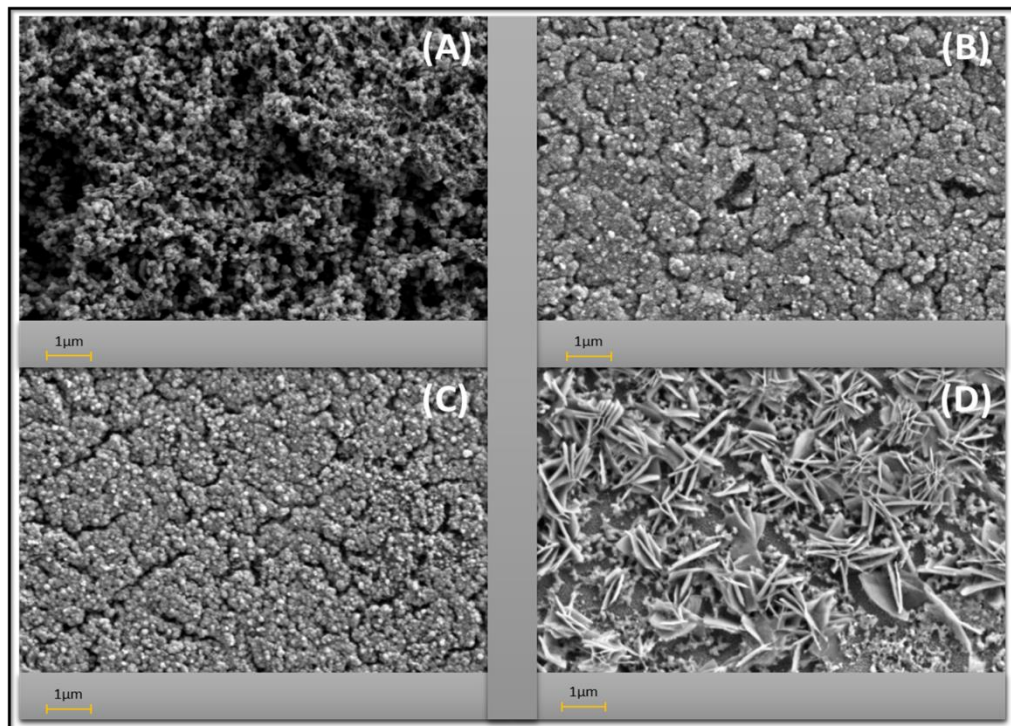

Figure 2. SEM images of glass/ITO/ZnO samples; (A) 2.5 min, (B) 5 min, (C) 7.5 min, (D) 10 min.

CONCLUSION

Unique 2-steps electrochemical process is faster, cheaper and simpler way to produce ZnO nanostructure. Metal layer thickness which depends on deposition time is important parameter for growth of nanostructures. With selecting proper parameter, surfaces covered with ZnO nanostructures can be obtained which are suitable for enzymatic biosensors to detect diseases like cholesterol.

REFERENCES

[1] A. Tereshchenko, M. Bechelany, R. Viter et al., Optical biosensors based on ZnO nanostructures: advantages and perspectives. A review, Sensors and Actuators B 229 (2016) 664–677.

[2] S. S. Bhat, A. Qurashi, F. A. Khanday, ZnO nanostructures based biosensors for cancer and infectious disease applications: Perspectives, prospects and promises, Trends in Analytical Chemistry 86 (2017) 1-13.

[3] A. Wei, X. Sun, J. X. Wang et al., Enzymatic glucose biosensor based on ZnO nanorod array grown by hydrothermal decomposition, Applied Physics Letters 89 (2006) 123902.

[4] S. K. Arya, S. Saha, J. E. Ramirez-Vick et al, Recent advances in ZnO nanostructures and thin films for biosensor applications: Review, Analytica Chimica Acta 737 (2012) 1– 21.

[5] S. Kumar, W. Ahlawat, R. Kumar, N. Dilbaghi, Graphene, carbon nanotubes, zinc oxide and gold as elite nanomaterials for fabrication of biosensors for healthcare, Biosensors and Bioelectronics 70 (2015) 498–503.

[6] R. Khan, A. Kaushik, P. R. Solanki, A. A. Ansari et al., Zinc oxide nanoparticles-chitosan composite film for cholesterol biosensor, Analytica Chimica Acta 616 (2008) 207–213.

[7] X. Liu, Q. Hu, Q. Wu, W. Zhang et al., Aligned ZnO nanorods: A useful film to fabricate amperometric glucose biosensor, Colloids and Surfaces B: Biointerfaces 74(1) (2009) 154-158.

[8] M. H. Asif, B. Danialsson, M. Willander, ZnO Nanostructure-Based Intracellular Sensor, Sensors 15 (2015) 11787-11804.

[9] Z. L. Wang, Nanostructures of zinc oxide. Materials Today 7(6) (2004) 26-33.

[10] F. Wang, R. Liu, A. Pan, et al., The optical properties of ZnO sheets electrodeposited on ITO glass, Materials Letters 61(10) (2007) 2000-2003.

[11] T. Dikici, Çelik malzeme yüzeyine elektrolitik yolla kaplanan Zn-Ni-Co alaşımının mekanik ve yapısal özelliklerinin incelenmesi, DEÜ Fen Bilimleri Enstitüsü Y.L. Tezi (2009).

Growth of Zinc Oxide Nanowires on Carbon Fiber through Hydrothermal Method

Irmak Tunç*, İzmir Katip Çelebi Univ., Dept. of Engineering Sciences, Çiğli Main Campus, İzmir, Türkiye
Mustafa Erol, Dokuz Eylul Univ., Dept. of Metallurgy and Materials Engineering, Tınaztepe Main Campus, İzmir, Türkiye
*Corresponding author: irmak.tunc@ikc.edu.tr

Abstract

In this study, ZnO nanowire coated carbon fiber composite was synthesized by a simple hydrothermal treatment. Aqueous suspension containing ZnO precursors with the carbon fibers was kept in the hydrothermal process at 90 ºC for 2 hour and 4 hour. As a result, a homogenous distribution of ZnO nanowires on the surface of carbon fibers is seen. Therefore, this work provides a facile method of the production of carbon fiber based composites which may have potential applications in the photocatalytic application.

Keywords: ZnO, carbon fiber, hydrothermal method
Discipline: Nanotechnology and Materials Science

1. INTRODUCTION

Over the last decades, zinc oxide nanostructures on flexible carbon fibers (ZnO/CF) have been widely studied due to their superior structural, electrical and optical properties. They have been employed in a wide range of application areas such as, solar cells, photovoltaic, piezoelectric, nano-generators, strain sensors, biosensors, chemical sensing devices and photocatalysts [1].

ZnO is a wide band gap (~3.37 eV) semiconductor photocatalyst activated under ultra-violet light. However, when ZnO structures are grown on such carbon based substrates or incorporated with some metals, narrower band gap structures are obtained and catalysts became active under visible light irradiation [2].As a motivation to decrease band gap by the formation of ZnO-carbon junction, carbon fiber is a promising substrate due to its chemical stability, high electrical conductivity, high specific surface area and suitable porosity for several applications.

Growth of ZnO structures can be performed by electrodeposition, hydrothermal method, sol–gel method, laser ablation technique or chemical vapor deposition, electrospinning [1,3]. Among these techniques hydrothermal method stands a step ahead since it leds to formation of nanostructures with enhanced surface areas. With this motivation, in this study, it is aimed to synthesize ZnO nanostructures on a conductive carbon fibers by hydrothermal synthesis under varying duration. As produced composites were characterized by scanning electron microscopy (SEM), energy dispersive x-ray spectroscopy (EDX), x-ray diffraction (XRD) and UV-Visible spectrophotometer.

2. MATERIALS AND METHODS

Zinc acetate dehydrate from Sigma Aldrich (5970-45-6), Zinc nitrate hexahydrate form Acros (10196-18-6), Hexamethylene tetramine (HMTA) form Sigma Aldrich (100-97-0), NaOH from Sigma Aldrich (1310-73-2) and Ethanol from Sigma Aldrich (32221) were employed for the development of CF/ZnO nanostructures. In addition to solution preparation materials carbon fiber substrate supplied by Aksaca (12K A-42). Throughout this study, the reagents and chemicals were used without further purification or process.

Carbon fibers first washed with nitric acid, acetone and ethanol to remove residual, and then dried in vacuum at 60 ºC. In order to form a seeding layer for hydrothermal treatment a thin ZnO film was dip coated on CF using zinc acetate dihydrate based solutions. To obtain ZnO nanowires, ZnO seed-coated CFs were immersed in zinc nitrate hexahydrate and hexamethylene-tetramine (HMTA) solution in Teflon-lined stainless autoclave. Heat treatment followed the process that led the transformation of amorphous structure in to crystalline phase. Samples were characterized by X-ray diffraction (XRD), scanning electron microscopy (SEM) and UV-Vis spectroscopy.

3. RESULTS AND DISCUSSION

XRD patterns of the samples are given in Figure 1. XRD results, demonstrates that structures are composed of zincite (JCPDS number: 00-036-1451) and Graphite-2H (JCPDS number: 00-041-1487). Obtained results points out that ZnO deposited on carbon fibers had crystalline structure similar to previous studies in literature [3, 4, 5].
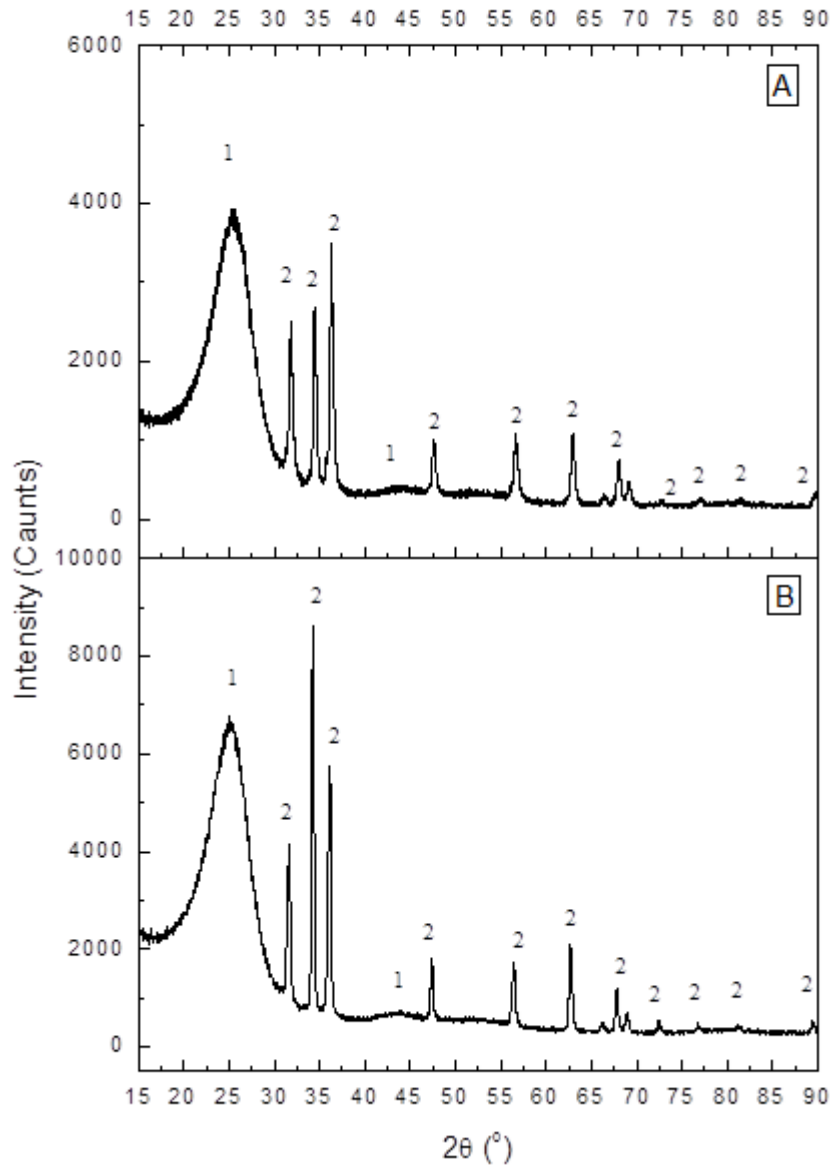

Figure 1. XRD patterns of ZnO NW-coated CFs produced for 2-hours (A) and 4-hours (B)
(1: Graphite-2H, 2: Zincate)

SEM images of the samples are given in Figure 2. It is seen that ZnO nanowires fabricated successfully. Generally, ZnO NWs stand almost vertical to the CFs. The comparative results of the samples of various treatment durations are given in Table 1. In a good agreement with the study of Lui et al., results shows that the length and aspect ratio of nanowires increases with increase in process time [2]. However, the aspect ratio increases with the time.
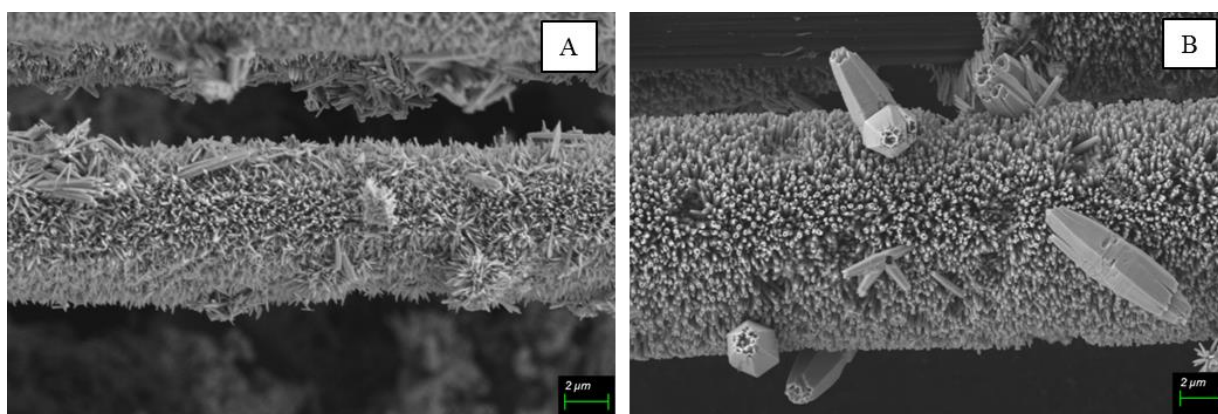
Figure 2. SEM images of ZnO NW-coated CFs produced for (A) 2-hours and (B) 4-hours

Table 1. The length and thickness of ZnO nanowires

Sample / Duration	2 hour	4 hour
Avr. Length/nm	822±215	1429±251
Max-Min length/nm	1227-437	1787-890
Avr. Thickness/nm	91±26	99±36
Max-Min Thickness /nm	135-44	166-53
Aspect ratio	9.0	14.4

In order to determine optical properties of ZnO/CF structure UV-Vis spectrum of the samples were taken (Figure 3). The optical band gap values were calculated by the extrapolation method using the tangent of the absorption curve to intercept the wavelength axis [6, 7]. The optical band gap values which are in a good agreement with the study of Zhang et al. were estimated as 2.78 eV and 2.75 eV, for the samples treated for 2 hours and 4 hours, respectively [8]. The calculation was conducted using the equation $E_g=1240/\lambda_i$, where Eg and λ_i are optical band gap and wavelength of intercept, respectively.
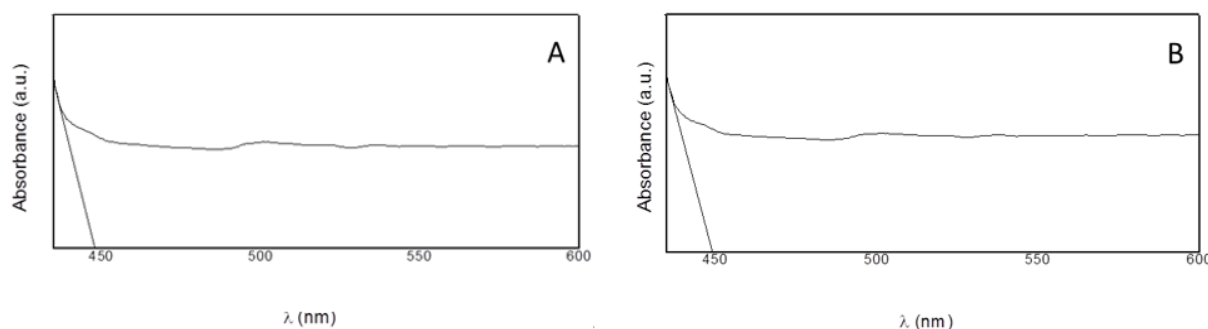
Figure 3. UV-Vis spectra of the samples produced for 2 hours (A) and 4 hours (B) process time.

4. CONCLUSION

In summary, well aligned ZnO NWs deposited on CFs by hydrothermal method successfully. The characterization results revealed that ZnO particles with hexagonal zincite phase were distributed over the surface of CF. Optical band gap of structures were estimates as 2.78 eV and 2.75 eV for the samples treated for 2 hours and 4 hours, respectively.

The effects of time of hydrothermal process on formation of ZnO nanowires have investigated. The growth of ZnO nanowires carried out at 2 different hydrothermal process time. 2 hour, 4 hour process time were tested. It has seen that, at longer time, longer length and higher aspect ratio were seen.

In future, we produce ZnO nanostructures on a conductive carbon fiber by hydrothermal synthesis method and determine the effect of the synthesis parameters in order to obtain optimum photocatalytic properties. The effects of temperature and concentration of solution on the formation of ZnO nanostructures on carbon fiber will be evaluated by means of morphological, structural and optical analyses and photocatalytic activity of the composites will be investigated.

As well as, it is planned to substitute metals into ZnO nano structures at different ratios, in order to shift the absorption spectra to the visible range and decrease the optical band gap with regarding to obtain most effective photocatalyst. Then, the obtained structures' elemental compositions will be characterized by X-Photon Spectroscopy (XPS). Also, using UV-Vis Spectroscopy, the change in absorption properties and band gap values of substituted and unsubstituted structures will be evaluated and compared.

REFERENCES

[1] Y.K. Kim, H.J. Seo, S. Kim, S.H. Hwang, H. Park, S.K. Lim, Effect of ZnO electrodeposited on carbon film and decorated with metal nanoparticles for solar hydrogen production, Journal of Materials Science & Technology 32 (2016) 1059-1065. http://dx.doi.org/10.1016/j.jmst.2016.08.010

[2] H. Liu, C. Gu, C. Hou, Z. Yin, K. Fan, M. Zhang, Plasma-assisted synthesis of carbon fibers/ZnO core-shell hybrids on carbon fiber templates for detection of ascorbic acid and uric acid, Sensors and Actuators B: Chemical 224 (2016) 857-862.

[3] B. Pant, M. Park, H. Kim, S-J. Park, Ag-ZnO photocatalyst anchored on carbon nanofibers: Synthesis, characterization, and photocatalytic activities, Synthetic Metals 220 (2016) 533–537. http://dx.doi.org/10.1016/j.synthmet.2016.07.027

[4] G. Chen, Y. Wang, Q. Shen, Y. Song, G. Chen, H. Yang, Synthesis and enhanced photocatalytic activity of 3D flowerlike ZnO micro structures on activated carbon fiber, Materials Letters 123 (2014) 145–148.

[5] L. Liu, Controllable ZnO nanorod arrays@carbon fibers composites: Towards advanced CO_2 photocatalytic reduction catalysts, Ceramic International 42(10) (2016) 12516-12520.

[6] S. Demirci, B. Öztürk, S. Yildirim, F. Bakal , M. Erol , O. Sancakoğlu , R. Yigit , E. Celik , T. Batar, Synthesis and comparison of the photocatalytic activities of flame spray pyrolysis and sol–gel derived magnesium oxide nano-scale particles, Materials Science in Semiconductor Processing 34 (2015) 154–161. http://dx.doi.org/10.1016/j.mssp.2015.02.029

[7] H. Xiao, W. Zhang, Y. Wei, L. Chen, Carbon/ZnO nanorods composites templated by TEMPO-oxidized cellulose and photocatalytic activity for dye degradation, Cellulose 25 (2018) 1809-1819.

[8] W. Zhang, Y. Sun, Z. Xiao, W. Li, B. Li, X. Huang, X. Liu, J. Hu, Heterostructures of CuS nanoparticle/ZnO nanorod arrays on carbon fibers with improved visible and solar light photocatalysis, Journal of Materials Chemistry: A 3 (2015) 7304-7309.

Carbon Fiber Reinforced Acrylic Bone Cements:
An Investigation on the Effects of Various Electrochemical Surface Modifications on the Mechanical Properties

Emine Özge Akkaş, İzmir Katip Çelebi Univ., Dept. of Nanoscience & Nanotechnology, Turkey
Gökçen Salman Akdeniz, İzmir Katip Çelebi Univ., Dept. of Nanoscience & Nanotechnology, Turkey
Ahmet Aykaç*, İzmir Katip Çelebi Univ., Dept. of Engineering Sciences, İzmir, Turkey
Mustafa Erol, Dokuz Eylül Univ., Dept. of Metallurgical and Materials Engineering, İzmir, Turkey
Mehmet Çevik, İzmir Katip Çelebi Univ., Dept. of Mechanical Engineering, İzmir, Turkey
Fethullah Güneş, İzmir Katip Çelebi Univ., Dept. of Materials Science and Engineering, İzmir, Turkey
*Corresponding author: ahmet.aykac@ikc.edu.tr

Abstract

Acrylic bone cement or surgical grade polymethylmethacrylate is weaker than compact bone and has a lower modulus of elasticity. Polymethylmethacrylate bone cement is weaker than compression stress. This disadvantage limits the use of orthopedics where stretching stresses are minimal. Many authors have attempted to improve their disadvantages by studying the mechanical properties of acrylic bone cement. In recent years, carbon-based nanometers have become important for acrylic bone cement applications due to their unique properties and have been extensively researched. In our work, we used carbon fiber as a carbon-based nanometer-scale. Nanostructured CF / Zn and CF / ZnO composites were produced by electroplating and anodization, respectively. The effect of zinc and zinc oxide structures on surface modification of carbon fiber has been investigated. The effect of nanostructured powders will be investigated by adding the obtained CF / Zn and CF / ZnO nanocomposites as reinforcing agent to polymethylmethacrylate (PMMA) at loads ranging from 0.1 to 1.0 wt% to bone cements. The mechanical, thermal and morphological properties of the resulting polymeric nanocomposites will be characterized. First samples of CF / Zn, CF / ZnO and bone cement composites were successfully produced. In our study, the effect of different parameters on composite structures will be examined and the most suitable parameters will be determined in terms of mechanical, thermal, economical and production methods and commercialization of composite structure will be started.

Keywords: bone cement, carbon fiber, laminates, nano-structures, interface/interphase, fiber/matrix bond
Discipline: Nanotechnology and Materials Science

INTRODUCTION

Acrylic bone cements have been used in orthopedic applications since the 60`s decade [1], being nowadays the most used fixation technique in the joint replacement surgeries. Nowadays, acrylic bone cements are primarily used as a grouting material in joint replacement surgeries, in an effort to transfer the load between the prosthetic implant and the bone [2]. The number of joint replacements performed in the West European countries has increased greatly over the last decade [3]. Several factors have contributed to this increase in the incidence of joint replacement procedures, e.g. an ageing population and the reduction in the patient average age due to obesity or lifestyle. [4]

Acrylic bone cements present many advantages over other fixation techniques (such ease of preparation and application, quick polymerization reaction and fast patient recuperation), but there are also several setbacks (weakened mechanical properties due to pore entrapment, thermal bone necrosis and leaching of unreacted monomer) [5].

The improvement of the bone cement properties is a challenging issue that has been the focus of much research; recently the incorporation of nano-sized materials has been widely explored as potential solutions to improve the mechanical properties [6]. Multiwalled carbon nanotube (MWCNT) powders, calcium carbonate nanoparticles, silica nanoparticles and core-shell nanoparticles are some examples of such materials [7, 8]. The main advantage of nano-sized materials is their high surface area to volume ratio, which provides interesting improvements in the mechanical properties at relatively low concentration levels.

Carbon based nanomaterials (CBNs) have particular types namely: carbon nanotubes (CNT), carbon fibers (CF), graphene (G), graphene oxide (GO) or fullerenes among others. These nanomaterials have become very essential due to their unique properties (ie. thermal and electrical conductivity, high mechanical strength etc.). Their uses have been widely researched in a great variety of applications; especially in the reinforcement of composite materials [9].

Among these CBNs, carbon fibers stand a step ahead, due to their availability in mass production and controlled production parameters. The carbon atoms in carbon fiber are bonded together in microscopic graphite crystals that are more or less aligned parallel to the long axis of the fiber. The resulting alignment brings out an enhanced specific strength in carbon fibers and the composites made up of carbon fibers [10].

Ormsby et al. [8, 11] reported that the most efficacious method to produce MWCNT-PMMA bone cements was to disperse the MWCNT powder in the liquid monomer component using ultrasonic disintegration prior to its introduction into the polymer powder. In this way, acrylic bone cements containing 0.1–0.25 wt. % loading of MWCNT powder have showed significant improvements in the static and fatigue properties, as well as low levels of cytotoxic response. These studies also showed the fundamental importance of the MWCNT functionalisation in order to achieve a good dispersion, and in turn improvements in mechanical performance.

MWCNT-PMMA bone cements have been extensively studied; however, in literature the number of the studies based on the effects of surface modifications on the mechanical behaviors of composite acrylic bone cements are limited. Therefore, in this study nanostructured CF/Zn and CF/ZnO composites were produced through electroplating and anodization, respectively. The structural, morphological and the mechanical properties of the composites modified under various processing parameters were investigated in detail.

METHODOLOGY

In this research, the aim was to obtain nanofibers (CF / Zn) at the most suitable interface by making experiments on important aspects such as zinc (Zn) coating on carbon fiber surfaces, chemical electroplating while varying pH, temperature, voltage, current and duration. It is required to make zinc oxide coated carbon fiber (CF / ZnO) nanostructures at the most suitable interface by making anodization of zinc coated carbon fibers (CF / Zn) by electrochemical method and by making experiments on important parameters such as pH, temperature, voltage, current and duration.

The bone cements containing the powders of the prepared nanowires at different loading levels (0.1, 0.25, 0.5 and 1 wt. %) were prepared. Nanomaterial powders are dispersed in liquid composition by ultrasonication. The powder and liquid phase of the bone cement must be prepared prior to mixing. For comparison, PMMA bone cement without nanomaterials should be used as cement.

The powder phase is prepared by gradually adding small amounts of barium sulfate to the PMMA. When some PMMA dust is added, the mixture should be shaken by hand until a total PMMA amount is achieved and a homogeneous mixture should be obtained.

The liquid phase is prepared by mixing the MMA and DmpT components. For these tests where the samples are manufactured, the cement is injected using a mold with the relevant size and geometry depending on the test conditions. Each bone cement sample is then removed from the bone. The bone cement samples are then stored at room temperature and humidity for 1 week before testing.

Mechanical properties of each of the different loading levels (0.1, 0.25, 0.5 and 1 wt. %) And thermal properties will be characterized by preparing 4 different nanocomposites for comparison (PMMA, PMMA / CF, PMMA / CF / Zn, PMMA / CF / ZnO) . SEM images of the prepared composites are taken and the interaction between the composites and the interactions between them will be examined.

The SEM will be used for the analysis of the fracture surfaces of the different bone cement combinations as well as the shape and dimensions of the powder nanomaterials (CF, CF / Zn and CF / ZnO). With the FTIR study, information about the chemical composition of composites will be provided. XRD images will be taken to examine the atomic and molecular structures of the prepared composites.

RESULTS

As a result of the experiments, the zinc coating process on the carbon fiber surfaces was successful without any problem by chemical electroplating. Characterization of coating experiments with different parameters was made by scanning electron spectrometry (SEM).(Figure 1) As a result of the SEM

2nd International Students Science Congress
4-5 May 2018, Izmir - Turkey

İZMİR
KÂTİP ÇELEBİ
UNIVERSITY
2010

İZMİR
Uluslararası
Misafir
Öğrenci
Derneği
♦ İZMİR International Guest Student Association

images, it is determined that the coating has continuity and the best coating is figure 1-b. Base on the results obtained from the electrochemical anodization process, the performed anodization process was successful without error.(Figure 2). However, different parameters will work for better results.
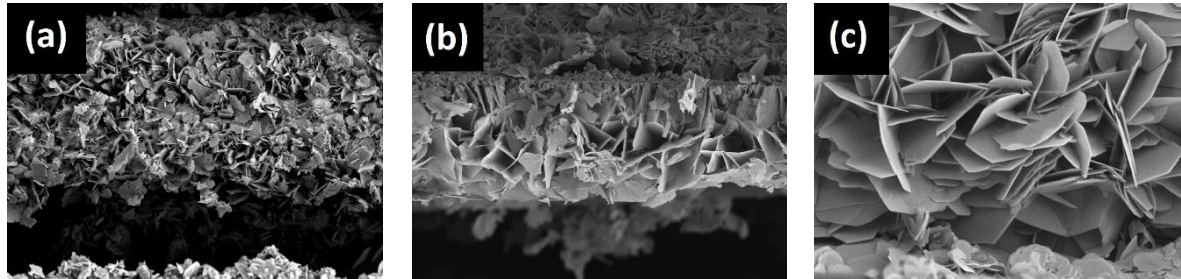

Figure 1: SEM images of CF / Zn composites coated by chemical electroplating method at different parameters (a) SEM image of carbon fibers coated at 0.9V for 10 min. (b) SEM image of carbon fibers coated at 0.9V for 15 min. (c) SEM image of carbon fibers coated at 0.9V for 20 min.
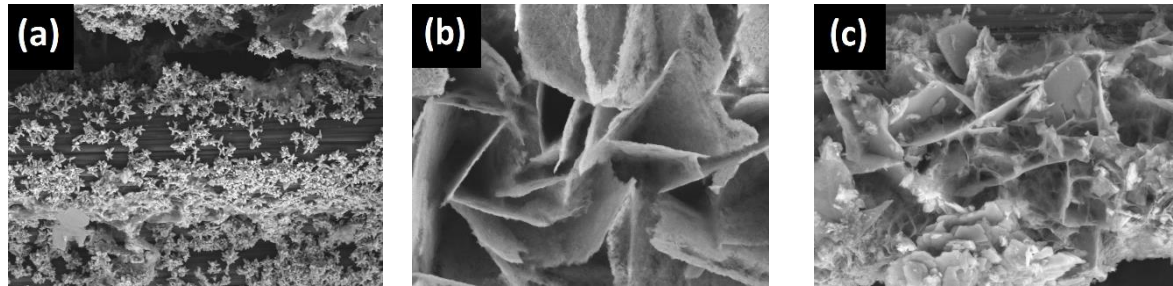

Figure 2: SEM images obtained by electrochemical anodization of zinc coated carbon fibers at different parameters. (a) and (b) SEM image of CF/Zn anodization at 30V for 10 min. (c) SEM image of CF/Zn anodization at 30V for 15 min.

Investigating different parameters and characterization procedures, we expect to identify the appropriate structure form of the carbon fiber. After electroplating and anodizing, bone cement, preparation studies were carried out. As described in the Methods section, the liquid and powder phases were separately prepared and the bone cements were mixed until hardened. As a result, in this experiment the appropriate formulation for the preparation of bone cement was identified. In order to move on to polymeric composite preparation processes we first have to complete characterization of bone cement studies and anodization studies. As shown in our results, it was determined that the coating and anodizing processes were carried out smoothly and the bone cement made are similar to commercial bone cements.

CONCLUSION

As a result of the studies made, surface modifications of carbon fiber have been changed by electrochemical coating and electrochemical anodization processes. It is envisaged that CF / Zn or CF / ZnO nanotozes may improve the mechanical performance of PMMA bone cement as a result of incorporating low loads (≤ 0.25 wt%). It is anticipated that in the PMMA bone cement matrix, sufficient interaction between the nanoscale additive and matrix is the key. Additionally, good distribution of CF / Zn and CF / ZnO can prevent crack propagation through bone cement because of mechanical tests.

REFERENCES

[1] J. Charnley, The Classic: The bonding of prostheses to bone by cement. Clinical Orthopaedics and Related Research 468 (2010) 3149-3159.

[2] J. Charnley, Anchorage of the femoral head prosthesis to the shaft of the femur, J. Bone Joint Surg. Br. 42-B (1960) 28–30.

[3] OECD and European Union, Health at a Glance: Europe, OECD Publishing, 2014.

[4] U. Holzwarth, G. Cotogno, Total hip Arthroplasty State of the art, Challenges and Prospects, Institute for Health and Consumer Protection, Luxembourg: Publications Office, 2011.

[5] N. Dunne, J. Clements, J.-S. Wang, in: Joint Replacement Technology, *ed.* P.A. Revell, Woodhead Publishing (2014) 212–256.

[6] N. Dunne, R. Ormsby, Carbon Nanotubes - Growth and Applications: MWCNT used in Orthopaedic Bone Cements, in M. Naraghi, editor, Carbon Nanotubes - Growth and Applications, In Tech. (2011) 337-392.

[7] J. Slane, J. Vivanco, J. Meyer, H.-L. Ploeg, M. Squire, Modification of acrylic bone cement with mesoporous silica nanoparticles: Effects on mechanical, fatigue and absorption properties, Journal of the Mechanical Behavior of Biomedical Materials 29 (2014) 451–461.

[8] R. Ormsby, T. McNally, C. Mitchell, N. Dunne, Incorporation of multiwalled carbon nanotubes to acrylic based bone cements: Effects on mechanical and thermal properties, Journal of the Mechanical Behavior of Biomedical Materials 3 (2010) 136–145.

[9] C. Cha, S.R. Shin, N. Annabi, M.R. Dokmeci, A. Khademhosseini, Carbon-based nanomaterials: Multifunctional materials for biomedical engineering. ACS Nano 7 (2013) 2891–2897.

[10] X. Yao, X. Gao, J. Jiang, C. Xu, C. Deng, J. Wang, Comparison of carbon nanotubes and graphene oxide coated carbon fiber for improving the interfacial properties of carbon fiber/epoxy composites, Composites Part B: Engineering 132 (2018) 170-177.

[11] R. Ormsby, T. McNally, P. O'Hare, G. Burke, C. Mitchell, N. Dunne, Fatigue and biocompatibility properties of a poly(methyl methacrylate) bone cement with multiwalled carbon nano-tubes, Acta Biomater. 8 (2012) 1201–1212.

2D Graphene Based Composite with Polyethylene Glycol

Çağlar Erdem, İzmir Katip Çelebi Univ., Dept. of Nanoscience and Nanotechnology, İzmir, Turkey
Büşra Beşli, İzmir Katip Çelebi Univ., Dept. of Materials Science and Engineering, İzmir, Turkey
Müge Çetin, İzmir Katip Çelebi Univ., Dept. of Materials Science and Engineering, İzmir, Turkey
Ahmet Aykaç, İzmir Katip Çelebi Univ., Dept of Engineering Science, Izmir, Turkey
Mustafa Erol, Dokuz Eylul Univ., Dept of Metallurgical and Materials Engineering, Izmir, Turkey
Evren Çulcular, Izmir Institute of Technology, Dept. of Physics, İzmir, Turkey
Fethullah Güneş[*], İzmir Katip Çelebi Univ., Dept. of Materials Science and Engineering, İzmir, Turkey*
[*]Corresponding Author: fethullah.gunes@ikc.edu.tr

Abstract

Graphene is a single-atom thick two-dimensional allotrope of carbon. It has a unique conic band structure allowing it high carrier speed, and high specific surface area. On the other hand, the low water-solubility and the irreversible aggregation due to the strong π-π stacking, hinders the biomedical application of graphene. Using polymers the water solubility could be improved significantly, resulting in biological compatibility of graphene,.

PEG (polyethylene glycol) polymer shows a very hydrophilic behavior and PEG chains have high mobility and flexibility in the coherent phases. Apart from these properties, PEG may also possess excellent characteristics such as very low toxicity and biocompatibility.

In this study, our purpose was graphene synthesis using Chemical Vapor Deposition (CVD) method and its surface functionalization with PEG for biological applications. In the first step of this study, graphene synthesis was carried out using CVD over copper foil and transferred onto an insulating Si/SiO$_2$ substrate. After that, the graphene film was coated by PEG using spin coating followed by furnace drying method. Final graphene-PEG composite material characterization was done via Scanning Electron Microscopy (SEM) and Raman spectroscopy techniques. As a result, few layered graphene was synthesized successfully and PEG nanoparticles were observed uniformly distributed on graphene surfaces.

Keywords: Graphene, Polyethylene-glycol, CVD method, Nanocomposite
Discipline: Nanoscience and Nanotechnology

INTRODUCTION

Graphene is a two-dimensional sheet of sp2-hybridized carbon atoms. These carbon atoms bound to each other within a plane by strong covalent bonds forming a honeycomb lattice structure. Graphene has one atom thickness which is formed by a covalent bond of adjacent carbon atoms in a single lattice. Many experiments demonstrate graphene's excellent theoretical limits such as electron mobility of 2.5 x 105 cm2.V-1.s-1 at room temperature, young modulus of 1 TPa and intrinsic strength of 130 GPa, good thermal conductivity above 3000 W mK-1, optical absorption of $\pi\alpha \approx 2.3\%$, exact tightness to any gas, ability to sustain extremely high densities of electric current; a million times higher than copper [1-5].

Graphene can be synthesized by different methods. The properties of graphene depend on preparation methods. In this study, the CVD method was chosen because CVD production of graphene is suitable for large area graphene with improved properties such as high specific surface area, crystallinity, and electron mobility [6-7].

Graphene has extraordinary properties; however, it has some limitation for biological application. Forming composite structures may improve graphene's properties due to additive material's biocompatibility or water solubility [8-9]. PEG was chosen as additive material which can be produced by the interaction of ethylene oxide with water, ethylene glycol, or ethylene glycol oligomers. Polymer chain length is hinged on the ratio of reactants. Based on the catalyst type, the mechanism of polymerization could be cationic or anionic. High-molecular mass polyethylene glycol is synthesized by suspension polymerization. It is essential to hold the growing polymer chain in solution during the polycondensation process. The reaction is catalyzed by magnesium-, aluminum-, or calcium-organoelement compounds [10]. PEG is a highly hydrophilic synthetic polymer with very high

biocompatibility. The molecular weight range is from 200 to 6000. Properties and areas of use vary depending on the molecular weight. PEG is one of the well known an uncharged, water-soluble, non-toxic, non-immunogenic polymer and is therefore an ideal material for coating biomolecules and to be used as protecting material. Water is miscible and soluble in many alcohols and organic solvents. It does not migrate or decompose at low vapor pressures [11].

METHODOLOGY

In this research, our main purpose was graphene synthesis by using the CVD method and surface functionalization with PEG 2000. CVD method was chosen because it is the most reliable and suitable method for high quality graphene synthesis in terms of high crystallinity, high electron conductivity and surface area. Surface functionalization was applied by using drop coating method.

The process was begun with the graphene synthesis. First of all, copper foil was cleaned with $FeCl_3$ and distilled water. Then the copper foil was put into the center point of CVD furnace that was heated near a temperature of copper's melting point with Argon (Ar) (1000 sccm) and Hydrogen (H_2) (80 sccm) gases. H_2 gases prevent to oxidation of surface and Ar gases clean to surface from impurities. Then, the annealing process was started. Annealing expands the grain boundaries of copper foil. It was continued for 40 minutes. Until this step, just Ar and H_2 gases flowed into the furnace. Now, methane (CH_4) (12 sccm) gases were flowed, additionally, as a source of carbon atoms. It reduced at high temperature and carbon atoms deposited on copper foil so these carbon atoms generated graphene film. This step was applied either 1 or 2 minutes. Growth time depends on a determination of the required graphene layers. The final step was slow cooling at room temperature with Ar and H_2 gases.

Graphene was grown on copper foil, the graphene film could be transferred onto Si/SiO_2 substrate because of the characterization process. The transfer process was begun with the poly (methylmethacrylate) (PMMA) coating of the graphene surface by using drop coating with a spin-coater device. PMMA protects graphene film from copper etchant. The sample was put into iron-chloride which was etched the copper foil when it was etched, the graphene/PMMA structure transferred into DI water in order to clean residual of a copper etchant. Graphene film was taken out, then from cleaning bath to Si/SiO_2 wafer. Furthermore, PMMA was removed from the graphene surface with hot acetone. Finally, graphene film was obtained on Si/SiO_2 wafer.

The graphene transferred on the Si/SiO_2 substrate was coated with PEG 2000 (Sigma-Aldrich) that was used for the coating process. PEG 2000 was mixed with different solvents to obtain homogeneous solutions. These are distilled water, ethanol and methanol. A sonic bath was used for the dissolving process. Two different coating method was used, these were spin coating and drying furnace. In the drop casting method, PEG solution was dropped on to graphene surface and coated using spin coating method. In the drying furnace method, the PEG solution was dropped onto the graphene surface and the sample was put in a drying-furnace at 50°C.

RESULTS

The samples characterization was done with Raman Spectroscopy and Scanning Electron Microscopy (SEM). The first characterization was done with Raman Spectroscopy which may give an idea on the quality of graphene. This characterization method was done with Renishaw InVia microscope at Katip Çelebi University central research laboratory and the spectrum was obtained by the excitation source of 532 nm and 2400 greeting. The working distance of wave is between from 1100 nm to 3000 nm. The Raman peaks showed single layer graphene because the ratio of 2D/G was 3.28.
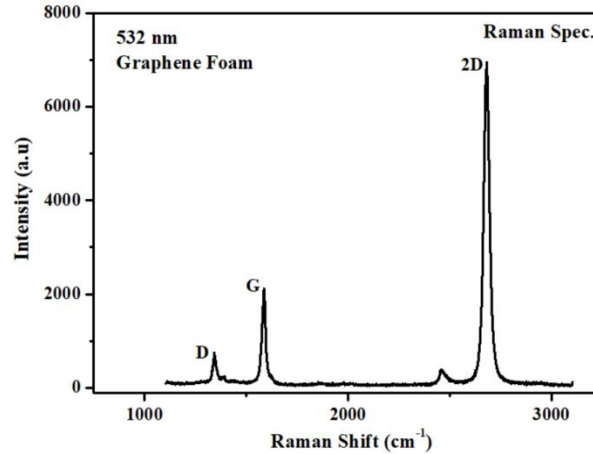
Figure 1. The Raman Spectroscopy of graphene

The characterization of scanning electron microscopy was done with Zeiss Sigma 300vp at İzmir Katip Çelebi University central research laboratory. SEM is working in high vacuum. Electron high tension value was between 2 kV and 5 kV and PEG/Graphene on Si/SiO2 wafer was viewed by a magnitude of 10K, 25K, 50K and 100K. Dispersed PEG was seen on graphene surface area with SEM. PEG may be found on graphene wrinkles because graphene wrinkles have different surface tension due to the difference in thermal expansion coefficients of graphene and that of copper.
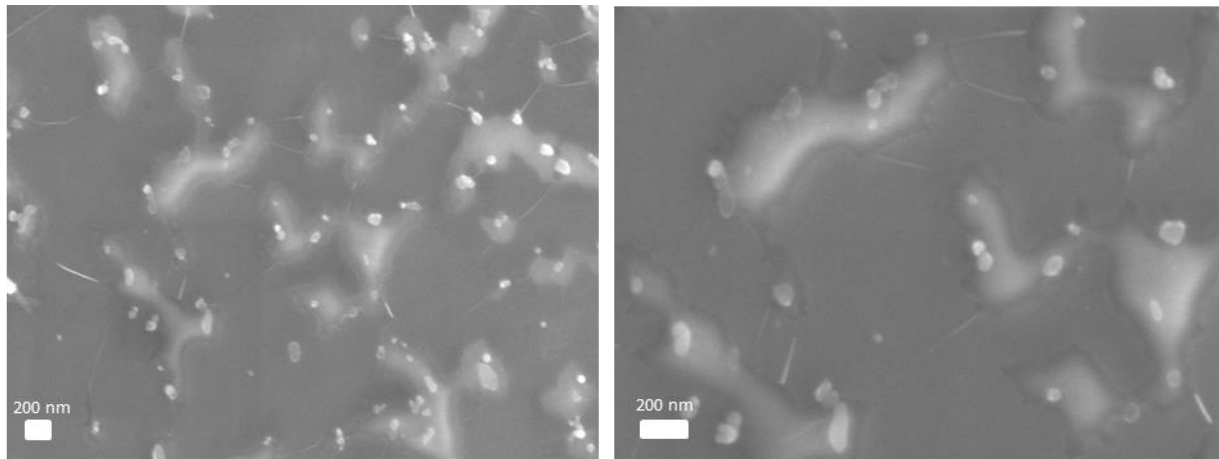

Figure 2. Images of SEM characterization.

CONCLUSIONS

In this study, graphene was synthesized via CVD method, and the Raman Spectroscopy results showed single layer graphene peaks with 2D/G ratio at 3.28, respectively. Graphene peaks are single layer because the ratio of 2D/G was over 2.5. Graphene surface was coated with PEG 2000 solution. SEM images show the drying furnace method was better than the spin coating method. PEG 2000 solution was well dispersed on graphene surface with drying furnace method. The structure of PEG on graphene improves the surface area and its biocompatibility. We believe that these results will open up possibilities for further studies.

REFERENCES

[1] K.S. Novoselov, V. I. Fal'ko, L. Colombo, P. R. Gellert, M. G. Schwab, K. Kim, A roadmap for graphene, Nature 490 (2012) 192-200.
[2] K.S. Novoselov, A.K. Geim, S.V. Morozov, D. Jiang, M.I. Katsnelson, I.V. Grigorieva, S.V. Dubonos, A.A. Firsov, Two-dimensional gas of massless Dirac fermions in graphene, Nature 438 (2005) 197-200.

[3] A.H. Castro Neto, K. Novoselov, New directions in science and technology: two-dimensional crystals, Reports on Progress in Physics 74 (2011) 082501.

[4] S. Chen, Q. Wu, C. Mishra, J. Kang, H. Zhang, K. Cho, A.A. Balandin, R.S. Ruoff, Thermal conductivity of isotopically modified graphene, Nature Materials 11 (2012) 203-207.

[5] J. Rafiee, X. Mi, H. Gullapalli, et al., Wetting transparency of graphene, Nature Materials 11 (2012) 217-222.

[6] C. Mattevi, H. Kim, M. Chhowalla, A review of chemical vapour deposition of graphene on copper, Journal of Materials Chemistry 21 (2011) 3324-3334.

[7] Y. Zhu, S. Murali, W. Cai, X. Li, J.W. Suk, J.R. Potts, R.S. Ruoff, Graphene and graphene oxide: synthesis, properties, and applications, Advanced Materials 22 (2010) 3906-3924.

[8] K. Yang, J. Wan, S. Zhang, Y. Zhang, S. Lee, Z. Liu, In vivo pharmacokinetics, long-term biodistribution, and toxicology of PEGylated graphene in mice, ACS Nano 5 (2011) 516-522.

[9] K. Yang, H. Gong, X. Shi, J. Wan, Y. Zhang, Z. Liu, In vivo biodistribution and toxicology of functionalized nano-graphene oxide in mice after oral and intraperitoneal administration, Biomaterials 34 (2013) 2787-2795.

[10] S. Kumbar, C. Laurencin, M. Deng, eds. Natural and Synthetic Biomedical Polymers. Elsevier, 2014.

[11] H.J. Milton, ed. Poly(Ethylene Glycol) Chemistry: Biotechnical and Biomedical Applications. Springer, 1992.

The Synthesis of Gold Nanoparticle Decorated 2D Graphene

Büşra Beşli, İzmir Katip Çelebi University, Department of Materials Science and Engineering, Izmir, Turkey
Çağlar Erdem, İzmir Katip Çelebi University, Department of Nanoscience and Nanotechnology, Izmir, Turkey
Ezgi Şahin, İzmir Katip Çelebi University, Department of Materials Science and Engineering, Izmir, Turkey
Fethullah Güneş, İzmir Katip Çelebi University, Department of Materials Science and Engineering, Izmir, Turkey
Mustafa Erol, Dokuz Eylul University, Department of Metallurgical and Materials Engineering, Izmir, Turkey
Evren Çulcular, Izmir Institude of Technology, Department of Physics, İzmir, Turkey
Ahmet Aykaç[*], İzmir Katip Çelebi University, Department of Engineering Science, Izmir, Turkey
[*]Corresponding Author: ahmet.aykac@ikc.edu.tr

Abstract

Graphene is a two-dimensional material and an allotrope of carbon that has a hexagonal honeycomb lattice and single atomic thickness [1]. Due to its large surface area, high electron mobility, thermal conductivity, and stability, it is a material known for outstanding chemical, electrical, optical and physical properties. In this study, single-layer graphene was synthesized by chemical vapor deposition (CVD) on the copper foil and transferred onto the insulator Si / SiO2 substrates [2].

Hybrid structures consist of graphene and metal nanoparticles are a class of nanocomposites which shows new physical properties by combining properties of graphene and the advantages of metallic nanoparticles. Gold nanoparticles (AuNP) have distinct physical and optical properties, which depend on their size, shape, surface structure and agglomeration state [3]. Adding of gold nanoparticles to graphene improves the properties such as effective surface area, catalytic activity, electrical conductivity, water solubility and biocompatibility; therefore, gold nanoparticles were selected for this study. Graphene decorated with gold nanoparticles is used for catalysis, biosensors, fuel cells, light emitting diodes, solar cells, advanced transparent conductors. Gold nanoparticles were produced around 10-20 nm in diameter using the Turkevich method. Finally, graphene foil was coated with gold nanoparticles [4].

After synthesis processes, graphene-AuNP hybrid nanocomposite was characterized by using SEM, AFM and Raman spectroscopy. Raman spectroscopy showed single-layer graphene peaks. SEM images showed graphene networks on Si / SiO2. AFM showed some ripples of Si wafer. It has been observed that the results of this experiment are close to the literature. The graphene-AuNp hybrid nanocomposite that is obtained in this study demonstrated that the chemical and electrical properties of graphene improved by modification with gold nanoparticles.

Keywords: Graphene, CVD, Au nanoparticles
Discipline: Nano Science and Nano Engineering

INTRODUCTION

A single layer of graphite is called graphene. It is an allotrope of carbon element and has sp2 hybridization. Graphene is a two-dimensional (2D) material that has a hexagonal honeycomb lattice and single atomic thickness [5]. Due to its large surface area, high electron mobility, thermal conductivity and stability, it is a material with outstanding chemical, electrical, optical and physical properties. Thermal, electrical and mechanical properties of graphene are much better than the other materials so preference of graphene increases in recent years. Graphene is the only material known to be the thinnest, lightest and two-dimensional. It is transparent and has a light transmittance of 97-98%. The electrical conductivity of graphene is much higher than copper. It is also the material with the highest thermal conductivity. It is hard, 200 times more resistant than steel, but at the same time flexible and easy to bend. Flexibility makes it possible to coat on different materials. The electron movement of the graphene is very fast, so it is an alternative material against silicon for electronic circuits [6-9].

Chemical vapor deposition (CVD) is one of the production methods of graphene. It is efficient, quite good quality and reproducible production method. It is known that graphene has defects in graphene oxide production. This method is a bottom-up method and is suitable for producing perfect graphite layers also the equipment for production is costly cheap compared to other methods. The graphene layers

were first deposited on nickel by CVD technique. Nowadays, deposition is carried out on transition metals such as nickel, palladium, iridium and copper [10].

The most common metal nanoparticles for scientific applications are gold. Bulk gold is a soft, malleable, transition metal and is one of the least chemically active elements [11]. Colloidal gold is submicrometer size particles of gold. Unlike bulk gold, colloidal gold is highly reactive and it can be used for new applications [12]. With advances in analytical technologies in the 20th century, studies of gold nanoparticles accelerated [13]. Gold particles are studied for practical uses because of their easy synthesis and high stability. Different types of gold nanoparticles are used in many industries, such as electronics and medicine.

METHODOLOGY

CVD method was chosen to produce graphene. CVD method is the most reliable and suitable method to produce few-layer high-quality graphene. Au nanoparticles that obtained via the Turkevich method was chosen for coating. Turkevich method is a reliable and low-cost method to produce AuNP's.

It was decided to produce a single-layered graphene on a copper plate. The copper plate was placed in the furnace for a preannealing process. Hydrogen (100 sccm) and Argon gas (100 sccm) were sent into the furnace. The oven was heated to 1079 °C for 56 minutes with the copper plate in it. This temperature is close to the melting point of copper and annealing is applied to obtain larger grain boundaries in order to maintain better graphene growth. It was then kept at 1079 °C for 120 minutes. After, the furnace is cooled in the room temperature. The copper plate was removed from the furnace and polished with FeCl3 (acid) and distilled water.

In graphene production part, the copper plate was put in the furnace again. Hydrogen (80 sccm) and Argon gases (1000 sccm) were sent into the furnace. The furnace was heated to 1079 °C at 56 minutes with the copper plate in it. It was then left at the same temperature for 40 minutes. Methane gas (CH4) (12 sccm) then flowed to the furnace at 1079 °C for 2 min. This allowed graphene growth on the copper plate. Then, the furnace was cooled and the graphene/Cu plate was removed from the furnace.

The deposited graphene on copper must be transferred to a substrate to measure its properties. A substrate can be Si wafer or ITO. The transfer was started by coating polymethylmethacrylate (PMMA) onto the graphene film. The graphene copper plate was coated with PMMA (2 ml) by using a spin coater (1000 rpm/60s).

Then the copper plate was put into the iron(III)chloride (FeCl3) (Cu etchant) bath until graphene film was floated without copper in the etchant bath. Then graphene film was transferred into the pure water in order to clean residuals from etchant and copper was completely removed from the graphene-coated PMMA.

The PMMA-coated graphene film was placed on a Si / SiO2 plate. For good drying, the sample was held in a drying oven at 80 °C. To remove the PMMA from the surface of the graphene, it was immersed in heated acetone, it was immersed for about 3 minutes in pure water and a graphene film was obtained on the all-free Si layer.

As a final step, nanoparticles dropped onto the graphene and waited for 5 minutes and dried in the furnace for 15 min. Also, a concentration of AuNP's was changed (50%, 75% and 87.5%). Thus, the gold nanoparticle-graphene hybrid nanocomposite is obtained.

RESULTS

Raman spectroscopy was used for the characterization of graphene. A number of graphene sheet layer and the quality of graphene were identified via Raman. The ratio of 2D/G should be higher than 2.50 to obtain single layer graphene.

2ⁿᵈ International Students Science Congress
4-5 May 2018, Izmir - Turkey

İZMİR
KÂTİP ÇELEBİ
UNIVERSITY
2010

İZMİR
Uluslararası
Misafir
Öğrenci
Derneği
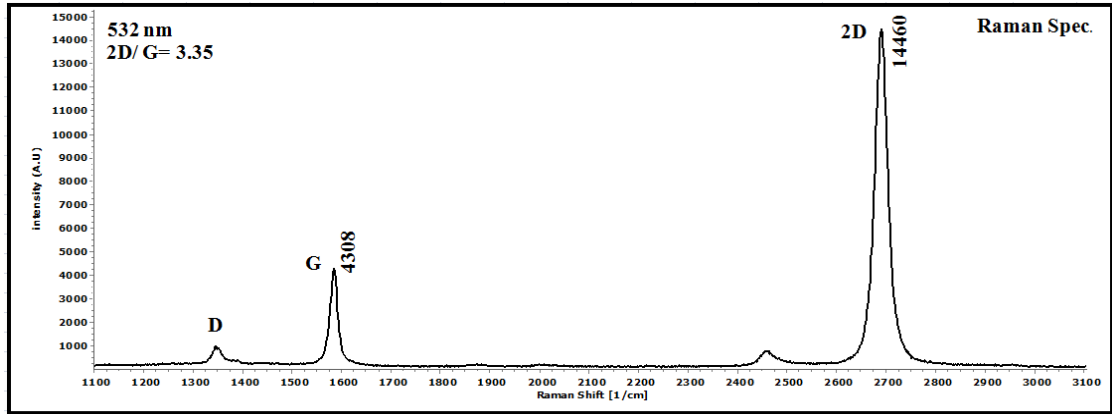◆İZMİR International Guest Student Association

Figure 1. Raman result of graphene

The Raman spectroscopy results show the peaks of single-layer graphene on the substrate. The intensity ratio of the specimens of the G band and 2D band show a few layers of graphene were synthesized. 2D band intensity is 14460, G band intensity is 4308 so the intensity ratio of bands is 3.35.

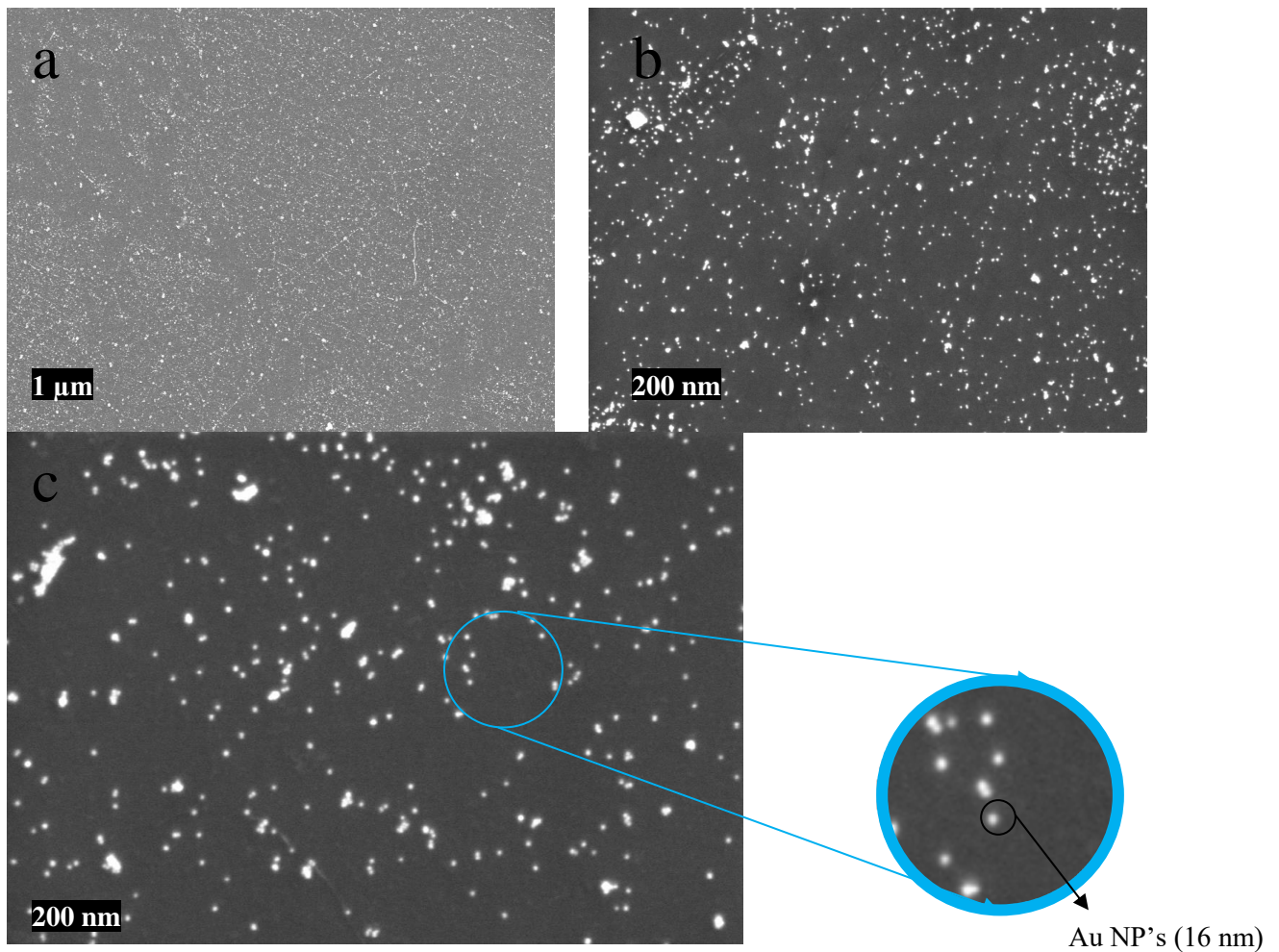SEM is used for image nanomaterials and characterize morphologies of graphene.

Figure 2. SEM results of graphene/AuNP.
(a) 1μm, (b) 200nm, (c) 200nm from the different part of the specimen

In this specimen gold nanoparticles dispersed properly. Wrinkles are too few as it can be seen in Figure 2(a). Little aggregation can be observed. Diameters of gold nanoparticles are about 16nm. There

are very little defects and residuals. Residuals can be PMMA or dust particles. These images are approximately similar to literature.

CONCLUSION

As a result of this study, graphene growth has been synthesized as a single layer on the copper plate via CVD method successfully. Also, the transferring process was completed successfully. Characterization results show us clearly.

Raman spectroscopy results show that single layer graphene was observed. SEM images were proved that Au NP's were dispersed on graphene properly. As a result, the gold nanoparticle-graphene hybrid nanocomposite was synthesized successfully.

Consequently, gold nanoparticle-graphene hybrid nanocomposite can be used for electronic devices such as transistors, super-fast computers, capacitors capable of fast charging, biosensors and touch screen, drug delivery, etc.

When the conditions became stable for the experimental process, the results can be developed. It is believed that these results will be helpful for further studies.

REFERENCES

[1] K.S. Novoselov, V. I. Fal'ko, L. Colombo, P. R. Gellert, M. G. Schwab, K. Kim, A roadmap for graphene, Nature 490 (2012) 192-200.

[2] C. Mattevi, H. Kim, M. Chhowalla, A review of chemical vapour deposition of graphene on copper, Journal of Materials Chemistry 21 (2011) 3324-3334.

[3] Z. Osváth, A. Deák, K. Kertész, Gy. Molnár, G. Vértesy, D. Zámbó, C., Hwang, L.P. Biró, The structure and properties of graphene on gold nanoparticles, Royal Society of Chemistry, Nanoscale 7 (2015) 5503-5509.

[4] J. Kimling, M. Maier, B. Okenve, V. Kotaidis, H. Ballot, A. Plech, Turkevich method for gold nanoparticle synthesis revisited, J. Phys. Chem. B. 110 (2006) 15700-15707.

[5] Boundless Chemistry, provided by Boundless Learning, Allotropes of Carbon.

[6] R. Prasher, Graphene spreads the heat, Science 328 (2010) 185-186.

[7] A.A. Balandin,S. Ghosh, W. Bao, I. Calizo, D. Teweldebrhan, F. Miao, C.N. Lau, Superior thermal conductivity of single-layer graphene, Nano Letters 8 (2008) 902-907.

[8] J.H. Seol, I. Jo, A.L: Moore, L. Lindsay, Z. H. Aitken, M. T. Pettes, Two-dimensional phonon transport in supported graphene Science 328 (2010) 213-216.

[9] Y.K. Koh, M.-H. Bae, D.G. Cahill, E. Pop, Heat conduction across monolayer and few-layer graphenes, Nano Letters 10 (2010) 4363-4368.

[10] P. Lenz-Solomun, M.-C. Wu, D. W. Goodman, Methane coupling at low temperatures on Ru (0001) and Ru (11‾20) catalysts, Catalysis Letters 25 (1994) 75-86.

[11] S. Link, M.A. El-Sayed, Spectral properties and relaxation dynamics of surface plasmon electronic oscillations in gold and silver nanodots and nanorods J. Phys. Chem. B. 103 (1999) 8410-8426.

[12] Gold. Retrieved July 26, 2013, from wikipedia.org: http://en.wikipedia.org/wiki/Gold

[13] R Rau, Have traditional DMARDs had their day? Effectiveness of parenteral gold compared to biologic agents, Clin. Rheumatol 24 (2005) 189-202.

Synthesis and Characterization of Biodegradable Sodium Alginate - Chitosan Polymeric Nanoparticles

Aylin Kazoluk, Ahmet Aykaç*
İzmir Katip Çelebi Univ., Institute of Natural & Appl. Sci., Nanoscience & Nanotechnology, İzmir, Turkey
*Corresponding author: ahmet.aykac@ikc.edu.tr

Abstract

The aim of this project is to investigate the encapsulation of antioxidants in nanoparticles that derived from sodium alginate and chitosan biopolymers. Furthermore, the characterizations, optimization of conditions, encapsulation ability of the polymeric NPs with an antioxidant.and release study of the encapsulated antioxidant will be carried out. As an encapsulation agent Pomegranate have been chosen. Both the pomegranate juice extract and the anthocyanin extract will be examined for their total anthocyanin content, total flavonoid, total phenolic substance and antioxidant capacity. The excreted anthocyanin, sodium alginate and chitosan, will be encapsulated by ionic gelation / dripping (cross-linking) method in the presence of calcium chloride. Characterization of nanoparticles based on the size, morphology and surface charge will be carried out by Scanning Electron Microscopy (SEM), Fourier Transform Infrared Spectroscopy (FT-IR) and UV-Vis spectroscopy. In order to determine the efficiency of nano-encapsulation, anthocyanin release experiments will be carried out in the artificial gastrointestinal media (biological buffer). So that, the study might be a model study for hydrophilic pharmaceutically active molecules.

Keywords: Sodium alginate, chitosan, nanoparticles, calcium, hydrocolloidal, biopolymer nanoparticles
Discipline: Nanoscience and Nanotechnology

INTRODUCTION

Many factors such as increasing environmental pollution, developing technology, pesticides used in food, smoking and alcohol drinking, ultraviolet rays cause people to be exposed to harmful effects. Environmental and psychological effects cause the formation of Free Radical (FR) in humans. With the radical increase, various illnesses increase and human health is adversely affected. For this purpose, consumption of natural foods and high antioxidant foods become important [1]. Antioxidants are chemicals that protect foodstuffs and the living organisms that consume them from the oxidative damage of free radical molecules such as nitrogen species and reactive oxygen. As antioxidants are the most important source of plant foods, antioxidants taken in the diet are often called phytochemical antioxidants. Antioxidants are substances that neutralize free radicals in living things, prevent cells from being affected by them, or make themselves renewable [2]. Pomegranate juice contains significant phenolic substances. Many studies have shown that pomegranate extracts have antimicrobial and antiviral activity.

Controlled release is the slow transfer of a substance / drug substance over time to the release medium after it has been placed in a trapping vehicle. This release can be carried out at various speeds with various mechanisms. It is an area of technology that has emerged and is developing with the basic advantages of controlled release due to the troublesome formation and economic difficulties of standard drug applications. Controlled release uses nanoparticles to remove adverse effects such as incorrect target site release or accumulation. Nanoparticles; matrix systems in which the active ingredients are dissolved, entrapped and / or adsorbed onto the surface of the particles, prepared using natural or synthetic polymers [3]. In addition, nanoparticles increase the stability of drugs / proteins or peptides. It can be easily sterilized and the loading capacity of the active substance is also high. In this respect, oral administration of the drug increases the release and bioavailability of the drug given in the form of nanoparticles [4]. Antioxidant substance encapsulation will be provided by the characterization of alginate and chitosan, which have many advantages in production applications and usage. The encapsulation; solid, liquid and gaseous components, enzymes, cells and other substances, microorganisms with a coating material based on proteins, carbohydrates or other substances [5]. Today more and more active food ingredients are used in new food products every day and methods are being sought to integrate and protect these ingredients in the products. In recent years, encapsulation

technology has been used to protect active lipophilic food components used in functional foods and antioxidants such as flavonoids, controlled release, prolong shelf life [6].

The use of biopolymers in drug release systems first started in the 1980s. Studies have shown that biopolymers can trap both hydrophilic and hydrophobic drugs and that there is no biocompatibility problem, and these properties have shown biopolymers to be one step ahead of synthetic polymers [7]. Alginate or alginic acid is a linear polysaccharide derived from the cell walls of some species of brown algae. Alginate has been reported to be non-toxic and biologically metabolized by oral route [8]. Alginate is a nontoxic, biodegradable and biocompatible substance [9]. Therefore, there are a wide range of uses in the field of encapsulation.

Studies have shown that CaCl2 is the most effective gelling calcium salt for alginate among various calcium salts [10]. Alginate can easily gel with calcium, a divalent cation. The resulting calcium alginate is used in many cell immobilization and encapsulation processes. Another feature of sodium alginate is that it can be used alone or in combination with other materials in some ocular delivery systems. From this feature, formation of chitosan / sodium alginate nanoparticles by gelling technique has been reported [11]. Chitosan is a cationic biopolymer that is most commonly found after cellulose in nature and widely used in drug release. The most prevalent form of chitosan is obtained from the kit, which is a waste of shells of living things such as α-chitosan crabs and shrimps.

In a more recent study, Rastogi et al. [12] examines the microspheres in which isoniazid (INH) release is extended and the sodium alginate produced by the modified emulsification method is used as a hydrophilic carrier. It has been determined that the surfaces of the microspheres are smooth and they have spherical shapes. The properties of the particles prolong the stay in the small intestine [12]. Again Sarmento et al. insulin molecule is trapped in chitosan / alginate nanoparticles. The nanoparticle system has been evaluated as a promising development in the oral use of insulin due to the preservation of the insulin structure and bioactivity [13]. In a study with antioxidant-induced lemon balm, calcium alginate hydrogels were encapsulated and, as a result, alginates were found to be suitable for encapsulation of phenolic materials such as antioxidants [14].

METHODOLOGY

Initially, studies were carried out to obtain empty nanoparticles by cross-linking of sodium alginate-chitosan in calcium chloride medium and to optimize them by changing ambient conditions. 0.037 g of sodium alginate was dissolved in 58.75 mL of distilled water at room temperature with constant stirring. 12.5 mL of calcium chloride solution (2.0 mg / mL) was added dropwise to the mixed sodium alginate with a syringe to give 1 drop per second. This step took 46 minutes. The solution was stirred for another 30 minutes at the same time. 1 mg of chitosan was dissolved in 12.5 mL of 1% acetic acid (v/v) solution with stirring for 20 minutes. The prepared chitosan solution was added to the sodium alginate at the rate of 1 drop / sec.this step took 55 minutes. The solution was sealed and left 1 night for stirring under darkness.

Three samples were prepared and labeled as Sample 1 (S1), Sample 2 (S2), Sample 3 (S3) respectively. 10 mL of each sample (S1, S2, S3) centrifuged three times at 2800 rpm for 40, 60 and 80 minutes, respectively. The supernatant remaining on the top was separated by pipette, the stack of nanoparticles at the bottom was spread to the petri dish for each sample and left to dry at 70°C for 4 days. Characterization of the P-NPs has done by using SEM, UV-Vis and FTIR. Size of the P-NPs that found via SEM images (Table 1.) showed that the synthesized biocompatible P-NPs might be suitable carrier for hydrophilic drugs.

Table 1. Parameter of nanoparticle processes

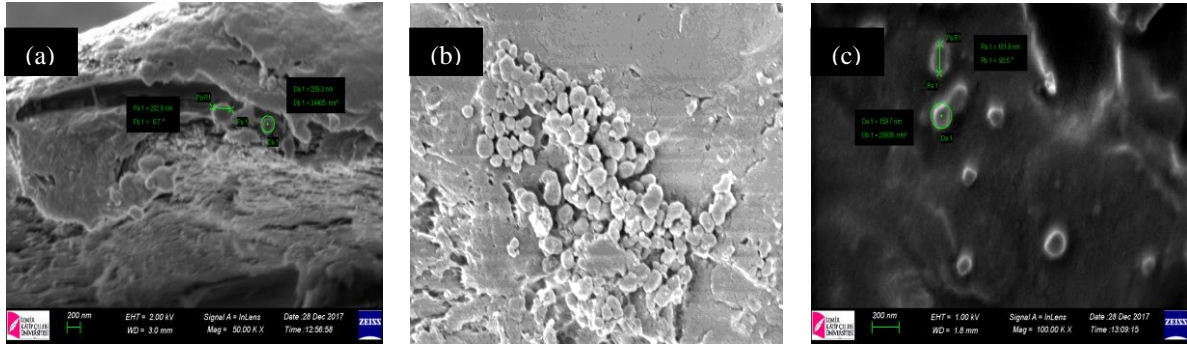| Sample Name	Centrifuged Time (minute)	Nanoparticle Size (nm)
S1	40	≈70
S2	60	≈90
S3	80	≈80

Figure 1. SEM images of nanoparticles of calcium alginate obtained by of calcium chloride cross-linker. (a) Sample 1 (S1), centrifuged at 2800 rpm for 40 minutes, (b) Sample 2 (S2), centrifuged at 2800 rpm for 60 minutes, (c) Sample 3 (S3), centrifuged at 2800 rpm for 80 minutes.
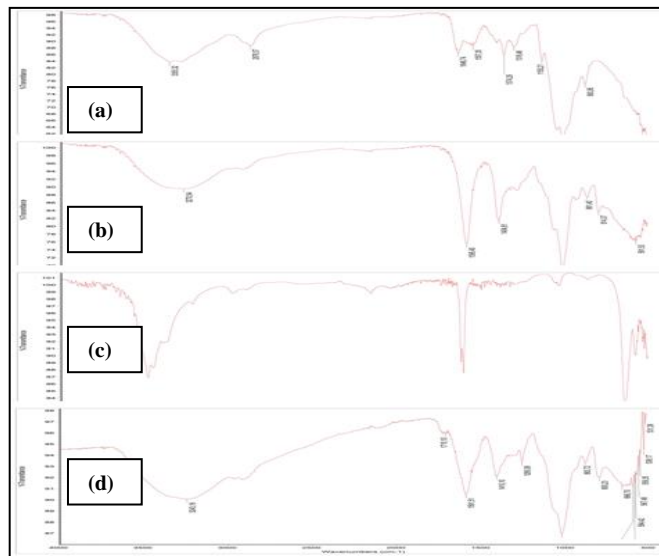

Figure 2. FTIR spectra of the polymers. (a) Chitosan; (b) Sodium alginate; (c) Calcium chloride; and (d) nanoparticles of sodium alginate and chitosan cross linker.

CONCLUSION

As a result of it has been found that different working conditions affect nanoparticle size and structures. Therefore, to optimize the condition, different parameters have been studied. Several experiments with different parameters and by changing the conditions were carried out. The most suitable nanoparticles structure and size range were obtained by centrifugation at 2800 rpm for 60 minutes according to the data obtained from SEM images in characterization studies. It has been understood that post-centrifugal flushing helps to get better quality images. The results have been compared with previous studies and reference work. A comparison of the results showed no noticeable difference between the reference work and our experiment. FTIR results are parallel to reference work and it clearly shows that the successful cross-linking has been done. The obtained polymeric nanoparticles were found to be ready for antioxidant loading. After the pomegranate juice is extracted, nanoparticle-loading studies will be carried out.

REFERENCES

[1] I..F. Benzie, Evolution of dietary antioxidants, Comparative Biochemistry and Physiology. Part A 136 (2003) 113-126.
[2] J. Lee, N. Koo, D.B. Min, Reactive oxygen species, aging, and antioxidative nutraceuticals, Comprehensive Reviews in Food Science and Food Safety 3 (2004) 21- 33.

[3] S. Derman, K. Kızılbey, Z.M. Akdeste, Polymeric nanoparticles, Sigma Journal of Engineering and Natural Sciences 31 (2013) 109-122.

[4] A. Kumari, S.K. Yadav, S.C. Yadav, Biodegradable polymeric nanoparticles based drug delivery systems, Colloids and Surfaces B: Biointerfaces 75 (2010) 1-18.

[5] A. Madene, M. Jacquot, J. Scher, S. Desobry, Flavour encapsulation and controlled release - a review, International Journal of Food Science and Technology 41 (2005) 1-21.

[6] S. Gouin, Microencapsulation: industrial appraisal of existing technologies and trends, Trends in Food Science and Technology 15 (2004) 330-347.

[7] V.V. Ranade and M. A. Hollinger, Drug Delivery Systems. CRC Press, Boca Raton, FL, 2004.

[8] M. Rinaudo, Main properties and current applications of some polysaccharides as biomaterials, Polymer International 57 (2008) 397-430.

[9] U. Cornelli, Antioxidant use in nutraceuticals, Clin Dermatol. 27 (2009) 175–94.

[10] I. Çakır, Fonksiyonel gıda bileşenleri ve probiyotiklerde mikroenkapsülasyon uygulamaları, 5. Gıda Mühendisliği Kongresi, Ankara 2007.

[11] X. Zhu, M. Su, S. Tang, L. Wang, X. Liang, F. Meng, Y. Hong, Z. Xu, Synthesis of thiolated chitosan and preparation nanoparticles with sodium alginate for ocular drug delivery, Molecular Vision 18 (2012) 1973-1982.

[12] R. Rastogi, Y., Sultana, M., Aqil, A., Ali, S., Kumar, Alginate microspheres of isoniazid for oral sustained drug delivery, International Journal of Pharmaceutics 334 (2007) 71-77.

[13] B. Sarmento, A. Ribeiro, F. Veiga, P. Sampaio, R. Neufeld, D. Ferreira, Alginate/chitosan nanoparticles are effective for oral insulin delivery, Pharmaceutical Research 24 (2007) 2198-2206.

[14] S. N. Soulari, H. Shekarchizade, M. Kadivar Encapsulation optimization of lemon balm antioxidants in calcium alginate hydrogels, Journal of Biomaterials Science, Polymer Edition 27 (2016) 1631-1644.

Production of Nanostructured Zinc Oxide Films on ITO/Glass Substrates through Hydrothermal Method

Irmak Tunç*, İzmir Katip Çelebi Univ., Dept. of Engineering Sciences, Çiğli Main Campus, Izmir, Turkey
Eyüp Yalçın, İzmir Katip Çelebi Univ., Dept. of Material Science and Engineering, Çiğli Main Campus, Izmir, Turkey
Mustafa Erol, Dokuz Eylül Univ., Dept. of Metallurgical and Materials Engineering, Tınaztepe Main Campus, Izmir, Turkey
Ahmet Aykaç, İzmir Katip Çelebi Univ., Dept. of Engineering Sciences, Çiğli Main Campus, Izmir, Turkey
Mustafa Can, İzmir Katip Çelebi Univ., Dept. of Engineering Sciences, Çiğli Main Campus, Izmir, Turkey
*Corresponding author: irmak.tunc@ikc.edu.tr

INTRODUCTION

ZnO has received broad attention because of its semiconductivity, large exciton binding energy, superior electrochemical stability, non-toxicity, suitability for doping, and low cost. Due to its electrical and optical properties it is intensively used for photonics, solar cells, piezoelectric devices, nano-generators, photovoltaic devices, strain sensors, biosensors, chemical sensing devices and photocatalysts [1, 2].

Production methods of ZnO on the substrates are hydrothermal method, electrodeposition, sol–gel method, laser ablation technique, chemical vapor deposition, electrospinning. Among these techniques hydrothermal method is a promising and practical technique [1].

Dye sensitized solar cells (DSSCs) have been intensively investigated as alternative candidates for the next generation photovoltaic cells due to their low cost and low environmental impact competed with conventional silicon based solar cells since they were first introduced by O'Regan and Grätzel in 1991. The structure of a typical DSSC consists of a photoanode containing with the wide bandgap semiconducting material TiO_2, a liquid electrolyte containing with I/I_3 redox couple and a platinum counter electrode. A photosensitizing dye, anchored to the surface of the wide bandgap semiconductor in the photoanode, absorbs light. Under illumination, the excited dye molecule releases photoelectrons and injects the electrons into the wide bandgap semiconductor. Therefore, an effective light harvest and a good electron transport in photoanode are necessary for obtaining high conversion efficiency of DSSCs. A schematic illustration is given in Figure 1 [3].
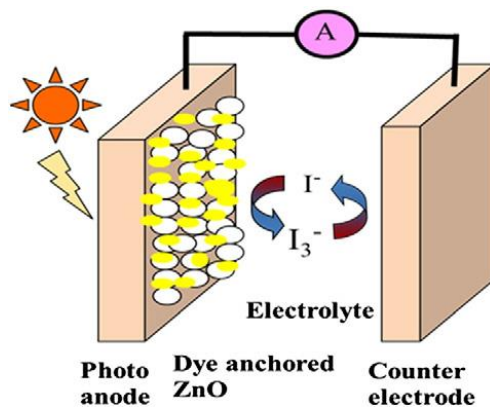

Figure 1. A schematic illustration

In this present work, production of nanostructured ZnO film have been performed on ITO coated glass substrate by hydrothermal method and characterized by X-ray diffraction (XRD) and scanning electron microscopy/energy-dispersive X-ray spectroscopy (SEM/EDS). It is also aimed to apply obtained structure on solar energy systems.

2nd International Students Science Congress
4-5 May 2018, Izmir - Turkey

İZMİR
KÂTİP ÇELEBİ
UNIVERSITY
2010

İZMİR
Uluslararası
Misafir
Öğrenci
Derneği
◆ IZMIR International Guest Student Association

MATERIALS

Throughout this study, the reagents and chemicals were used without further purification or process. Zinc acetate dehydrate from Sigma Aldrich (5970-45-6), Zinc nitrate hexahydrate form Acros (10196-18-6), Hexamethylene tetramine (HMTA) form Sigma Aldrich (100-97-0), NaOH from Sigma Aldrich (1310-73-2) and Ethanol from Sigma Aldrich (32221) were employed for the development of CF/ZnO nanostructures. In addition to solution preparation materials carbon fiber substrate supplied by Aksaca (12K A-42).

EXPERIMENTAL PROCEDURE

The ZnO films were growth on ITO by hydrothermal method. In order to provide growth of ZnO on ITO, a seeding layer coated on ITO using zinc acetate dihydrate solution. After that, to growth of ZnO film, ITO was dipped into Zinc nitrate hexahydrate and Hexamethylene-tetramine (HMTA) solution. Hydrothermal process was conducted in Teflon-lined stainless autoclave. The chemical composition, structure and morphology were characterized by X-ray diffraction (XRD) and scanning electron microscopy/energy-dispersive X-ray spectroscopy (SEM/EDS). In order to obtain the most stable and suitable sample, ZnO film production parameters will be investigated.

RESULTS AND DISCUSSION

Nanostructure and Morphology

Morphological structure of produced samples analyzed with Scanning Electron Microscope. It is seen that from Scanning Electron Microscopy images ZnO nanowires fabricated successfully. Generally, ZnO NWs stand almost vertical to the CFs (Figure 2). The length and thickness of ZnO nanowires measured by Image J software. The results are given in Table 1.
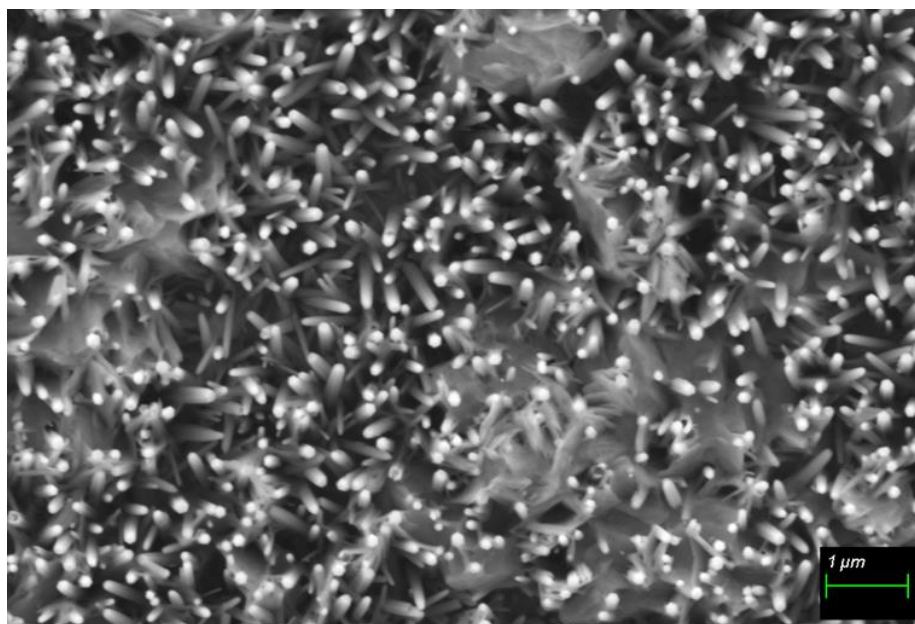

Figure 2. SEM images of ZnO NW-coated ITO/glass.

Table 1. The length and thickness of ZnO nanowires

Avr. length/nm	840±76
Max-Min length/nm	917-700
Avr. thickness /nm	78±29
Max-Min thickness/nm	147-32
Aspect ratio	10.7

Crystal Structure

In order to reveal the crystallographic structure of the ZnO/CF structures, XRD analyses was performed and patterns is given in Figure 3. According to XRD results, their elemental compositions appear to be similar. Search-match process demonstrates that structure composed of zincite phase that has hegzagonal crystal structure (common name: Chinese white) (JCPDS number: 00-036-1451).
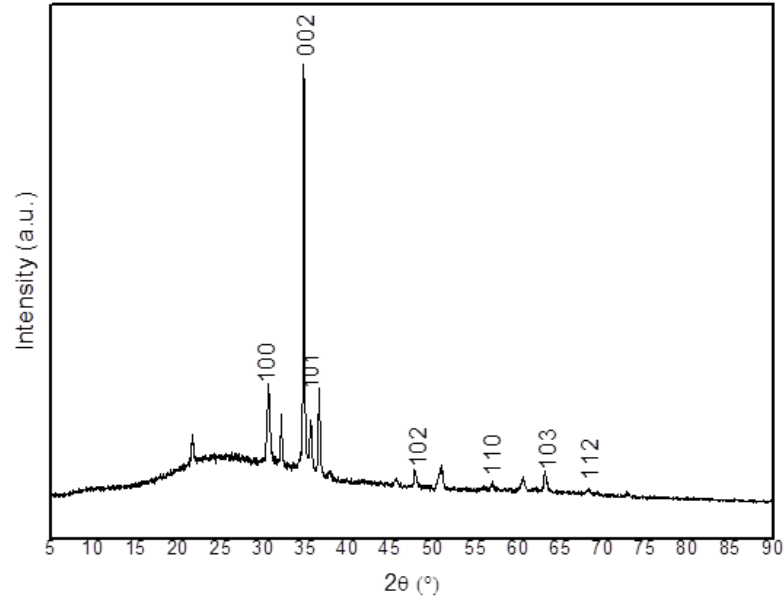

Figure 3. XRD patterns of ZnO NW-coated ITO/glass.

Optical Properties

In order to determine optical properties of ZnO/ITO glass structure Ultraviolet spectroscopy (UV) analyses was performed. The optical band gap can be calculated by the extrapolation method that is the tangent of the absorption curve to intercept the wavelength axis. The optical band gap was found using the formula given below [4, 5]. Eg is band gap and λa is the wavelength of the intercept. In Figure 4, UV result is given. Herein, the absorption on sets is approximately 350nm. The optical band gap was estimated so as to be 3.5 eV.

$$Eg(\text{eV}) = \frac{1240}{\lambda a}$$

CONCLUSION

The results shows that ZnO NWs deposited on ITO/glass by hydrothermal method successfully. SEM, XRD and UV spectroscopy analyses were performed. The length, thickness and aspect ratio were measured as 840±76 nm, 78±29 nm, 10.7 nm, respectively. The XRD results revealed that ZnO growth with hegzagonal zincite phase on ITO/ glass. Obtical band gap of structures were estimates as 3.5 eV. In future, we will apply obtained structure on solar energy systems.
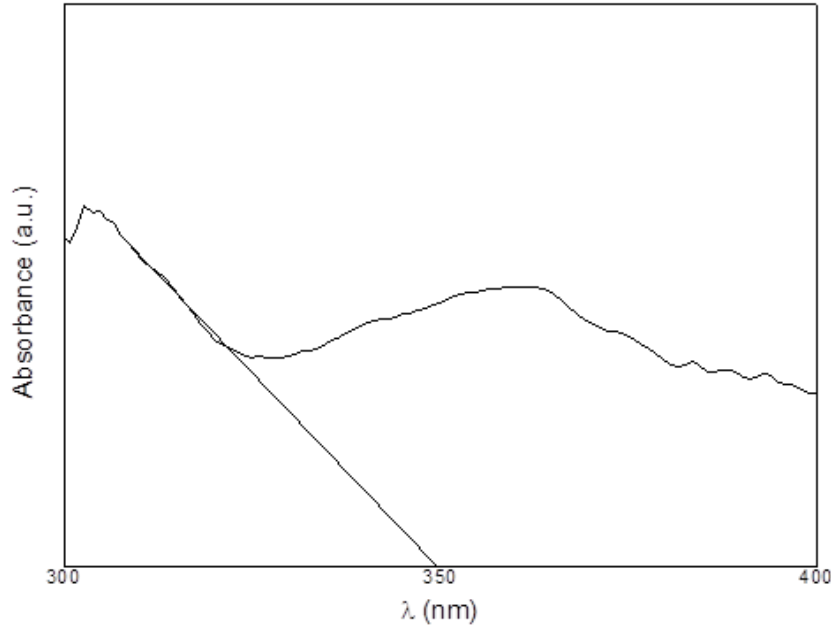
Figure 4. UV result of ZnO NW-coated ITO/glass.

REFERENCES

[1] Y.K. Kim, H.J. Seo, S. Kim, S.H. Hwang, H. Park, S.K. Lim, Effect of ZnO electrodeposited on carbon film and decorated with metal nanoparticles for solar hydrogen production, Journal of Materials Science & Technology 32 (2016) 1059-1065.

[2] Y. Zhang, ZnO Nanostructures: Fabrication and Applications. Nanoscience & Nanotechnology, The Royal Society of Chemistry (2017). doi: 10.1039/9781788010238-00001

[3] D. Sinha, D. De, A. Ayaz. Performance and stability analysis of curcumin dye as a photo sensitizer used in nanostructured ZnO based DSSC, Spectrochimica Acta Part A: Molecular and Biomolecular Spectroscopy 193 (2018) 467-474. https://doi.org/10.1016/j.saa.2017.12.058

[4] S. Demirci, B. Öztürk, S. Yildirim, F. Bakal , M. Erol , O. Sancakoğlu , R. Yigit , E. Celik , T. Batar, Synthesis and comparison of the photocatalytic activities of flame spray pyrolysis and sol–gel derived magnesium oxide nano-scale particles, Materials Science in Semiconductor Processing 34 (2015) 154–161. http://dx.doi.org/10.1016/j.mssp.2015.02.029

[5] H. Xiao, W. Zhang, Y. Wei, L. Chen, Carbon/ZnO nanorods composites templated by TEMPO-oxidized cellulose and photocatalytic activity for dye degradation, Cellulose 25 (2018) 1809-1819.

2nd International Students Science Congress
4-5 May 2018, Izmir - Turkey

İZMİR KÂTİP ÇELEBİ UNIVERSITY
2010

İZMİR Uluslararası Misafir Öğrenci Derneği
◆IZMIR International Guest Student Association

Calculating the Efficiency of Silicon Solar Cell

Ala Jehad, Ibrahim Hamammu
Physics Department, Dokuz Eylul University, Izmir- Turkey
Corresponding author: alasamsom@gmail.com

Abstract

The aim of this paper is to understand how the solar cell works and how the performance of the cell can be analyzed in terms of basic parameters. The single junction crystalline silicon solar cell with (np) type has been studied with analytical method, for three regions of solar cell, which are emitter, base and space charge region (SCR) region. By solving solar cell's equations: Poisson's equation, current density equations, and continuity equations for both types of charge carriers, the results were obtained for each of the current contribution for parts of the cell, internal quantum efficiency, internal spectral response, and the characteristic I-V curve of cell. While I-V curve shows the electrical characteristics of a solar cell, by determining the solar cell's output performance and solar efficiency, the spectral response and quantum efficiency curves show how the cell react with the light spectrum. From I-V curve the efficiency of the cell is proportional to the value of the three main photovoltaic parameters: short circuit current I_{sc}, open circuit voltage V_{oc}, fill factor FF and efficiency η have been determined. The result shows that the base component has the main contributing to the total current in almost all wavelengths except in the shorter wavelengths, where the emitter layer contribution dominates. The efficiency of the cell obtained to be 13%.

Keywords: solar cell, silicon, I-V curve, quantum efficiency
Discipline: Physics

INTRODUCTION

With the increasing consumption of non-renewable energy sources and their adverse effect to the environment, the search for renewable energy sources must be carried out to meet the increased demand for energy.

Sun is one of the most important sources, where its illuminates our planet by energy which is 8000 times more than the current rate of global consumption of energy [1]. One of the solar energy conversion technologies is 'Photovoltaic Technique'. This technique directly converts the sunlight into electricity using a unique device known as solar cell.

The mono-junction silicon solar cell is formed by a very thin layer n-type region is called the emitter as a front surface, and a thick layer and less doped p-type region is called the base as a back surface (see Figure 1). When n-type and p-type put together, the depletion region formed, which is empty form free carriers [2].
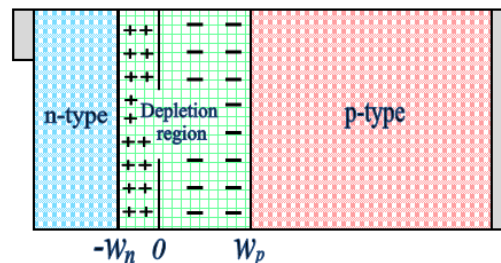

Figure 1. Simple structure of solar cell

When sunlight illuminates solar cells, the electron-hole pairs generates inside the cell. Electric field at the pn junction works to separate the electrons to n-type and the holes to the p-type. Then the front grid contacts work to pull electrons to external circuit to dissipated their energy, then come back to the base region to recombine again with holes, waiting for another photon from the sun to generate new pairs.

THEORY

As solar cell is semiconductor device, so it is underlying to semiconductor equations. There are five non-linear differential equations [2]. These equations has been solved analytically by using suitable boundary condition [3]. The calculations involved the light generated current for three parts of cell, dark current, internal quantum efficiency, internal spectral response, and I-V curve respectively as following:

1) *Light generated current density in emitter, base and depletion region*

$$J_E(\lambda) = \frac{q\alpha\phi_o(1-R)L_p}{(\alpha L_p)^2 - 1} \times$$

$$\left[-\alpha L_p e^{-\alpha w_e} + \frac{S_e + \dfrac{L_p}{D_p} + \beta L_p - e^{-\alpha w_e}\left(S_e \dfrac{L_p}{D_p}\cosh\dfrac{w_e}{L_p} + \sinh\dfrac{w_e}{L_p}\right)}{\cosh\dfrac{w_e}{L_p} + S_e \dfrac{L_p}{D_p}\sinh\dfrac{w_e}{L_p}} \right] \qquad (1)$$

$$J_B(\lambda) = \frac{q\alpha\phi_o'(1-r)L_n}{(\alpha L_n)^2 - 1} \times$$

$$\left[-\alpha L_n - \frac{S_b + \dfrac{L_n}{D_n} + \left(\cosh\dfrac{w_b}{L_n} - e^{-\alpha w_b}\right) + \sinh\dfrac{w_b}{L_n} + \alpha L_n e^{-\alpha w_b}}{\cosh\dfrac{w_b}{L_n} + S_b \dfrac{L_n}{D_n}\sinh\dfrac{w_b}{L_n}} \right] \qquad (2)$$

$$I_{SCR}(\lambda) = qF(1-R)\exp(-\alpha xj)(1 - \exp(-\alpha w_D)) \qquad (3)$$

2) *Dark current density in emitter and base*

$$J_{darkE} = q\frac{n_i^2 D_p}{N_D L_p}\left[\frac{S_e \dfrac{L_p}{D_p}\cosh\dfrac{w_e}{L_p} + \sinh\dfrac{w_e}{L_p}}{S_e \dfrac{L_p}{D_p}\sinh\dfrac{w_e}{L_p} + \cosh\dfrac{w_e}{L_p}} \right]\left[e^{\frac{V}{V_T}} - 1 \right] \qquad (4)$$

$$J_{darkB} = q\frac{n_i^2 D_n}{N_A L_n}\left[\frac{S_b \dfrac{L_n}{D_n}\cosh\dfrac{w_b}{L_n} + \sinh\dfrac{w_b}{L_n}}{S_b \dfrac{L_n}{D_n}\sinh\dfrac{w_b}{L_n} + \cosh\dfrac{w_b}{L_n}} \right]\left[e^{\frac{V}{V_T}} - 1 \right] \qquad (5)$$

3) *Total current density*

$$J = J_L - J_{dark} \qquad (6)$$

4) *Internal Quantum Efficiency (IQE)*

$$IQE = \frac{J_L}{q\varphi_o(1-R)} \qquad (7)$$

5) *Internal Spectral Response (ISR)*

$$ISR = \frac{J_L}{F(1-R)} \qquad (8)$$

The cell parameters chosen for the simulation for the present model are summarized in Table 1.

Table 1. Parameters used in the simulation

Parameter		Value	Unit
n_i	Intrinsic carrier concentration	1.45×10^{10}	cm^{-3}
N_D	Donor carrier concentration	1×10^{16}	cm^{-3}
N_A	Acceptor carrier concentration	1×10^{16}	cm^{-3}
L_n	Diffusion length in base	162×10^{-4}	Cm
L_p	Diffusion length in emitter	0.43×10^{-4}	cm
D_n	Diffusion coefficient in base	36.33	cm^2/s
D_p	Diffusion coefficient in emitter	3.4	cm^2/s
S_e	Surface recombination velocity in emitter	2×10^5	cm/s
S_b	Surface recombination velocity in base	1×10^3	cm/s
w_e	Emitter thickness	0.3×10^{-4}	cm
w_b	Base thickness	300×10^{-4}	cm
α	Absorption coefficient		cm^{-1}
φ_0	Spectral photon flux in emitter	From database of Silicon [4,5]	#/cm^{2}μms
φ'_0	Spectral photon flux in base		#/cm^{2}μms
R	Reflectivity of Silicon		___

RESULTS

Cell that has been studied in this research, was np-type mono-crystalline single junction solar cell, with equal doping concentration, where the donor concentration is equal to the acceptor concentration $N_D = N_A = 10^{16}$ cm^{-3}.
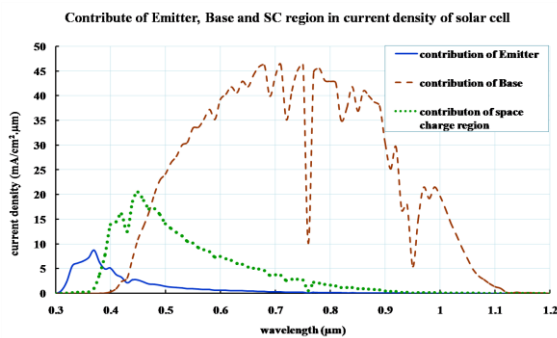

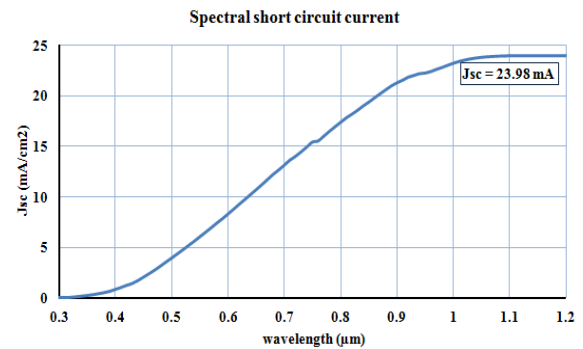Figure 2. Contribution parts of cell in light generated current.

Figure 3. Spectral short circuit current density.

Figure 2 shows the contribution of emitter, base and space charge regions in generated current density. The base component is the main component contributing to the total current in almost all wavelengths except in the shorter wavelengths, where the emitter layer contribution dominates. The contribution of space charge density is medium between emitter and base regions.

Figure 3 shows the spectral current density for generated light and dark current where the current maximum value reached to 24 mA.

2ⁿᵈ International Students Science Congress
4-5 May 2018, Izmir - Turkey

İZMİR
KÂTİP ÇELEBİ
UNIVERSITY
2010

İZMİR
Uluslararası
Misafir
Öğrenci
Derneği
◆ İZMİR International Guest Student Association

Figure 4 shows the Internal Quantum Efficiency (IQE) curve. The internal quantum efficiency has a maximum of around 98% at 0.7µm of wavelength and fades away from the maximum value at the two ends of the cell; this reduction is because of the surface recombination velocity at front and back surface of cell, and due to reach to the band-gap wavelength of silicon.
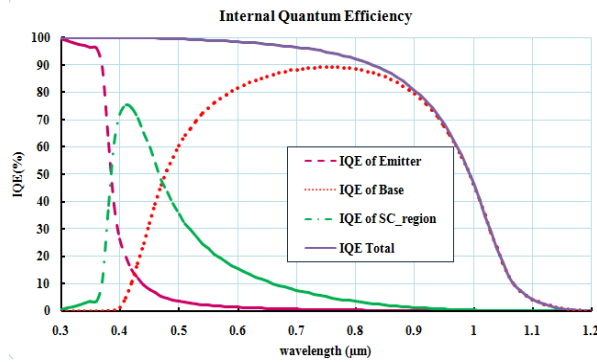
Figure 4. Internal Quantum Efficiency
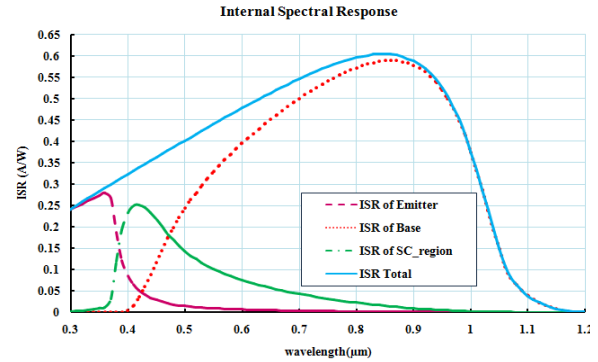
Figure 5. Internal Spectral Response

Figure 5 shows the internal spectral response, has a maximum of around 0.62A/W at 0.8µm where at short wavelengths are absorbed at the beginning of the spectrum thus, the response spectrum is reduced. At medium wavelengths, the cell is act as the ideal cell and at long wavelengths, the spectral response tends to zero.

Figure 6 shows the I-V characteristic curve of solar cell where the basic parameters of solar cell are illustrated in Table 2.

Figure 6. I-V curve of solar cell

Table 2. Basic parameters of cell

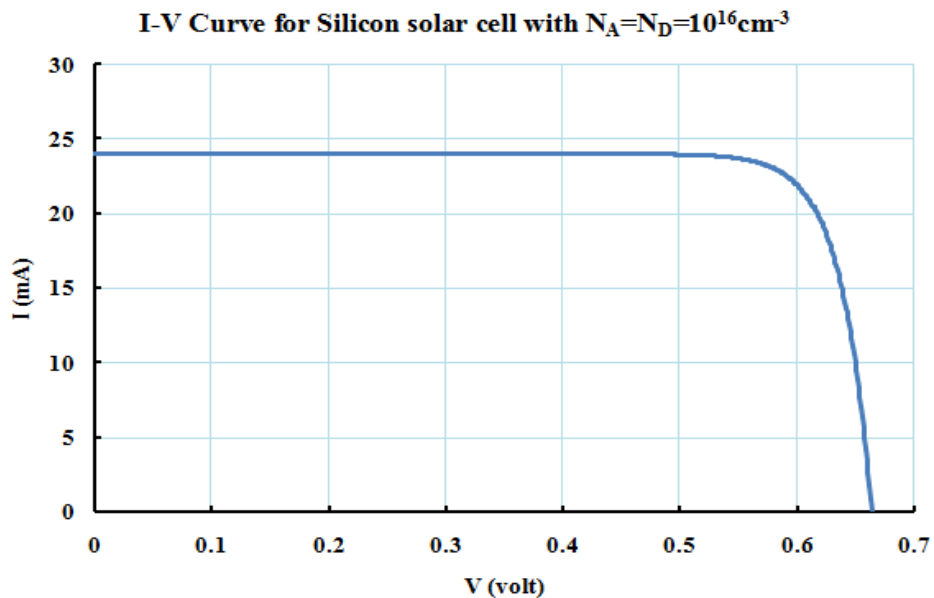|	
Area of cell = 1cm^2	
Power point at 0.58 volt	
V_{mp} (volt)	0.58
I_{mp} (mA)	23.10
V_{oc} (volt)	0.66
I_{sc} (mA)	24.00
FF = $(V_{mp}*I_{mp})/(V_{oc}*I_{sc})$	84.5
$P_{out} = V_{mp}*I_{mp}$	0.13
P_{in} for 1cm^2	0.01
$\eta = (P_{out}/P_{in})*100$ %	13.5 %

CONCLUSION

In this paper, we analyzed the contribution of each part of cell in electrical power cell. This would contribute to improve the design and performance of the solar cell. The depending of solar cell current on doping concentration depends on other variables, which are a thickness of active region, positions of carriers, diffusion coefficients and carrier lifetime of solar cell. With a deeper study of what is happening inside the cell and how to get the largest possible number of charge carriers would raise the efficiency of solar cell.

REFERENCES

[1] R. D. Rugescu, Solar Energy, Intech Publications (2010) pp. 432.
[2] A. Luque, S. Hegedus, Handbook of Photovoltaic Science and Engineering, John Wiley and Sons Ltd. (2003) pp. 1164.
[3] L. Castaner, S. Silvestre, Modelling Photovoltaic Systems Using PSpice, John Wiley and Sons Ltd. (2002) pp. 376.
[4] Database of spectral AM1.5G, from ASTM Standard G173-03. Retrieved from http://www.pveducation.org/pvcdrom/appendicies/standard-solar-spectra
[5] Database of optical properties of Silicon. Retrieved from
http://www.pveducation.org/pvcdrom/appendicies/optical-properties-of-silicon

Consideration of Urban Regeneration as an Approach in Slum Transformation in Ghana[1]

Abubakar Sadiq Abass*, Mehmet Küçükmehmetoğlu
Gebze Technical University, Dept. of City and Regional Planning, Gebze, 41400 Kocaeli, Turkey
*Corresponding author: s.abass@gtu.edu.tr

INTRODUCTION

The slum concept is one of the most intensely debated concepts in the academic spectrum. Its uniqueness with changing geographic location contributes to the difficulty in arriving at a universally accepted definition. Different local connotations are used to refer to what can be said to imply 'slum'. The terms shantytowns [1], ghettos [2] and redline district among others are mostly used in North America whereas the term, decaying inner-city is often found in European literature [3]. In South America, the terms, Favela and Corticos are used in the case of Brazil [4] for example. Despite efforts to distinguish between the traditional slum from the gecekondu in Turkey, Doğan [5] finally underscored the reality that there was no significant difference between slum and the gecekondu in Turkey.

Understandably, 'slum' does not only imply a human settlement deprived of any of the five shelter indicators proposed by the United Nations Human Settlement Programme (UN-Habitat) but in addition to this physical indication is the social profile of the dwellers. The five-shelter deprivation as outlined by the UN-Habitat [6] include; adequate access to safe water; adequate access to sanitation and infrastructure; structural quality of housing; sufficient living space; and secure residential status.

In Ghana, despite the existence of slums, there has not been a formal definition of the term [7]. However, the Ghana Statistical Services (GSS) indicates that slums are generally defined as settlements that fall below a certain standard 'necessary for human development'. In this work, the definition provided by the UN-Habitat (2007) [6] is adopted as the working definition despite its shortcomings as identified by other scholars. Ashaiman is selected as the study area mainly because it is made up of the three main slum types identified in Ghana [8] which makes it possible to investigate all at once.

Slums in Ghana were said to be the results of discriminatory colonial planning policies [9, 10], as well as the inadequate investments by governments in urban areas [11]. Over the years, various policies were implemented to transform the Ghanaian slum communities. Interventions such as clearance were implemented in slums like Old Fadama; demolition and resettlement; and regularisation across the Tema Acquisition Area (TAA) which also includes Ashaiman. It has been witnessed however that, these policies have failed to deal with the slum problem as evident in its continued existence. Urban regeneration having been implemented in countries such as Turkey has been seen to yield the desire result of transforming slum communities by reducing the slum prevalence from about 30% in the 1990's [12] to about 11% in 2014 [13].

Roberts (2000) [14] defined urban regeneration as "a comprehensive and integrated vision and action which leads to the resolution of urban problems and which seeks to bring about a lasting improvement in the economic, physical, social and environmental conditions of an area that has been subject to change". This means that any urban regeneration project must endeavour to embrace each of economic, socio-cultural as well as the physical/environmental dimensions of the community it is implemented. Urban regeneration therefore comes in handy in the solution of wide array of urban problems which include slum. The Ashaiman slum was studied with the aim of determining the potential acceptability (or otherwise) of this policy in Ghana.

---

[1] This work is culled from the master's degree thesis of the main author, which was also prepared on the same topic.

METHODOLOGY

The main data collection method employed here was the systematic random sampling method. Household heads within the study area were systematically sampled and questionnaire administered such that each 30th household head formed part of the sample frame. In the end, a total of 322 respondents were reached. This count was carried out systematically across the 6 blocks within the study area as indicated below:

Figure 1. Study area, Ashaiman, Ghana
(Source: Google Earth; markings by authors)

Another non-random sampling method, the purposive sampling method was also employed in the selection of professionals within the built environment in Ghana. 25 professionals were reached in the process. This was done to elicit some expert views concerning the subject matter and its applicability in Ghana.

The data collection tool used in this work was the questionnaire as previously indicated. Two sets of questionnaires were designed; one for the resident household heads of the study area and the other issued to professionals within the built environment in Ghana. Questions within the questionnaires were obtained from the literature related to the topic. The questions were of two main categories, viz; objective questions comprising the observed characteristics of the study area and subjective questions which also comprised views of respondents on relevant aspects of the study. Descriptive statistics were then extracted from the collected data. The differences noted in the descriptive statistics were tested using the Chi-square and ANOVA to see if any significant relationships exist between selected variables relevant to this paper. Thus, for the purpose of this paper, only selected variables were analysed and presented in the next section.

RESULTS

For a patriarchal society, household heads in Ghana are predominantly males. This work also revealed a similar trend where female household heads constituted only about 7% (22) of the entire sample. These female household heads were usually from households with absentee male spouses due to divorce (7), separation (4), death (4), spinsterhood (5) or spouse currently abroad or in another city (2). Majority (89%) of respondents are migrants from other parts of the country or from other West African countries (ECOWAS) as shown on the map below:
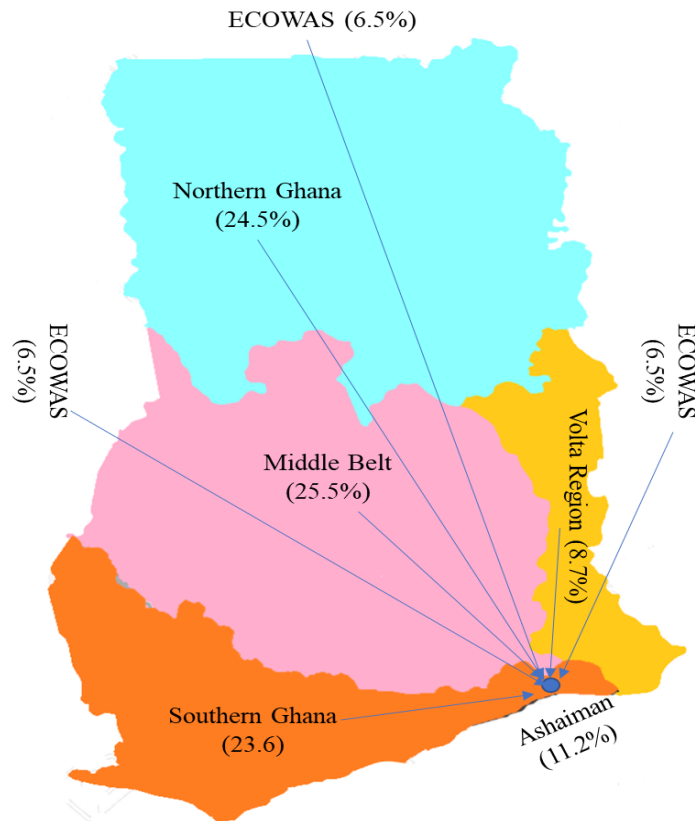
Figure 2. Map of Ghana[1] showing the origins of respondents

The dominant economic activities are within the informal sector (77.1%) which is in line with other slum studies across the world [see, 15,16] as well as within Ghana [see, 17,18,19]. Majority (58.4%) of respondents work outside of Ashaiman in Tema (52.5%) and Accra (5.9%) and this was found to significantly affect the income levels of respondents as those working in Accra were found to earn higher monthly incomes on average than those working in either Ashaiman or Tema as shown on Table 1.

Table 1. Descriptive: Monthly income of household heads

Place	N	Mean	Std. Deviation	Std. Error	95% Confidence Interval for Mean		Minimum	Maximum
					Lower Bound	Upper Bound		
Accra	19	2,663.16	1853.289	425.174	1769.90	3556.41	700	7000
Ashaiman	127	1,728.35	1795.050	159.285	1413.13	2043.57	200	15000
Tema	169	2,281.95	2001.573	153.967	1977.99	2585.91	200	10000
Total	315	2,081.75	1930.263	108.758	1867.76	2295.73	200	15000

ANOVA: Monthly income of household heads

	Sum of Squares	df	Mean Square	F	Sig.
Between Groups	2.906E7	2	1.453E7	3.973	0.020
Within Groups	1.141E9	312	3,656,665.445		
Total	1.170E9	314			

---

[1] This map does not show the 10 administrative regions of Ghana. Some regions were merged in this map to give simplified geographic places of origin of respondents.

However, in general, with an average monthly household income of GH¢ 3600, Ashaiman, unlike the slums of Ivory Coast [20] cannot be described as a place of 'squalor and wanton poverty'.

Table 2. Monthly income (in GH¢) statistics

	Monthly Income of Household Head	Total Monthly Income of Household
Valid	322	322
Missing	0	0
Mean	2,037	3,614
Median	1,500	2,300
Mode	800	1,500
Std. Deviation	1,933.2	3,953.5
Minimum	0	0
Maximum	15,000	35,600

For a compound-house dominated community, majority of respondents were tenants (68%) with landlords constituting only about 19%. This again does not contradict the general home tenure arrangement across the country (GSS, 2014). Almost half (49.1%) of households live in single rooms. Owing to reasons such as; weak/old buildings, insufficient living space, pollution/filth as well as lack of basic facilities within the housing units and across the community in general, overwhelming majority (90%) expressed dissatisfaction with living in the community.

URBAN REGENERATION IN ASHAIMAN

Over 90% of household heads indicated their support for a possible urban regeneration (SUR) in Ashaiman. Within this composite figure include groups of different kinds. In determining which groups within the community are more likely to support urban regeneration in Ashaiman, various chi-square tests were done. It was thus revealed that, migrants were more likely to support UR than indigenes after a significant relationship (p=.001) between place of origin and support for UR was determined (see, Table 3). The reason for this was found to be the hope by migrants to become homeowners under UR in Ashaiman whereas natives were seen to harbour the fear of losing their community to migrants under UR.

Table 3. Relationship between SUR and the birth places of respondents

Birth Place of Household		I will Support Urban Regeneration in Ashaiman			Total
		I am indifferent / I (strongly) disagree	I agree	I strongly agree	
Ashaiman	Count	10	9	17	36
	Expected Count	2.9	5.6	27.5	36.0
	% within Birth Place of Respondents	27.8%	25.0%	47.2%	100.0%
	% within I will Support Urban Regeneration in Ashaiman	38.5%	18.0%	6.9%	11.2%
	% of Total	3.1%	2.8%	5.3%	11.2%
Outside Ashaiman	Count	16	41	229	286
	Expected Count	23.1	44.4	218.5	286.0
	% within Birth Place of Respondents	5.6%	14.3%	80.1%	100.0%
	% within I will Support Urban Regeneration in Ashaiman	61.5%	82.0%	93.1%	88.8%
	% of Total	5.0%	12.7%	71.1%	88.8%
Total	Count	26	50	246	322
	Expected Count	26.0	50.0	246.0	322.0
	% within Birth Place of Respondents	8.1%	15.5%	76.4%	100.0%
	% within I will Support Urban Regeneration in Ashaiman	100.0%	100.0%	100.0%	100.0%
	% of Total	8.1%	15.5%	76.4%	100.0%

Chi-square value: 26.345, df: 2, *p* value: .001
1 cell (16.7%) has expected count less than 5. The minimum expected count is 2.91

Also, those resident within locations that have weaker or poorly constructed buildings were more in support of UR than those living in relatively durable houses. This is because there was a significant [χ^2(4, N=322)=44.021, p=0.001) relationship between residential blocks and construction materials. Weaker building materials such as wood and mud were mostly concentrated within the EF Block while sandcrete block buildings were found to concentrate more within the AB and CD Blocks. Consequently, residents within EF Blocks were found to be more likely to support UR than those from the other blocks. A statistically significant relationship (p=0.006) was found between residential blocks and SUR as presented below.

Table 4. Relationship between SUR in Ashaiman and locality of respondents

Location of Buildings		I will Support Urban Regeneration in Ashaiman			
		I am indifferent / I (strongly) disagree	I agree	I strongly agree	Total
AB Block	Count	11	23	67	101
	Expected Count	8.2	15.7	77.2	101.0
	% within Location of Buildings	10.9%	22.8%	66.3%	100.0%
	% within I will Support Urban Regeneration in Ashaiman	42.3%	46.0%	27.2%	31.4%
	% of Total	3.4%	7.1%	20.8%	31.4%
CD Block	Count	6	19	76	101
	Expected Count	8.2	15.7	77.2	101.0
	% within Location of Buildings	5.9%	18.8%	75.2%	100.0%
	% within I will Support Urban Regeneration in Ashaiman	23.1%	38.0%	30.9%	31.4%
	% of Total	1.9%	5.9%	23.6%	31.4%
EF Block	Count	9	8	103	120
	Expected Count	9.7	18.6	91.7	120.0
	% within Location of Buildings	7.5%	6.7%	85.8%	100.0%
	% within I will Support Urban Regeneration in Ashaiman	34.6%	16.0%	41.9%	37.3%
	% of Total	2.8%	2.5%	32.0%	37.3%
Total	Count	26	50	246	322
	Expected Count	26.0	50.0	246.0	322,0
	% within Location of Buildings	8.1%	15.5%	76.4%	100.0%
	% within I will Support Urban Regeneration in Ashaiman	100.0%	100.0%	100.0%	100.0%
	% of Total	8.1%	15.5%	76.4%	100.0%

Chi-square value: 14.548, df: 4, p value: .006
0 cells (0.0%) have expected count less than 5. The minimum expected count is 8.16

In terms of income level, those earning not more than GH¢ 1500 a month showed more support than those earning above this amount. The reason could be the support those earning below the stated amount hope to get from both government and other family members.

FUNDING UR IN GHANA

Of the 25 professionals who took part in this work which comprise planners, engineers, land economists among others working in both the public and private sector, over 90% also showed strong support for any possible UR in Ghana. They viewed UR 'as the way to go' in dealing with slum in Ghana. They were also of the view that a special fund which may be called the urban regeneration fund (URF) be created to fund this policy. Also, a strong partnership between the public and private sector be created in order to ensure sufficient funding for this policy. Foreign private entities may also be involved in this venture. However, the involvement of foreign governments and international funding agencies were widely discouraged by experts who took part in this survey.

Table 5. Relationship between SUR and the monthly income of respondents

Monthly Income of Respondents (GH¢)		I am indifferent / I (strongly) disagree	I agree	I strongly agree	Total
		I will Support Urban Regeneration in Ashaiman			
≤ 1500	Count	21	36	130	187
	Expected Count	15.1	29.0	142.9	187.0
	% within Monthly Income of Respondents	11.2%	19.3%	69.5%	100.0%
	% within I will Support Urban Regeneration in Ashaiman	80.8%	72.0%	52.8%	58.1%
	% of Total	6.5%	11.2%	40.4%	58.1%
≥ 1501	Count	5	14	116	135
	Expected Count	10.9	21.0	103.1	135.0
	% within Monthly Income of Respondents	3.7%	10.4%	85.9%	100.0%
	% within I will Support Urban Regeneration in Ashaiman	19.2%	28.0%	47.2%	41.9%
	% of Total	1.6%	4.3%	36.0%	41.9%
Total	Count	26	50	246	322
	Expected Count	26.0	50.0	246.0	322.0
	% within Monthly Income of Respondents	8.1%	15.5%	76.4%	100.0%
	% within I will Support Urban Regeneration in Ashaiman	100.0%	100.0%	100.0%	100.0%
	% of Total	8.1%	15.5%	76.4%	100.0%

Chi-square value: 12.245, df: 2, p value: .002
0 cells (0.0%) have expected count less than 5. The minimum expected count is 10.9

CONCLUSION

With majority of respondents in support of a possible urban regeneration in Ashaiman, it provides an opportunity to implement this policy in the area. Despite this huge support, any such project in Ashaiman must involve the participation of all relevant stakeholders including the residents themselves. It has been demonstrated in this work that, contrary to popular views about the residents of slum communities especially in Ashaiman, income levels of residents are not low. Despite this, it is suggested that any URP taking place in Ashaiman be focused more on rental units than on sales because majority (72%) of households earn over GH¢ 1,500.00 (US$ 330.00)[1] a month and so affordable rental units will enable them to independently rent without any support. Special subsidies should be made available to those who earn less than this amount to ensure that gentrification is controlled. With predominantly one storey buildings spread across the community coupled with the willingness of respondents to live in medium to high-rise buildings, this is again an opportunity to create more housing units while at the same time providing enough space for other social amenities in the community. Having observed that that majority of the residents ply their trades in either Tema or Ashaiman, any urban regeneration project in Ashaiman must consider and provide avenues for residents to continue their occupations within these places. It must not lead to job losses but on the contrary, it must enhance job creation opportunities.

It is also recognised that this work, just like any other research constrained by time and material resources did not cover all aspects of urban regeneration. It is therefore suggested that efforts be considered in exploring areas that this work could not capture. These include among other topics relating to; funding of UR in developing nations, roles of UR in city branding, roles of UR in solving housing deficits (in developing nations) and the financial viability of UR from the private sector perspective.

REFERENCES

[1] L. Goff, *Shantytown, USA: Forgotten Landscapes of the Working Poor*. Harvard University Press. (2016) Cambridge Massachusetts, USA

[2] M. Cross, The Ghetto and the underclass, Journal of Ethnic and Migration Studies 17 (1990) 141-149 DOI: 10.1080/1369183X.1990.9976229

[3] H. Carter, From Slums to Slums in Three Generations; Housing Policy and the Political Economy of the Welfare State, 1945-2005 (Number 98) [Discussion Papers in Economic and Social History] (2012) University of Oxford, UK

[4] G. O'hare, M. Barke, The Favelas of Rio de Janeiro: A Temporal and Spatial Analysis, Geojournal 56 (2003) 225-240

[5] M.C. Doğan, Türkiye'de Gecekondu Meselesi ve Ümraniye Mustafa Paşa Gecekondu Bölgelerinde Bir Saha Araştırması (Doctoral Dissertation). (1990). Retrieved from the Turkish Board of Higher Education (YÖK) Dissertations and Theses database. (8427)

[6] UN-Habitat (2007). *State of the World Cities 2006/7: The Millennium Development Goals and Urban Sustainability: 30 Years of Shaping the Habitat Agenda*. Retrieved from https://unhabitat.org/books/state-of-the-worlds-cities-20062007/

[7] GSS. (2014). *2010 Population and Housing Census District Analytical Report – Tema Metropolitan*. Retrieved from
http://www.statsghana.gov.gh/docfiles/2010_District_Report/Greater%20Accra/Tema%20Metro.pdf

[8] J. W. Paller, Informal networks and access to power to obtain housing in urban slums in Ghana. Indiana University Press (2015) International African Bibliography Online.

[9] K.K. Adarkwa, The changing face of Ghanaian towns. African Review of Economics and Finance, 4 (2012) 1-29.

[10] P.B. Cobbinah, R. Niminga-Beka, Urbanisation in Ghana: Residential land use under siege in Kumasi central, Cities 60 (2017) 388-401.

[11] S. Fox, The political economy of slums: Theory and evidence from Sub-Saharan Africa, World Development 54 (2014) 191-203.

---

[1] A rate of GH¢ 4.5 to a USD was used because it was the highest quote during the month of March 2018 (see, https://currencies.zone/historic/us-dollar/ghanian-cedi/march-2018) during which time the field survey for this work was completed.

[12] B. Uzun, M. Cete, H.M. Palancıoğlu, Legalizing and upgrading illegal settlements in Turkey. Habitat International 34 (2010) 204-209. doi: 10.1016/j.habitatint.2009.09.004

[13] UNStat (2014). *Slum population as percentage of urban, percentage*. United Nations' MDG's. Retrieved from https://mdgs.un.org/unsd/mdg/SeriesDetail.aspx?srid=710

[14] P. Roberts, (2000). The Evolution, Definition and Purpose of Urban Regeneration. In: Roberts P. & Sykes, H. (eds.) *Urban Regeneration: A Handbook. London*: SAGE.

[15] T. Erman, Squatter (gecekondu) housing versus apartment housing: Turkish rural-to-urban migrant residents' perspectives Habitat International 21 (1997) 91-106

[16] T. Şenyapılı, (1998). Gecekondu Olgusuna Dönemsel Yaklaşımlar. In A. Eraydın (Ed.), *Değişen Mekân: Mekânsal Süreçlere İlişkin Tartışma ve Araştırmalara Toplu Bakış: 1923 – 2003* (pp. 84-122). Ankara, Turkey: Dost Kitabevi Publications.

[17] G. Razzu, Urban redevelopment, cultural heritage, poverty and redistribution: the case of Old Accra and Adawso House, Habitat International 29 (2005) 399-419. doi:10.1016/j.habitatint.2003.12.002

[18] K. Adubofour, K. Obiri-Danso, C. Quansah, Sanitation survey of two urban slum Muslim communities in the Kumasi metropolis, Ghana, Environment and Urbanization 25 (2012) 189-207 doi: 10.1177/0956247812468255

[19] F.K. Aseye, M. Opoku, Agyeman-Duah, (2015). Potential of slum tourism in Urban Ghana: A case study of Old Fadama (Sodom and Gomorra) slum in Accra, Journal of Social and Development Sciences 6 (2015) 39-45.

[20] UN-Habitat (2003). *The Challenge of Slums: Global Report on Human Settlements 2003*, Earthscan Publications, London and Sterling, VA.

The Urban Gap between the Inner City and its Districts in Algeria: the Case of Batna Province

Nağme Ebru Karabage, Yasar University, Dept. of Interior Architecture, İzmir, Türkiye
Nadjla Fellahi*, Izmir Institute of Technology, Dept. of Architecture, İzmir, Türkiye
*Corresponding author: nadjlafellahi14@gmail.com

Keywords: Algeria, Batna, inner city, districts, urban, incomes, social facilities
Discipline: Urban and Regional Planning

INTRODUCTION

The hard climatic conditions of the desert of Algeria, which covers 83% from the total surface leaded to a high population concentration in the North and the inner cities which present 17% of the whole surface of Algeria. This latter was facing a very rapid and massive population growth which forced the authorities concerned to build housing units and creating new neighborhoods in order to solve the high demand of housing problem for the Algerian inhabitants. However, this problem was solved in one side, but in other did not, like main cities saturation, the strong emergence of slums, and the unorganized neighborhoods around the main and big cities as in Batna city which located in the east part side of Algeria, which faced a fast urban progress which changed the urban city textile.

The Algerian government after the independence had so much pressure from the demand of building housing settlements for the Algerian families, especially due to the increasing of birth rate after the nation got its freedom to compensate the human losses (more than one and half million people died in the revolution of 8 years) [1]. The Algerian cities after the independence experienced a rapid and massive population growth, which made the Algerian government, had to build new cities and neighborhoods which unfortunately not all of them were done in a measured manner [2].

THE CITY OF BATNA

Batna city located (Figure 1) in the northeast side of the semi-arid part of Algeria ranked the fifth biggest city in the country. Batna had a fast urban progress, which changed the urban city textile. People who have their properties as lands and houses outside the inner city live in the surrounded districts (Figure 2), in order to protect it. Batna as an inner big city has all the required facilities which are needed for the everyday life. Thus, people who live there have an easy life, administrative, education, health, transport, fun, etc. of building facilities, which are organized in a way to be close and suitable for the inner city [3].

Figure 1. Location of Batna

Figure 2. Batna's inner city and its surrounded districts

Nowadays, Batna city (Figure 3) is facing an important urban problem which is the irregular, unorganized continuous progress of the urban textile from Zone C to B, and its negative effects and results not only on the urban character of Batna but also on the everyday life of the inhabitants [4].
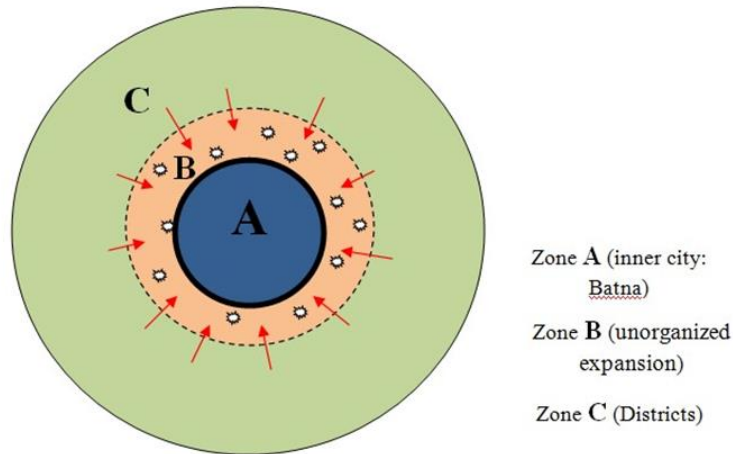

Figure 3. The three urban zones of Batna

Zone A:

The inner city of Batna which characterized by the urban areas or organized neighborhoods, known as the center which provides the conditions that satisfy human needs spiritually and physically; educational institutions, youth clubs, cinema, cafes, etc. Arranged roads, public and green spaces. The ecological consideration in order to protect the natural environment. In addition, taking into account population data; the size of the family, population density per hectare or per square kilometer. The lands are divided according to the housing, social, urban areas, roads, streets, parks, playgrounds, etc., in accordance with the criteria set and established by the government [5].

Zone C:

The Zone C represents the districts which surrounded the inner city of Batna. It characterized by the existence of medium sized populated and small villages, with a population of 1000 to 4000 people [6]. The families' class in Zone C is a mix between rich, medium and poor, but the majority are medium and low income families.

Low income families have communities which do not exceed 100 people. located near to the transport routes in order to sale their lands' products (fruits, vegetables) on the streets to the route passengers, this is the only way for them to get money and to live. The inhabitants in this zone live in very hard conditions due to the total absence of education, health, administrative, transportation, and fun facilities. Mostly, they are not educated neither the parents nor their children. Some of them like this

way of life, they say that it is better to live in nature, far from the noise of the city, and the dirty air. Some, they do not like this way of living but they just surrender and got used of this, but they wish to leave it and live in the city center. Others do not like the quality of life there; their only wish is to have money and settle in the center of Batna [7].

Middle income families in Zone C, the majority of families live in houses which they built themselves on their lands, and they have some other incomes like commercial sources in the city center. Mostly, some of them travel everyday to the center where their shops there for work and come back in the evening [8]. They sale their lands' products in the city center, or the sale it to the tradesmen of the center, this is their way to get money. People of this class spend too much money for transportation to the inner city, whether for work, education of their children, health, or administration issues. Thus, they plan to find a way to get into the inner city or just to be close to it because they know that their income is not enough to buy a house in the heart of the city.

Zone B:

All families who live in Zone B are the ones with middle income, they wish to live in the city center, but their limited income does not allow them to buy a house there, so they collect money and buy a land in Zone B, and build a house to live. They came from Zone C and settle in Zone B, because of the following reasons:

- To be close to the inner city of Batna.
- To have a better safe life, education, and health.
- To pay less for transportation.
- The easy process way to buy a land from private landowners.
- They can buy any size of land according to the money they have.
- No rules from the government which can stop anyone to buy a lands. [9].

There is an important aspect which should be taken into consideration in the Zone B, due to increasing demand and pressure of the middle income people to the government to care and make equality between all the citizens of Batna to live in the city center which is already saturated, and their demand for their right to live an easy life in good conditions [10].

The people of Zone C started to settle in Zone B, they were constructing their new individual houses in an unorganized way which created a big messy urban zone. Then, when the municipality started to build collective housing units, it did the same thing, no urban organization at all. The government was constructing according to the number of demands of the people, this was her only concern [11]. Thus, the main problem in the Zone B is containing only individual and collective housing units, no education, no administrative, and no health facilities were built and took into consideration to be building in the future, only small number of shops which were distributed far from each other, where inhabitants can buy food from it.

CONCLUSION

The case in Batna city is the same, according to what we have seen in this paper; the three zones which compose the whole city have different character, life, and urban organization. Zone A expresses the civilized life of the city, the good conditions which are needed for the everyday life, the accessibility to different services; education, health, administrative, fun, etc., where only high income families have the change to live on this zone (the inner city center). Zone B expresses the middle income families whom could not endure the hard life in Zone C, in the same time, they could not buy a house in the inner city (Zone A), this leaded them to create their own area and build their houses in Zone B which is outside and close to the Zone A and far from Zone C, people on this zone prefer to be close to the city center than to stay and live in the hard life conditions as they were before. Zone C shows the low income families who cannot leave their homes in this zone due to their financial conditions to buy a house or a land, so the only thing they can do is staying in this zone and face the hard life conditions everyday; no transportation, no education, no health services, etc.

Due to the increasing demand of housing units, the government started to build collective housing units in the Zone B to calm down the people, in the same time people keep building freely their individual housing. Thus, made Zone B became an urban mess, which we can call it the slums' zone of

Batna city, which characterized by the only presence of housing units, no education no health, no security and no fun services for the inhabitants, etc.

The slums in the Zone B do not only need individual or collective housing units, the people or the inhabitants have the right to have the same facilities as the inhabitants in the Zone A have. The government or the municipality of Batna should care about how to make Zone B suitable more for living and for affording everyday life needs to the inhabitants there without the need to make them travel everyday to the inner city center for their daily issues. If Zone B has at least the required facilities needed it would be more organized, safer, enjoyable, and suitable for living.

The neglect from the government to care about the rights of the inhabitants of both Zone B and C should be stopped. The inequality which is seen and clear between the income levels of people should be stopped as well. The difference between the urban organization and contents of the three zones should be taken into consideration, because every human being wants to live a good life, an easy life, happy, being safe, educated, and healthy. Thus, authorities should make new studies to achieve that, in order to create the needed daily services for both zones B and C.

REFERENCES

[1] A. Bouanaka, Unplanned neighborhoods and their social and psychological implications, University Publications, Algiers (1987).

[2] A. Boudraa, Urban development and urban underdeveloped cities, Batna University Publications, (1997).

[3] I. Bouzida, Urbanization in Algeria is a reality and a challenge, Jazayris Journal, August (2015).

[4] A. Hafiane, Urban planning standards and urban practice, les mondes urbaines (2013).

[5] B. Masoudane, City of Batna: A study in the geographic geography of the population, PhD Thesis, University of Mentouri, Constantine (2009).

[6] F. Mechnan, The illicit neighborhoods to the city of Batna and carried out in the urban fabric, Journal of Humanities and Social Sciences, 20 (2015) 25-26. University of Hadj Lakhdar, Batna.

[7] T. Said, Informal urban and new centrality of Batna, Algiers, University of Constantine, (1999).

[8] M. Saidouni, The land problem in Algeria, parallel cities, (2003).

[9] F. Sousi, The growth of the city of Batna and the inevitability of the transition towards the parties, Master Thesis, Batna University, (2006).

[10] B. Tidjani, Urbanization in Algeria, University Publications, Algiers, (2000).

[11] A. Weld, A. Sawt, Algerian urbanization: a loss of heritage and an urgent modernity, Ghardaia, (2017).

Water Resource Management Using RS and GIS in Arid and Semi-arid Regions of Somalia

Abdirahman Ahmed Omar*, Urban Regeneration Department, Institute of Natural and Applied Sciences, İzmir Kâtip Çelebi University, İzmir Turkey
Özşen Çorumluoğlu, Geomatics Engineering Department, İzmir Kâtip Çelebi University, İzmir Turkey
*Corresponding author: shaati31@gmail.com

Abstract

This research will mainly focus on Somalia, a country located in the Horn of Africa with two perennial rivers, Juba and Shabelle. These two rivers can provide enough water for irrigation and other uses, but the lack of reliable data and an appropriate spatial management system has resulted in the disuse of these abundant resources. Limited water resources and tough competitions among various water demand create new challenges on the economic development of the country. In order to overcome these challenges, water resource management has to articulate and combine the necessary resources which can preserve the ecological quality of the environment and society. During this research we will use combinations of technologies such as remote sensing data which has a great promise to improve hydrological forecasting, land use, and water resource management, and Geographic Information System (GIS) technology particularly Water Evaluation and Planning (WEAP) Model to consolidate water-related data and to simulate current and future water management to allocate a sustainable rule for surface and groundwater.

Keywords: water resources, remote sensing, local planning, GIS
Discipline: Urban and Regional Planning

INTRODUCTION

Somalia is a slowly developing country; it is also recovering from long termed conflicts and civil strife that hampered the development of every sector in the country. Consequently, water resource management in the country was dramatically weakened.

Water resource management including water distribution, sanitation, and water drilling services was formally organized by the Central Government of the country but due to chaotic political situations, continuous economic crises, unstable security and transitioning from the Central Government to Federal Government which has not carefully planned constitutional infrastructure worsened water resource management.

Local public entities were standing the role of the government [1] but these local public entities were only focusing on water drilling and distributions in urban areas more than water resource management as a holistic approach, while the rural areas are in between floods and droughts.

In some regions of the country, particularly North-West (Somaliland) and Northeast (Puntland) have more deteriorated water resources due to the aridity of the climate, geological, geomorphological and hydrogeological effects [2]. Most parts of these regions water supplies were drawn from the groundwater but this system is insignificant due to the overstretched population in urban areas and increasing water demand from rural populations in long dry seasons, as a result, people of this area suffer from inadequate water supply and have fewer opportunities to meet their water needs.

Over 90% of annual rainfall evaporates in dryland, and this evapotranspiration is essential component in land-atmosphere interaction [3]. Sun radiations as a result of the global warming increase the evapotranspiration which creates great loss of surface water and this will turn the harshness of the environment to even more desolate and inhospitable; furthermore, the swampy and lushness of the alluvial in North-West regions change into more devastating and may be irreversible environmental situation, while the economic development will cripple and social fragmentation inevitable.

Despite the importance of groundwater for human, livestock, and agriculture there are no hydrogeological maps for groundwater management and exploration in these regions. Strangely enough, the state of knowledge about quality and quantity of groundwater resource is limited. Moreover, information on hydrogeology to develop a strategic water resource management and to facilitate drilling groundwater is either scattered or limited or even some cases non-existent, and this results unguided water drilling projects which lead into low success rate [4].

Although the groundwater is one of the most important water sources for surviving and sustainability of the population in these regions, acidity and alkalinity, salinity and dissolved solids – minerals made the quality of the water low and not suitable for drinking with only 40 – 50% of groundwater suitable for drinking, furthermore, the majority of the water source have excessive level of salinity, approximately 70%, when compared to the WHO standards for drinking water (1500µS/cm) [5].

North part of the country has little surface runoff and rainfall which almost all of the rainfalls and runoffs are lost through infiltration and evaporation. Although there are some short streams in the mountainous regions that flow throughout the year in some stretches.

Gulf of Aden Basin and Darror Basin are among the major drainage basin in the Northern regions (Figure 1), in addition to this there are, however, some natural springs in the mountainous regions of the north and shallow and deeper aquifers which are important source of water for people and livestock in these drainage basins. Small scale dams (manmade dams also known warr in Somali language) play essential role for rainfall water catchments and harvesting.

Figure 1. Major Drainage Basins in Northern regions of Somalia

The Gulf of Aden basin covers the area drained by small streams (Waadi) passing through the mountain range extending in an east – west direction. It covers about $74442 km^2$ and lies roughly between $42°42`$ and $51°22`$ east and between $9°28`$ and $12°1`$ and north [2].

This drainage basin includes a variety of morphological features (Figure 2) such as coastal plains and steep slopes. The mountainous range in this drainage basin has numerous water streams (Toggag) that flow towards the Gulf of Aden [6–9]. Most of the water from these streams barely reaches the sea but infiltrates in the coastal plains.

Darror Basin is third drainage basin in the northern part of the country (Figure 1), it covers an area of $34194 km^2$. Due to the harshness and inhospitable of the climate the population in this basin are scattered and moving from place to place by seeking suitable place to sustain the livelihoods.

Poor land cover and the nature of the rocks in the mountainous area in this basin make the livelihood activities more difficulty but there are small farming scales in the Darror Valley. [2]

Main characteristics of this basin are high temperature level throughout a year, daily mean temperature in the coolest month of the year is in between $20 - 23℃$, and high rate of evaporation which always exceeds the expected rainfall throughout a year.
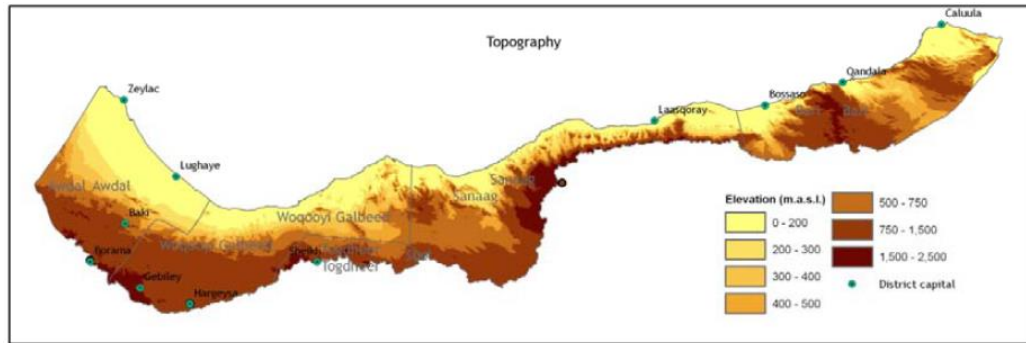

Figure 2. General description maps of Gulf of Aden drainage basin

Closed basins occur whenever the total actual evapotranspiration (ET) has exceeded the gross inflow from rainfall and inter-basin transfers [10]. The average potential evapotranspiration (PET) is about $2700mm$ a year, while yearly rainfall mean is around $100mm$[2] as shown in the climate maps in (Figure 3).
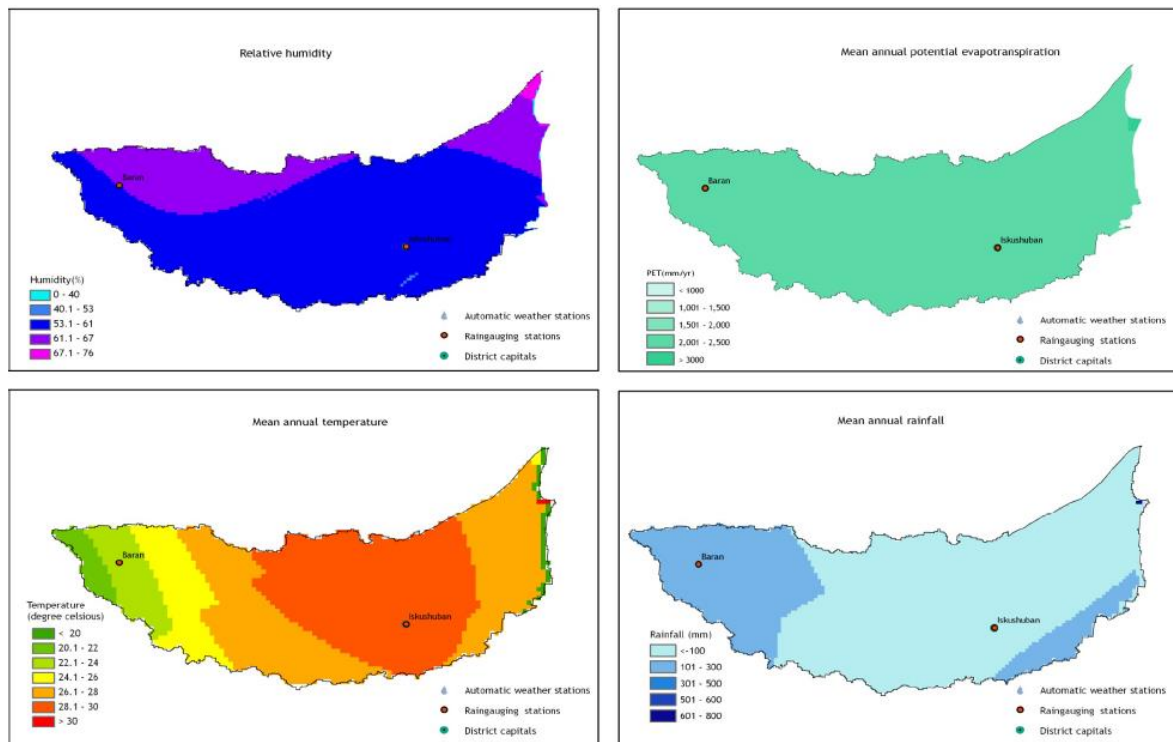

Figure 3. Mean annual weather pattern maps for Darror Basin

Somalia's surface water resources are limited mainly along the two perennial rivers which are located in the Southern regions, thus the population of these regions have higher opportunity of accessing surface water. Furthermore, the deterioration of the river regulation infrastructure and the flood control increase the vulnerability of the riparian community to the floods and progressively smaller peak floods which occurs once every three to four years [9].

The climate of these regions fall under moisture semiarid and small scales of forest to tropical climatic conditions with very little of other surface water resource such as dams [11]. Juba and Shabelle

occupy small percent inside Somalia's territory, while two-third of the river is outside of the country. Juba river plays essential geo-politics role for the east African countries. It demarcates the border of three neighbor countries, Kenya-Ethiopia border, Somalia-Kenya border and Somalia-Ethiopia border [12].

The combination of three main tributaries Wabi Gerstro, Wabi Dawa and Ganale, which are all in Ethiopia territory, form the Juba river (Figure 4). The river covers about $1808km$ of $804km$ in lies in Ethiopia and $1004km$ lies in Somalia based on SRTM $30M$ derived stream from USGS [13].
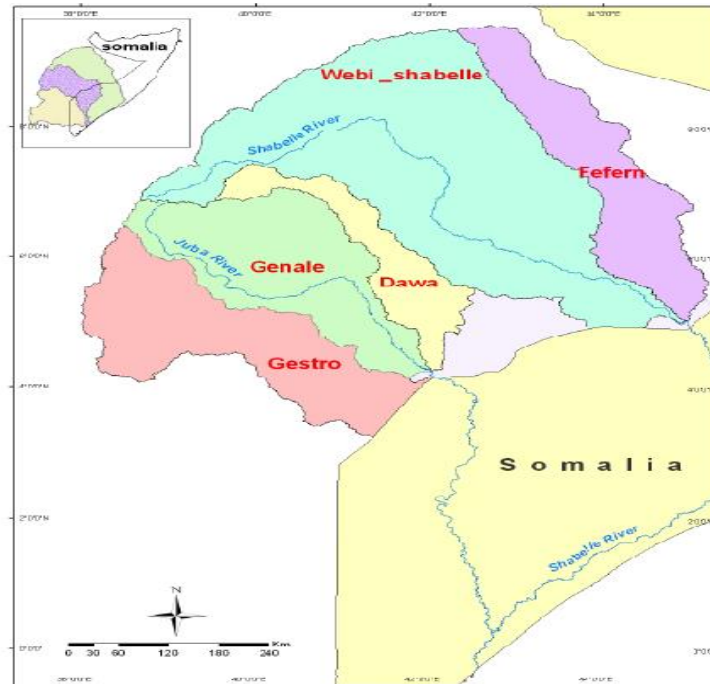

Figure 4. Sub-basins of the Juba and Shabelle Rivers within Ethiopia

Shabelle river covers an area about $108300km^2$ in Somalia and two-third of the river lies in Ethiopia [14]. The Shabelle river is a combination of two main tributaries in Ethiopia Fafan and Wabi Shabelle (Figure 5). It covers longer distance inside Somalia than Juba river, while it enters to the southeast of Somali-Ethiopia border. Shabelle river moves to south of the country parallel to the coastline from which it is separated by a range of sound dunes. The flow of the river discharges into the Juba river only during high rainfall periods.

This research exams the physical development of land and water resource management as holistic approach using a linked GIS and Remote Sensing (RS) technology. Water resources management is a complex system that integrates several spatial features. Thus, to deal with such multi-functional system it is needed to use a powerful technological tool which facilitate and provide some of the most comprehensive techniques for storing, manipulating and analyzing geo-referenced spatial data [15]. The combination of RS and GIS ensure more efficient use of the natural resource with time flexible and scale. These technologies have capability in handling both digital spatial features and the associated databases of attribute information for map features [16]. Groundwater exploration by using traditional means consumes lot of time, energy and money, and requires skilled manpower. In contrast, RS and GIS technology have great advantages of spatial, spectral and temporal availability of data covering and inaccessible area within a short time [17].

Ref. [10] defines water scarcity as the threat to people's livelihoods due to lack of access to safe and affordable water for drinking, and food production. To overcome this threat and maximize food production it is required informed decisions within the water and related sectors. However, using RS and GIS technology will effectively facilitate required information on how much water is available and how much is being consumed for different purpose, and therefore, will lead us to know how availability will change under future scenarios. Ground-based water resources observations using various

instruments such as rain gauges and weather radar give insufficient information. Space-based observations are the solution and used as a promising alternative sources. There are high-resolution satellite-based products which are recently functioning to provide an unprecedented opportunity for hydrologist to monitor the spatial distribution [18].
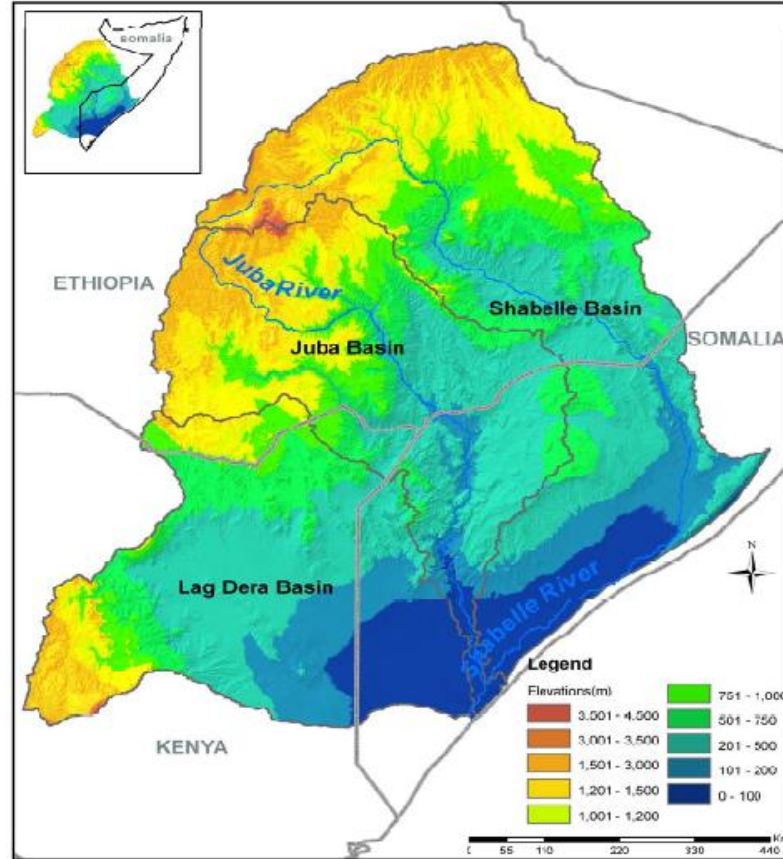

Figure 5. Elevation Variations of the Juba and Shabelle River Basins within Ethiopia and Somalia

MATERIALS AND METHODOLOGY

Through this research, we will use quantitative data which have being collected in different periods of time and in different places. Although there is no enough ground data but remote sensing products have great promise to improve hydrological forecasting, also remote sensing can provide fundamental biophysical information, including temperature, moisture contents as well as coordinate locations. In this sense, remote sensing derived information has great impact to the successful modeling of numerous natural (water supply estimation) and cultural (water demand estimation population estimation) processes which are the focal point of our research in order to model a successful planning of water management which is fulfilling urban water requirement and the water requirements of modern societies.

Remote Sensing technology has been widely used in water resource applications, especially multispectral imagery has been used as the data resource of a long time but it collects data in 3-6 spectral bands in a single observation from the visible and near-infrared region of the electromagnetic spectrum [19]. Therefore, multispectral imagery depends on the reflected and emitted energy from the earth which is referred as the primary limiting factor of multispectral sensors system. Meanwhile hyperspectral systems have great possibility for the collection of several hundred spectral bands in a single acquisition, thus producing many more detailed spectral data. Thus, the development of scientific research resulted to develop airborne hyperspectral imagers such as CASI and HYMAP and satellite – based sensors such as HYPERION which has the mainstream of remote sensing in our research.

However, remote sensing is not a panacea that will provide all the information needed to conduct hydrological information but at least we can improve some models which identify the water use patterns and thus from these patterns we can extract information which enables us to measure the capacity of the

future water use for irrigation and water requirements for modern societies. GIS technology has great possibility to assess the criteria which defines the sustainability of water resources, in this technology we particularly use WEAP (Water Evaluation and Planning) system in which we use to consolidate water related data and to simulate current and future management and allocating sustainable methods for surface and ground water. WEAP is GIS based system and it operates on the basic principles of water balance accounting, it can be either used as a database, as forecasting tool or as a policy analysis tool. Using data from FAO – SWALIM (Somali water and land information management) database to simulate the model and thus this model can account hydrologic processes within a watershed system can capture the propagating and nonlinear effects of water withdrawal for different uses. WEAP21 is latest version incorporates a range of physical hydrological processes in a watershed with the management of demand and installed infrastructure in a seamless and coherent manner.
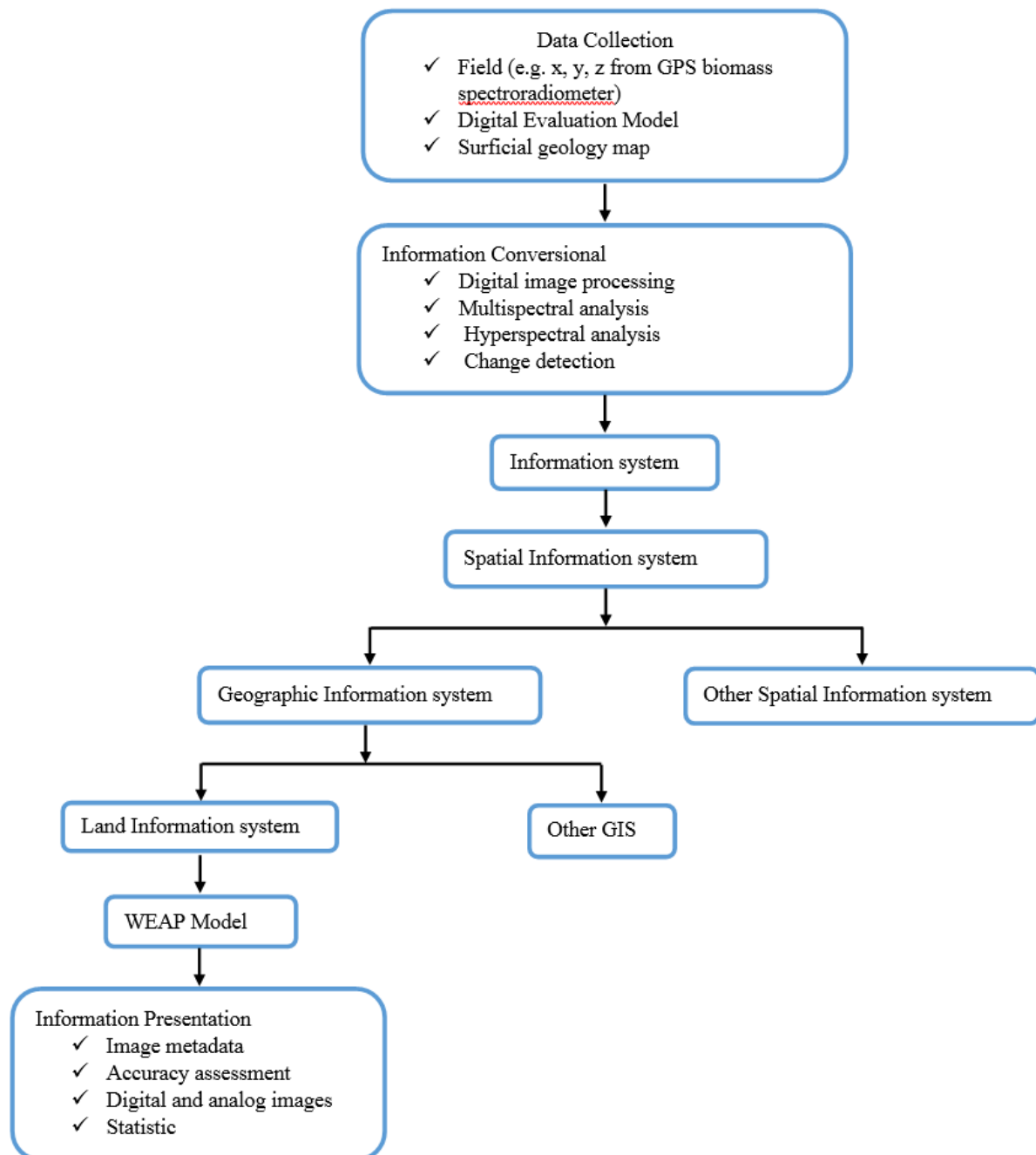
REMOTE SENSING AND GIS STRUCTURE PROCESS

Figure 6. Algorithm process of RS and GIS

STUDY AREA

Somalia is located in between 1°40' south of the Equator to 11° 58'° north and from 40°59' west to 51° 24' east, and it covers an area of $673660\ km2$ which 45% of the land area is classified as a rangelands suitable for livestock, and grazing. After continuously problems of degradations and deforestation 30% of the land area is desert, while 14% is covered by forest and 11% is arid and semiarid [20]. Somalia has border with Djibouti to north west, Gulf of Aden to the north, Indian Ocean to the east and Kenya and Ethiopia to the south and west respectively.

RESULTS AND DISCUSSION

Annual runoff of Shabelle river is estimated by $2500 Mm^3$ with higher proportion of runoff coming from Ethiopia. According to [6] more than 90% of the total volume runoff is generated from Ethiopian parts while less than 10% of the river flow contributes to Somalia because of low rainfall in the Somalia [9]. Result of 15 years of the river flow records are indicating that there is inter-annual variability in annual discharge with peak flow registered in 2006, 2013, 2016 and mid of 2018 while the smallest flow record on 2004, 2011 and early of 2018. In general, about 50% of observation period shows runoff discharge below the average [6]. Figure 7 shows the discharge scenario between 2003–2014.
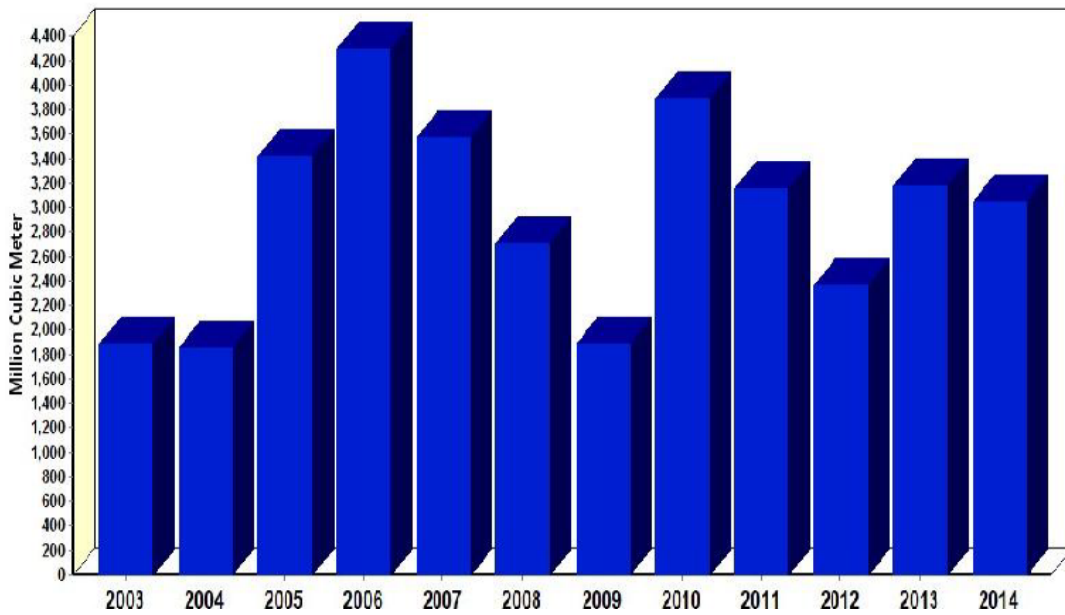

Figure 7. Annual flows of Shabelle river

Table 1. Total monthly water demand (Mm^3) in along river Shabelle

Months	Agriculture	Domestic	Livestock	Environmental	Total
Jan	135.6	2.2	3.7	7.07	148.57
Feb	152.1	2.0	3.4	5.95	163.45
Mar	0.0	2.2	3.7	8.83	14.73
Apr	5.7	2.2	3.6	27.63	39.13
May	16.1	2.2	3.7	52.03	74.03
Jun	8.0	2.2	3.6	35.41	49.21
July	20.6	2.2	3.7	16.54	43.04
Aug	64.9	2.2	3.7	21.32	92.12
Sep	88.9	2.2	3.6	33.49	128.19
Oct	68.9	2.2	3.7	36.86	111.66
Nov	53.2	2.2	3.6	37.7	96.7
Dec	57.6	2.2	3.7	21.31	84.81

As indicated in Table 1, Somalia has utilized very little of the Shabelle river because of its inaccessibility, and major irrigation schemes collapsed.

In this study, we have developed five different scenarios using WEAP Model which considers the availability of irrigable land and infrastructure extension and population growth.

FIRST SCENARIO. Current Water Demand

It is estimated that the current water demand for irrigation for Shabelle and Juba is about $1829 m^3/ha$ and $11428 m^3/ha$ respectively while the irrigated land alongside Shabelle and Juba river basin is $50000 ha$ and $15000 ha$ respectively (Figure 8).
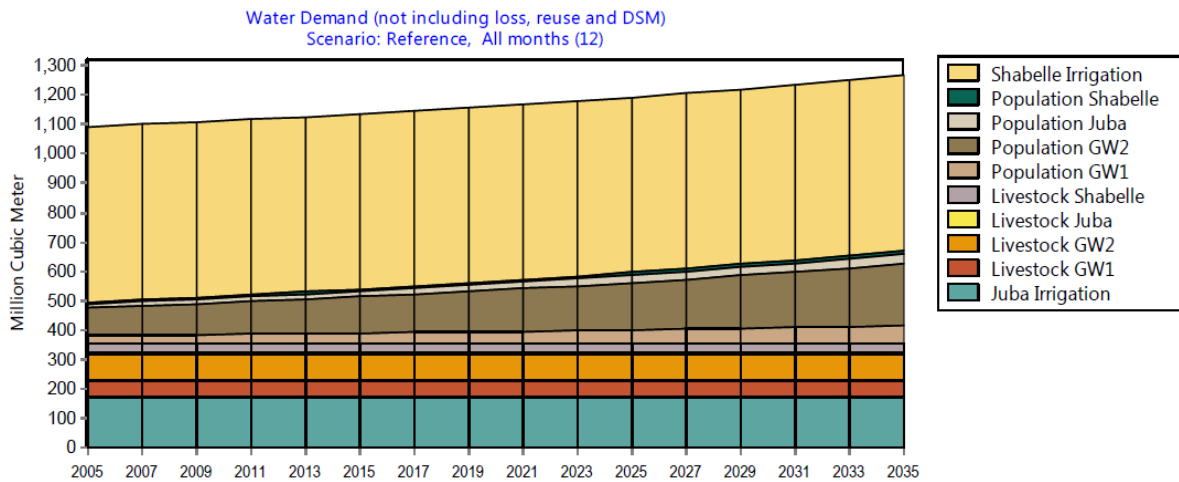

Figure 8. Water Demand

SECOND SCENARIO. Existent Schemes Demand

Current irrigation infrastructure alongside the rivers can cover $135000 ha$ in the Shabelle river basin and $25000 ha$ in the Juba river basin.

If the irrigation infrastructure along the river basins is maintained, irrigation water demands in 2035 are $337.6 MCM$ and $2195.3 MCM$ along the Juba and Shabelle river basins, respectively, as in Figure 9.
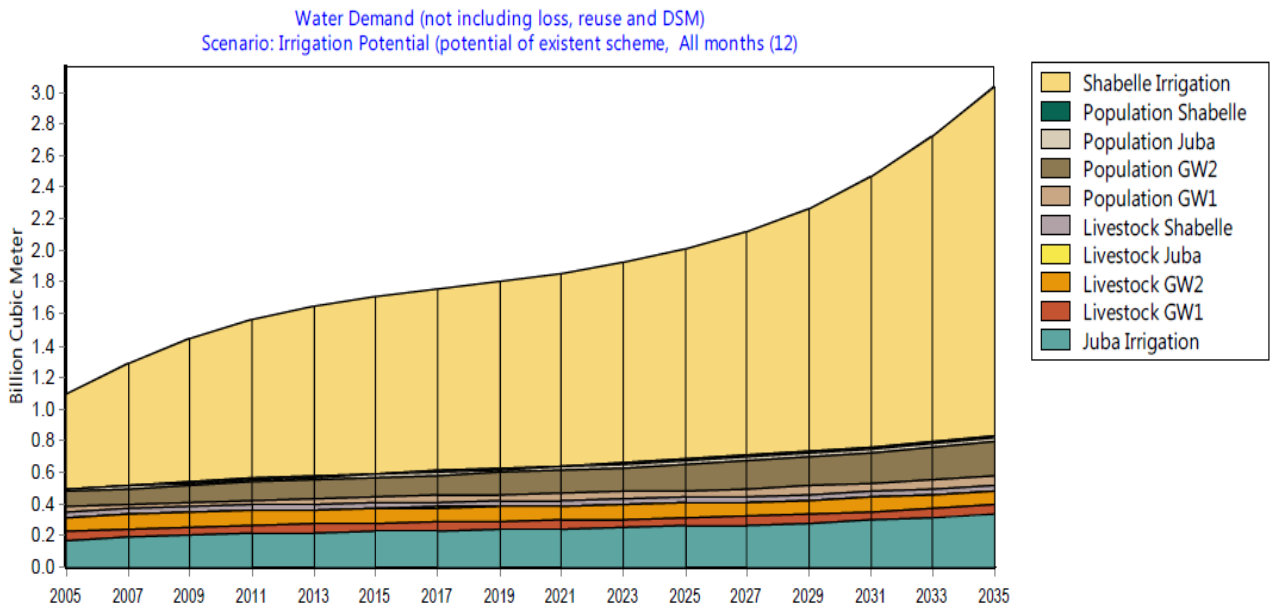

Figure 9. Existent Schemes Demand

270

THIRD SCENARIO. Water Demand during Minimum Flow

In the dry season Juba river flows higher than Shabelle river flow. It is possible to irrigate up to $17000ha$ and $50000ha$ along Shabelle and Juba river basins respectively, meanwhile the irrigation water demand for 2035 goes up to $764.7MCM$ and $53.8MCM$ along Juba and Shabelle rivers (Figure 10).

Figure 10. Water Demand During minimum river flow
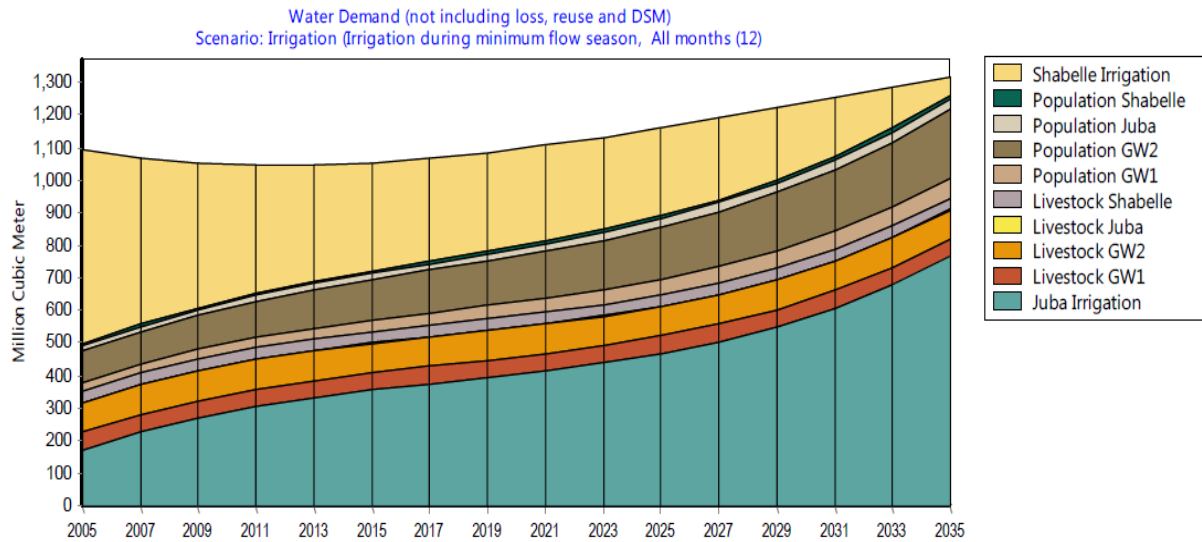
FOURTH SCENARIO. Water Demand during Maximum Flow

During maximum river flow, only Juba river can irrigate $170000ha$ while $80000ha$ is irrigated alongside Shabelle river. In the same scenario if the irrigation infrastructural extensions schemes are made, the annual irrigation water demand during 2035 will be $2077.6MCM$ along Juba river and $1073.3MCM$ along Shabelle river basin (Figure 11).

Figure 11. Demand during maximum river basins flow
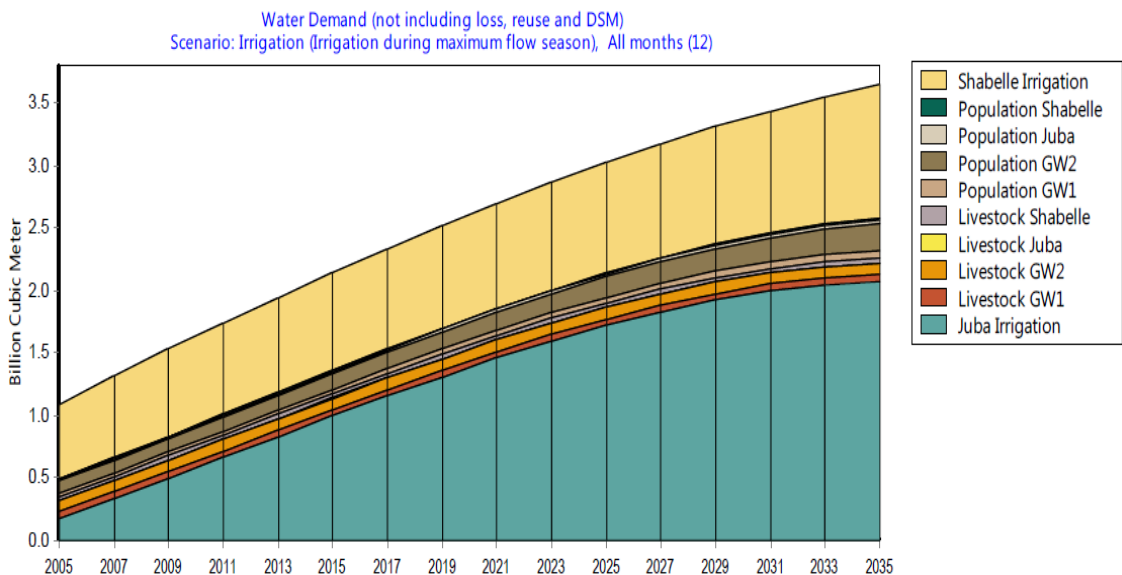
FIFTH SCENARIO. High Population Growth Demand

Water demand alongside the river basins is proportional to the rate of population growth in the basin. Water demand in the riparian area will reach $32.5MCM$ for Shabelle river and $13.3MCM$ for the Juba river basin in 2035 (Figure 12).

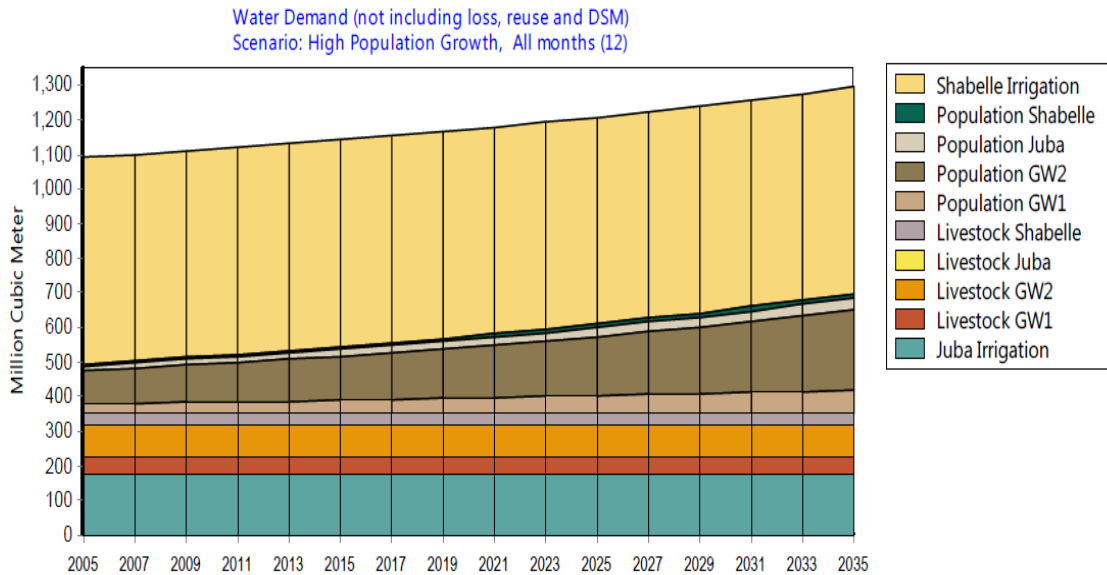Figure 12. Population growth and water demand in riparian areas.

CONCLUSION AND RECOMMENDATION

During our research, our main objective was to undertake the availability of water resource in the country as holistic approach and to compare to the water demand and analyze the outcome for enhancing water resource planning in the country particularly riparian areas using some technologies such as RS and GIS/WEAP Model.

Based on the findings of our study the following conclusion were drawn. The water sources inventory was done only on the strategic water points, as the resources available could not allow complete coverage of all water sources. There are many seasonal water sources, mainly small-scale dams and some shallow wells across the country. However, these sources do not last long into the dry season, hence the reason why they were not prioritized in trying to make the best use of the available resources for the survey.

The changes in water demand for the domestic, livestock, and irrigation will have significant impacts on the basin. The model simulations indicate that approximately 90% of irrigation demand has been met and the extending irrigated area will be broadly match the potential until the current scenarios of the 2015-2040.

Several recommendations can be derived from the results.

- Further development of the assessment model for the water resource management is recommended in order to investigate the hydrological response and its consequences for the sake of the future water demand.
- Consideration of integrated approach for water resource management between neighbor countries is recommended.
- Major adaptation of cropping patterns and their water demand is recommended to address irrigation systems

REFERENCES

[1] G. Petersen, H.M. Gadain, Water demand assessment for the Juba and Shabelle rivers, Technical Report No W-22, (2012) FAO-SWALIM, Nairobi, Kenya, 9-57.

[2] P. W. Muchiri, Inventory of northern Somalia drainage basins, Technical Report NoW-18, (2009) FAO-SWALIM, Nairobi, Kenya, 1-50.

[3] H. Alemu, G. B. Senay, A. T. Kaptue, V. Kovalskyy, Evapotranspiration variability and its association with vegetation dynamics in the Nile basin, 2002–2011, Remote Sens. 6 (2014) 5885-5908.

[4] G. Artan, H.M. Gadain, F.M. Muthusi, P.W. Muchiri, Improving flood forecasting and early warning in Somalia, feasibility study, Technical Report No W-10, (2007) FAO-SWALIM, Nairobi, Kenya, 4-19.

[5] Z. Balint, H. Gadain, F. Muthusi, M. Shaie, J. Ngochoch, A. Ismail, O. Abdulle, Hydrogeological survey and assessment of selected areas in Somaliland and Puntland, Technical Report No. W-20, (2012) FAO-SWALIM, Nairobi, Kenya, 1-74.

[6] D. B. Basnyat, Water resources of Somalia. Technical Report No W-11, (2007), FAO-SWALIM, Nairobi, Kenya, 2-102.

[7] G. Mahamud, A. Abdalle, H. Gadain,Urban water supply assessment – monitoring the progress of the Somali urban water supply towards the millennium development goals, Project Publication No W-07, (2006), FAO-SWALIM, Nairobi, Kenya, 7-52.

[8] F.M. Muthusi, G. Mahamud, A. Abdalle, H. M. Gadain,Rural water supply assessment, Technical Report No-08, (2007), FAO-SWALIM, Nairobi, Kenya, 3-30.

[9] H. M. Gadain, A. M., Jama, Flood risk and response management, Technical Report No W-15, (2009), FAO-SWALIM,Nairobi, Kenya, 13-57.

[10] W. G.M. Bastiaanssen, P. Karimi, L. Rebelo, Z. Duan, G. Senay, L. Muthuwatte, V. Smakhtin, Earth observation based assessment of the water production and water consumption of Nile basin agro-ecosystems, Remote Sens. 6/11, (2014) 10306-10334.

[11] G. Petersen, H. M Gadain, Climate change impacts on water resources of Somaliland and Puntland. Technical Report No W-21, (2012), FAO-SWALIM, Nairobi, Kenya, 8-58.

[12] A. E. Mohamed, Sharing water in Africa: comparative analysis of the limpopo and orange-senqu river basins in SADC and the Juba and Shabelle river basins in the horn of Africa, PhD Thesis, TRITA LWR PHD (2014) 1-57.

[13] A. M. Hassan, Surface water availability and demand analysis: implication for enhancing water resource planning at Shabelle basin in southern Somalia, institute of water and environment, Master thesis, (2015) 1-19.

[14] A. E. Mohamed,Managing shared basins in the horn of Africa-Ethiopian projects on the Juba and Shabelle rivers and downstream effects in Somalia, natural resources and conservation1 (2013), 35-49.

[15] A. Ryan, GIS and water resource management in water-scarce regions, Indian society of Remote Sensing 19 (2005) 563-575.

[16] A. Akbari, R. B. Varadharajan,Application of GIS and RS in rural water supply systems, The 28th Asian Conference on Remote Sensing, 12-16 November 2007, 1-5.

[17] M. I. Malik, M. S. Bhat, SH. A. Najar, Remote sensing and GIS based groundwater potential mapping for sustainable water resource management of Lidder catchment in Kashmir Valley, India, Journal Geological Society of India 87 (2016) 716-726.

[18] W. Muhammad, H. Yang, H. Lei, A. Muhammad, D. Yang, Improving the regional applicability of satellite precipitation products by ensemble algorithm Remote Sens. 10(4) (2018) 1-19.

[19] M. Rasmy, T. Koike, Xin Li, Applicability of multi-frequency passive microwave observations and data assimilation methods for improving numerical weather forecasting in Niger, Africa, Remote Sens. 6 (2014) 5306-5324.

[20] M. Y. Sebhat, Assessments of water demands for the Juba and Shabelle rivers in Somalia, Journal of agriculture and environment for international development (JAEID) 109 (2015) 165 – 177.

Congress Photo Gallery

2nd International Students Science Congress
4-5 May 2018, Izmir - Turkey

İZMİR
KÂTİP ÇELEBİ
UNIVERSITY

İZMİR
Uluslararası
Misafir
Öğrenci
Derneği
◆ İZMİR International Guest Student Association